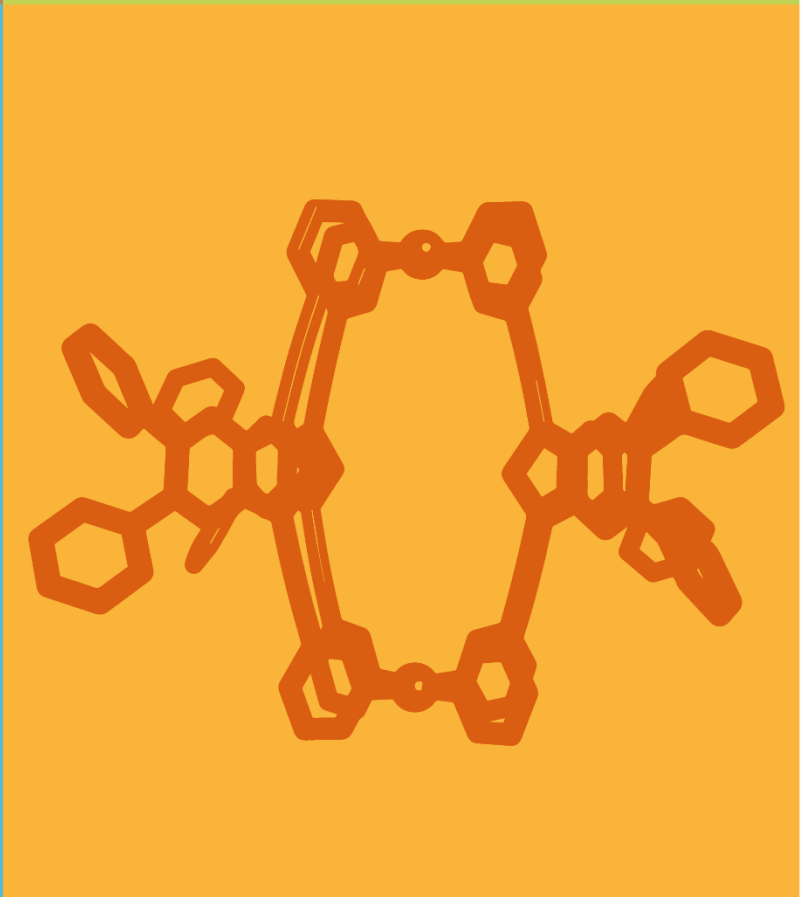
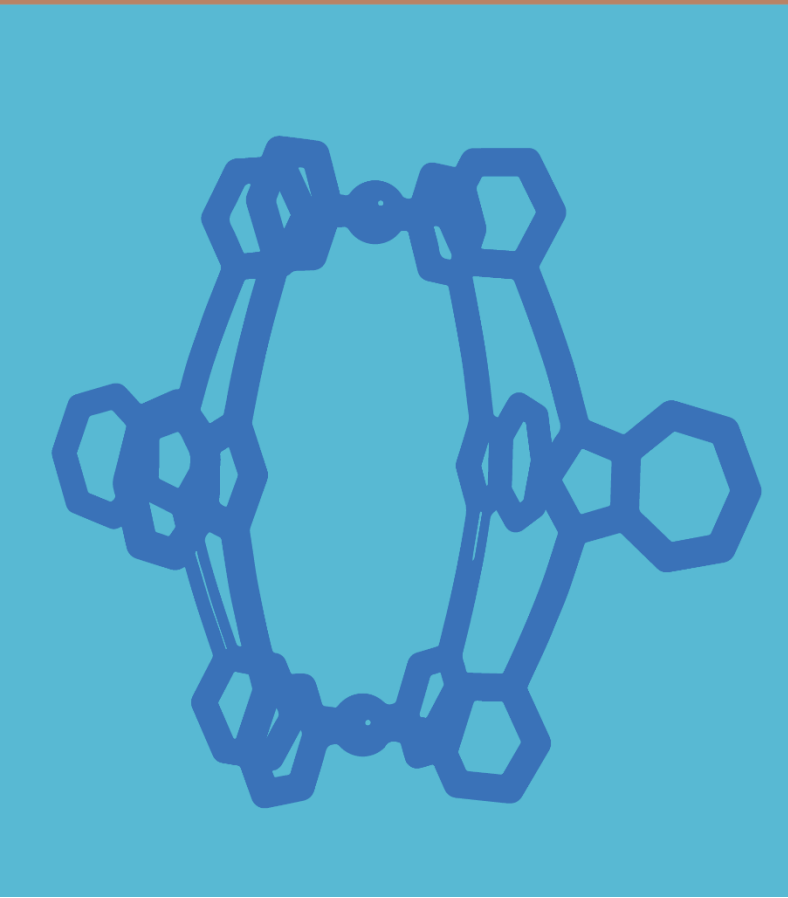
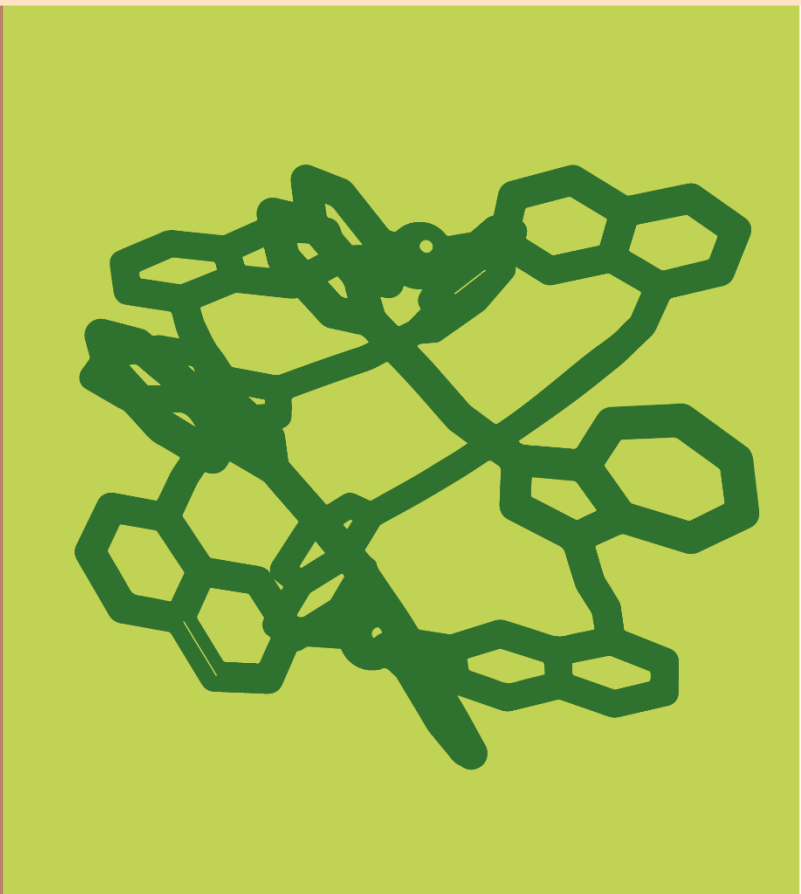
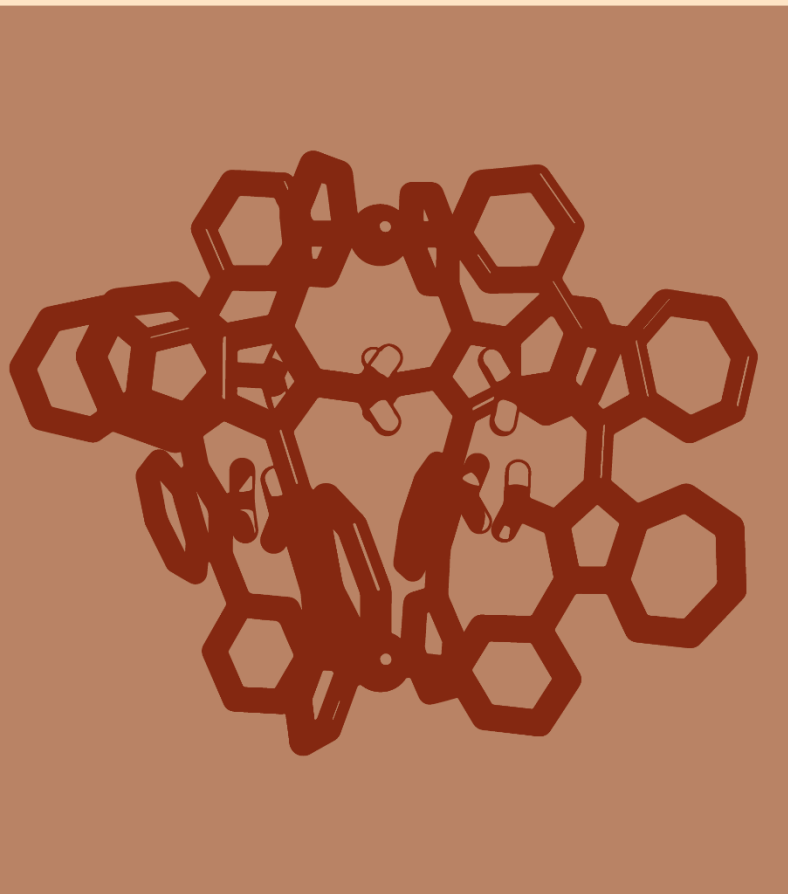


Alexandre Walther

CHROMOPHORIC COORDINATION CAGES

PHD THESIS



CHROMOPHORIC COORDINATION CAGES

This dissertation is submitted for the degree of
“Doctor rerum naturalium”
TU Dortmund
Department of Chemistry and Chemical Biology

Alexandre Walther



tu technische universität
dortmund

This work has been conducted from October 2020 to June 2024 at the Department of Chemistry and Chemical Biology at TU Dortmund.

Principal Advisor: Prof. Dr. Guido H. Clever
Department of Chemistry and Chemical Biology
TU Dortmund

Co-examiner: Prof. Dr. Arne Lützen
Kekulé-Institut für Organische Chemie und Biochemie
Universität Bonn

Submission date: 13/09/2024

« C'est une bonne situation, ça, scribe ?

« Mais, vous savez, moi je ne crois pas qu'il y ait de bonne ou de mauvaise situation. Moi, si je devais résumer ma vie aujourd'hui avec vous, je dirais que c'est d'abord des rencontres, des gens qui m'ont tendu la main, peut-être à un moment où je ne pouvais pas, où j'étais seul chez moi. Et

c'est assez curieux de se dire que les hasards, les rencontres forment une destinée... Parce que quand on a le goût de la chose, quand on a le goût de la chose bien faite, le beau geste, parfois on ne trouve pas l'interlocuteur en face, je dirais, le miroir qui vous aide à avancer. Alors ce n'est pas mon cas, comme je le disais là, puisque moi au contraire, j'ai pu ; et je dis merci à la vie, je lui dis merci, je chante la vie, je danse la vie... Je ne suis qu'amour !

Et finalement, quand beaucoup de gens aujourd'hui me disent : « Mais comment fais-tu pour avoir cette humanité ? » Eh bien je leur réponds très simplement, je leur dis que c'est ce goût de l'amour, ce goût donc qui m'a poussé aujourd'hui à entreprendre une construction mécanique, mais demain, qui sait, peut-être simplement à me mettre au service de la communauté, à faire le don, le don de soi... »

Astérix & Obélix : Mission Cléopâtre (2002)

Eidesstattliche Versicherung (Affidavit)

Name, Vorname
(Surname, first name)

Matrikel-Nr.
(Enrolment number)

Belehrung:

Wer vorsätzlich gegen eine die Täuschung über Prüfungsleistungen betreffende Regelung einer Hochschulprüfungsordnung verstößt, handelt ordnungswidrig. Die Ordnungswidrigkeit kann mit einer Geldbuße von bis zu 50.000,00 € geahndet werden. Zuständige Verwaltungsbehörde für die Verfolgung und Ahndung von Ordnungswidrigkeiten ist der Kanzler/die Kanzlerin der Technischen Universität Dortmund. Im Falle eines mehrfachen oder sonstigen schwerwiegenden Täuschungsversuchs kann der Prüfling zudem exmatrikuliert werden, § 63 Abs. 5 Hochschulgesetz NRW.

Die Abgabe einer falschen Versicherung an Eides statt ist strafbar.

Wer vorsätzlich eine falsche Versicherung an Eides statt abgibt, kann mit einer Freiheitsstrafe bis zu drei Jahren oder mit Geldstrafe bestraft werden, § 156 StGB. Die fahrlässige Abgabe einer falschen Versicherung an Eides statt kann mit einer Freiheitsstrafe bis zu einem Jahr oder Geldstrafe bestraft werden, § 161 StGB.

Die oben stehende Belehrung habe ich zur Kenntnis genommen:

Official notification:

Any person who intentionally breaches any regulation of university examination regulations relating to deception in examination performance is acting improperly. This offence can be punished with a fine of up to EUR 50,000.00. The competent administrative authority for the pursuit and prosecution of offences of this type is the chancellor of the TU Dortmund University. In the case of multiple or other serious attempts at deception, the candidate can also be unenrolled, Section 63, paragraph 5 of the Universities Act of North Rhine-Westphalia.

The submission of a false affidavit is punishable.

Any person who intentionally submits a false affidavit can be punished with a prison sentence of up to three years or a fine, Section 156 of the Criminal Code. The negligent submission of a false affidavit can be punished with a prison sentence of up to one year or a fine, Section 161 of the Criminal Code.

I have taken note of the above official notification.

Ort, Datum
(Place, date)

Unterschrift
(Signature)

Titel der Dissertation:
(Title of the thesis):

Ich versichere hiermit an Eides statt, dass ich die vorliegende Dissertation mit dem Titel selbstständig und ohne unzulässige fremde Hilfe angefertigt habe. Ich habe keine anderen als die angegebenen Quellen und Hilfsmittel benutzt sowie wörtliche und sinngemäße Zitate kenntlich gemacht.

Die Arbeit hat in gegenwärtiger oder in einer anderen Fassung weder der TU Dortmund noch einer anderen Hochschule im Zusammenhang mit einer staatlichen oder akademischen Prüfung vorgelegen.

I hereby swear that I have completed the present dissertation independently and without inadmissible external support. I have not used any sources or tools other than those indicated and have identified literal and analogous quotations.

The thesis in its current version or another version has not been presented to the TU Dortmund University or another university in connection with a state or academic examination.*

***Please be aware that solely the German version of the affidavit ("Eidesstattliche Versicherung") for the PhD thesis is the official and legally binding version.**

Ort, Datum
(Place, date)

Unterschrift
(Signature)

ABSTRACT

One of the principal reasons for the extensive study of coordination cages in the last few decades is the promise they hold for their use as artificial analogues to biological systems, and more specifically artificial enzymes. Indeed, like this class of catalytically active proteins, coordination cages and capsules possess a central cavity able to bind guest molecules. In turn, it has been shown by the supramolecular community that catalytic processes can happen in coordination cages, by the specific arrangement of guest molecules in the cavity. However, unlike enzymes, coordination cages have been seen as rather conformationally or topologically static, in contrast to the vast changes ternary and quaternary structure that may take place upon the binding of a substrate to an enzyme. Moreover, the cavity of non-chiral homoleptic coordination cages do not allow for the asymmetric catalysis enabled by the chirotopic and low-symmetry catalytic pocket of enzymes. Therefore, to better mimic biological systems with coordination cages, the study of low-symmetry systems that are responsive to external stimuli is of interest.

In the first project of this thesis, I present an azulene-based Pd₂L₄ lantern-shaped cage that transforms into a Pd₄L₈ tetrahedral complex upon addition of benzene disulfonate guests. This geometrical change is clean, efficient, and rapid. The final structure was determined by single crystal X-ray crystallography. The use of azulene, a simple, but coloured two-ring aromatic hydrocarbon allows for an easy monitoring of the progress of the transformation by eye only. Using a second coordination cage based on methylene blue, the transformation was shown to be reversible, thanks to the transfer of the guest from the tetrahedron to the newly added cage, which has a higher affinity for the disulfonates. This experiment demonstrates several key principles of advanced coordination cage chemistry, such as multi-component non-statistical systems of narcissistically self-sorting cages, or guest transfer. Several other azulene-based ligands were synthesised as well, but none of their corresponding homoleptic assemblies could undergo the same cage-to-cage transformation, highlighting the sensitivity of the first system to shape and size.

A second azulene-based family of ligands was prepared next, but this time with a chiral amino-biazulene backbone, isomeric to the widely adopted BINOL moiety. Two ligands were thus synthesised, the first of them bearing two pyridine donor groups. Using the racemate of the first ligand for the formation of the Pd(II)-cage ultimately resulted in the formation of a single *meso-trans* isomer of the Pd₂L₄ cage in acetonitrile and DMSO, instead of a statistical mixture. X-ray structure analysis of the cage unexpectedly revealed that discrete solvent molecules were responsible for the non-statistical arrangement, by acting as tethers between the amino groups of the ligands, through hydrogen bonding. This is the first time that single solvent molecules were shown to directly influence the outcome of the chiral self-sorting of a coordination cage. This observation was supplemented with experimental and computational models. A larger ligand with 7-isoquinoline groups was also synthesised. Due to the larger donor groups, the amino groups are pulled further away from each-other in the final coordination assembly. This greater distance means that the solvent molecules were not able to bridge the ligands anymore, and therefore a statistical mixture was observed in this case.

Finally, thiophene- and thieno[3,4b]pyrazine-based ligands were used to potentially recreate the cage-to-tetrahedron transformation described in the first part. The transformation was successful due to the similar geometry imparted by the five-membered rings. In addition, the thieno[3,4b]pyrazine-based ligands were observed to be highly luminescent, and the resulting Pd₂L₄ cages were as well. This is an interesting result, as the fluorescence of palladium(II) assemblies are generally quenched, and therefore their use as fluorescent probes can be limited. Moreover, the emission colour of those ligands could be modulated by electron withdrawing or donating substituents.

ZUSAMMENFASSUNG

Einer der Hauptgründe für die umfangreiche Erforschung von Koordinationskäfigen in den letzten Jahrzehnten ist das Versprechen, dass sie als künstliche Analoga zu biologischen Systemen und insbesondere als künstlichen Enzymen verwendet werden können. Wie diese Klasse katalytisch aktiver Proteine verfügen Koordinationskäfige und -kapseln über einen zentralen Hohlraum, der Gastmoleküle binden kann. Die supramolekulare Gemeinschaft hat wiederum gezeigt, dass in Koordinationskäfigen durch die spezifische Anordnung von Gastmolekülen im Hohlraum katalytische Prozesse ablaufen können. Im Gegensatz zu Enzymen wurden Koordinationskäfige jedoch als eher strukturell oder topologisch statisch angesehen, im Gegensatz zu den enormen Veränderungen der ternären und quaternären Struktur, die bei der Bindung eines Substrats an ein Enzym stattfinden können. Darüber hinaus ermöglicht der Hohlraum von nicht-chiralen homoleptischen Koordinationskäfigen nicht die asymmetrische Katalyse, die durch die chirotopische und wenig symmetrische katalytische Tasche von Enzymen ermöglicht wird. Um biologische Systeme mit Koordinationskäfigen besser nachahmen zu können, ist daher die Untersuchung von Systemen mit geringer Symmetrie, die auf externe Stimuli reagieren, von Interesse.

Im ersten Projekt dieser Arbeit stelle ich einen laternenförmigen Pd₂L₄-Käfig auf Azulenbasis vor, der sich bei Zugabe von Benzoldisulfonat-Gästen in einen tetraedrischen Pd₄L₈-Komplex verwandelt. Diese geometrische Veränderung ist sauber, effizient und schnell. Die endgültige Struktur wurde durch Einkristall-Röntgenkristallographie bestimmt. Die Verwendung von Azulen, einem einfachen, aber farbigen aromatischen Kohlenwasserstoff mit zwei Ringen, ermöglicht eine einfache Überwachung des Fortschritts der Umwandlung allein mit dem Auge. Bei Verwendung eines zweiten Koordinationskäfigs auf der Basis von Methylenblau konnte gezeigt werden, dass die Umwandlung reversibel ist, da der Gast vom Tetraeder auf den neu hinzugefügten Käfig übertragen wird, der eine höhere Affinität für die Disulfonate hat. Dieses Experiment demonstriert mehrere Schlüsselprinzipien der fortgeschrittenen Chemie von Koordinationskäfigen, wie z. B. nichtstatische Mehrkomponentensysteme von narzisstisch selbstsortierenden Käfigen oder Gasttransfer. Es wurden auch mehrere andere Liganden auf Azulenbasis synthetisiert, aber keine der entsprechenden homoleptischen Assemblierungen konnte die gleiche Käfig-zu-Käfig-Transformation durchlaufen, was die Empfindlichkeit des ersten Systems gegenüber Form und Größe unterstreicht.

Als Nächstes wurde eine zweite Familie von Liganden auf Azulenbasis hergestellt, diesmal jedoch mit einem chiralen Amino-Biazulen-Grundgerüst, das isomer zum weit verbreiteten BINOL-Motiv ist. Auf diese Weise wurden zwei Liganden synthetisiert, von denen der erste zwei Pyridin-Donorgruppen trägt. Die Verwendung des Racemats des ersten Liganden für die Bildung des Pd(II)-Käfigs führte schließlich zur Bildung eines einzigen meso-trans-Isomers des Pd₂L₄-Käfigs in Acetonitril und DMSO anstelle einer statistischen Mischung. Die Röntgenstrukturanalyse des Käfigs ergab überraschenderweise, dass einzelne Lösungsmittelmoleküle für die nicht statistische Anordnung verantwortlich waren, indem sie über Wasserstoffbrückenbindungen als Bindeglied zwischen den Aminogruppen der Liganden fungierten. Dies ist das erste Mal, dass einzelne Lösungsmittelmoleküle nachweislich einen direkten Einfluss auf das Ergebnis der chiralen Selbstsortierung eines Koordinationskäfigs haben. Diese Beobachtung wurde durch experimentelle und rechnerische Modelle ergänzt. Ein größerer Ligand mit 7-Isochinolingruppen wurde ebenfalls synthetisiert. Aufgrund der größeren Donorgruppen werden die Aminogruppen in der endgültigen Koordinationsanordnung weiter voneinander weggezogen. Dieser größere Abstand bedeutet, dass die Lösungsmittelmoleküle nicht mehr in der Lage waren, die Liganden zu überbrücken, so dass in diesem Fall eine statistische Mischung beobachtet wurde.

Schließlich wurden Liganden auf Thiophen- und Thieno[3,4b]pyrazin-Basis verwendet, um die im ersten Teil beschriebene Umwandlung von Käfigen in Tetraeder nachzustellen. Die Umwandlung war aufgrund der ähnlichen Geometrie der fünfgliedrigen Ringe erfolgreich. Darüber hinaus wurde beobachtet, dass die Thieno[3,4b]pyrazin-basierten Liganden und die daraus resultierenden Pd₂L₄-Käfige stark lumineszieren. Dies ist ein interessantes Ergebnis, da die Fluoreszenz von Palladium(II)-Verbindungen oft gequenchet sind und daher nur begrenzt als Fluoreszenzsonden verwendet werden konnte. Außerdem könnte die Emissionsfarbe dieser Liganden durch elektronenziehende oder -abgebende Substituenten moduliert werden.

Awards

2019	Best Master thesis poster of the 2019 promotion of the Chemistry section of the EPFL
2024	Poster award at SupraChem 2024 in Ulm
2024	Oral communication award at the Girona Seminar, 2 nd place

Conferences and contributions

<i>Poster presentations</i>	December 2021	MASC2021, online
	May-June 2022	1st International Supramolecular Chemistry Summer School, Cagliari, Italy
	July 2022	SupraChem 2022, Mainz, Germany
	September 2022	International Symposium on Confinement-controlled Chemistry 2022
	June 2023	International Symposium on Macrocyclic and Supramolecular Chemistry, Reykjavik, Iceland
	February May 2024	SupraChem 2024, Ulm, Germany SupraParis
<i>Oral presentations</i>	September 2023	796 th Heraeus-Seminar, Bad Honnef, Germany
	December 2023	PhD seminar, TU Dortmund
	February 2024	Tag der Chemie, TU Dortmund
	June 2024	Girona Seminar, Spain

Publications

- **A. Walther**, I. Regeni, J. J. Holstein, G. H. Clever, “*Guest-Induced Reversible Transformation between an Azulene-Based Pd₂L₄ Lantern-Shaped Cage and a Pd₄L₈ Tetrahedron*” *J. Am. Chem. Soc.* **2023**, 145, 46, 25365–25371.
- E. Benchimol, K. E. Ebbert, **A. Walther**, J. J. Holstein, G. H. Clever, “*Ligand Conformation Controls Assembly of a Helicate/Mesocate, Heteroleptic [Pd₂L₂L’₂] Cages and a Six-Jagged [Pd₆L₁₂] Ring*” *Chem. Eur. J.* **2024**, e202401850.
- W. Xue, E. Benchimol, **A. Walther**, *et al.* “*Interplay of stereochemistry and charge governs guest binding in flexible Zn^{II}₄L₄ cages*”, submitted.
- **A. Walther**, G. Tusha, J. J. Holstein, L. Schäffer, G. H. Clever, “*Solvent-directed social chiral self-sorting in Pd₂L₄ coordination cages via hydrogen bonding*”, submitted.
- E. Benchimol*, L. Neukirch*, **A. Walther***, G. H. Clever, “*Chromophore-based coordination cages*” (review), in preparation (*: equal contribution).

CONTENT

Abstract	i
1 General Introduction	1
1.1 Coordination cages	1
1.2 Self-correction and guest-triggered transformations.....	4
1.3 (Chiral) Self-sorting.....	13
1.4 Chromophoric coordination cages.....	18
1.5 References.....	26
2 Scope of the thesis.....	31
3 Guest-induced transformation of an azulene-based Pd₂L₄ cage to a Pd₄L₈ tetrahedron	33
3.1 Azulene	33
3.2 Azulene-based coordination assemblies	35
3.3 Guest encapsulation experiments.....	45
3.4 Guest-induced transformation of Pd ₂ AZU1 ₄	47
3.5 Guest experiments with AZU2 to AZU5 coordination species	54
3.6 Conclusion	63
3.7 Experimental part.....	65
3.8 References	124
4 Solvent-directed chiral self-sorting of an azulene-based coordination cage ...	127
4.1 Chirality in coordination cages.....	127
4.2 Synthesis of [1,1'-biazulene]-2,2'-diamine ("BAAZU")-based ligands	129
4.3 BAAZU-based coordination assemblies.....	130
4.4 Assignment of the absolute configuration	142
4.5 Guest encapsulation	146
4.6 Racemisation behaviour	150
4.7 Perspective	152
4.8 Conclusion	152
4.9 Experimental part.....	154
4.10 References	210
5 Thieno[3,4-b]pyrazine-based Pd₂L₄ luminescent assemblies.....	213
5.1 Reproducing the cage-to-tetrahedron transformation.....	213
5.2 Thieno[3,4-b]pyrazine-based ligands and cages	215
5.3 Heteroleptic assemblies	222
5.4 Perspective	228
5.5 Conclusion	228
5.6 Experimental part.....	230
5.7 References	266
6 Conclusion and Outlook	269
Acknowledgement.....	273

1 GENERAL INTRODUCTION

1.1 COORDINATION CAGES

The concept of coordination cages can seem relatively evident to the supramolecular chemist: combining metal centres with polytopic ligands capable of bridging several of said metal centres to form discrete three-dimensional assemblies. It is therefore intriguing that the first of such a species was discovered only serendipitously: in 1988, Saalfrank *et al.* reported the formation of tetrahedron Mg_4L^1_6 (Fig. 1.1) upon mixing diethyl malonate, oxalyl chloride, and methylmagnesium iodide.^[1] While fully unexpected, this result opened the door for further research in three-dimensional self-assembled coordination assemblies.

In the following years, the directed preparation of supramolecular coordination species was more extensively studied, starting from the self-assembly of coordination squares by the groups of Fujita,^[2-4] Stang,^[5-8] and Lippert,^[9,10] to name but a few. Those examples have all in common their use of *cis*-protected square-planar metal cations such as Pd(II) or Pt(II) and bis-monodentate organic ligands. It is by using this same technique, but changing the ligand to a tris-pyridyl type, that the group of Fujita obtained their now iconic Pd_6L_4 octahedron.^[11] Comprised of four 1,3,5-tris(4-pyridyl)triazine panels (or “walls”) held together by six ethylenediamine-Pd(II) metal vertices, this supramolecular container can be dissolved in water, and thanks to its hydrophobic cavity limited by the electron-poor organic panels, is capable of encapsulating molecules normally insoluble in aqueous media. In turn, the limited size and shape of the cavity of the cage preorganises the guest molecules and can be used to enantiomerically and regioselectively catalyse the transformation of said guest molecules, where conventional catalysts would struggle to achieve such selectivity.^[12-19] The group of Stang would also use the same type of *cis*-protected Pt(II) or Pd(II) vertices for the preparation of larger coordination species.^[20-22]

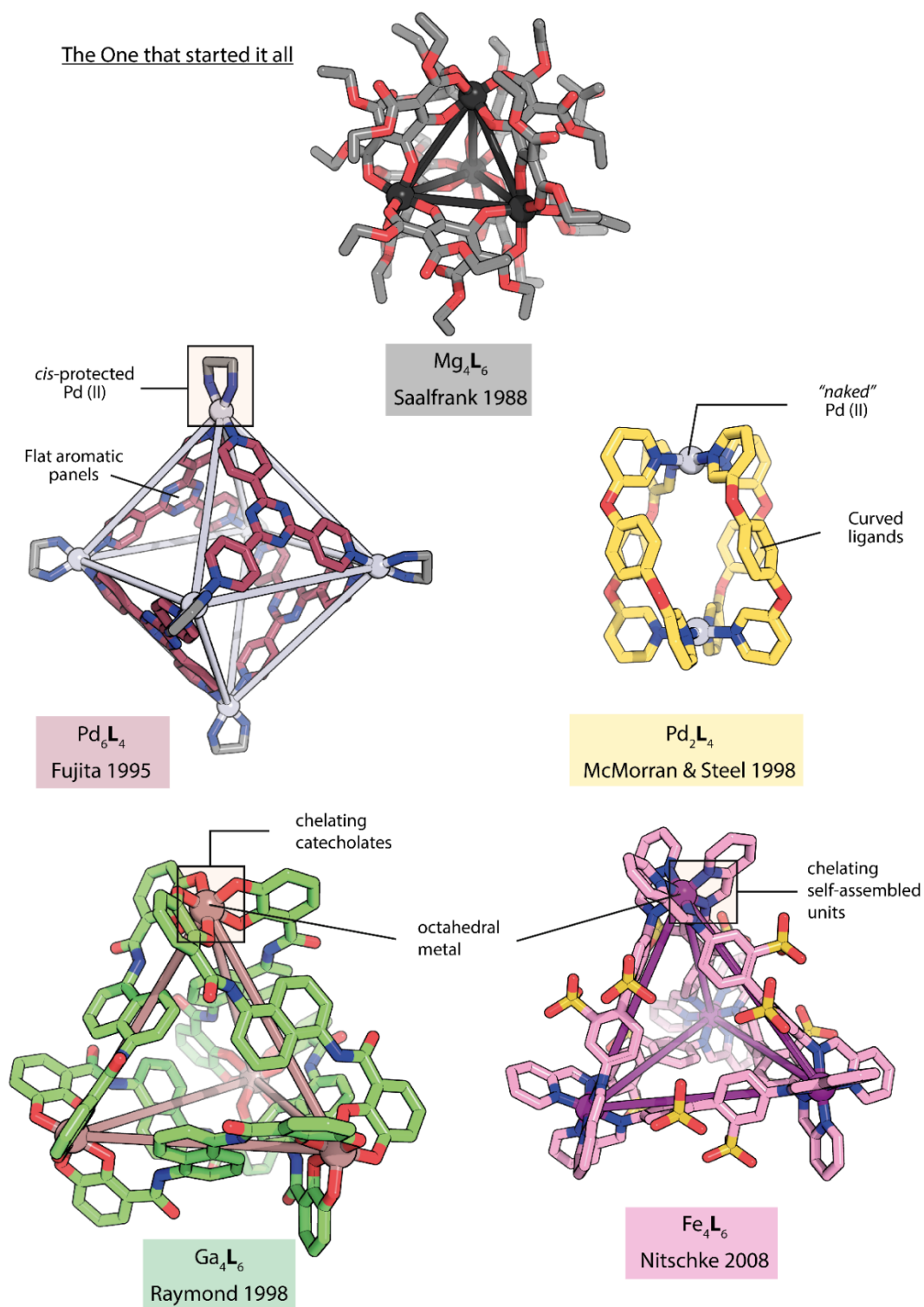


Figure 1.1: Five historical examples of the main methods of assembling coordination cages. Firstly, there is the historical serendipitous example of Saalfrank. Then, we see the two different way of assembling cages with square-planar metals, either with *cis*-protected or “naked” ions, such as Pd(II). Finally, the use of octahedral metals is exemplified with the work of Raymond with catecholates-based ligands or the work of Nitschke with sub-component self-assembly.

At the same time, the group of Raymond developed a different methodology to obtain coordination cages: instead of the aforementioned tris-pyridine ligands and square planar metals, they combined octahedral metal cations with ligands possessing two anionic chelating units to form

negatively charged M_4L_6 tetrahedra, a technique reminiscent of the original tetrahedron by Saalfrank.^[1] Those chelating groups can be hydroxamates,^[23,24] or more commonly catecholates.^[25] Thanks to their overall negative charges, those containers can encapsulate positively charged guest molecules through electrostatic interactions,^[26] and have thus also been used over the years as catalysts for reactions involving positively charged species and intermediates, such as aza-Cope rearrangement,^[27-29] Nazarov cyclisation,^[30,31] and many more.^[32-35]

Iterating on the work of Stang and Fujita on square-planar metals, the use of non-protected metal centres for the preparation of M_2L_4 “lantern-shaped” cages was investigated first by Atwood and co-workers^[36] with Cu(II) as metal centre, and later with Pd(II) by McMorran and Steel.^[37] The use of bent bis-monodentate ligands allows for a unidirectionality of the coordination vectors of the donors, and therefore when a metal is added, the two sub-components can form a discrete assembly. If the vectors were too divergent, a coordination polymer or network would be formed instead. While the aforementioned first example used Cu(II) centres, its paramagnetism makes it unsuited for standard NMR analysis. Therefore, it was promptly replaced by Pd(II) for its many advantages, such as strict square planar coordination geometry, diamagnetism (suitable for routine NMR analysis), and kinetic lability. Pt(II) as metal centre has also been used, but in a limited fashion due to its kinetic inertness. Since the inception of this cage design, many groups have experimented with different shapes and functions for the ligands^[38] (with the Clever lab being one of the most prominent). The specifics of such lantern-shaped cages will be discussed in a later section.

Finally, the fourth main method of coordination cage preparation is called sub-component self-assembly and has been most extensively and successfully studied by the group of Nitschke.^[39] In its most common occurrence, this method consists in an imine condensation between two sub-components, one functionalised with amines and the other one with 2-formylpyridine groups, and a metal cation. While imine groups are in dynamic exchange with their constituents and a water molecule, the chelation of an octahedral transition metal cation stabilises the 2-pyridine imine. With a suitable bis- or multi-substituted ligand, a coordination cage can be assembled from those chelated metal centres. The group of Nitschke have shown over the years many uses and designs for their cages, such as the stabilisation of white phosphorus (P_4) in air,^[40] chemical separation of steroids in a photoresponsive cage,^[41] or regio- and enantio-specific functionalisation of fullerene C_{60} ,^[42] to cite but a few.

As eluded above, two of the key features of most of the structures described here are: **(1)** a cavity, delimited from the bulk of the media by the walls of the cage, capable of encapsulating foreign molecules (or “guests”), and **(2)** the lability of the coordination bond between the metal centres and the donor groups of the ligands, which allows for self-correction during the self-assembly of the cage, as well as in the case of a change in the conditions of the system, such as a change in temperature, pressure, or the addition of guest molecules.

Guest encapsulation goes hand-in-hand with the attempt to mimic enzymatic processes with those artificial metallocontainers. However, before the study of such interactions can be undertaken, one has to understand that the lability of the coordination bond is the one reason such artificial

supramolecular constructs are possible in the first place, and why their preparation is (on paper) so easy and elegant. Moreover, combined with the vast number of possibilities for different structures of the organic ligands, and the possibility to combine several of them in a heteroleptic structure, it is possible to envision a near-infinite range of structures allowed in great part by the lability of the coordination bond. However, like many subjects, it is important to first understand the underlying principles governing the assembly of cages and their dynamic nature before digging deeper into their structure and functionalities.

1.2 SELF-CORRECTION AND GUEST-TRIGGERED TRANSFORMATIONS

Exchange rate of coordinated ligands around metal centres varies greatly depending on the metal itself and on its oxidation state. Looking only at d^8 square planar metals Pd(II) and Pt(II), the exchange rate of a water molecule in the first coordination sphere is nearly six orders of magnitude slower around Pt(II) than around Pd(II) (10^{-4} vs. 10^2 s^{-1}).^[43] If we accept that this trend is similar with pyridine-type ligands, the assembly of supramolecular species with Pd(II) becomes much more advantageous than with Pt(II), as far as the rate of formation is concerned. Moreover, the problem of kinetics versus thermodynamics plays a large role in the formation of coordination cages. Indeed, even if thermodynamically the cage is favoured, its immediate self-assembly is not a given, especially if the pathway to it is laden with kinetic traps, products whose activation barriers are lower than the one of the final thermodynamic product (Fig. 1.2). Therefore, a large input of energy over a long period of time would be required to insure the assembly of the desired cage when using a kinetically inert metal such as Pt(II), with the added risk of side-reactions with the ligands themselves (decomposition, polymerisation, etc...). The kinetic inertness of platinum coordination bonds might however be an advantage when mixed with competitive ligands, such as carboxylates. Pd(II) on the other hand makes much more labile bonds with its ligands, and is therefore preferred in general for the very mild conditions required for the self-assembly of coordination cages and for easily reaching the thermodynamic product of the system. This high lability of the coordination bond allows for a highly important feature of the self-assembly of supramolecular coordination species: self-correction.

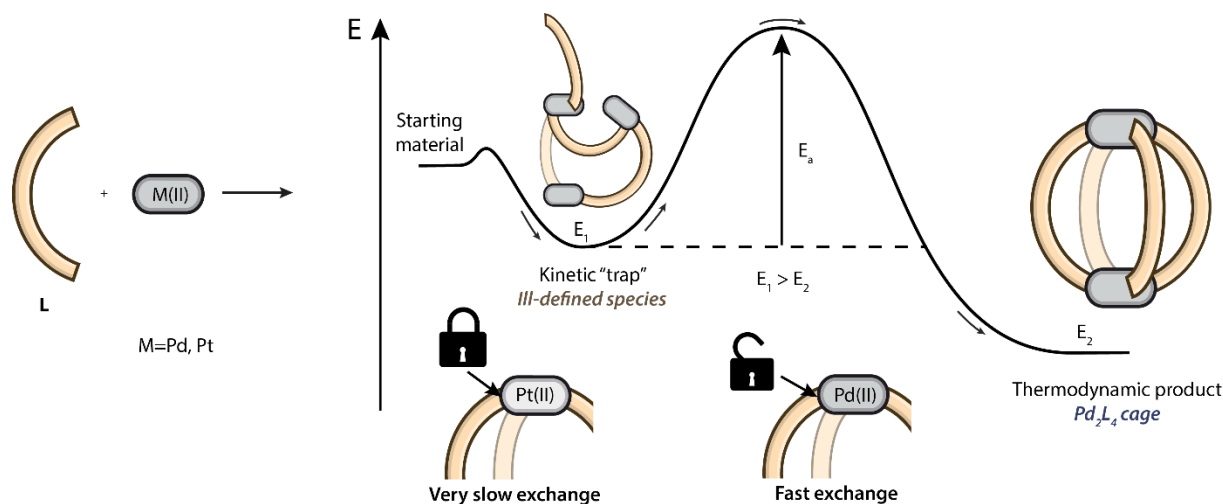


Figure 1.2: The self-assembly pathway from a mixture of ligand and metal salt to form the final coordination cage as the thermodynamic product needs to overcome the formation of potentially undesirable kinetic species. Therefore, the ability of the system to self-correct through the exchange of ligands around the metal centre is paramount and is driven by the input of energy to overcome the activation barrier (E_a). The kinetics of such exchange is dependent on the chosen metal: ligands experience much slower exchange around Pt(II) centres compared to Pd(II).

As mentioned above, the pathway towards the coordination cage might be hampered by kinetic products, such as coordination polymers or undefined larger species. If the lability of the coordination bond is too low, overcoming the barrier to break again those bonds and reform them in a more favourable way might be prohibitive. This would lock the system in an ill-defined mess, and fully unusable. However, with a larger lability of the coordination bonds, the system can rearrange itself much more easily and quickly to form the desired discrete assemblies. This property of the system is called self-correction.

Not only is it desirable during the initial formation of the cage(s), but it also allows for a reactivity and a plasticity of the system towards external stimuli that changes the thermodynamic minimum. Moreover, two or more different thermodynamic minima can be close in energy, with low exchange barriers. Therefore, a change in concentration, pressure, or temperature change, or the addition of an external species such as a guest molecule,^[44] or another coordination species^[45] can be used to shift the equilibrium, and thus influence the relative amount of each species.

As mentioned earlier, many of coordination cages possess, by definition, a cavity separated from the bulk of the media by the metaphorical walls or bars of the cages. Guest molecules can in turn bind these cavities, like substrates bind to the pocket of enzymes. In many cases, the guest and the host are content to simply associate, leading to a host-guest complex. However, it may happen that the interaction between the two species leads to a change in the nuclearity of the host, in a case where the guest templates a new structure.

A notable early example was reported by Raymond *et al.* in 1999, where the authors described the transformation of a Ti(IV)- or Ga(III)-based M_2L_3 helicate into a M_4L_6 tetrahedron upon the addition of tetramethyl ammonium cation, forming a $NMe_4@M_4L_6$ host-guest complex (Fig. 1.3).^[46] In this publication, the transformation is first observed for the system with Ti(IV) as vertices. However, the system is then changed to Ga(III) because of its greater lability, connecting to the

talking point of the first paragraph of this section. Despite this, the full transformation still takes 5 days under heating at 40°C. As for the reason of the transformation, one can see on the X-ray structure and on the $^1\text{H-NMR}$ that the methyl groups of the NMe_4^+ cations interact closely with the aromatic panels of the cage, and these favourable $\text{CH}-\pi$ interactions might be enough to offset the entropy penalty for the formation of a larger structure and host-guest complex instead of the smaller helicate (which does not possess a large enough cavity to bind the guest).

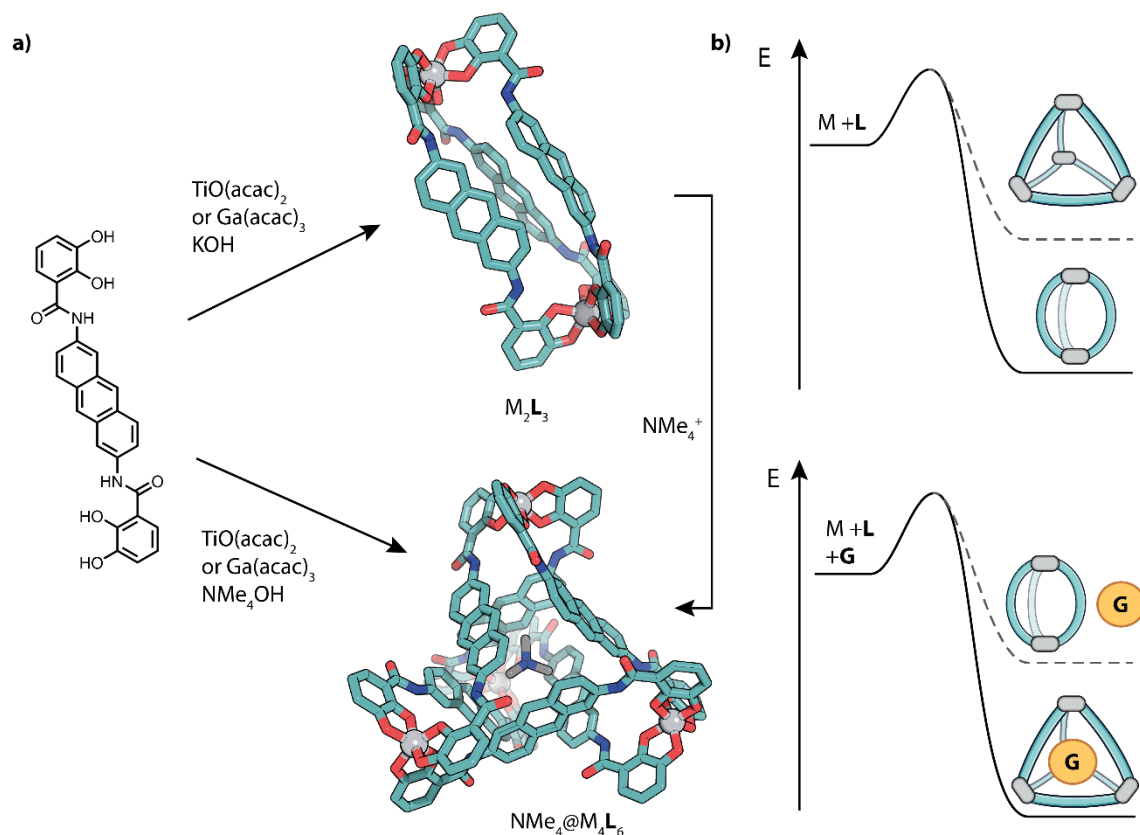


Figure 1.3: With the same anthracene-based ligand L , two structures can be formed: if KOH is used as a base during the assembly, a triply stranded helicate M_2L_3 is formed, whereas a tetrahedron M_4L_6 is formed if NMe_4OH is used instead. The tetramethyl ammonium cation templates the formation of the tetrahedron by binding to its cavity and favourably interacting with the aromatic panels of the cage. If NMe_4^+ is added to the helicate, it triggers a transformation from the helicate to the tetrahedron.

Since this discovery, many more examples of cage systems experiencing a change in their nuclearity and topology have been reported. This subject has been extensively reviewed by Percástegui^[44] and Nitschke.^[45] Thus, I will only present in this chapter notable and most relevant examples. Both neutral and charged guests have been shown to trigger cage-to-cage transformations, and one such notable neutral guest is fullerene.

The host-guest chemistry of fullerenes in coordination cages is well studied and has been used for many applications, such as purification,^[47] or region-specific functionalisation of fullerenes.^[48-50] In 2015, the group of Nitschke showed that a tetrahedral cage Fe_4L_6 with porphyrin-based ligands could rearrange to a smaller Fe_3L_4 structure upon binding of one equivalent of fullerene C_{70} .^[51] Porphyrin-based metallo-containers are particularly well suited to the binding of fullerenes, thanks to the large

aromatic surface they create and leading to strong π - π interactions between the electron-poor fullerene and the electron-rich porphyrins.^[52] In the present example, the cage rearranges itself to create a species with a smaller but better fitting cavity for the C_{70} . In addition, the lower nuclearity of the newly formed host-guest complex means that one of the Fe(II) centres is left unsaturated, binding only two ligands. Remarkably, this metal centre can be replaced by a tetrahedral Cu(I) cation, further transforming the system to an unusual bimetallic $C_{70}@CuFe_2L_4$ host-guest complex.

The same group the same year showed that a $Co_{12}L_6$ cuboctahedron with ligands also based on porphyrin could undergo significant rearrangement upon binding of fullerene (Fig. 1.4a).^[53] Indeed, the O -symmetric cage (thermodynamic product) or its D_4 kinetic counterpart could bind two fullerenes (C_{60} or C_{70}) and rearrange into a S_6 isomer of the $(C_{60}/C_{70})_2@Co_{12}L_6$ host-guest complex. This broad range of structural isomers underlines the stereochemical plasticity of the system that, contrary to the previous example, did not need to change its nuclearity to accommodate the two guest molecules.

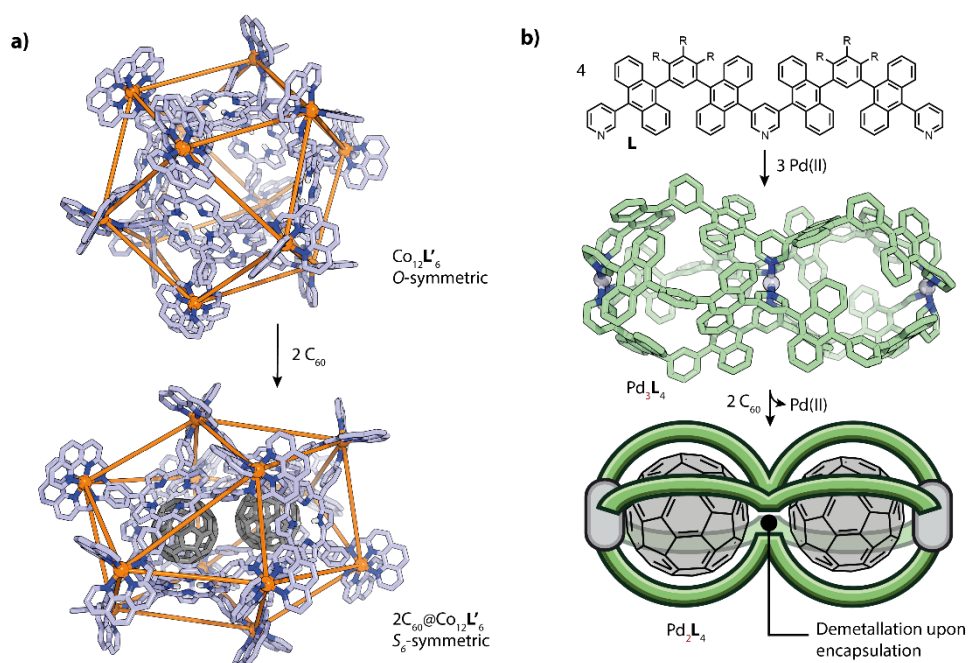


Figure 1.4: (a) Change in overall symmetry of a $Co_{12}L_6$ capsule from its O -symmetric initial shape to the S_6 -symmetric $2C_{60}@Co_{12}L_6$ host-guest complex. (b) Formation of peanut-like cage Pd_3L_4 , and the subsequent encapsulation of two equivalents of C_{60} , accompanied by the demetallation of the central donor position to form host-guest complex $2C_{60}@Pd_2L_4$.

The group of Yoshizawa have also experienced the encapsulation of fullerenes in coordination cages with large aromatic panels. In their case, they generally use anthracene-based ligands in cages assembled with Pd(II) cations. In one example, they prepared a Pd_3L_4 ‘‘molecular peanut’’ from W-shaped organic ligands, with Pd(II) cations coordinating to pyridine donors at both ends, as well as at the middle point of the ligand (Fig. 1.4b).^[54] This unusual ‘‘peanut’’ thus possesses two distinct cavities capable of binding fullerenes, among others. Unexpectedly however, in order to bind two C_{60} molecules, the peanut has to undergo a demetallation and get rid of the central Pd(II) cation; the

final host-guest complex therefore has a $2C_{60}@Pd_2L_4$ formula. This suggests a remarkable stability of the host-guest complex, strong enough to largely compensate the loss of four favourable Pd(II)-pyridine coordination bonds. The stabilisation of a single species was also shown by the same group in an example where a statistical mixture of $Pd_2L_n^A L_{(4-n)}^B$ would reconfigure into a single heteroleptic $C_{60}@cis-Pd_2L^A_2L^B_2$ host-guest complex.^[55] In a more recent article, the group of Yoshizawa also described a complex Pd_2L_4 cage system prepared with a desymmetrised ligand with dynamic naphthalene moieties.^[56] Thus, when assembled into a cage, the ligand can show three distinct atropoisomers: *anti*, *syn*, and *anti'*, depending on the relative orientation of the naphthalene moieties. The authors calculated that 42 possible of fast exchanging isomers are found in solution. However, upon addition fullerene C_{60} to the system in D_2O , the cage binds the guest and forms the unique isomer $C_{60}@Pd_2syn-L_4$. Again, this system does not undergo a change in nuclearity, but the binding of the guest selects for a specific isomer.

While fullerenes are the most notable examples of neutral guest-triggered cage-to-cage transformation, other types of guests have been studied over the years as well. For example, in the last discussed system, other guests such as triphenylene, adamantane, or corannulene have also selected for a specific isomer of Pd_2L_4 , although not to the same degree of efficiency as fullerene C_{60} .

The group of Fujita showed in 2004 that a $Pd_{12}L_4$ structure formed from large hexatopic ligands with pyridyl donor groups could encapsulate two triphenylene guests (G_1) in aqueous media, each sandwiched between two of the flat ligands.^[57] Interestingly, upon addition of larger triphenyl triazine guests (G_2) to the system, the system underwent shrinkage to yield the smaller $G_2@Pd_6L_2$ host-guest complex. The authors explain that the smaller “naked” assembly is less favoured over the $Pd_{12}L_4$ complex, despite entropic penalties, because large distortions in the ligand are necessary to reach the smaller assembly. However, upon complexation with G_2 , the hydrophobic π - π interactions between the cage and the guests are enough to overcome the energetic barrier and thus to yield the $G_2@Pd_6L_2$ host-guest complex. The same group reported later a $Pd_{18}L_6$ trigonal bipyramidal capsule capable of undergoing reversible size extension to a $Pd_{24}L_6$ octahedron upon coordination of several neutral guests, such as acenaphthylene or calix[4]arene.^[58] Despite its strong binding to the cage, acenaphthylene could be removed from the system by heating a biphasic mixture of the aqueous cage solution and chloroform for 24 h. Deprived of the guest, the capsule reverted to its original $Pd_{18}L_6$ state.

Finally, more exotic neutral guests were used recently by the group of Nitschke to drive the selective formation of a single $M_6A_3B_2$ ($M=Co(II)$ or $Zn(II)$) heteroleptic capsule from a mixture of orientation isomers.^[59] Indeed, the addition of a series of highly chlorinated pesticides (such as Mirex) drove the system to a single isomer of the cage.

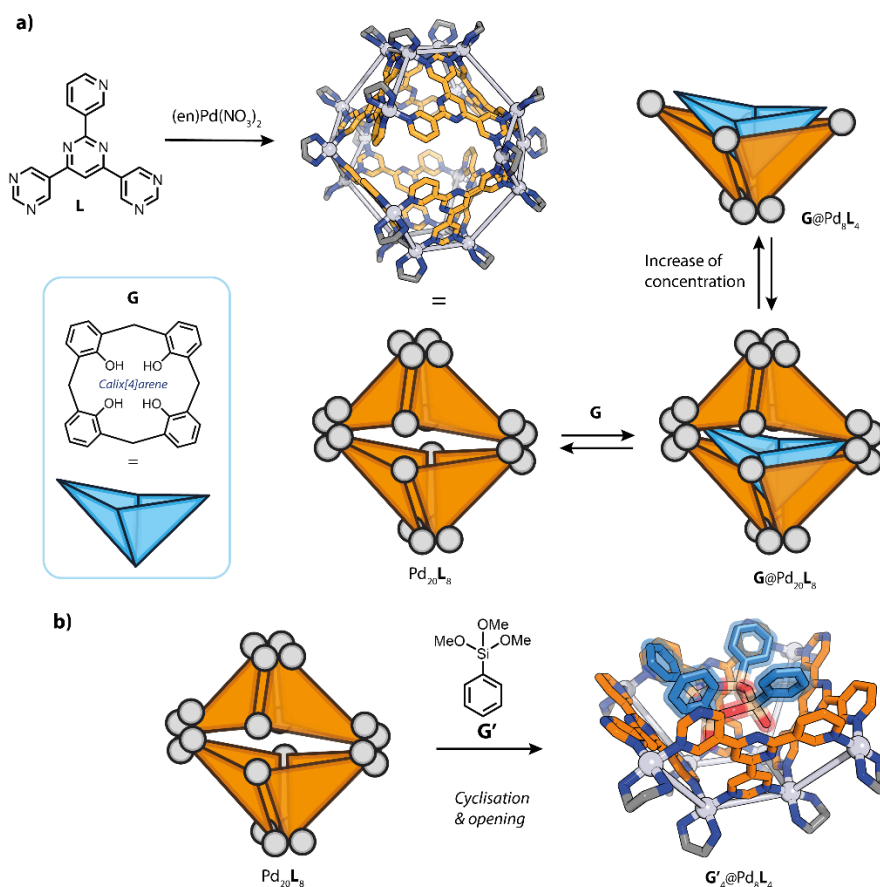


Figure 1.5: (a) formation of the $Pd_{20}L_8$ capsule, followed by the encapsulation of the calix[4]arene guest and the subsequent transformation of the capsule into a Pd_8L_4 bowl upon increase of the concentration of guest or of the overall system. (b) Concerted encapsulation into $Pd_{20}L_8$ and cyclisation of guest G' into the tetramer G'_4 bound inside of the cavity of the newly formed Pd_8L_4 bowl.

Until now, I only focussed on guests with a specific size and shape that did not undergo chemical transformation upon binding to cages. However, two rare examples of host-guest systems where the guest is chemically transformed, thus leading to a change in the host, have been reported. In a 2016 article, the group of Fujita described a $Pd_{20}L_8$ octahedral capsule capable of splitting into two Pd_8L_4 bowls and releasing four Pd(II) centres upon addition of excess calix[4]arene as a guest (Fig. 1.5a).^[60] A low concentration also favoured the formation of the smaller bowl-guest complex, while a higher concentration favoured the larger capsule-guest complex. Building on that observation, the authors then attempted to encapsulate phenyl trimethoxysilane and hydrolyse it (Fig. 1.5b). Results showed that a cyclic isomer of tetrasiloxane had formed and was bound into a Pd_8L_4 bowl, similarly as to the calix[4]arene. While the authors do not demonstrate that the monomeric guest binds first to the cage, and then undergoes oligomerisation, they underline that only a *cis* isomer of the tetramer has been formed. Indeed, the controlled and stereospecific preparation of cyclic siloxanes is difficult, but can be tamed and template inside of coordination cages.^[61] More recently, the group of Sun published a system where a Pd_4L_2 cage undergoes a “cell mitosis” when guest 1-hydroxymethyl-2-naphthol dimerises in the cavity of the cage and thus triggers a transformation to a “conjoined

Pd₆L₃ twin-cage”.^[62] The transformation was shown to be reversible upon change from an aqueous solution to a DMSO environment, capable of efficiently dissolving the guest. Moreover, addition of EtOAc to the DMSO solution precipitated the initial Pd₄L₂, allowing for its full recovery for a second cycle.

As most of the coordination cages are assembled from neutral organic ligands and metallic cations, they present an overall positive charge. Therefore, many examples exist of anionic guests interacting with cages and causing changes in their structure. For example, the group of Sun presented a Pd-based ring system capable of showing every nuclearity of Pd_nL_{2n} (n=3-7) depending on the templating anion and capable of undergoing transformation upon addition of another anionic guest.^[63,64] To clarify the terms used here, anionic guests are used to describe externally added anions, and not anions that exist in solution as charge-balancing species to the positively charged cages. As we previously observed in quadruply catenated double Pd₂L₄ cages, the addition of an anionic guest can sometimes lead to only minor changes in the size of the overall assembly.^[65] However, in many other cases, the presence of external anions is crucial in modulating the catenation of Pd₂L₄ lantern-shaped cages. Indeed, Kuroda *et al.* showed in 2008 the first example of quadruply interpenetrated double Pd₂L₄ cages, whose structure is promoted by the favourable electrostatic interaction between the positively charged Pd(II) centres of the cages, and of the NO₃⁻ counter-anions, yielding the overall structure 3(NO₃)@Pd₄L₈.^[66] However, they later showed that the interpenetration could be broken by the addition of an excess of anionic guest naphthalene-2-sulfonate (**NAP2**) to form host-guest complex 2**NAP2**@Pd₂L₄.^[67] The catenated structure could in turn be obtained again by the addition of more nitrate, demonstrating that the interpenetration was dependent on a subtle balance between the two anions in solution.

Early in the Clever group’s history, work was focussed on those quadruply catenated double Pd₂L₄ cages. The group first showed that they could be templated by a BF₄⁻ counteranion tightly bound in the central cavity between the two internal Pd(II) cations,^[68] and that their two external cavities could accommodate external halide anions, leading to a slight contraction of the size of the cage along the Pd-Pd-Pd-Pd axis as seen by DOSY (Fig. 1.6a). However, due to the inherent presence of templating BF₄⁻ in the system and the impossibility to obtain the non-catenated Pd₂L₄ cage first under thermodynamic control, a new system based on ligands with bulkier internal substituents was envisioned; the steric bulk of those substituents should be enough to prevent the catenation of the cage. And indeed, upon addition of Pd(II), the system self-assembled into the non-catenated Pd₂L₄ cage. Next, the subsequent addition of 0.5 equivalents of chloride drove the system towards the formation of the Cl@Pd₄L₈ complex (Fig. 1.6b).^[69] The two external cavities of this complex were also large enough to accommodate one bulky anion (such as ClO₄⁻, PF₆⁻, or ReO₄⁻) each. A similar behaviour was observed later with carbazole-based ligands **L³** self-assembling with [Pd(MeCN)₄](BF₄)₂ to form the monomeric Pd₂L₃₄.^[70] Due to their shorter length, those ligands cannot yield a large enough double cage capable of accommodating tetrafluoroborate anions tightly sandwiched between the Pd(II) centres. Therefore, only a monomeric cage is obtained when using

BF_4^- . However, the addition of 1.5 equivalents of halide (Cl^- or Br^-) was shown to trigger the catenation of the cages to form the $3\text{X}@\text{Pd}_4\text{L}^2_8$ complex, where the cavities in-between the Pd(II) centres were large enough to allow for the binding of the anions (Fig. 1.6c). Surprisingly, upon addition of excess bromide, a new triply interlocked species $\{\text{trans}[(\text{PdBr}_2)_2\text{L}_2]\}_3$ could be isolated, where each palladium centre was *trans*-coordinated with two Br^- . It is worth noting that the progressive addition of halides to the starting cage is paramount for the obtention of the triply catenated species, as it cannot be obtained starting from PdCl_2 or PdBr_2 .

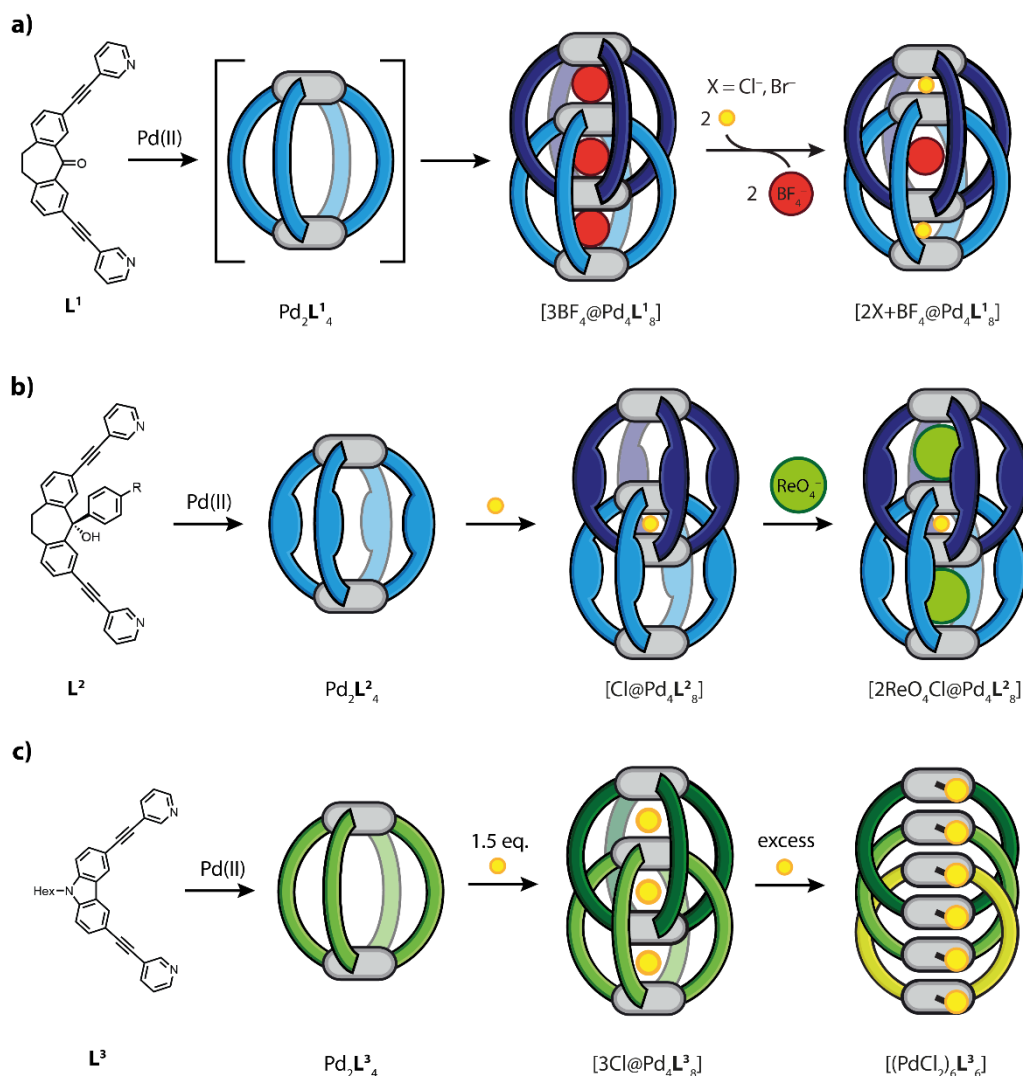


Figure 1.6: (a) Formation of the Pd_4L^1_8 double cage from a suberone-based ligand L^1 with a strongly bound BF_4^- in the central cavity. The other two BF_4^- in the two outermost cavities can be replaced by two halides, leading to a contraction of the double cage. (b) Adding bulk to the middle of the suberone-based ligand doesn't lead to the direct formation of a double cage upon coordination with Pd(II) and BF_4^- counteranions. However, the subsequent addition of Cl^- allows the Pd_2L^2_4 cage to catenate and form the $\text{Cl}@\text{Pd}_4\text{L}^2_8$ complex. The outer cavities are large enough in this case to bind large anions such as ReO_4^- . (c) Carbazole-based ligand L^3 forms a Pd_2L^3_4 cage, which can be converted to the catenated $3\text{Cl}@\text{Pd}_4\text{L}^3_8$ complex. Upon further addition of chloride anions, a neutral $(\text{PdCl}_2)_6\text{L}^3_6$ triply catenated species was formed.

Expanding on this work, the group showed that a peanut-like Pd_3L_4 species could similarly catenate upon the addition of halides to form the $5\text{Cl}@\text{Pd}_6\text{L}_8$ inclusion complex.^[71] Finally, they

showed that a phenanthrene-based ligand self-assembled with $[\text{Pd}(\text{MeCN})_4](\text{BF}_4)_2$ to form a mixture of $\text{Pd}_3\mathbf{L}_6$ triangles and $\text{Pd}_4\mathbf{L}_8$ squares and tetrahedra, but formed exclusively a [2]-catenated $(\text{Pd}_4\mathbf{L}_8)_2$ species of two interlocked squares when starting from $\text{Pd}(\text{NO}_3)_2$.^[72] This species was shown to form as well starting from the tetrafluoroborate mixture and adding 8 equivalents of nitrates. The nitrates are essential to template the catenated structure, as they fit in-between the four Pd(II) centres which are aligned on the C_2 axis. A heteroleptic system $\text{Pd}_4\mathbf{A}_2\mathbf{B}_4$, where **A** is a bridged tetratopic carbazole ligand, was also shown to encapsulate two equivalents of guest naphthalene-2,7-disulfonate (**NAP27**) in solution.^[73] Surprisingly however, upon crystal growth and analysis by single crystal X-ray diffraction, the solid-state structure was found to be the larger $\text{Pd}_6\mathbf{A}_3\mathbf{B}_6$.

While the Clever group has shown extensive and exciting results in the domain of the catenation of $\text{Pd}_2\mathbf{L}_4$ cages, there had yet to be an example of a more dramatic change in topology and number of sub-components, for this type and nuclearity of cage.

Straying away from palladium-based assemblies, let us now have a look at different examples of transformations in assemblies with different transition metals. For example, in 2017, the group of Duan presented a $\text{Zn}_4\mathbf{L}_6$ tetrahedron assembled through sub-component assembly, capable of triply interlocking upon addition of a bromide anion.^[74] Moreover, the group of Nitschke developed systems based on Cd(II)-assemblies capable of undergoing distinct transformations upon the step-wise addition of different anions.^[75,76] The same team also published a heteroleptic system where a $\text{Zn}_4\mathbf{A}_4$ tetrahedron and a $\text{Zn}_8\mathbf{B}_6$ cube narcissistically self-sort, but could be driven to a heteroleptic $\text{Zn}_6\mathbf{A}_2\mathbf{B}_3$ triangular prism by the addition of $\text{CoC}_4\text{B}_{18}\text{H}_{22}^-$ or testosterone by templation.^[77]

On a last note, the group of Fujita have introduced in the last years a new class of large and highly intricate structures based on tripodal ligands possessing both pyridyl donor groups and alkyne linkers, both capable of coordinating Cu(I) or Ag(I) cations to form those highly tangled coordination species.^[78,79] Interestingly, the final nuclearity and topology depend on the counteranions used, and can be interconverted by the addition of an external anion, such as nitrate.

Those varied examples underline the sometimes-unpredictable nature of supramolecular coordination assemblies, governed by subtle entropic and enthalpic considerations. If smaller assemblies tend to be favoured because of the higher entropy of the system, it was shown that those entropic gains can be compensated by tight interactions between a larger assembly and guest molecules. Moreover, those tight interactions can change the energy landscape by selecting for a specific structure out of a mixture of possible isomers and nuclearities. Furthermore, the lability of the coordination bond is paramount to make the transformations possible and to drive the systems to their thermodynamic minima. While I mentioned in the present section heteroleptic systems and the challenges of self-sorting, I shall now present the matter in a more detailed way.

1.3 (CHIRAL) SELF-SORTING

Theoretically, when mixing two or more different ligands with a metal source, several thermodynamic outcomes are possible, depending on the nature of the ligands (Fig. 1.7). First in one extreme end, a statistical mixture can be formed, where any possible stoichiometry of the cage is formed, without any bias. On the opposite end, a narcissistic self-sorting may occur, where the ligands form their respective homoleptic species without interacting with one another. Finally, in the middle, we find the aptly named integrative self-sorting,^[80-82] relating to systems where several different building blocks combine to form a well-defined complex structure. To create well-defined multifunctional low symmetry species as mimics to artificial enzymes, a statistical distribution is wholly uninteresting. Therefore, to avoid such outcomes, strategies in the design of the ligands have been developed over the years to yield non-statistical systems (Fig. 1.8).^[83] As the subject is vast and most is outside of the scope of this introduction, I will focus more on non-protected Pd-based assemblies.

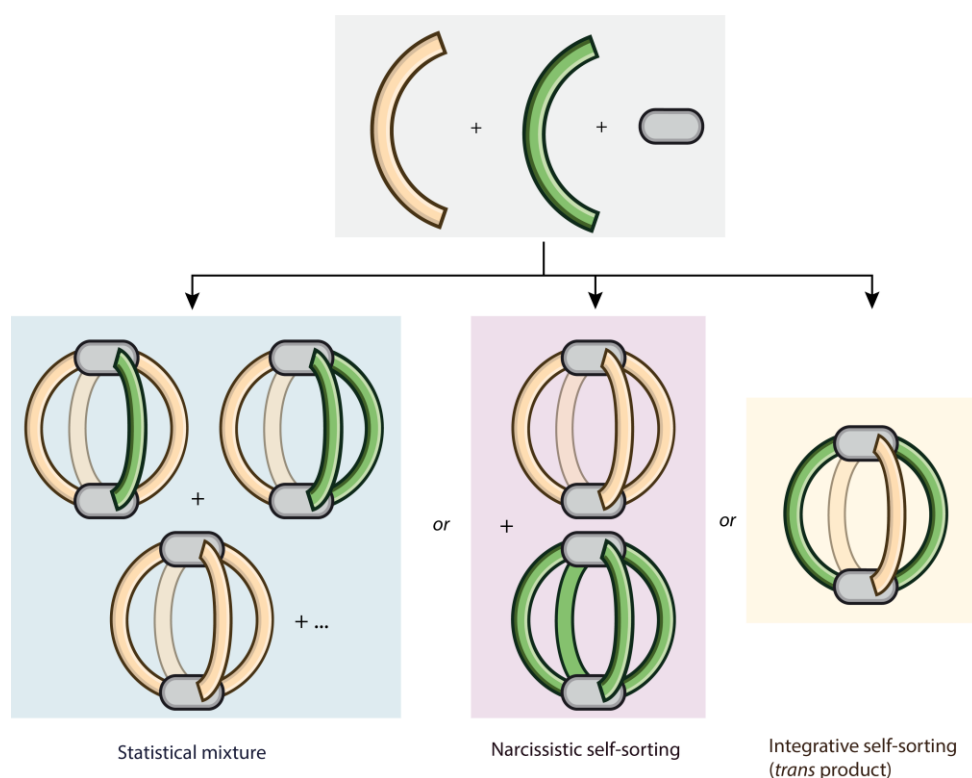


Figure 1.7: The three types of outcomes possible in a heteroleptic system (here only two different types of ligands): a statistical mixture, or a narcissistic self-sorting (where every ligand only interacts with itself), or an integrative self-sorting, where only one product is formed and includes every type of ligand in a regular and consistent position.

A first technique, that has already been discussed in the previous section, is self-sorting through **guest encapsulation**.^[55,59,84] However, systems capable of this are rather scarce, and the technique relies on an external factor rather than on the design of the container itself. Finally, the examples lack as of now a predictive power to reliably design such a system from scratch. A second technique was introduced by Hooley in 2011, coined “**ligand interaction**”, where bulky substituents on one of the ligands points towards the cavity and thus biases the system to form a Pd₂A₃B

assembly.^[85] However, this technique negates the cavity in the final assembly, making it useless for the study of guest encapsulation in low-symmetry cages. Crowley *et al.* have also prepared a system capable of self-sorting by ligand interactions on the outside of the cage by adding amino group in the 2-position of the pyridine donor group (\mathbf{L}^{NH_2}).^[86] When combined in equimolar amounts with the corresponding unsubstituted ligand (\mathbf{L}) and a Pd(II) source, the authors found that the *cis*- $[\text{Pd}_2\mathbf{L}^{\text{NH}_2}_2\mathbf{L}_2]$ cage had formed, but under kinetic control only. The role of the amino groups in the self-sorting consists of the hydrogen bonds they can create with the adjacent hydrogens on the non-substituted pyridyl donor groups. Having iterated on this concept, I will present an example of self-sorting through ligand interactions that does not negate the cavity in Chapter 5. A final example of ligand interactions driving the non-statistical assembly of a supramolecular coordination species was demonstrated by Tessarolo, Clever, and co-workers in a heteroleptic $\text{Pd}_4\mathbf{L}_4\mathbf{L}'_4$ tetrahedron.^[87] Two ligands of similar shape and size were employed. When carbazole-based ligand \mathbf{L} is mixed with Pd(II), a mixture of $\text{Pd}_3\mathbf{L}_6$, $\text{Pd}_4\mathbf{L}_6$, and $\text{Pd}_6\mathbf{L}_{12}$ species is obtained. On the other hand, dihexylfluorene-based ligand \mathbf{L}' exclusively forms a $\text{Pd}_6\mathbf{L}_{12}$ octahedron, thanks to the added steric bulk on its backbone. Combining the two ligands with Pd(II) leads to a single $\text{Pd}_4\mathbf{L}_4\mathbf{L}'_4$ tetrahedron, where the bulky \mathbf{L}' ligands occupy the singly-bridged edges of the species, and the less-hindered \mathbf{L} can occupy the doubly-bridged edges. To regroup those several disparate examples of ligand interactions driving integrative self-sorting, our group has recently coined the term “**adjacent backbone interaction**” (ABI).

The assembly of such low-symmetry non-statistical heteroleptic systems has been one of the main goals of the Clever lab, notably in the preparation of Pd_2 lantern-shaped cages. One strategy we employed early on was “**coordination sphere engineering**” (CSE): this method consists in using ligands with donor groups of a specific size and/or property so that more than one type of donor coordinates around the metal centre in a non-statistical manner. More precisely, the use of bulky donors on one ligand might sterically hinder the coordination of enough ligands to saturate the metal centre and consequently only smaller ligands are able to coordinate to the metal. This concept had already been demonstrated by Fujita *et al.* for *cis*-protected Pd(II)-based squares with the use of methyl groups next to the nitrogen of the pyridine donor group.^[88] It was then adapted to $\text{Pd}_2\mathbf{L}_4$ lantern-shaped ligands by the Clever lab using *o*-picoline (2-methylpyridine) donor groups on ligands to selectively form *cis*- $[\text{Pd}_2\mathbf{L}^{\mathbf{A},\mathbf{i}_2}\mathbf{L}^{\mathbf{B},\mathbf{o}_2}]$ cages, with ligands of the same shape and size, but with differing backbones (\mathbf{i} =methyl group inside, \mathbf{o} =methyl group outside).^[89] Another approach to CSE developed by our lab is the use of bulky donor groups, such as quinolines, naphthyridines, or even acridines to selectively form $\text{Pd}_2\mathbf{L}_4$ cages, $\text{Pd}_2\mathbf{L}_3$ bowls, or $\text{Pd}_2\mathbf{L}_2$ rings.^[90,91] The play on the bulkiness of different types of ligands was furthermore successfully exploited to form a wide net of heteroleptic assemblies.^[92,93]

A second approach to integrative self-sorting was developed by our lab, the now called “**shape complementary assembly**” (SCA) in 2016.^[94] Its principle lies in combining two different ligands (in its first iteration) with opposing coordination vectors and matching size, *i.e.* one long ligand with converging vectors, and one smaller ligand with diverging coordination vectors. Upon coordination

with Pd(II), the heteroleptic species Pd₂A₂B₂ can thus be formed, with the coordination planes of the two metal centres not being parallel, unlike most heteroleptic Pd₂L₄ cages. It is worth noting that Fujita and co-workers had previously reported a larger species assembled from two ligands of different length but with the same coordination vectors, playing on the size of the ligands rather than on their shape.^[95] The principle of SCA had not been properly developed at the time however. Since then many examples of binary heteroleptic assemblies through SCA by both our group and others have been reported.^[96–102]

Self-sorting strategies for heteroleptic Pd₂L₄ cages

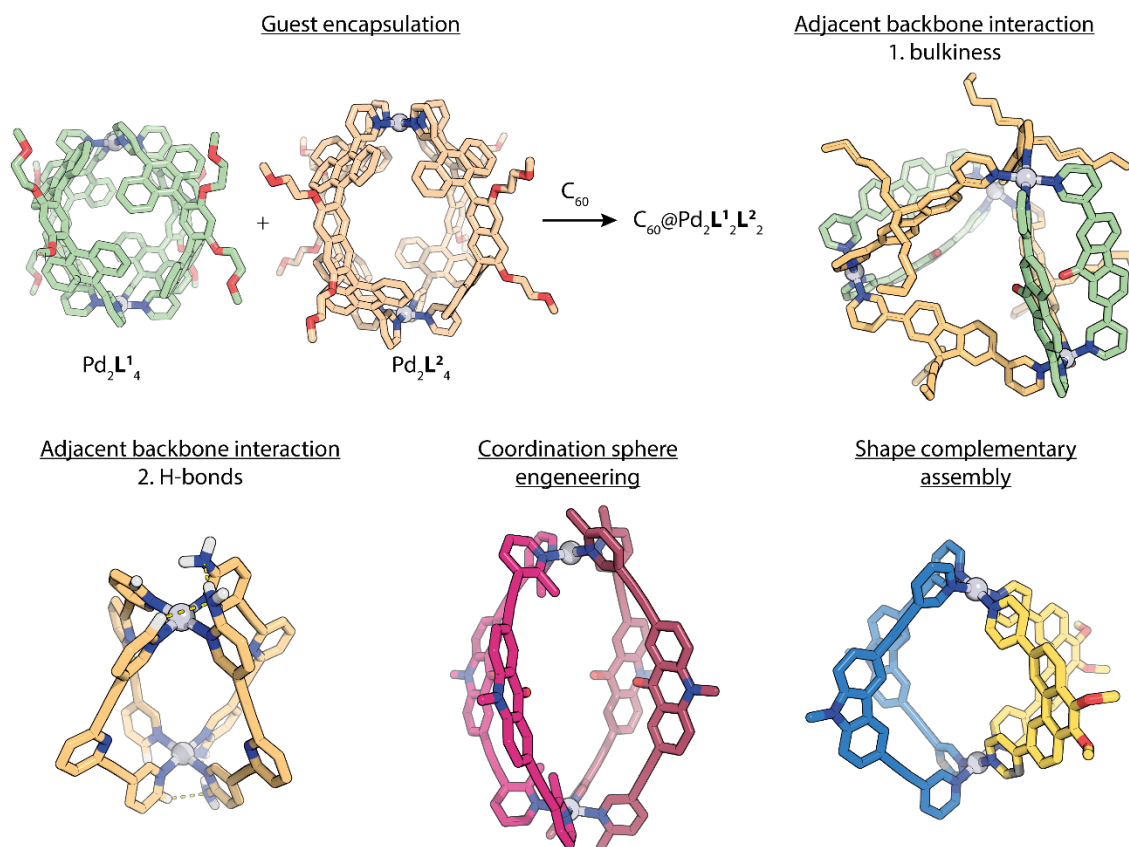


Figure 1.8: Ensemble of the different strategies to assemble non-statistical Pd₂L₄ cages.

In pursuit of lower symmetry assemblies, several Pd₂A₂BC and Pd₂ABCD cages were prepared in the recent years. For example, Lu et al. prepared a *trans*-Pd₂A₂BC by using a modified version of Hooley's^[85] backbone bulk technique.^[103] Our group has also prepared a system showing heteromeric competitive self-sorting with two coexisting Pd₂A₂B₂ and Pd₂A₂C₂ assemblies, capable of undergoing a transformation towards a unique Pd₂A₂BC cage simply by changing the ratio of the ligands in solution.^[104] Finally, we have shown recently the formation of the first examples of non-statistically assembled Pd₂ABCD cages, existing under thermodynamic control, by carefully considering the ligand combinations, and stabilising the assemblies by ligand-ligand CH-π interactions.^[105] The group of Hiraoka also proposed examples of Pd₂ABCD assemblies, but only

under kinetic control.^[106] On a slightly different note, we have also recently prepared an example of a Co(III)-salphen-based $\text{Co}_2\mathbf{ABCD}$ cage, where \mathbf{AB} is an asymmetric macrocycle.^[107] This approach, although different from the previously mentioned examples, has the advantage of starting from the kinetically labile Co(II) ion, allowing for rapid self-correction of the system, and locking the system through aerobic oxidation with the much less labile Co(III) centre.

A specific case of self-sorting happens when one uses the racemate of a ligand. Indeed, despite there being only one type of ligand, the two enantiomers have mirror images and their association inside of a supramolecular species is not necessarily trivial. Just like if there were two chemically different ligands, a system self-assembled from a racemate can have the same outcomes: a statistical mixture of every possible diastereoisomer, a narcissistic self-sorting leading to the formation of both enantiomers of the homochiral cage, and finally a social integrative self-sorting, where both enantiomers of the ligand find a defined position in the final assembly. Many examples of both types of self-sorting exist and most have been compiled into a review by Zhang and co-workers.^[108] Here, we will mostly focus on examples from Pd(II)-based assemblies.

The first example of such a system was reported by Claessens and Torres in 2002 in a subphthalocyanine-based $\text{Pd}_3\mathbf{L}_2$ cage. When used as a racemate, the clockface-chiral ligand self-assembles into a *meso* compound, making this an example of social self-sorting.^[109] Another example of social chiral self-sorting came from our group more recently, where [6]-helicene ligands formed a *meso-cis* $\text{Pd}_2\mathbf{L}^{\text{P}}_2\mathbf{L}^{\text{M}}_2$ cage upon coordination with Pd(II) (Fig. 1.9a).^[110] Interestingly, when the linkers between the helicene backbone and the pyridyl donors were elongated, no self-sorting was observed anymore, suggesting that the self-sorting was promoted by sterics and/or interactions between the ligands; the longer linkers negated those effects by bringing the bulky backbones further apart of each other. Recently, the group of Natarajan has explored a series of assemblies made from axially chiral bimesityl-based ligands. In a first study, they have shown a remarkable control over the type of self-sorting a $\text{Pd}_2\mathbf{L}_4$ cage was undergoing by changing the counteranion and the solvent (Fig. 1.9c).^[111] For example, while a *meso-cis* cage is formed with NO_3^- , the cage undergoes a change to a mixture of the two enantiomers of the homochiral cage upon addition of BF_4^- , PF_6^- , or OTf^- . Next, by changing the donor group of the ligand to 4-pyridyl, the authors managed to prepare a pair of enantiomers of a D_3 -symmetric $\text{Pd}_6\mathbf{L}^{\text{S}}_6\mathbf{L}^{\text{R}}_6$ octahedron.^[112]

Narcissistic self-sorting was observed by Lützen and co-workers in BINOL-based cages in 2013 (Fig. 1.9b).^[113] Experimentally, they found that the NMR signals of the final $\text{Pd}_2\mathbf{L}_4$ assembly were the same whether they used the enantio-pure ligand, or its racemate. The group of Hiraoka later studied the system more in-depth through NMR and ESI-MS kinetic experiments, and concluded that, while a complicated mixture of heterochiral species was formed at the early moments of the reaction, the rate of ligand exchange was faster in homochiral intermediates, leading to an early formation of the homochiral cages.^[114] Then, the heterochiral intermediates lead to the formation of heterochiral cages, which then slowly interconvert into the thermodynamically favoured homochiral cages through ligand exchange in a complicated pathway. Finally, the group of Feringa reported in 2019 a $\text{Pd}_2\mathbf{L}_4$ cage system based on their famous photoresponsive molecular motors.^[115] Using the

racemate or the enantiopure ligand led to the same NMR signals, a sign of chiral narcissistic self-sorting. Moreover, upon irradiation with light, the motor moieties can undergo rotation, and therefore two isomers of the cage could be obtained, both under the control of narcissistic self-sorting.

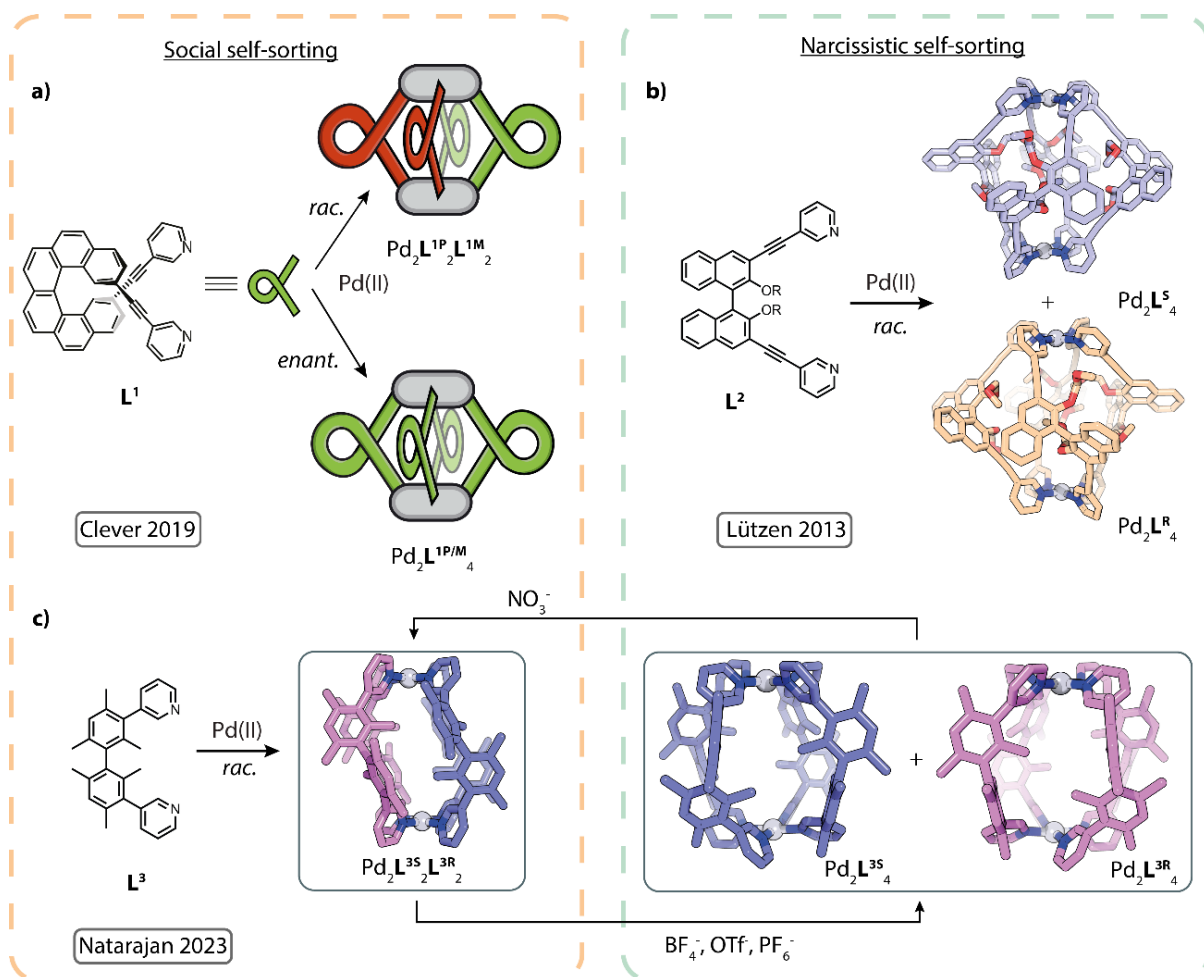


Figure 1.9: (a) Example of chiral social self-sorting with helicene-based ligand L^1 . When using its racemate, a single *meso-cis* $Pd_2L^1_4$ cage is formed upon addition of $Pd(II)$. (b) BINOL-based ligand L^1 narcissistically self-sorts into a pair of homochiral $Pd_2L^2_4$ cages. (c) The recent system of Natarajan can undergo either social or narcissistic chiral self-sorting, depending on the counteranion of the cage.

In conclusion, the combination of two or more ligands in a heteroleptic system can lead to a statistical mess if one does not have a strategy in advance to mitigate this undesirable outcome. Over the last years, several of such strategies have been developed to access low-symmetry coordination assemblies, by either controlling the coordination sphere, or carefully choosing the shape and geometry of the ligands' backbones. A specific case of self-sorting is observed when the racemate of a chiral ligand is used. Few examples of chiral self-sorting have yet been reported in Pd_2L_4 cages and the mechanism of their formation is not yet very-well understood. However, such insights are necessary to directly prepare ligands capable of self-sorting upon self-assembly, without relying on serendipity. On a positive note, recent works pave the way for more dynamic systems, reactive to both anions and solvents.

By combining the principles governing the non-statistical preparation of low symmetry assemblies and using functional ligands, one might envision in the near future the facile preparation of multifunctional cages. While the functionalities that can be integrated into the cages are numerous, I will focus more particularly in this work on molecules that interact with light, as it is a notable commonality between the different ligands I studied during my time in the Clever group.

1.4 CHROMOPHORIC COORDINATION CAGES

Harvesting light and converting it into usable energy through its interaction with matter is a crucial phenomenon for many living organisms on Earth through photosynthesis.^[116] And while Nature has had billions of years of evolution to optimise this process, the design of efficient artificial light harvesting systems remains a challenge for humans. Supramolecular chemistry has emerged in the last few decades as a potential tool for the precise arrangement of chromophores in structures resembling the strategies employed by biological systems. The design of coordination cages, with their ligands occupying a fully defined position in the assembly, is ripe with potential for emergent properties in self-assembled structures bearing chromophoric moieties, such as photocatalysis,^[117,118] sensing,^[119] molecular recognition,^[120] etc...^[121]

The world of chromophoric cages is extremely vast, and this section is only supposed to be an introduction to the subject and is in no way going to cover every detail in an exhaustive manner. Should the reader want to know more about it, our group has recently written a much more comprehensive and in-depth review of chromophoric coordination cages (still in preparation as I write those lines) and I highly recommend giving it a glance (once it is published).

The interaction of light with matter, and more specifically coordination cages, can be summarised in a Jablonski diagram (Fig. 1.10). However, due to the length and subjects covered by the present work, I will only focus here on systems with absorbing and/or emissive properties. Energy and electron transfer, as well as photoswitching will not be discussed.

1.4.1 Absorbance

In this section, I will discuss coordination cages whose absorption of light in the visible range of the electromagnetic spectrum (380-800 nm) plays an at least notable role in their study. Two main ways have been established to give cages colours: the first consists in using the ligands as the source of the colour by incorporating chromophores in the backbone, or to use the transition metal centre.

In the first case, among the simplest organic chromophores are polyaromatic hydrocarbons, such as anthracene. This backbone was used for example in a work previously mentioned by Raymond and co-workers, in which a M_2L_3 helicate could interconvert to a M_4L_6 tetrahedron upon the addition of a tetramethyl ammonium guest.^[46] The group of Yoshizawa has also made extensive use of anthracene-based ligands in their work.^[122,123] Despite the weak colour imparted by the ligands to the

assemblies, the same authors have used their strong guest-binding ability to encapsulate a diverse range of dyes and polyaromatic hydrocarbons, which in turn impart a colour to the newly formed host-guest complexes.^[124–127] I have also recently introduced the use of azulene as a small but colourful aromatic backbone,^[128] and this work will be the subject of Chapters 3 and 4.

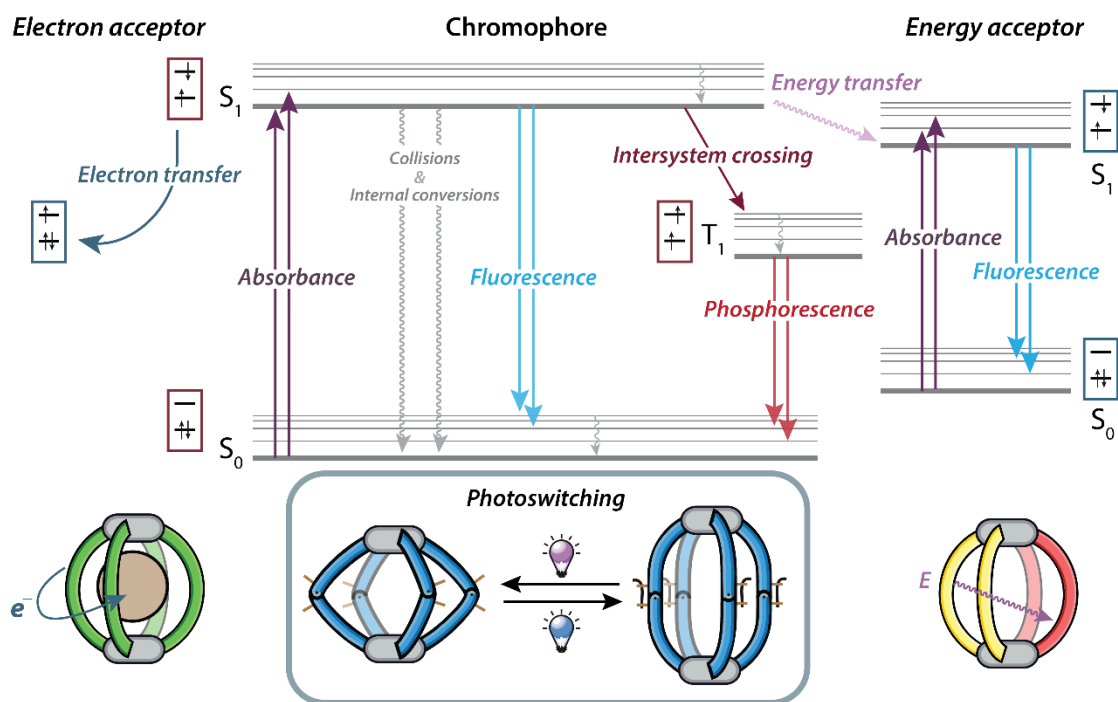


Figure 1.10: Jablonsky diagram describing the different outcomes of the absorption of a photon by a chromophore in a coordination cage. Based on an original work by E. Benchimol.

In addition to the work on azulene-based coordination cages, the Clever lab has also recently introduced the use of coal-tar dyes, such as methylene blue or Rhodamine B, as deeply coloured backbones in coordination cages (Fig. 1.11a-c).^[129] This class of dyes is formed from large π -surfaces substituted with auxochromic groups (substituents which cause the chromophore to absorb light in the visible range). In this particular case, the linker between the coordination donor groups and the backbones of the ligands was chosen to be piperazine instead of the more commonly used alkyne or phenyl groups. Indeed, piperazine here plays the role of the auxochromic electron donor group, necessary for the colour of the dyes to emerge. In addition, the use of both pyridine and isoquinoline as coordination donor groups allowed for the preparation of eight different cages and helicates. The integration of the chromophore in the backbone of the assemblies was exploited for the enhanced chiroptical detection in the visible range of anionic guests with weak absorption in the UV through guest-to-host chirality transfer^[129] or of a wide range of DNA strands by electrostatic interactions between the positively charged helicates and the negatively charged nucleic acid^[130].

After having worked of coal-tar dyes, our group introduced diketopyrrolopyrrole (DPP) as another dye in the backbones of coordination cages (Fig. 1.11d).^[131] This dye has also been nicknamed “Ferrari Red”, due to its association with the brightly painted cars of the famed automobile manufacturer. The integration into Pd(II)-based assemblies of DPP ligands was shown to extensively

modify their photophysical properties, including absorbance and fluorescence: by modifying the donor groups of the ligands, by-then PhD student Irene Regeni was able to obtain four different assemblies, with an increasing number of stacked DPP units. Interestingly, the absorbance of the DPP units undergoes a red-shift with an increase of the number of stacked units (Fig. 1.11e,f)

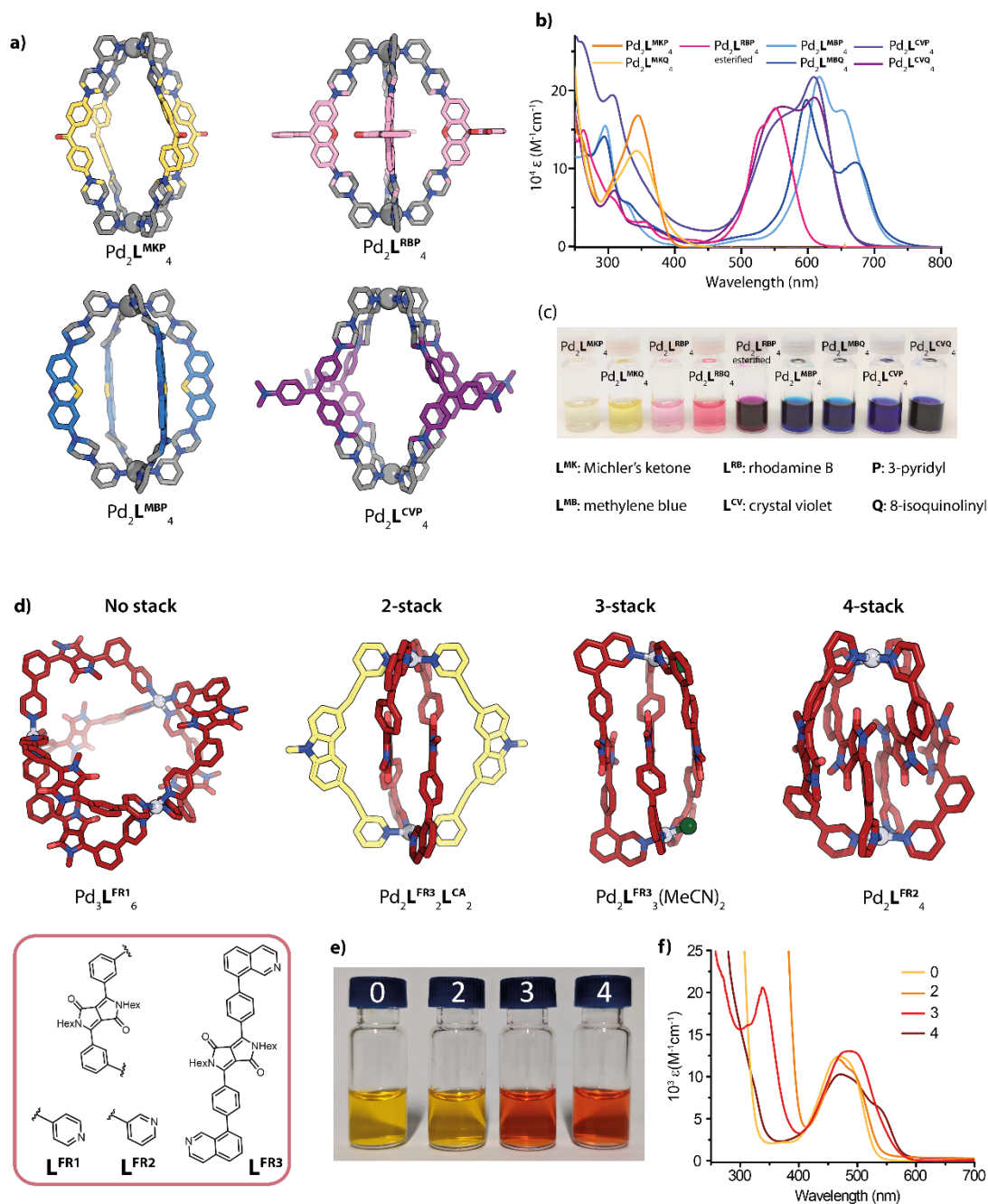


Figure 1.11: (a) Structure of the four pyridine-based Pd₂L₄ cages with coal-tar dyes as backbones. (b) UV-Vis spectra of the coal-tar dyes assemblies. (c) Photographs of the same species (esterified: to be kept in the chromophoric open structure, the carboxylic acid of rhodamine B was esterified with an ethyl group). (d) X-ray and DFT structures of the four different Ferrari Red assemblies, in order of increasing number of DPP units stacked. (e) Photographs of the four DPP assemblies with the number of stacked units. (f) UV-Vis spectra of the four assemblies.

BODIPY dyes are another family of organic dyes whose integration within coordination cages have been studied. For example, in 2013, Nitschke and co-workers have shown that a Zn_4L_6 tetrahedron based on such a dye could be used as an efficient probe for the selective detection of OAc^- , N_3^- , F^- and Cl^- , turning from purple to turquoise upon contact with those anions.^[132] Further articles on BODIPY-based cages include a study by Nitschke of the influence of the arrangement of the dyes in a Zn_4L_6 tetrahedron on their photophysical properties^[133] or the presentation of a new $\{[Pd_2L_4]@[Pd_4L_8]\}$ “cage-in-ring” assembly by Lützen and Clever.^[134]

Finally, porphyrins are one the most employed dyes in supramolecular coordination chemistry, primarily for their large planar aromatic surfaces, which are very well suited to serve as hydrophobic walls in coordination cages. Thus, many systems based on porphyrins or backbones of the same family have been described for example by Stang,^[135] Fujita,^[136] Torres and de la Torre,^[109,137-139] Heitz,^[140] or Yamaguchi.^[141] The group of Ribas has used a series of heteroleptic $Pd_3A_2B_4$ cages (where **A** is based on porphyrin) to bind different guests, including fullerene C_{60} ^[142-144] and studied the photosensitising properties of porphyrins when incorporated into supramolecular coordination assemblies.^[145] Indeed, they observed a longer lifetime of the porphyrins, the chromophores being better protected from photobleaching when part of the cage. In addition, in collaboration with the group of Von Delius, they employed the excellent fullerene binding properties of their porphyrin assemblies for regioselective functionalisation of C_{60} and C_{70} .^[48-50]

While porphyrins lie midway between organic and inorganic chromophores, our attention now shifts to species whose colours predominantly arise from metal centres, particularly through transition metal complexes. Two cases are to be considered here: the first is when metals responsible for the colour are directly incorporated into a metalloligand, and the second is when a coloured metal complex is used as the vertices of the self-assembled species.

In the first case, many different backbones incorporating a metal centres were used to assemble coordination cages, such as ferrocene,^[146] (cyclopentadienyl)(cyclobutadienyl) cobalt (CpCoCb),^[147] Fe(II) clathrochelates^[148-150] or Ru(II)(bipy)₃.^[151-153] Those backbones were not used for their absorbing properties however, but rather for their photophysical properties such as photosensitisation or emission, or for geometrical considerations.

The second case is dominated by examples from the group of Nitschke, as they are assembled from chelating ligands and transition metals, commonly leading to a strong metal-to-ligand charge transfer (MLCT) character, observable through a marked absorption band in the visible range.^[154,155] Most examples of such coloured cages come from examples with Fe(II), Cu(I), Co(II), or Cd(II). On the opposite, Zn(II) chelating cages do not lead to MLCT in the visible.^[156]

The group of Nitschke has used the colourful properties of their cages for several applications, such as a naked eye indicator for the phase transfer of cage $Fe_4L^1_4$ upon counteranion exchange (Fig. 1.12a-c),^[157] easy detection of the specific solubility of three different cages in three immiscible layers of water and ionic liquids **IL1** and **IL2** (Fig. 1.12f)^[158] and observation of molecular cargoes between immiscible layers.^[159,160] The principle was expanded to the preparation of a thermoresponsive $Fe_4L^2C_4$ cage capable of transferring from an aqueous/ionic liquid layer to an ethyl acetate organic layer and

vice-versa upon cooling and heating.^[161] The location of the cage can then be nicely followed by its bright purple hue (Fig 1.12e).

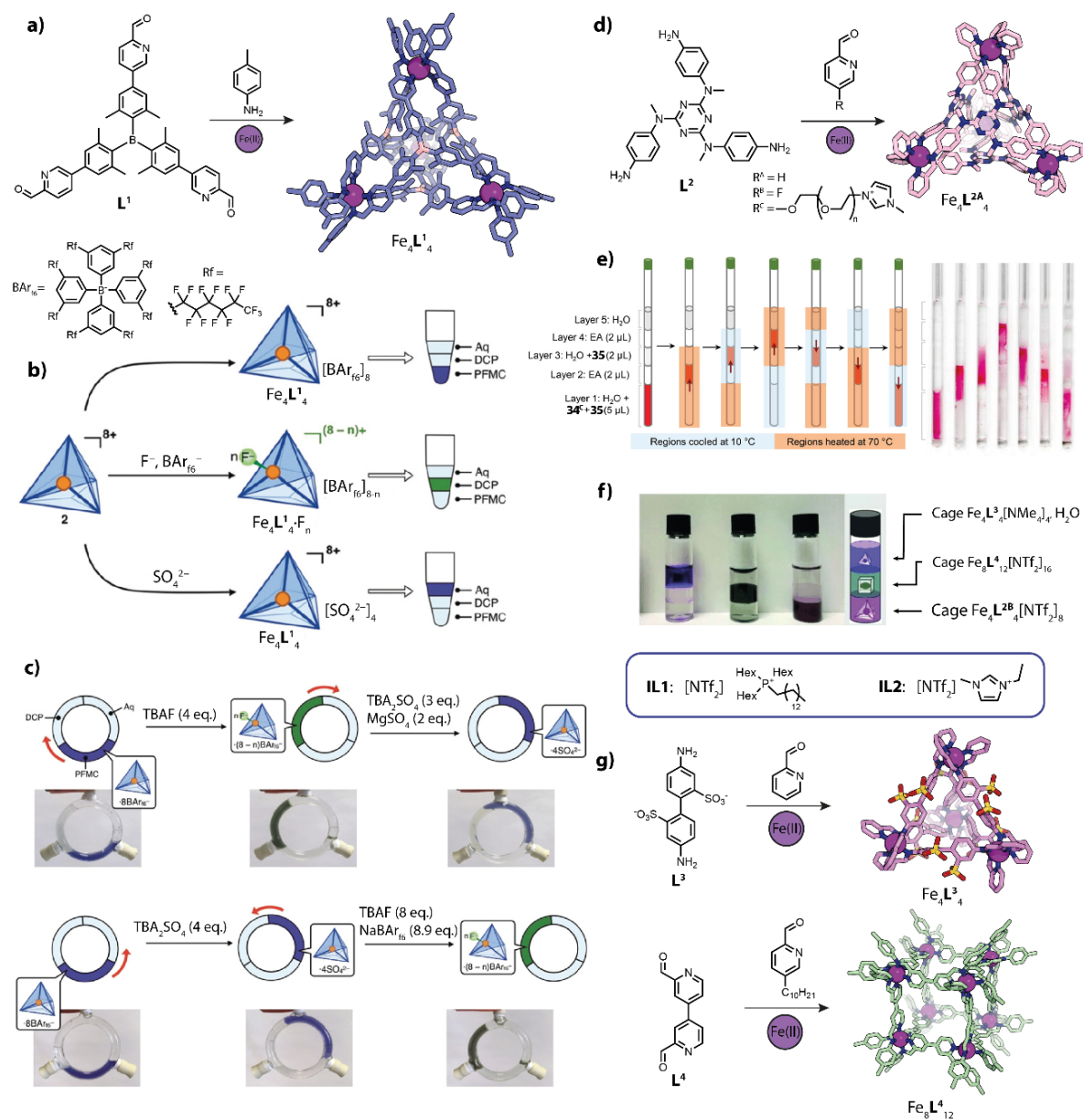


Figure 1.12: (a) Formation of cage Fe_4L^1_4 and its X-ray structure. (b) The three conditions allowing for the cage Fe_4L^1_4 to become soluble in three different immiscible solvents. (c) Transfer experiments of the cage into the three different solvents by addition of various additives. (d) Formation of cages Fe_4L^2_4 and the X-ray structure of $\text{Fe}_4\text{L}^2\text{A}_4$. (e) Phase transfer of the cage $\text{Fe}_4\text{L}^2\text{C}_4$ through selective heating and cooling of a glass tube. The cage is visible as the pink species in solution. (f) Selective solubility of three different cages Fe_4L^3_4 , $\text{Fe}_8\text{L}^4_{12}$, and $\text{Fe}_4\text{L}^2\text{B}_4$ in water and ionic liquids **IL1** and **IL2**. (g) Formation of Fe_4L^3_4 and $\text{Fe}_8\text{L}^4_{12}$ and their X-ray structures. The X-ray structure chosen to represent cage **32** is of its methyl-capped derivative. Rights of the illustrations: (b), (c), and (e) figures reused from refs. 157 and 161 (CC BY licence). (f) photograph reused with permission from Wiley, ref. 158.

1.4.2 Fluorescence

Fluorescence refers to the spontaneous emission of a photon from a singlet excited state of a molecule (called fluorophore). Thanks to the emission of said photon, the molecule can then relax to its ground state.

The construction of a fluorescent coordination cage is dependent on the integration of fluorophores as building blocks in its design, may it be as fluorescent ligands or metal nodes.^[121] However, one needs to stay cautious about the metals used to self-assemble the cage, as certain transition metals (such as Pd(II)) may lead to the quenching of the luminescence of the assembly. Zn(II) and other d^{10} metals are generally preferred due to their closed electronic shells as they prevent the quenching to photoelectron transfers. Therefore, the luminescent properties of the cages are not only dictated by the backbone, but also by the metal chosen to assemble the cage.

As an introduction fluorescent cages and Chapter 5, and to keep the length of this chapter from ballooning out of control, this section will only cover select examples of cages who gain their luminescent properties from their ligand. Therefore, I will not mention lanthanide-based cages and other similar systems.

To start off, let us have a look into assemblies based on tetraphenylene (TPE) ligands. This backbone has been extensively used over the years to prepare emissive metal-organic assemblies^[162-165] For example, the group of Stang has reported in 2015 a luminescent heteroleptic $Pt_8A_2B_4$ capsule.^[166] Interestingly, TPE-based ligand **A** is not fluorescent on its own but becomes emissive when incorporated into the supramolecular coordination assembly. Indeed, the relaxation from the excited state cannot proceed through molecular deformation as much as in the case of the free ligand. Therefore, the surplus energy is liberated as a photon. Moreover, the authors tested the aggregation-induced emission of the cage, and observed an increase in the quantum yield from 23.2% in pure DCM to 60.6% in 90% hexane, accompanied by a strong blue shift of the emission, going from yellow to cyan.

Next, the group of Sun has incorporated TPE as a bis-monodentate ligand in a lantern-shaped Pd_2L_4 cage.^[167] While the cage itself does not show emission, the authors have observed that its luminescence was greatly improved upon encapsulation of anions such as HCO_3^- , F^- , Cl^- and Br^- (Fig. 1.13a). In another work, Ming and co-workers have associated a TPE- or benzophenone-based metalloligand with a luminescent triphenylamine ligand to form two heteroleptic assemblies in which the luminophore is highly curved, which prevents aggregation and restricts the rotation of the phenyl rings, leading to luminescence of the coordination species in both solid and solution state.^[168] The problem of the aggregation of chromophores was also recently tackled by Nitschke and Feldmann in their study of a perylene diimide (PDI)-based Zn_8L_6 cubic assembly.^[169] Indeed, they observed that the integration of the PDI ligand into the supramolecular species preserved its electronic purity by preventing the dyes from aggregating. Specifically, this translates to a dramatic 100-fold increase in the emission of the embedded dye, a narrow linewidth of the absorbance bands, and a notably prolonged lifetime of the excited state into nanoseconds.

An interesting radical organic luminophore was recently used by Wang *et al.* to form a Zn_3L_2 emissive assembly.^[170] As mentioned before, the Zn(II) centre does not quench the emission of the ligand. Interestingly, the emission of the cage embedded in PMAA films was greatly increased and was subject to a red-shift upon the application of a 7 Tesla magnetic field, thanks to its radical nature.

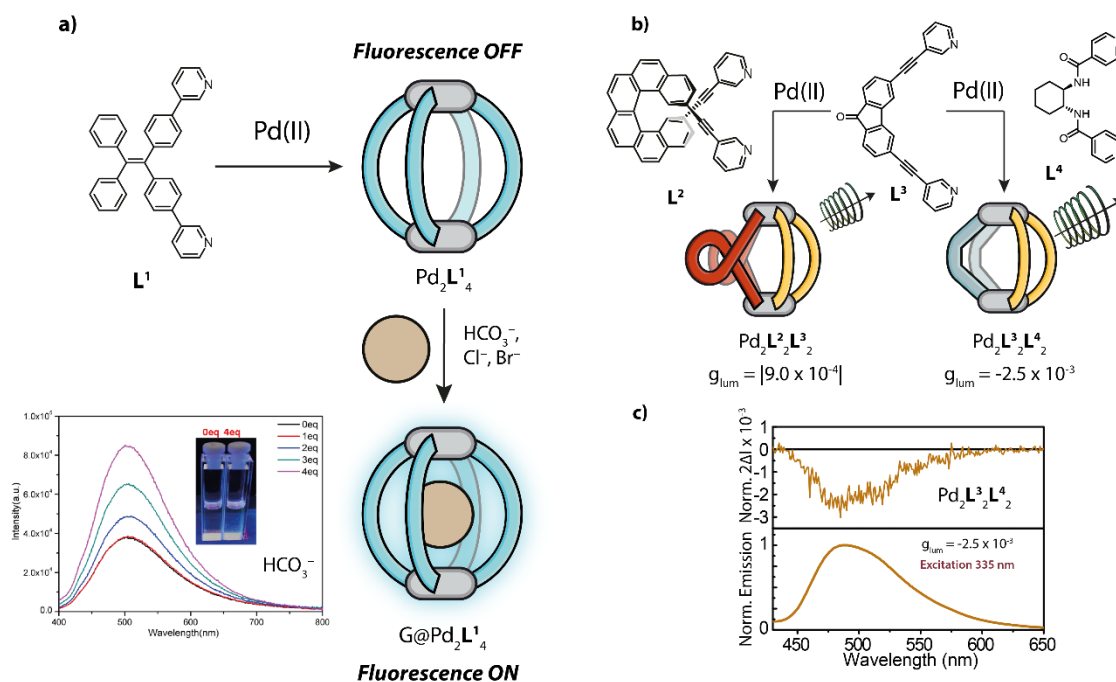


Figure 1.13: (a) Increase in fluorescence of cage Pd_2L^1_4 upon encapsulation of guest anions. Emission spectrum of cage titrated with HCO_3^- (Adapted with permission from Zhang, Sun, *et al. Inorg. Chem.* **2018**. Copyright 2018 American Chemical Society). (b) Formation of heteroleptic chiral emissive cages $\text{Pd}_2\text{L}^2_2\text{L}^3_2$ and $\text{Pd}_2\text{L}^3_2\text{L}^4_2$ from their respective ligands and the corresponding g_{lum} factors of their circularly polarised luminescence. (c) CPL spectrum of cage $\text{Pd}_2\text{L}^3_2\text{L}^4_2$.

Fluorescent cages were used by several authors as sensors for the encapsulation of guests through the quenching of their fluorescence (an opposite behaviour as the above-described encapsulation-induced emission). For example, Würthner and co-workers reported a PDI-based tetrahedron whose fluorescence was quenched upon the addition of PAHs.^[171] In addition, the group of Nitschke prepared a similar system with an emissive cationic ligand.^[172] This species was able to bind nucleotides monophosphates, and its fluorescence was in turn quenched upon the binding of AMP in its cavity.

While I previously discussed examples of assemblies with only one luminophore, the construction of heteroleptic cages allows for the integration of several emissive dyes into one supramolecular species. A notable example was reported by the group of Nitschke with a BODIPY-based Zn_4L_4 tetrahedron (red emission), end-capped with pyrene groups (green emission), and capable of encapsulating a perylene guest molecule (blue emission).^[132] The combination of three emissive moiety with their specific range of emission over the visible spectrum into a single assembly created a system capable of emitting a near-white light with a quantum yield of 11%.

Our group has recently introduced the fluorenone backbone in the assembly of Pd₃L₆ rings and Pd₄L₄L'₄ heteroleptic tetrahedra.^[87] Upon self-assembly with Pd(II), the emission of the fluorenone was conserved, but was blue-shifted. However, the quantum yields of the different species were not determined, making it difficult to assess to what extent the luminescence of the fluorenone was quenched. In a more recent study, chiral and non-chiral ligands were combined into emissive assemblies, capable of showing CPL through ligand-to-ligand chirality transfer (Fig. 1.13b). In more details, a Pd₂A₂B₂ assembly was prepared, where **A** is based on a fluorenone backbone and **B** is a chiral [6]-helicene-based ligand.^[99] Both ligands show luminescence by themselves (QY(**B**)=6.1%), but the emission of the heteroleptic assembly is greatly quenched (QY=1.5%), due to the presence of the Pd(II) centres.^[110,173] CD analysis confirmed that the chirality of ligand **B** is transferred to **A** thanks to the presence of CD signals in a region of the spectrum where only bands of **A** are visible. Despite the quenching of the luminescence, Circularly Polarised Luminescence (CPL) of the assembly could be measured; a signal in the characteristic band of fluorenone at around 500 nm was measured with a g_{lum} factor of 9.0·10⁻⁴ (free helicene ligand: g_{lum}=2.5·10⁻²). Furthermore, this factor could be increased to 3.5·10⁻³ upon encapsulation of a disulfonate guest. No signal could be recorded in the range of the emission of ligand **B**. In a follow-up study, the helicene ligand was replaced by a diaminocyclohexane-based counterpart.^[101] There, the g_{lum} factor of the free cage was enhanced, reaching 2.5·10⁻³ (Fig. 1.13c).

Finally, as mentioned previously, our group has introduced emissive DPP cores in the assembly of supramolecular Pd(II) assemblies (Fig. 1.11d).^[131] Just like for absorption, the emission maximum undergoes a red-shift upon an increase in the number of DPP cores stacked together. The highest quantum yield was measured to be 51.30% for the heteroleptic assembly Pd₂L^{FR3}₂L^{CA}₂, an incredible value for Pd(II) assemblies. With the aid of time-resolved photoluminescence spectroscopy, it was hypothesised that such a strong emission is caused by a strong communication between the two chromophores, DPP and carbazole, resulting in an intra-assembly excitation transfer from L^{CA} to L^{FR3}.

As the examples above have shown, only a small handful of fluorescent Pd₂L₄ exist, and no homoleptic structure can reach a quantum yield of two digits. A highly fluorescent Pd₂L₄ lantern-shaped cage can however be desirable, notably to be as a probe for the detection of analytes. Chapter 5 will introduce a new ligand for the preparation of fluorescent homo- and heteroleptic Pd₂L₄ cages.

1.5 REFERENCES

- [1] R. W. Saalfrank, A. Stark, K. Peters, H. G. von Schnering, *Angew. Chem. Int. Ed. Engl.* **1988**, *27*, 851–853.
- [2] M. Fujita, J. Yazaki, K. Ogura, *J. Am. Chem. Soc.* **1990**, *112*, 5645–5647.
- [3] M. Fujita, F. Ibukuro, K. Yamaguchi, K. Ogura, *J. Am. Chem. Soc.* **1995**, *117*, 4175–4176.
- [4] M. Fujita, S. Nagao, M. Iida, K. Ogata, K. Ogura, *J. Am. Chem. Soc.* **1993**, *115*, 1574–1576.
- [5] P. J. Stang, V. V. Zhdankin, *J. Am. Chem. Soc.* **1993**, *115*, 9808–9809.
- [6] P. J. Stang, J. A. Whiteford, *Organometallics* **1994**, *13*, 3776–3777.
- [7] P. J. Stang, D. H. Cao, S. Saito, A. M. Arif, *J. Am. Chem. Soc.* **1995**, *117*, 6273–6283.
- [8] P. J. Stang, D. H. Cao, *J. Am. Chem. Soc.* **1994**, *116*, 4981–4982.
- [9] M. Wienken, B. Lippert, E. Zangrando, L. Randaccio, *Inorg. Chem.* **1992**, *31*, 1983–1985.
- [10] H. Rauter, E. C. Hillgeris, A. Erxleben, B. Lippert, *J. Am. Chem. Soc.* **1994**, *116*, 616–624.
- [11] M. Fujita, D. Oguro, M. Miyazawa, H. Oka, K. Yamaguchi, K. Ogura, *Nature* **1995**, *378*, 469–471.
- [12] T. Kusukawa, T. Nakai, T. Okano, M. Fujita, *Chem. Lett.* **2003**, *32*, 284–285.
- [13] M. Yoshizawa, M. Tamura, M. Fujita, *Science* **2006**, *312*, 251–254.
- [14] Y. Nishioka, T. Yamaguchi, M. Kawano, M. Fujita, *J. Am. Chem. Soc.* **2008**, *130*, 8160–8161.
- [15] T. Murase, S. Horiuchi, M. Fujita, *J. Am. Chem. Soc.* **2010**, *132*, 2866–2867.
- [16] T. Murase, M. Fujita, *Chem. Rec.* **2010**, *10*, 342–347.
- [17] S. Horiuchi, T. Murase, M. Fujita, *Chem. Asian J.* **2011**, *6*, 1839–1847.
- [18] Y. Fang, T. Murase, M. Fujita, *Chem. Lett.* **2015**, *44*, 1095–1097.
- [19] H. Takezawa, T. Kanda, H. Nanjo, M. Fujita, *J. Am. Chem. Soc.* **2019**, *141*, 5112–5115.
- [20] B. Olenyuk, J. A. Whiteford, A. Fechtenkötter, P. J. Stang, *Nature* **1999**, *398*, 796.
- [21] S. Leininger, J. Fan, M. Schmitz, P. J. Stang, *Proc. Natl. Acad. Sci. U.S.A.* **2000**, *97*, 1380–1384.
- [22] S. R. Seidel, P. J. Stang, *Acc. Chem. Res.* **2002**, *35*, 972–983.
- [23] T. Beissel, R. E. Powers, K. N. Raymond, *Angew. Chem. Int. Ed. Engl.* **1996**, *35*, 1084–1086.
- [24] T. Beissel, R. E. Powers, T. N. Parac, K. N. Raymond, *J. Am. Chem. Soc.* **1999**, *121*, 4200–4206.
- [25] D. L. Caulder, R. E. Powers, T. N. Parac, K. N. Raymond, *Angew. Chem. Int. Ed.* **1998**, *37*, 1840–1843.
- [26] T. N. Parac, D. L. Caulder, K. N. Raymond, *J. Am. Chem. Soc.* **1998**, *120*, 8003–8004.
- [27] D. Fiedler, R. G. Bergman, K. N. Raymond, *Angew. Chem. Int. Ed.* **2004**, *43*, 6748–6751.
- [28] D. Fiedler, H. van Halbeek, R. G. Bergman, K. N. Raymond, *J. Am. Chem. Soc.* **2006**, *128*, 10240–10252.
- [29] C. J. Hastings, D. Fiedler, R. G. Bergman, K. N. Raymond, *J. Am. Chem. Soc.* **2008**, *130*, 10977–10983.
- [30] C. J. Hastings, M. D. Pluth, R. G. Bergman, K. N. Raymond, *J. Am. Chem. Soc.* **2010**, *132*, 6938–6940.
- [31] C. J. Hastings, R. G. Bergman, K. N. Raymond, *Chem. Eur. J.* **2014**, *20*, 3966–3973.
- [32] D. H. Leung, R. G. Bergman, K. N. Raymond, *J. Am. Chem. Soc.* **2006**, *128*, 9781–9797.
- [33] C. J. Brown, G. M. Miller, M. W. Johnson, R. G. Bergman, K. N. Raymond, *J. Am. Chem. Soc.* **2011**, *133*, 11964–11966.
- [34] W. M. Hart-Cooper, C. Zhao, R. M. Triano, P. Yaghoubi, H. L. Ozores, K. N. Burford, F. D. Toste, R. G. Bergman, K. N. Raymond, *Chem. Sci.* **2014**, *6*, 1383–1393.
- [35] D. M. Kaphan, F. D. Toste, R. G. Bergman, K. N. Raymond, *J. Am. Chem. Soc.* **2015**, *137*, 9202–9205.
- [36] L. J. Barbour, G. W. Orr, J. L. Atwood, *Nature* **1998**, *393*, 671–673.
- [37] D. McMorran, P. Steel, *Angew. Chem. Int. Ed.* **1998**, *37*, 3295–3297.
- [38] M. Han, D. M. Engelhard, G. H. Clever, *Chem. Soc. Rev.* **2014**, *43*, 1848–1860.
- [39] T. K. Ronson, S. Zarra, S. P. Black, J. R. Nitschke, *Chem. Commun.* **2012**, *49*, 2476–2490.
- [40] P. Mal, B. Breiner, K. Rissanen, J. R. Nitschke, *Science* **2009**, *324*, 1697–1699.
- [41] A. Ghosh, J. Pruchyathamkorn, C. F. Espinosa, J. R. Nitschke, *J. Am. Chem. Soc.* **2024**, *146*, 2568–2573.
- [42] Z. Lu, T. K. Ronson, A. W. Heard, S. Feldmann, N. Vanthuyne, A. Martinez, J. R. Nitschke, *Nat. Chem.* **2023**, *15*, 405–412.
- [43] S. F. Lincoln, *Helv. Chim. Acta* **2005**, *88*, 523–545.

- [44] E. G. Percástegui, *Eur. J. Inorg. Chem.* **2021**, 2021, 4425–4438.
- [45] E. Benchimol, B.-N. T. Nguyen, T. K. Ronson, J. R. Nitschke, *Chem. Soc. Rev.* **2022**, 51, 5101–5135.
- [46] M. Scherer, D. L. Caulder, D. W. Johnson, K. N. Raymond, *Angew. Chem. Int. Ed.* **1999**, 38, 1587–1592.
- [47] C. García-Simón, M. Costas, X. Ribas, *Chem. Soc. Rev.* **2015**, 45, 40–62.
- [48] E. Ubasart, O. Borodin, C. Fuertes-Espinosa, Y. Xu, C. García-Simón, L. Gómez, J. Juanhuix, F. Gándara, I. Imaz, D. MasPOCH, M. von Delius, X. Ribas, *Nat. Chem.* **2021**, 13, 420–427.
- [49] F. M. Steudel, E. Ubasart, L. Leanza, M. Pujals, T. Parella, G. M. Pavan, X. Ribas, M. von Delius, *Angew. Chem. Int. Ed.* **2023**, 62, e202309393.
- [50] V. Iannace, C. Sabrià, Y. Xu, M. von Delius, I. Imaz, D. MasPOCH, F. Feixas, X. Ribas, *J. Am. Chem. Soc.* **2024**, 146, 5186–5194.
- [51] D. M. Wood, W. Meng, T. K. Ronson, A. R. Stefankiewicz, J. K. M. Sanders, J. R. Nitschke, *Angew. Chem. Int. Ed.* **2015**, 54, 3988–3992.
- [52] E. G. Percástegui, V. Jancik, *Coord. Chem. Rev.* **2020**, 407, 213165.
- [53] F. J. Rizzuto, J. R. Nitschke, *Nat. Chem.* **2017**, 9, 903–908.
- [54] K. Yazaki, M. Akita, S. Prusty, D. K. Chand, T. Kikuchi, H. Sato, M. Yoshizawa, *Nat. Commun.* **2017**, 8, 15914.
- [55] M. Yamashina, T. Yuki, Y. Sei, M. Akita, M. Yoshizawa, *Chem. Eur. J.* **2015**, 21, 4200–4204.
- [56] T. Tsutsui, L. Catti, K. Yoza, M. Yoshizawa, *Chem. Sci.* **2020**, 11, 8145–8150.
- [57] K. Kumazawa, Y. Yamanoi, M. Yoshizawa, T. Kusukawa, M. Fujita, *Angew. Chem. Int. Ed.* **2004**, 43, 5936–5940.
- [58] S. Wang, T. Sawada, K. Ohara, K. Yamaguchi, M. Fujita, *Angew. Chem. Int. Ed.* **2016**, 55, 2063–2066.
- [59] T. K. Ronson, J. P. Carpenter, J. R. Nitschke, *Chem* **2022**, 8, 557–568.
- [60] S. Wang, T. Sawada, M. Fujita, *Chem. Commun.* **2016**, 52, 11653–11656.
- [61] M. Yoshizawa, T. Kusukawa, M. Fujita, S. Sakamoto, K. Yamaguchi, *J. Am. Chem. Soc.* **2001**, 123, 10454–10459.
- [62] P. Cheng, L. Cai, S. Li, S. Hu, D. Yan, L. Zhou, Q. Sun, *Angew. Chem. Int. Ed.* **2020**, 59, 23569–23573.
- [63] T. Zhang, L.-P. Zhou, X.-Q. Guo, L.-X. Cai, Q.-F. Sun, *Nat. Commun.* **2017**, 8, 15898.
- [64] S.-C. Li, T. Zhang, X.-P. Deng, X.-Q. Guo, L.-P. Zhou, F. Guo, Q.-F. Sun, *Inorg. Chem. Commun.* **2018**, 92, 69–73.
- [65] S. Löffler, J. Lübben, L. Krause, D. Stalke, B. Dittrich, G. H. Clever, *J. Am. Chem. Soc.* **2015**, 137, 1060–1063.
- [66] M. Fukuda, R. Sekiya, R. Kuroda, *Angew. Chem. Int. Ed.* **2008**, 47, 706–710.
- [67] R. Sekiya, M. Fukuda, R. Kuroda, *J. Am. Chem. Soc.* **2012**, 134, 10987–10997.
- [68] S. Freye, J. Hey, A. Torras-Galán, D. Stalke, R. Herbst-Irmer, M. John, G. H. Clever, *Angew. Chem. Int. Ed.* **2012**, 51, 2191–2194.
- [69] S. Freye, R. Michel, D. Stalke, M. Pawliczek, H. Frauendorf, G. H. Clever, *J. Am. Chem. Soc.* **2013**, 135, 8476–8479.
- [70] R. Zhu, J. Lübben, B. Dittrich, G. H. Clever, *Angew. Chem. Int. Ed.* **2015**, 54, 2796–2800.
- [71] R. Zhu, I. Regeni, J. J. Holstein, B. Dittrich, M. Simon, S. Prévost, M. Gradziński, G. H. Clever, *Angew. Chem. Int. Ed.* **2018**, 57, 13652–13656.
- [72] W. M. Bloch, J. J. Holstein, B. Dittrich, W. Hiller, G. H. Clever, *Angew. Chem. Int. Ed.* **2018**, 57, 5534–5538.
- [73] K. Wu, B. Zhang, C. Drechsler, J. J. Holstein, G. H. Clever, *Angew. Chem. Int. Ed.* **2020**, 60, 6403–6407.
- [74] L. Yang, X. Jing, B. An, C. He, Y. Yang, C. Duan, *Chem. Sci.* **2017**, 9, 1050–1057.
- [75] I. A. Riddell, T. K. Ronson, J. K. Clegg, C. S. Wood, R. A. Bilbeisi, J. R. Nitschke, *J. Am. Chem. Soc.* **2014**, 136, 9491–9498.
- [76] J. Mosquera, T. K. Ronson, J. R. Nitschke, *J. Am. Chem. Soc.* **2016**, 138, 1812–1815.
- [77] F. J. Rizzuto, J. P. Carpenter, J. R. Nitschke, *J. Am. Chem. Soc.* **2019**, 141, 9087–9095.
- [78] Y. Domoto, M. Abe, T. Kikuchi, M. Fujita, *Angew. Chem. Int. Ed.* **2020**, 59, 3450–3454.
- [79] Y. Domoto, M. Abe, M. Fujita, *J. Am. Chem. Soc.* **2021**, 143, 8578–8582.
- [80] W. Jiang, C. A. Schalley, *Proc. Natl. Acad. Sci.* **2009**, 106, 10425–10429.
- [81] Z. He, W. Jiang, C. A. Schalley, *Chem. Soc. Rev.* **2014**, 44, 779–789.
- [82] W. M. Bloch, G. H. Clever, *Chem. Commun.* **2017**, 53, 8506–8516.
- [83] S. Pullen, J. Tessarolo, G. H. Clever, *Chem. Sci.* **2021**, 12, 7269–7293.
- [84] Felix. J. Rizzuto, J. R. Nitschke, *J. Am. Chem. Soc.* **2020**, 142, 7749–7753.

- [85] A. M. Johnson, R. J. Hooley, *Inorg. Chem.* **2011**, *50*, 4671–4673.
- [86] D. Preston, J. E. Barnsley, K. C. Gordon, J. D. Crowley, *J. Am. Chem. Soc.* **2016**, *138*, 10578–85.
- [87] J. Tessarolo, H. Lee, E. Sakuda, K. Umakoshi, G. H. Clever, *J. Am. Chem. Soc.* **2021**, *143*, 6339–6344.
- [88] M. Yoshizawa, M. Nagao, K. Kumazawa, M. Fujita, *J. Organomet. Chem.* **2005**, *690*, 5383–5388.
- [89] R. Zhu, W. M. Bloch, J. J. Holstein, S. Mandal, L. V. Schäfer, G. H. Clever, *Chem. Eur. J.* **2018**, *24*, 12976–12982.
- [90] B. Chen, J. J. Holstein, S. Horiuchi, W. G. Hiller, G. H. Clever, *J. Am. Chem. Soc.* **2019**, *141*, 8907–8913.
- [91] B. Chen, S. Horiuchi, J. J. Holstein, J. Tessarolo, G. H. Clever, *Chem. Eur. J.* **2019**, *25*, 14921–14927.
- [92] B. Chen, J. J. Holstein, A. Platzek, L. Schneider, K. Wu, G. H. Clever, *Chem. Sci.* **2022**, *13*, 1829–1834.
- [93] R.-J. Li, J. Tessarolo, H. Lee, G. H. Clever, *J. Am. Chem. Soc.* **2021**, *143*, 3865–3873.
- [94] W. M. Bloch, Y. Abe, J. J. Holstein, C. M. Wandtke, B. Dittrich, G. H. Clever, *J. Am. Chem. Soc.* **2016**, *138*, 13750–13755.
- [95] Q. Sun, S. Sato, M. Fujita, *Angew. Chem. Int. Ed.* **2014**, *53*, 13510–13513.
- [96] W. M. Bloch, J. J. Holstein, W. Hiller, G. H. Clever, *Angew. Chem. Int. Ed.* **2017**, *56*, 8285–8289.
- [97] S. Saha, B. Holzapfel, Y.-T. Chen, K. Terlinden, P. Lill, C. Gatsogiannis, H. Rehage, G. H. Clever, *J. Am. Chem. Soc.* **2018**, *140*, 17384–17388.
- [98] A. Platzek, S. Juber, C. Yurtseven, S. Hasegawa, L. Schneider, C. Drechsler, K. E. Ebbert, R. Rudolf, Q. Yan, J. J. Holstein, L. V. Schäfer, G. H. Clever, *Angew. Chem. Int. Ed.* **2022**, *61*, e202209305.
- [99] K. Wu, J. Tessarolo, A. Baksi, G. H. Clever, *Angew. Chem. Int. Ed.* **2022**, *61*, e202205725.
- [100] S. Sudan, R.-J. Li, S. M. Jansze, A. Platzek, R. Rudolf, G. H. Clever, F. Fadaei-Tirani, R. Scopelliti, K. Severin, *J. Am. Chem. Soc.* **2021**, *143*, 1773–1778.
- [101] J. Tessarolo, E. Benchimol, A. Jouaiti, M. W. Hosseini, G. H. Clever, *Chem. Commun.* **2023**, *59*, 3467–3470.
- [102] R. G. DiNardi, S. Rasheed, S. S. Capomolla, M. H. Chak, I. A. Middleton, L. K. Macreadie, J. P. Violi, W. A. Donald, P. J. Lusby, J. E. Beves, *J. Am. Chem. Soc.* **2024**, *146*, 21196–21202.
- [103] Y. Liu, S. Liao, W. Dai, Q. Bai, S. Lu, H. Wang, X. Li, Z. Zhang, P. Wang, W. Lu, Q. Zhang, *Angew. Chem. Int. Ed.* **2023**, *62*, e202217215.
- [104] E. Benchimol, I. Regeni, B. Zhang, M. Kabiri, J. J. Holstein, G. H. Clever, *J. Am. Chem. Soc.* **2024**, *146*, 6905–6911.
- [105] K. Wu, E. Benchimol, A. Baksi, G. H. Clever, *Nat. Chem.* **2024**, 1–8.
- [106] T. Abe, N. Sanada, K. Takeuchi, A. Okazawa, S. Hiraoka, *J. Am. Chem. Soc.* **2023**, *145*, 28061–28074.
- [107] B. Zhang, H. Lee, J. J. Holstein, G. H. Clever, *Angew. Chem. Int. Ed.* **2024**, e202404682.
- [108] C. Li, Y. Zuo, Y.-Q. Zhao, S. Zhang, *Chem. Lett.* **2020**, *49*, 1356–1366.
- [109] C. G. Claessens, T. Torres, *J. Am. Chem. Soc.* **2002**, *124*, 14522–14523.
- [110] T. R. Schulte, J. J. Holstein, G. H. Clever, *Angew. Chem. Int. Ed.* **2019**, *58*, 5562–5566.
- [111] S. Ghorai, R. Natarajan, *Chem. A Eur. J.* **2023**, *29*, e202203085.
- [112] S. Ghorai, S. Maji, B. Paul, K. Samanta, S. K. Sen, R. Natarajan, *Chem. Asian J.* **2023**, e202201312.
- [113] C. Gütz, R. Hovorka, G. Schnakenburg, A. Lützen, *Chem. Eur. J.* **2013**, *19*, 10890–10894.
- [114] T. Tateishi, T. Kojima, S. Hiraoka, *Commun. Chem.* **2018**, *1*, 20.
- [115] C. Stuckhardt, D. Roke, W. Danowski, E. Otten, S. J. Wezenberg, B. L. Feringa, *Beilstein. J. Org. Chem.* **2019**, *15*, 2767–2773.
- [116] T. Mirkovic, E. E. Ostroumov, J. M. Anna, R. van Grondelle, Govindjee, G. D. Scholes, *Chem. Rev.* **2017**, *117*, 249–293.
- [117] R. Ham, C. J. Nielsen, S. Pullen, J. N. H. Reek, *Chem Rev* **2023**, *123*, 5225–5261.
- [118] T. K. Piskorz, V. Martí-Centelles, R. L. Spicer, F. Duarte, P. J. Lusby, *Chem. Sci.* **2023**, *14*, 11300–11331.
- [119] A. Brzechwa-Chodzyńska, W. Drożdż, J. Harrowfield, A. R. Stefankiewicz, *Coordin. Chem. Rev.* **2021**, *434*, 213820.
- [120] C. T. McTernan, J. A. Davies, J. R. Nitschke, *Chem. Rev.* **2022**, *122*, 10393–10437.
- [121] Y. Jiao, Y. Zuo, H. Yang, X. Gao, C. Duan, *Coord. Chem. Rev.* **2021**, *430*, 213648.
- [122] Z. Li, N. Kishi, K. Hasegawa, M. Akita, M. Yoshizawa, *Chem. Commun.* **2011**, *47*, 8605–8607.
- [123] Z. Li, N. Kishi, K. Yoza, M. Akita, M. Yoshizawa, *Chem. Eur. J.* **2012**, *18*, 8358–8365.
- [124] T. Tsutsui, S. Kusaba, M. Yamashina, M. Akita, M. Yoshizawa, *Chem. Eur. J.* **2019**, *25*, 4320–4324.
- [125] H. Dobashi, L. Catti, Y. Tanaka, M. Akita, M. Yoshizawa, *Angew. Chem. Int. Ed.* **2020**, *59*, 11881–11885.

- [126] N. Kishida, K. Matsumoto, Y. Tanaka, M. Akita, H. Sakurai, M. Yoshizawa, *J. Am. Chem. Soc.* **2020**, *142*, 9599–9603.
- [127] M. Ueda, N. Kishida, L. Catti, M. Yoshizawa, *Chem. Sci.* **2022**, *13*, 8642–8648.
- [128] A. Walther, I. Regeni, J. J. Holstein, G. H. Clever, *J. Am. Chem. Soc.* **2023**, *145*, 25365–25371.
- [129] I. Regeni, B. Chen, M. Frank, A. Baksi, J. J. Holstein, G. H. Clever, *Angew. Chem. Int. Ed.* **2021**, *60*, 5673–5678.
- [130] I. Regeni, Dye-Based Coordination Cages, **2020**, PhD thesis
- [131] I. Regeni, R. Chowdhury, K. Terlinden, S. Horiuchi, J. J. Holstein, S. Feldmann, G. H. Clever, *Angew. Chem. Int. Ed.* **2023**, *62*, e202308288.
- [132] P. P. Neelakandan, A. Jiménez, J. R. Nitschke, *Chem. Sci.* **2014**, *5*, 908–915.
- [133] A. J. Musser, P. P. Neelakandan, J. M. Richter, H. Mori, R. H. Friend, J. R. Nitschke, *J. Am. Chem. Soc.* **2017**, *139*, 12050–12059.
- [134] M. Käseborn, J. J. Holstein, G. H. Clever, A. Lützen, *Angew. Chem. Int. Ed.* **2018**, *57*, 12171–12175.
- [135] Y. Shi, I. Sánchez-Molina, C. Cao, T. R. Cook, P. J. Stang, *Proc. Natl. Acad. Sci. U.S.A.* **2014**, *111*, 9390–9395.
- [136] N. Fujita, K. Biradha, M. Fujita, S. Sakamoto, K. Yamaguchi, *Angew. Chem. Int. Ed.* **2001**, *40*, 1718–1721.
- [137] C. G. Claessens, M. J. Vicente-Arana, T. Torres, *Chem. Commun.* **2008**, *0*, 6378–6380.
- [138] E. Fazio, C. J. E. Haynes, G. de la Torre, J. R. Nitschke, T. Torres, *Chem. Comm.* **2018**, *54*, 2651–2654.
- [139] A. Salazar, M. Moreno-Simoni, S. Kumar, J. Labella, T. Torres, G. de la Torre, *Angew. Chem. Int. Ed.* **2023**, e202311255.
- [140] P. Ballester, M. Claudel, S. Durot, L. Kocher, L. Schoepff, V. Heitz, *Chem. Eur. J.* **2015**, *21*, 15339–15348.
- [141] A. Ikeda, M. Ayabe, S. Shinkai, S. Sakamoto, K. Yamaguchi, *Org. Lett.* **2000**, *2*, 3707–3710.
- [142] C. García-Simón, M. Garcia-Borràs, L. Gómez, T. Parella, S. Osuna, J. Juanhuix, I. Imaz, D. MasPOCH, M. Costas, X. Ribas, *Nat. Commun.* **2014**, *5*, 5557.
- [143] C. García-Simón, M. Garcia-Borràs, L. Gómez, I. Garcia-Bosch, S. Osuna, M. Swart, J. M. Luis, C. Rovira, M. Almeida, I. Imaz, D. MasPOCH, M. Costas, X. Ribas, *Chem. Eur. J.* **2013**, *19*, 1445–1456.
- [144] C. Colombar, G. Szalóki, M. Allain, L. Gómez, S. Goeb, M. Sallé, M. Costas, X. Ribas, *Chem. Eur. J.* **2017**, *23*, 3016–3022.
- [145] C. Colombar, C. Fuertes-Espinosa, S. Goeb, M. Sallé, M. Costas, L. Blancafort, X. Ribas, *Chem. Eur. J.* **2018**, *24*, 4371–4381.
- [146] R. A. S. Vasdev, J. A. Findlay, A. L. Garden, J. D. Crowley, *Chem. Commun.* **2019**, *55*, 7506–7509.
- [147] Q. Gan, T. K. Ronson, D. A. Vosburg, J. D. Thoburn, J. R. Nitschke, *J. Am. Chem. Soc.* **2015**, *137*, 1770–1773.
- [148] M. D. Wise, J. J. Holstein, P. Pattison, C. Besnard, E. Solari, R. Scopelliti, G. Bricogne, K. Severin, *Chem. Sci.* **2015**, *6*, 1004–1010.
- [149] S. M. Jansze, M. D. Wise, A. V. Vologzhanina, R. Scopelliti, K. Severin, *Chem. Sci.* **2017**, *8*, 1901–1908.
- [150] S. M. Jansze, D. Ortiz, F. F. Tirani, R. Scopelliti, L. Menin, K. Severin, *Chem. Commun.* **2018**, *54*, 9529–9532.
- [151] A. J. Metherell, M. D. Ward, *Chem. Commun.* **2014**, *50*, 10979–10982.
- [152] C. E. Hauke, A. N. Oldacre, C. R. P. Fulong, A. E. Friedman, T. R. Cook, *Inorg. Chem.* **2018**, *57*, 3587–3595.
- [153] S. Oldknow, D. R. Martir, V. E. Pritchard, M. A. Blitz, C. W. G. Fishwick, E. Zysman-Colman, M. J. Hardie, *Chem. Sci.* **2018**, *9*, 8150–8159.
- [154] S. Schenker, A. Hauser, W. Wang, I. Y. Chan, *J. Chem. Phys.* **1998**, *109*, 9870–9878.
- [155] M. Hutin, C. J. Cramer, L. Gagliardi, A. R. M. Shahi, G. Bernardinelli, R. Cerny, J. R. Nitschke, *J. Am. Chem. Soc.* **2007**, *129*, 8774–8780.
- [156] S. E. Howson, L. E. N. Allan, N. P. Chmel, G. J. Clarkson, R. J. Deeth, A. D. Faulkner, D. H. Simpson, P. Scott, *Dalton Trans.* **2011**, *40*, 10416–10433.
- [157] N. Mihara, T. K. Ronson, J. R. Nitschke, *Angew. Chem. Int. Ed.* **2019**, *58*, 12497–12501.
- [158] A. B. Grommet, J. L. Bolliger, C. Browne, J. R. Nitschke, *Angew. Chem. Int. Ed.* **2015**, *54*, 15100–15104.
- [159] A. B. Grommet, J. R. Nitschke, *J. Am. Chem. Soc.* **2017**, *139*, 2176–2179.
- [160] Angela B. Grommet, J. B. Hoffman, E. G. Percástegui, J. Mosquera, D. J. Howe, J. L. Bolliger, J. R. Nitschke, *J. Am. Chem. Soc.* **2018**, *140*, 14770–14776.
- [161] B. T. Nguyen, A. B. Grommet, A. Tron, M. C. A. Georges, J. R. Nitschke, *Adv. Mater.* **2020**, *32*, 1907241.
- [162] X. Yan, P. Wei, Y. Liu, M. Wang, C. Chen, J. Zhao, G. Li, M. L. Saha, Z. Zhou, Z. An, X. Li, P. J. Stang, *J. Am. Chem. Soc.* **2019**, *141*, 9673–9679.
- [163] C. Mu, Z. Zhang, Y. Hou, H. Liu, L. Ma, X. Li, S. Ling, G. He, M. Zhang, *Angew. Chem. Int. Ed.* **2021**, *60*, 12293–12297.

- [164] M. Li, S. Jiang, Z. Zhang, X.-Q. Hao, X. Jiang, H. Yu, P. Wang, B. Xu, M. Wang, W. Tian, *CCS Chem.* **2020**, *2*, 337–348.
- [165] L. Bian, Y. Liang, Z. Liu, *Acs Appl. Nano. Mater* **2022**, *5*, 13940–13958
- [166] X. Yan, T. R. Cook, P. Wang, F. Huang, P. J. Stang, *Nat. Chem.* **2015**, *7*, 342–348.
- [167] T. Zhang, G.-L. Zhang, Q.-Q. Yan, L.-P. Zhou, L.-X. Cai, X.-Q. Guo, Q.-F. Sun, *Inorg. Chem.* **2017**, *57*, 3596–3601.
- [168] Y. Zeng, J. Shi, Z. Wang, X. Zhang, J. Li, H. Su, F. Fang, H. Zhang, M. Wang, *Inorg. Chem.* **2023**, *62*, 17150–17156.
- [169] I. Heckelmann, Z. Lu, J. C. A. Prentice, F. Auras, T. K. Ronson, R. H. Friend, J. R. Nitschke, S. Feldmann, *Angew. Chem.* **2023**, *135*, e202216729
- [170] J. Shi, W. Xu, H. Yu, X. Wang, F. Jin, Q. Zhang, H. Zhang, Q. Peng, A. Abdurahman, M. Wang, *J. Am. Chem. Soc.* **2023**, *145*, 24081–24088
- [171] P. D. Frischmann, V. Kunz, F. Würthner, *Angew. Chem. Int. Ed.* **2015**, *54*, 7285–7289.
- [172] A. J. Plajer, E. G. Percástegui, M. Santella, F. J. Rizzuto, Q. Gan, B. W. Laursen, J. R. Nitschke, *Angew. Chem. Int. Ed.* **2019**, *58*, 4200–4204.
- [173] M. Frank, M. D. Johnstone, G. H. Clever, *Chem. Eur. J.* **2016**, *22*, 14104–14125.

2 SCOPE OF THE THESIS

The present work will delve into the preparation and characterisation of palladium(II)-based coordination cages which integrate a chromophore into the structure of their organic ligands. Much effort has been made by our group, as well as other research laboratories, to bring functionalities into the structure of coordination cages, and that effort has notably included the use of supramolecular assemblies as tools for sensing, photocatalysis, or molecular recognition, by constructing them with chromophoric building blocks. Indeed, emergent photophysical properties may be observed when dyes become spatially arranged in specific ways in larger structures, as compared to free-moving dyes in solutions. By studying the properties of coordination cages made from chromophoric ligands, we may gain greater insight into the future possibilities offered by such designs in real-world applications. While our group has recently introduced coal-tar dyes and diketopyrrolopyrrole as colourful cores for the assembly of coordination cages, we were also interested in using a much simpler (structurally speaking) molecule: azulene. Despite its structural isomerism with naphthalene, this small aromatic hydrocarbon possesses interesting electronic properties leading it to show colours, among others. Moreover, this core has barely been studied in relation to supramolecular systems and could potentially bear a lot of potential there. Therefore, initial steps were taken to introduce this building block, as well as derivatives of fluorescent thieno[3,4-b]pyrazine, into our family of palladium-based coordination cages.

Based on this premise, the main steps for this work are the following:

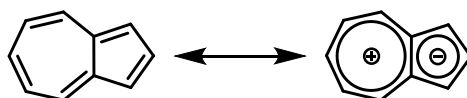
- Construction of **chromophoric coordination cages**: design of several ligands bis-monodentate ligands based on the two aforementioned backbones, and the construction of homo- and heteroleptic Pd(II) assemblies from the said ligands. Study of the resulting structures by NMR, mass spectrometry (ESI-MS), and X-ray diffraction. Characterisation of their photophysical properties by UV-Vis, CD, emission, and CPL spectroscopy.
- Study of the binding of negatively charged guests to the cages, and the study of their host-guest complexes as well as the potential transformations induced by the binding events.
- Synthesis of chiral biazulene ligands, and the study of the chiral self-sorting of the cages made from them, as well as the chiral recognition between chiral cages and chiral guests.

The first chapter of the thesis covers the preparation of cages based on 1,3-substituted azulene. Next, by complexifying the ligand, the study of chiral biazulene cages is presented in the second chapter. Finally, the last chapter presents several structures made from the thieno[3,4-b]pyrazine backbone.

3 GUEST-INDUCED TRANSFORMATION OF AN AZULENE-BASED Pd_2L_4 CAGE TO A Pd_4L_8 TETRAHEDRON

3.1 AZULENE

Azulene is a bicyclic aromatic hydrocarbon, isomeric to naphthalene, with the formula $C_{10}H_8$. Unlike its even-ringed isomer, azulene is composed of one five-membered ring fused to a seven-membered ring. This asymmetry is the source of the peculiar electronic and visual properties of azulene. Indeed, pure azulene presents as dark blue crystals in the solid state, an unusual feature for such a small hydrocarbon, especially compared to its colourless cousin, naphthalene. This colour has been explained by the electronic delocalisation between the seven-membered to the five-membered ring that enables both halves to be stabilised by a 6π -electron aromatic system.^[1] In that regard, the structure of azulene can be visualised as fused tropylium and cyclopentadienyl ions, imparting a zwitterionic character to the structure (Scheme 3.1). This lends it a notable 1.08 D dipole, a rarely observed property for small aromatic hydrocarbons.^[2] Moreover, thanks to the electronic delocalisation, the energy between the HOMO and the LUMO of azulene is lowered compared to naphthalene, thus imparting a transition band in the visible range of the electromagnetic spectrum.^[3]



Scheme 3.1: neutral and zwitterionic resonance structures of azulene.

However, the intensity of this transition is much lower than expected for π - π^* transition absorptions.^[4] This has been explained by a special mismatch in the overlap between the HOMO and the LUMO, making the transition more difficult between those two orbitals than for example between their HOMO and LUMO+1.^[3,5] A more recent computational work by Ottson, Slanina, and co-workers^[6] has also demonstrated that the S_1 state of azulene is anti-aromatic, thereby making the S_0 - S_1 transition forbidden. This also explains the anti-Kasha fluorescence of azulene, where an emission from the S_2 to the S_0 state is observed, rather than from the S_1 .^[7]

Despite its peculiar properties, azulene has attracted significantly less attention in chemistry in general than its cousin naphthalene. For example, at the time of writing these lines (4th of April, 2024), a search for the term “azulene” on SciFinder returned 5’255 documents (excluding patents), while “naphthalene” returned 81’970 documents. This staggering difference may be explained in part by the scarcity of azulene derivatives in nature (found for instance in some steam-distilled essential oils^[8]) and its need to be synthesised rather than extracted from petrochemical starting material,^[1]

leading it to be an expensive product (2024 prices): 167€⁹/g at Sigma,^[9] compared to 1.78€¹⁰/g for naphthalene.^[10]

This rarity and relative anonymity of azulene means that it has barely been used in supramolecular chemistry to this day. The most prominent derivatives of azulene used in the field have been “calix-azulenes”, analogues of the famous calix[n]arene class of molecules.^[11] Several syntheses have been reported to date.^[12–14] However, the study of their properties as guest binding hosts has only been limited to fullerene C₆₀^[15] and a series of tetraalkylammonium salts.^[16]

Azulene derivatives have also been used as colour-changing probes for the detection of anions such as fluorides^[17] or a broader range of analytes.^[18–20] Closer to the subject of the present study, Mazaki and co-workers have shown the preparation of a self-assembled Pd₃L₃Cl₆ triangular coordination compound from a chiral 2,2'-dipyridyl-1,1'-biazulene ligand (Fig. 3.1).^[21]

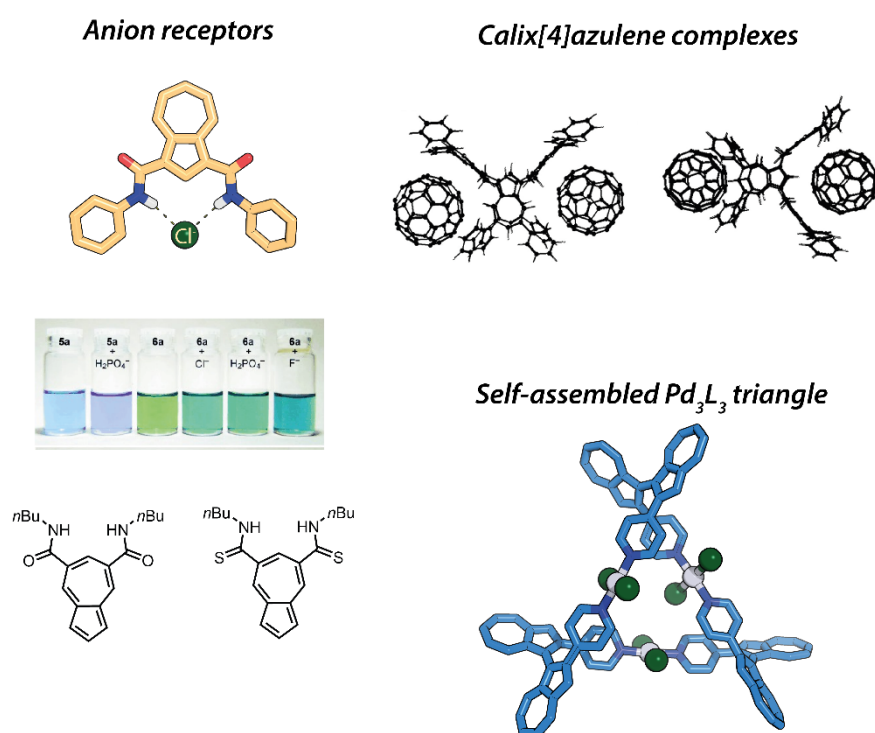


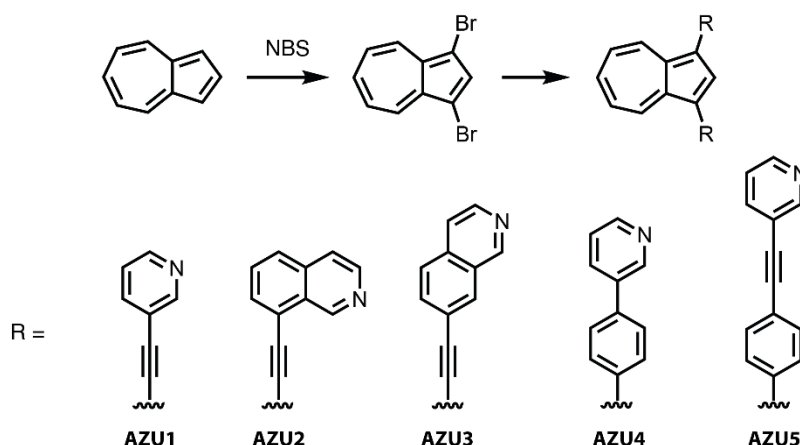
Figure 3.1: 3 different azulene-based supramolecular systems: chromophoric anion receptors (photograph reproduced by authorisation of Elsevier, Copyright 2005, ref. 18), calix[4]azulene-C₆₀ complex (figure reused with the authorisation of Taylor & Francis, Copyright 2017, ref. 15), and self-assembled Pd₃L₃Cl₆ triangle.

Recognising the interesting potential of azulene in self-assembled nano-containers, I decided to integrate those chromophores into our group’s “lantern-shaped” Pd₂L₄-type coordination cages. The interesting colour changing properties of some azulene-based anion hosts, as well as the unusual polarisation of the aromatic system inspired us to attempt to bring those properties into our own systems. Our lab, through the work of Dr. Irene Regeni, recently has integrated coal-tar dyes^[22] or diketopyrrolopyrroles^[23] as strongly coloured backbones in our cages to expand their functionalities as probes for host-guest interactions, and the goal of my current work is to bring a new type of chromophore into our assemblies to expand our library of colourful cages.

3.2 AZULENE-BASED COORDINATION ASSEMBLIES

Note: parts of this chapter were published in the article “Guest-Induced Reversible Transformation between an Azulene-Based Pd_2L_4 Lantern-Shaped Cage and a Pd_4L_8 Tetrahedron”.^[24] Ligands **AZU4** and **AZU5** and every derived data have not yet been published.

In the first iteration of our azulene-based assemblies, five different azulene-based ligands were synthesised, starting from 1,3-dibromoazulene:^[25] **AZU1** (1,3-bis(pyridin-3-ylethynyl)azulene), **AZU2** (1,3-bis(isoquinolin-8-ylethynyl)azulene), **AZU3** (1,3-bis(isoquinolin-7-ylethynyl)azulene), **AZU4** (1,3-bis(4-(pyridin-3-yl)phenyl)azulene), and **AZU5** (1,3-bis(4-(pyridin-3-ylethynyl)phenyl)azulene). The synthetic routes are shown in Scheme 3.2. The complete synthetic protocols and full characterisation are provided in the experimental part (Section 3.7) of the present chapter.



Scheme 3.2: General synthetic pathway for the preparation of ligands **AZU1** to **AZU5**. The first step comprises of a bromination of azulene in positions 1 and 3. The second step consists in Sonogashira or Suzuki C-C cross coupling reactions to form the final ligand.

The first step for the synthesis of all ligands is a bromination of positions 1 and 3 of azulene with *N*-bromosuccinimide in pentane. The reaction was performed at 0°C for 30 minutes. The solution can then be filtered and evaporated to yield pure 1,3-dibromoazulene.

Ligands **AZU1** to **AZU3** were synthesised through Sonogashira cross-coupling between 1,3-dibromoazulene and the corresponding terminal alkynes. **AZU4** was synthesised from the commercially available 3-(4-(BPin)phenyl)pyridine through Suzuki cross-coupling. Finally, **AZU5** was synthesised in two steps from a Suzuki cross-coupling between 1,3-dibromoazulene and (4-bromophenyl)BPin, followed by a Sonogashira cross-coupling with commercially available 3-ethynylpyridine. All ligands were thoroughly purified by Gel Permeation Chromatography (GPC) before the preparation of the coordination species.

3.2.1 General protocol for the formation of the cages

All cages have either been prepared in deuterated acetonitrile (CD_3CN) or $DMSO-d_6$. Ligands were dissolved or suspended in the solvent of choice to form solutions at 3.11 mM. Palladium(II) stock solutions at 15 mM were also prepared from the commercially available salts $Pd(CH_3CN)_4(BF_4)_2$ or $Pd(CH_3CN)_4OTf_2$. To form the cages, the two stock solutions were mixed: 450 μ l of the ligand, and 50 μ l of the Pd(II), resulting in a 2:1 ratio, with a slight excess of the metal cation. To ensure all ligand had reacted, the solutions were heated at 70°C for 1 hour, except when otherwise stated.

3.2.2 Pd_2AZU1_4

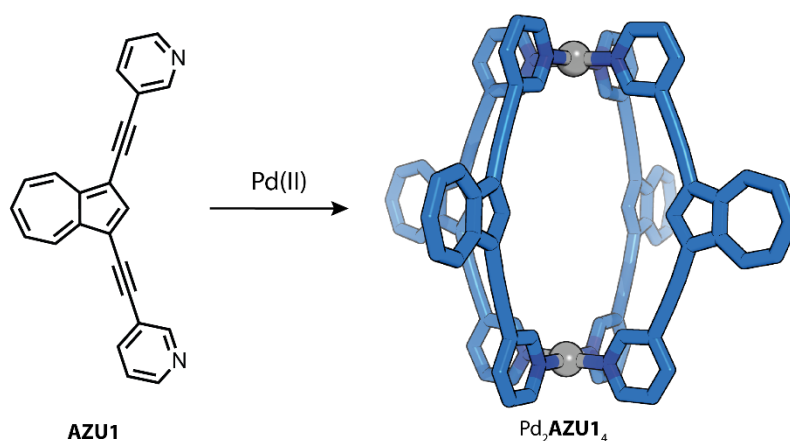


Figure 3.2: Schematic representation of the formation of cage Pd_2AZU1_4 (X-ray structure) from ligand **AZU1**.

The first synthesised ligand **AZU1** possesses two *meta*-pyridine donor groups with an alkyne linker and due to the coordination vectors being close to parallel, the resulting Pd(II)-cage is expected to be lantern-shaped. The initial ligand solution in $DMSO-d_6$ was a dark turquoise, and turned a greener shade upon addition of Pd(II). The cage was characterised by NMR, ESI-MS, UV-Vis absorption spectroscopy, and Single Crystal X-ray Diffraction Crystallography (SCXRD) (Section 3.7.7.1).

The 1H -NMR data shows a downfield shift of most of the signals of the protons of the ligands, with the most important ones being the a and b, situated on the pyridine donor group, right next to the Pd(II) center (Fig. 3.3). This behaviour is consistent with previous reports for lantern-shaped cages. In addition, ESI-MS confirmed the formation of a Pd_2AZU1_4 species (Fig. 3.4b).

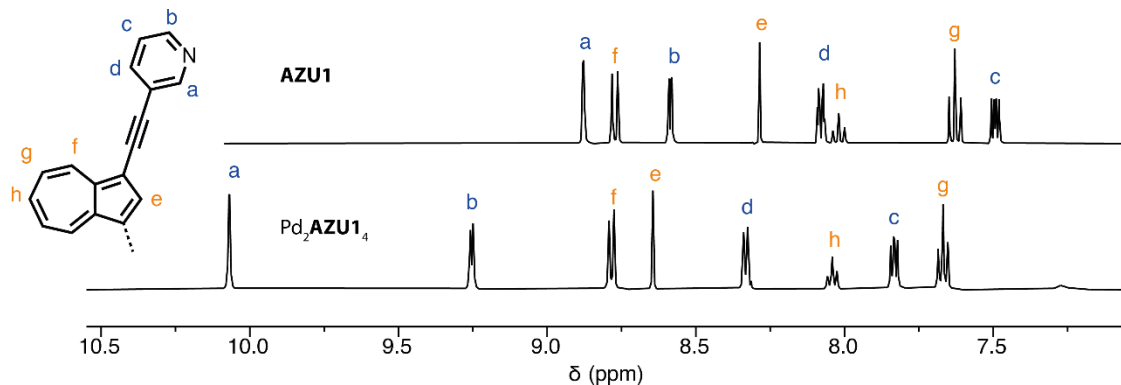


Figure 3.3: ¹H-NMR (500 MHz, 298 K, DMSO-*d*₆) of ligand **AZU1** (top), and of the corresponding Pd₂**AZU1**₄ cage (bottom) after addition of 0.5 eq. of Pd(CH₃CN)₄OTf₂.

The absorption spectra of both ligand and cages were also measured. Similar to other azulene derivatives,^[26] they present strong bands in the UV region. However, the S₀-S₁ band in the visible range is weak and broadened, as expected for azulene and its derivatives. The formation of the cage blue-shifted the S₀-S₁ transition maxima from 614 nm to 591 nm, but red-shifted the first local maximum in the higher energy bands from 421 to 435 nm.

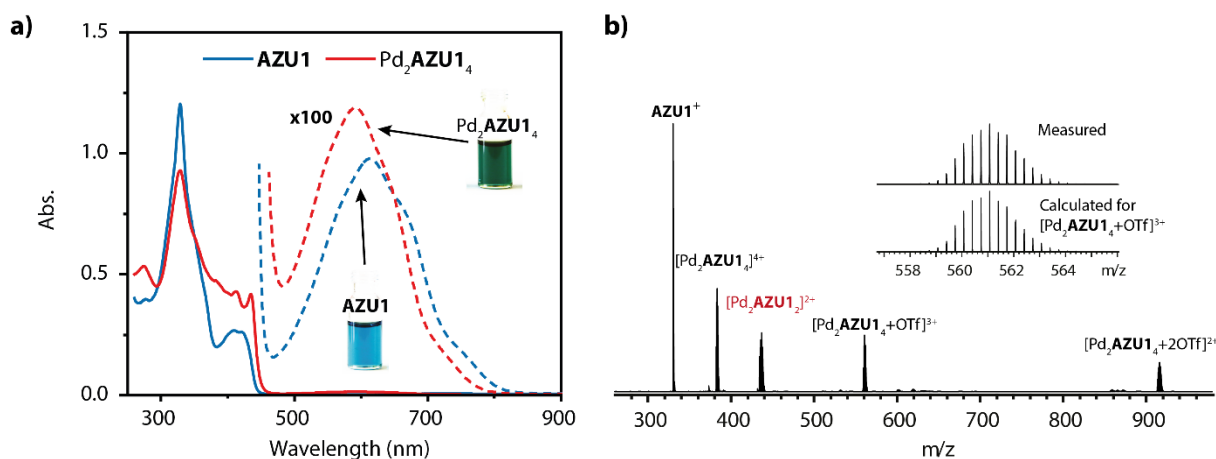


Figure 3.4: (a) Absorption spectra of **AZU1** and Pd₂**AZU1**₄ in DMSO (cuvette length: 1 cm, concentration (in ligand equivalent): 0.02 mM and 2 mM, except for Pd₂**AZU1**₄ at low concentration: 1 mM and 0.2 mM). Photographs of the concentrated solutions are provided as inserts. (b) ESI-MS spectrum of cage Pd₂**AZU1**₄.

Fluorescence spectra of both species was also recorded. As expected for azulene, the emission of both the ligand and the cage happens from the S₂ level instead of S₁ and their maxima were measured at 460 nm and 462 nm respectively. The emission of the ligand was weak, but the one of the cage was even weaker, as observed from many Pd(II) assemblies (Section 3.7.6).

Finally, single crystals fit for X-ray diffraction measurements were obtained from slow vapour diffusion of ethyl acetate (EtOAc) into a DMSO-*d*₆ solution of [Pd₂**AZU1**₄](OTf)₄. Due to their small size, they were measured with synchrotron X-ray radiation at DESY, Hamburg. The obtained structure reveals the lantern-shaped cage Pd₂**AZU1**₄ as expected. The compound crystallised in the

orthorhombic Fmmm (no. 69) space group, and the asymmetric unit cell was composed of only one eighth of the cage. The full structure can then be reconstructed by symmetry operations (Section 3.7.7.1).

3.2.3 Pd₂AZU₂₄

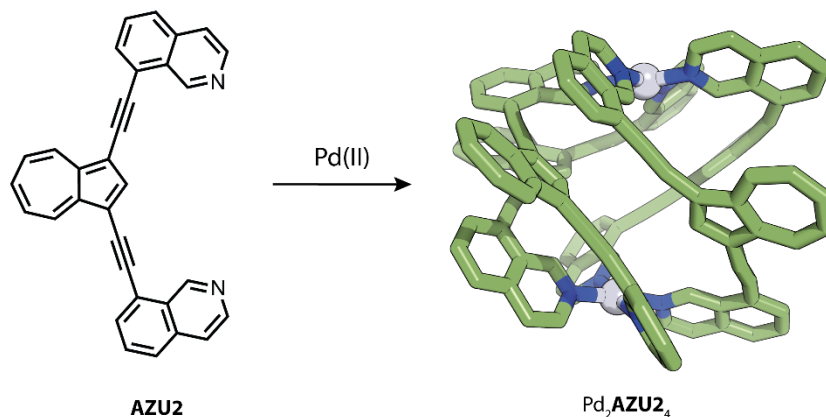


Figure 3.5: Schematic representation of the formation of cage Pd₂AZU₂₄ (X-ray structure) from ligand AZU₂.

Ligand **AZU₂** differs from the previously described **AZU₁** ligand by its 8-isoquinoline donor group. The coordination vectors here are very convergent, and according to previous reports should yield a quadruply stranded helicate upon coordination with Pd(II).^[27]

The ligand is almost insoluble in acetonitrile, and only partially in DMSO. Upon addition of Pd(II) and heating however, the solution cleared up. The ligand forms a green solution in DMSO, but the colour drastically changes into a yellow-brown upon formation of the coordination species. Like the previous species, it was characterised by NMR, ESI-MS, UV-Vis absorption spectroscopy, and SCXRD.

Contrary to Pd₂AZU₁₄, most of the ¹H-NMR signals of the free ligand shifted upfield upon formation of the coordination species (Fig. 3.6), consistent with the formation of a helicate.^[27] The solution also had to be heated overnight to ensure full conversion. Here, the formation of the new species was performed both in CD₃CN and DMSO-*d*₆, with BF₄⁻ as counteranion. No significant differences were noted between the two solvents, implying the same species forms independently of the tested conditions. ESI-MS also confirmed the formation of a Pd₂AZU₂₄ species (Fig. 3.7b).

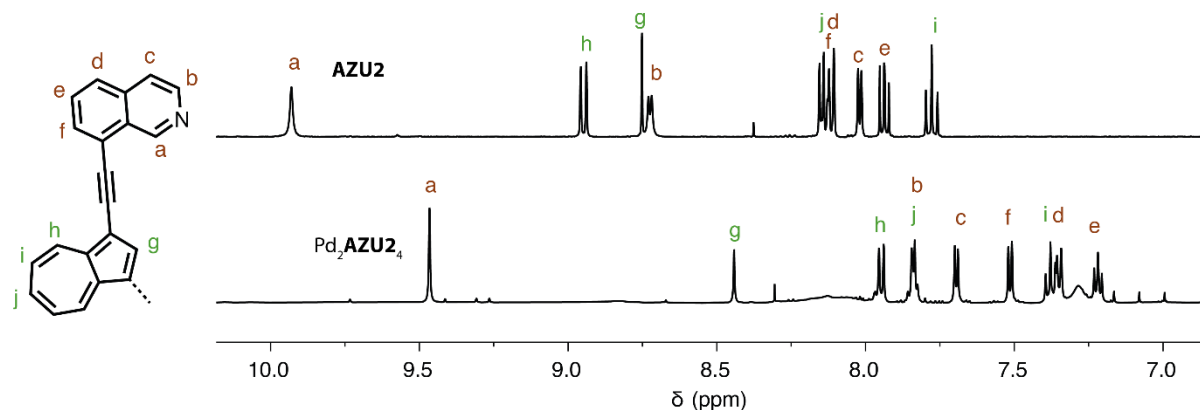


Figure 3.6: ¹H-NMR (500 MHz, 298 K, DMSO-*d*₆) of ligand **AZU2** (top), and of the corresponding [Pd₂**AZU2**₄](BF₄)₄ cage (bottom) after addition of 0.5 eq. of Pd(CH₃CN)₄(BF₄)₂

UV-Vis spectroscopy showed a blue-shift of the S₀-S₁ transition maxima from 616 nm for the ligand to 601 nm for the helicate, similarly to **AZU1**. However, a significant red shift occurs for the S₀-S₂ transition, going from 401 nm for the ligand, to 434 nm for the cage. Moreover, the S₀-S₂ transition of the cage (approx. 450 nm) was significantly red-shifted and broadened compared to **AZU2** (approx. 410 nm) (Fig. 3.7a). This broadening is a possible evidence of inter-ligand interactions, as the organic components are much closer to each other in the helicate structure than in the previously described lantern-shaped cage. However, further experiments are needed to confirm this behaviour.

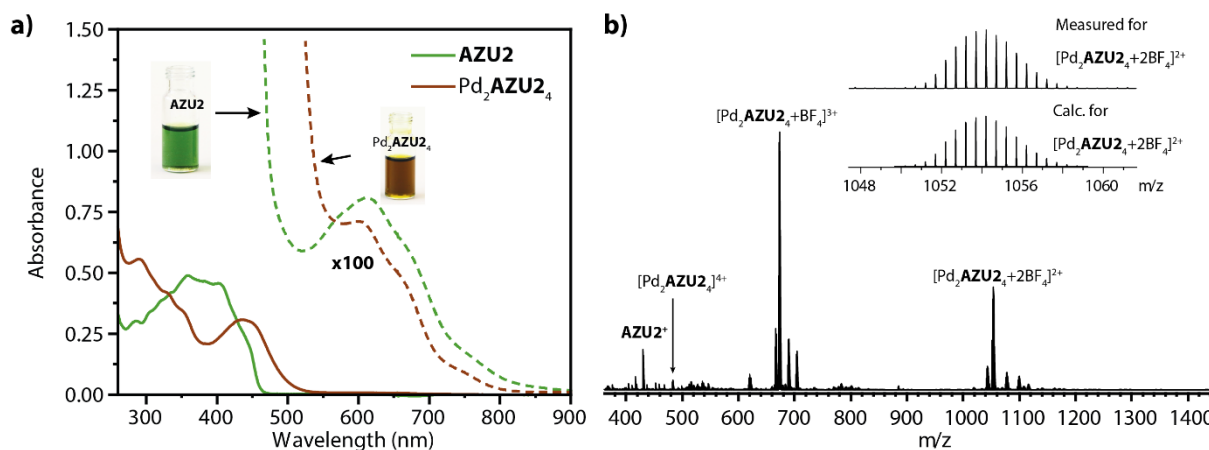


Figure 3.7: (a) Absorption spectra of **AZU2** and Pd₂**AZU2**₄ in DMSO (cuvette length: 1 cm, concentration (in ligand equivalent): 0.02 mM and 2 mM, except for Pd₂**AZU2**₄ at low concentration: 1 mM and 0.2 mM). Photographs of the concentrated solutions are provided as inserts. (b) ESI-MS spectrum of cage [Pd₂**AZU2**₄](BF₄)₄.

Fluorescence of the ligand is weak, but still measurable, and has a maximum at 470 nm. The emission of the helicate is mostly quenched, however. Two local maxima are observed at around 400 nm and 490 nm (Section 3.7.6.).

The helicate structure of Pd₂**AZU2**₄ was definitely confirmed by SCXRD (Section 3.7.7.2). Crystals fit for synchrotron radiation were grown from slow diffusion of diisopropylether in the CD₃CN solution of the coordination species. The obtained structure showed that the helicate crystallised as

both enantiomers, in very close proximity, in the triclinic P-1 (no. 2) space group. Indeed, the ligands of the two enantiomers interact through π - π and CH- π stacking to form dimers in the solid state. Moreover, because of the stacking, a deformation of the helicates occurs and results in a non-symmetric structure. However, as shown earlier, the lack of splitting in the ¹H-NMR spectrum of Pd₂AZU₂ indicates that this deformation only occurs in the solid state or is too fast to be measured by NMR.

3.2.4 Pd₂AZU₃₄

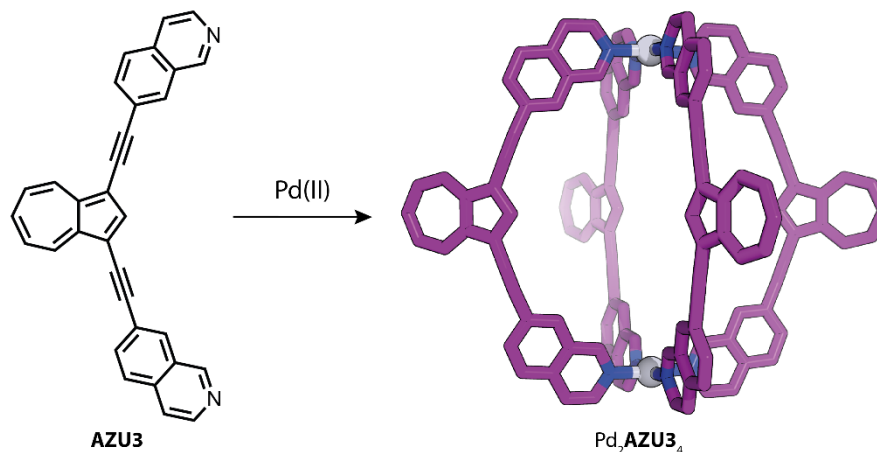


Figure 3.8: Schematic representation of the formation of cage Pd₂AZU₃₄ (X-ray structure) from ligand AZU₃.

Like AZU₂, AZU₃ possesses an isoquinoline donor group. However, its substitution in the 7- position imparts it with coordination vectors similar to AZU₁ and should yield a cage similar, but larger, to Pd₂AZU₁₄ (Fig. 3.8).

The formation of the cage was measured in DMSO-*d*₆, with OTf⁻ as counteranion. Upon addition of Pd(II), the solution of the ligand went from a dark turquoise colour to a greener shade. Like Pd₂AZU₁₄, most of the ¹H-NMR signals shifted downfield, giving strong evidence for the formation of a lantern-shaped cage (Fig. 3.9). Moreover, ESI-MS confirmed that a Pd₂AZU₃₄ species is formed (Fig. 3.10b).

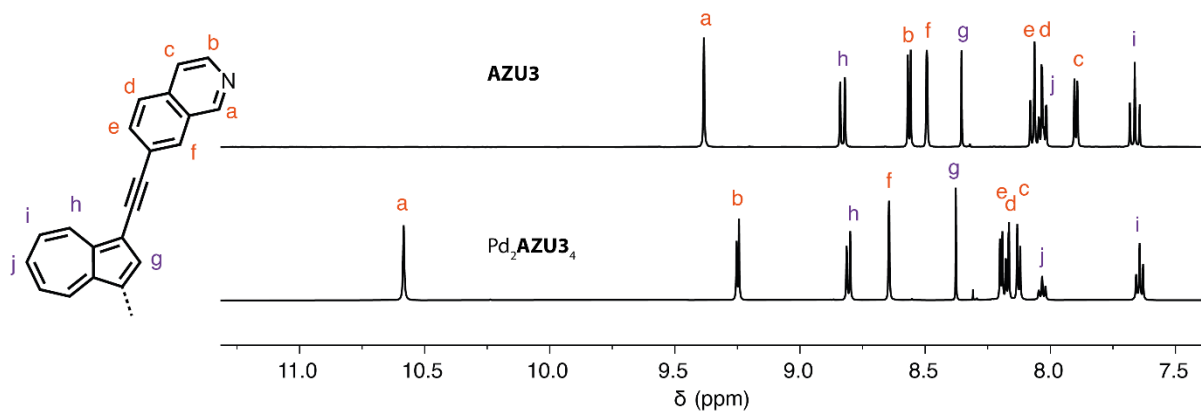


Figure 3.9: $^1\text{H-NMR}$ (500 MHz, 298 K, $\text{DMSO-}d_6$) of ligand **AZU3** (top), and of the corresponding $[\text{Pd}_2\text{AZU3}_4](\text{OTf})_4$ cage (bottom) after addition of 0.5 eq. of $\text{Pd}(\text{CH}_3\text{CN})_4\text{OTf}_2$

Similar to the previous two species, the UV-Vis spectroscopy showed that the S_0 - S_1 transition maximum is blue-shifted from 619 nm for the ligand to 611 nm for the cage (Fig. 3.10a). This smaller difference in shift compared to lantern-shaped $\text{Pd}_2\text{AZU1}_4$ probably stems from the larger distance between the chromophoric azulene core of the ligand and the coordinated $\text{Pd}(\text{II})$ cations in the present case, entailing a weaker electronic interaction between the chromophore and the metal. Moreover, the S_0 - S_2 bands are also red-shifted in the cage compared to the ligand. However, in the absence of a clear local maximum, the extent of the shift is delicate to quantify.

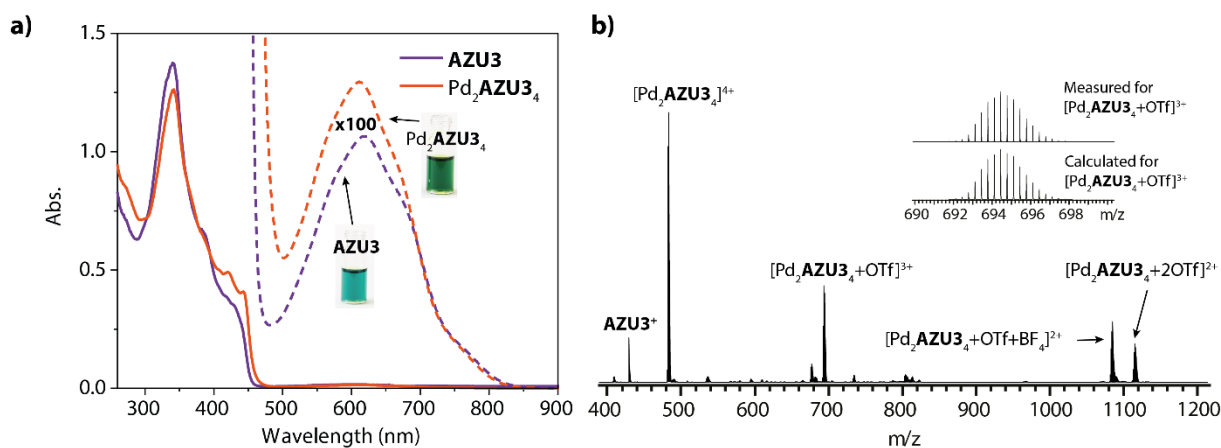


Figure 3.10: (a) Absorption spectra of **AZU3** and $\text{Pd}_2\text{AZU3}_4$ in DMSO (cuvette length: 1 cm, concentration (in ligand equivalent): 0.02 mM and 2 mM, except for $\text{Pd}_2\text{AZU3}_4$ at low concentration: 1 mM and 0.2 mM). Photographs of the concentrated solutions are provided as inserts. (b) ESI-MS spectrum of cage $\text{Pd}_2\text{AZU3}_4$.

The lantern-shaped structure of the cage was confirmed by SCXRD of a host-guest complex with the cage and will be discussed in the next section.

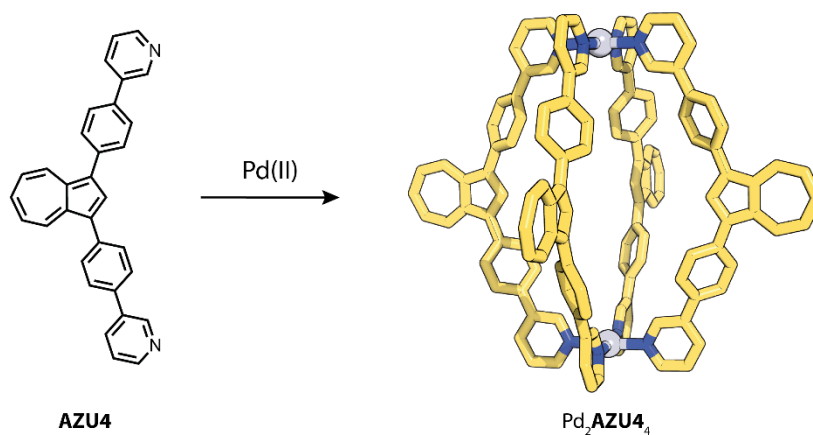
3.2.5 Pd₂AZU₄

Figure 3.11: Schematic representation of the formation of cage Pd₂AZU₄ (DFT structure, B3LYP/def2-SVP) from ligand AZU₄.

Like AZU₁, AZU₄ possesses two *meta*-pyridine donor groups, but unlike its cousin with alkyne linkers, AZU₄ has phenyl rings as linkers, which renders its structure less flexible.

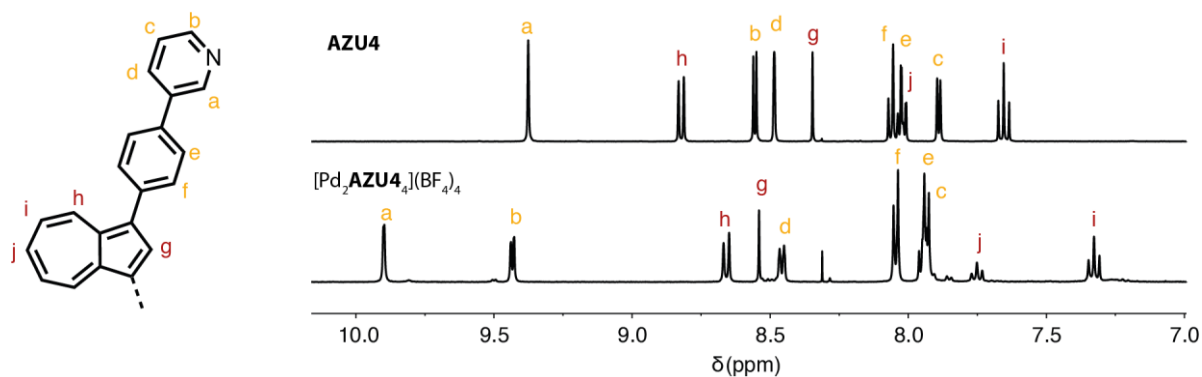


Figure 3.12: ¹H-NMR (500 MHz, 298 K, DMSO-*d*₆) of ligand AZU₄ (top), and of the corresponding [Pd₂AZU₄](BF₄)₄ cage (bottom) after addition of 0.5 eq. of Pd(CH₃CN)₄(BF₄)₂.

The formation of the cage was verified like the previous species by ¹H-NMR (Fig. 3.12) and ESI-MS (Fig. 3.13b). As usual, the formation of the cage was accompanied by a change in colour of the solution, this time from blue to teal.

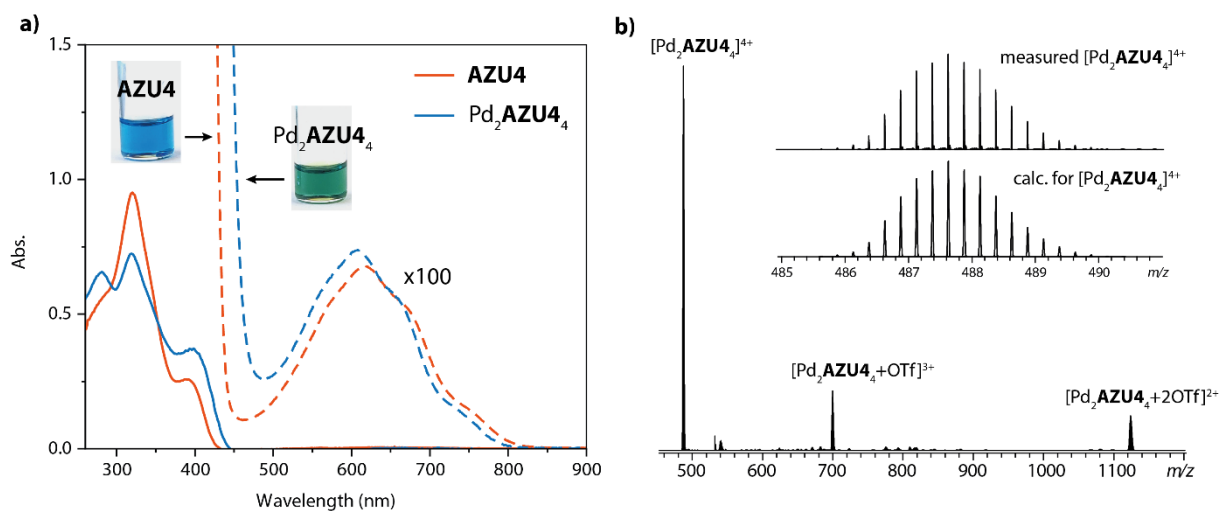


Figure 3.13: (a) UV-Vis spectra of **AZU4** and Pd_2AZU_4 in DMSO (cuvette length: 1 cm, concentration (in ligand equivalent): 0.02 mM and 2 mM, except for Pd_2AZU_4 at low concentration: 1 mM and 0.2 mM). Photographs of the concentrated solutions are provided as inserts. (b) ESI-MS spectrum of cage Pd_2AZU_4 .

No crystal of sufficient quality could be grown from solutions of Pd_2AZU_4 . A DFT model (ω B97X-D/def2SVP) was used in place of an X-ray structure (Fig. 3.11).

3.2.6 Pd_2AZU_5

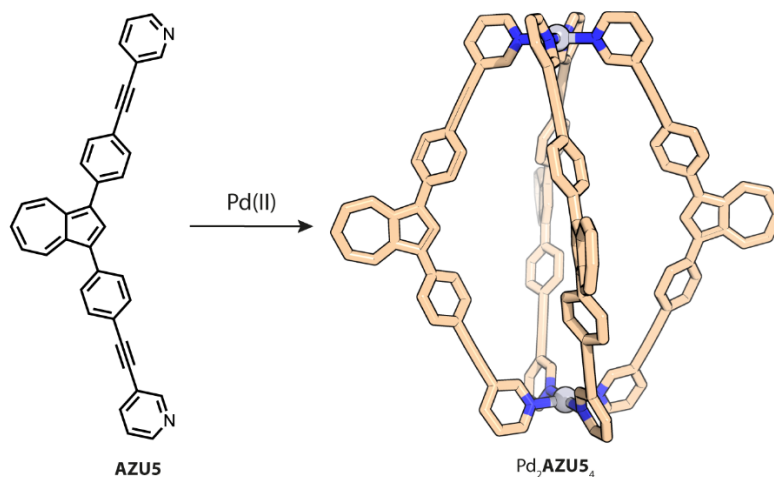


Figure 3.14: Schematic representation of the formation of cage Pd_2AZU_5 (DFT structure, B3LYP/def2-SVP) from ligand **AZU5**.

Of all five of the azulene-derived ligands, **AZU5** is the longest, with both phenyl and alkyne linkers. Upon addition of Pd(II), the solution turns from teal to green.

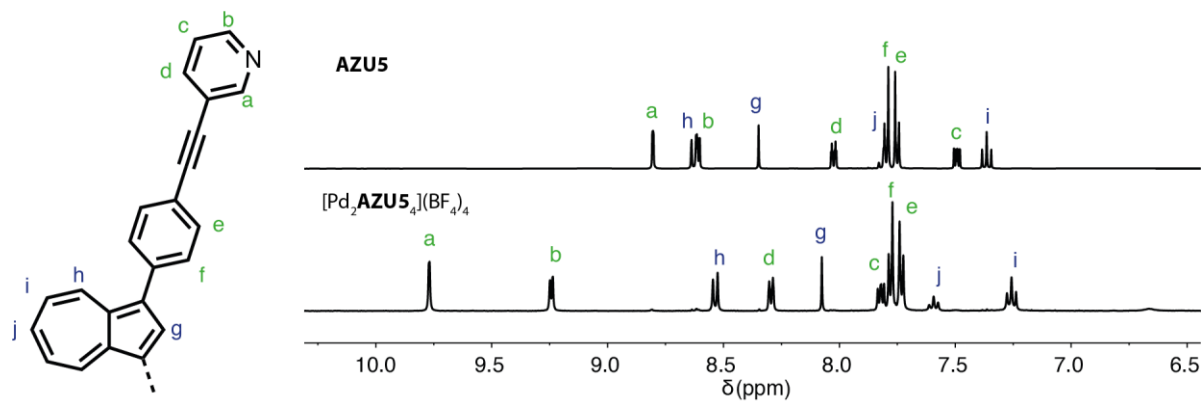


Figure 3.15: $^1\text{H-NMR}$ (500 MHz, 298 K, $\text{DMSO-}d_6$) of ligand **AZU5** (top), and of the corresponding $[\text{Pd}_2\text{AZU5}_4](\text{BF}_4)_4$ cage (bottom) after addition of 0.5 eq. of $\text{Pd}(\text{CH}_3\text{CN})_4(\text{BF}_4)_2$.

The formation of the cage was verified like the previous species by $^1\text{H-NMR}$ (Fig. 3.15) and ESI-MS (Fig. 3.16b). Like for cage $\text{Pd}_2\text{AZU3}_4$, I was unable to obtain single crystals of sufficient quality for SCXRD of the free cage $\text{Pd}_2\text{AZU5}_4$. However, I was able to obtain crystals of a host-guest complex, and therefore that structure will be discussed later in section 3.5.4.

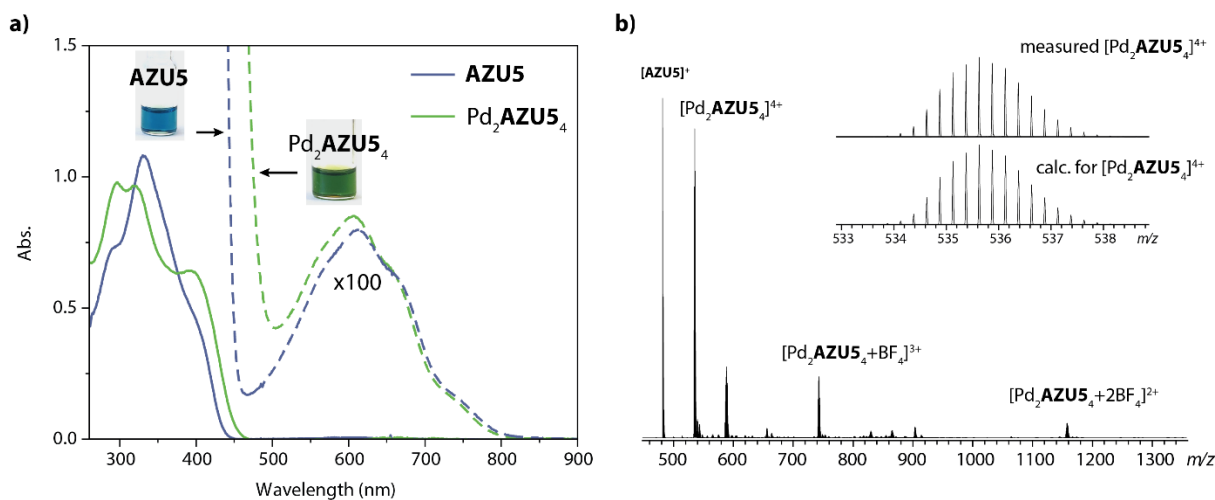


Figure 3.16: (a) UV-Vis spectra of **AZU5** and $\text{Pd}_2\text{AZU5}_4$ in DMSO (cuvette length: 1 cm, concentration (in ligand equivalent): 0.02 mM and 2 mM, except for $\text{Pd}_2\text{AZU5}_4$ at low concentration: 1 mM and 0.2 mM). Photographs of the concentrated solutions are provided as inserts. (b) ESI-MS spectrum of cage $[\text{Pd}_2\text{AZU5}_4](\text{BF}_4)_4$.

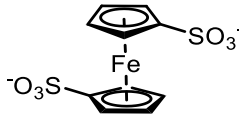
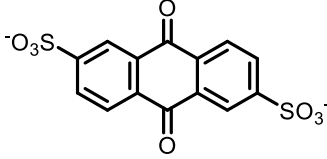
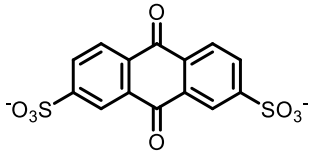
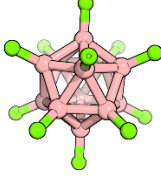
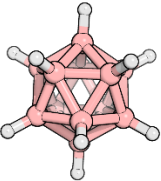
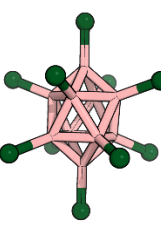
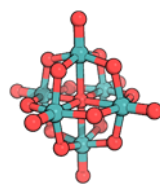
3.3 GUEST ENCAPSULATION EXPERIMENTS

After their synthesis, the cages and helicate were tested for their guest encapsulation properties with negatively charged molecules. The test consisted in the addition of 1 equivalent of the guest to the cage in solution, heating for 10 minutes to allow full equilibration of the system and recording the ¹H-NMR. Most guests presented here are based on aromatic disulfonates, and the next table recaps all the guests used in this section, together with their abbreviations.

Table 3.1: List of the guests used in this study, with their abbreviations.

Abbreviation	Full name	Structure	Counterion
PRO	propan-1,3-disulfonate		TBA ⁺
BEN13	benzene-1,3-disulfonate		TBA ⁺
BEN14	benzene-1,4-disulfonate		TBA ⁺
NAP15	naphthalene-1,5-disulfonate		TBA ⁺
NAP26	naphthalene-2,6-disulfonate		TBA ⁺
NAP27	naphthalene-2,7-disulfonate		TBA ⁺
BINSA	(<i>R</i>)- [1,1'-binaphthalene]-2,2'-disulfonate		K ⁺
CSA	(<i>R</i>)-camphor sulfonate		TBA ⁺

3 – Guest-induced transformation of an azulene-based Pd_2L_4 cage to a Pd_4L_8 tetrahedron

FEC	ferrocene-1,1'-disulfonate		TBA ⁺
26ANQ	anthraquinone-2,6-disulfonate		Na ⁺
27ANQ	anthraquinone-2,7-disulfonate		Na ⁺
B12F12	dodecafluorododecaborate		Cs ⁺
B12H12	dodecaborate		NEt ₃ H ⁺
B10Cl10	decachlorodecaborate		TBA ⁺
Mo6O19	Hexamolybdate (Mo ₆ O ₁₉ ²⁻)		TBA ⁺

3.4 GUEST-INDUCED TRANSFORMATION OF Pd₂AZU₁₄

3.4.1 Characterisation of tetrahedron 2G@Pd₄AZU₁₈

The first coordination species tested for guest interactions was Pd₂AZU₁₄. Due to its small cavity, only small disulfonates were screened. No significant interaction was observed for the guests based on a naphthalene core (**NAP26** and **NAP27**). However, when guests **BEN13** and **BEN14** were used, a noticeable colour change occurred rapidly upon heating, the solution going from a teal hue to a greener shade. The ¹H-NMR of both solutions revealed then that the signals of the cage had unexpectedly split in two sets of signals, in a 1:1 fashion (Fig. 3.17). In general, host-guest interactions do not lead to a splitting of the signals, as they do not break the symmetry of the host.^[28] Therefore, the interaction between Pd₂AZU₁₄ and **BEN13** or **BEN14** must yield an interesting new species, with reduced symmetry compared to the initial lantern-shaped cage. It is worth noting that the transformation of the cage to the new species is only complete if OTf⁻ is used as a counteranion to the cage. Indeed, if BF₄⁻ is chosen instead, the transformation is only partial, as seen by NMR (Fig S3.32), a precipitation is observed if more of the guest is added. The reason of such a different behaviour is not clear at the moment, but BF₄⁻ might be binding more strongly to the cavity of the Pd₂AZU₁₄ cage, competing with the guests, whereas OTf⁻ does not.

ESI-MS of the newly formed species revealed that in both cases a 2G@Pd₄AZU₁₈ (**G** = **BEN13** or **BEN14**) host-guest complex had formed (Fig. S3.31 & 35). This constitutes an extremely interesting result, as this was the first time that a larger species was observed to arise from the interaction between a disulfonate guest and a lantern-shaped Pd₂L₄ cage in our lab. It had been observed previously that the addition of halides to a some Pd₂L₄ cages would trigger their catenation through favourable electrostatic interactions between positively charged Pd(II) cations and the newly added anions.^[29]

In the initial absence of a crystal structure for the newly formed 2G@Pd₄AZU₁₈, I wondered about its actual structure. Pd₄L₈ species have already been reported by several groups, including ours. Quadruply catenated Pd₂L₄ cages give rise to two sets of NMR signals.^[30] However, I rejected this topology due to the very small size of the resulting cavities, unable to hold the benzene-disulfonate guests. Next, Pd₄L₈ squares were also rejected due to their non-split NMR signals. As an exception to this rule however, Lützen and co-workers have reported a chiral Pd₄L₈ square with split NMR signals.^[31] In addition, a unique Pd₄L₈ topology was recently published by Severin and co-workers, as a sort of doubly bridged twisted Pd₂L₃ bowls.^[32] This structure in turn has too low of a symmetry to yield only two sets of signals. Therefore, having eliminated all other topologies for the reasons discussed above, I concluded that my newly formed species must have a tetrahedral shape, which would fit the splitting of the NMR signals, and possess a cavity large enough to contain two of the guests.

DOSY analysis also confirmed an increase of the hydrodynamic radius from 10.5 Å for Pd₂AZU1₄ to 13.2 Å and 14.3 Å for the newly formed species, respectively, containing **BEN13** or **BEN14** (Fig. 3.17).

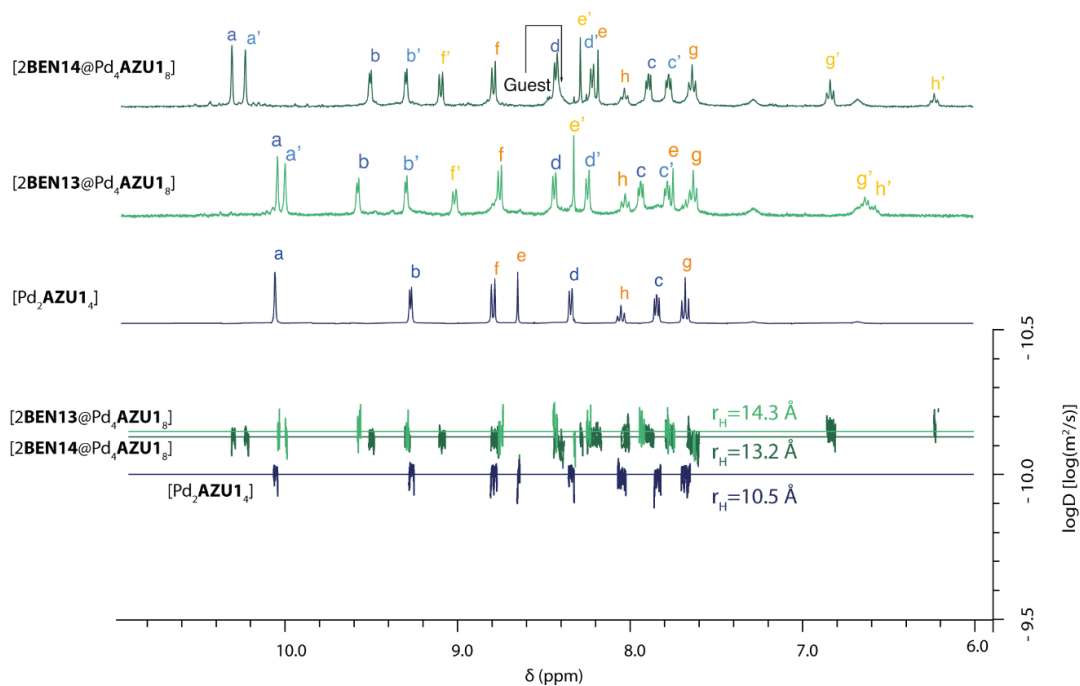


Figure 3.17: ¹H-NMR (500 MHz, 298 K, DMSO-*d*₆) of Pd₂AZU1₄ and 2**BEN13**@Pd₄AZU1₈ and 2**BEN14**@Pd₄AZU1₈, with their corresponding DOSY traces.

With the aid of 2D-NMR, I assigned the signals of the ¹H-NMR spectrum, and using NOE contacts, I determined that the ligand **AZU1** possessed two different orientations with respect to the rotation of the pyridine donor group around the alkyne linker (Fig. 3.18). With that information, I managed to construct a DFT model of the 2**G**@Pd₄AZU1₈ tetrahedron (Fig S3.67).

However, after several unsuccessful attempts, good quality single crystals of 2**BEN14**@Pd₄AZU1₈ were obtained. Toluene was slowly diffused into a 0.35 mM DMSO solution of the tetrahedron mixed one-to-one with a 15 mM solution of NBu₄ReO₄. The crystals were measured using synchrotron radiation at DESY, and the resulting tetrahedral structure confirmed the accuracy of the DFT calculation I performed previously (Fig. 3.19).

The host-guest complex crystallises in the triclinic space group P-1 (no. 2), and the results show that the asymmetric unit cell is composed of two different tetrahedra, as well as one ReO₄⁻ anion disordered over two positions. Some **BEN14** guests can also be found outside of the tetrahedra. Finally, some solvent molecules DMSO and toluene can be resolved in the proximity of the main coordination species (Section 3.7.7.4.).

This confirmation of the formation of a Pd₄L₈ tetrahedron by the addition of guest molecules to a smaller Pd₂L₄ cage is a remarkable result, as no other similar transformation has yet been reported. Moreover, the reaction produces a clean and unique product after the addition of just one

equivalent of guest and is complete after only 5 minutes of heating at 70°C. While it is not yet clear what the driving force of the reaction is, I can make a few observations to clue us into the mechanism of the transformation.

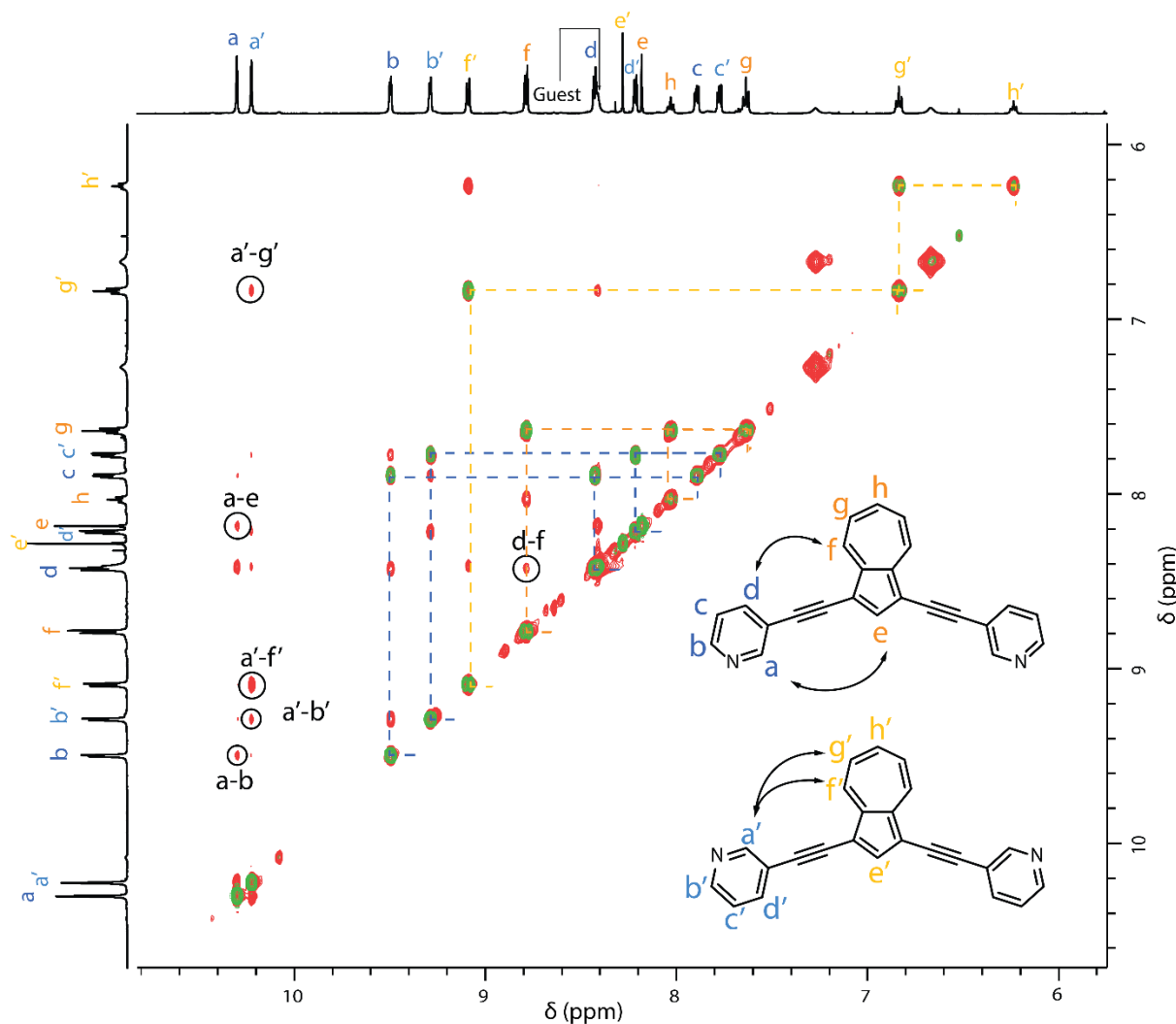


Figure 3.18: Overlay of COSY (green) and NOESY (red) 1H - 1H -NMR spectra (700 MHz, 298 K, $DMSO-d_6$) of $2BEN14@Pd_4AZU1_8$. Important COSY correlations are labelled in dashed lines. The orientation of the pyridine donor group respective to the azulene backbone was determined by the circled NOE peaks and are indicated by arrows on the Lewis structures of **AZU1**.

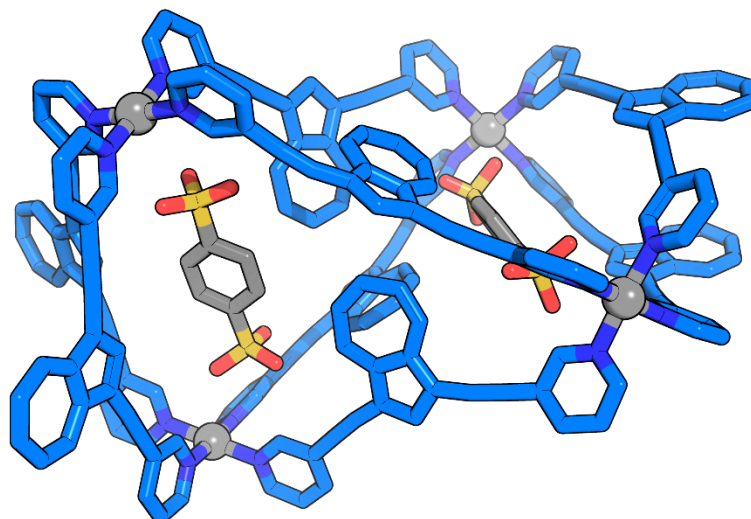


Figure 3.19: X-ray structure of $2\text{BEN14@Pd}_4\text{AZU18}$. Counteranions and solvents molecules are omitted for the sake of clarity.

Firstly, analysis of the cavity volumes of the different structures reveals that the guests benefit from larger cavities in the tetrahedron as compared to the $\text{Pd}_2\text{AZU14}$ cage ($321\text{--}345 \text{ \AA}^3$ vs 221 \AA^3 per cavity) (Table S3.5 and Fig. S3.66). The distance between the Pd atoms also increases from 12.3 \AA in the cage to 14.0 \AA (shortest) in the tetrahedron. This increase in volume and space between the two cations may be one of the driving forces of the transformation from cage to tetrahedron. Indeed, a larger distance between the palladium centres allows the doubly negatively charged guest to fit in-between the two positively charged metallic centres, and thus maximises the electrostatic interactions.

Secondly, upon closer inspection of the X-ray structure of the $2\text{BEN14@Pd}_4\text{AZU18}$ tetrahedron, the arrangement of the four central azulene moieties in a square-like fashion caught our interest. Indeed, in that peculiar case, the positively polarised seven-membered ring of every aromatic unit is pointing perpendicularly towards their neighbour. The “h” protons of the affected azulenes are therefore experiencing a shielding effect, visible by NMR as an important shift from approximately 8 ppm (in the $\text{Pd}_2\text{AZU14}$ cage) to 6.1 ppm (Fig. 3.17)

To assess whether this peculiar arrangement has any effect on the stabilisation of the structure, we performed DFT computations, comparing the stabilisation energies of four azulene moieties in the previously mentioned arrangement and four naphthalene units in a similar pattern. The energies were computed at the $\omega\text{B97X-D/def2-TZVP}$ level, and they showed that the four azulenes units experience a higher stabilisation (-75 kJ/mol) when arranged in a square than four naphthalenes in a similar $\text{CH}\text{--}\pi$ configuration (-58 kJ/mol) (Fig. 3.20). We attribute this increase in stabilisation to more favourable $\text{CH}\text{--}\pi$ interactions between the negatively polarised five-membered rings and the positively polarised seven-membered rings of the azulenes.

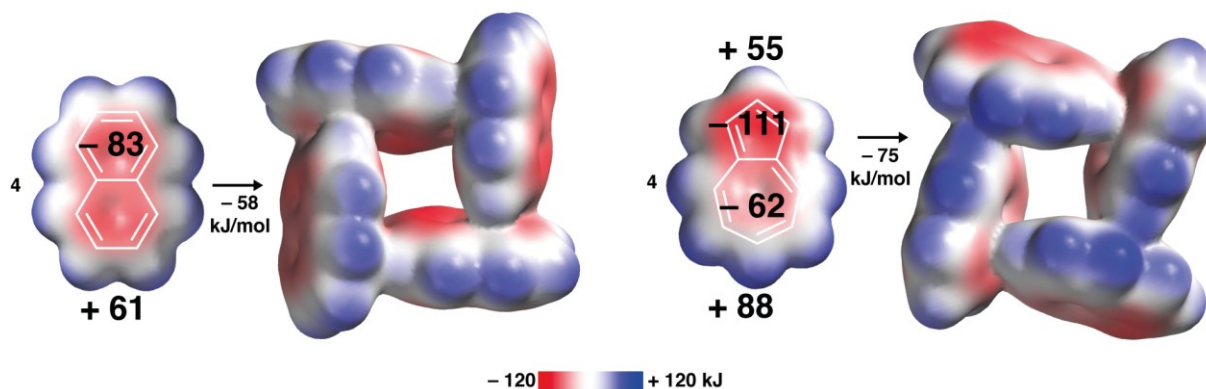


Figure 3.20: four naphthalenes (left) and four azulenes (right) were arranged as observed in the central part of the X-ray structure of $2BEN14@Pd_4AZU1_8$ (with respect to the nearest CH- π contacts) and association energies as well as electrostatic potential maps computed (max/min values given for π -surfaces and terminal hydrogens).

3.4.2 Kinetics of the transformation

As the product of the transformation was determined to be a Pd_4L_8 tetrahedron, I next wondered about the mechanism that allowed such a change to take place. Therefore, as an initial experiment, I went on to measure the kinetic parameters. Such values may help us to shed some light into what is happening at the supramolecular level.

To determine the kinetic parameters, I followed the transformation by 1H -NMR (Fig. 3.21a) at five different temperatures. With the recorded data, the concentration of both cage and tetrahedron was determined by integration of their respective signals, with 1,3,5-trimethoxybenzene serving as an internal standard. The reaction was determined to be of the first order by plotting the natural logarithm of the cage concentration over time and observing a linear relation (Fig. 3.21b). Finally, the reaction rates could be determined and used to construct an Eyring plot (Fig. 3.21c). During all measurements, only signals from the cage and the tetrahedron were observed; no clear intermediate was detected in the mixture.

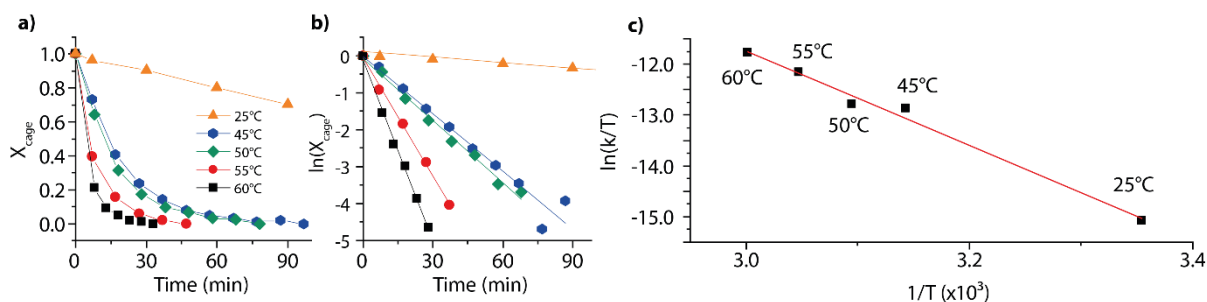


Figure 3.21: (a) fraction of the cage during the cage to tetrahedron transformation as a function of time, as determined by NMR at different temperatures. (b) $\ln(X_{\text{cage}})$ during the same transformation. (c) Eyring plot of the transformation, with the linear regression (red line).

The Eyring plot allowed us to determine an activation enthalpy ΔH^\ddagger of 77.2 kJ/mol and entropy ΔS^\ddagger of -64 J/mol·K, thus equating to an activation Gibbs free energy ΔG^\ddagger of 96.1 kJ/mol at 298 K. The negative activation entropy may suggest that a rate determining step consists in the association of two individual cages to form one larger assembly (through loss of degrees of freedom).

The apparent first order kinetics is puzzling, as seemingly four reactant (supra)molecules are required to form one product. This could be partially explained by imagining that the cages and the guests are interacting electrostatically at the beginning of the reaction, preforming a loose reactive complex precursor, and therefore do not need to “meet” randomly during the process. However, again, more experiments would be needed to validate this hypothesis.

3.4.3 Reversibility

Having now observed and studied the transformation from the cage to the tetrahedron, I next wondered if the tetrahedral species would still be favoured were the guests to be removed. Can an empty Pd₄AZU₁₈ still exist, or would the system revert back to the Pd₂AZU₁₄ cage? The removal of neutral guests from supramolecular coordination species were achieved previously in examples by Fujita^[33] and Klajn^[34] by washing the host-guest complex with a solvent in which the guest, but not the capsule, was soluble in. As both cage and guest are soluble in the same range of solvents in the present case, that technique was not applicable. Another technique our group previously employed was the precipitation of cage-bound Br⁻ anions by the addition of a Ag⁺ salt, causing the precipitation of AgBr.^[35] Again, this second strategy was not feasible here.

Taking advantage of the vast library of our previously prepared systems, I envisioned that the addition of another Pd(II)-based cage with a higher affinity for the guest than the tetrahedron would lead to a guest transfer between the two hosts. In other words, the newly added cage would “steal” the guests away from the tetrahedron. As mentioned in the introduction, the dynamic nature of the Pd(II) coordination bonds can cause a scrambling of the ligands when two cages are mixed if the two systems are not capable of narcissistically self-sorting. Therefore, I needed to find a species that would narcissistically self-sort in the presence of Pd₄AZU₁₈, so that the guest transfer could be the only possible interaction between the two cages.

3 – Guest-induced transformation of an azulene-based Pd₂L₄ cage to a Pd₄L₈ tetrahedron

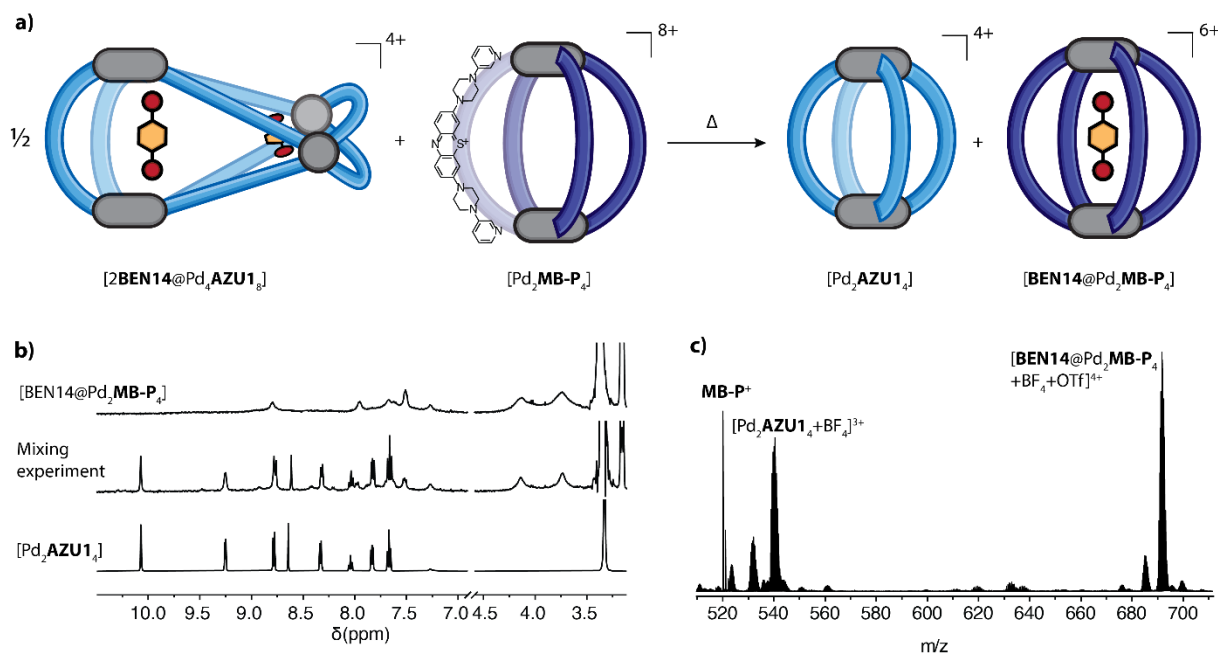


Figure 3.22: a) Schematic representation of the guest transfer between the tetrahedron 2BEN14@Pd₄AZU1₈ to the cage Pd₂MB-P₄. The cage Pd₂AZU1₄ is reformed in the process, while new host guest 2BEN14@Pd₂MB-P₄ is formed. (b) ¹H-NMR (500 MHz, 298 K, DMSO-*d*₆) of the cage Pd₂AZU1₄ (top) and of host-guest complex 2BEN14@Pd₂MB-P₄ (bottom), and of the solution of the two starting species, after 1 h. of heating at 70°C (middle), showing an overlap of the two top and bottom species, confirming the transfer and transformation had taken place. (c) ESI-MS spectrum of the same mixture. Adapted with permission from ref. 24, Copyright 2023 American Chemical Society.

A screening of already known cages from our group was performed to find a species adapted to the guest transfer experiment. After a few trials, cage Pd₂MB-P₄ was found to narcissistically self-sort from Pd₂AZU1₄ (Fig. 3.22a). The MB-P ligand is based on the methylene-blue dye and had been prepared by Dr. Irene Regeni.^[22] In addition, the positive charge carried by the ligand leads to the formation of a coordination species with an 8+ total charge. We assumed that this high charge could favour the transfer of the anionic guest from the tetrahedron to the newly added cage. To help us quantify the binding affinity of BEN14 to Pd₂MB-P₄, a UV-Vis titration was performed. The experiment suggested a strong binding affinity of the guest from the host. Unfortunately, I met difficulties fitting the data to a 1:1 or 1:2 binding model and therefore could not obtain a reliable binding constant (Fig. S3.54).

Despite this hurdle, the guest transfer experiment was a success. A mixture of 2BEN14@Pd₄AZU1₈ and Pd₂MB-P₄ in a 1:2 ratio was heated for 60 minutes at 70 °C, and subsequent ¹H-NMR analysis showed that the tetrahedron had completely transformed back into the cage (Fig. 3.22b). This was evidenced by the disappearance of the 1:1-split signals of the tetrahedron and the reappearance of the signals of the cage. This result was further confirmed by ESI-MS, which showed in addition the formation of the host-guest complex BEN14@Pd₂MB-P₄ (difficult to see in the NMR spectrum due to broadening) (Fig. 3.22c). Thus, I definitely demonstrated that our system is reversible and that the final geometry and nuclearity of the Pd_nAZU1_{2n} assemblies are dictated

by the presence of the anionic disulfonate guest molecules, which can template the formation of a larger species.

3.5 GUEST EXPERIMENTS WITH AZU2 TO AZU5 COORDINATION SPECIES

In order to further understand the transformation mechanism of Pd₂AZU1₄ into 2BEN14@Pd₄AZU1₈ and what conditions are needed to be fulfilled to observe the guest templation of a larger species, four other ligands of varying lengths and coordination vectors based on 1,3-azulenyl were prepared and their corresponding Pd₂L₄ cages were studied for their host-guest interactions.

3.5.1 Pd₂AZU2₄

To determine if guests would bind to helicate Pd₂AZU2₄, an initial NMR screening was performed, where 1 eq. of the guest as a DMSO-*d*₆ solution was added to a solution of the helicate in the same solvent. The mixture was then left to equilibrate at RT for 5 minutes before a spectrum was recorded. The tested guests were: **BEN13**, **BEN14**, **NAP15**, **NAP26**, **NAP27**, and **BINSA**.

No shift of any signals was recorded in any of the helicate-guest mixture (Fig. S3.45), meaning no binding event. This was expected, as the cavity of the helicate is much too small to accommodate any of the tested guests (49 Å³, Table S3.5), even the smaller benzene-disulfonates.

3.5.2 Pd₂AZU3₄

The larger Pd₂AZU3₄ was tested for host-guest interactions as well. Of similar shape as Pd₂AZU1₄, its only difference with its cousin is the presence of 7-isoquinoline donor groups, resulting in a larger cavity. Therefore, I expect the same guests that trigger transformation from cage to tetrahedron in Pd₂AZU1₄ to only be encapsulated in the present species. The tested guests were **PRO**, **BEN13**, **BEN14**, and **BINSA**.

The initial NMR screening with 1 equivalent of guest showed shifts of the internal protons of the cage for every case. The strongest shift was observed for **BEN14** (Fig. 3.23). A ¹H-NMR titration was attempted for this host-guest combination and showed a fast exchange regime through the shifts of the signals. However, precipitation was observed after the addition of more than 1 equivalent of the guest (Fig S3.50). Moreover, a colour change from deep green to olive green was observed. A second titration through UV-Vis spectroscopy was thus performed and allowed us to calculate a binding constant through BindFit: $K_{11} = 6'557 \text{ M}^{-1} \pm 4\%$. (Fig. 3.24 and S3.51)

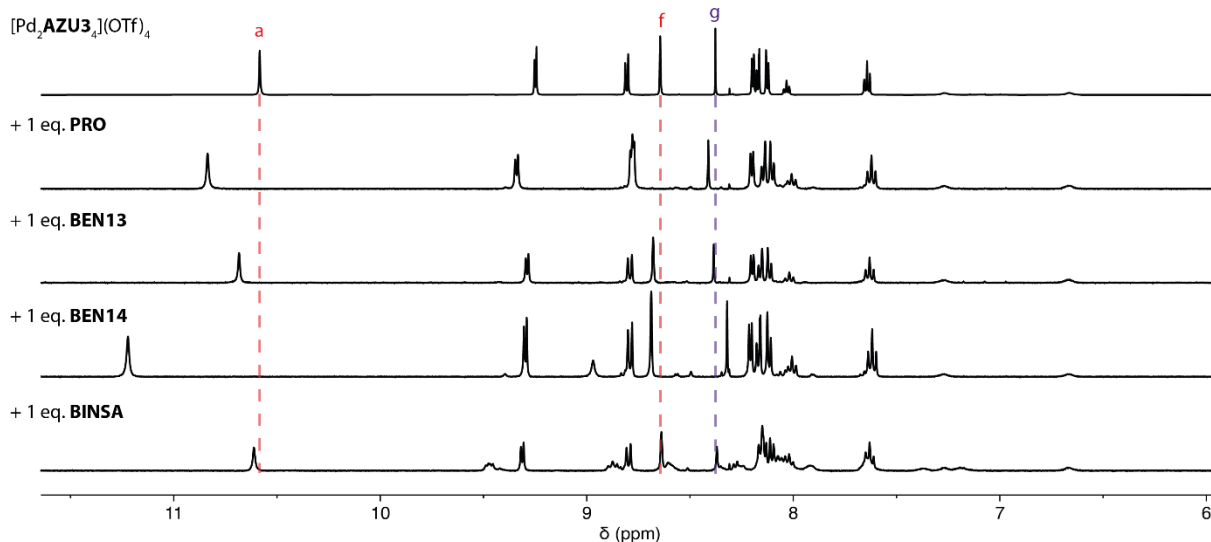


Figure 3.23: $^1\text{H-NMR}$ (500 MHz, $\text{DMSO-}d_6$, 298 K) of $[\text{Pd}_2\text{AZU}_3_4](\text{OTf})_4$ and with 1 equivalent of guest added.

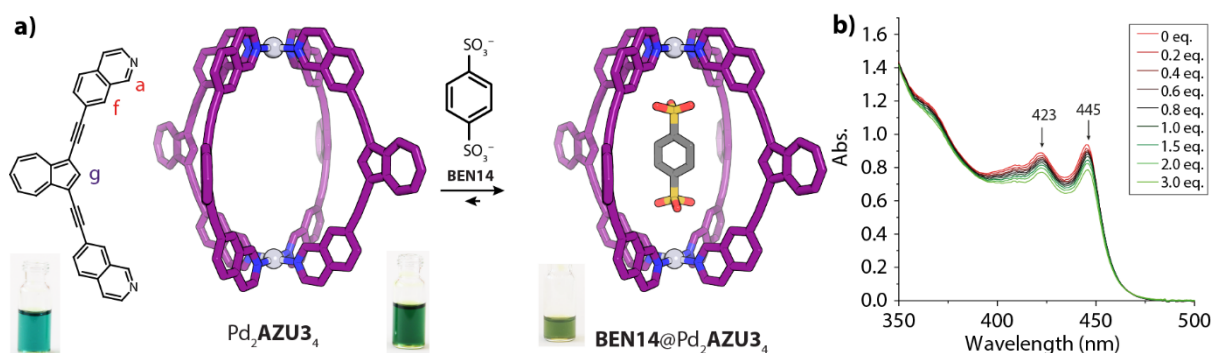


Figure 3.24: (a) host-guest equilibrium of $\text{BEN14@Pd}_2\text{AZU}_3_4$, and photographs of the coloured solutions of each species. (b) UV-Vis titration of $\text{Pd}_2\text{AZU}_3_4$ with BEN14 in DMSO . The two local maxima are indicated, with the value of their wavelength (in nm).

Finally, single crystals of $[\text{BEN14@Pd}_2\text{AZU}_3_4](\text{OTf})_4$ could be grown from the DMSO solution by slow diffusion of toluene and could be analysed by SCXRD: the cage crystallised in the C2/m (no. 12) monoclinic space group, and the asymmetric unit cell contains only one fourth of the complex. As expected, guest BEN14 sits in the middle of the cavity of the cage, its two sulfonate groups pointing towards the nearest Pd(II) cations to maximise electrostatic interactions^[36] (Fig 3.24a and Section 3.7.7.3.).

The absence of transformation when combining the present cage and guests BEN13 or BEN14 confirms that at least one of the factors contributing to the special reactivity of $\text{Pd}_2\text{AZU1}_4$ is related to the size of its cavity and the distance between the two palladium centres.

3.5.3 $\text{Pd}_2\text{AZU}_4_4$

Similar to $\text{Pd}_2\text{AZU}_3_4$, $\text{Pd}_2\text{AZU}_4_4$ and $\text{Pd}_2\text{AZU}_5_4$ were prepared to assess the possibility of recreating the transformation from cage to a higher nuclearity structure upon addition of a guest

molecule. The longer linkers between the backbone and the donor groups would in turn impart a longer distance between the two palladium centres, and therefore larger guests could be accommodated in the cavity. If their size is just in the right spot, they could potentially trigger a transformation of the cage.

For Pd₂AZU₄, the following guests were tested: **BEN13**, **BEN14**, **NAP26**, **NAP27**, **NAP15**, **BINSA**, and **CSA**. Of those, only **BEN14** was measured by NMR to bind inside the cavity, as evidenced by the shifting of the inside pointing protons, notably **a** and **g** (Fig 3.25). In addition, the addition of **NAP15** caused immediate precipitation.

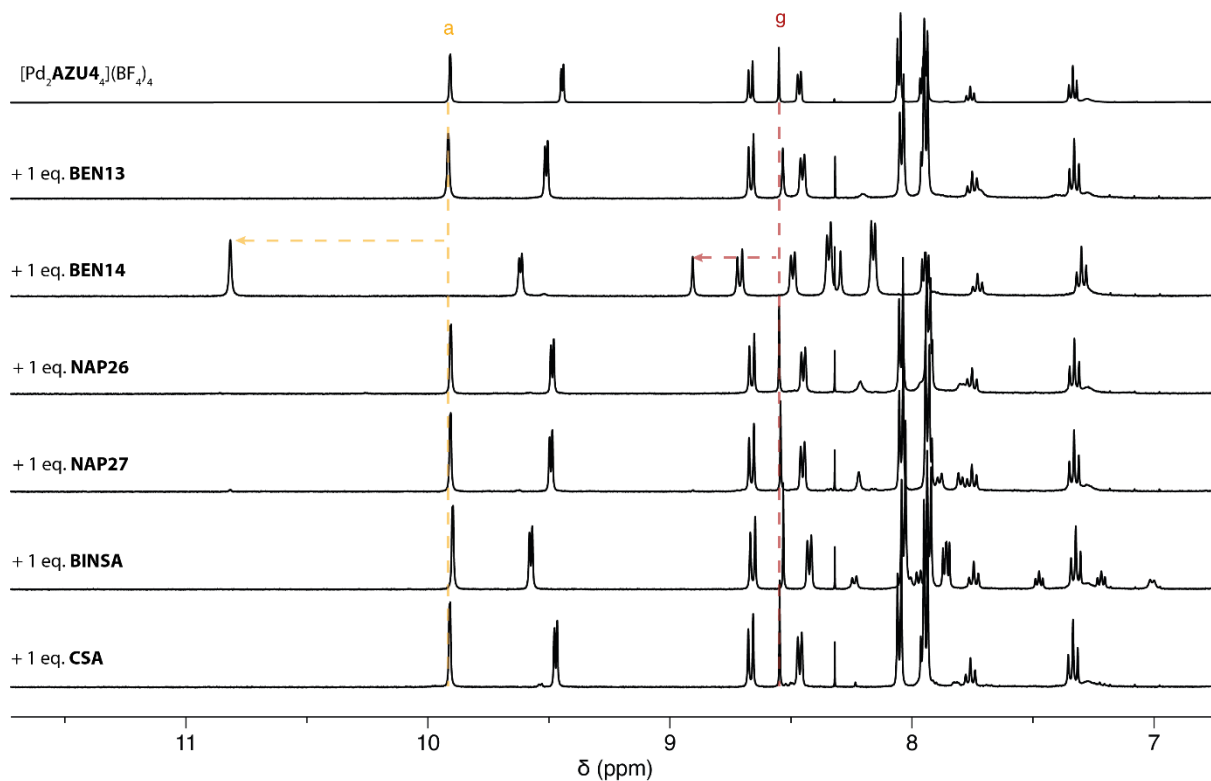


Figure 3.25: ¹H-NMR (500 MHz, DMSO-*d*₆, 298 K) of Pd₂AZU₄ and of its tested host-guest complexes, with 1 equivalent of guest added.

An NMR titration of **BEN14** in Pd₂AZU₄ was performed to determine the binding constant. The rise of new signals and the disappearance of the signals of the free cage demonstrated that the guest exchange rate was slow on the NMR time scale (Fig. 3.26). Moreover, the signals of the free host were completely gone after the addition of 1 equivalent of the guest, precluding us from measuring an accurate binding constant. We can however conclude that the binding constant is higher than 10⁵ M⁻¹. In addition, the host-guest complex was characterised by ESI-MS (Fig. S3.52) and confirmed 1:1 binding.

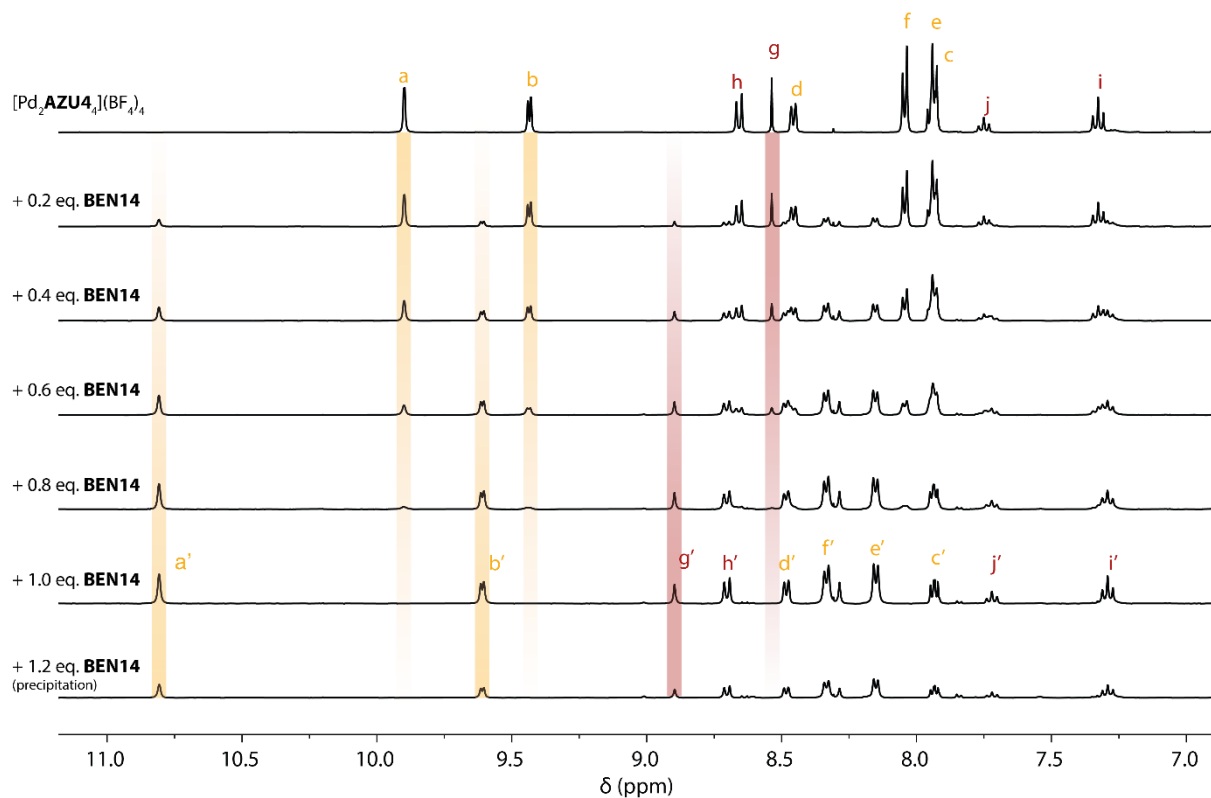


Figure 3.26: $^1\text{H-NMR}$ (500 MHz, $\text{DMSO-}d_6$, 298 K) titration of Pd_2AZU_4 with guest **BEN14**. The slow exchange can be seen by the rising of the host-guest complex signals and the decrease of the signals of the free cage.

In the absence of an X-ray structure of the host-guest complex, a DFT model was prepared (B3LYP/def2-SVP) (Fig. 3.27). A similar distance between the S-atoms of the guest and the nearest Pd-centres was found between Pd_2AZU_4 (4.25 Å, DFT) and Pd_2AZU_3 (4.42 Å, X-ray). However, the distance between opposite azulene moieties (hydrogen position 2 of the azulene backbone) is of 9.9 Å in Pd_2AZU_4 , but of 11.8 Å in Pd_2AZU_3 . The narrower cavity of the **AZU4** cage probably explains its strong selectivity for the exclusive binding of the linear guest **BEN14**, over the similar sized but bent **BEN13**. This exclusivity however means that larger guests were found not to bind, and therefore could not potentially trigger a transformation.

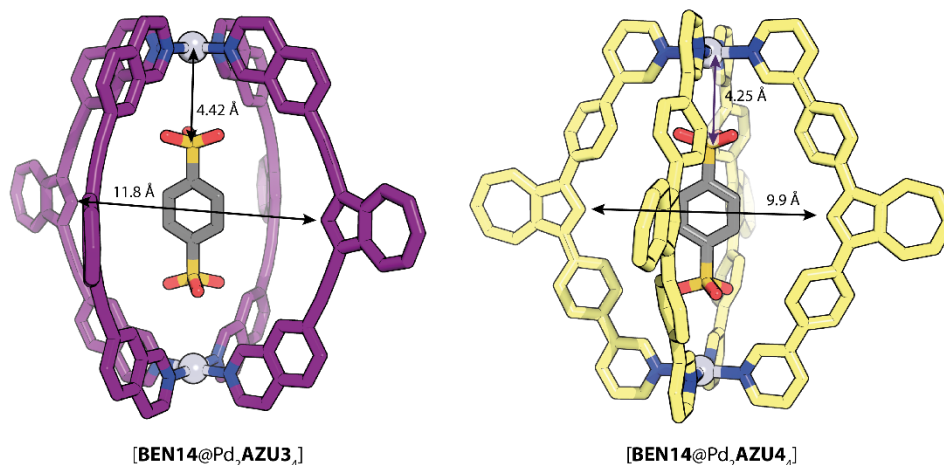


Figure 3.27: comparison of the sizes of the host-guest complexes **BEN14@Pd₂AZU₃** (X-ray structure) and **BEN14@Pd₂AZU₄** (DFT model, B3LYP/def2-SVP).

3.5.4 $Pd_2AZU_5_4$

As no guests except **BEN14** were found to bind to Pd_2AZU_4 , a larger structure was envisioned: cage $Pd_2AZU_5_4$ was prepared from ligand **AZU5**, which possesses an even longer linker, combining both alkyne and phenyl groups. The same guests as previously were screened for interaction with the cage: **BEN13**, **BEN14**, **NAP26**, **NAP27**, **NAP15**, **BINSA**, and **CSA**. By shift of the NMR signals of the internal protons after the addition of 1 equivalent, every guest listed here was found to bind, with the largest shift of the **a** proton being recorded with **NAP27** (Fig. 3.28). The case of **BINSA** is more delicate to assess: indeed, the **a** proton does not shift. However, the **g** and **b** protons do, indicating a possible outside binding from both the top and the side of the cage. However, host-guest mixtures formed with **BEN13**, **BEN14**, and **NAP15** were found to precipitate after cooling down.

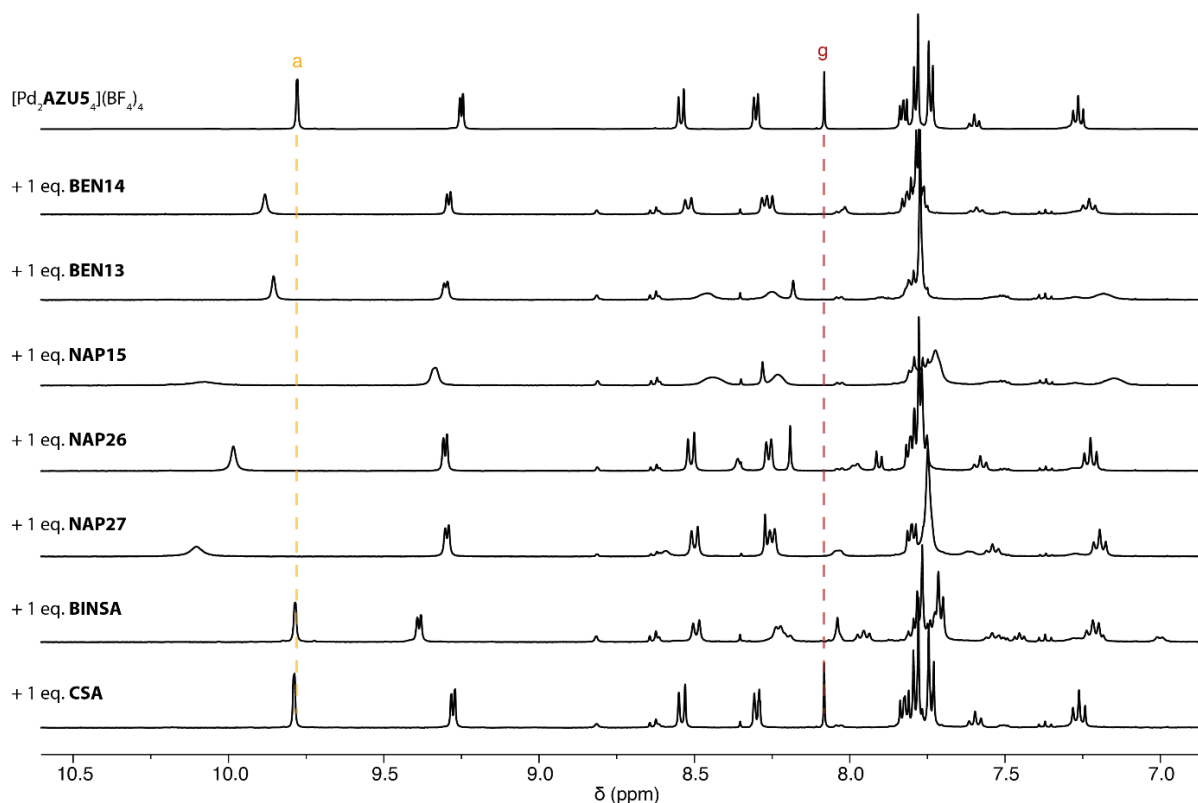


Figure 3.28: ¹H-NMR (500 MHz, DMSO-*d*₆, 298 K) of Pd₂AZU₅₄ and of the first half of the tested host-guest complexes, with 1 equivalent of guest added.

In addition to the previously mentioned guests, larger ones were also screened: **FEC**, **26ANQ**, **27ANQ**, **B12H12**, **B12F12**, **B10C110**, and **Mo6O19**. Of those seven new guests, **FEC**, **26ANQ**, **27ANQ**, and **B12F12** were shown to bind to the cage. The addition of **B12H12** and **Mo6O19** caused precipitation, and **B10C110** showed no binding (Fig. 3.29).

The exchange rate of the host-guest complexes (fast or slow on the NMR timescale) was not determined for any of the guests during the screening process, as only 1 equivalent was added at this stage. However, no spectra showed an overlap of signals of the free cage and of the host-guest complex. This potential case would have meant that the guest bound in a slow process and a moderately strong association constant ($K_a < 10^5 \text{ M}^{-1}$). On the other hand, **BEN14** was previously shown to fully saturate Pd₂AZU₄ after only one equivalent, meaning a strong association constant ($K_a < 10^5 \text{ M}^{-1}$).

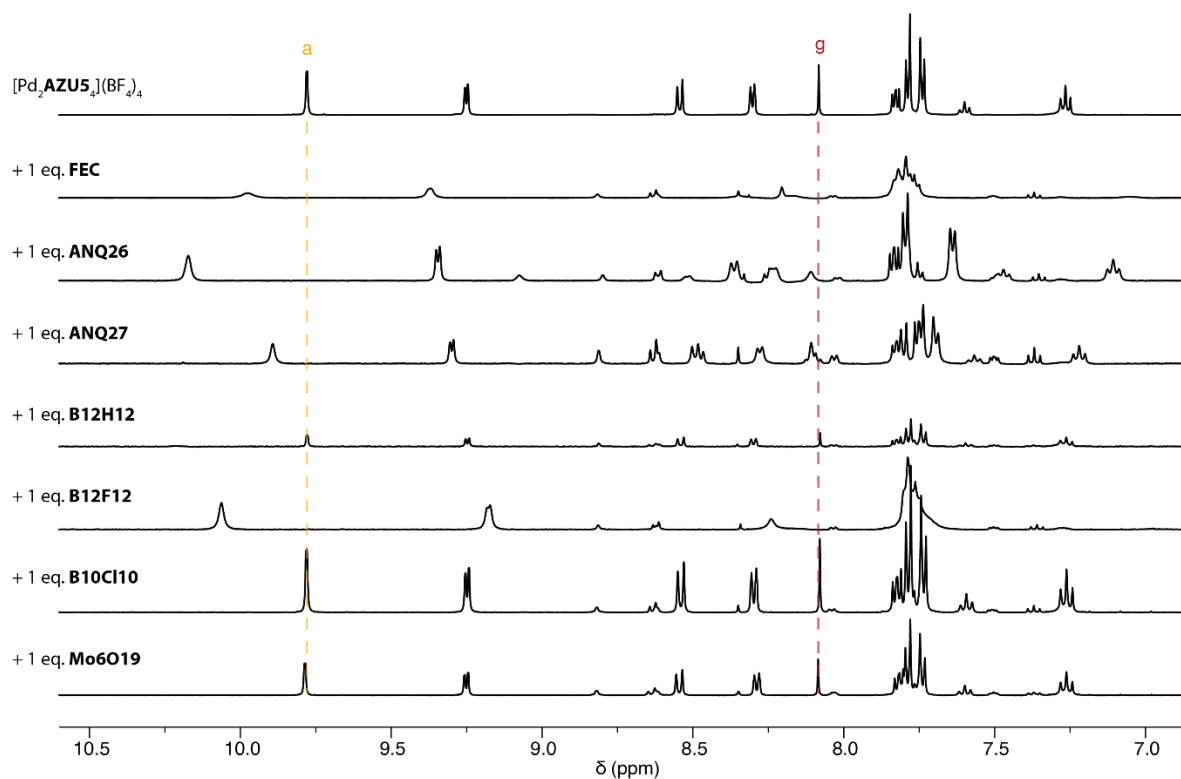


Figure 3.29: ¹H-NMR (500 MHz, DMSO-*d*₆, 298 K) of [Pd₂AZU₅]₄(BF₄)₄ and of the second half of the tested host-guest complexes, with 1 equivalent of guest added.

Host-guest complex **B12F12**@Pd₂AZU₅₄ could be crystallised by slow diffusion of toluene into the DMSO solution. X-ray diffraction analysis showed that the compound crystallises into the monoclinic C2/c (no. 15) space group, with the asymmetric unit cell containing one host-guest complex, and guest **B12F12** binding to the centre of the cavity as expected (Fig. 3.30 and Section 3.7.7.5). The azulene moieties of two neighbouring ligands are parallel to each other, resulting from π -stacking with the ligands of a neighbouring cage in the crystal lattice. The distance between the two azulene moieties (plane to centroid) was measured to be 3.5 Å, a value in good agreement with π - π stacking.^[37] Moreover, the stacking of the complex in the crystal lattice creates large pores, which constitute around 40% of the total volume of the crystal as calculated with Mercury.

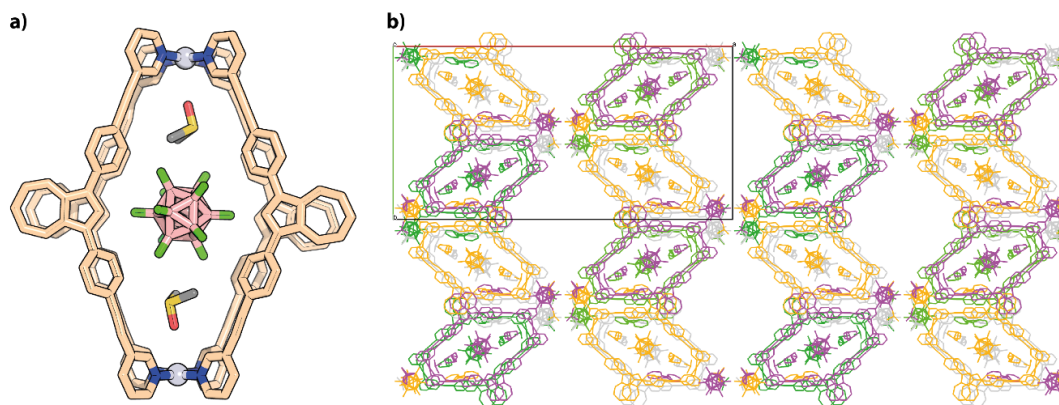


Figure 3.30: (a) X-ray structure of the host-guest complex **B12F12@Pd₂AZU₅₄**. Most of the solvent molecules and counteranions were omitted for clarity. (b) packing of the crystal of the host-guest complex viewed along the c axis. Notice the jagged arrangement of the cages and the large resulting solvent channels.

The binding constant of guests **NAP26**, **NAP27**, and **B12F12** was determined by NMR titration and the BindFit app. Every guest tested is in rapid exchange.

B12F12 could be fitted to a 1:1 binding model, in accordance with the X-ray structure, and the binding constant was calculated as $K_{11} = 18'907 \text{ M}^{-1} \pm 10.6 \%$ (Fig. 3.31).

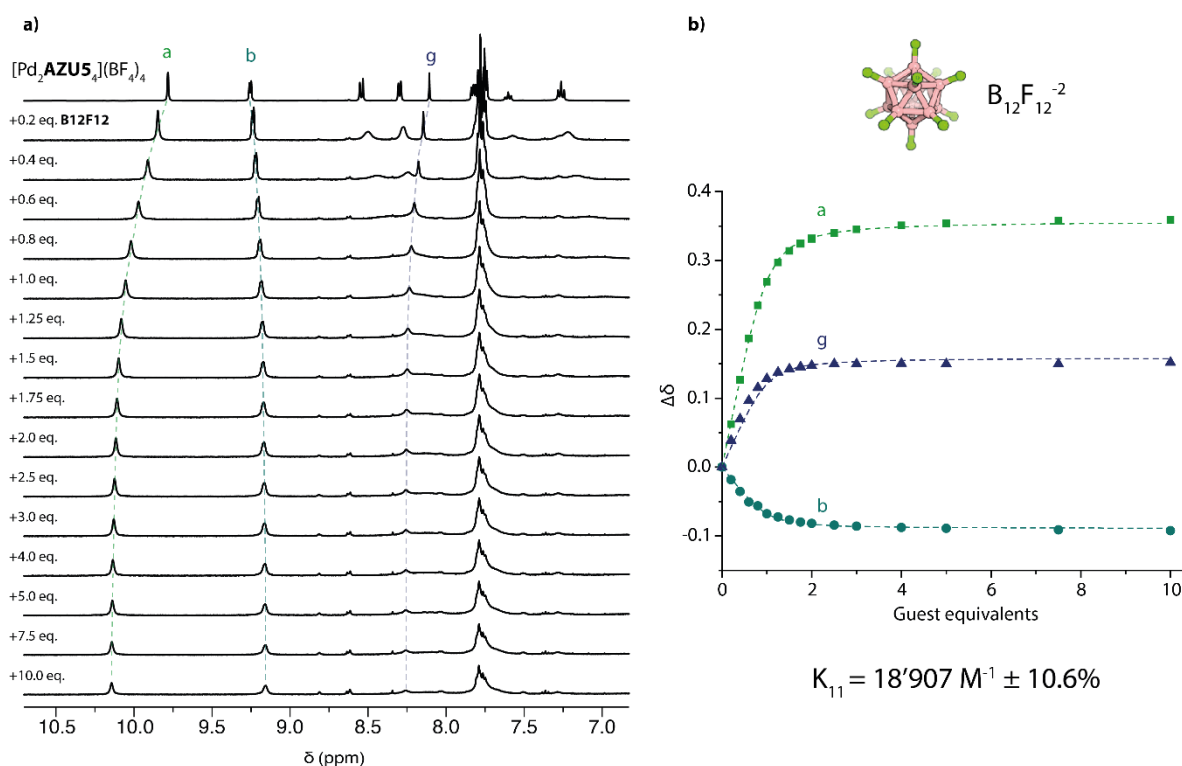


Figure 3.31: (a) ¹H-NMR (500 MHz, DMSO-*d*₆, 298 K) of the titration of **B12F12** into Pd₂AZU₅₄. (b) graph of the shift of the signals **a**, **b**, and **g** used for the determination of the binding constant (scatter) and the fit of the data by BindFit (dashed lines).

The titration of guests **NAP26** and **NAP27** revealed a different behaviour, as in both NMR titrations the **g** proton (on the azulene, inward pointing) would initially experience a downfield shift,

followed by an upfield shift after the addition of 1.5 eq. of guest (Fig. 3.32a & 3.33a). This inflexion behaviour is potentially an evidence for a more complex binding stoichiometry, likely a 1:2 (host:guest) binding mode. Unfortunately, the host-guest complexes could not be detected by ESI-MS. A fit of the **NAP26** NMR data to a 1:2 mode with BindFit gave the following values: $K_{11} = 32'016 \text{ M}^{-1} \pm 29 \%$ and $K_{12} = 674 \text{ M}^{-1} \pm 32 \%$. While the errors are large, the values themselves are in agreement with a potential non-cooperative 1:2 binding mode: a first strong binding event, followed by a much weaker one. To overcome the large errors of the binding constants obtained by NMR, the same titration was performed at 50 μM by UV-Vis spectroscopy (Fig. 3.32b) and similar binding constants were calculated: $K_{11} = 25'458 \text{ M}^{-1} \pm 12 \%$ and $K_{12} = 640 \text{ M}^{-1} \pm 5 \%$ (Fig. 3.32c). Those values confirm the NMR titration, but with better uncertainty values. The second binding event is probably an outside interaction, as seen by the comparatively very weak value. In addition, the absence of an isosbestic point in the UV-Vis data seems to confirm the presence of more than two supramolecular species during the titration.

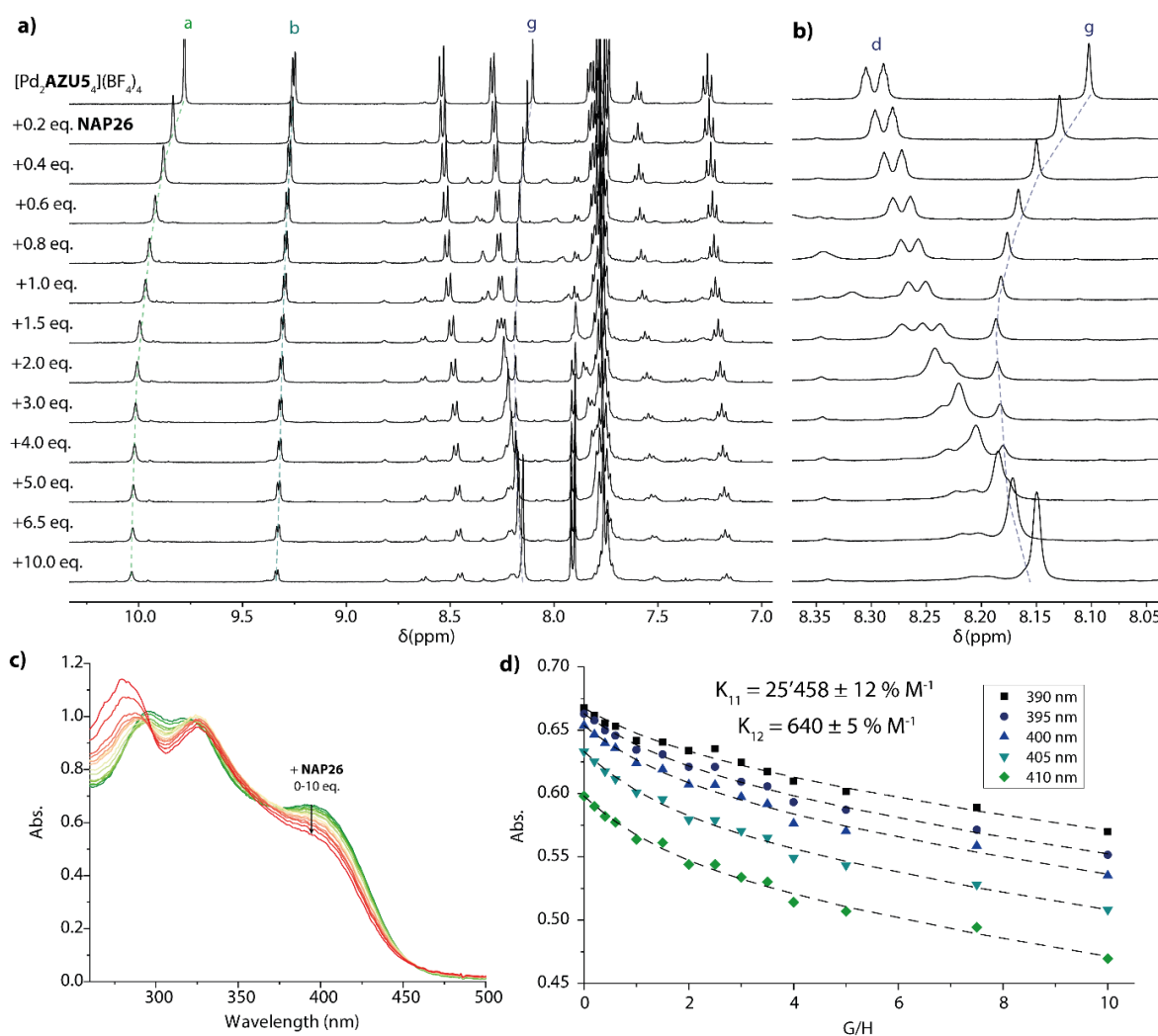


Figure 3.32: (a) $^1\text{H-NMR}$ (500 MHz, $\text{DMSO-}d_6$, 298 K) of the titration of **NAP26** into $[\text{Pd}_2\text{AZU5}_d](\text{BF}_4)_4$. (b) zoom in the d and g proton area. (c) UV-Vis absorbance spectra of the titration. (d) graph of the evolution of the absorbance at selected wavelengths used for the determination of the binding constant (scatter) and the fit of the data by BindFit (dashed lines).

Similarly, the **NAP27** NMR data gave the following values: $K_{11}=83'098 \pm 22 \% M^{-1}$ and $K_{12}=3'657 \pm 18 \% M^{-1}$ (Fig. 3.33). The more than threefold increase in association constant compared to **NAP26** could be explained by shape complementarity between the host and the guest.^[38] However, the sulfonates in **NAP26** are positioned in a linear fashion (180°), easily bridging the two Pd(II) centres of the cage. On the opposite, the sulfonates in **NAP27** are positioned with a 120° angle, a less favourable angle for electrostatic interactions between the two palladium centres with parallel coordination planes. A UV-Vis titration was performed similarly as with **NAP26**, but the negligible change in the spectrum precluded us from measuring any reliable data with this method (Fig. S3.53).

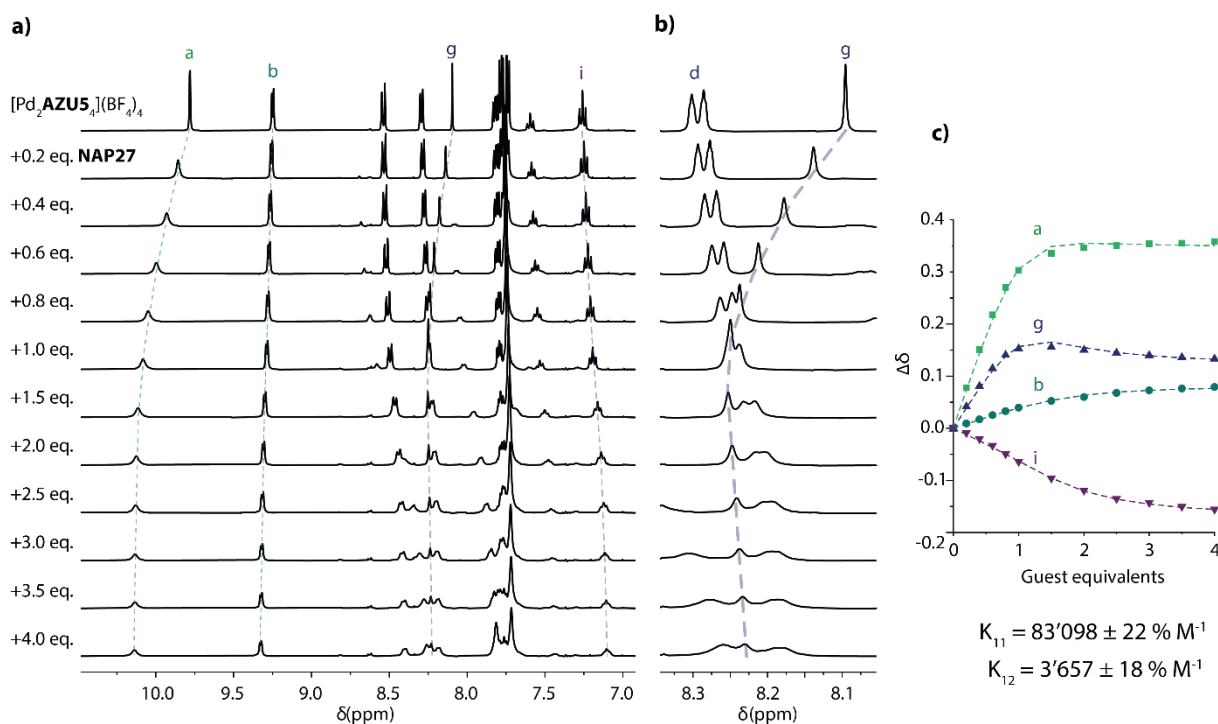


Figure 3.33: (a) ¹H-NMR (500 MHz, DMSO-*d*₆, 298 K) of the titration of **NAP27** into $[Pd_2AZU_5](BF_4)_4$. (b) zoom in the **d** and **g** proton area. (c) graph of the shift of the signals **a**, **b**, **g**, and **i** used for the determination of the binding constant (scatter) and the fit of the data by BindFit (dashed lines).

3.6 CONCLUSION

In conclusion, I have prepared a series of Pd₂L₄ coordination cages with ligands of different sizes based on the 1,3-azulene backbone. By varying the length of the linkers and the type of donor groups, we can control their cavity volumes and their guest uptake behaviour. The smallest cage, Pd₂AZU1₄, can undergo a dramatic transformation between its initial lantern-shaped topology to a twice as large Pd₄AZU1₈ tetrahedron upon a stoichiometric addition of disulfonate guests **BEN13** and **BEN14**. In addition, the transformation can be reversed by the addition of a second coordination cage based on the dye methylene blue, which will preferentially bind the guests, and release the initial

Pd₂AZU₁₄ cage. The addition of the azulene chromophore into the ligands has two implications: first, it allows for an easy following of the cage formation and transformation upon guest binding by the naked eye, as the colour of the azulene core is highly dependent on its electronic environment. Moreover, DFT calculations suggest that the structure of the tetrahedron is stabilised by favourable polarised CH- π interactions between the central four azulene units.

Attempts to replicate the guest-triggered transformation between a cage and a larger species by working with larger ligands based on azulene were unsuccessful, only leading to the formation of classic host-guest complexes, without any observable transformations.

3.7 EXPERIMENTAL PART

3.7.1 General methods

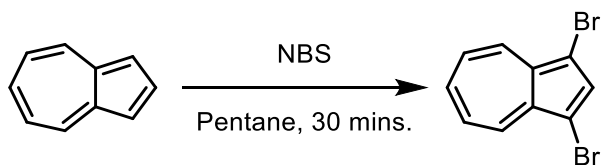
Where necessary, experiments were performed under argon atmosphere using standard Schlenk techniques. Chemicals and standard solvents were purchased from Sigma Aldrich, Acros Organics, Carl Roth, TCI Europe, VWR, ABCR and used as received, if not mentioned differently. Dry solvents were purchased or purified and dried over absorbent-filled columns on a GS-Systems solvent purification system (SPS). Reactions were monitored with thin layer chromatography (TLC) using silica coated aluminium plates (Merck, silica 60, fluorescence indicator F254, thickness 0.25 mm). For column chromatography, silica (Merck, silica 60, 0.02–0.063 mesh ASTM) was used as the stationary phase. Gel permeation chromatography (GPC) purification of ligands were performed on a JAI 9210-II NEXT GPC System with a JAIGEL HH-2/HH-1 column combination running with CHCl₃ (HPLC grade). UV-vis spectra were recorded on a DAD HP-8453 UV-Vis spectrometer. Cuvette path length 1 cm, unless otherwise stated; wavelength: 270 nm – 900 nm, step size: 1 nm. Fluorescence spectra were recorded on a Jasco FP-8300 fluorescence spectrometer. Cuvette path length 2 mm, step size 0.5 nm.

High resolution Electrospray ionization (ESI) mass spectra were recorded on Bruker ESI timsTOF (trapped ion mobility-time of flight) and Compact mass spectrometers (positive mode). All samples were diluted with spectroscopy-grade CH₃CN (1:10).

NMR experiments were performed on Bruker AVANCE III 500, 600 or 700 MHz spectrometers. Chemical shifts for ¹H and ¹³C are reported in ppm with residual solvent as reference: acetonitrile (1.94 ppm for ¹H, 1.32 ppm for ¹³C), DMSO-*d*₆ (2.50 ppm for ¹H, 39.52 ppm for ¹³C) and CDCl₃ (7.26 ppm for ¹H, 77.16 ppm for ¹³C). Abbreviations for signal multiplicity in the ¹H-NMR spectra are indicated as following: s: singlet, d: doublet, t: triplet, dd: doublet of doublets; dt: doublet of triplets; m: multiplet, b: broad.

3.7.2 Synthesis of the ligands

3.7.2.1 Synthesis of 1,3-Dibromoazulene



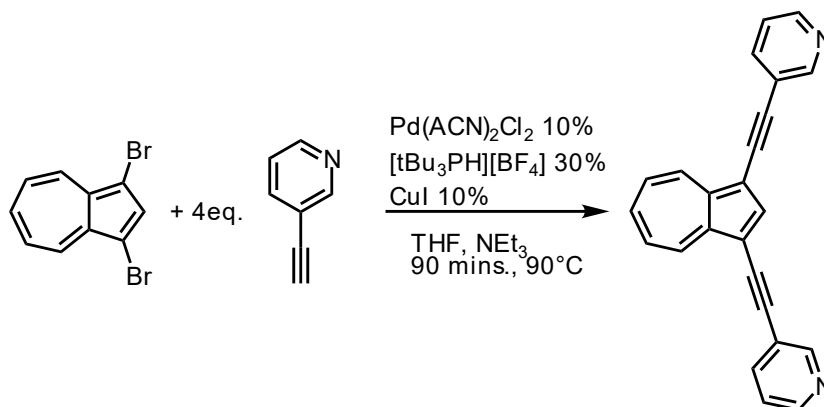
Scheme S3.1

Azulene (1 mmol, 128.2 mg) was dissolved in pentane (10 ml), and the solution was cooled down to 0°C in an ice bath. *N*-bromo succinimide (4 mmol, 712.0 mg) was then added in portions. After the addition was complete, the ice-bath was removed, and the solution was stirred for 30 min.

at RT. It was then filtered, and the solvent was removed by evaporation to afford the product as puffy dark green crystals (0.8 mmol, 288.8 mg, yield: 80%)

¹H-NMR (500 MHz, CDCl₃) δ 8.41 – 8.24 (m, 2H), 7.81 (s, 1H), 7.72 – 7.64 (m, 1H), 7.28 (d, 2H).

3.7.2.2 Synthesis of ligand **AZU1** (1,3-bis(pyridin-3-ylethynyl)azulene)



Scheme S3.2

1,3-Dibromoazulene (0.5 mmol, 143.0 mg) and 3-ethynylpyridine (2 mmol, 206.2 mg) were added to a pressure-proof Schlenk flask, as well as a magnetic stirrer and 10 ml of a 1:1 mixture of dry THF and triethylamine. The solution was degassed by the freeze-pump-thaw technique. Then, under a stream of argon, the catalysts were added: Bis(acetonitrile)palladium(II) dichloride (0.05 mmol, 13.0 mg), tri-*tert*-butylphosphonium tetrafluoroborate (0.15 mmol, 43.5 mg), and copper(I) iodide (0.05 mmol, 9.5 mg). The mixture was then stirred for 90 minutes at 90°C.

Afterwards, the solution was filtered, and the solvents evaporated. The crude product was purified by flash column chromatography (EtOAc, MeOH 10%) and GPC to yield ligand **AZU1** as a dark green powder (blue in solution in all tested solvents). (0.35 mmol, 115.6 mg, yield: 70%)

¹H-NMR (600 MHz, 298K, CDCl₃) δ 8.86 (d, *J* = 2.2 Hz, 2H), 8.63 (d, *J* = 9.5 Hz, 2H), 8.58 – 8.54 (m, 2H), 8.16 (s, 1H), 7.89 (dt, *J* = 7.8, 2.0 Hz, 2H), 7.77 (t, *J* = 9.8 Hz, 1H), 7.41 (t, *J* = 9.7 Hz, 2H), 7.32 (dd, *J* = 7.9, 4.9 Hz, 2H).

¹³C-NMR (151 MHz, 298K, CDCl₃) δ 152.19, 148.36, 142.39, 141.92, 140.56, 138.25, 137.46, 126.53, 123.24, 121.17, 110.05, 90.92, 88.25.

ESI-MS: calculated for [C₂₄H₁₄N₂+H⁺]: 331.1230, found: 331.1221

3 – Guest-induced transformation of an azulene-based Pd_2L_4 cage to a Pd_4L_8 tetrahedron

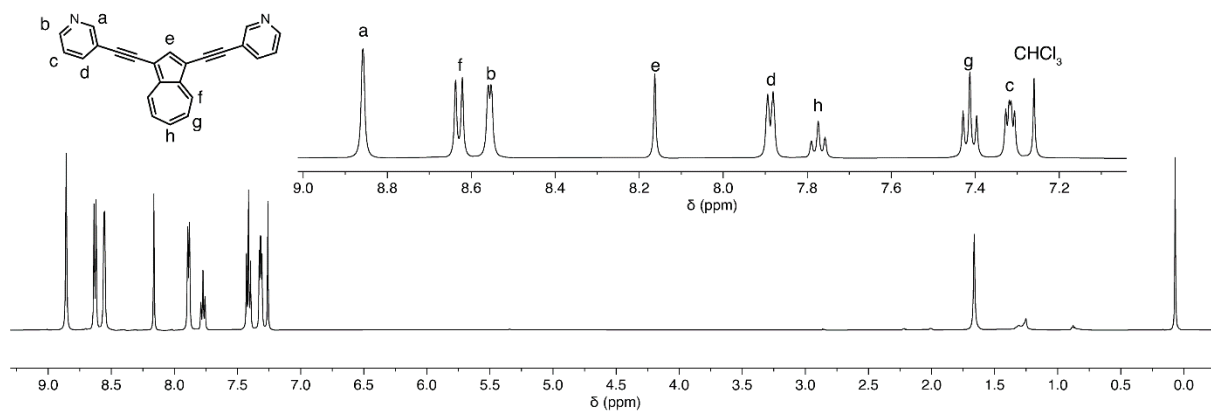


Figure S3.1: 1H -NMR spectrum (600MHz, 298K, $CDCl_3$) of ligand AZU1. The aromatic region is presented in the insert.

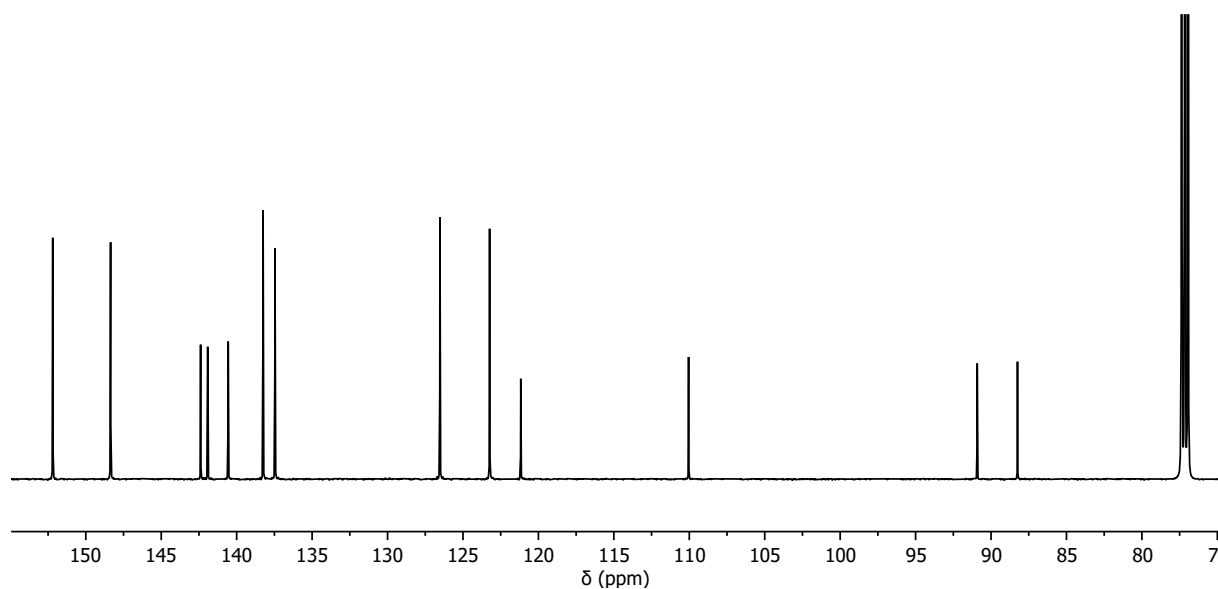
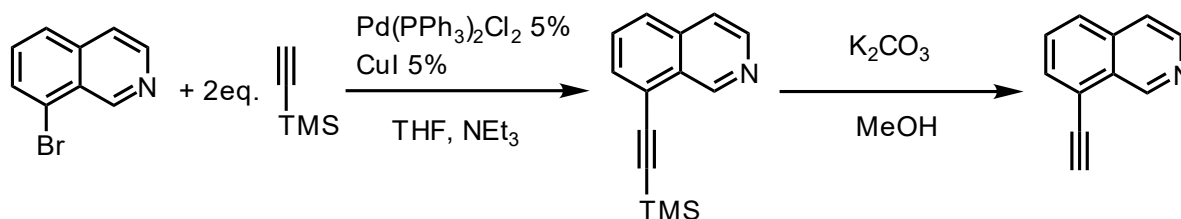


Figure S3.2: ^{13}C -NMR spectrum (151MHz, 298K, $CDCl_3$) of ligand AZU1.

3.7.2.3 Synthesis of 8-ethynylisoquinoline



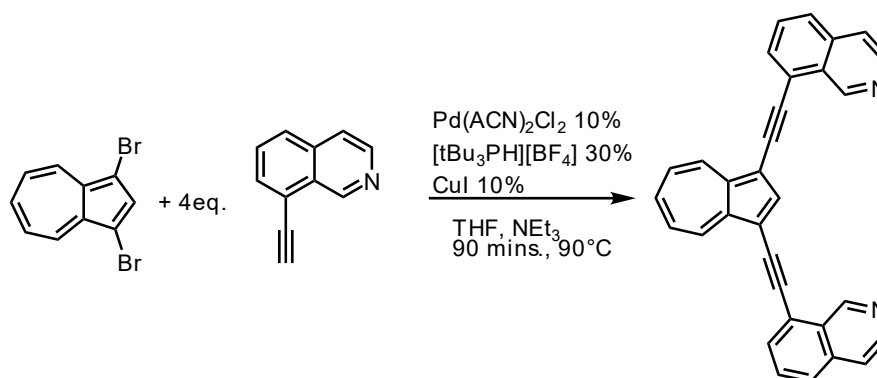
Scheme S3.3

8-Bromoisoquinoline (500 mg, 2.4 mmol) was added to a Schlenk flask, as well as a magnetic stirrer and 10 ml of a 1:1 mixture of dry THF and triethylamine (30 ml). The solution was degassed

by the freeze-pump-thaw technique. Then, under a stream of argon, the catalysts were added: bis(triphenylphosphine)palladium(II) dichloride (84.2 mg, 0.12 mmol) and copper iodide (23.0 mg, 0.12 mmol). Finally, ethynyltrimethylsilane (707.2 mg, 1.02 ml, 7.2 mmol) was added. The mixture was then stirred at 60°C for 10 hours. Afterwards, the solution was filtered, and the solvents evaporated. The crude product was purified by flash column chromatography (DCM/EtOAc 2:1). The resulting off-white product (intermediate 8-((trimethylsilyl)ethynyl)isoquinoline) was then dissolved in 20 ml of methanol under argon, and potassium carbonate (1 g) was added. The mixture was stirred for 1h at RT. The contents were filtered, and the solvent was evaporated. The crude was purified flash column chromatography (DCM/EtOAc 2:1) to yield the title compound as an off-white powder (202.1 mg, 1.32 mmol, total yield over two steps: 55%).

¹H-NMR (500 MHz, CDCl₃) δ 9.73 (s, 1H), 8.60 (d, *J* = 5.7 Hz, 1H), 7.86 – 7.79 (m, 2H), 7.67 – 7.62 (m, 2H), 3.56 (s, 1H).

3.7.2.4 Synthesis of ligand **AZU2** (1,3-bis(isoquinolin-8-ylethynyl)azulene)



Scheme S3.4

1,3-Dibromoazulene (0.5 mmol, 143.0 mg) and 8-ethynylisoquinoline (2 mmol, 306.4 mg) were added to a pressure-proof Schlenk flask, as well as a magnetic stirrer and 10 ml of a 1:1 mixture of dry THF and triethylamine. The solution was degassed by the freeze-pump-thaw technique. Then, under a stream of argon, the catalysts were added: Bis(acetonitrile)palladium(II) dichloride (0.05 mmol, 13.0 mg), tri-*tert*-butylphosphonium tetrafluoroborate (0.15 mmol, 43.5 mg), and copper(I) iodide (0.05 mmol, 9.5 mg). The mixture was then stirred for 90 minutes at 90°C.

Afterwards, the solution was filtered and the solvents evaporated. The crude product was purified by flash column chromatography (EtOAc, MeOH 5%) and GPC to yield ligand **AZU2** as an olive-green powder. (66%)

¹H-NMR (600 MHz, CDCl₃) δ 9.98 (s, 2H), 8.78 (d, *J* = 9.4 Hz, 2H), 8.63 (d, *J* = 5.6 Hz, 2H), 8.36 (s, 1H), 7.92 (d, *J* = 7.1 Hz, 2H), 7.81 (m, 3H), 7.75 – 7.66 (m, 4H), 7.48 (t, *J* = 9.7 Hz, 2H).

¹³C-NMR (151 MHz, CDCl₃) δ 205.94, 150.35, 142.71, 141.46, 139.53, 136.44, 134.88, 130.16, 128.91, 126.77, 125.66, 125.44, 121.30, 119.58, 109.30, 90.38, 89.58.

ESI-MS: calculated for [C₃₂H₁₈N₂+H⁺]: 431.1543, found: 431.1568

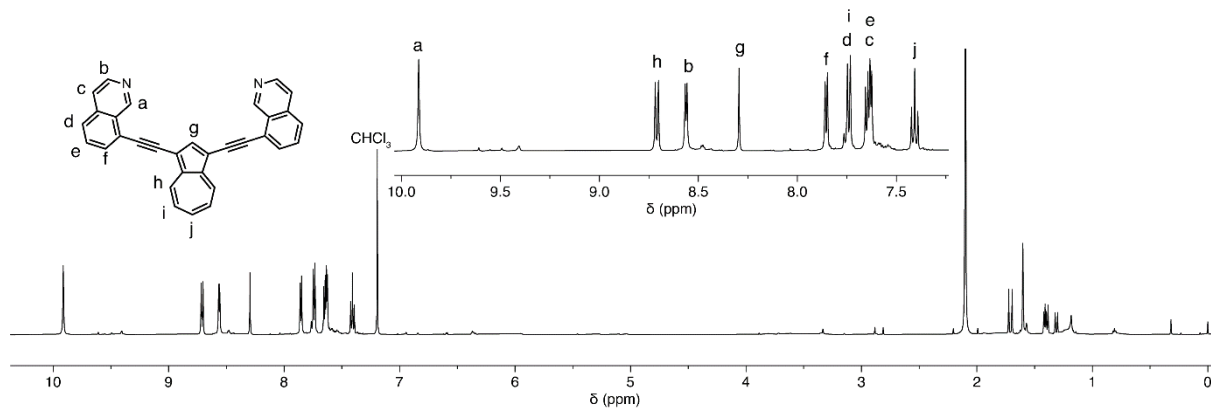


Figure S3.3: ¹H-NMR spectrum (600MHz, 298K, CDCl₃) of ligand **AZU2**. The aromatic region is presented in the insert.

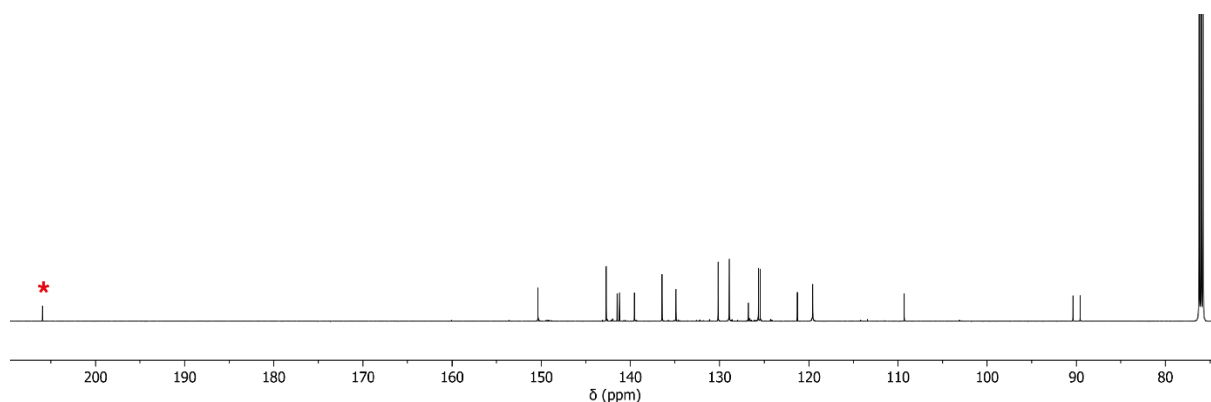
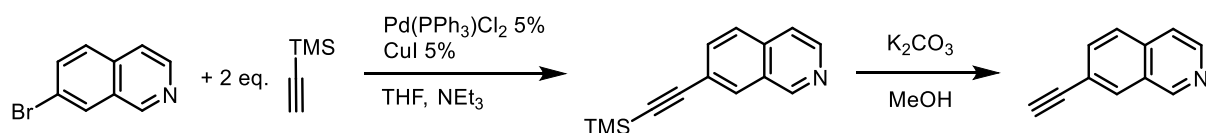


Figure S3.4: ¹³C-NMR spectrum (151MHz, 298K, CDCl₃) of ligand **AZU2**. Signal from acetone impurity is labelled with an asterisk.

3.7.2.5 Synthesis of 7-ethynylisoquinoline



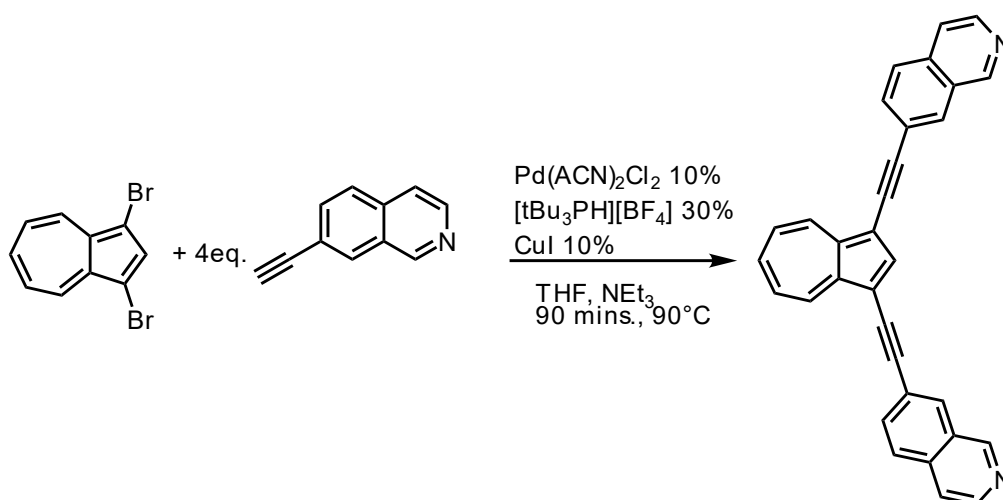
Scheme S3.5

7-Bromoisoquinoline (500mg, 2.4mmol) was added to a Schlenk flask, as well as a magnetic stirrer and 10ml of a 1:1 mixture of dry THF and triethylamine (10ml). The solution was degassed by the freeze-pump-thaw technique. Then, under a stream of argon, the catalysts were added: bis(triphenylphosphine)palladium(II) dichloride (84.2mg, 0.12mmol) and copper iodide (23.0mg, 0.12

mmol). Finally, ethynyltrimethylsilane (707.2mg, 1.02ml, 7.2mmol) was added. The mixture was then stirred at 70°C overnight. Afterwards, the solution was filtered and the solvents evaporated. The crude product was purified by flash column chromatography (DCM/EtOAc 4:1). The resulting off-white product (intermediate 7-((trimethylsilyl)ethynyl)isoquinoline, 322.2 mg, 1.43 mmol, intermediate yield: 60%) was then dissolved in 20 ml of methanol under argon, and potassium carbonate (1 g) was added. The mixture was stirred for 1h at RT. The contents were filtered, and the solvent was evaporated. The crude material was purified by flash column chromatography (DCM/EtOAc 4:1) to yield the title compound as an off-white powder (157.3 mg, 1.03 mmol, total yield over two steps: 43%).

¹H-NMR (500 MHz, CDCl₃) δ 9.23 (s, 1H), 8.55 (d, *J* = 5.7 Hz, 1H), 8.15 (d, *J* = 1.4 Hz, 1H), 7.79 (d, *J* = 8.5 Hz, 1H), 7.74 (dd, *J* = 8.5, 1.5 Hz, 1H), 7.64 (d, *J* = 5.8 Hz, 1H), 3.21 (s, 1H).

3.7.2.6 Synthesis of ligand **AZU3** (1,3-bis(isoquinolin-7-ylethynyl)azulene)



Scheme S3.6

1,3-Dibromoazulene (0.175 mmol, 50 mg) and 7-ethynylisoquinoline (0.875 mmol, 134 mg) were added to a pressure-proof Schlenk flask, as well as a magnetic stirrer and 10 ml of a 1:1 mixture of dry THF and triethylamine. The solution was degassed by the freeze-pump-thaw technique. Then, under a stream of argon, the catalysts were added: Bis(acetonitrile)palladium(II) dichloride (0.018 mmol, 4.7 mg), tri-*tert*-butylphosphonium tetrafluoroborate (0.09 mmol, 26.1 mg), and copper(I) iodide (0.018 mmol, 3.4 mg). The mixture was then stirred for 90 minutes at 90°C.

Afterwards, the solution was filtered, and the solvents evaporated. The crude product was purified by flash column chromatography (EtOAc, MeOH 5%) and GPC to yield ligand **AZU3** as a green powder (33.5 mg, 0.078 mmol, yield: 44.5%).

¹H-NMR (700 MHz, CDCl₃) δ 9.27 (s, 2H), 8.72 – 8.66 (m, 2H), 8.55 (d, *J* = 5.7 Hz, 2H), 8.25 (dd, *J* = 1.7, 0.9 Hz, 2H), 8.22 (s, 1H), 7.89 (dd, *J* = 8.4, 1.6 Hz, 2H), 7.86 – 7.82 (m, 2H), 7.78 (ddt, *J* = 10.7, 9.8, 1.2 Hz, 1H), 7.66 (dd, *J* = 5.7, 1.0 Hz, 2H), 7.46 – 7.38 (m, 2H).

¹³C-NMR (176 MHz, CDCl₃) δ 152.34, 143.73, 142.49, 141.93, 140.54, 137.48, 135.06, 133.04, 130.46, 128.69, 126.84, 126.42, 123.06, 120.54, 110.43, 93.93, 86.58.

ESI-MS: calculated for [C₃₂H₁₈N₂]⁺: 430.1465, found: 430.1483

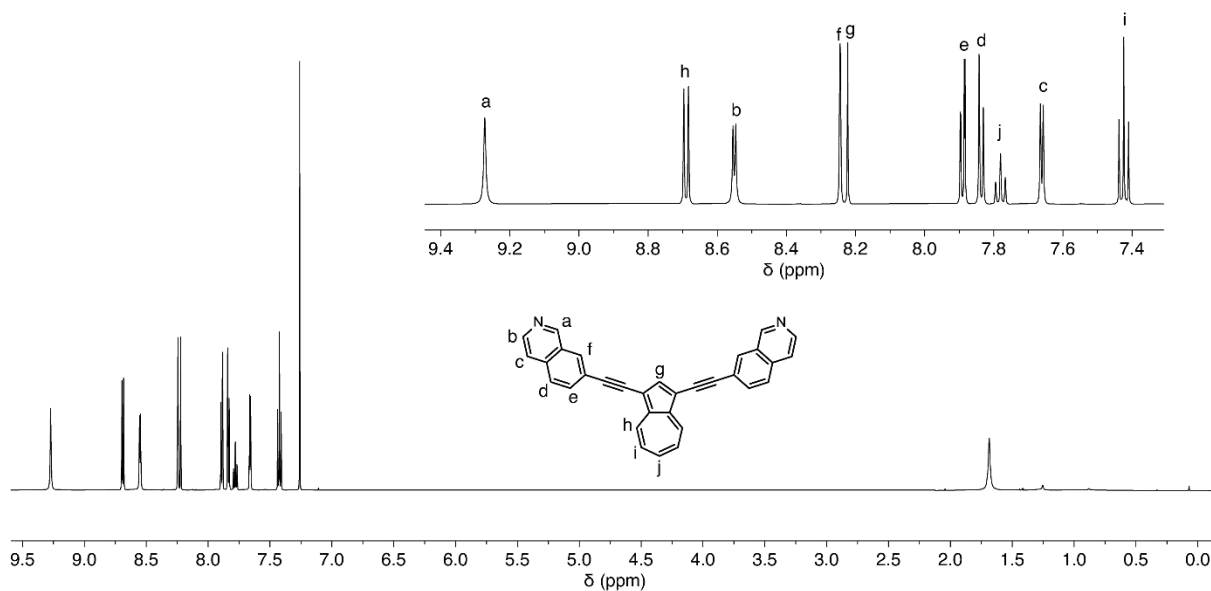


Figure S3.5: ¹H-NMR spectrum (700MHz, 298K, CDCl₃) of ligand **AZU3**. The aromatic region is presented in the insert.

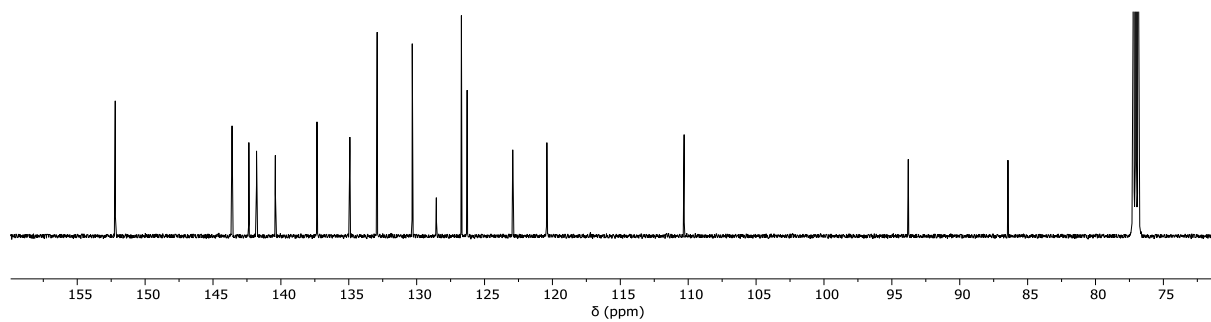
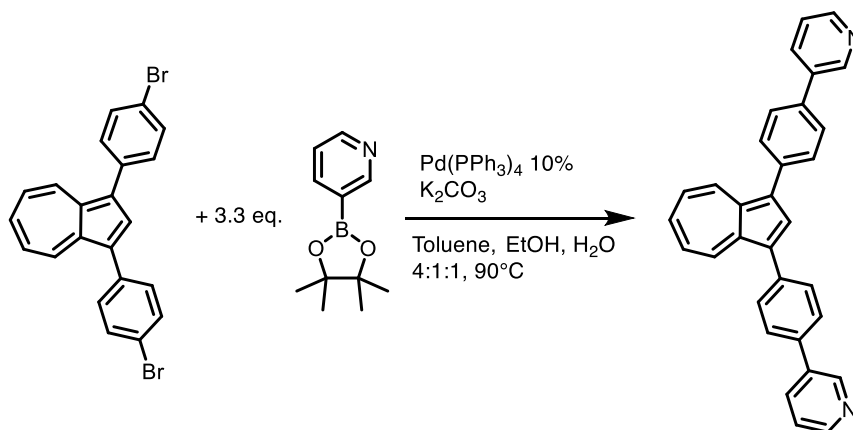


Figure S3.6: ¹³C-NMR spectrum (151MHz, 298K, CDCl₃) of ligand **AZU3**.

3.7.2.7 Synthesis of ligand AZU4 (1,3-bis(4-(pyridin-3-yl)phenyl)azulene)

Scheme S3.7

1,3-bis(4-bromophenyl)azulene^[39] (219 mg, 0.5 mmol), 3-pyridine-BPin (412 mg, 1.15 mmol), and K₂CO₃ (276 mg, 2 mmol) were added to a Schlenk flask with a mixture of 20 ml of toluene, 5 ml of EtOH, and 5 ml of water, and the whole was degassed by bubbling argon through it for 15 min. Then, Pd(PPh₃)₄ (58 mg, 0.05 mmol) was added to it, the flask was sealed and heated at 90°C and stirred overnight. After it was cooled down, the mixture was poured in water and extracted with DCM. The organic layer was dried with MgSO₄ and evaporated under reduced pressure. The crude was chromatographed on silica with DCM, 5% MeOH to yield **AZU4** as a blue product. It was then further purified by GPC. The final yield was 135 mg (62%).

¹H-NMR (600 MHz, CDCl₃) δ 8.99 (s, 2H), 8.64 (s, 2H), 8.62 (d, *J* = 49.3 Hz, 2H), 8.21 (s, 1H), 8.00 (dt, *J* = 8.0, 1.7 Hz, 2H), 7.82 – 7.73 (m, 8H), 7.65 (t, *J* = 10.0 Hz, 1H), 7.44 (d, *J* = 4.4 Hz, 2H), 7.21 (t, *J* = 10.0 Hz, 2H).

¹³C-NMR (151 MHz, CDCl₃) δ 148.47, 148.29, 139.60, 137.29, 137.28, 136.80, 136.55, 136.02, 134.56, 130.69, 130.06, 127.68, 124.30, 124.00.

ESI-MS (pos. mode): calculated for [C₃₂H₂₂N₂+H]⁺: 435.1842, found 435.1856

3 – Guest-induced transformation of an azulene-based Pd_2L_4 cage to a Pd_4L_8 tetrahedron

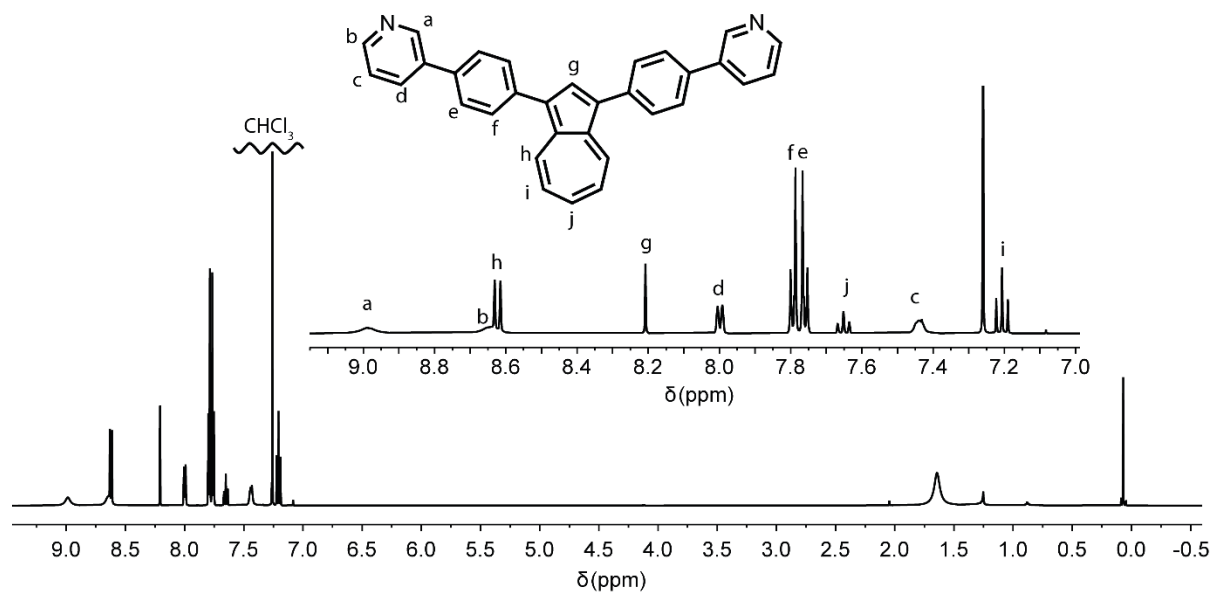


Figure S3.7: 1H -NMR spectrum (600MHz, 298K, $CDCl_3$) of ligand AZU4. The aromatic region is presented in the insert.

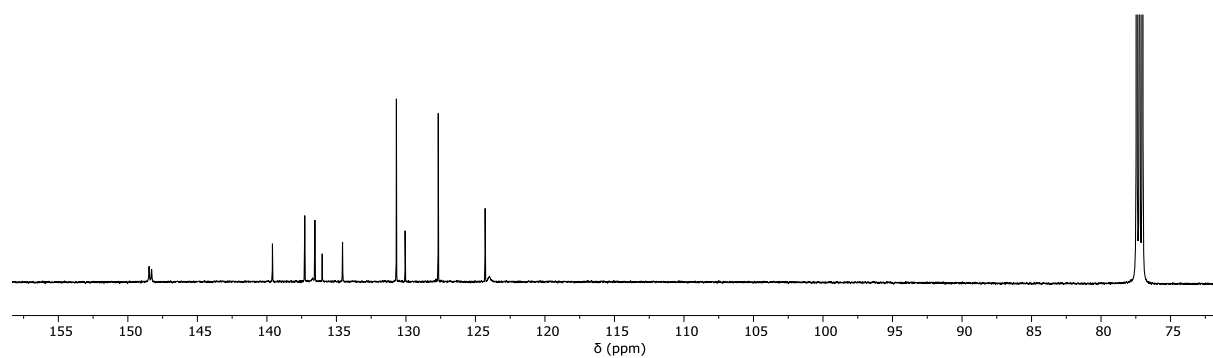
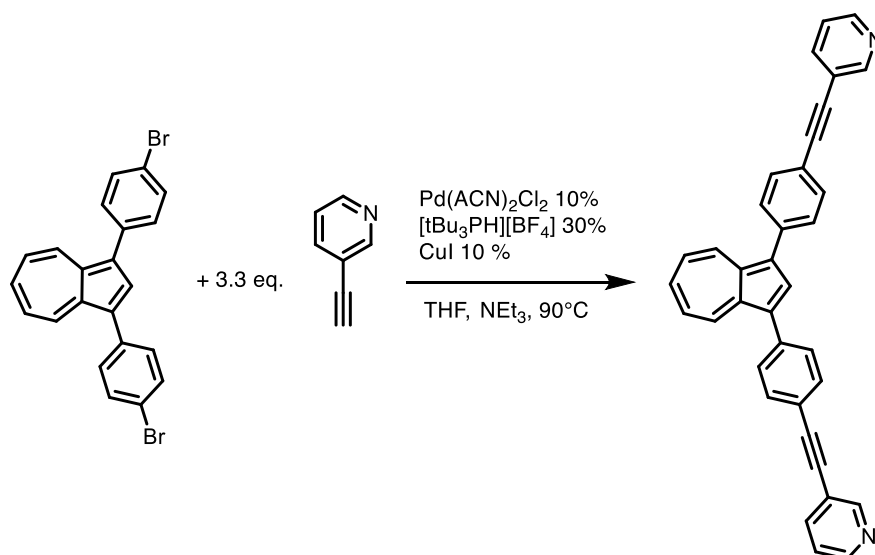


Figure S3.8: ^{13}C -NMR spectrum (151MHz, 298K, $CDCl_3$) of ligand AZU4

3.7.2.8 Synthesis of ligand **AZU5**

1,3-bis(4-bromophenyl)azulene^[39] (80 mg, 0.183 mmol) and 3-ethynylpyridine (75 mg, 0.73 mmol) were added to a Schlenk flask with 5 ml of THF and 5 ml of NEt₃, and the solution was degassed three times by the freeze-pump-thaw technique. Then, under a stream of argon, the catalysts were added: Bis(acetonitrile)palladium(II) dichloride (0.02 mmol, 5.2 mg), tri-*tert*-butylphosphonium tetrafluoroborate (0.06 mmol, 17.4 mg), and copper(I) iodide (0.02 mmol, 3.8 mg). The mixture was then stirred for 45 minutes at 90°C.

Afterwards, the solution was filtered, and the solvents evaporated. The crude product was purified by flash column chromatography (DCM, MeOH 5%) and GPC to yield ligand **AZU5** as a green powder (69 mg, 0.143 mmol, yield: 78%).

¹H-NMR (600 MHz, DMSO) δ 8.81 (d, *J* = 2.5 Hz, 2H), 8.64 (d, *J* = 9.8 Hz, 2H), 8.62 (dd, *J* = 4.8, 1.7 Hz, 2H), 8.36 (s, 1H), 8.03 (dt, *J* = 7.9, 1.9 Hz, 2H), 7.85 – 7.78 (m, 6H), 7.76 (d, *J* = 8.2 Hz, 5H), 7.53 – 7.48 (m, 2H), 7.37 (t, *J* = 9.8 Hz, 2H).

¹³C-NMR (151 MHz, DMSO) δ 152.11, 149.46, 140.70, 139.02, 137.68, 137.64, 137.01, 136.74, 132.49, 130.15, 129.21, 125.67, 124.16, 120.01, 93.05, 87.18.

ESI-MS: calculated for [C₃₆H₂₂N₂]⁺: 482.1778, found 482.1761

3 – Guest-induced transformation of an azulene-based Pd_2L_4 cage to a Pd_4L_8 tetrahedron

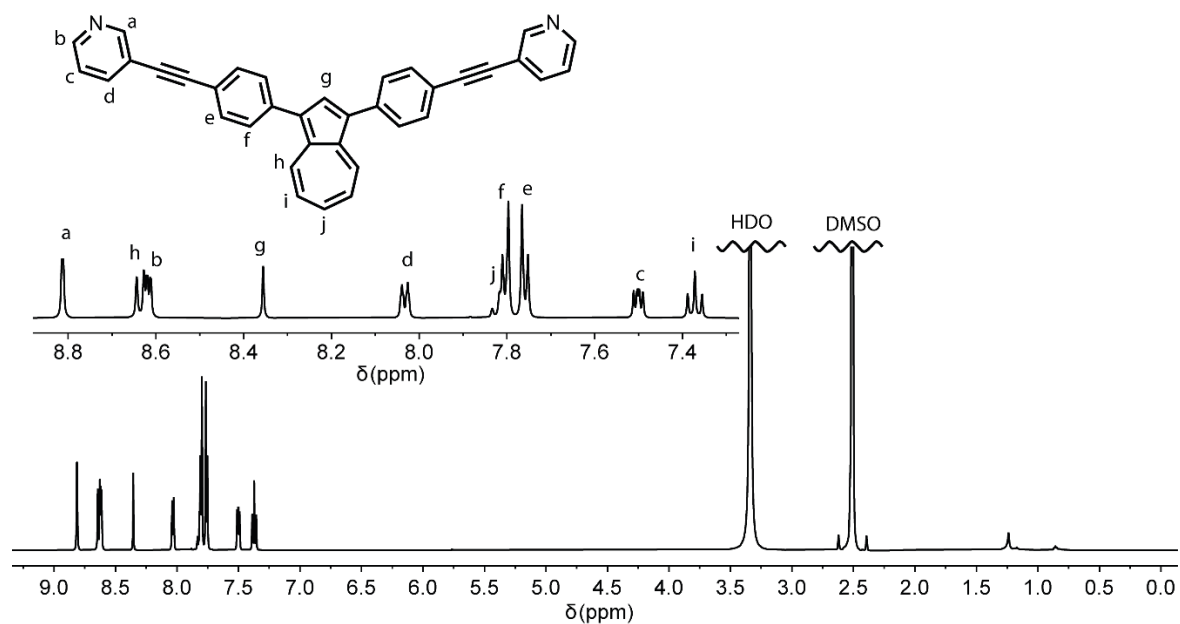


Figure S3.9: 1H -NMR spectrum (600MHz, 298K, $DMSO-d_6$) of ligand **AZU5**. The aromatic region is presented in the insert.

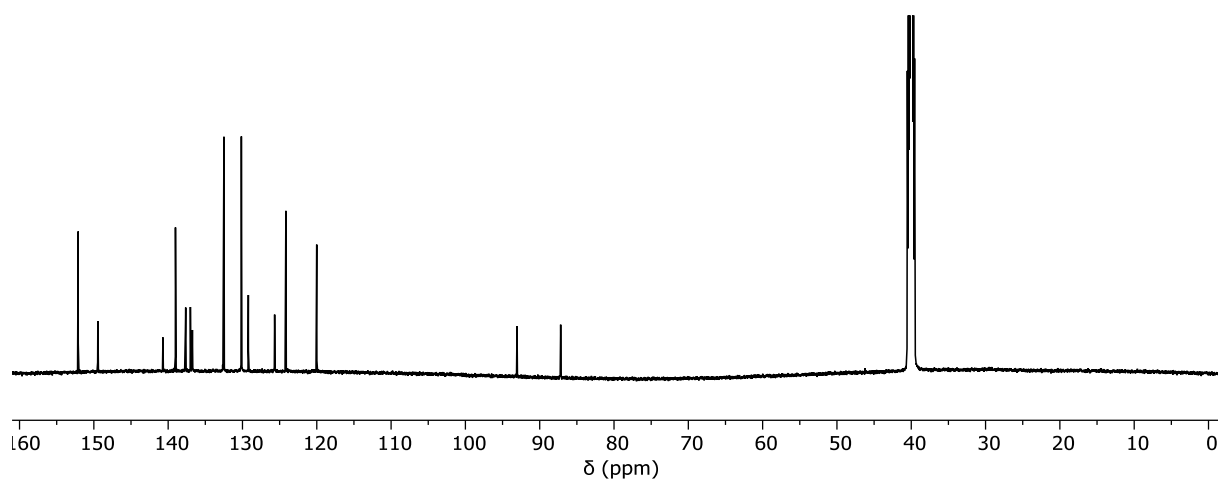
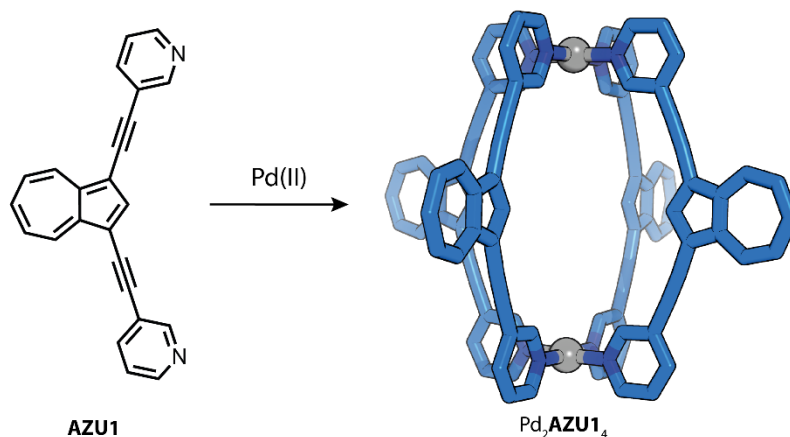


Figure S3.10: ^{13}C -NMR spectrum (151MHz, 298K, $DMSO-d_6$) of ligand **AZU5**

3.7.3 Assembly of the cages and helicates

All of the Pd₂L₄ species were assembled according to the same procedure: to 450 μl of a 3.11mM solution of the ligand in DMSO-*d*₆, 50 μl of 15 mM solution of the Pd(II) salt in the same solvent were added. The mixture was then heated to 70°C for 10 minutes (unless otherwise stated) to yield the coordination species as a 0.7 mM solution.

3.7.3.1 [Pd₂AZU1₄](OTf)₄



The coordination cage [Pd₂AZU1₄](OTf)₄ was synthesised as a 0.7mM solution in DMSO-*d*₆ according to the general procedure, using [Pd(CH₃CN)₄]OTf₂ as the palladium(II) salt. The solution turned from blue to green upon formation of the cage.

¹H-NMR (600 MHz, 298K, DMSO-*d*₆) δ 10.08 (d, *J* = 2.1 Hz, 2H), 9.26 (dd, *J* = 5.9, 1.4 Hz, 2H), 8.79 (d, *J* = 9.8 Hz, 2H), 8.65 (s, 1H), 8.34 (dt, *J* = 8.0, 1.6 Hz, 2H), 8.05 (t, *J* = 9.6 Hz, 1H), 7.84 (dd, *J* = 7.9, 5.9 Hz, 2H), 7.68 (t, *J* = 9.8 Hz, 2H).

3 – Guest-induced transformation of an azulene-based Pd_2L_4 cage to a Pd_4L_8 tetrahedron

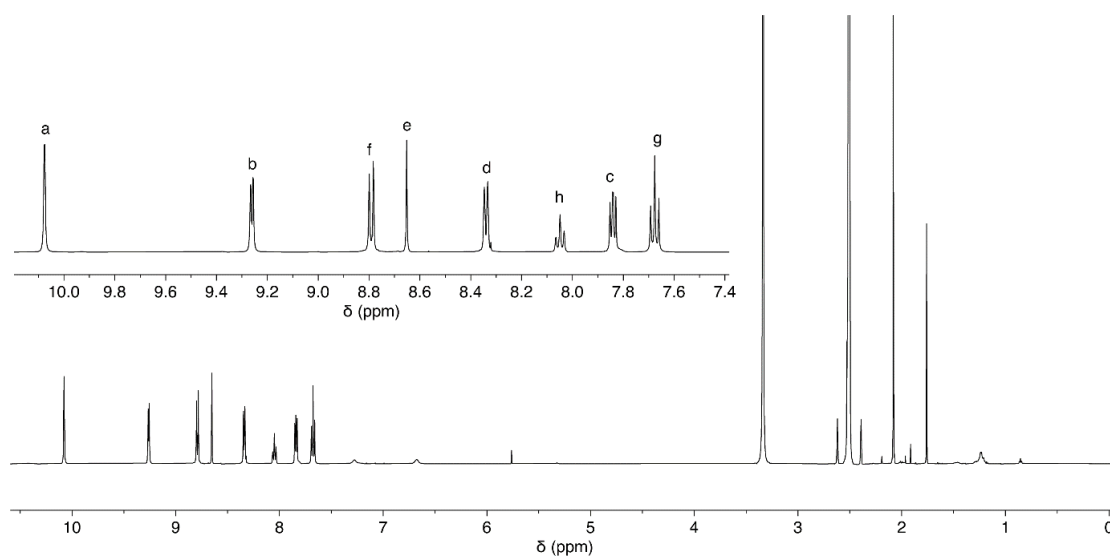


Figure S3.11: 1H -NMR spectra (600MHz, 298K, $DMSO-d_6$) of cage $[Pd_2AZU14](OTf)_4$. The aromatic region is presented in the insert.

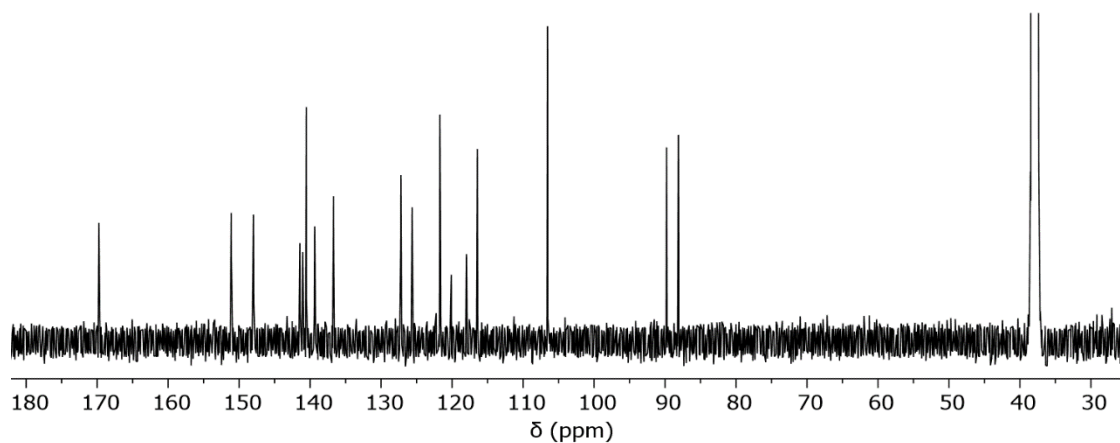


Figure S3.12: ^{13}C -NMR spectrum (150MHz, 298K, $DMSO-d_6$) of cage $[Pd_2AZU14](OTf)_4$.

3 – Guest-induced transformation of an azulene-based Pd_2L_4 cage to a Pd_4L_8 tetrahedron

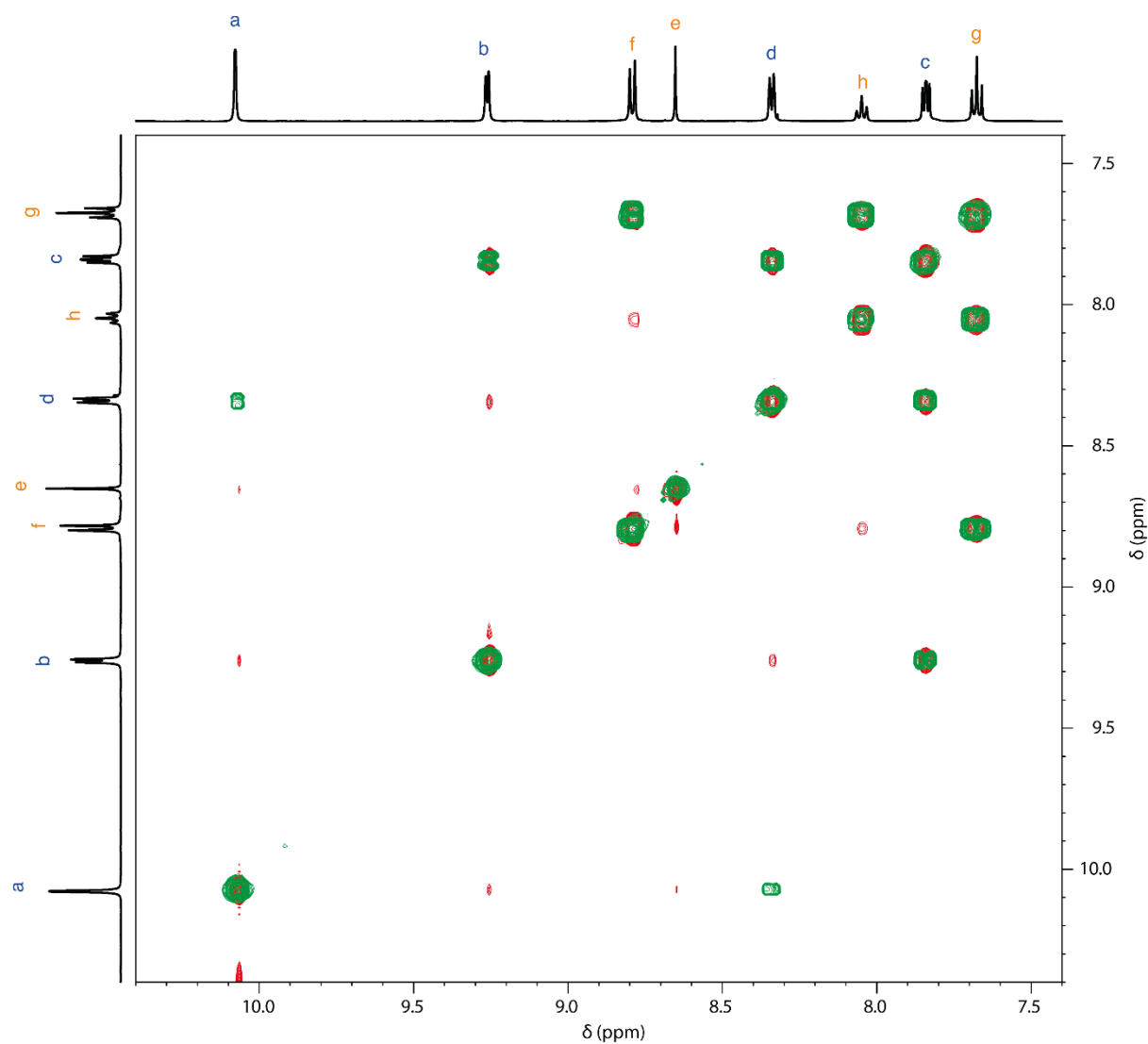


Figure S9: 1H - 1H COSY (green) and 1H - 1H NOESY (red) spectra (600MHz, 298K, $DMSO-d_6$) of cage $[Pd_2AZU1_4](OTf)_4$.

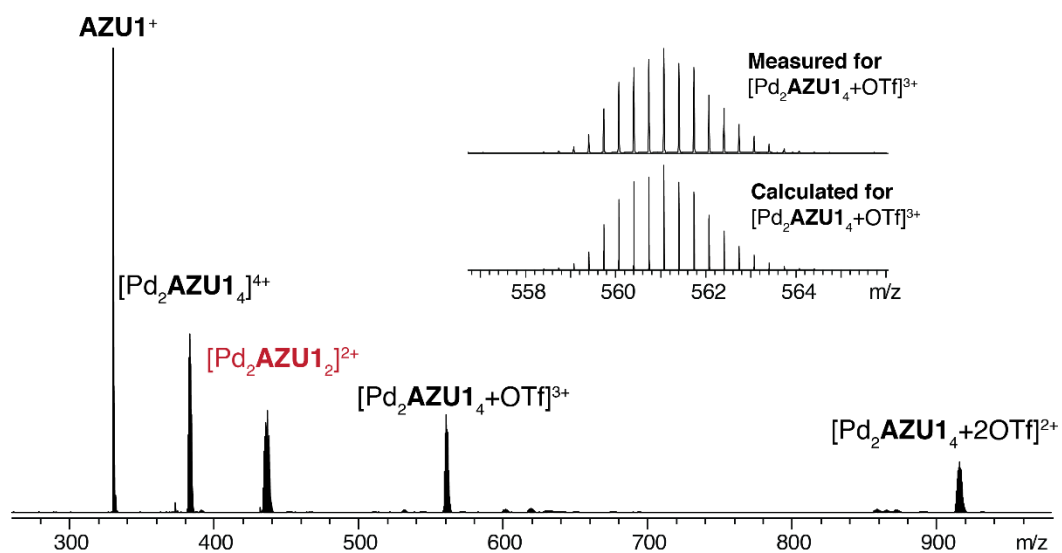
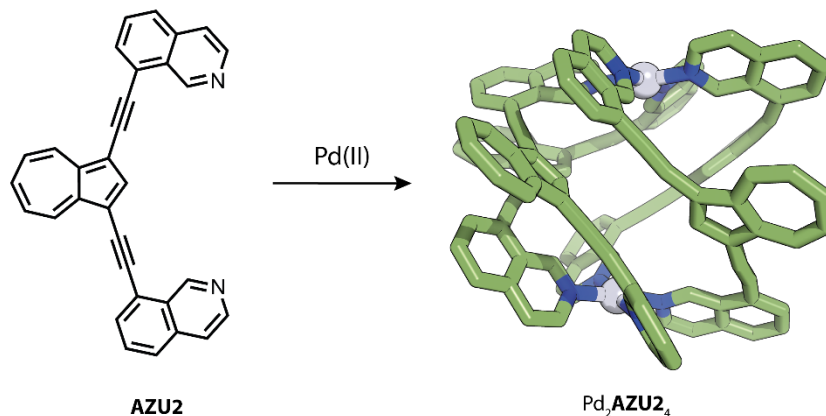


Figure S3.13: ESI-MS spectrum of $[Pd_2AZU1_4](OTf)_{0.2}$. The insert shows the measured (top) and calculated (bottom) isotopic pattern of species $[Pd_2AZU1_4+OTf]^{3+}$. A peak corresponding to $[Pd_2AZU1_2]^{2+}$ was also detected and labelled in red.

3.7.3.2 [Pd₂AZU₂]₄(BF₄)₄

The coordination cage [Pd₂AZU₂]₄(BF₄)₄ was synthesised as a 0.7 mM solution in DMSO-*d*₆ according to the general procedure, using [Pd(CH₃CN)₄](BF₄)₂ as the palladium(II) salt. The solution turned from green to yellow-brown upon formation of the cage.

¹H-NMR (600 MHz, DMSO-*d*₆) δ 9.47 (s, 2H), 8.45 (s, 1H), 7.96 (d, *J* = 9.5 Hz, 2H), 7.89 – 7.79 (m, 3H), 7.70 (d, *J* = 6.4 Hz, 2H), 7.41 – 7.34 (m, 4H), 7.23 (t, *J* = 7.8 Hz, 2H).

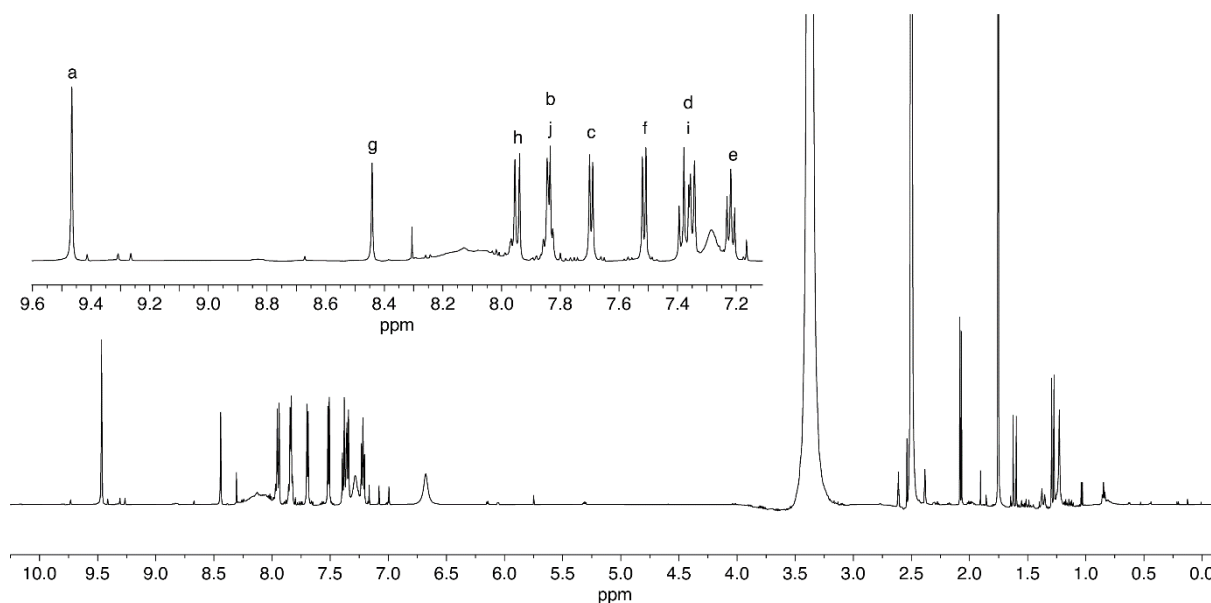


Figure S3.14: ¹H-NMR spectrum (600MHz, 298K, DMSO-*d*₆) of cage [Pd₂AZU₂]₄(BF₄)₄. The aromatic region is presented in the insert.

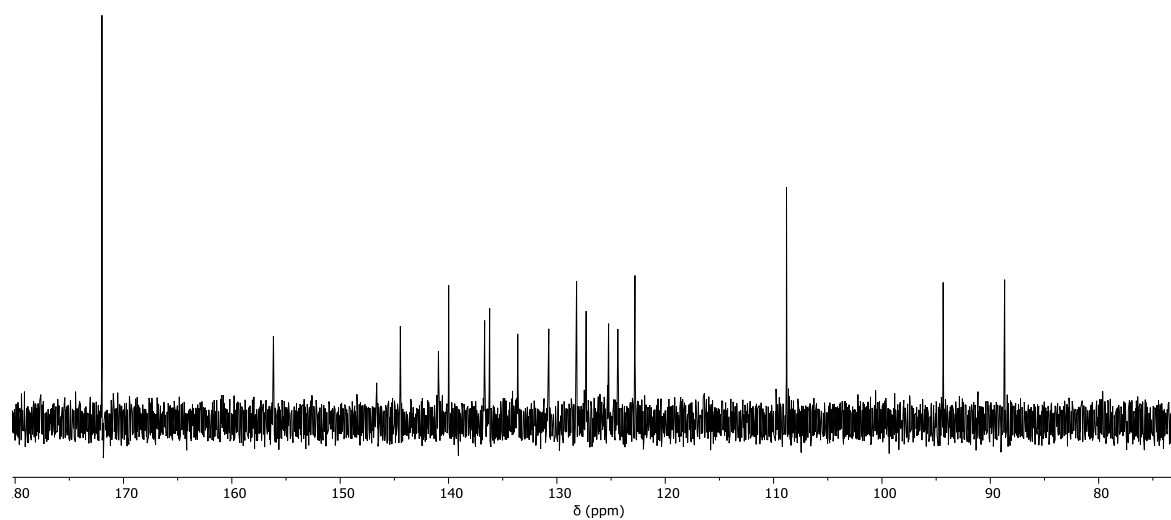


Figure S3.15: ^{13}C -NMR spectrum (150MHz, 298K, DMSO- d_6) of cage $[Pd_2AZU2_4](BF_4)_4$

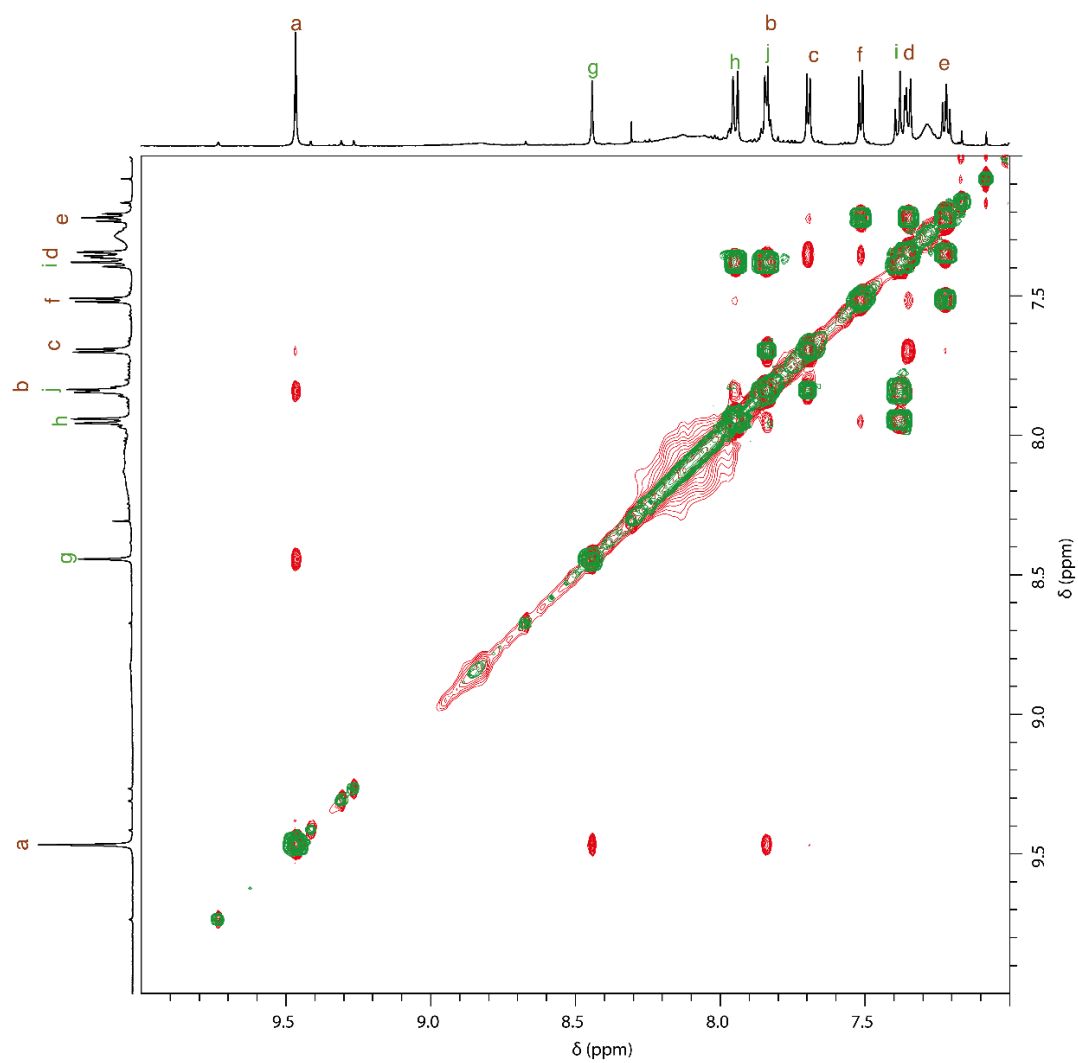


Figure S3.16: 1H - 1H COSY (green) and 1H - 1H NOESY (red) spectra (600MHz, 298K, DMSO- d_6) of cage $[Pd_2AZU2_4](BF_4)_4$.

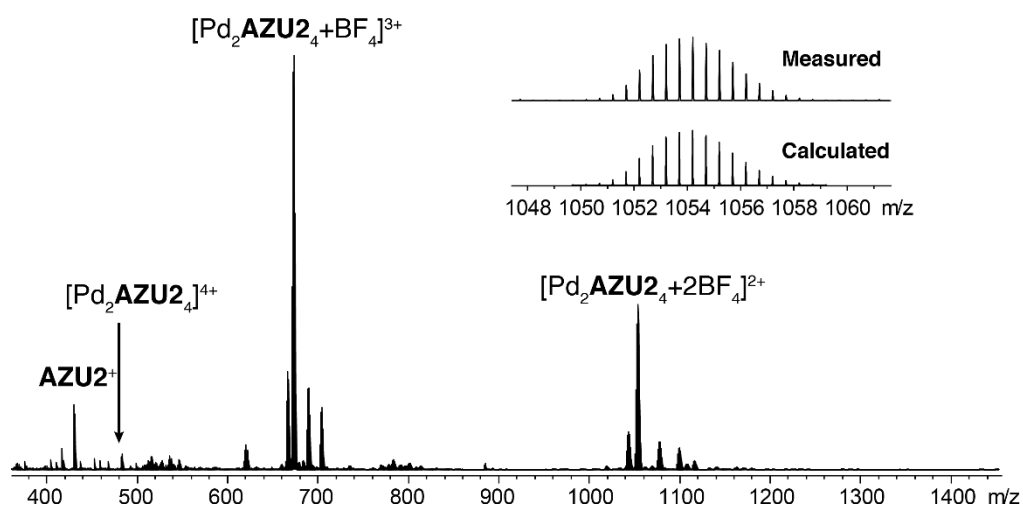
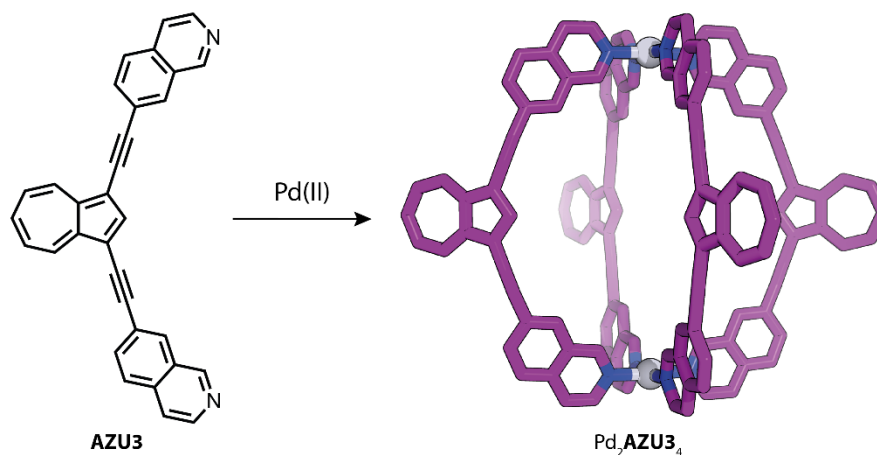


Figure S3.17: ESI-MS TOF spectrum of [Pd₂AZU₂]₄(BF₄)_{0.2}. The inset shows the measured isotopic pattern of [Pd₂AZU₂+2BF₄]₂²⁺ (top) and calculated (bottom).

3.7.3.3 [Pd₂AZU₃]₄(OTf)₄



The coordination cage [Pd₂AZU₃]₄(OTf)₄ was synthesised as a 0.7mM solution in DMSO-*d*₆ according to the general procedure, using [Pd(CH₃CN)₄]OTf₂ as the palladium(II) salt. The solution turned from teal to green upon formation of the cage.

¹H-NMR (700 MHz, DMSO-*d*₆) δ 10.59 (s, 2H), 9.26 (d, *J* = 6.8 Hz, 2H), 8.81 (d, *J* = 9.9 Hz, 2H), 8.65 (d, *J* = 1.7 Hz, 2H), 8.38 (s, 1H), 8.22 – 8.16 (m, 4H), 8.13 (d, *J* = 8.2 Hz, 2H), 8.04 (t, *J* = 9.4 Hz, 1H), 7.65 (t, *J* = 9.7 Hz, 2H).

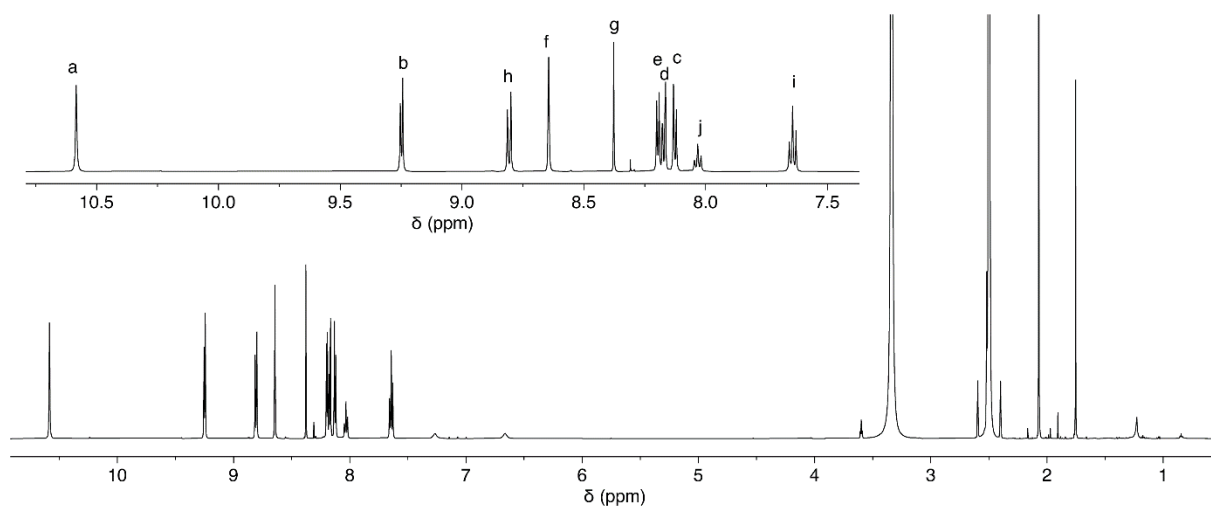


Figure S3.18: ¹H-NMR spectrum (700MHz, 298K, DMSO-*d*₆) of cage [Pd₂AZU₃₄](OTf)₄. The aromatic region is presented in the inset.

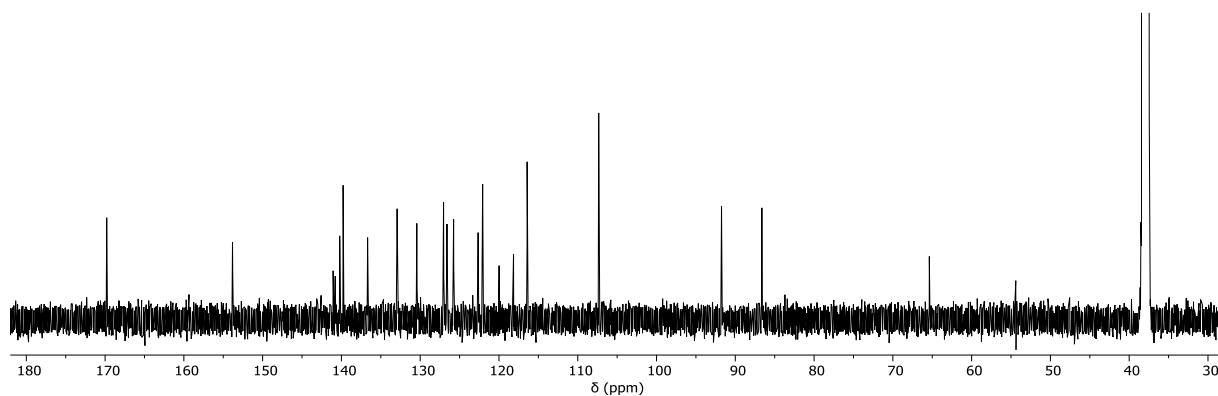


Figure S3.19: ¹³C-NMR spectrum (175MHz, 298K, DMSO-*d*₆) of cage [Pd₂AZU₃₄](OTf)₄

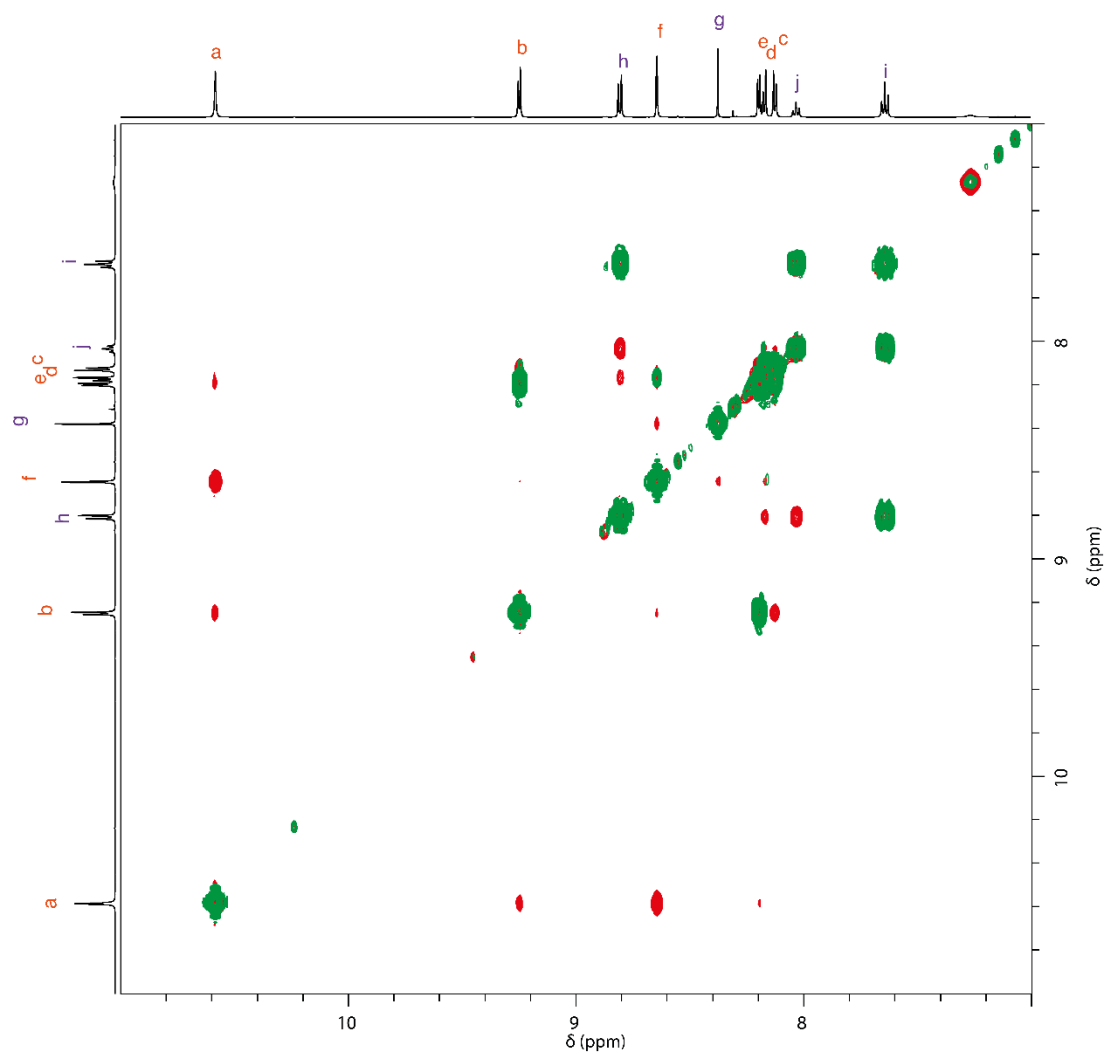


Figure S3.20: 1H - 1H COSY (green) and 1H - 1H NOESY (red) spectra (700MHz, 298K, DMSO- d_6) of cage $[Pd_2AZU34](OTf)_4$

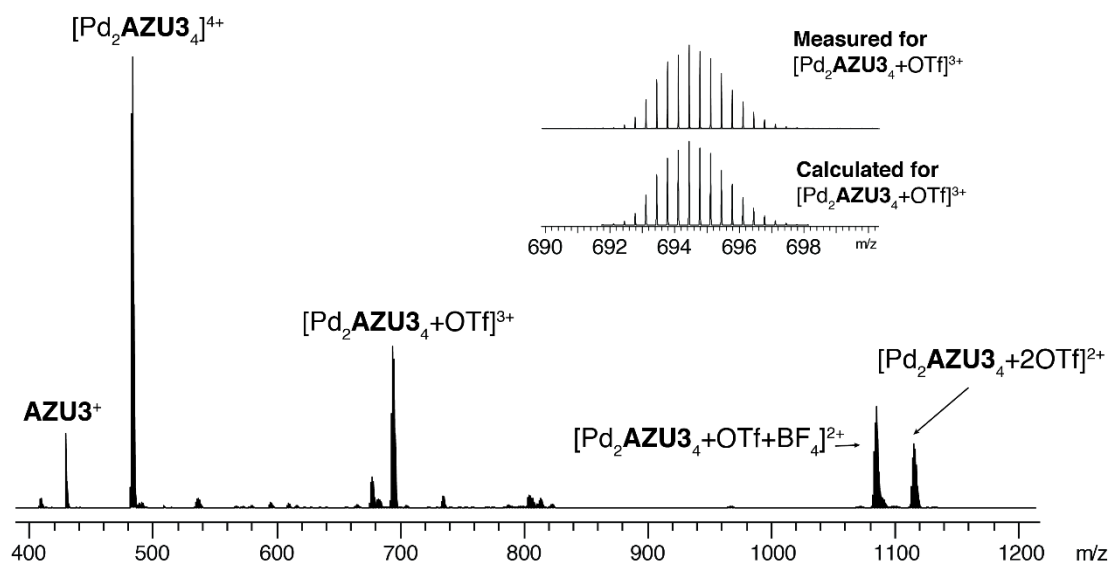
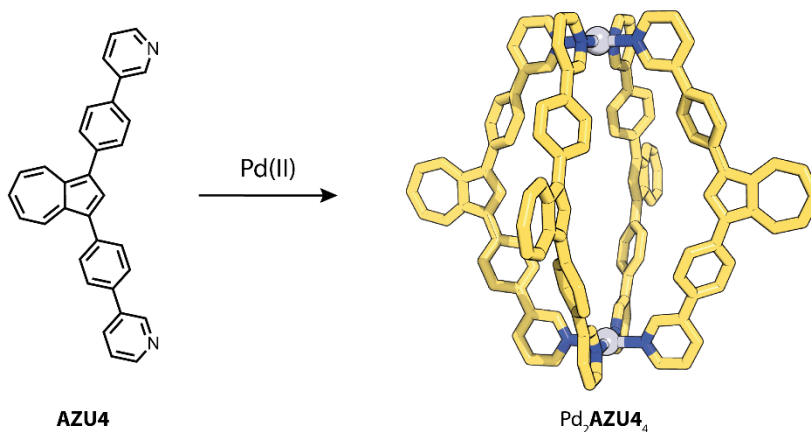


Figure S3.21: ESI-MS spectrum of [Pd₂AZU₃]₄(OTf)_{0.2}. The inset shows the measured (top) and calculated (bottom) isotopic pattern of species [Pd₂AZU₃]₄+OTf)³⁺.

3.7.3.4 [Pd₂AZU₄]₄(BF₄)₄



The coordination cage [Pd₂(AZU₄)₄](BF₄)₄ was synthesised as a 0.7 mM solution in DMSO-*d*₆ according to the general procedure, using [Pd(CH₃CN)₄](BF₄)₂ or [Pd(CH₃CN)₄](OTf)₂ as the palladium(II) salt. The solution turned from blue to green upon formation of the cage.

¹H-NMR (600 MHz, DMSO) δ 9.91 (d, *J* = 2.2 Hz, 2H), 9.44 (dd, *J* = 5.8, 1.3 Hz, 2H), 8.67 (d, *J* = 10.0 Hz, 2H), 8.55 (s, 1H), 8.47 (dt, *J* = 7.9, 1.7 Hz, 2H), 8.05 (d, *J* = 7.7 Hz, 4H), 7.98 – 7.92 (m, 6H), 7.76 (t, *J* = 9.5 Hz, 1H), 7.33 (t, *J* = 9.8 Hz, 2H).

¹³C-NMR (151 MHz, DMSO) δ 169.77, 147.88, 146.48, 138.54, 137.40, 136.87, 136.08, 134.73, 134.44, 130.80, 128.50, 126.28, 126.15, 123.77, 116.43.

3 – Guest-induced transformation of an azulene-based Pd₂L₄ cage to a Pd₄L₈ tetrahedron

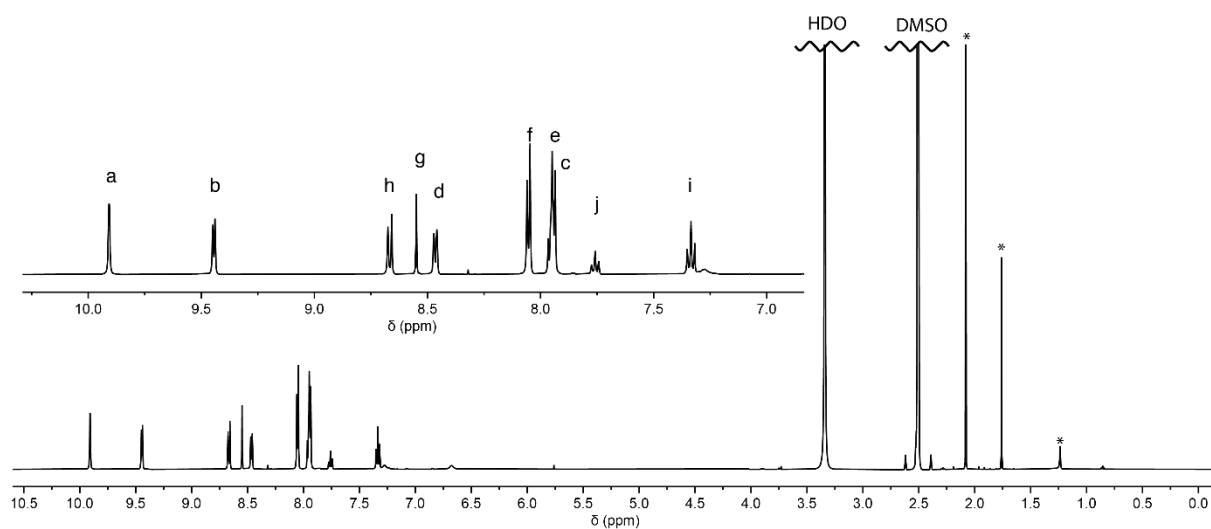


Figure S3.22: ¹H-NMR spectrum (600MHz, 298K, DMSO-*d*₆) of cage [Pd₂AZU₄](BF₄)₄. The aromatic region is presented in the inset.

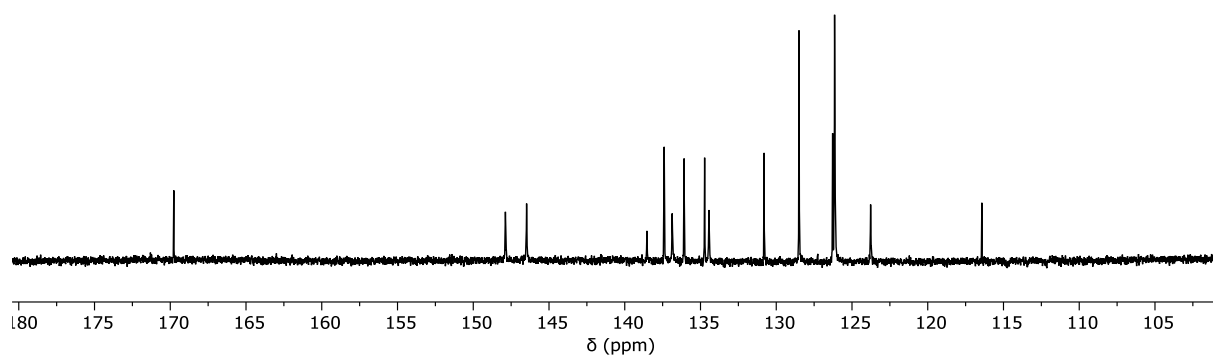


Figure S3.23: ¹³C-NMR spectrum (151 MHz, 298K, DMSO-*d*₆) of cage [Pd₂AZU₄](BF₄)₄.

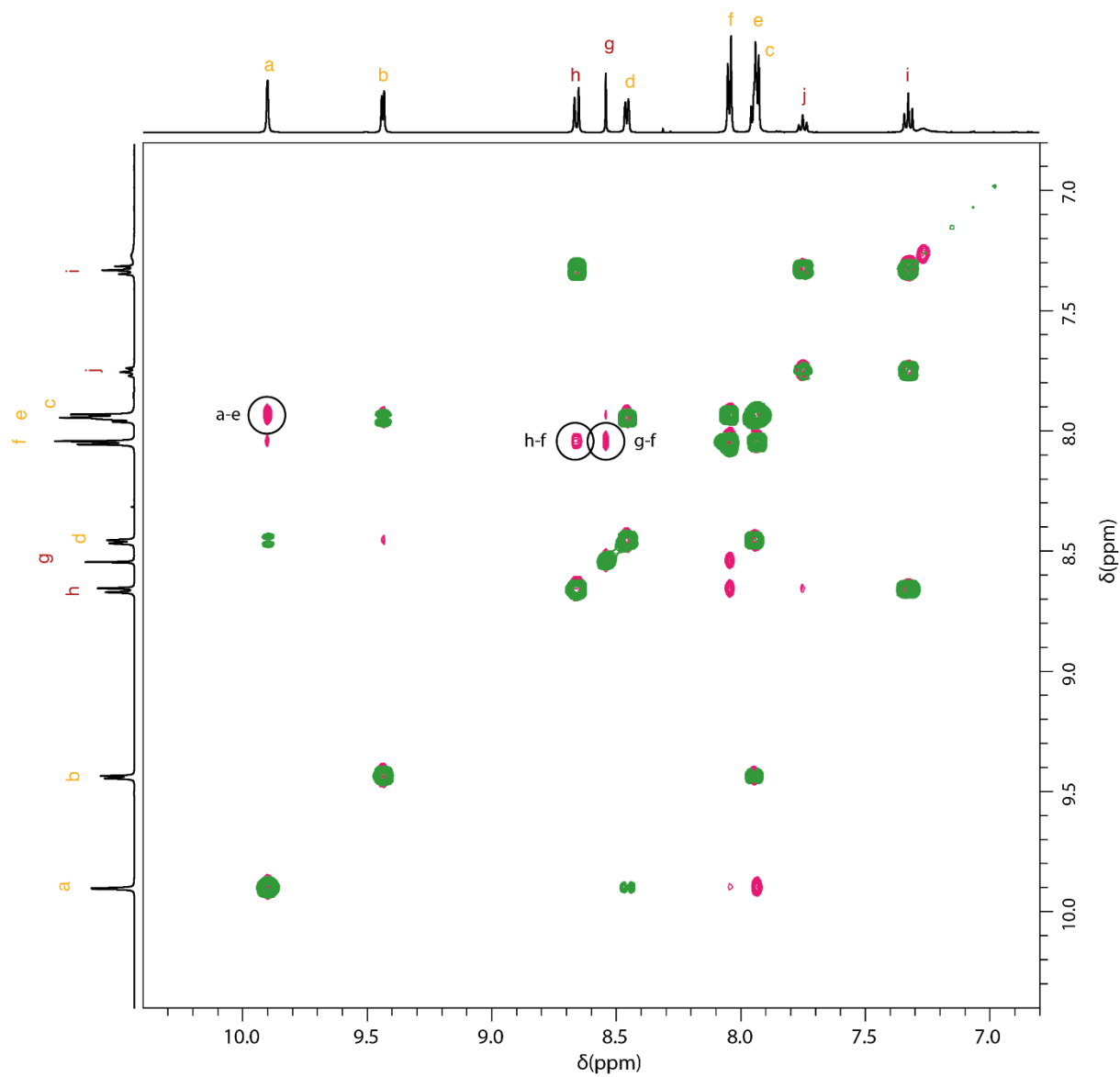


Figure S3.24: 1H - 1H COSY (green) and 1H - 1H NOESY (red) spectra (600MHz, 298K, DMSO- d_6) of cage $[Pd_2AZU_4](BF_4)_4$

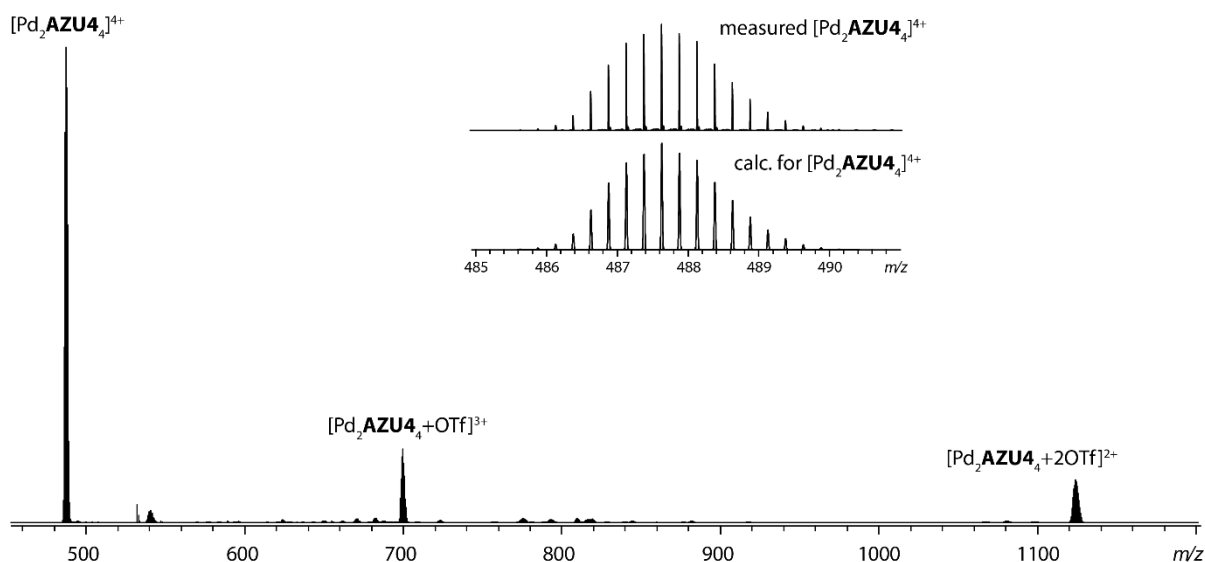
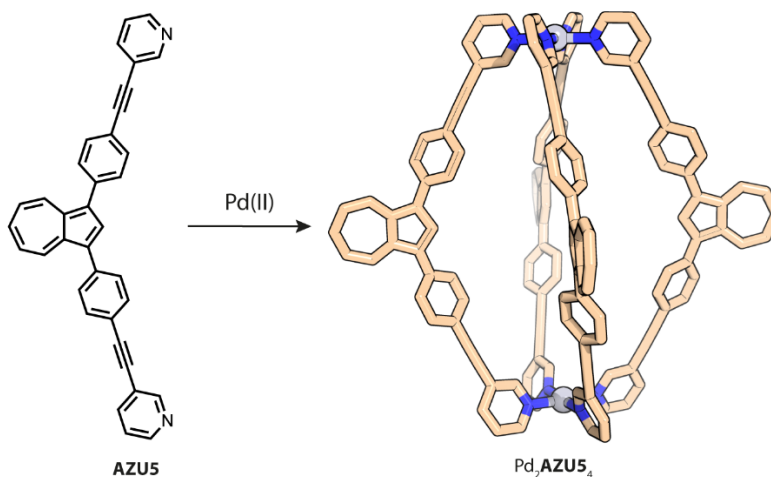


Figure S3.25: ESI-MS spectrum of [Pd₂AZU₄](OTf)_{0.2}. The inset shows the measured (top) and calculated (bottom) isotopic pattern of species [Pd₂AZU₄]⁴⁺.

3.7.3.5 [Pd₂AZU₅](BF₄)₄



The coordination cage [Pd₂(AZU₄)₄](BF₄)₄ was synthesised as a 0.7 mM solution in DMSO-*d*₆ according to the general procedure, using [Pd(CH₃CN)₄](BF₄)₂ as the palladium(II) salt. The solution turned from blue to green upon formation of the cage.

¹H-NMR (600 MHz, DMSO) δ 9.79 (d, *J* = 2.1 Hz, 2H), 9.26 (dd, *J* = 5.8, 1.4 Hz, 2H), 8.54 (d, *J* = 10.0 Hz, 2H), 8.33 – 8.27 (m, 2H), 8.08 (s, 1H), 7.82 (dd, *J* = 7.8, 5.9 Hz, 2H), 7.79 (d, *J* = 7.9 Hz, 4H), 7.74 (d, *J* = 8.0 Hz, 4H), 7.60 (t, *J* = 9.5 Hz, 1H), 7.26 (t, *J* = 9.8 Hz, 2H).

¹³C-NMR (151 MHz, DMSO) δ 169.82, 151.62, 148.63, 140.38, 138.61, 136.21, 135.10, 134.89, 134.49, 130.57, 127.97, 126.51, 125.68, 123.88, 120.98, 116.70, 116.44, 93.54, 82.76, 77.52.

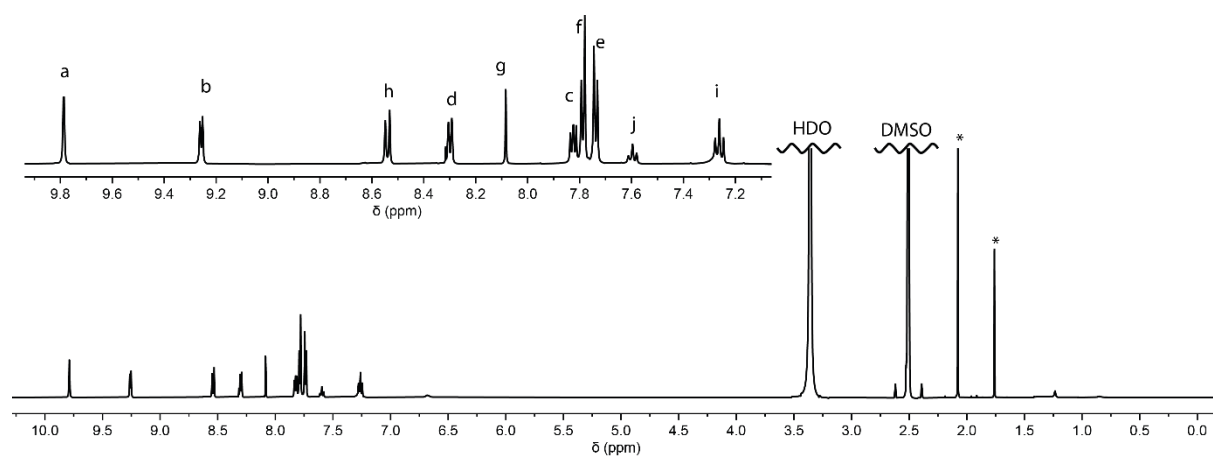


Figure S3.26: ¹H-NMR spectrum (600MHz, 298K, DMSO-*d*₆) of cage [Pd₂AZU₅₄](BF₄)₄. The aromatic region is presented in the inset.

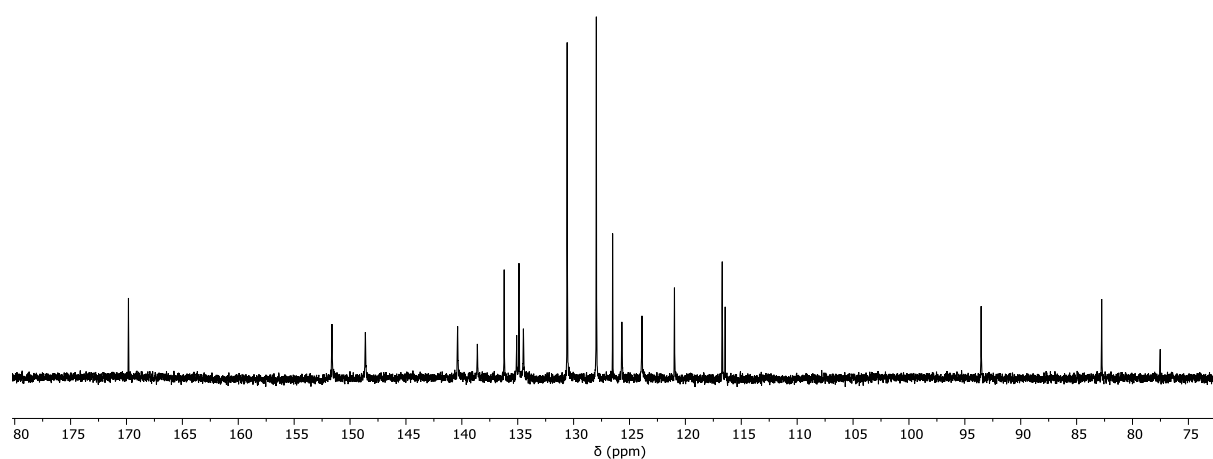


Figure S3.27: ¹³C-NMR spectrum (151 MHz, 298K, DMSO-*d*₆) of cage [Pd₂AZU₅₄](BF₄)₄.

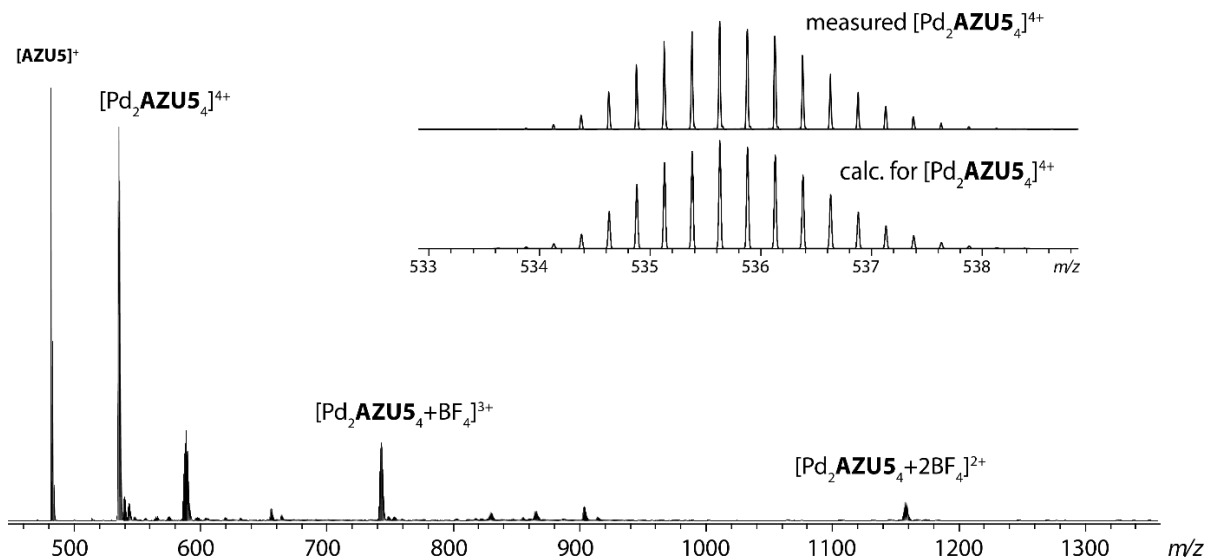
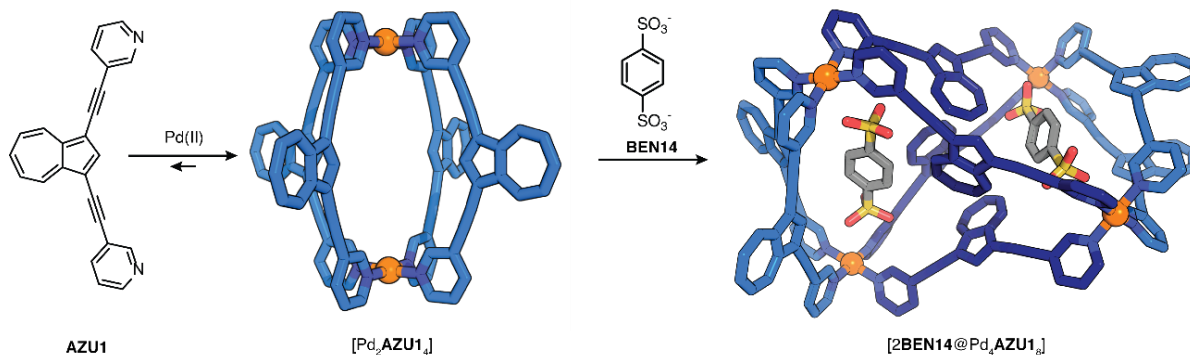


Figure S3.28: ESI-MS spectrum of $[\text{Pd}_2\text{AZU5}_4](\text{OTf})_{0.2}$. The inset shows the measured (top) and calculated (bottom) isotopic pattern of species $[\text{Pd}_2\text{AZU5}_4]^{4+}$.

3.7.4 Host-guest complexes

3.7.4.1 $[\text{2BEN14@Pd}_4\text{AZU1}_8](\text{OTf})_4$



The distorted tetrahedral host-guest complex $[\text{2BEN14@Pd}_4\text{AZU1}_8](\text{OTf})_4$ was prepared by adding 25 μl of a 15mM DMSO-*d*₆ solution of the guest **BEN14** as the tetrabutylammonium salt to 500 μl of a 0.7mM DMSO-*d*₆ solution of the cage $[\text{Pd}_2\text{AZU1}_4](\text{OTf})_2$. The resulting solution was heated for 5 minutes at 70°C to yield the tetrahedron.

¹H-NMR (700 MHz, DMSO-*d*₆) δ 10.29 (s, 2H), 10.22 (s, 2H), 9.50 – 9.47 (m, 2H), 9.30 – 9.26 (m, 2H), 9.08 (d, *J* = 9.4 Hz, 2H), 8.78 (d, *J* = 9.5 Hz, 2H), 8.44 – 8.39 (m, 4H), 8.27 (s, 1H), 8.21 (dt, *J* = 8.1, 1.5 Hz, 2H), 8.17 (s, 1H), 8.02 (t, *J* = 9.9 Hz, 1H), 7.91 – 7.86 (m, 2H), 7.77 (dd, *J* = 8.2, 5.7 Hz, 2H), 7.63 (t, *J* = 9.7 Hz, 2H), 6.83 (t, *J* = 9.7 Hz, 2H), 6.23 (t, *J* = 9.9 Hz, 1H), 3.18 – 3.13 (m, 12H), 1.60 – 1.53 (m, 12H), 1.35 – 1.27 (m, 12H), 0.94 (t, *J* = 7.4 Hz, 16H).

3 – Guest-induced transformation of an azulene-based Pd_2L_4 cage to a Pd_4L_8 tetrahedron

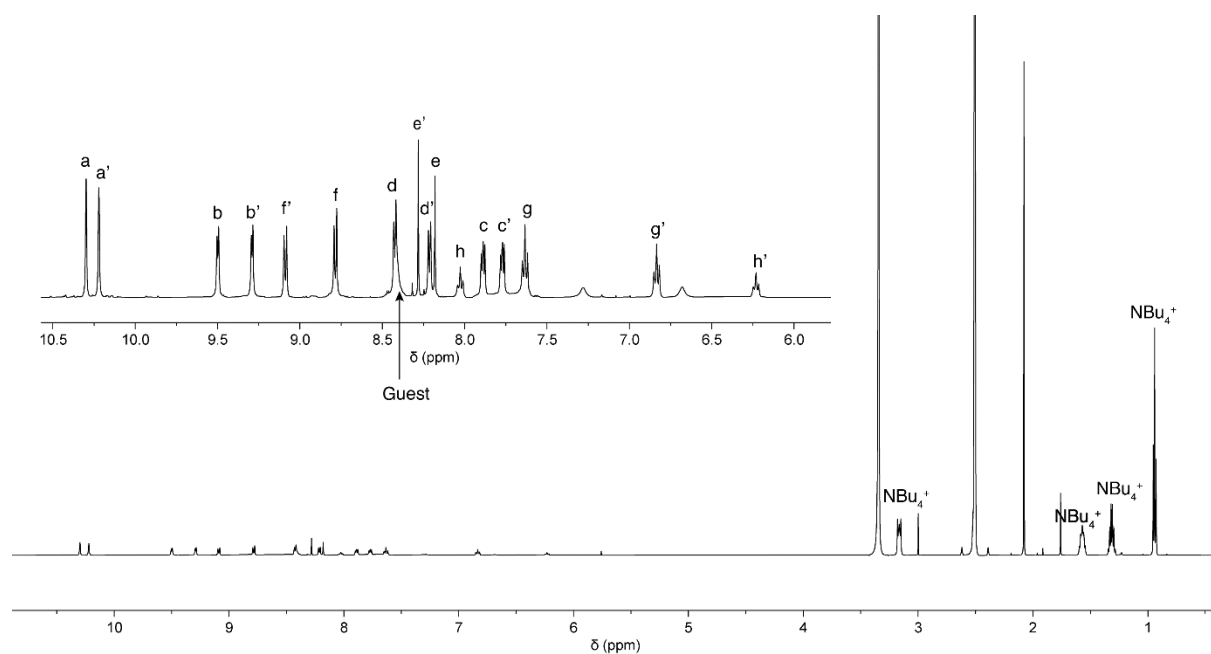


Figure S3.29: 1H -NMR spectrum (700MHz, 298K, $DMSO-d_6$) of tetrahedron $[2BEN14@Pd_4AZU1_8](OTf)_4$ with an inset of the aromatic protons.

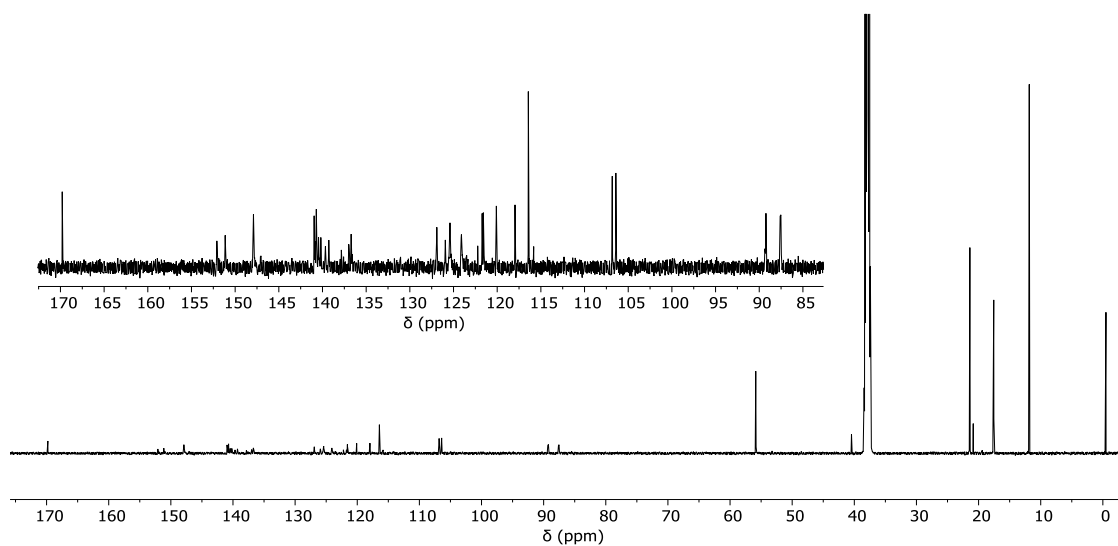


Figure S3.30: ^{13}C -NMR spectrum (175MHz, 298K, $DMSO-d_6$) of tetrahedron $[2BEN14@Pd_4AZU1_8](OTf)_4$ with an inset of the aromatic region.

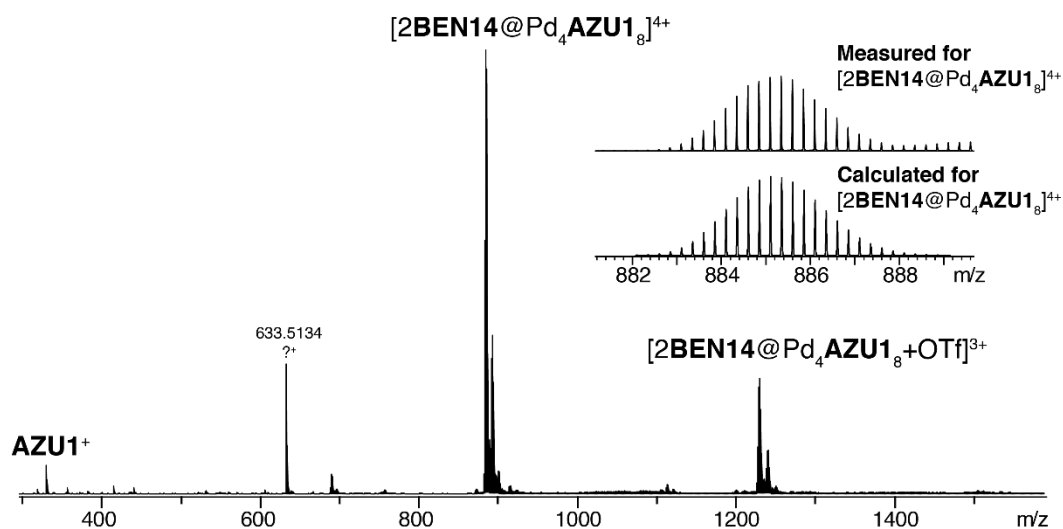


Figure S3.31: ESI-MS spectrum of $[2BEN14@Pd_4AZU1_8](OTf)_{0-1}$. The inset shows the measured (top) and calculated (bottom) isotopic pattern of species $[2BEN14@Pd_4AZU1_8]^{4+}$.

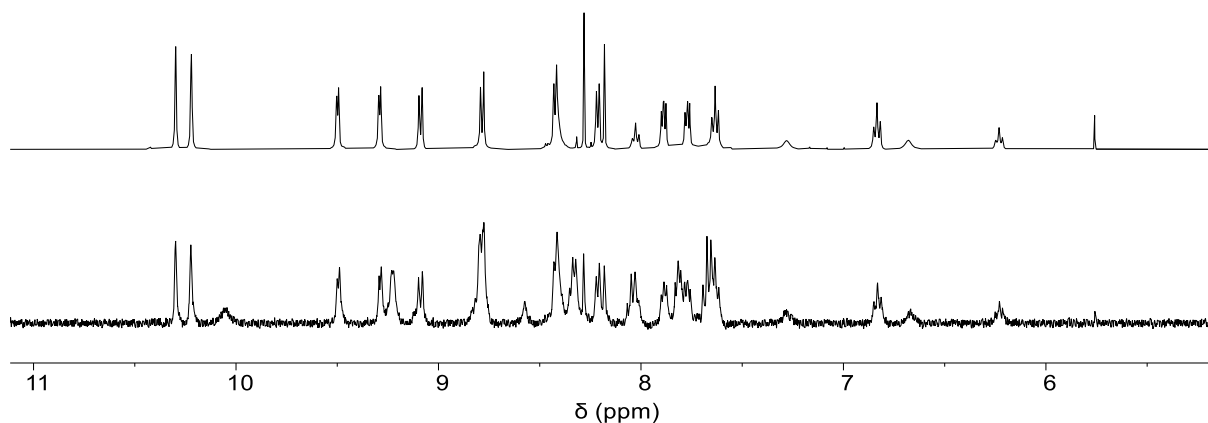
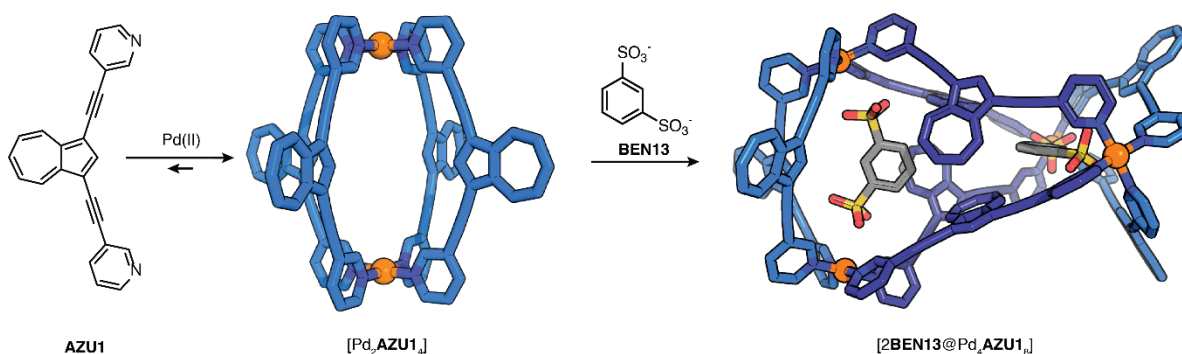


Figure S3.32: 1H -NMR spectra (500-700MHz, 298K, $DMSO-d_6$) of the addition of 1 eq. of guest **BEN14** to a solution of $[Pd_2AZU1_4](OTf)_4$ (top) and $[Pd_2AZU1_4](BF_4)_4$ (bottom).

3.7.4.2 $[2BEN13@Pd_4AZU1_8](OTf)_4$



The distorted tetrahedral host-guest complex $[2BEN13@Pd_4AZU1_8](OTf)_4$ was prepared by adding 25 μ l of a 15mM $DMSO-d_6$ solution of the guest **BEN13** as the tetrabutylammonium salt

3 – Guest-induced transformation of an azulene-based Pd₂L₄ cage to a Pd₄L₈ tetrahedron

to 500 µl of a 0.7mM DMSO-*d*₆ solution of the cage [Pd₂AZU1₄](OTf)₄. The resulting solution was heated for 5 minutes at 70°C to yield the tetrahedron.

Due to the convoluted ¹H-NMR of the reaction mixture, the shifts are not reported here, only the spectrum. A precise assignment of the main species is included in **Figure S29**. Due to solubility issues, the ¹³C-NMR spectra could not be properly measured, despite using 10'000 scans.

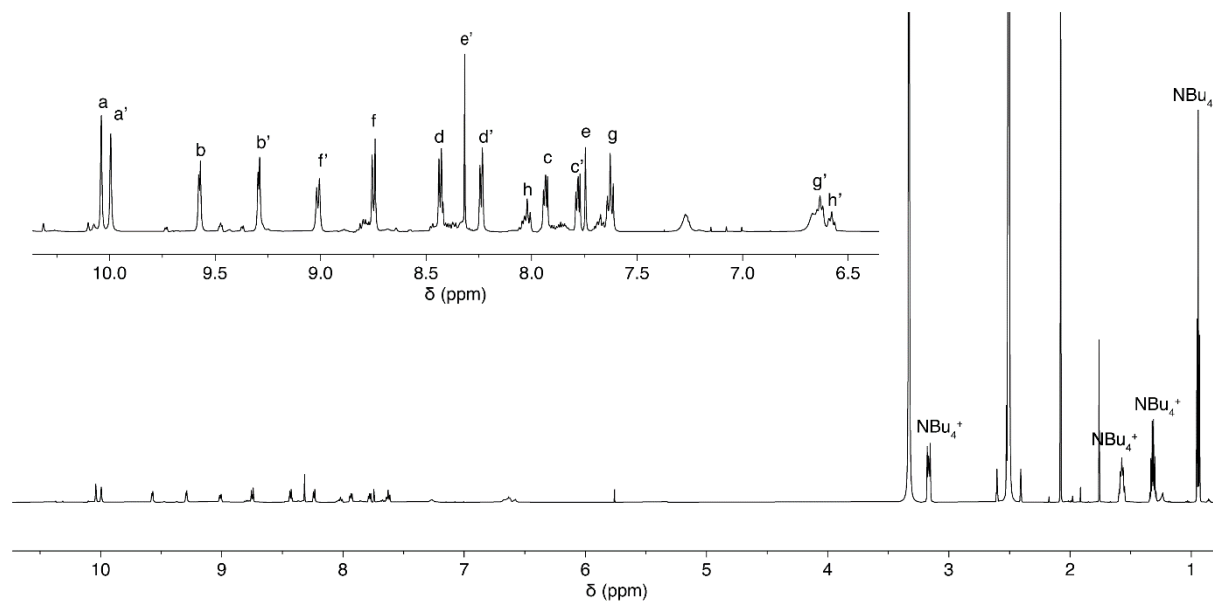


Figure S3.33: ¹H-NMR spectrum (700MHz, 298K, DMSO-*d*₆) of tetrahedron [2BEN13@Pd₄AZU1₈](OTf)₄ with an inset of the aromatic protons.

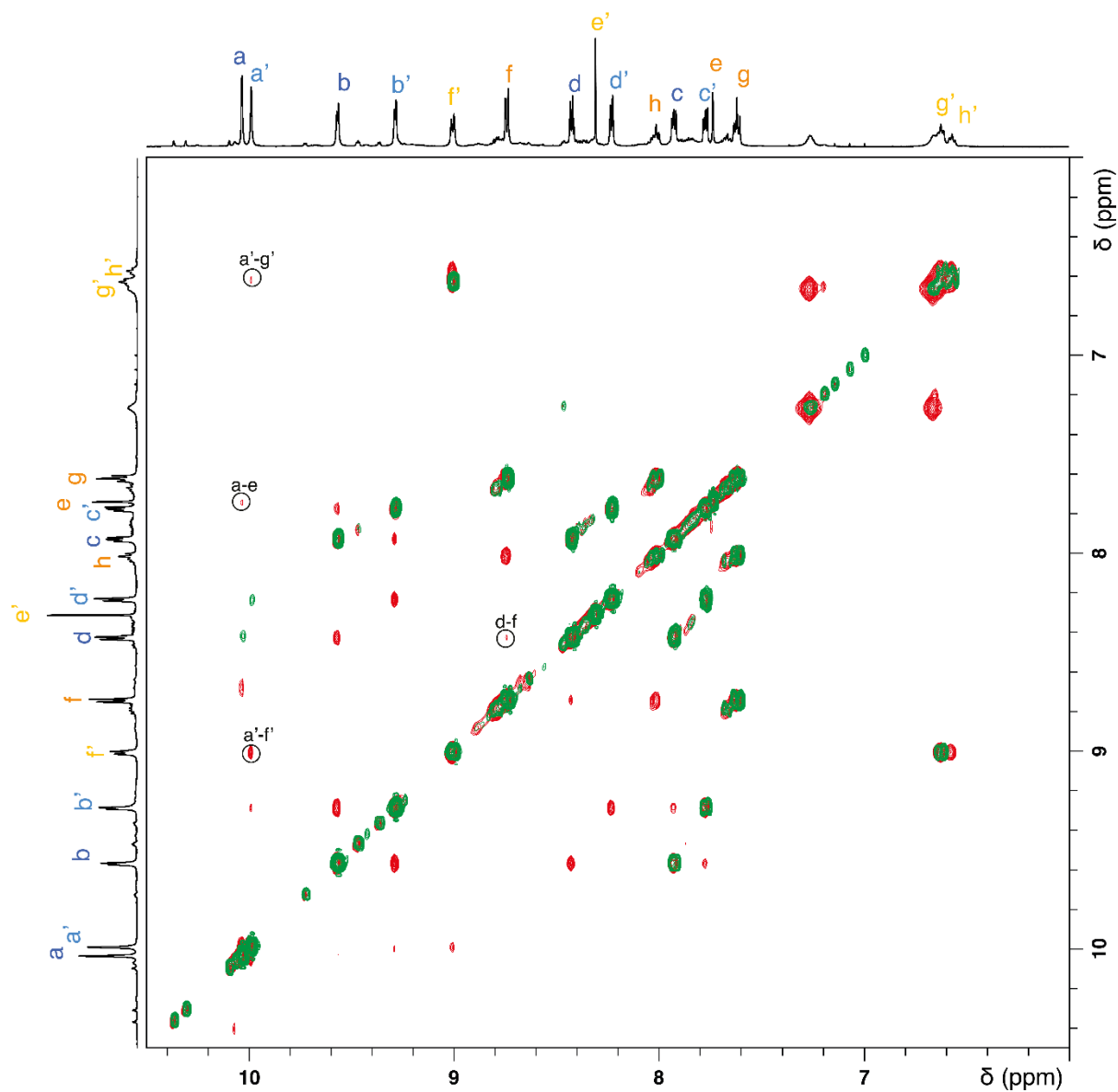
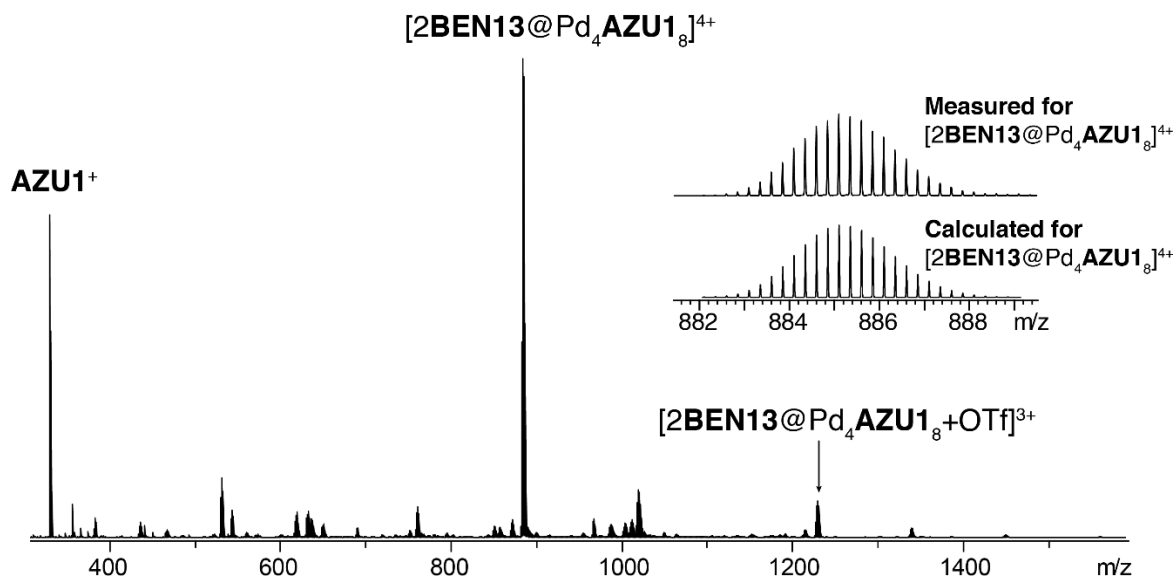
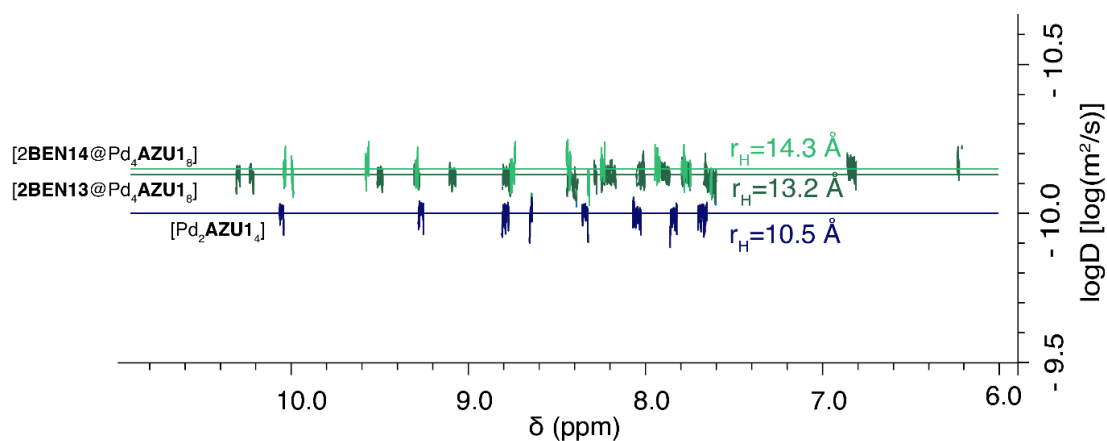


Figure S3.34: 1H - 1H COSY (green) and 1H - 1H NOESY (red) spectra (700MHz, 298K, $DMSO-d_6$) of complex $[2BEN13@Pd_4AZU18](OTf)_4$ with assignment of the protons (see Fig. S24 for the ligand structures).

Figure S3.35: ESI-MS of [2BEN13@Pd₄AZU1₈](OTf)₄3.7.4.3 DOSYFigure S3.36: Superimposed ¹H-NMR DOSY spectra (500MHz, 298K, DMSO-*d*₆) of cage [Pd₂AZU1₄] and tetrahedra [2BEN13@Pd₄AZU1₈] and [2BEN14@Pd₄AZU1₈].Table S3.1: Diffusion coefficients D and corresponding hydrodynamic radii of cage [Pd₂AZU1₄] and tetrahedra [2BEN13@Pd₄AZU1₈] and [2BEN14@Pd₄AZU1₈].

	[Pd ₂ AZU1 ₄]	[2BEN13@Pd ₄ AZU1 ₈]	[2BEN14@Pd ₄ AZU1 ₈]
D [m ² /s]	9.53 E-11	7.57 E-11	6.97 E-11
Radius [Å]	10.5	13.2	14.3

The Stokes-Einstein relation was used to calculate the hydrodynamic radius of the species, with a viscosity of DMSO-*d*₆ of $\eta=2.19 \cdot 10^{-3}$ Pa·s, and a temperature of 298 K.

3.7.4.4 NMR kinetic study of the formation of tetrahedron $[2BEN14@Pd_4AZU1_8]$

The evolution of the different species in solution was monitored by integration of their respective signals relative to the internal standard 1,3,5-trimethoxybenzene (its aromatic protons are labelled as Ref.). It is worth mentioning that the effective concentration in cage and tetrahedron was found to be slightly lower than calculated from the initial concentration of ligand **AZU1** (2.8 mM). This could be explained by the formation of some coordination polymers and aggregates that do not show up in the NMR spectra.^[40] The calculated kinetics were based on the actual concentrations as determined with the internal standard.

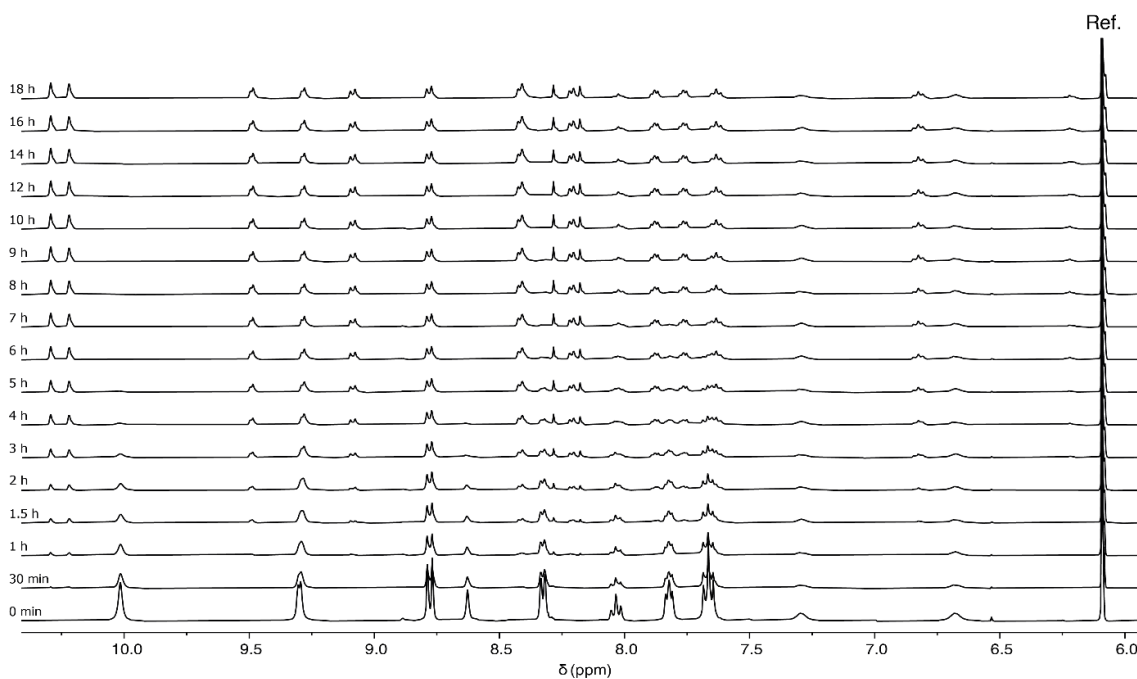


Figure S3.37: $^1\text{H-NMR}$ spectrum (500MHz, 298K, $\text{DMSO-}d_6$) of the formation of tetrahedron $[2BEN14@Pd_4AZU1_8](\text{OTf})_4$ from cage $[Pd_2AZU1_4](\text{OTf})_4$ recorded at 25°C.

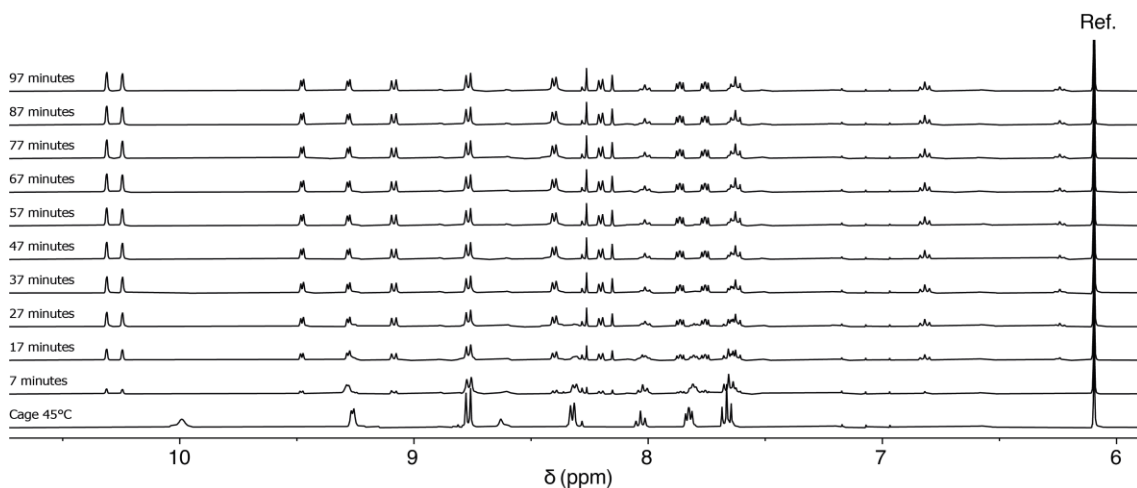


Figure S3.38: $^1\text{H-NMR}$ spectrum (500MHz, 298K, $\text{DMSO-}d_6$) of the formation of tetrahedron $[2BEN14@Pd_4AZU1_8](\text{OTf})_4$ from cage $[Pd_2AZU1_4](\text{OTf})_4$ recorded at 45°C.

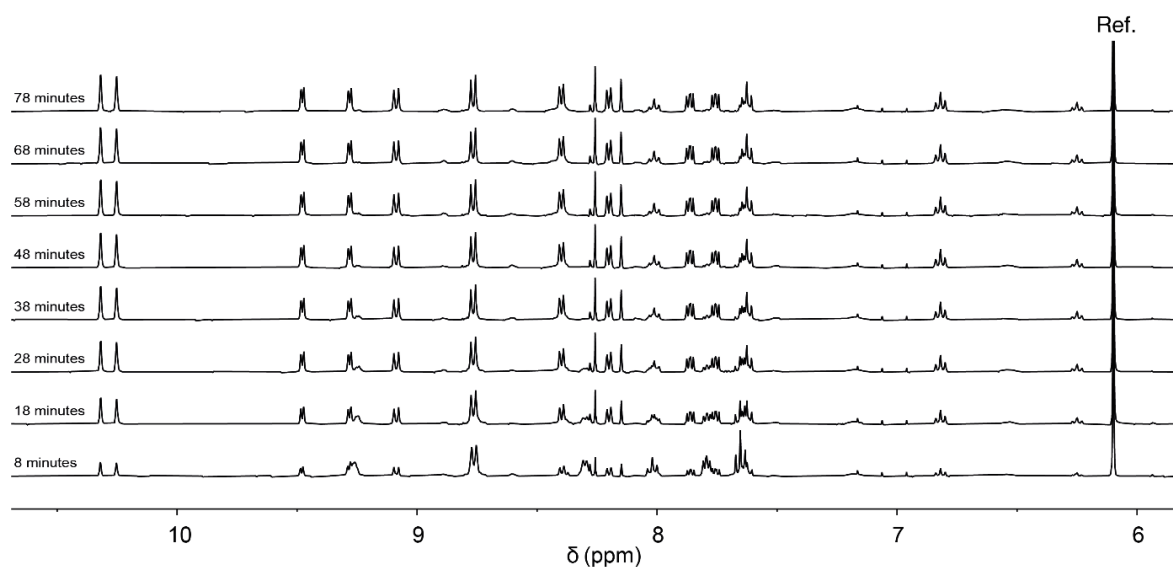


Figure S3.39: ¹H-NMR spectrum (500MHz, 298K, DMSO-*d*₆) of the formation of tetrahedron [2BEN14@Pd₄AZU1₈](OTf)₄ from cage [Pd₂AZU1₄](OTf)₄ recorded at 50°C.

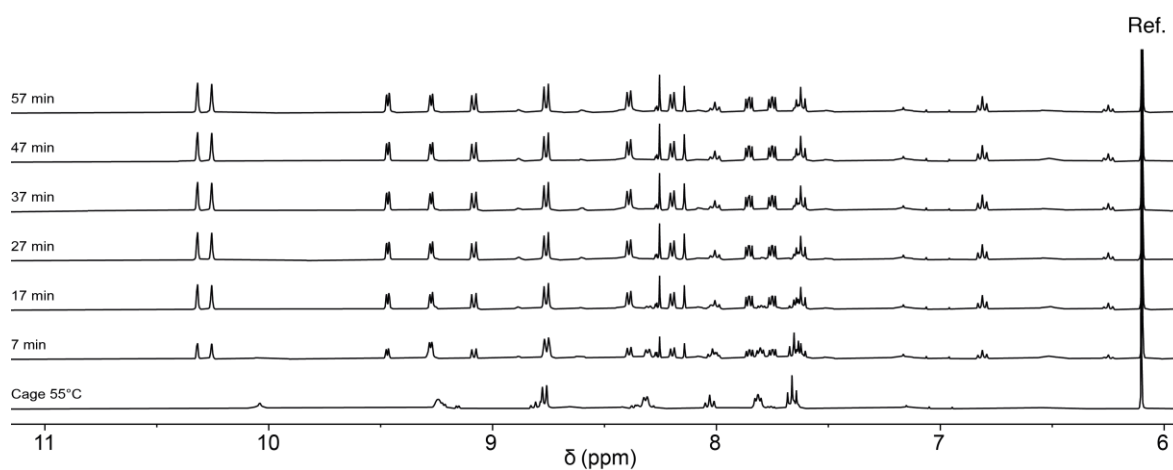


Figure S3.40: ¹H-NMR spectrum (500MHz, 298K, DMSO-*d*₆) of the formation of tetrahedron [2BEN14@Pd₄AZU1₈](OTf)₄ from cage [Pd₂AZU1₄](OTf)₄ recorded at 55°C.

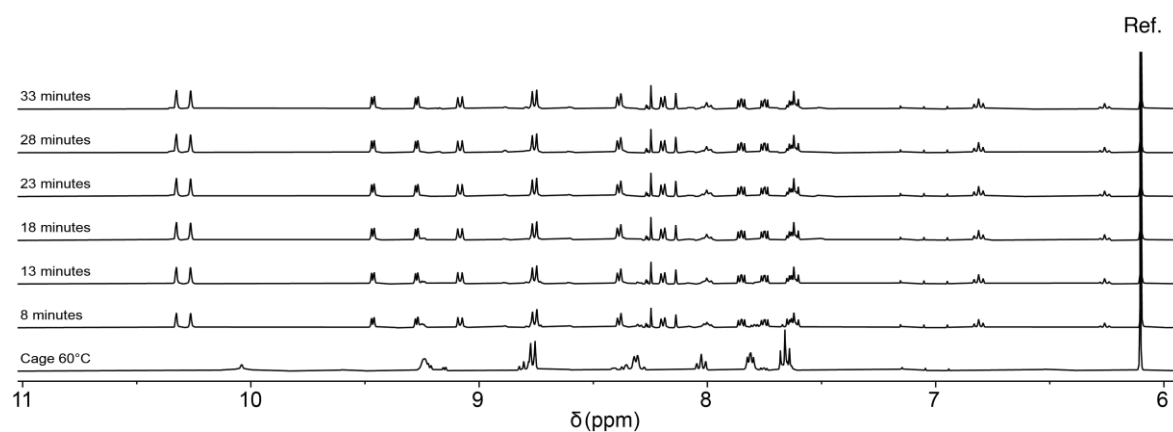


Figure S3.41: ¹H-NMR spectrum (500MHz, 298K, DMSO-*d*₆) of the formation of tetrahedron [2BEN14@Pd₄AZU1₈](OTf)₄ from cage [Pd₂AZU1₄](OTf)₄ recorded at 60°C.

3 – Guest-induced transformation of an azulene-based Pd_2L_4 cage to a Pd_4L_8 tetrahedron

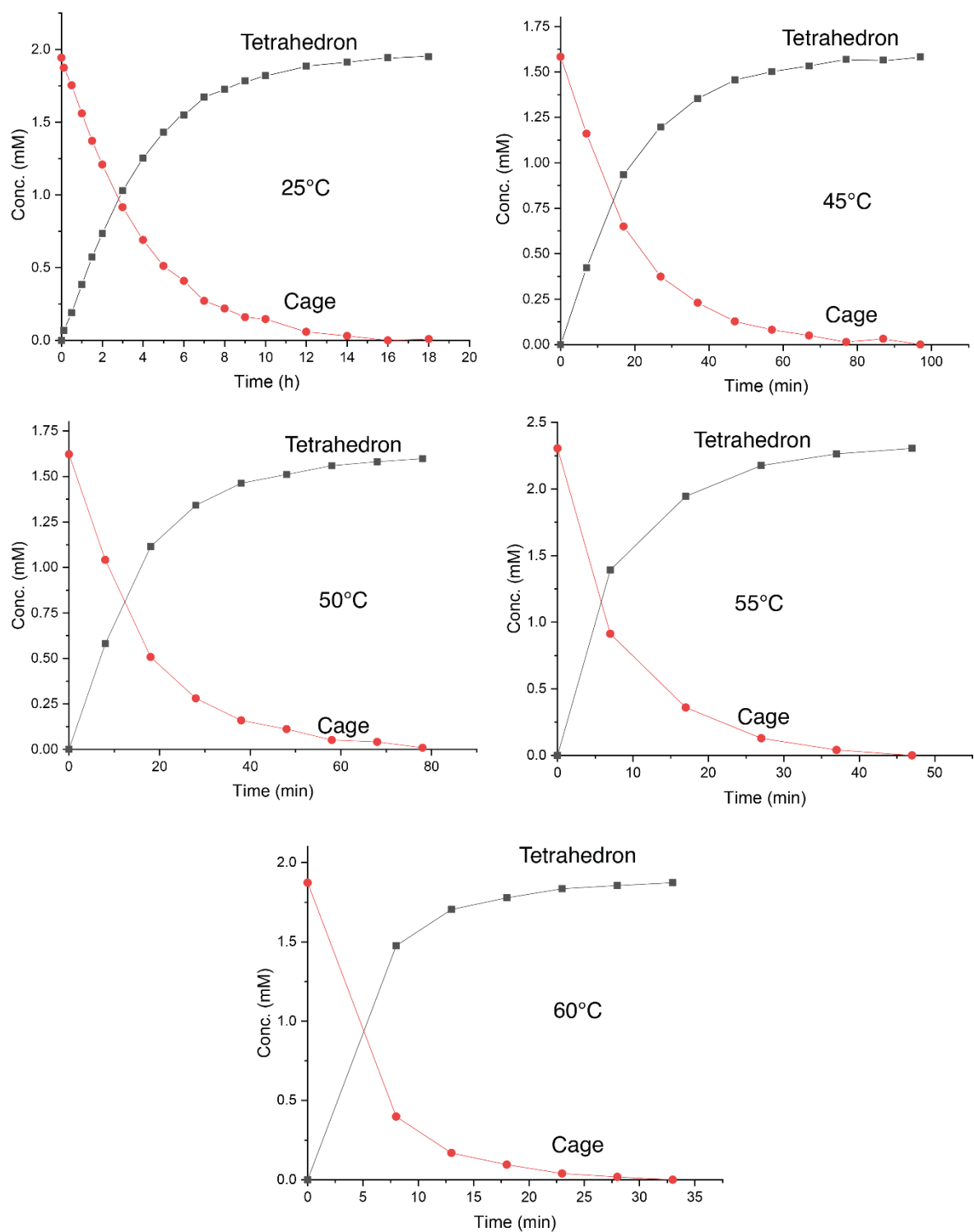


Figure S3.42: Evolution of species $[Pd_2AZU_{14}](OTf)_4$ (red traces) and $[2BEN_{14}@Pd_4AZU_{18}](OTf)_4$ (black traces) at all measured temperatures. The concentrations are given in ligand equivalents.

3 – Guest-induced transformation of an azulene-based Pd_2L_4 cage to a Pd_4L_8 tetrahedron

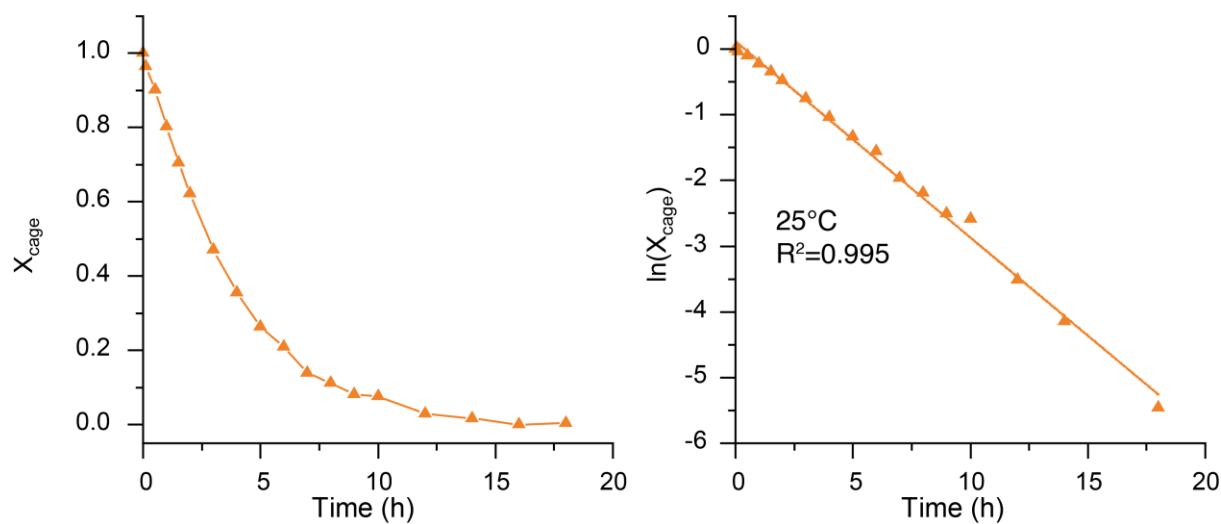


Figure S3.43: (left) Fraction of cage $[Pd_2AZU1_4](OTf)_4$ at 25°C over time during transformation to the tetrahedron. (right) natural logarithm of the fraction of cage $[Pd_2AZU1_4](OTf)_4$ at 25°C over time, with linear regression.

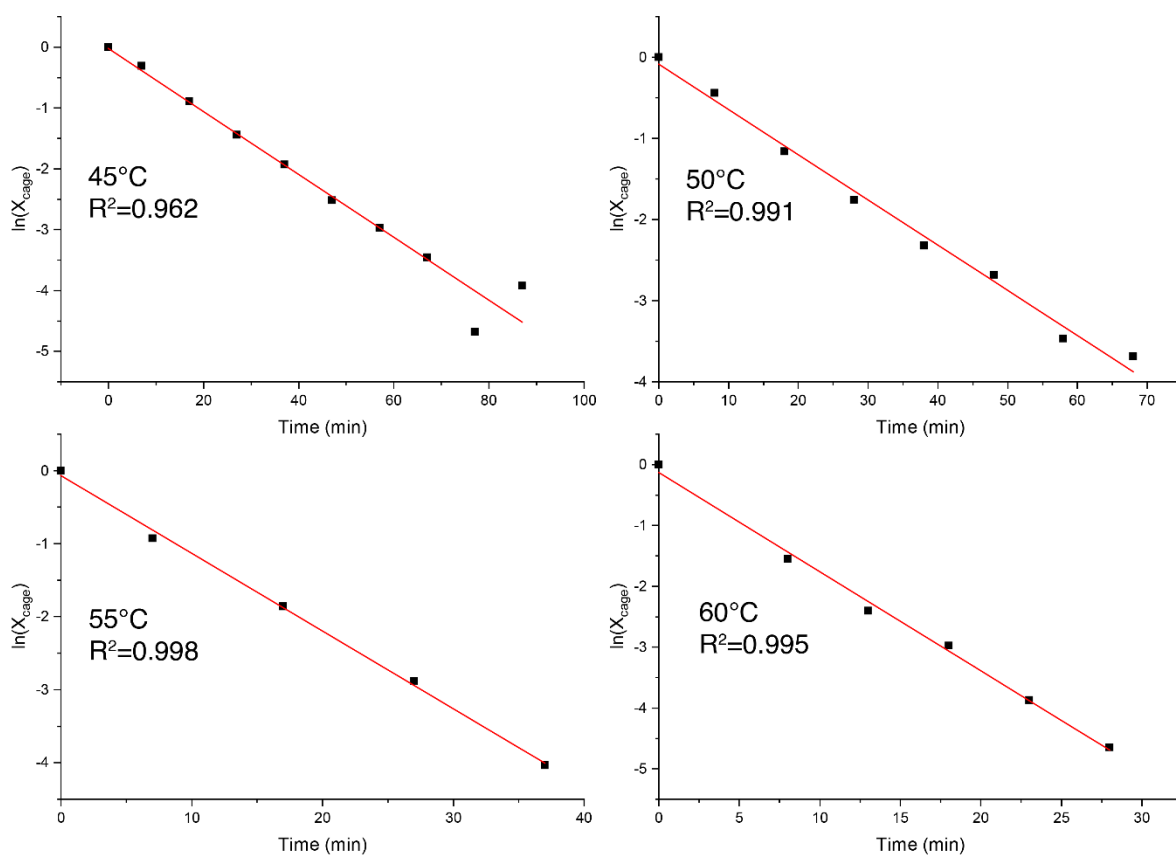


Figure S3.44: Natural logarithm of the fraction of cage $[Pd_2AZU1_4](OTf)_4$ at 45°C, 50°C, 55°C, and 60°C over time, with linear regression (red lines).

3.7.4.5 $Pd_2AZU_2_4$

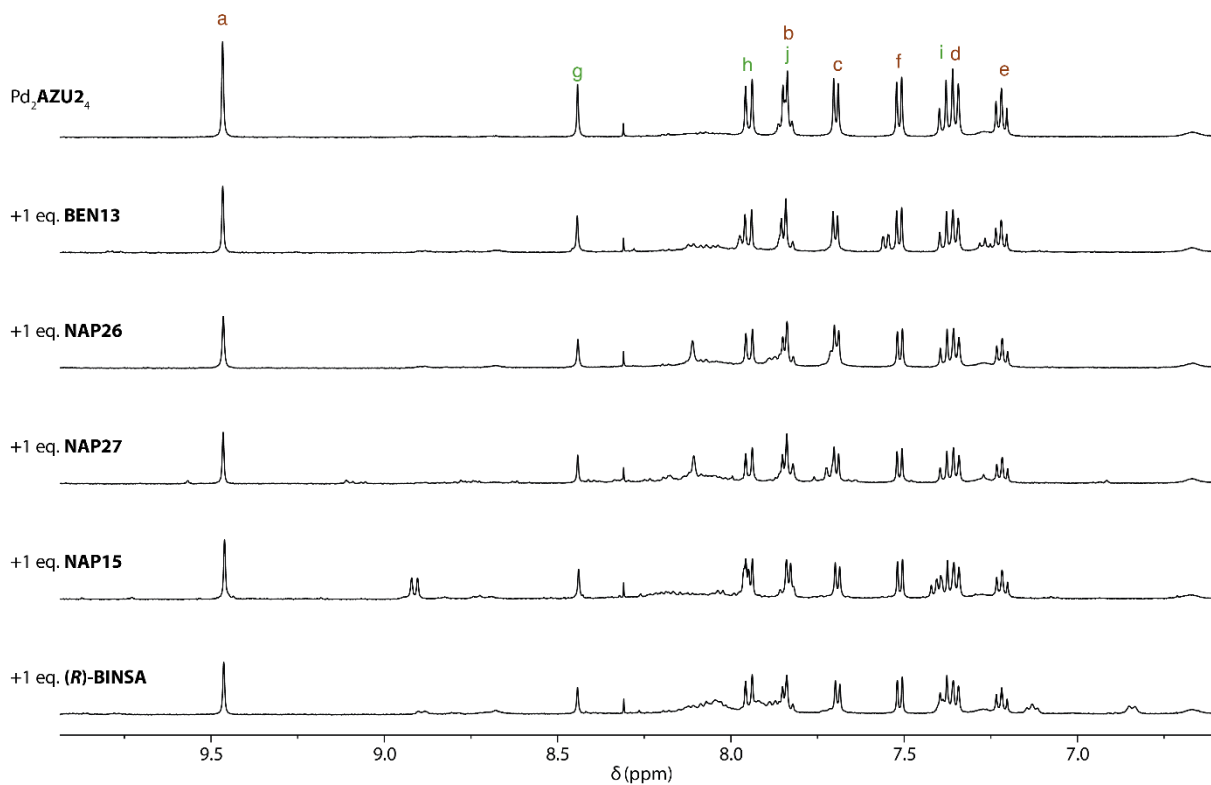
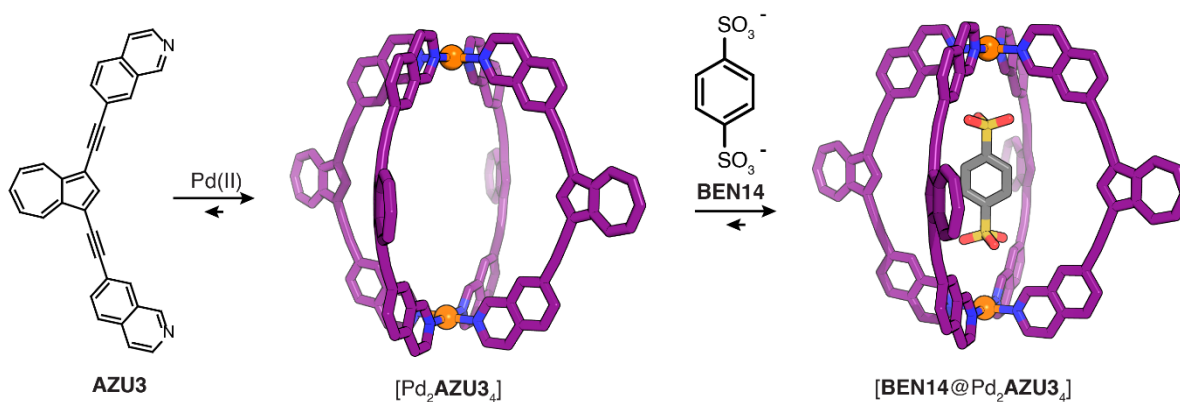


Figure S3.45: 1H -NMR (500 MHz, 298 K, $DMSO-d_6$) of cage $Pd_2AZU_2_4$ with the addition of five different guests.

3.7.4.6 $[BEN14@Pd_2AZU_3_4](OTf)_2$ and $[BEN13@Pd_2AZU_3_4](OTf)_2$



The host-guest complex $[BEN14@Pd_2AZU_3_4](OTf)_2$ was prepared by adding 25 μ l of a 15mM $DMSO-d_6$ solution of the guest **BEN14** as the tetrabutylammonium salt to 500 μ l of a 0.7mM $DMSO-d_6$ solution of the cage $[Pd_2AZU_3_4](OTf)_4$.

3 – Guest-induced transformation of an azulene-based Pd_2L_4 cage to a Pd_4L_8 tetrahedron

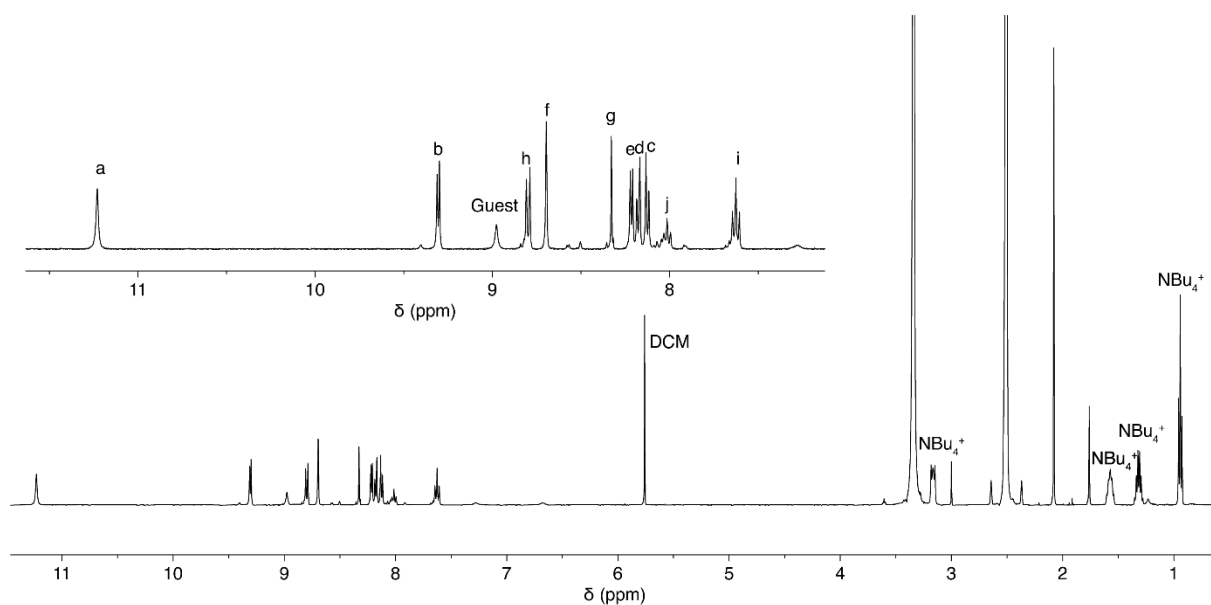


Figure S3.46: ^1H -NMR spectrum (500MHz, 298K, $\text{DMSO-}d_6$) of host-guest complex $[\text{BEN14@Pd}_2\text{AZU3}_4](\text{OTf})_2$ with an inset of the aromatic protons.

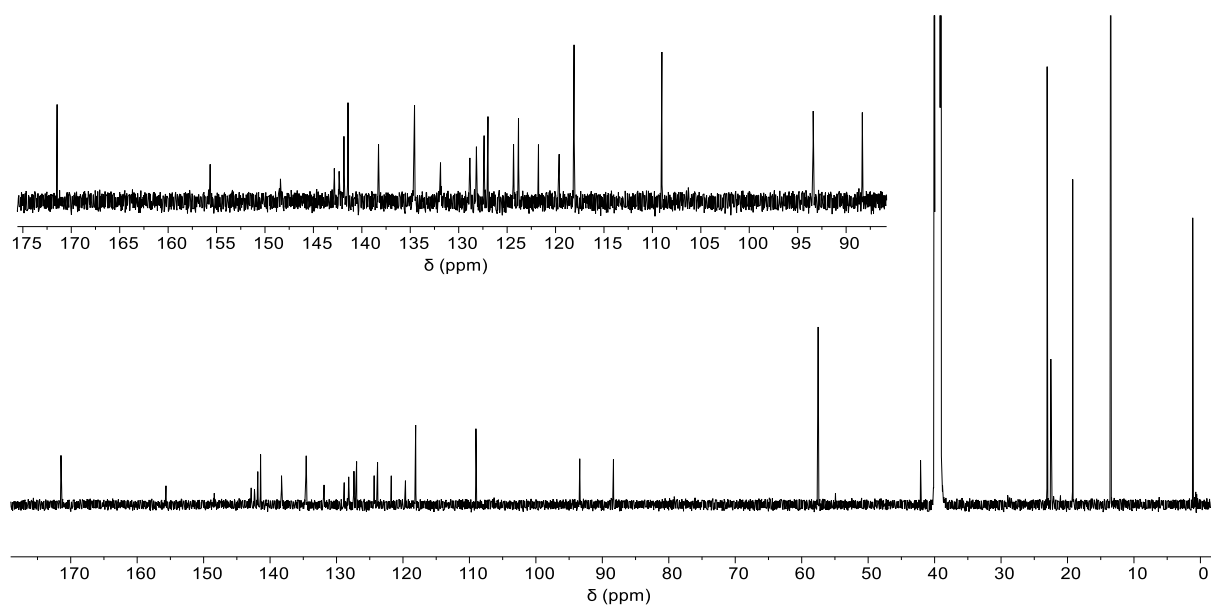


Figure S3.47: ^{13}C -NMR spectrum (175MHz, 298K, $\text{DMSO-}d_6$) of host-guest complex $[\text{BEN14@Pd}_2\text{AZU3}_4](\text{OTf})_2$ with an inset of the aromatic region.

3 – Guest-induced transformation of an azulene-based Pd_2L_4 cage to a Pd_4L_8 tetrahedron

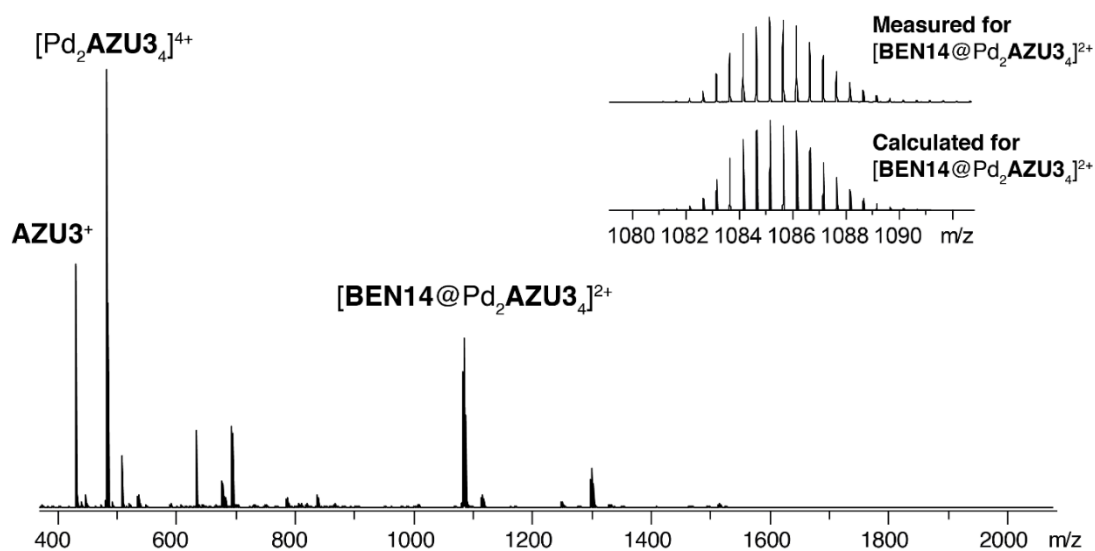


Figure S3.48: ESI-MS of host-guest complex $[BEN14@Pd_2AZU_3_4](OTf)_2$.

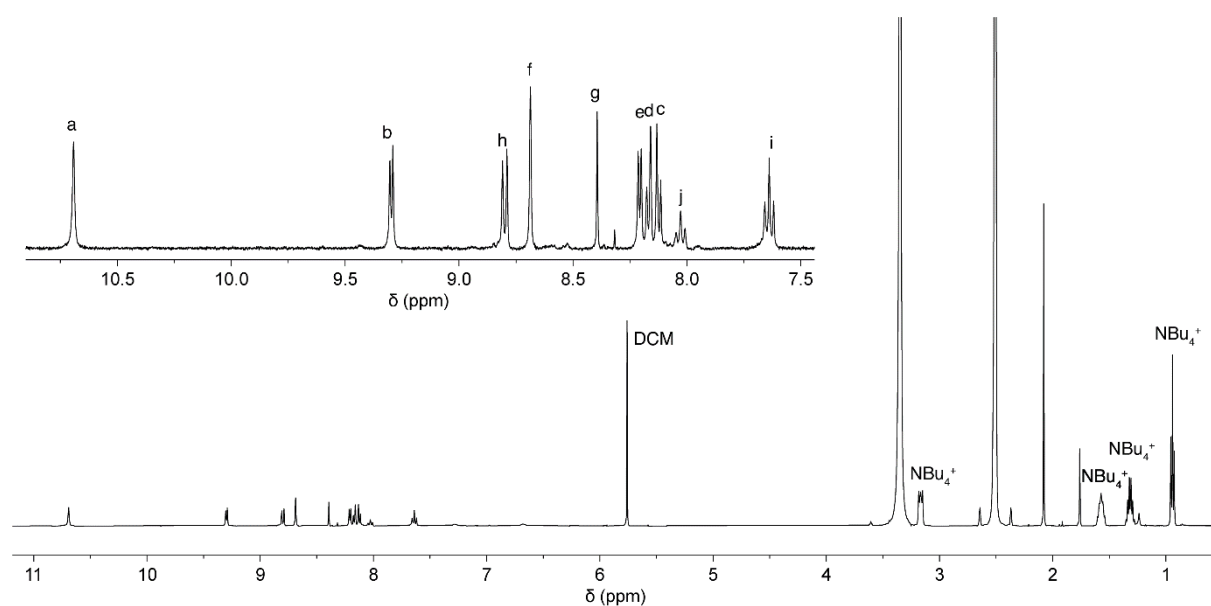


Figure S3.49: 1H -NMR spectrum (500MHz, 298K, $DMSO-d_6$) of host-guest complex $[BEN13@Pd_2AZU_3_4](OTf)_2$ with an insert of the aromatic protons.

Due to solubility issues, the ^{13}C -NMR could not be properly measured, despite using 10'000 scans.

3 – Guest-induced transformation of an azulene-based Pd₂L₄ cage to a Pd₄L₈ tetrahedron

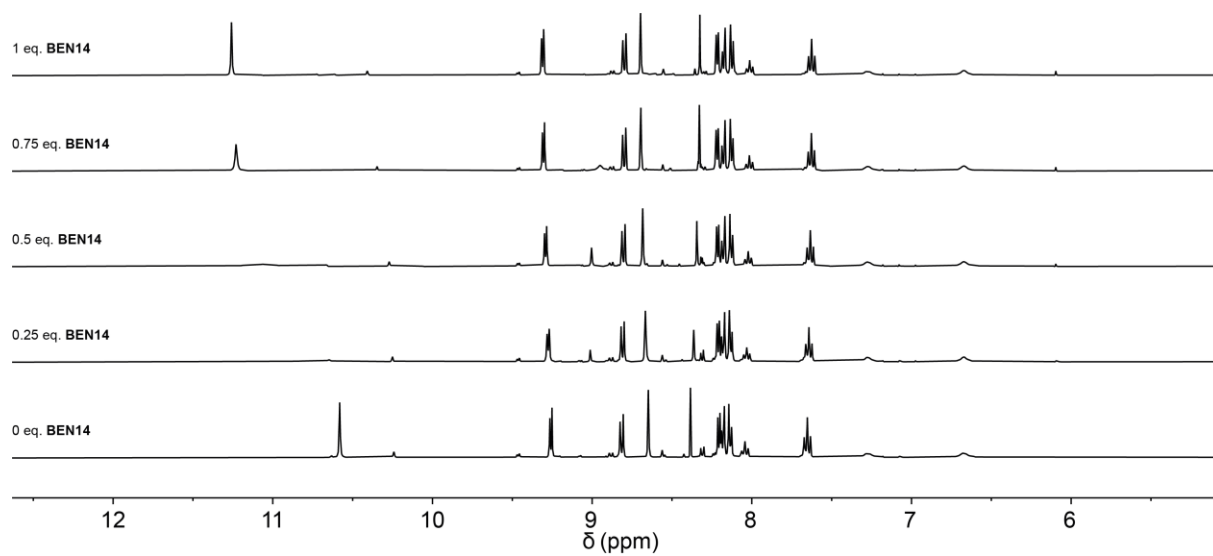


Figure S3.50: ¹H-NMR spectra (500MHz, 298K, DMSO-*d*₆) of cage [Pd₂AZU₃](OTf)₄ titrated with guest BEN14. Precipitation was observed after 1 eq. of guest was added.

3.7.4.7 UV-Vis titration of [Pd₂AZU₃](OTf)₂ with BEN14

The binding constant was determined with Bindfit (<http://supramolecular.org>)^[41]. Despite precipitation occurring after the addition of 3 equivalents of BEN14 before a plateau was reached, a binding constant could still be calculated.

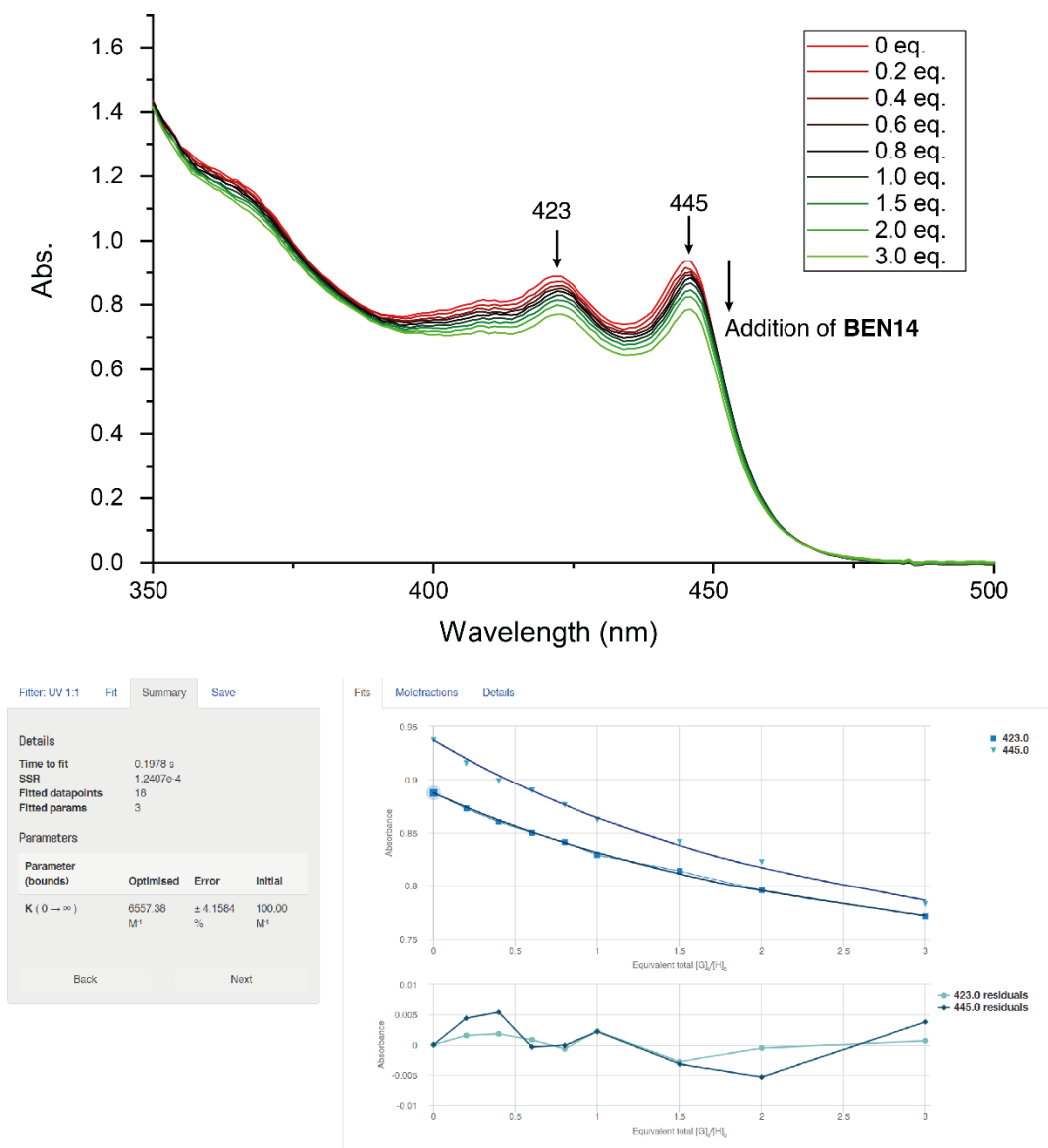


Figure S3.51: Top: UV-Vis titration of [Pd₂AZU₃](OTf)₄ with BEN14. Concentration of the cage (in ligand): 0.3 mM, cuvette thickness: 1 mm, solvent: DMSO. The amount of guest added is expressed in equivalents of cage. The arrows point towards the peaks at which the absorbance values were chosen for the binding constant calculation. Bottom: Bindfit window of the binding constant calculation.

3.7.4.8 BEN14@Pd₂AZU₄

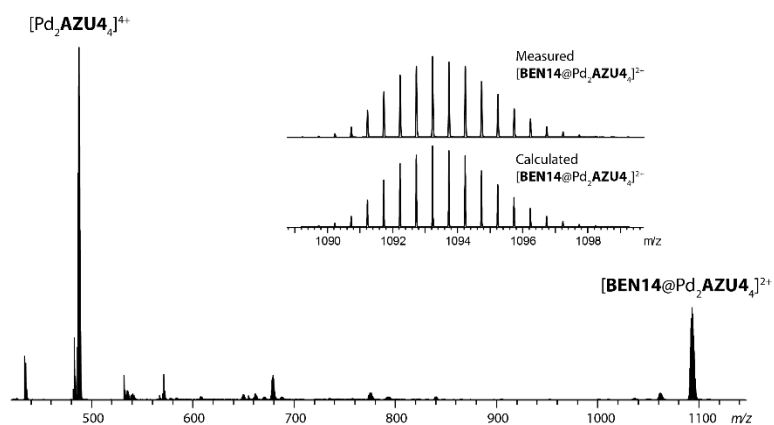


Figure S3.52: ESI-MS spectrum of the host-guest complex BEN14@Pd₂AZU₄.

3.7.4.9 NAP27@Pd₂AZU₅

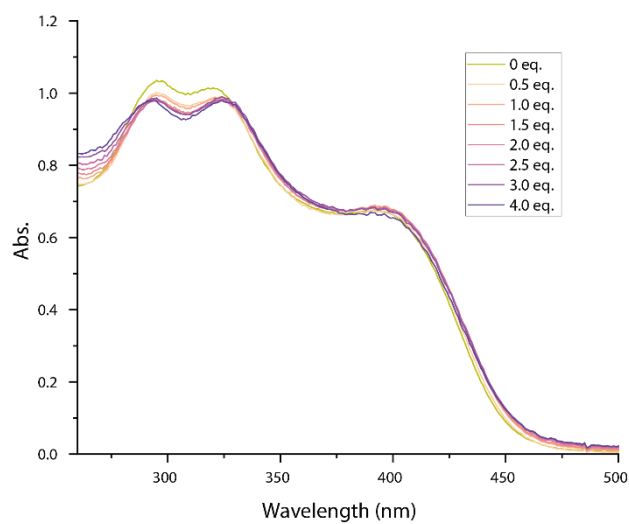


Figure S3.53: UV-Vis titration of Pd₂AZU₅ with NAP27 in DMSO.

3.7.5 Tetrahedron to cage transformation

3.7.5.1 Synthesis of cage [Pd₂MB-P₄](BF₄)₈ or (OTf)₈

Cage MB-P was prepared as previously described,^[42] as a 0.7mM solution in DMSO-*d*₆.

3.7.5.2 Titration of cage [Pd₂(MB-P)₄](OTf)₈ with BEN14

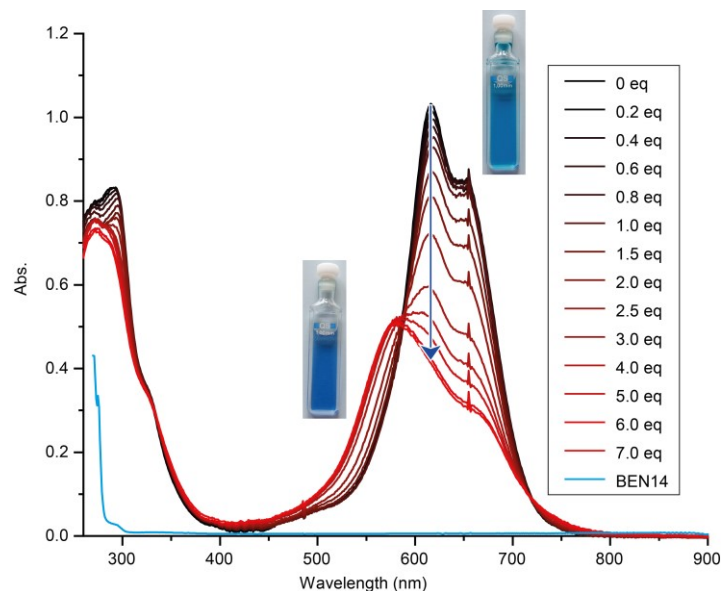


Figure S3.54: UV-Vis titration of [Pd₂(MB-P)₄](OTf)₈ with BEN14. Concentration of the cage (in ligand): 0.3 mM, cuvette thickness: 1 mm, solvent: DMSO. The amount of guest added is expressed in equivalents of cage. Concentration of free BEN14 for the spectrum: 1.5 mM.

3.7.5.3 Guest transfer experiments

0.25 ml of a 0.35mM solution of [2BEN14@Pd₄AZU1₈](OTf)₄ or [2BEN13@Pd₄AZU1₈](OTf)₄ and 0.25ml of a 0.7mM solution of [Pd₂MB-P₄](OTf)₈ in DMSO-*d*₆ were mixed and heated at 70°C for 1 hour. The ¹H-NMR was then recorded and showed a disappearance of the signals of [2GUEST@Pd₄AZU1₈](OTf)₄ and a reappearance of the signals of cage [Pd₂AZU1₄](OTf)₄.

We further tried a separation of these species by precipitation of the [Pd₂AZU1₄] cage via addition of water to the DMSO mixture of the two cages, knowing that the [Pd₂MB-P₄] cage is soluble in water. However, no precipitation was observed. On the other hand, the addition of a second equivalent of BEN14 causes precipitation of almost everything in the solution.

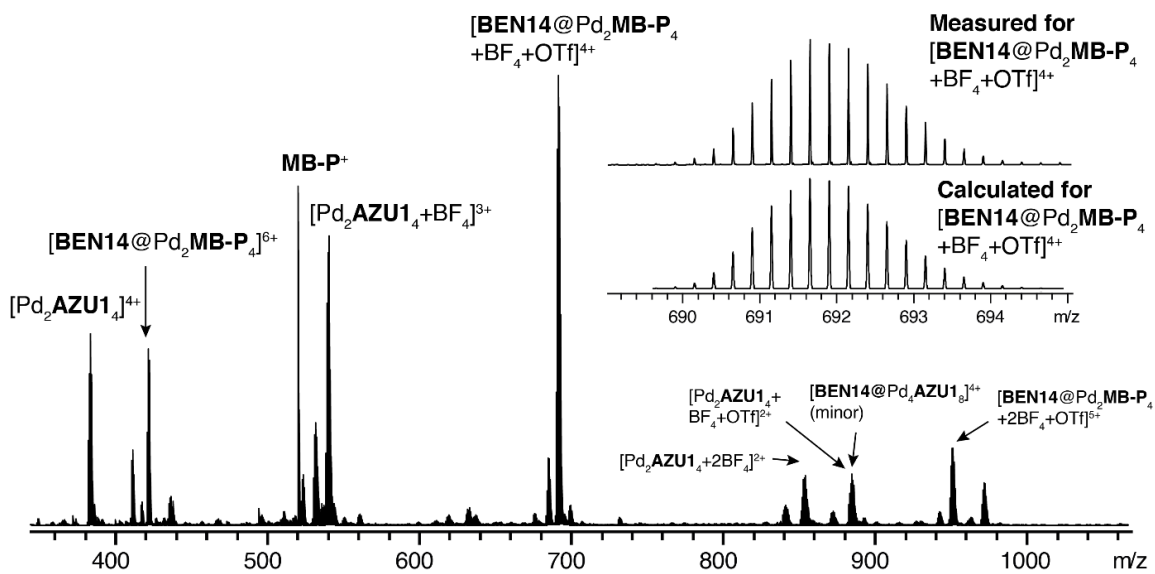


Figure S3.55: ESI-MS of the guest-exchange experiment with **BEN14** after heating at 70°C for 1 hour. The experiment was recorded with BF_4^- as a counter-anion to the **MB-P** cage.

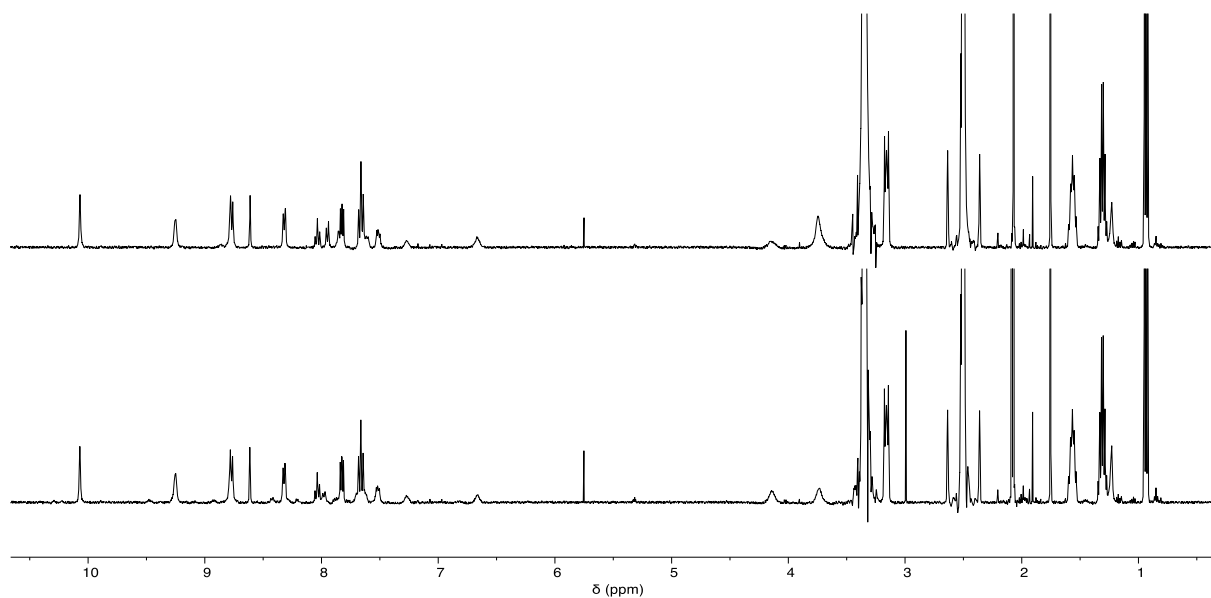


Figure S3.56: 1H -NMR spectra (500MHz, 298K, $DMSO-d_6$) of the guest-exchange experiment with **BEN13** (top) and **BEN14** (bottom) after heating at 70°C for 1 hour. The experiment was recorded with OTf^- as a counter-anion to the **MB-P** cage. The highest peaks were clipped for the sake of clarity.

3.7.5.4 NMR evolution of the system at 25°C

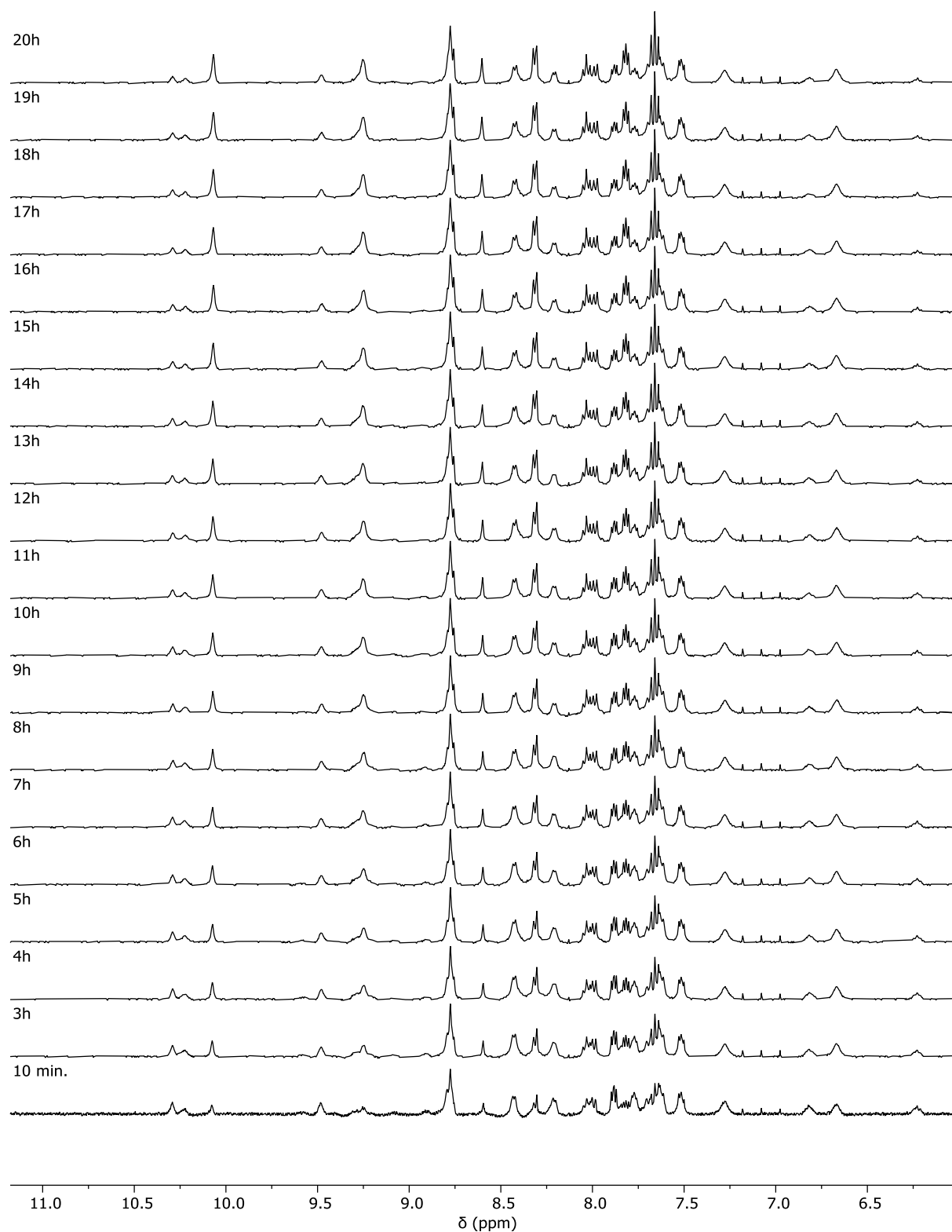


Figure S3.57: Evolution of the guest transfer with BEN14 monitored for 20 h by ¹H-NMR (500MHz, 298K, DMSO-*d*₆) at 25°C.

3.7.6 Fluorescence data (AZU1 to AZU3)

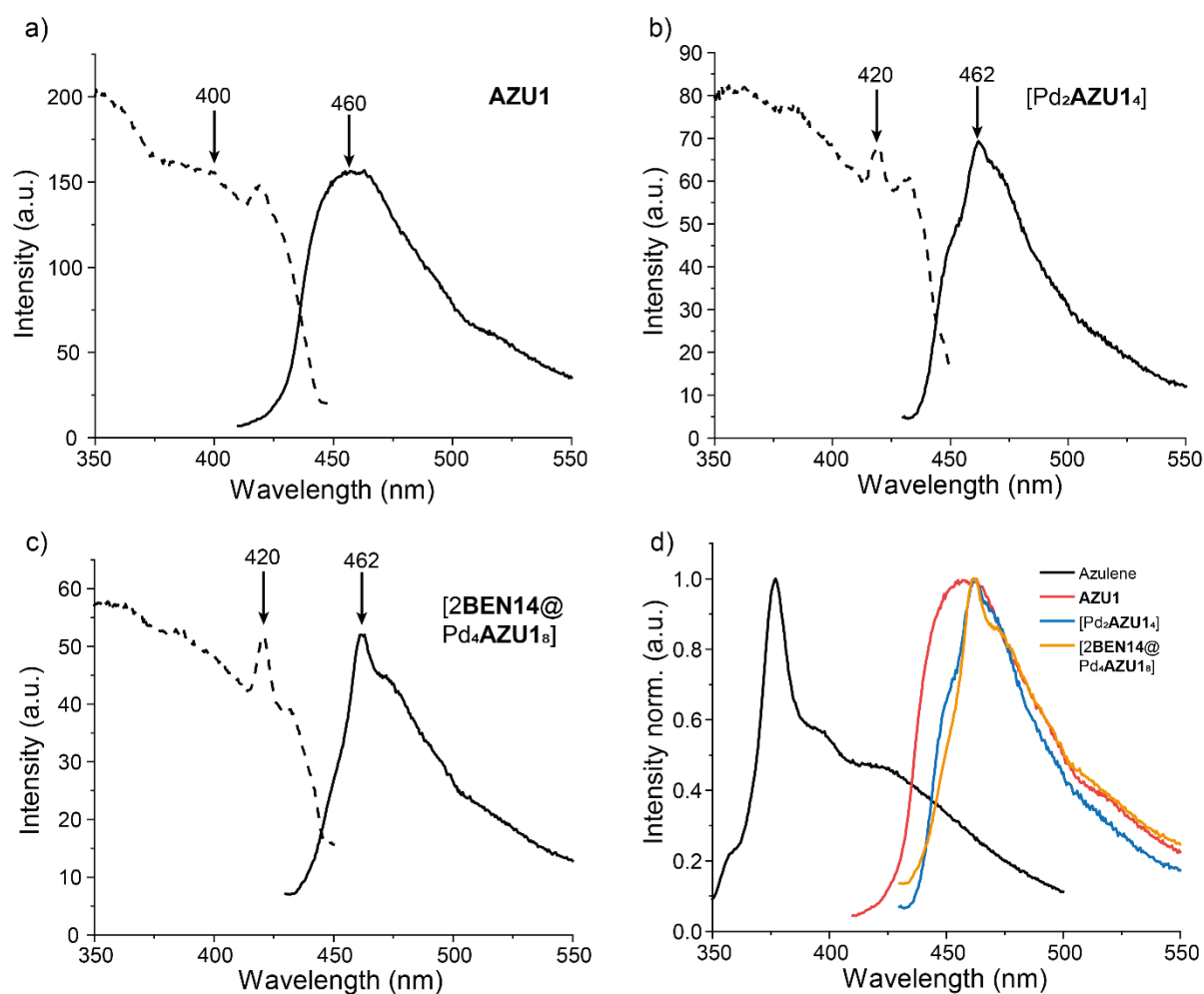
3.7.6.1 AZU1 species

Figure S3.58: (a), (b) and (c): excitation (dashed lines) and emission spectra (full lines) of **AZU1**, $[Pd_2AZU1_4](OTf)_4$ and $[2BEN14@Pd_4AZU1_8](OTf)_4$. The arrows point to the respective emission or excitation wavelength (in nm). (d): normalised emission spectra of azulene and of the three previous species.

3.7.6.2 **AZU2** species

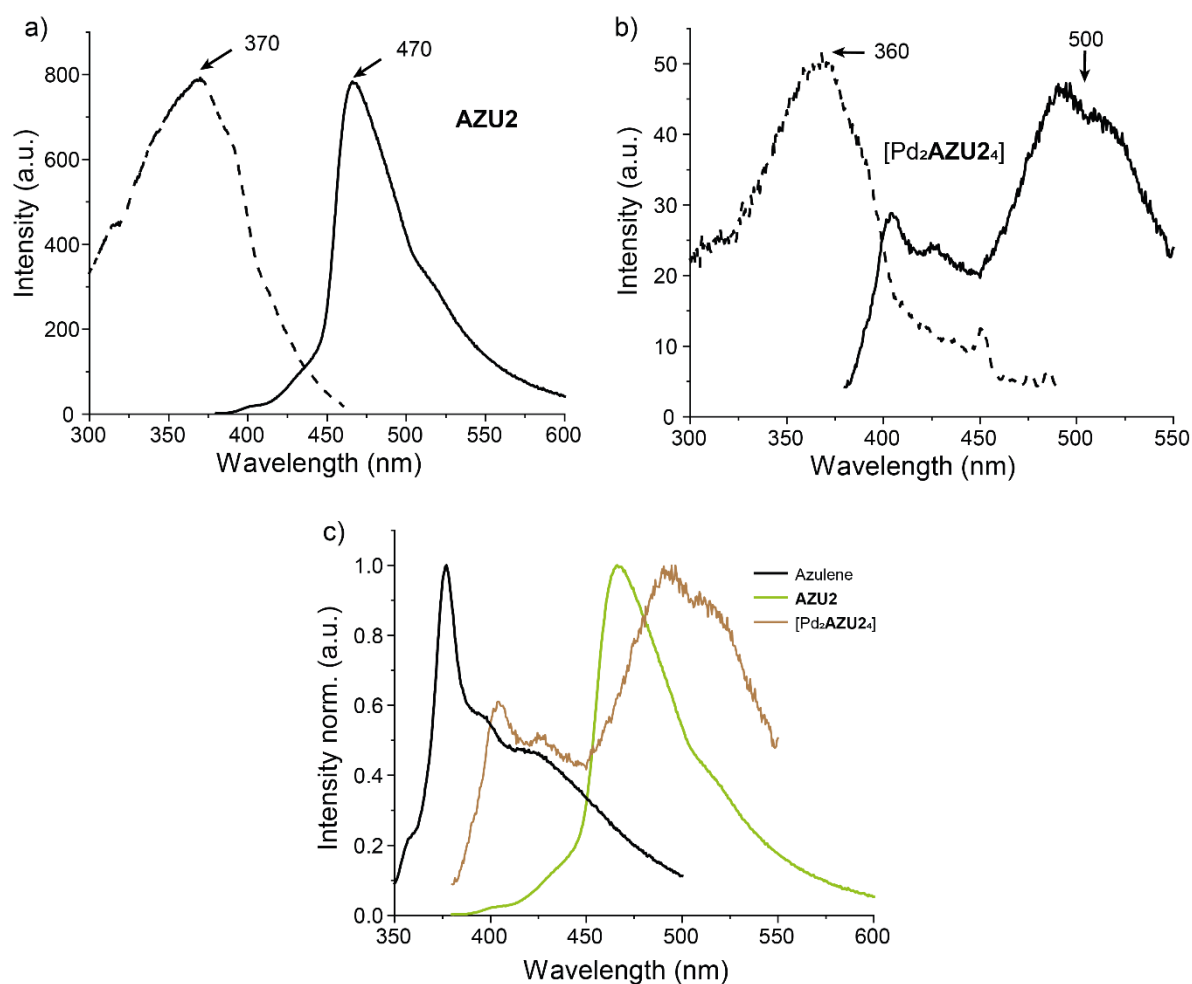


Figure S3.59: (a) and (b): excitation (dashed lines) and emission spectra (full lines) of **AZU2** and $[Pd_2AZU_2]_4(OTf)_4$. The arrows point to the respective emission or excitation wavelength (in nm). (c): normalised emission spectra of azulene and of the two previous species.

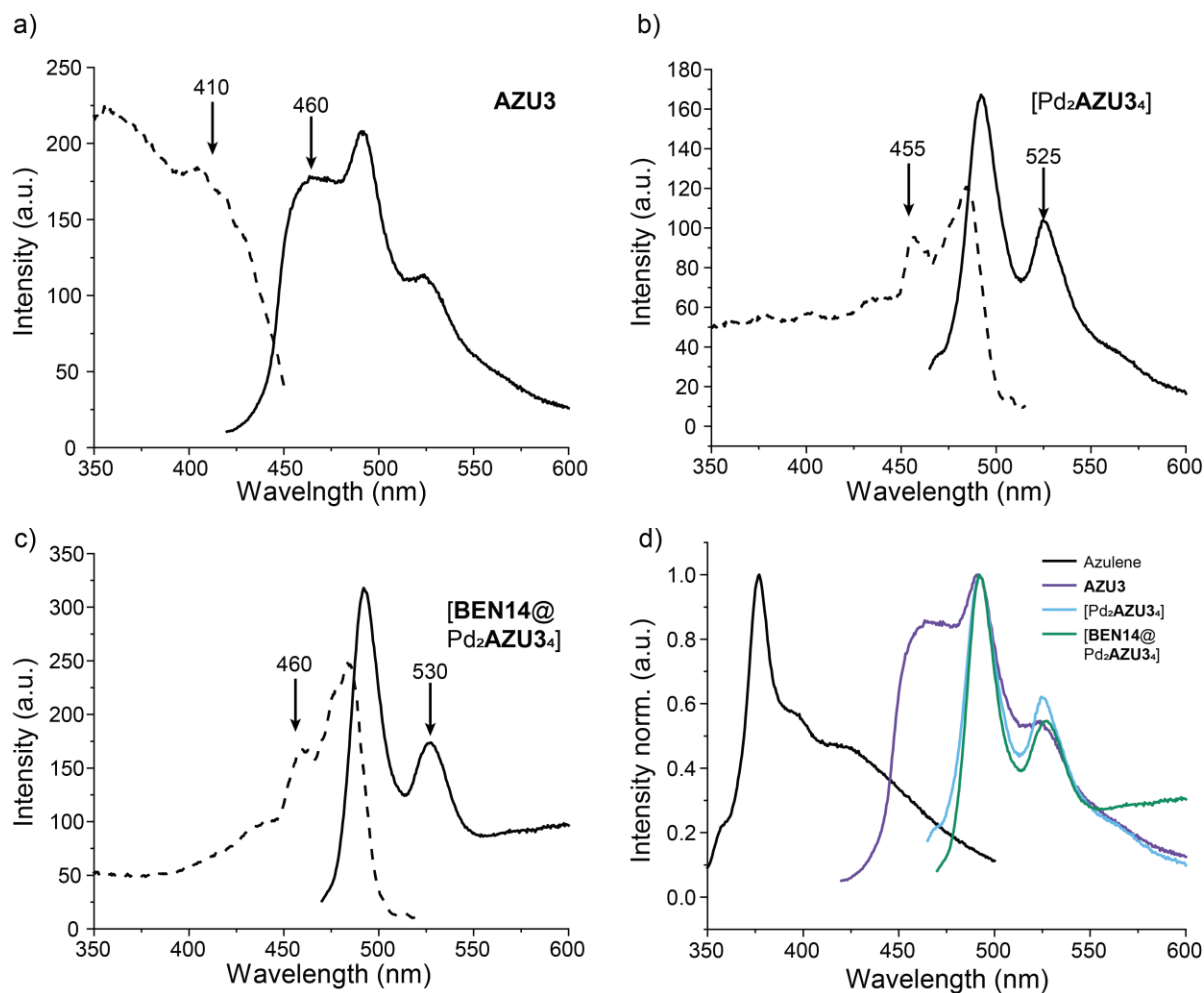
3.7.6.3 **AZU3** species

Figure S3.60: (a), (b) and (c): excitation (dashed lines) and emission spectra (full lines) of **AZU3**, **[Pd₂AZU₃]₄**(OTf)₄ and **[BEN14@Pd₂AZU₃]₄**(OTf)₂ (2 equivalents of guest added). The arrows point to the respective emission or excitation wavelength (in nm). (d): normalised emission spectra of azulene and of the three previous species.

3.7.7 X-ray structures

Five different supramolecular assemblies **Pd₂AZU1₄**, **Pd₂AZU2₄**, **BEN14@Pd₂AZU3**, **2BEN14@Pd₄AZU1₈**, and **B12F12@Pd₂AZU5₄** were studied using single crystal X-ray crystallography. The crystals of those supramolecular assemblies were extremely sensitive to organic solvent loss. Moreover, due to small block or thin plate shaped crystals, the analysis required cryogenic handling and highly brilliant synchrotron radiation. Hence, diffraction data of the supramolecular assemblies was collected during four beamtime shifts at macromolecular synchrotron beamline P11, PETRA III, DESY.^[43] Counterion and solvent flexibility required carefully adapted macromolecular refinement protocols employing geometrical restraint dictionaries, similarity restraints and restraints for anisotropic displacement parameters (ADPs).

Table S3.2: Crystal data and structure refinement for supramolecular assemblies Pd₂AZU₁₄ and Pd₂AZU₂₄

Compound	Pd ₂ AZU ₁₄	Pd ₂ AZU ₂₄
CIF ID	aw1e	aw2i
CCDC no	2256445	2256446
Empirical formula	C ₉₈ H ₆₂ B ₃ F ₁₂ N ₈ OPd ₂ S	C ₁₃₄ H ₈₁ B ₄ F ₁₆ N ₁₁ Pd ₂
Formula weight	1872.84	2405.13
Temperature [K]	100(2)	100(2)
Crystal system	orthorhombic	triclinic
Space group (number)	<i>Fm</i> mm (69)	<i>P</i> $\bar{1}$ (2)
<i>a</i> [Å]	20.935(6)	16.435(5)
<i>b</i> [Å]	28.101(9)	17.268(4)
<i>c</i> [Å]	20.868(12)	21.662(4)
α [Å]	90	82.850(7)
β [Å]	90	80.648(18)
γ [Å]	90	73.438(14)
Volume [Å ³]	12277(9)	5794(3)
<i>Z</i>	4	2
ρ_{calc} [g/cm ³]	1.013	1.379
μ [mm ⁻¹]	0.333	0.357
<i>F</i> (000)	3780	2436
Crystal size [mm ³]	0.100× 0.080× 0.040	0.120× 0.100× 0.005
Crystal color	green	yellow
Crystal shape	block	plate
Radiation	synchrotron ($\lambda=0.6888$ Å)	synchrotron ($\lambda=0.6888$ Å)
2 θ range [°]	3.02 to 53.92 (0.76 Å)	2.39 to 53.92 (0.76 Å)
Index ranges	-27 ≤ <i>h</i> ≤ 27 -35 ≤ <i>k</i> ≤ 35 -27 ≤ <i>l</i> ≤ 27	-21 ≤ <i>h</i> ≤ 21 -20 ≤ <i>k</i> ≤ 20 -28 ≤ <i>l</i> ≤ 27
Reflections collected	37344	69610
Independent reflections	3630 <i>R</i> _{int} = 0.0343 <i>R</i> _{sigma} = 0.0195	18977 <i>R</i> _{int} = 0.0287 <i>R</i> _{sigma} = 0.0262
Completeness	99.3 %	83.0 %
Data / Restraints / Parameters	3630/320/231	18977/3880/1734
Goodness-of-fit on <i>F</i> ²	1.892	1.026
Final <i>R</i> indexes [<i>I</i> ≥ 2 σ (<i>I</i>)]	<i>R</i> ₁ = 0.1186 <i>wR</i> ₂ = 0.3630	<i>R</i> ₁ = 0.0743 <i>wR</i> ₂ = 0.2368
Final <i>R</i> indexes [all data]	<i>R</i> ₁ = 0.1205 <i>wR</i> ₂ = 0.3704	<i>R</i> ₁ = 0.0876 <i>wR</i> ₂ = 0.2531
Largest peak/hole [eÅ ³]	2.43/-1.57	2.08/-0.82

Table S3.3: Crystal data and structure refinement for supramolecular assemblies **BEN14@Pd₂AZU₃₄** and **2BEN14@Pd₄AZU₁₈**.

Compound	BEN14@Pd₂AZU₃₄	2BEN14@Pd₄AZU₁₈
CIF ID	aw25t	aw48t
CCDC no	2256447	2256448
Empirical formula	C ₈₆ H ₆₆ F ₃ N ₄ O ₈ Pd ₄ S ₄	C _{482.01} H _{375.44} N ₃₂ O ₆₂ Pd ₈ ReS ₃₀
Formula weight	1575.06	9606.88
Temperature [K]	100(2)	100(2)
Crystal system	monoclinic	triclinic
Space group (number)	<i>C</i> 2/ <i>m</i> (12)	<i>P</i> $\bar{1}$ (2)
<i>a</i> [Å]	14.662(7)	22.049(4)
<i>b</i> [Å]	46.468(10)	34.177(7)
<i>c</i> [Å]	15.844(3)	42.927(9)
α [Å]	90	83.40(3)
β [Å]	113.561(17)	76.38(3)
γ [Å]	90	81.01(3)
Volume [Å ³]	9895(6)	30949(12)
<i>Z</i>	4	2
ρ_{calc} [g/cm ³]	1.057	1.031
μ [mm ⁻¹]	0.294	0.525
<i>F</i> (000)	3244	9821
Crystal size [mm ³]	0.120×0.030×0.010	0.200×0.200×0.050
Crystal color	green	green
Crystal shape	plate	block
Radiation	synchrotron ($\lambda=0.6888$ Å)	synchrotron ($\lambda=0.6888$ Å)
2 θ range [°]	1.70 to 52.40 (0.78 Å)	1.17 to 56.20 (0.73 Å)
Index ranges	-18 ≤ <i>h</i> ≤ 18 -57 ≤ <i>k</i> ≤ 56 -19 ≤ <i>l</i> ≤ 19	-25 ≤ <i>h</i> ≤ 26 -42 ≤ <i>k</i> ≤ 43 -51 ≤ <i>l</i> ≤ 51
Reflections collected	62219	395374
Independent reflections	9801 <i>R</i> _{int} = 0.0368 <i>R</i> _{sigma} = 0.0222	107668 <i>R</i> _{int} = 0.0241 <i>R</i> _{sigma} = 0.0214
Completeness	95.8 %	86.1 %
Data / Restraints / Parameters	9801/953/535	107668/12867/6150
Goodness-of-fit on <i>F</i> ²	1.183	1.601
Final <i>R</i> indexes [<i>I</i> ≥ 2 σ (<i>I</i>)]	<i>R</i> ₁ = 0.0724 <i>wR</i> ₂ = 0.2484	<i>R</i> ₁ = 0.0942 <i>wR</i> ₂ = 0.3340
Final <i>R</i> indexes [all data]	<i>R</i> ₁ = 0.0769 <i>wR</i> ₂ = 0.2571	<i>R</i> ₁ = 0.0989 <i>wR</i> ₂ = 0.3421
Largest peak/hole [eÅ ³]	1.56/-1.17	5.01/-1.72

Table S3.4: Crystal data and structure refinement for supramolecular assemblies B12F12@Pd₂AZU5₄

Compound	B12F12@Pd₂AZU5₄
CIF ID	aw41t
CCDC number	Unpublished
Empirical formula	C ₁₆₁ H ₁₂₆ B ₂₄ F ₂₄ N ₈ O ₅ Pd ₂ S ₅
Formula weight	3341.23
Temperature [K]	100(2)
Crystal system	monoclinic
Space group (number)	<i>C2/c</i> (15)
<i>a</i> [Å]	61.31(2)
<i>b</i> [Å]	31.000(7)
<i>c</i> [Å]	28.894(7)
α [°]	90
β [°]	96.949(8)
γ [°]	90
Volume [Å ³]	54511(27)
<i>Z</i>	8
ρ_{calc} [gcm ⁻³]	0.814
μ [mm ⁻¹]	0.597
<i>F</i> (000)	13568
Crystal size [mm ³]	0.300×0.010×0.005
Crystal colour	brown
Crystal shape	block
Radiation	synchrotron ($\lambda=1.0332$ Å)
2 θ range [°]	1.95 to 51.00 (1.20 Å)
Index ranges	-47 ≤ <i>h</i> ≤ 47 -24 ≤ <i>k</i> ≤ 24 -20 ≤ <i>l</i> ≤ 20
Reflections collected	98711
Independent reflections	14395 <i>R</i> _{int} = 0.0446 <i>R</i> _{sigma} = 0.0255
Completeness to $\vartheta = 25.499^\circ$	87.1 %
Data / Restraints / Parameters	14395/5422/2237
Goodness-of-fit on <i>F</i> ²	1.904
Final <i>R</i> indexes [$\geq 2\sigma(I)$]	<i>R</i> ₁ = 0.1221 <i>wR</i> ₂ = 0.3908
Final <i>R</i> indexes [all data]	<i>R</i> ₁ = 0.1343 <i>wR</i> ₂ = 0.4089
Largest peak/hole [eÅ ⁻³]	0.81/-0.45

3.7.7.1 Crystal structure of Pd₂AZU1₄

Green block shaped crystals of Pd₂AZU1₄ were grown by slow vapour diffusion of ethyl acetate (EtOAc) into a 0.7mM DMSO solution of [Pd₂AZU1₄](BF₄)₄ at room temperature. Single crystals in mother liquor were pipetted onto a glass slide containing NVH oil. To avoid collapse of the crystal lattice, several crystals were quickly mounted on micro loops and immediately flash-cooled in liquid nitrogen. Crystals were stored at cryogenic temperature in dry shippers, in which they were safely transported to macromolecular beamline P11 at Petra III,^[43] DESY, Hamburg, Germany. A wavelength of $\lambda = 0.6888 \text{ \AA}$ was chosen using a liquid N₂ cooled double crystal monochromator. Single crystal X-ray diffraction data was collected at 100(2) K on a single axis goniometer, equipped with an Oxford Cryostream 800 and an Eiger2x 16M detector. 3600 diffraction images were collected in a 360° φ sweep at a detector distance of 154 mm, 100% filter transmission, 0.1° step width and 0.05 seconds exposure time per image. Data integration and reduction were undertaken using XDS.^[44] The structure was solved by intrinsic phasing/direct methods using SHELXT^[45] and refined with SHELXL^[46] using 22 CPU cores for full-matrix least-squares routines on F^2 and ShelXle^[47] as a graphical user interface and the DSR program plugin was employed for modeling.^[48,49]

Specific refinement details

Stereochemical restraints for the AZU1 ligands (residue A3P), dimethylsulfoxide solvent molecule (residue DMS) and tetrafluoroborate counter ions (residue BF4) were generated by the GRADE program using the GRADE Web Server (<http://grade.globalphasing.org>) and applied in the refinement. A GRADE dictionary for SHELXL contains target values and standard deviations for 1,2-distances (DFIX) and 1,3-distances (DANG), as well as restraints for planar groups (FLAT). All displacements for non-hydrogen atoms were refined anisotropically. The refinement of ADPs for carbon, nitrogen and oxygen atoms was enabled by a combination of similarity restraints (SIMU) and rigid bond restraints (RIGU).^[50] The contribution of the electron density from disordered counterions and solvent molecules, which could not be modeled with discrete atomic positions were handled using the SQUEEZE^[51] routine in PLATON.^[52] The solvent mask file (.fab), computed by PLATON, was included in the SHELXL refinement via the ABIN instruction leaving the measured intensities untouched.

The compound crystalized in orthorhombic space group *Fm*mm (69). Due to strong overlap of molecular point group symmetry with crystallographic symmetry in the crystal structure, the asymmetric unit only contains one eighth of a cage (one half AZU1 ligand and one quarter of a Pd ion), two tetrafluoroborate counterions, both occupied by one fourth as being close to crystallographic mirror planes, as well as one eighth of a Dimethylsulfoxide solvent molecule close to crystallographic mirror planes in the inner cage cavity.

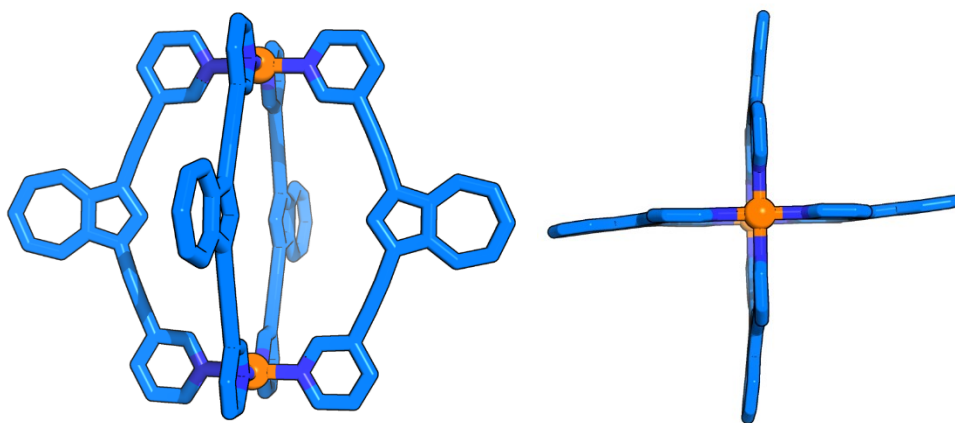


Figure S3.61: Two views of the X-ray crystal structure of [Pd₂AZU₁₄]. Counterions and solvent molecules have been omitted for clarity.

3.7.7.2 Crystal structure of Pd₂AZU₂₄

Yellow plate shaped crystals of [Pd₂AZU₂₄] were grown by slow vapour diffusion of diisopropylether (ⁱPr₂O) into a 0.7mM acetonitrile solution of [Pd₂AZU₂₄](BF₄)₄ at room temperature. Single crystals in mother liquor were pipetted onto a glass slide containing NVH oil. To avoid collapse of the crystal lattice, several crystals were quickly mounted on micro loops and immediately flash-cooled in liquid nitrogen. Crystals were stored at cryogenic temperature in dry shippers, in which they were safely transported to macromolecular beamline P11 at Petra III,^[43] DESY, Hamburg, Germany. A wavelength of $\lambda = 0.6888 \text{ \AA}$ was chosen using a liquid N₂ cooled double crystal monochromator. Single crystal X-ray diffraction data was collected at 100(2) K on a single axis goniometer, equipped with an Oxford Cryostream 800 and an Eiger2x 16M detector. 3600 diffraction images were collected in a 360° φ sweep at a detector distance of 154 mm, 100% filter transmission, 0.1° step width and 0.1 seconds exposure time per image. Data integration and reduction were undertaken using XDS.^[44] The structure was solved by intrinsic phasing/direct methods using SHELXT^[45] and refined with SHELXL^[46] using 22 CPU cores for full-matrix least-squares routines on F^2 and ShelXle^[47] as a graphical user interface and the DSR program plugin was employed for modeling.^[48,49]

Specific refinement details

Stereochemical restraints for the AZU₂ ligands (residue AQ1), acetonitrile solvent molecule (residue ACN) and tetrafluoroborate counter ions (residue BF4) were generated by the GRADE program using the GRADE Web Server (<http://grade.globalphasing.org>) and applied in the refinement. A GRADE dictionary for SHELXL contains target values and standard deviations for 1,2-distances (DFIX) and 1,3-distances (DANG), as well as restraints for planar groups (FLAT). All displacements for non-hydrogen atoms were refined anisotropically. The refinement of ADPs for

carbon, nitrogen and oxygen atoms was enabled by a combination of similarity restraints (SIMU) and rigid bond restraints (RIGU).^[50]

The compound crystallized in triclinic space group P-1 (no. 2). The asymmetric unit contains one full cage and four tetrafluoroborate counterions. One of them serves as guest in the inner cage cavity. Three of the four tetrafluoroborate counterions were modelled as disordered over two conformations using free individual variables for refinement of occupancy factors. Additionally, three acetonitrile solvent molecules could be modelled successfully yielding a complete model of the crystal structure in this case.

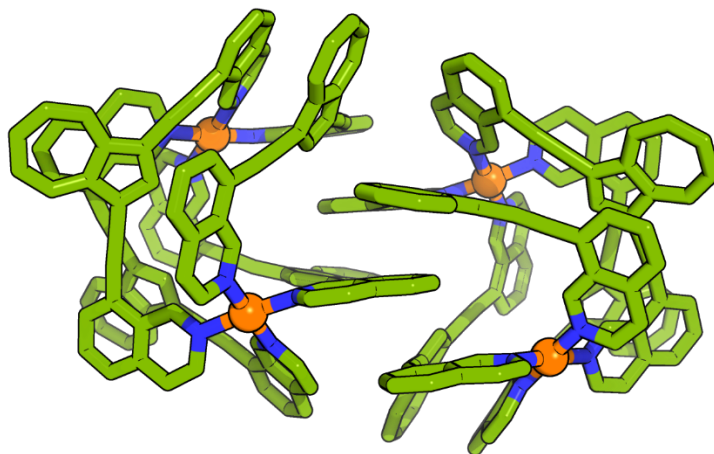


Figure S3.62: View of the X-ray crystal structure of Pd₂AZU₂₄ showing the aromatic stacking happening between the two enantiomers of the helicate. Counterions, solvent molecules and disorders have been omitted for clarity.

3.7.7.3 Crystal structure of BEN14@Pd₂AZU₃₄

Dark green plate shaped crystals of **BEN14@Pd₂AZU₃₄** were grown by slow vapour diffusion of toluene into a 0.7mM DMSO solution of [**BEN14@Pd₂AZU₃₄**](OTf)₂ at room temperature. Single crystals in mother liquor were pipetted onto a glass slide containing NVH oil. To avoid collapse of the crystal lattice, several crystals were quickly mounted on micro loops and immediately flash-cooled in liquid nitrogen. Crystals were stored at cryogenic temperature in dry shippers, in which they were safely transported to macromolecular beamline P11 at Petra III,^[43] DESY, Hamburg, Germany. A wavelength of $\lambda = 0.6888 \text{ \AA}$ was chosen using a liquid N₂ cooled double crystal monochromator. Single crystal X-ray diffraction data was collected at 100(2) K on a single axis goniometer, equipped with an Oxford Cryostream 800 and an Eiger2x 16M detector. 3600 diffraction images were collected in a 360° φ sweep at a detector distance of 154 mm, 100% filter transmission, 0.1° step width and 0.04 seconds exposure time per image. Data integration and reduction were undertaken using XDS.^[44] The structure was solved by intrinsic phasing/direct methods using SHELXT^[45] and refined with SHELXL^[46] using 22 CPU cores for full-matrix least-

squares routines on F^2 and ShelXle^[47] as a graphical user interface and the DSR program plugin was employed for modeling.^[48,49]

Specific refinement details

Stereochemical restraints for the **AZU3** ligands (residue A27), **BEN14** guest (residue B14), dimethylsulfoxide solvent molecule (residue DMS), toluene solvent molecules (residue TOL) and triflate counterions (residue OTF) and were generated by the GRADE program using the GRADE Web Server (<http://grade.globalphasing.org>) and applied in the refinement. A GRADE dictionary for SHELXL contains target values and standard deviations for 1,2-distances (DFIX) and 1,3-distances (DANG), as well as restraints for planar groups (FLAT). Additionally, similar distance restraints (SADI) for 1.2 distances were employed to the sulfonate S—O bonds of **BEN14** guest. All displacements for non-hydrogen atoms were refined anisotropically. The refinement of ADPs for carbon, nitrogen and oxygen atoms was enabled by a combination of similarity restraints (SIMU) and rigid bond restraints (RIGU).^[50] The contribution of the electron density from disordered counterions and solvent molecules, which could not be modeled with discrete atomic positions were handled using the SQUEEZE^[51] routine in PLATON.^[52] The solvent mask file (.fab), computed by PLATON, was included in the SHELXL refinement via the ABIN instruction leaving the measured intensities untouched.

The compound has crystallized in monoclinic space group $C2/m$ (no.12). Due to strong overlap of molecular point group symmetry with crystallographic symmetry in the crystal structure the asymmetric unit only contains one fourth of a cage (two half **AZU3** ligands and one half of a Pd ion), one half **BEN14** guest (residue B14) sitting on the crystallographic twofold axis and the crystallographic mirror planes in the inner cage cavity, one half triflate counterion close to special position (inversion centre), one full dimethylsulfoxide solvent molecule and one toluene solvent molecule.

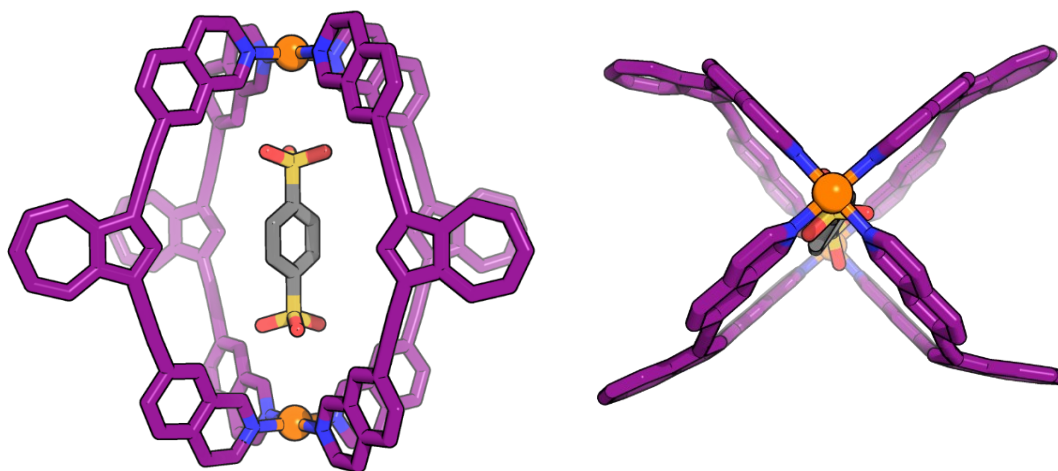


Figure S3.63: Two views of the X-ray crystal structure of **BEN14@Pd₂AZU₃**. Counterions and solvent molecules have been omitted for clarity.

3.7.7.4 Crystal structure of 2BEN14@Pd₄AZU1₈

Dark green block shaped crystals of 2BEN14@Pd₄AZU1₈ were grown by slow vapour diffusion of toluene into a 1:1 mixture of a 0.35mM solution of [2BEN14@Pd₄AZU1₈](OTf)₄ and a 15mM solution of NBu₄ReO₄. Single crystals in mother liquor were pipetted onto a glass slide containing NVH oil. To avoid collapse of the crystal lattice, several crystals were quickly mounted on micro loops and immediately flash-cooled in liquid nitrogen. Crystals were stored at cryogenic temperature in dry shippers, in which they were safely transported to macromolecular beamline P11 at Petra III,^[43] DESY, Hamburg, Germany. A wavelength of $\lambda = 0.6888 \text{ \AA}$ was chosen using a liquid N₂ cooled double crystal monochromator. Single crystal X-ray diffraction data was collected at 100(2) K on a single axis goniometer, equipped with an Oxford Cryostream 800 and an Eiger2x 16M detector. 3600 diffraction images were collected in a 360° φ sweep at a detector distance of 154 mm, 100% filter transmission, 0.1° step width and 0.01 seconds exposure time per image. Data integration and reduction were undertaken using XDS.^[44] The structure was solved by intrinsic phasing/direct methods using SHELXT^[45] and refined with SHELXL^[46] using 22 CPU cores for full-matrix least-squares routines on F^2 and ShelXle^[47] as a graphical user interface and the DSR program plugin was employed for modeling.^[48,49]

Specific refinement details

Stereochemical restraints for the AZU1 ligands (residue AZP), BEN14 guest (residue B14), dimethylsulfoxide solvent molecule (residue DMS) and toluene solvent molecules (residue TOL) were generated by the GRADE program using the GRADE Web Server (<http://grade.globalphasing.org>) and applied in the refinement. A GRADE dictionary for SHELXL contains target values and standard deviations for 1,2-distances (DFIX) and 1,3-distances (DANG), as well as restraints for planar groups (FLAT). All displacements for non-hydrogen atoms were refined anisotropically. The refinement of ADPs for carbon, nitrogen and oxygen atoms was enabled by a combination of similarity restraints (SIMU) and rigid bond restraints (RIGU).^[50]

The compound crystallized in triclinic space group $P\bar{1}$ (no. 2) and is by far the largest structure of this series. The asymmetric unit contains two full tetramers. In tetramer A only one of the eight AZU1 ligands was disordered over two conformation, while in tetramer B three AZU1 ligands were disordered. Additionally, the asymmetric unit contains six BEN14 guests, two of which showing partial and one which showing full molecule disorder, one perrhenate counterion, which was disordered over two positions, 18 dimethylsulfoxide solvent molecules (two of which disordered over two conformations) and four toluene solvent molecules. While in tetramer A, the inner cavity is occupied by one BEN14 guest, the inner cavity of tetramer B is occupied by the three disordered AZU1 ligands. However, by expanding the packing, it is visible that every tetrahedron's cavity is occupied by two guest molecules.

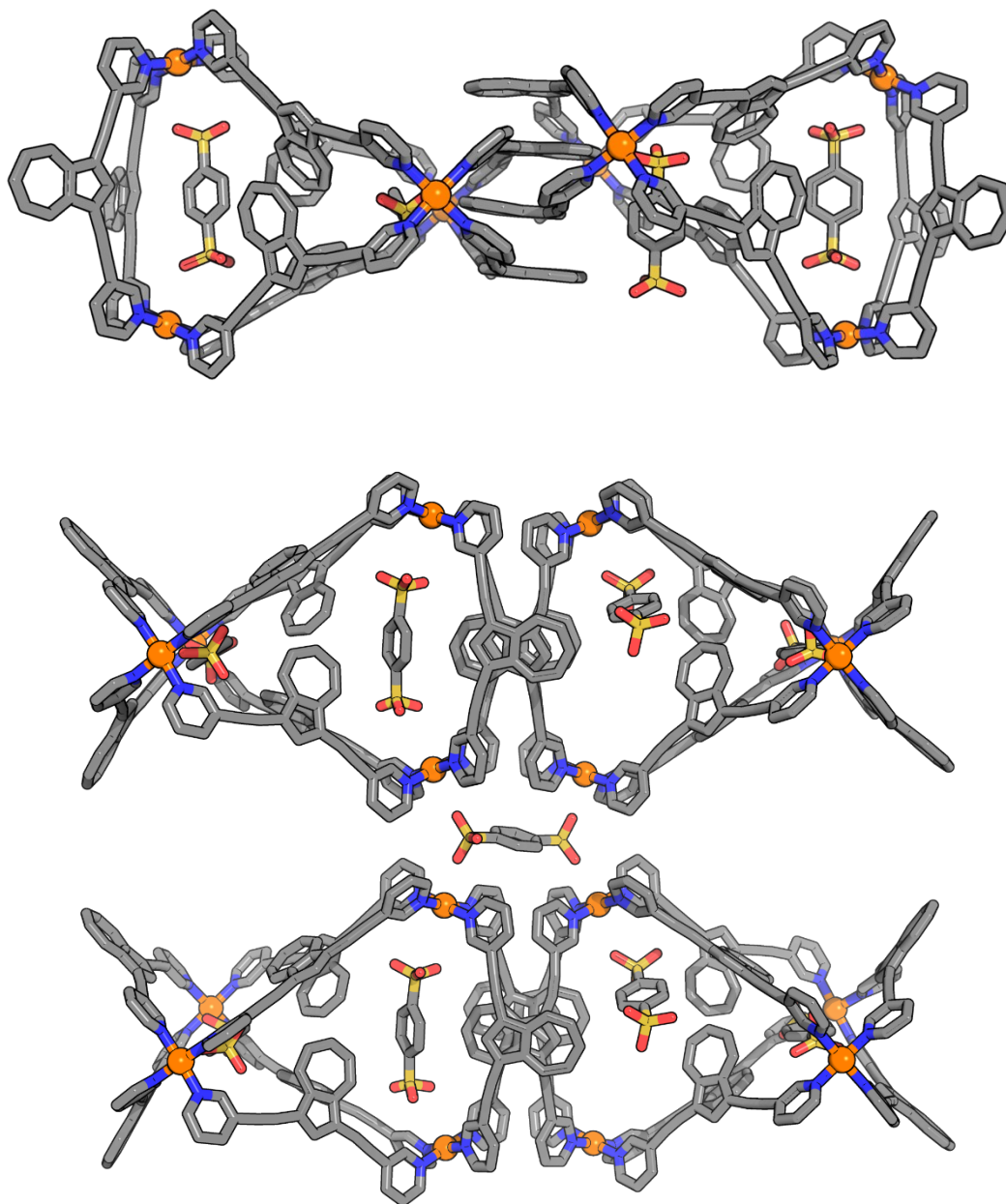


Figure S3.64: Two views of the X-ray crystal structure of $2BEN14@Pd_4AZU1_8$ showing the aromatic stacking happening between the ligands of two tetrahedra (top), and the bridging of four Pd(II) centres by a single **BEN14** molecule (bottom). Counterions (except some **BEN14** guests), solvent molecules and disorders have been omitted for clarity.

3.7.7.5 Crystal structure of $B12F12@Pd_2AZU5_4$

Brown block shaped crystals of $B12F12@Pd_2AZU5_4$ were grown by slow vapour diffusion of toluene into mixture of a 0.7mM solution of $[B12F12@Pd_2AZU5_4](BF_4)_4$. Single crystals in mother liquor were pipetted onto a glass slide containing NVH oil. To avoid collapse of the crystal lattice, several crystals were quickly mounted on micro loops and immediately flash-cooled in liquid nitrogen. Crystals were stored at cryogenic temperature in dry shippers, in which they were safely

transported to macromolecular beamline P11 at Petra III,^[43] DESY, Hamburg, Germany. A wavelength of $\lambda = 1.0332 \text{ \AA}$ was chosen using a liquid N₂ cooled double crystal monochromator. Single crystal X-ray diffraction data was collected at 100(2) K on a single axis goniometer, equipped with an Oxford Cryostream 800 and an Eiger2x 16M detector. 3600 diffraction images were collected in a 360° φ sweep at a detector distance of 154 mm, 100% filter transmission, 0.1° step width and 0.01 seconds exposure time per image. Data integration and reduction were undertaken using XDS.^[44] The structure was solved by intrinsic phasing/direct methods using SHELXT^[45] and refined with SHELXL^[46] using 22 CPU cores for full-matrix least-squares routines on F^2 and ShelXle^[47] as a graphical user interface and the DSR program plugin was employed for modeling.^[48,49]

Specific refinement details

Stereochemical restraints for the **AZU5** ligands (residue AP5), **B12F12** guest (residue BFF), dimethylsulfoxide solvent molecule (residue DMS) and toluene solvent molecules (residue TOL) were generated by the GRADE program using the GRADE Web Server (<http://grade.globalphasing.org>) and applied in the refinement. A GRADE dictionary for SHELXL contains target values and standard deviations for 1,2-distances (DFIX) and 1,3-distances (DANG), as well as restraints for planar groups (FLAT). All displacements for non-hydrogen atoms were refined anisotropically. The refinement of ADPs for carbon, nitrogen and oxygen atoms was enabled by a combination of similarity restraints (SIMU) and rigid bond restraints (RIGU).^[50]

The compound crystallized in monoclinic space group C2/c (no. 15). The asymmetric unit cell contains one host-guest structure, with one residue of **B12F12** and two disordered DMSO molecules located in-between the guest and the two Pd centres. A second **B12F12** can be found crystallised outside of the cage. In addition, three more DMSO molecules can be found outside of the cage (one disordered), and one disordered toluene molecule.

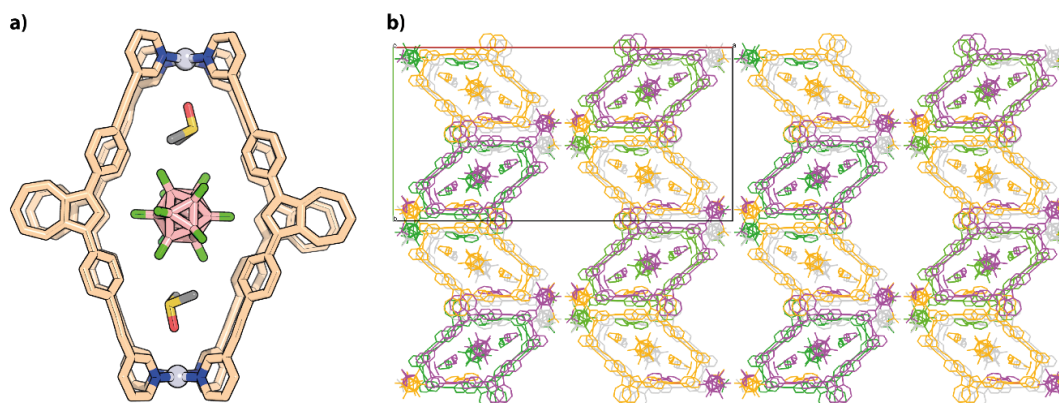


Figure 3.65: (a) X-ray structure of the host-guest complex **B12F12@Pd₂AZU₅**. Most of the solvent molecules and counteranions were omitted for clarity. (b) packing of the crystal of the host-guest complex viewed along the *c* axis. Notice the jagged arrangement of the cages and the large resulting solvent channels.

3.7.8 Cavity volume calculations

The volumes of the cavities of the four different coordination species were calculated using Molovol,^[53] based on the X-ray structures. Note that due to the different sizes for probes used here, the values presented here are just to get an idea of the relative space that can be occupied by a guest molecule, and not for direct comparison.

Table S3.5: volume of the cavities of the structures

Species	Large probe radius (Å)	Small probe radius (Å)	Cavity volume (Å ³)
Pd ₂ AZU1 ₄	3.3	1.8	225
Pd ₂ AZU2 ₄	-	1.8	49
Pd ₂ AZU3 ₄	4.7	3.5	487
Pd ₂ AZU4 ₄	3.5	1.8	383
Pd ₂ AZU5 ₄	4.5	2.0	954
Pd ₄ AZU1 ₈	3.3	1.8	321, 345

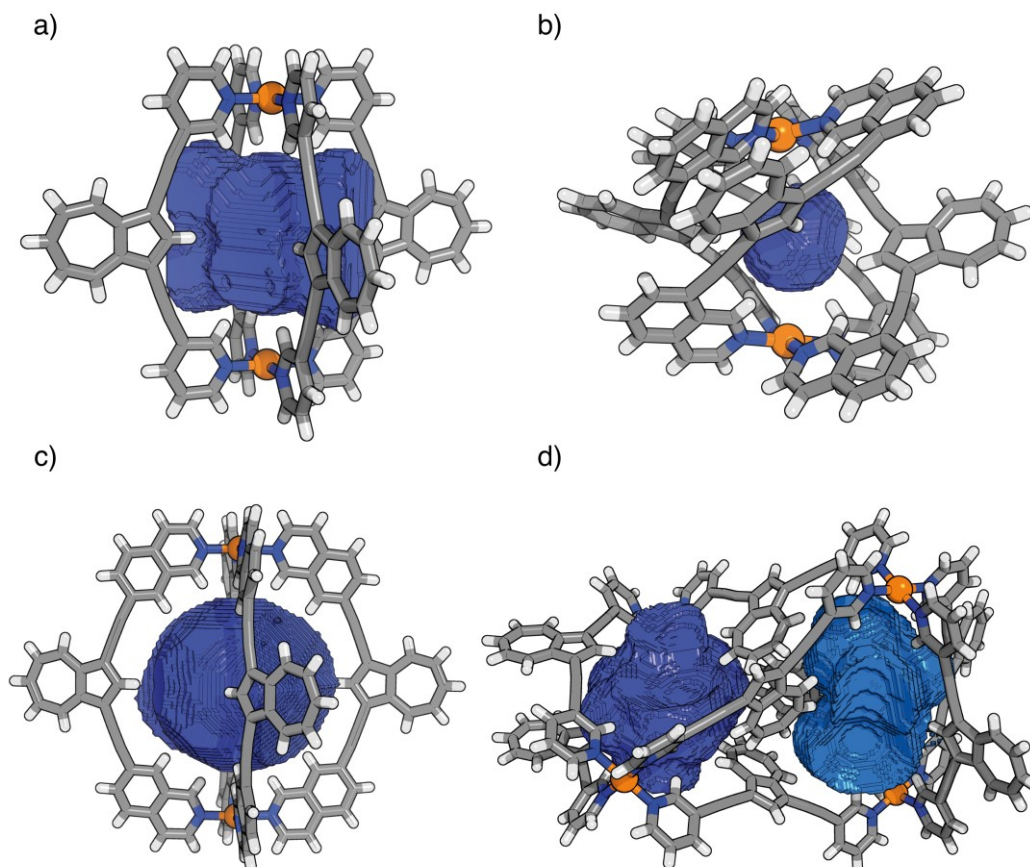


Figure S3.66: calculated cavities of the four different cages and host-guest complex.

3.7.9 Computations

The .xyz coordinate files of the following structures are available on the shared folder of the group, under \User\Thesis_group_members\PhD\2024_10_Alexandre_Walther. The DFT models are based on initial models constructed in Wavefunction SPARTAN'18,^[54] and then optimised by the semi-empirical PM6 method in Gaussian 16.^[55] The final DFT model was geometry-optimised in the same programme.

3.7.9.1 [Pd₂AZU₄]⁴⁺ and host-guest complex with BEN14

These models were optimised in the gas phase, at the B3LYP/def2-SVP level.

3.7.9.2 [Pd₂AZU₅]⁴⁺

This model was optimised in the gas phase, at the B3LYP/def2-SVP level.

3.7.9.3 [2BEN13@Pd₄AZU₁₈]⁴⁺

This model was optimised in the gas-phase at the ωB97X-D/def2-SVP level.

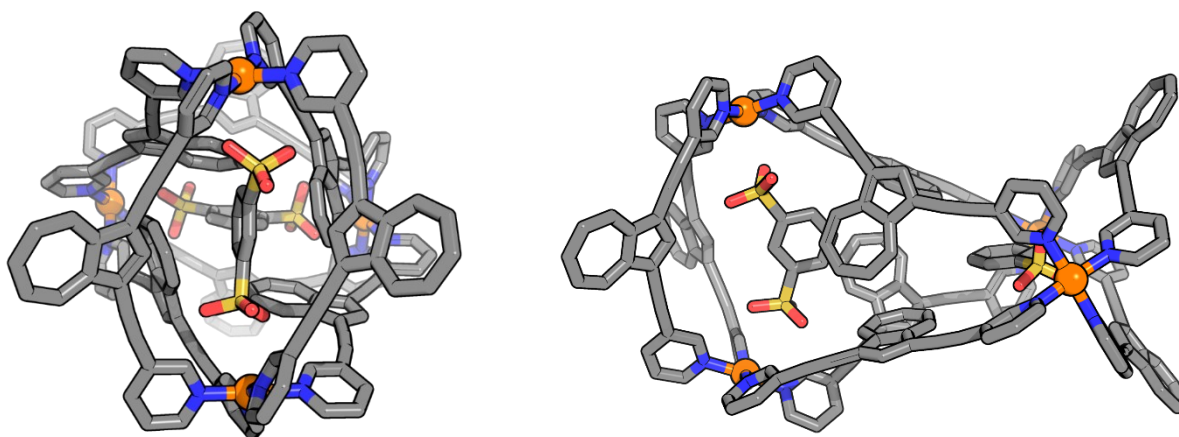


Figure S3.67: DFT structure of the [2BEN13@Pd₄AZU₁₈]⁴⁺ host-guest complex, optimised in the gas-phase, at the ωB97X-D/def2-SVP level.

3.7.9.4 [Azulene]₄ and [Naphthalene]₄

The two tetramers as well as the monomers of azulene and naphthalene were modelled and computed in SPARTAN'18,^[54] at the ωB97X-D/def2-SVP level of theory.

3.8 REFERENCES

- [1] D. M. Lemal, G. D. Goldman, *J. Chem. Educ.* **1988**, *65*, 923.
- [2] A. G. Anderson, B. M. Steckler, *J. Am. Chem. Soc.* **1959**, *81*, 4941–4946.
- [3] J. Michl, E. W. Thulstrup, *Tetrahedron* **1976**, *32*, 205–209.
- [4] T. Tsuchiya, T. Hamano, M. Inoue, T. Nakamura, A. Wakamiya, Y. Mazaki, *Chem. Commun.* **2023**, DOI 10.1039/d3cc02311g.
- [5] R. S. H. Liu, *J. Chem. Educ.* **2002**, *79*, 183.
- [6] D. Dunlop, L. Ludvíková, A. Banerjee, H. Ottosson, T. Slanina, *J. Am. Chem. Soc.* **2023**, *145*, 21569–21575.
- [7] G. Viswanath, M. Kasha, *J. Chem. Phys.* **1956**, *24*, 574–577.
- [8] M. Gordon, *Chem. Rev.* **1952**, *50*, 127–200.
- [9] “Azulene Sigma-Aldrich,” can be found under <https://www.sigmaaldrich.com/DE/en/product/aldrich/a97203>, **2024**.
- [10] “Naphthalene Sigma-Aldrich,” can be found under <https://www.sigmaaldrich.com/DE/en/product/aldrich/147141>, **2024**.
- [11] J. W. Steed, J. L. Atwood, in *Supramolecular Chemistry, 3rd Edition*, Wiley, **2022**, pp. 235–244.
- [12] T. Asao, S. Ito, N. Morita, *Tetrahedron Lett.* **1988**, *29*, 2839–2842.
- [13] D. A. Colby, T. D. Lash, *J. Org. Chem.* **2002**, *67*, 1031–1033.
- [14] T. D. Lash, J. A. El-Beck, D. A. Colby, *J. Org. Chem.* **2009**, *74*, 8830–8833.
- [15] C. Schneider, H. Nishimura, J. Lee, L. T. Scott, A. Wakamiya, R. Forbes, P. E. Georghiou, *Supramol. Chem.* **2017**, *30*, 1–8.
- [16] S. Rahman, A. Zein, L. N. Dawe, G. Shamov, P. Thordarson, P. E. Georghiou, *Rsc Adv.* **2015**, *5*, 54848–54852.
- [17] H. Salman, Y. Abraham, S. Tal, S. Meltzman, M. Kapon, N. Tessler, S. Speiser, Y. Eichen, *Eur. J. Org. Chem.* **2005**, *2005*, 2207–2212.
- [18] T. Zieliński, M. Kędziołek, J. Jurczak, *Tetrahedron Lett.* **2005**, *46*, 6231–6234.
- [19] T. Zieliński, M. Kędziołek, J. Jurczak, *Chem. Eur. J.* **2008**, *14*, 838–846.
- [20] D. Lichosyt, P. Dydio, J. Jurczak, *Chem. Eur. J.* **2016**, *22*, 17673–17680.
- [21] T. Tsuchiya, Y. Katsuoka, K. Yoza, H. Sato, Y. Mazaki, *Chempluschem* **2019**, *84*, 1659–1667.
- [22] I. Regeni, B. Chen, M. Frank, A. Baksi, J. J. Holstein, G. H. Clever, *Angew. Chem. Int. Ed.* **2021**, *60*, 5673–5678.
- [23] I. Regeni, R. Chowdhury, K. Terlinden, S. Horiuchi, J. J. Holstein, S. Feldmann, G. H. Clever, *Angew. Chem. Int. Ed.* **2023**, *62*, e202308288.
- [24] A. Walther, I. Regeni, J. J. Holstein, G. H. Clever, *J. Am. Chem. Soc.* **2023**, *145*, 25365–25371.
- [25] M. Iyoda, K. Sato, M. Oda, *Tetrahedron Lett.* **1985**, *26*, 3829–3832.
- [26] R. P. Steer, *J. Photochem. Photobiol. C: Photochem. Rev.* **2019**, *40*, 68–80.
- [27] W. M. Bloch, S. Horiuchi, J. J. Holstein, C. Drechsler, A. Wuttke, W. Hiller, R. A. Mata, G. H. Clever, *Chem. Sci.* **2023**, *14*, 1524–1531.
- [28] M. D. Johnstone, E. K. Schwarze, J. Ahrens, D. Schwarzer, J. J. Holstein, B. Dittrich, F. M. Pfeffer, G. H. Clever, *Chem. Eur. J.* **2016**, *22*, 10791–10795.
- [29] R. Zhu, J. Lübben, B. Dittrich, G. H. Clever, *Angew. Chem. Int. Ed.* **2015**, *54*, 2796–2800.
- [30] S. Freye, J. Hey, A. Torras-Galán, D. Stalke, R. Herbst-Irmer, M. John, G. H. Clever, *Angew. Chem. Int. Ed.* **2012**, *51*, 2191–2194.
- [31] C. Klein, C. Gütz, M. Bogner, F. Topić, K. Rissanen, A. Lützen, *Angew. Chem. Int. Ed.* **2014**, *53*, 3739–3742.
- [32] S. Sudan, F. Fadaei-Tirani, R. Scopelliti, K. E. Ebbert, G. H. Clever, K. Severin, *Angew. Chem. Int. Ed.* **2022**, *61*, e202201823.
- [33] S. Wang, T. Sawada, K. Ohara, K. Yamaguchi, M. Fujita, *Angew. Chem. Int. Ed.* **2016**, *55*, 2063–2066.
- [34] K. Hema, A. B. Grommet, M. J. Białek, J. Wang, L. Schneider, C. Drechsler, O. Yanshyna, Y. Diskin-Posner, G. H. Clever, R. Klajn, *J. Am. Chem. Soc.* **2023**, *145*, 24755–24764.
- [35] S. Freye, J. Hey, A. Torras-Galán, D. Stalke, R. Herbst-Irmer, M. John, G. H. Clever, *Angew. Chem. Int. Ed.* **2012**, *51*, 2191–2194.
- [36] G. H. Clever, S. Tashiro, M. Shionoya, *Angew. Chem. Int. Ed.* **2009**, *48*, 7010–7012.
- [37] I. Dance, *N. J. Chem.* **2002**, *27*, 22–27.
- [38] W. M. Bloch, Y. Abe, J. J. Holstein, C. M. Wandtke, B. Dittrich, G. H. Clever, *J. Am. Chem. Soc.* **2016**, *138*, 13750–13755.
- [39] M. Oda, N. C. Thanh, M. Ikai, T. Kajioaka, H. Fujikawa, Y. Taga, S. Ogawa, H. Shimada, S. Kuroda, *Chem. Lett.* **2005**, *34*, 754–755.

- [40] L. H. Foianesi-Takeshige, S. Takahashi, T. Tateishi, R. Sekine, A. Okazawa, W. Zhu, T. Kojima, K. Harano, E. Nakamura, H. Sato, S. Hiraoka, *Commun. Chem.* **2019**, *2*, 128.
- [41] P. Thordarson, *Chem. Soc. Rev.* **2010**, *40*, 1305–1323.
- [42] I. Regeni, B. Chen, M. Frank, A. Baksi, J. J. Holstein, G. H. Clever, *Angew. Chem. Int. Ed.* **2021**, *60*, 5673–5678.
- [43] A. Burkhardt, T. Pakendorf, B. Reime, J. Meyer, P. Fischer, N. Stübe, S. Panneerselvam, O. Lorbeer, K. Stachnik, M. Warmer, P. Rödig, D. Göries, A. Meents, *Eur. Phys. J. Plus* **2016**, *131*, 56.
- [44] W. Kabsch, *Acta Crystallogr., Sect. D: Biol. Crystallogr.* **2010**, *66*, 125–132.
- [45] G. M. Sheldrick, *Acta Crystallogr., Sect. A: Found. Adv.* **2015**, *71*, 3–8.
- [46] G. M. Sheldrick, *Acta Crystallogr., Sect. C: Struct. Chem.* **2015**, *71*, 3–8.
- [47] C. B. Hübschle, G. M. Sheldrick, B. Dittrich, *J. Appl. Crystallogr.* **2011**, *44*, 1281–1284.
- [48] D. Kratzert, J. J. Holstein, I. Krossing, *J. Appl. Crystallogr.* **2015**, *48*, 933–938.
- [49] D. Kratzert, I. Krossing, *J. Appl. Crystallogr.* **2018**, *51*, 928–934.
- [50] A. Thorn, B. Dittrich, G. M. Sheldrick, *Acta Crystallogr., Sect. A: Found. Crystallogr.* **2012**, *68*, 448–451.
- [51] A. L. Spek, *Acta Crystallogr., Sect. C: Struct. Chem.* **2015**, *71*, 9–18.
- [52] A. L. Spek, *Acta Crystallogr., Sect. D: Biol. Crystallogr.* **2009**, *65*, 148–155.
- [53] J. B. Maglic, R. Lavendomme, *J. Appl. Crystallogr.* **2022**, *55*, 1033–1044.
- [54] Spartan'18, Wavefunction Inc., Irvine,
- [55] M. J. Frisch, G. W. Trucks, H. B. Schlegel, G. E. Scuseria, M. A. Robb, J. R. Cheeseman, G. Scalmani, V. Barone, G. A. Petersson, H. Nakatsuji, X. Li, M. Caricato, A. V. Marenich, J. Bloino, B. G. Janesko, R. Gomperts, B. Mennucci, H. P. Hratchian, J. V. Ortiz, A. F. Izmaylov, J. L. Sonnenberg, D. Williams-Young, F. Ding, F. Lipparini, F. Egidi, J. Goings, B. Peng, A. Petrone, T. Henderson, D. Ranasinghe, V. G. Zakrzewski, J. Gao, N. Rega, G. Zheng, W. Liang, M. Hada, M. Ehara, K. Toyota, R. Fukuda, J. Hasegawa, M. Ishida, T. Nakajima, Y. Honda, O. Kitao, H. Nakai, T. Vreven, K. Throssell, Jr. Montgomery, J. E. Peralta, F. Ogliaro, M. J. Bearpark, J. J. Heyd, E. N. Brothers, K. N. Kudin, V. N. Staroverov, T. A. Keith, R. Kobayashi, J. Normand, K. Raghavachari, A. P. Rendell, J. C. Burant, S. S. Iyengar, J. Tomasi, M. Cossi, J. M. Millam, M. Klene, C. Adamo, R. Cammi, J. W. Ochterski, R. L. Martin, K. Morokuma, O. Farkas, J. B. Foresman, D. J. Fox, *Gaussian'16 Revision C.01*, Gaussian Inc., Wallingford CT.

4 SOLVENT-DIRECTED CHIRAL SELF-SORTING OF AN AZULENE-BASED COORDINATION CAGE

4.1 CHIRALITY IN COORDINATION CAGES

Installing chirality in coordination cages is one of the numerous ways that the supramolecular chemistry community has devised to increase the structural complexity thereof. Indeed, as one of the goals of the study of coordination cages is to eventually mimic the binding pockets of enzymes for signalling and catalytic processes, it is desirable to include chiral ligands in our toolbox to design low-symmetry, bio-mimicking nanocavities.

Several ways have been developed over the years to add chiral information into coordination cages. The first consists in adding a stereogenic centre on the vertices of the object. For example, BINAP (2,2'-bis(diphenylphosphino)-1,1'-binaphthyl) was used as a *cis*-protecting group of square-planar Pd(II) or Pt(II) by Stang and co-workers to prepare a Pd/Pt₆L₄ octahedron with chiral groups at the vertices.^[1] Similarly, Fujita and co-workers have used a (*R,R*)-diaminocyclohexane chelating group to their famous Pd₆L₄ tetrahedral cage to form a chiral version thereof,^[2] which they demonstrated could catalyse asymmetric photoaddition reactions.^[3,4] Several more examples of such systems have been published by the groups of Mukherjee,^[5,6] Yan,^[7] or Lusby.^[8] While the chiral chelating groups are easy to procure from chemical vendors and thus make preparing chiral coordination cages easy through this method, they also limit the number of ligands able to coordinate to the metal centres. Therefore, this technique is only applicable in certain systems.

The second way is the addition of a chiral pending residue on the coordinating groups. This can be done either by sub-component self-assembly by the use of a chiral auxiliary, such as a chiral amine, or by installing a chiral residue directly onto the donor groups of the free ligand. Many of Nitschke's systems have been prepared from sub-component self-assembly, mostly from the imine condensation between an amine and an aldehyde. A simple example of a tetrahedral Fe₄L₆ chiral cage can be obtained from ligand **L**, auxiliary 1-phenylethylamine, and a Fe(II) source.^[9] Because of steric bulk, using the (*S*)- or (*R*)- enantiomer of the auxiliary amine induces a unique Δ or Λ configuration around the octahedral metal centre,^[10] respectively. Therefore, enantiopure cages Δ_4 - or Λ_4 - Fe₄L₆ can be prepared. Such cages possessing chirotopic cavities have been used with much success by Nitschke

and co-workers for the preparation of enantiomerically pure C₆₀-anthracene adducts,^[11] for example, or to show that certain steroids have a high and specific affinity for one enantiomer of a Fe₄L₆ cage.^[12]

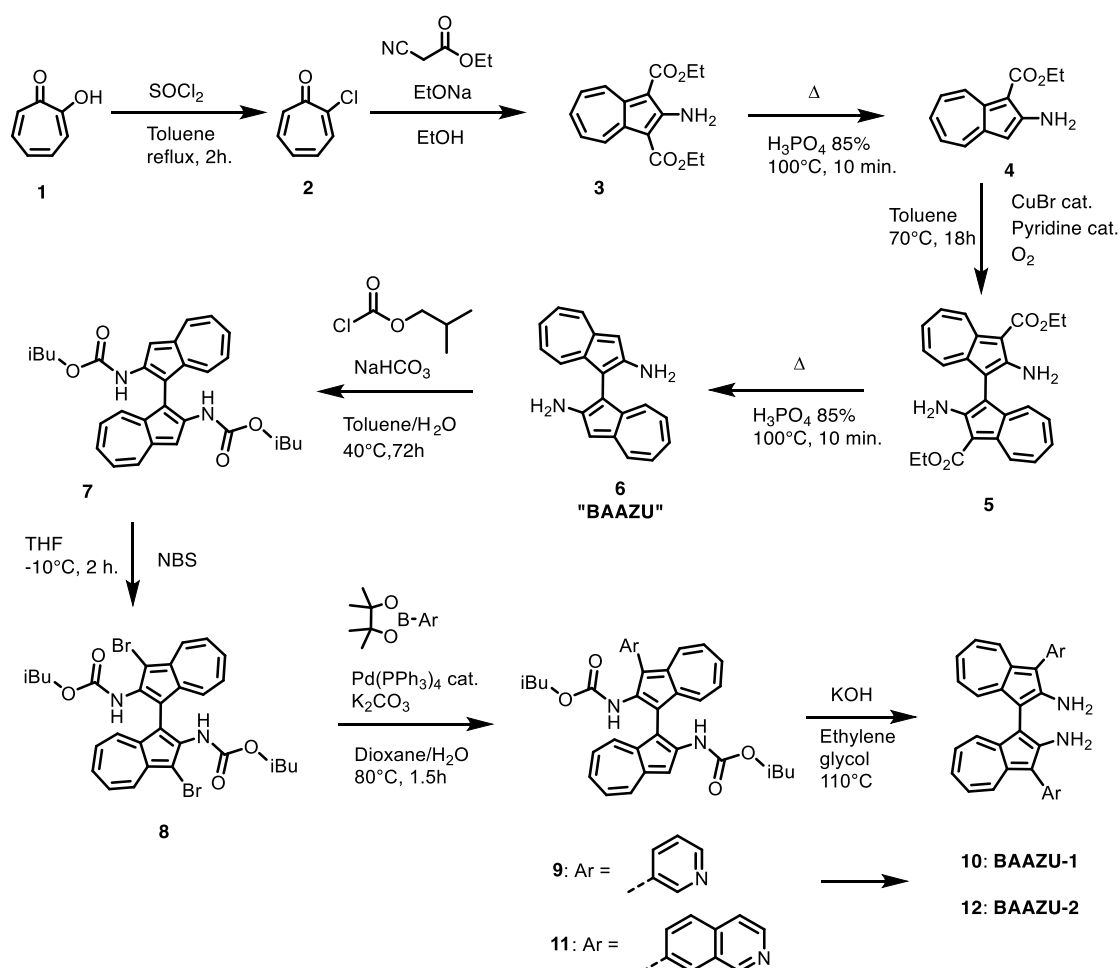
Finally, one can directly use a chiral ligand to assemble chiral coordination cages, without the need of a chiral auxiliary. This technique can be traced back to the late 1990',^[13,14] early 2000', notably to the pioneering work of Arne Lützen. He and his group have shown a number of examples involving BINOL ligands for the formation of Pd₂L₄ and larger assemblies.^[15-17]

As described in the General Introduction, our group has also produced an example of a chiral Pd₂L₄ cage, with ligands based on [6]-helicene.^[18] The cage formed from the smaller ligand is capable of undergoing chiral self-sorting when using the racemate, to form the *meso-cis* diastereoisomer of the cage. Moreover, the homochiral cage can discriminate between the two enantiomers of a camphorsulfonate guest thanks to its chirotopic cavity.

Following my work on the integration of azulenes in coordination cages as described in the previous chapter, I thought about increasing the complexity of the ligand while still retaining the azulene core. As azulene is an isomer of naphthalene, and as naphthalene can be used to form axial chiral BINOL and many derivatives thereof, I wondered if a bis-azulene chiral backbone could be incorporated into the structure of a coordination cage to impart it with both chirality and an absorbance in the visible. Indeed, the synthesis of a [1,1'-biazulene]-2,2'-diamine derivative had already been reported, but more as a curiosity and it had not received much publicity upon its publication.^[19] Therefore, I decided to use this precursor to synthesise chiral ligands to assemble chiral coordination cages with azulene backbones, and to expand our toolbox for the preparation of multi-functional low-symmetry cages. Moreover, the behaviour of this ligand could be compared to the BINOL assemblies previously prepared by Lützen and co-workers.^[17]

Note: the contents of this chapter have been submitted as an article entitled “Solvent-directed Social Chiral Self-Sorting in Pd₂L₄ Coordination Cages” to the J. Am. Chem. Soc. at the time of submitting this thesis.

4.2 SYNTHESIS OF [1,1'-BIAZULENE]-2,2'-DIAMINE (“BAAZU”)-BASED LIGANDS



Scheme 4.1: General synthesis scheme of ligands **BAAZU-1** and **BAAZU-2**. Full conditions are provided in Section 4.9.

The synthesis of the two ligands **BAAZU-1** and **BAAZU-2** was achieved in nine steps, starting from commercially available tropolone (**1**). A treatment with thionyl chloride (SOCl_2) afforded 2-chlorotropolone (**2**). Next, it was reacted with ethyl cyanoacetate to form diethyl 2-aminoazulene-1,3-dicarboxylate (**3**), which was in turn decarboxylated (**4**) by heating in concentrated H_3PO_4 . Then, two units were conjoined by oxidative coupling to form intermediate **5**. It is worth noting that the first four steps have been already published.^[19–22] The decarboxylation step with H_3PO_4 was then repeated to afford [1,1'-biazulene]-2,2'-diamine (**6**, “**BAAZU**”). Next, the amines were protected with isobutyl carbamate groups using isobutyl chloroformate. On a side note, a first attempt to protect the amines with Boc_2O failed and produced a “urea bridge” between the two amino groups. While an interesting structure, it was not desirable and has not been studied further. The protected product (**7**) was then brominated with *N*-bromosuccinimide. This intermediate (**8**) could then be involved in a Suzuki coupling with 3-pyridine or 7-isoquinoline boronic esters to yield the

protected final ligands (**9** or **11**). The ligands were deprotected by treatment with KOH in hot ethylene glycol to yield **BAAZU-1** or **BAAZU-2**.

4.3 BAAZU-BASED COORDINATION ASSEMBLIES

Note: the computations performed in this chapter have been mostly prepared by our collaborator Gers Tusha, from the group of Prof. Dr. Lars Schäfer, at Ruhr-Universität Bochum.

4.3.1 BAAZU-1 racemate

Firstly, the racemate of **BAAZU-1** was tested for its ability to form cages. A stock solution (partial suspension) of the ligand at 3.11 mM in CD₃CN was prepared, and 450 µl of it was combined with a 50 µl of a 15 mM solution of [Pd(CH₃CN)₄](BF₄)₂. The new mixture was heated at 70°C for 1 hour. Subsequently, a ¹H-NMR spectrum was measured and showed a forest of peaks, with no clearly identifiable species (Fig. 4.1b). An ESI-MS of the mixture revealed however the presence of only one Pd₂**BAAZU-1**₄ species (Fig. S4.28). As the starting material is a racemate, this result would suggest that a mixture of the possible diastereoisomers of the cage is formed.

To verify if the thermodynamic product had been reached, the mixture was heated for longer, and ¹H-NMR spectra were measured at 5 and 24 hours. They revealed that the composition of the mixture gradually changed to a single species, largely the major product after 1 day of heating (Fig. 4.1b and S4.25). Moreover, this main thermodynamic species was characterised by ESI-MS to still be a Pd₂**BAAZU-1**₄ cage (Fig. S4.29). The obtention of a single diastereoisomer of the larger coordination species instead of a mixture, despite starting from a racemate of the ligand, is a clear sign of chiral self-sorting. By consequent, the next step consisted in determining which stereoisomer was formed.

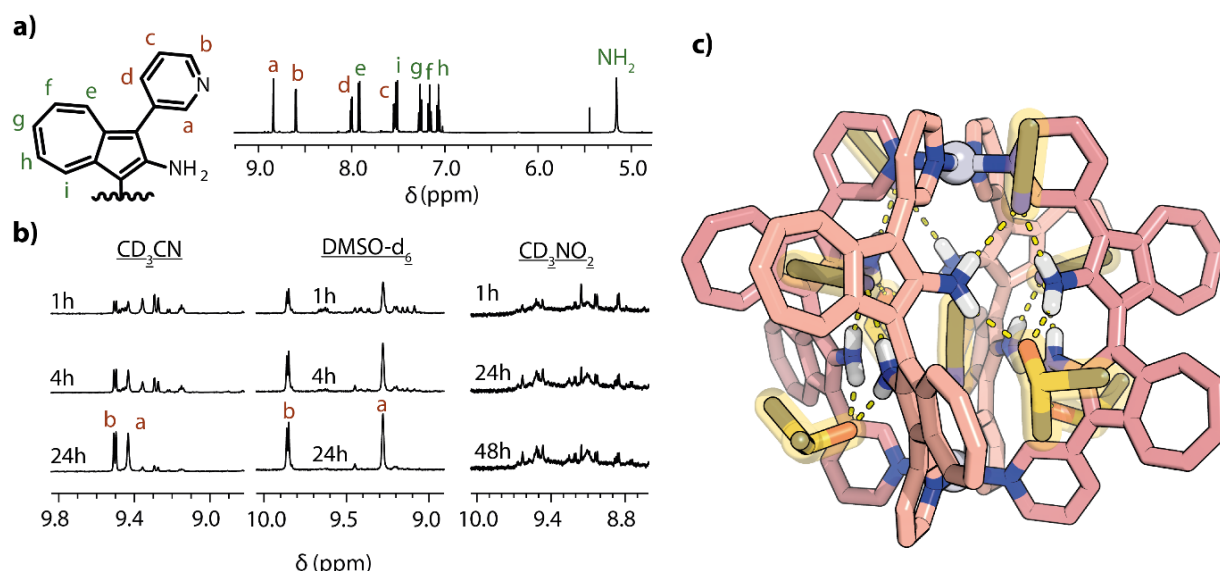


Figure 4.1: (a) structure and $^1\text{H-NMR}$ spectrum (500 MHz, CD_3CN , 298 K) of **BAAZU-1**. (b) evolution of the $^1\text{H-NMR}$ spectra of $[\text{Pd}_2\text{BAAZU-1}^{\text{rac}}_4](\text{BF}_4)_4$ over time in CD_3CN , $\text{DMSO-}d_6$, and CD_3NO_2 . (c) crystal structure of *meso-trans* $\text{Pd}_2\text{BAAZU-1}^{\text{rac}}_4$ with hydrogen bonds shown as yellow dash lines.

The NMR spectrum of the cage presents only one set of signals compared to the free ligand, meaning that the self-assembled species is highly symmetrical. Four different diastereoisomers of a Pd_2L_4 cage are possible if one starts from a racemic ligand: the homochiral *RRRR/SSSS* pair, the *RRRS/SSSR* pair, and the two possible *meso* isomers: *RRSS (cis)*, or *SRSR (trans)*. Of those four possibilities, only the homochiral and the *meso-trans* cage would have a symmetry high enough to give rise to only one set of signals for the four ligands. However, NMR analysis alone cannot help us determine which species is formed here.

To achieve this goal, DFT modelling was initially employed (performed by Gers Tusha from the group of Prof. Dr. Lars Schäffer at Ruhr-Universität Bochum). Models of four isomers were geometry optimised at the $\omega\text{B97X-D3/def2-SVP}$ level with implicit CPCM solvation in acetonitrile. The energies were then calculated at the $\text{DSD-PBEP86 D3BJ/def2-TZVP}$ level. The lowest energy was achieved for the homochiral *RRRR/SSSS* cage, followed by *SSSR/RRRS* by 4 kcal/mol, *meso-trans RRSR* by 7 kcal/mol, and *meso-cis RRSS* by 8 kcal/mol (Fig. 4.2). The ranking predicts therefore that the two enantiomers of the homochiral cage are preferred. This would fit with the absence of splitting in the measured NMR spectrum.

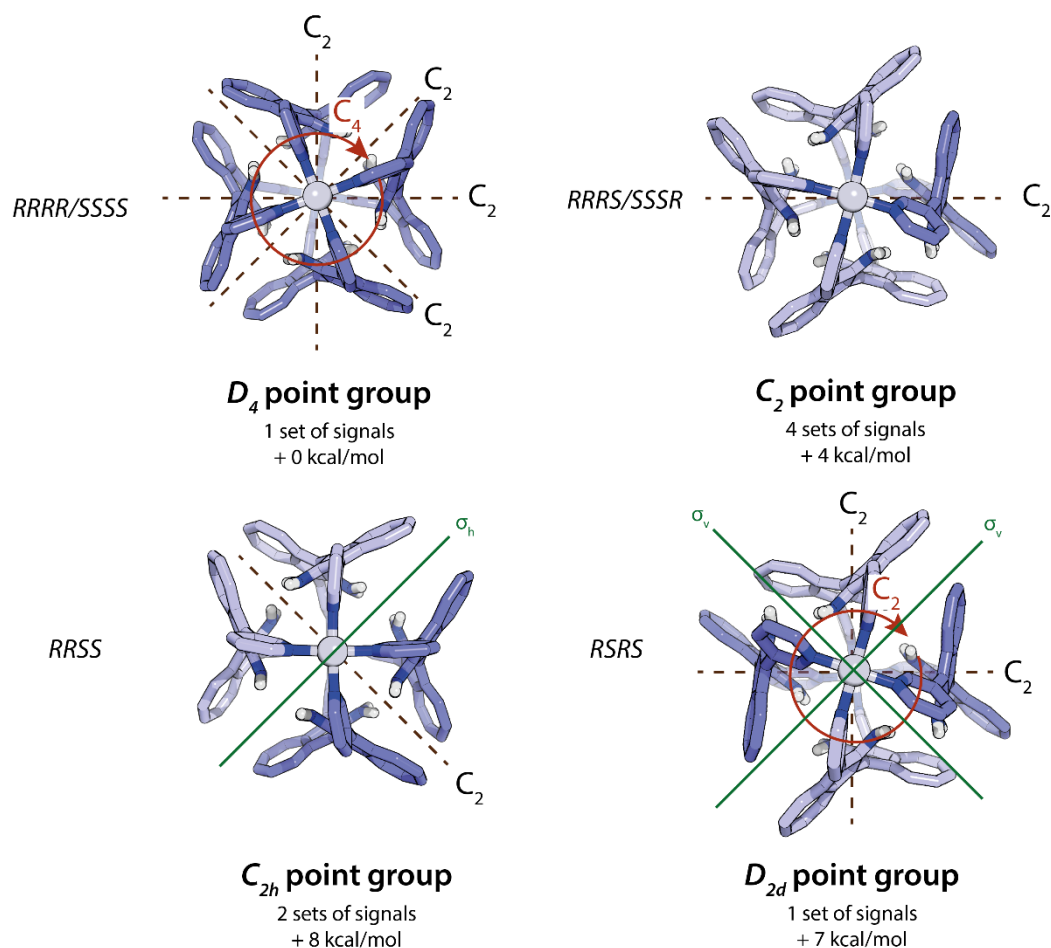


Figure 4.2: The four different possible diastereoisomers of $\text{Pd}_2\text{BAAZU-1}^{\text{rac}}_4$ with their relative energies computed by DFT without explicit solvent molecules, and their elements of symmetry justifying the number of predicted signals in their NMR spectrum.

Thankfully, single crystals of sufficient quality for X-ray diffraction analysis were grown by slow diffusion of diisopropylether into a solution of the cage in acetonitrile (10% DMSO). The newly revealed structure of the cage was however not the predicted homochiral, but instead the *meso-trans* isomer (Fig. 4.1c). The cage crystallised in the triclinic P-1 (no. 2) space group, with one cage per asymmetric unit cell, and two cages per unit cell. One striking detail about the solid-state structure of the assembly is the presence of eight very well-resolved acetonitrile (and DMSO overlapping on some positions) molecules around the cage, their nitrogens (or oxygens) pointing towards the amino groups of the ligands, in distances and angles that would suggest hydrogen bonding (2.0-2.4 Å). Those amino groups are themselves very close to their neighbouring group, and in addition the azulene moieties of the ligands are aligned on almost the same plane as their neighbour. Looking at the overall structure, it would seem that two solvent molecules per face of the cage act as tethers between the amino groups as “hydrogen bond bridges”, bringing the ligands together in a certain geometry that yields the overall *meso-cis* cage.

To test this hypothesis, the formation of the cage was monitored in two other solvents, $\text{DMSO-}d_6$ and nitromethane (CD_3NO_2). With its sulfoxide group, DMSO is a good hydrogen bond acceptor, while the nitro group of nitromethane is not. Therefore, the cage in DMSO should also self-sort, but

not the one in nitromethane. In DMSO, NMR revealed that the self-sorting was achieved after only 5 hours (Fig. 4.1b and S4.26), while no self-sorting was observed in the case of nitromethane, even after heating for 48 hours; only a forest of peaks was visible (Fig. 4.1b and S4.27). Moreover, this solution in nitromethane was titrated with DMSO to measure the amount of the hydrogen bond accepting solvent that would be needed to drive the self-sorting to its (near) completion. A single set of signals was obtained after the addition of about 5% vol. of DMSO in the cage solution in nitromethane, thereby confirming the necessity of hydrogen bond acceptors to drive the system towards a single diastereoisomer (Fig. 4.3).

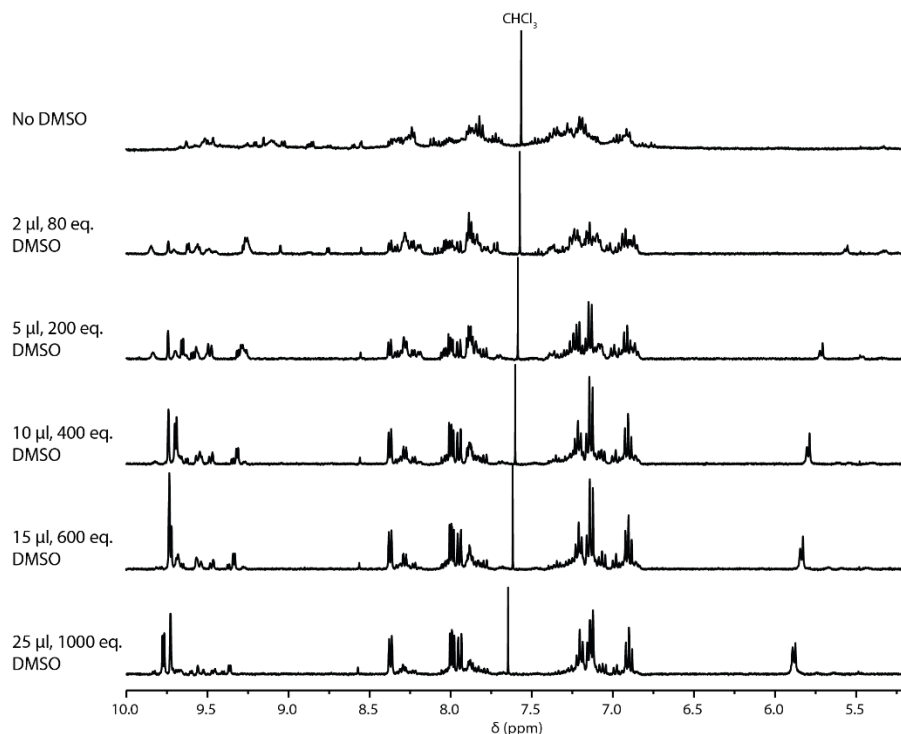


Figure 4.3: $^1\text{H-NMR}$ (500 MHz, CD_3NO_2 , 298 K) of $[\text{Pd}_2\text{BAAZU-1}^{\text{rac}}_4](\text{BF}_4)_4$ (0.35 mM) titrated with $\text{DMSO-}d_6$. The DMSO amount is expressed as equivalents to the cage.

As far as I know, this is the first time that a precise, observable reason could be attributed to the non-statistical chiral self-sorting of Pd(II)-assemblies. Indeed, in the previously published cases discussed above, the rationale behind the self-sorting is either not explained or explained through steric hinderance between the ligands. For example, in our report on [6]helicene-based cages self-sorting into a *meso-cis* isomer,^[23] the extension of the length of the linker between the backbone and the donors leads to a loss of the self-sorting property; the backbones of the ligands being pushed further apart from each other in the larger assembly probably causes the formation of a mixture of isomers instead of a single one. In the present case, the direct and indirect observation that the hydrogen bond acceptor capacity of the solvent dictates the self-sorting is unique. One could relate this system to the hexameric resorcinarene capsule published by Atwood *et al.* in 1997,^[24] where the six monomers are held together by eight molecules of water in a non-competitive solvent. In another instance, the specific selection of a constitutional isomer of an asymmetric Pd_2L_4 cage with a ligand based on a

steroid backbone was shown by Natarajan and co-workers to be caused by inter-ligand H-bonds.^[25] However, contrary to the present work, the solvent was not involved in the selectivity of the isomer, and the authors could only rely on computational evidence. Recently still, the group of Lewis published another Pd₂L₄ cage assembled from asymmetric ligands with both pyridine and quinoline donors capable of switching from the *trans* to the *cis* isomer upon changing the solvent from acetonitrile to DMSO.^[26] The authors attribute this selectivity by a strong interaction of a DMSO molecule with the polarised C-H bonds around the coordination sphere, leading to a change in isomer to accommodate the solvent molecule in that region.

However, at this point a doubt still lingered on the assignment of the *meso-trans* isomer to the cage formed from the racemate of **BAAZU-1** in solution. Indeed, it could have possible that the crystal structure of the assembly differs from the one in solution because of ligand exchange during the crystallisation process to form an isomer more favourable in the solid state. Therefore, I sought to form the homochiral cage by using the enantiopure ligand to compare the results of the self-assembly of both species.

4.3.2 BAAZU-1 enantiopure

To separate the two enantiomers of **BAAZU-1**, chiral HPLC separation was employed. CHIRALPAK IC columns were used with a dichloromethane (with 0.05% NEt₃)/isopropanol (97%/3%) mixture as eluent (Fig. 4.4).

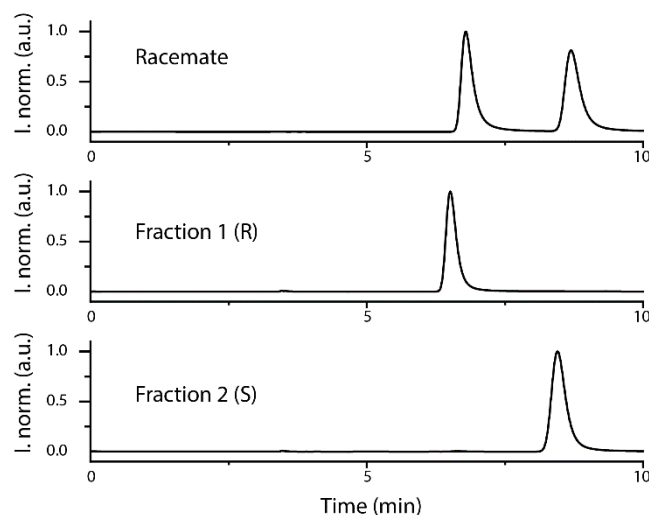


Figure 4.4: chiral HPLC chromatograms of **BAAZU-1** as racemate (top), of the first fraction (middle), and of the second fraction (bottom).

The enantiopure ligand was then used to form the homochiral cage: similar to the other cages, a 3.11 mM stock solution of the ligand was prepared in acetonitrile. To save up on the limited amount of available compound, the cage was formed at half of the usual concentration, i.e. 225 μ l of the stock solution were mixed with 25 μ l of a 15 mM stock solution of [Pd(CH₃CN)₄](BF₄)₂, and the rest was

completed with 250 μl of CD_3CN . Due to concerns of racemisation, the mixture was stirred at room temperature for twelve hours, and then it was measured by $^1\text{H-NMR}$. To my delight, the cage formed cleanly and showed only one set of signals, as expected for the homochiral isomer of the cage (Fig. 4.5a). The shift of those signals is however different than the ones from the cage prepared with the racemate of **BAAZU-1**, confirming that the *meso-trans* cage is formed from the racemate instead of a pair of the homochiral enantiomers of the cage. The homochiral cage will be referred to as $\text{Pd}_2\text{BAAZU-1}^{\text{enant}_4}$ hereafter.

Single crystals for X-ray diffraction were grown by slow diffusion of diethylether into the solution of the cage. The compound crystallises in the triclinic P1 (no. 1) space group, with one cage per unit cell. The structure revealed here is, as expected, the homochiral cage (Fig. 4.5b). Like in the *meso-trans* cage, the amino groups are bridged with two acetonitrile solvent molecules, underlining the importance of this process in this family of cages. However, here the distances between the two neighbouring nitrogen atoms of the amino groups are slightly higher (3.57 Å for the *meso-trans* and 3.75 Å for the homochiral cage). In turn, these longer distances between the amino groups decrease the overall strength of the hydrogen bonds, and this may explain the preference for the *meso-trans* cage to form when starting from the racemate.

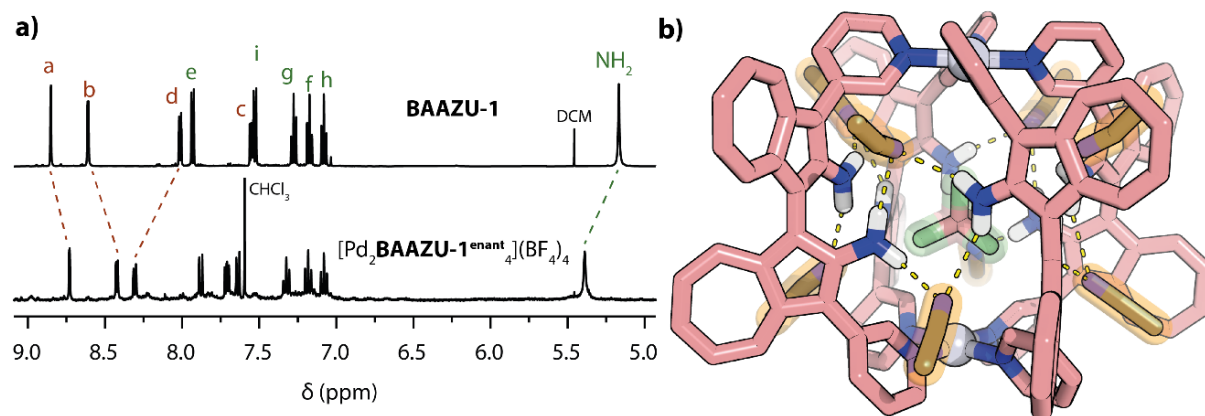


Figure 4.5: (a) $^1\text{H-NMR}$ (500 MHz, CD_3CN , 298 K) of **BAAZU-1** (top) and of cage $[\text{Pd}_2\text{BAAZU-1}^{\text{enant}_4}](\text{BF}_4)_4$ (bottom). (b) X-ray structure of the cage. The counter anions and some of the solvent molecules were omitted for clarity. The H-bonds between the surrounding MeCN molecules and the ligands of the cage are highlighted in dashed yellow lines.

CD spectra of the cage and of the ligands were measured as well (Fig. 4.6). The broad and weak So-S_1 transition of the azulene can be observed between 450-700 nm, although a 10x higher concentration was needed to properly measure this region by CD. Higher intensity bands were also visible in the 400-200 nm range. Overall, the signal intensity of the cage is higher than the free ligand's, but far from the immense increase that was observed by Lützen and co-workers in their work on BINOL-based coordination assemblies.^[16] They explained this increase by a change in the dihedral angle between the naphthyl sub-units from the free ligand to the final large assemblies. In the present case, the small increase in CD intensity would suggest that the angle between the azulene sub-units of the free ligands does not change much upon formation of the cage.

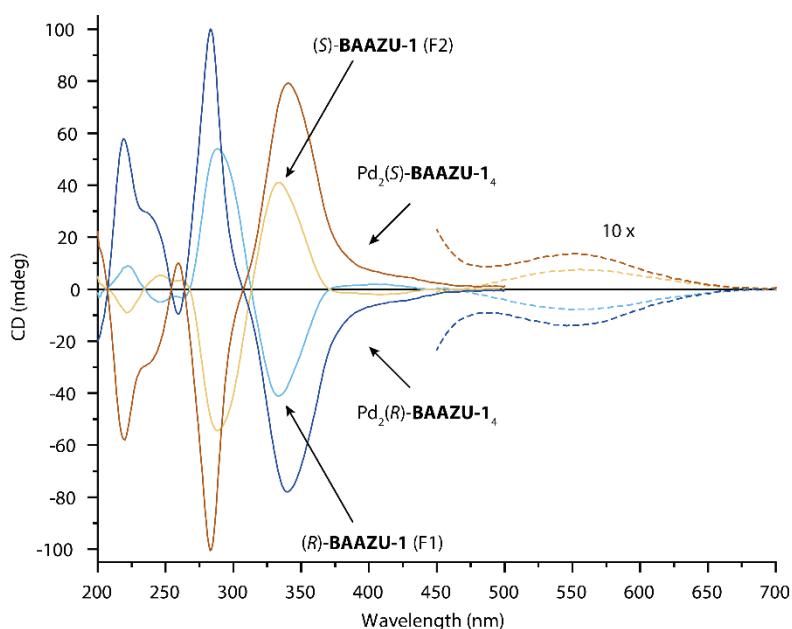


Figure 4.6: Circular dichroism of the two fractions of the **BAAZU-1** ligand and of the corresponding $[\text{Pd}_2\text{BAAZU-1}^{\text{enant}_4}](\text{BF}_4)_4$ in acetonitrile (0.125 mM: continuous lines, 1.25 mM: dashed lines, 2 mm cuvette). Due to its low solubility, the higher concentration data for pure ligand **BAAZU-1** was recorded at 0.25 mM with a cuvette with a 1 cm path length.

Now with a better understanding of the role that solvent molecules play in the mechanism of self-sorting of the cage, I attempted to explain the discrepancy between the homochiral cage predicted by the DFT models and the *meso-trans* isomer observed experimentally by X-ray crystallography.

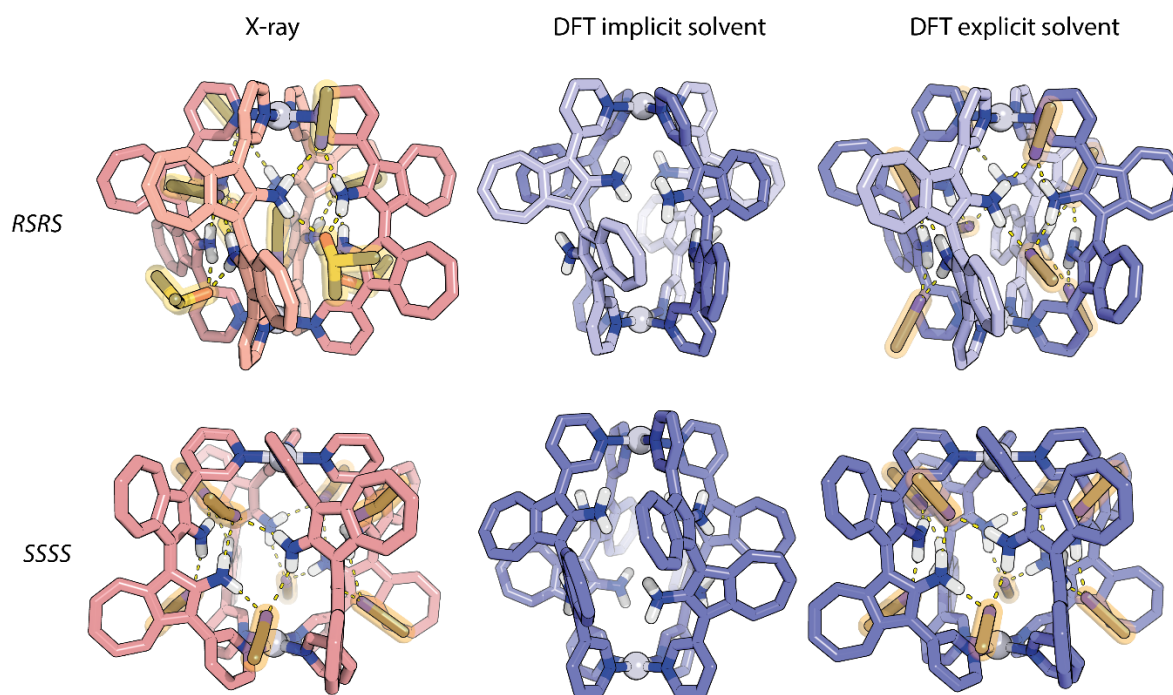
The main simplification made when modelling cage structures by DFT is to ignore the presence of solvent molecules, as the large increase in atom count and in degrees of freedom would drastically increase the already long and costly computation times. This generalisation is sound most of the time, as solvent molecules tend to interact very loosely with the cage, and do not contribute in general to the overall structure of the coordination species. However, in the present case, as I observed in the X-ray structure, the presence of solvent molecules interacting strongly with the amino groups of the ligands is essential for the *meso-trans* isomer of the cage to be formed. Therefore, we decided to add eight solvent molecules in our DFT models, prepared by our collaborators, in the same positions that are observed in the solid-state structure.

Firstly, the structure of the *meso-trans* obtained during the geometry optimisation phase is a much better match with the X-ray structure, with the solvent molecules forming the hydrogen bond bridges between the amino groups (Fig. 4.7). Secondly, the energies of the isomers were calculated, and a new ranking of the isomers was established (Table 4.1):

Table 4.1: Ranking of the energies of the isomers without and with the presence of explicit solvent molecules.

Isomers	ΔE (kcal / mol)				
	Implicit Solvent (MeCN)	8 MeCN	8 DMSO	4 MeCN + 4 DMSO	8 MeCN + 1 BF_4^- + 1 MeCN
<i>RRRR</i>	0	0	3	0	5
<i>RRSS</i>	8	7	11	13	-
<i>RSRS</i>	7	3	0	0	0
<i>SRRR</i>	4	6	7	8	-

As the X-ray structure contains some DMSO molecules, and as the self-sorting was also observed in that solvent, the structures were calculated with either 8 molecules of MeCN, 8 molecules of DMSO, or 4 molecules of each. In the first case, the homochiral cage is still favoured, but only 3 kcal/mol from the *meso-trans*. This trend is then reversed in the case of DMSO, and the two structures have equal energies when a mixture of MeCN and DMSO is used. In turn, the other two isomers have much higher energies compared to the low symmetry ones, probably due to the reduced number of possible hydrogen bond bridges owing to the arrangement of their ligands.

**Figure 4.7:** comparison of the experimental structures of cages *RSRS* and *SSSS* with the DFT models computed without and with explicit MeCN solvent molecules.

While these results do not yet fully explain why the *meso-trans* cage is favoured compared to the homochiral one, they still confirm that the presence of discrete solvent molecules bridging the amino groups of the ligands is necessary to describe the structure of the cages more accurately. They also give more credence to the fact that the chiral self-sorting in this case is a phenomenon driven by discrete molecules of solvent, a yet unique observation in the world of coordination cages.

However, the models are not yet fully reproducing the structures revealed by X-ray. Indeed, the cavity of the computational models is left empty. Still, one molecule of acetonitrile is observed in the cavity of the *meso-trans* cage, and one BF_4^- anion in the homochiral cage. Therefore, we worked on a third batch of computations, this time adding one more molecule of acetonitrile and one more BF_4^- in locations observed by X-ray crystallography. The models were then optimised, and their energies calculated with the same methods as the previous batch. In addition, to save up on time, only models of the *meso-trans* and the homochiral cage were considered. The results now showed a definitive energetic advantage to the *meso-trans*, favoured by 5 kcal/mol over its other isomer.

After increasing the complexity of our computational models twice from the starting structures, we have finally obtained results agreeing with the experimental observations. In that particular system, it is of the utmost importance to consider the cages as not isolated structures, but as a complex supramolecular cluster. However, it is also certain that, were it not for the crystal structures, the specific interactions between the solvent and the cages would have been much more difficult to uncover, and a thorough computational and experimental work would have been necessary to accurately model the structures.

4.3.3 BAAZU-2 racemate

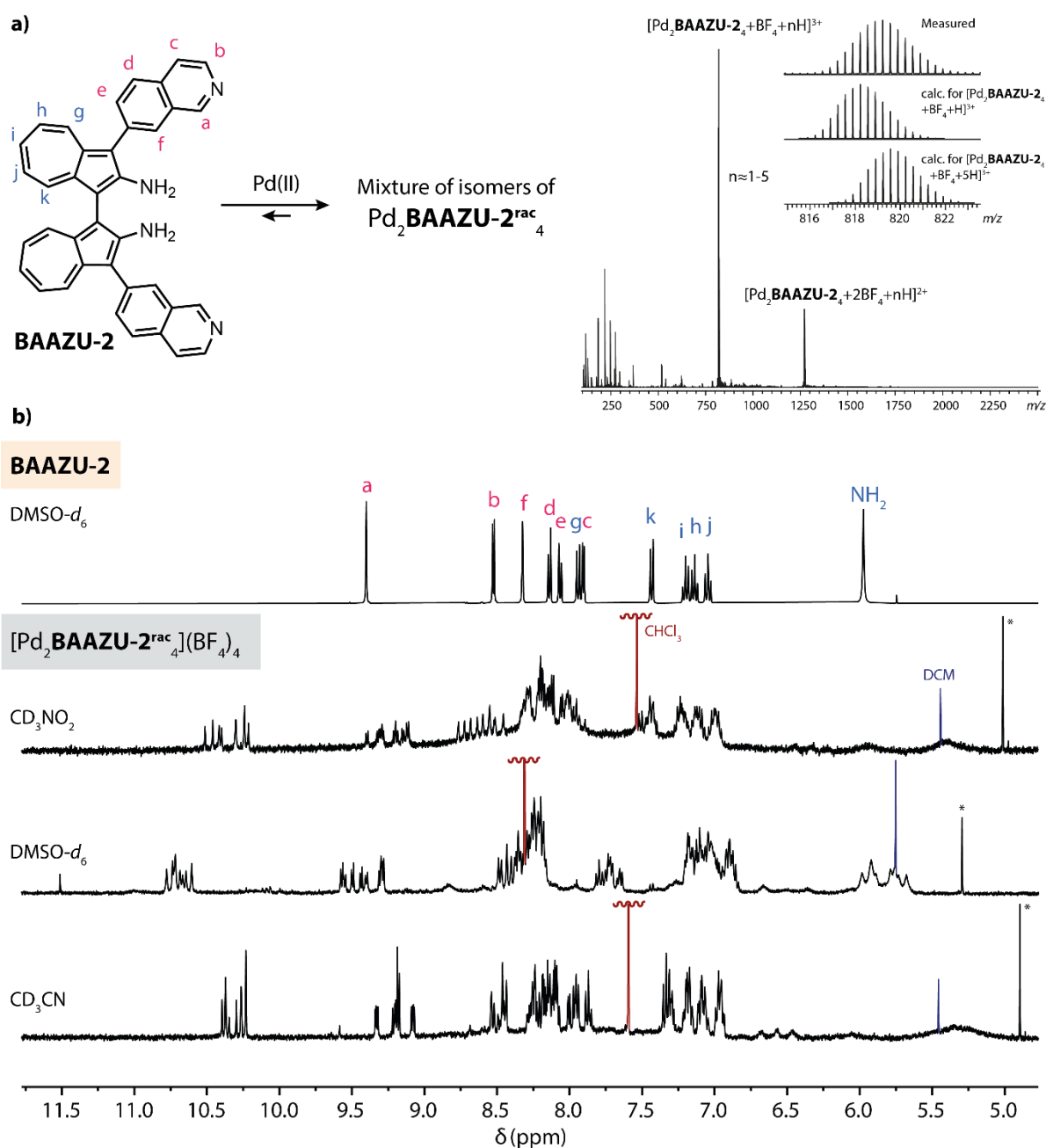


Figure 4.8: (a) scheme of the formation of the $\text{Pd}_2\text{BAAZU-2}^{\text{rac}}_4$ mixture of cage isomers. (b) ESI-MS of the mixture of cages. The main species corresponds to the cage, with approximately 1 to 5 neutral hydrogens added to the formula. The provenance of those extra hydrogens is unknown. (c) $^1\text{H-NMR}$ (500 MHz, 298 K) of ligand **BAAZU-2** in DMSO- d_6 , and of the mixture of the isomers of $[\text{Pd}_2\text{BAAZU-2}^{\text{rac}}_4](\text{BF}_4)_4$ in CD_3NO_2 , DMSO- d_6 , and CD_3CN (*=unknown impurity).

To confirm that the hydrogen bonds between ligands and solvent molecules in indeed a determining factor in the chiral self-sorting of $\text{Pd}_2\text{BAAZU-1}^{\text{rac}}_4$, I prepared a similar ligand, called **BAAZU-2**, but with a 7-isoquinoline donor group in place of the 3-pyridine of **BAAZU-1** (Fig. 4.8a). The only difference between those two ligands is their overall length, which would cause their BAAZU backbones to be pulled further apart in the structure of the $\text{Pd}_2\text{BAAZU-2}_4$ cage.

Consequently, the increased distance between the amino groups would mean that the hydrogen bond bridges could not form anymore, which would prevent the chiral self-sorting.

When preparing the cage with the racemate of **BAAZU-2** in the same conditions as previously, the $^1\text{H-NMR}$ spectra confirmed that a mixture of species were formed in CD_3CN , $\text{DMSO-}d_6$, and CD_3NO_2 , unlike with **BAAZU-1** (Fig. 4.8c). ESI-MS also confirmed the only presence of $\text{Pd}_2\text{BAAZU-2}_4$ (Fig. 4.8b), meaning that no chiral self-sorting had happened, further confirming the hypothesis that the distance between the NH groups of the ligands in the final assembly is paramount for the system to yield a single diastereoisomer over a choice of four.

4.3.4 BAAZU-2 enantiopure

While not undergoing chiral self-sorting as a racemate, **BAAZU-2** was of further interest because of the larger cavity of the cage it would form as an enantiopure ligand and of the guest binding opportunities it would open. Therefore, the two enantiomers were separated by chiral HPLC (Fig. 4.9). Similarly as for the first ligand, CHIRALPAK IC columns were used with dichloromethane (with 0.05% NEt_3)/isopropanol (92.5%/7.5%) mixture as eluent. A 10-minute cleaning of the column with 80% methanol and 20% n-hexane after the separation was needed to keep the two enantiomers from gradually eluting closer and closer after repeated runs. A consistent time of elution could not be achieved for the ligand, and great care had to be taken during the semi-preparatory separation to avoid the fractions eluting together.

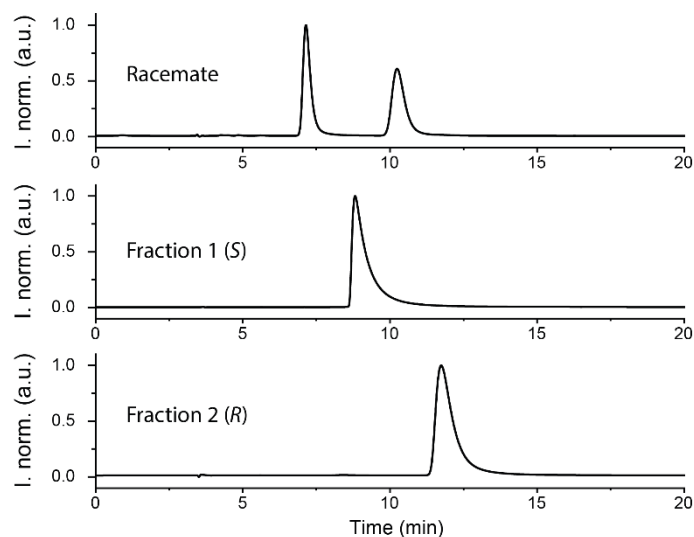


Figure 4.9: chiral HPLC chromatograms of **BAAZU-2** as racemate (top), of the first fraction (middle), and of the second fraction (bottom).

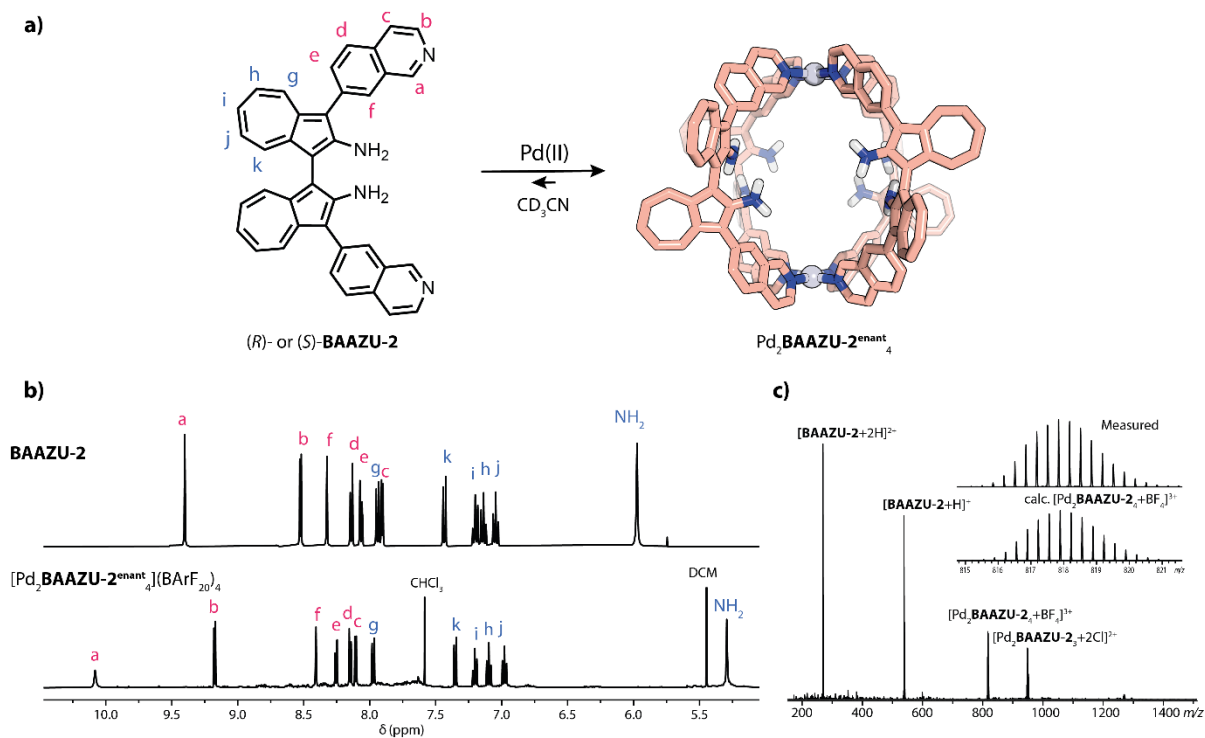


Figure 4.10: (a) formation of cage **Pd₂BAAZU-2^{enant}₄** (DFT structure, ω B97X-D/def2-SVP). (b) ¹H-NMR (500 MHz, 298 K) of ligand **BAAZU-2** (top, DMSO-*d*₆) and cage **[Pd₂BAAZU-2^{enant}₄](BArF₂₀)₄** (bottom, CD₃CN). (c) ESI-MS spectrum of **[Pd₂BAAZU-2^{enant}₄](BF₄)₄**.

The enantiopure ligand was then used to form the homochiral **Pd₂BAAZU-2^{enant}₄** according to the general procedure with either BF₄⁻ or BArF₂₀⁻ (tetrakis(pentafluorophenyl)borate) as a counteranion (Fig. 4.10a). Characteristic shifts of the protons in the ¹H-NMR spectrum (Fig. 4.10b), as well as ESI-MS (Fig. 4.10c) confirmed the formation of the cage. CD spectra of both enantiomers of the ligand and cage were also recorded (Fig. 4.11). Interestingly, the sign of the Cotton effect of the corresponding fractions are reversed compared to the **BAAZU-1** species. This discrepancy, as well as the assignment of the absolute configuration of both ligands, will be discussed in the next section.

The larger chirotopic cavity, as well as the eight -NH₂ groups lining the inside of the cage, were further studied for their guest binding abilities. This will be discussed in section 4.5.

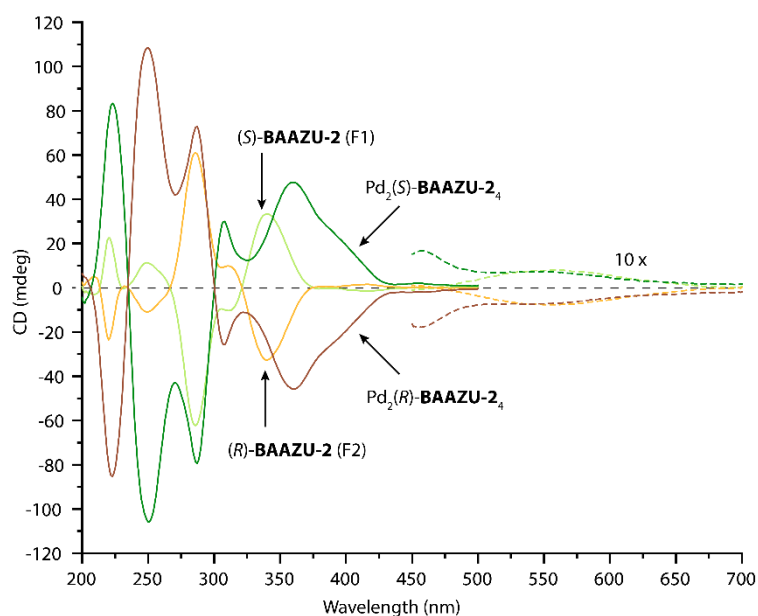


Figure 4.11: CD spectra of the two fractions of the **BAAZU-2** ligand and of the corresponding $[\text{Pd}_2\text{BAAZU-2}^{\text{enant}}_4](\text{BF}_4)_4$ in acetonitrile (0.125 mM: continuous lines, 1.25 mM: dashed lines).

4.4 ASSIGNMENT OF THE ABSOLUTE CONFIGURATION

As the **BAAZU**-based ligands are separated by chiral HPLC and not prepared from a precursor of known chirality, their absolute configuration had to be determined.

Crystals of enantiopure **BAAZU-1** could be grown from slow diffusion of diethylether into a DCM solution of the ligand. Unfortunately, only twinned crystals could be obtained. From this study, only one crystal of fraction 1 of **BAAZU-1** gave results of acceptable quality. The crystal was measured with $\text{CuK}\alpha$ radiation to maximise the anomalous dispersion. The compound crystallises in the monoclinic P2_1 (no. 4) space group and its asymmetric unit cell is comprised of two ligands of the (R)-enantiomer (Fig. 4.12). Software PLATON^[27] was used to determine the twin law, and it was inserted in the .res refinement file:

TWIN -1 0 0 0 -1 0 0 0 1

BASF 0.41872

The Flack parameter according to Parson's method was measured to be 0.05 (8).

Due to the lack of better, non-twinned crystals, comparisons between experimental and calculated CD spectra were used to supplement the assignment of the absolute configuration. Fraction 1 was observed to cause a negative Cotton effect. Time-dependant DFT (TD-DFT) calculations on the (R)-enantiomer were performed with a def2-TZVP basis set and both $\omega\text{B2PLYP}^{[28]}$ and $\text{BHandHLYP}^{[29]}$ functionals for comparison. Both functionals predicted a negative Cotton effect for

(*R*)-**BAAZU-1** in the visible range (450-700 nm). They were also effective in predicting the sign of the bands in the 250-450 nm region, with an advantage to BHandHLYP for the relative intensity of said bands. Interestingly, ω B2PLYP managed to predict more accurately the absorbance maximum of the S_0 - S_1 transition (Fig. 4.13). Therefore, we are confident in assigning Fraction 1 to (*R*)-**BAAZU-1** and Fraction 2 to (*S*)-**BAAZU-1**.

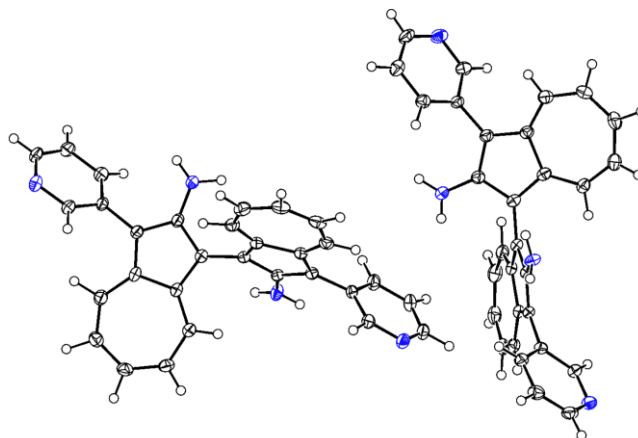


Figure 4.12: ORTEP representation of the asymmetric cell of (*R*)-**BAAZU-1**. Ellipsoids drawn at 50% probability.

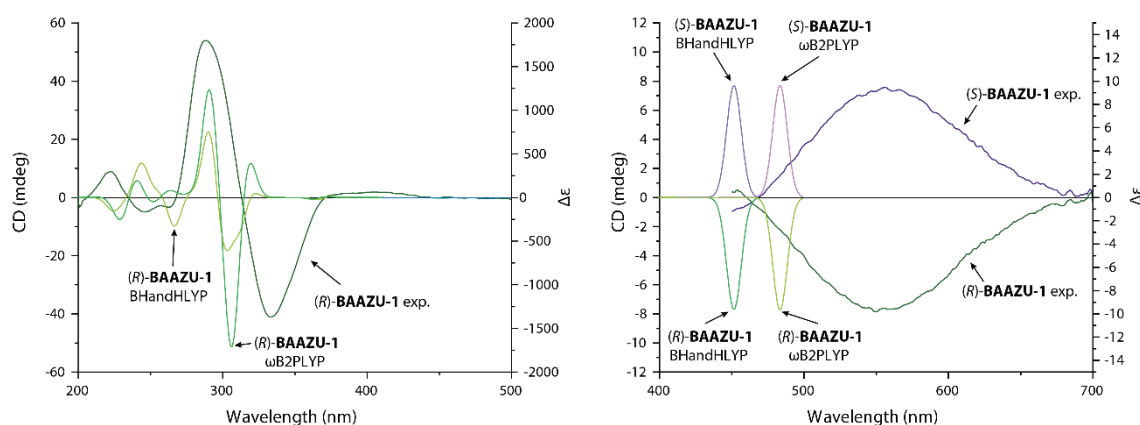


Figure 4.13: Experimental (left axis) vs. calculated (right axis) CD spectra of **BAAZU-1**.

Non-twinned crystals of enantiopure **BAAZU-2** could be grown. Due to their small size however, they could only be measured with synchrotron radiation. The compound crystallises in the monoclinic $P2_1$ (no. 4) space group and its asymmetric unit cell is comprised of one ligand (Section 4.9.9.6). However, the Flack parameter (-4.3 (10)) was fully out of range and thus could not help us assign the absolute configuration. TD-DFT predicted that Fraction 1 (with a positive Cotton effect) corresponded to (*S*)-**BAAZU-2** (Fig. 4.14).

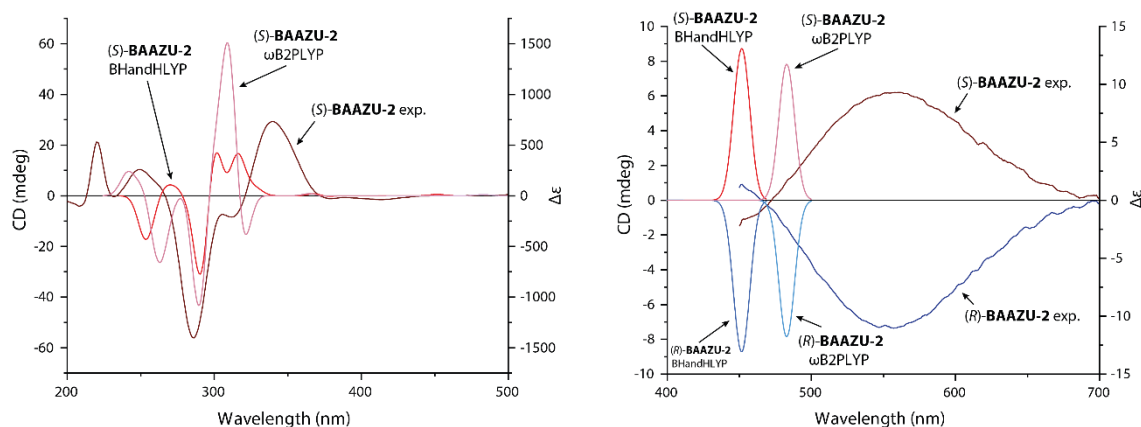


Figure 4.14: Experimental (left axis) vs. calculated (right axis) CD spectra of **BAAZU-2**

To confirm that the computations were accurate, I studied a third BAAZU-derivative, intermediate **8**, bearing two heavy bromine atoms to maximise anomalous dispersion. The two enantiomers could be separated by chiral HPLC on a CHIRALPAK IC column with a dichloromethane/*n*-hexane (70%/30%) mixture as eluent (Fig. S4.18). Fraction 1 showed a negative Cotton effect on the low intensity 450-750 nm broad S_0 - S_1 transition (Fig. 4.15).

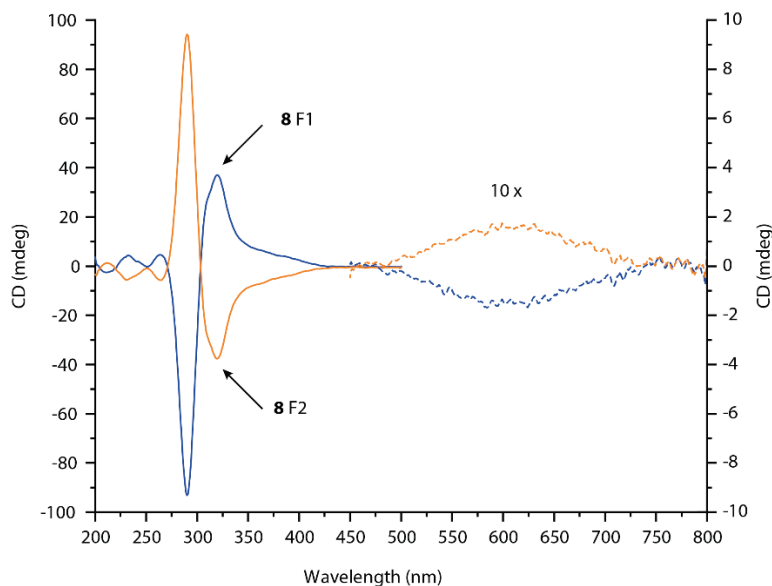


Figure 4.15: Circular dichroism of the two fractions of the intermediate **8**. The 450-800 nm concentrated spectra are plotted on the right y-axis.

Crystals of enantiopure **8** could be grown from the separated fractions and measured by SCXRD. The compound crystallises in the orthorhombic $P2_12_12_1$ (no. 19) space group. One unit of **8** is found in the asymmetric unit cell (Fig. 4.16). Fraction 1 was assigned to the (*S*)-enantiomer of **8**, while Fraction 2 was assigned to the (*R*)-enantiomer, with Flack parameters of 0.044 (4) and 0.059(5), respectively.

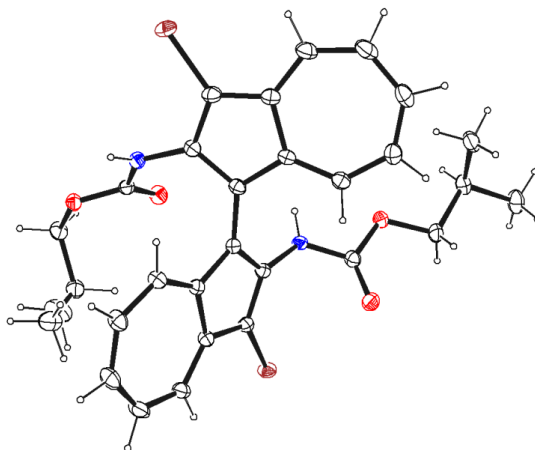


Figure 4.16: ORTEP representation of (*S*)-**8** (fraction 1). Ellipsoids drawn at 50% probability.

TD-DFT calculations performed on both enantiomers again were able to predict the sign of the Cotton effect of both enantiomers, as well as the higher energy bands in the 250–450 nm region (Fig. 4.17). However, functional BHandHLYP was in that case the only method that could predict the overall shape of the spectrum. We can therefore conclude that, in the absence of any contrary evidence, TD-DFT is an accurate method to assign the absolute configuration of the BAAZU-derivatives presented in this chapter, but with the caveat of having to choose an accurate functional.

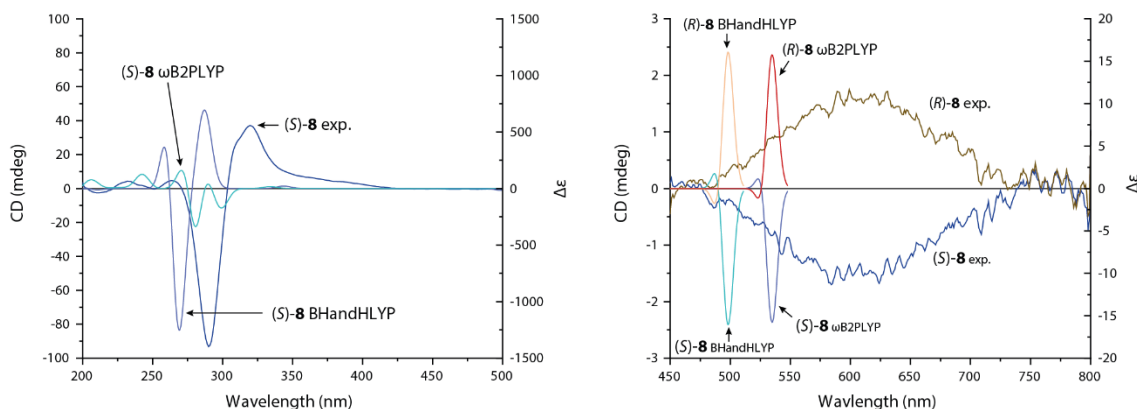


Figure 4.17: Experimental (left axis) vs. calculated (right axis) CD spectra of intermediate **8**

Table 4.2: Correspondence between the order of elution of the enantiomers of the three measured chiral compounds and of their absolute configuration and of the sign of the Cotton effect.

Compound	Intermediate 8	BAAZU-1	BAAZU-2
Fraction 1	<i>S</i> (negative)	<i>R</i> (negative)	<i>S</i> (positive)
Fraction 2	<i>R</i> (positive)	<i>S</i> (positive)	<i>R</i> (negative)

4.5 GUEST ENCAPSULATION

While the cavity of Pd₂BAAZU-1^{enant}₄ is small, it can still accommodate a BF₄⁻ anion, as seen by X-ray crystallography. However, the larger size of the cavity of Pd₂BAAZU-2^{enant}₄ has the potential of accommodating much larger and interesting guests, for example in asymmetric catalysis or chiral guest segregation. In addition, thanks to the structure of the ligand, the side of the cavity is lined with eight amino groups, bringing potential for the binding of neutral guest compounds with hydrogen bonds acceptors.

The size and functionality of Pd₂BAAZU-2^{enant}₄ was compared to a previously prepared Pd₂L₄ cage from our group, endohedrally functionalised with four inwards-pointing succinimide groups.^[30] Thanks to the H-bond donating character of the cavity, the cage is capable of binding several neutral and anionic transition metal complexes with carbonyl and cyanide ligands. Despite the open sides of the cage and the competition of acetonitrile molecules, the neutral octahedral M(CO)₆ guests are capable of binding the cage (albeit weakly, $K_a \approx 10^2$ - 10^3 M⁻¹) because of the cooperativity of the four H-bond sites lining the inside of the cavity and the six H-bond donors on the guests. Moreover, octahedral guest [Pt(CN)₆]²⁻ was found to be desymmetrised when bound to the cavity, as observed by IR spectroscopy: the C≡N stretching band was split into two separate bands, with different wavenumbers than the unique band observed for the free guest.

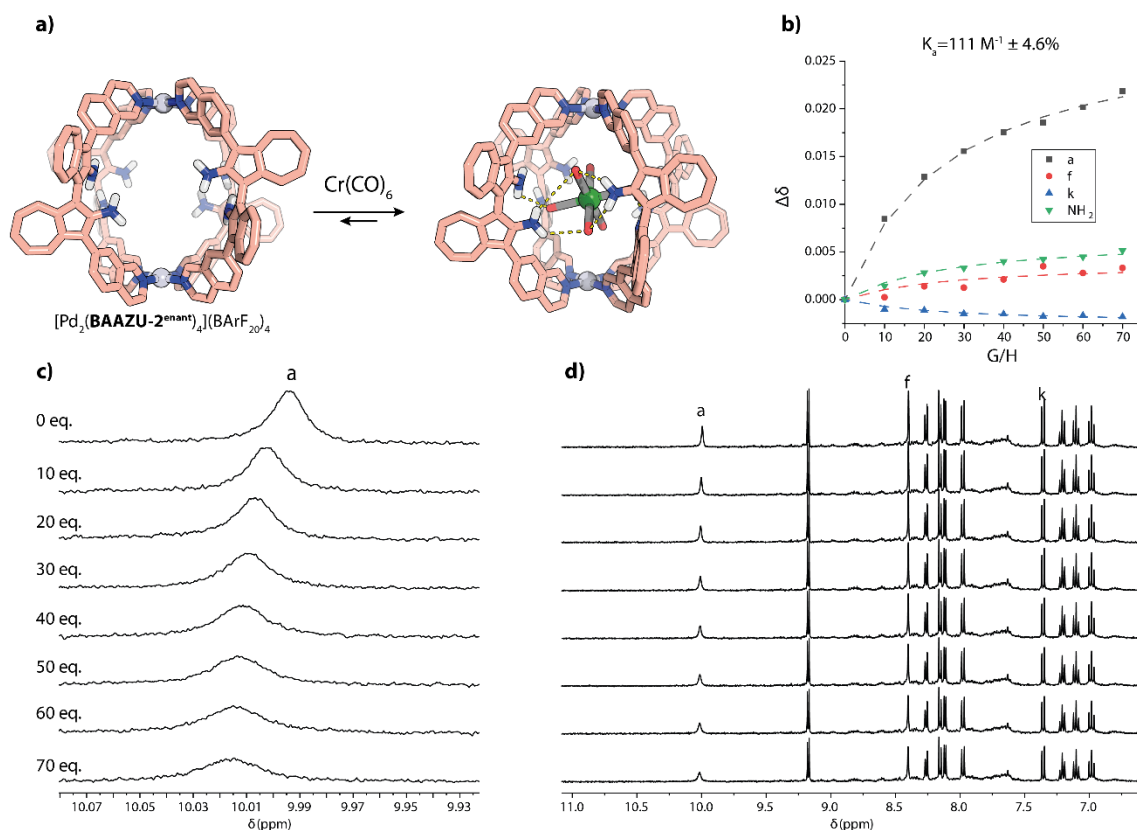


Figure 4.18: (a) DFT structures (ω B97X-D/def2-SVP) of the free cage and of its complex with Cr(CO)₆. (b) Graph of the shifts of selected protons (scatter) and the BindFit fitting model (dashed lines). (c) and (d) ¹H-NMR (500 MHz, 298 K, CD₃CN) of the titration of the cage with Cr(CO)₆.

Similar distances between the Pd(II) and between the opposite NH groups of both cages lead us to try to attempt to bind the same guests, as Pd₂**BAAZU-2^{enant}₄** possesses in addition a chiral cavity, which also could lead to further desymmetrisation of the guests. Titrations of [Pd₂**BAAZU-2^{enant}₄**](BArF₂₀)₄ with Cr(CO)₆ and (NBu₄)₂[Pt(CN)₆] were monitored by ¹H-NMR in CD₃CN. BArF₂₀⁻ (tetrakis(pentafluorophenyl)borate) was chosen as a large non-competitive counteranion for this experiment to limit the potential interactions between the smaller BF₄⁻ and the interior of the cage.

Cr(CO)₆ was added as a partial suspension in CD₃CN to the cage solution, and NMR spectra were measured until 70 equivalents of the guest was added. Shift of the inwards-pointing protons was weak but still measurable (Fig. 4.18), which allowed me to calculate the binding constant through BindFit (<http://app.supramolecular.org/bindfit/>). The value was measured to be $K_a = 111.4 \text{ M}^{-1} \pm 4.6 \%$. While weak, the binding is still observable and is in the same order of magnitude as with the previously published Pd₂**L₄** cage,^[30] despite Pd₂**BAAZU-2^{enant}₄** possessing twice as many H-bond donors as Pd₂**L₄** and the experiment being performed with a non-competitive counteranion. Those values may be explained by the fact that the amino groups of Pd₂**BAAZU-2^{enant}₄** do not point directly towards the centre of the cage and have a higher degree of movement, owing to the rotation of the ligand around its chiral axis. Moreover, by looking at the DFT model, it seems that the guest is relatively small for the cavity of the cage, and thus may only fit loosely.

The titration of [Pt(CN)₆]²⁻ was performed in the same manner. The guest was found to bind in a rapid exchange on the NMR time scale (Fig. 4.19c), but the association was much stronger than in the case of Cr(CO)₆, and precipitation from solution was observed after 1.2 equivalent of the guest was added. Because of this, a precise value for the binding constant could not be determined ($K_a = 86'681 \text{ M}^{-1} \pm 47\%$). A measurement was attempted by CD at a lower concentration to mitigate the precipitation risk (Fig. S4.54). However, precipitation was also observed at 1.2 eq. Thus, I can only conclude that the binding constant has a magnitude of $K_a \approx 10^5 \text{ M}^{-1}$. The 3 orders of magnitude difference in binding strength between the two guests is easily explained by the dianionic nature of [Pt(CN)₆]²⁻. ESI-MS confirmed the 1:1 binding ratio of the host-guest complex (Fig. 4.19d).

IR spectra of the [Pt(CN)₆@Pd₂**BAAZU-2^{enant}₄**] system were measured in addition (Fig. S4.56). However, unlike the previously published Pd₂**L₄** with endohedral NH groups,^[30] where the stretching of the C≡N bonds of the guest were visible and split in two, no signal was detected in the region of interest (2300-2000 cm⁻¹). While I am unsure of the reason of the disappearance of the signal, I suppose that the low symmetry of the cavity in addition to a more loosely fitting guest may create a situation where the hexacyanoplatinate does not have a precisely determined position. It thus results in a multitude of different states whose signals are lost in the noise of the IR spectrum.

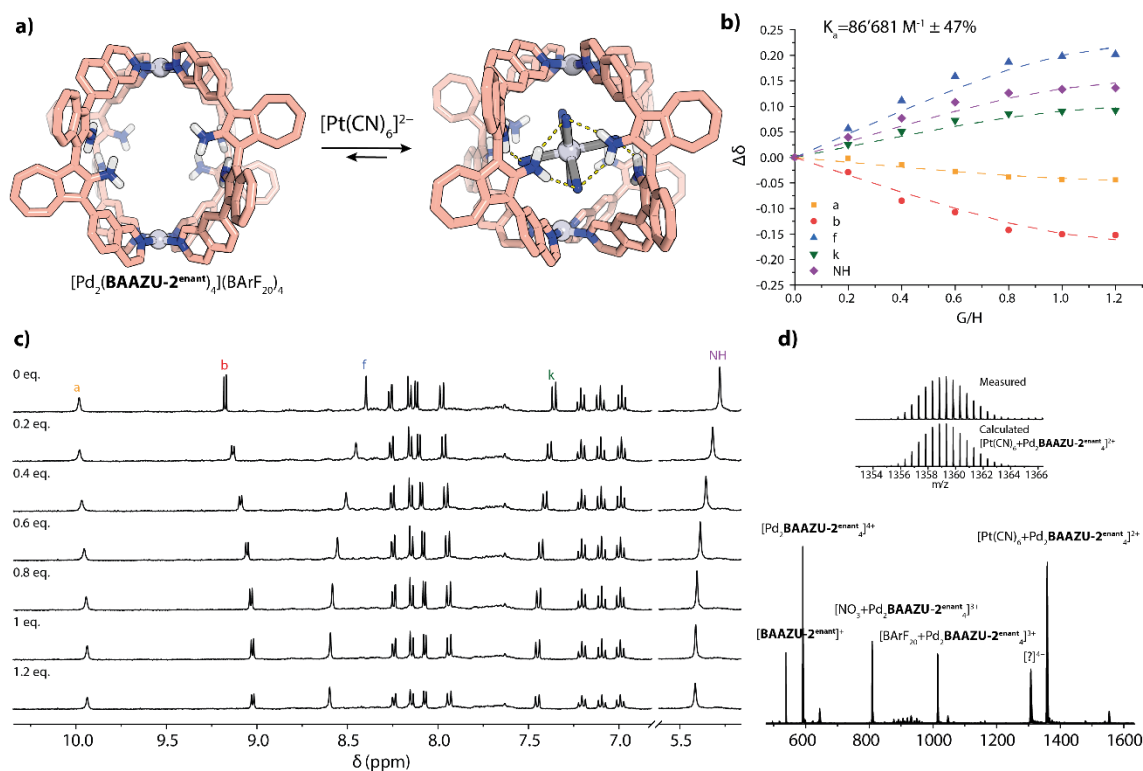


Figure 4.19: (a) DFT structures (ω B97X-D/def2-SVP) of $\text{Pd}_2\text{BAAZU-2}^{\text{enant}}_4$ and of its host-guest complex with $[\text{Pt}(\text{CN})_6]^{2-}$. (b) NMR shifts of selected protons of the cage upon titration of $[\text{Pt}(\text{CN})_6]^{2-}$ (scatter) and fitting of the data by BindFit (dashed lines). (c) $^1\text{H-NMR}$ (500 MHz, CD_3CN , 298 K) of the titration of $[\text{Pd}_2\text{BAAZU-2}^{\text{enant}}_4](\text{BArF}_{20})_4$ with $(\text{NBu}_4)_2[\text{Pt}(\text{CN})_6]$. (d) ESI-MS spectrum of the host-guest complex.

Finally, DFT models of the cage and of the two host-guest complexes were prepared to attempt to elucidate the binding mode of the guests inside the cavity. In both cases, during the optimisation process, the guests left their initial positions at the centre of the cavity and drifted towards the edges of the cage, turning, and pointing two of their ligands in positions between the amino groups of neighbouring ligands, thus creating a sort of “bridge” between them (Fig. 4.18a & 4.19a) This may be reminding of the way solvent molecules are bridging the amino groups in the $\text{Pd}_2\text{BAAZU-1}^{\text{rac}}_4$ and $\text{Pd}_2\text{BAAZU-1}^{\text{enant}}_4$. A similar behaviour was already observed experimentally by the group of Amouri in a Pd_2L_4 cage endohedrally functionalised with four amino groups.^[31] The authors managed to obtain an X-ray structure of the host-guest complex $[\text{Pt}(\text{NO}_3)_4]@[\text{Pd}_2\text{L}_4]$ where the platinate guest was disordered over two positions: in the first, the guest lies in the middle of the cage, with one of its coordination axes oriented along the Pd-Pd axis of the cage. In the second position, the guest was decentred and the nitro groups were bridging the amino groups of the cage, in a similar fashion as the DFT structure of $[\text{Pt}(\text{CN})_6]@[\text{Pd}_2\text{BAAZU-2}^{\text{enant}}_4]$. While the two cages and guests are obviously different, this older result gives credibility to the DFT structure of the present host-guest complex.

The chirotopic cavity of the cage was next examined for its chiral guest discrimination potential. Indeed, in our previously prepared cage based on [6]-helicene, we demonstrated that the binding of one enantiomer of camphorsulfonate was doubly preferred over the second one.^[18]

Therefore, we tested whether the present cage could also be used to separate the two enantiomers of the same guest. The titration of both enantiomers of **CSA** to the (*S*)-enantiomer of the homochiral cage was followed by $^1\text{H-NMR}$ (Fig. 4.20a). Both enantiomers were binding in a 2:1 model, as seen by the inflection of the signal of protons **a** and **NH** (Fig. 4.20b). The formation of the 1:1 complex [**CSA**@ $\text{Pd}_2(\text{S})\text{-BAAZU-2}_4$] was extremely favoured, and approximately 3 times as strong for (*S*)-**CSA** compared to its enantiomer ($15 \cdot 10^4 \text{ M}^{-1}$ vs $5 \cdot 10^4 \text{ M}^{-1}$) (Fig. 4.20c). The very strong binding of both guests may stem from a very favourable fit between the shape of the guest and of the cage, as well as a potential H-bond between the amino groups of the cage and the carbonyl group of the guest (Fig. 4.21 for DFT structures). The second binding was much weaker for both guests, and due to the size of the cavity, the relative weakness can probably be attributed to an outside binding. The 1:1 and 1:2 complexes could also both be detected by ESI-MS (Fig. S4.57).

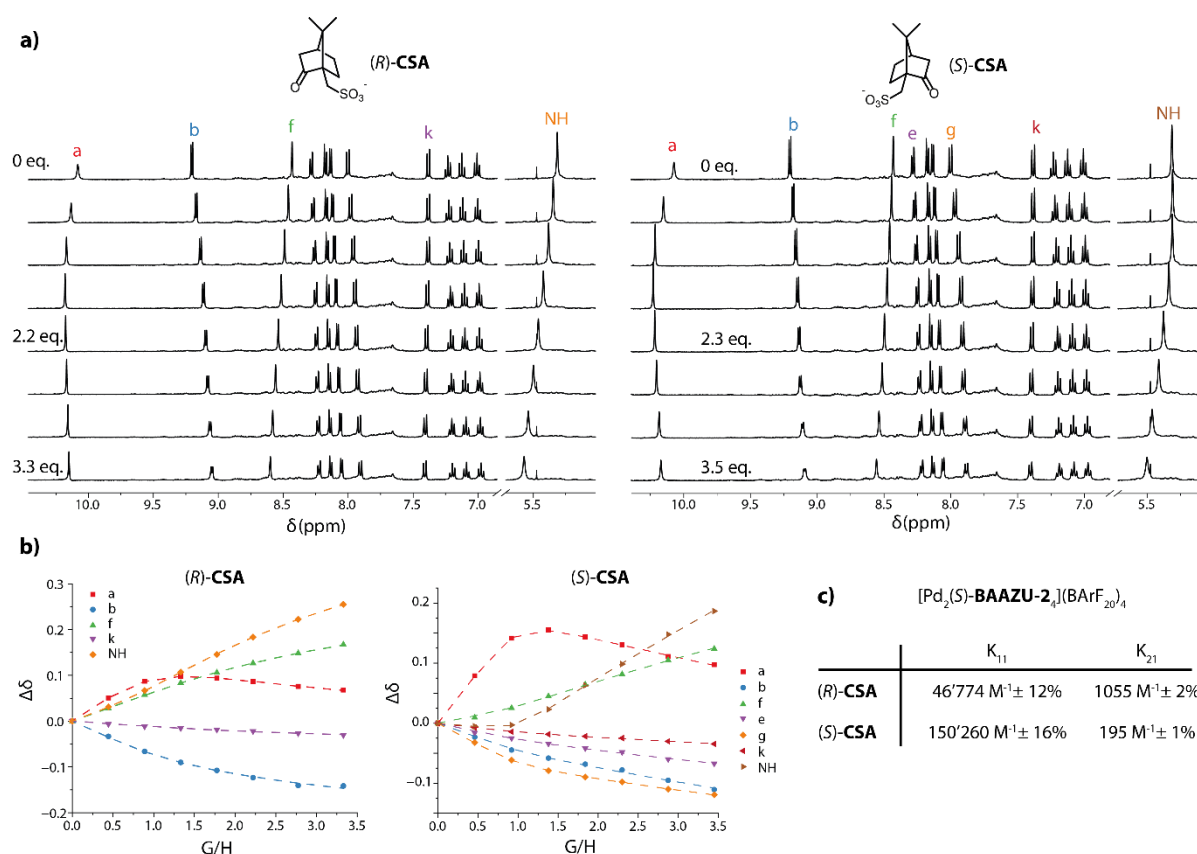


Figure 4.20: (a) $^1\text{H-NMR}$ (500 MHz, CD_3CN , 298 K) of the titration of [$\text{Pd}_2(\text{S})\text{-BAAZU-2}_4$](BArF_{20}) $_4$ with (*R*)- and (*S*)-**CSA**. The equivalents in guest were corrected through integration of the signals of tetrabutylammonium and of the cage. (b) Graph of the shifts of the signals of both titrations (scatter) and the BindFit fitting curve (dashed lines). (c) Binding constants of the two enantiomers of **CSA** to the cage [$\text{Pd}_2(\text{S})\text{-BAAZU-2}_4$](BArF_{20}) $_4$.

Thus, I have shown that the chiral $\text{Pd}_2\text{BAAZU-2}^{\text{enant}}_4$ can bind neutral guests thanks to its endohedral amino groups, as well as charged guests. Moreover, the cage can discriminate between the two enantiomers of **CSA** with a threefold difference in association constant.

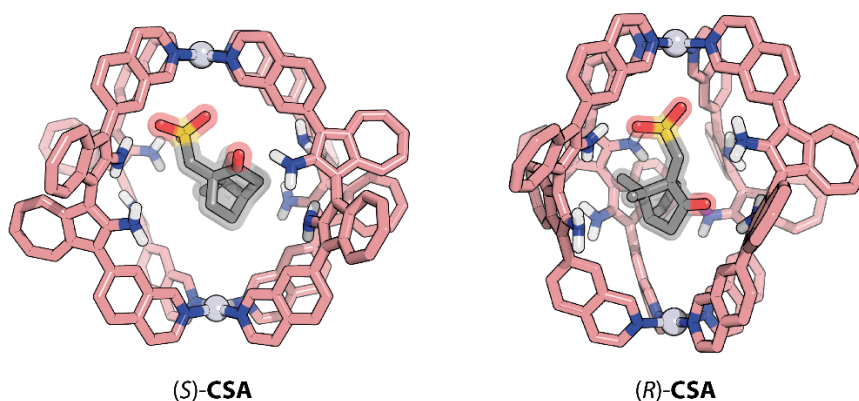


Figure 4.21: DFT structures (ω B97X-D3/def2-SVP) of the host-guest complexes of Pd₂(S)-BAAZU-2₄ with both camphorsulfonate enantiomers.

4.6 RACEMISATION BEHAVIOUR

The rotational barrier of the two azulene subunits around the 1,1' bond was studied as well. Indeed, I wondered if the inclusion of the ligand in a cage would lock its conformation in place (or at least slow its racemisation down) because of a reduced degree of freedom when included in the coordination assembly.

First, the racemisation of ligand **BAAZU-1** was measured in MeCN by the decay of the CD signal at elevated temperatures (Fig. 4.21a). As expected, the racemisation follows a first order reaction and by construction of an Eyring plot, the kinetic parameters could be determined. The racemisation Gibbs free energy of activation ΔG^\ddagger was calculated to be 110.3 kJ/mol (26.4 kcal/mol) in MeCN at 298 K (Fig. 4.21c).

To supplement this measurement, DFT calculations were also performed by G. Tusha: the transition states were located with the aid of NEB calculations^[32] at the def2-SVP/ ω B97X-D3 level of theory in MeCN with an implicit solvation model. Then, single point energies were calculated at the DLPNO-CCSD(T)^[33]/def2-TZVP level of theory in order to accurately compute the energy barriers associated with the isomerization process. The results show a racemisation barrier of 28 kcal/mol for both crossing points (either the two NH₂ groups pass on top of each other, or they pass on top of the seven-membered ring of the opposite azulene moiety).

Then, I measured the decay of the CD signal of cage [Pd₂**BAAZU-1**^{enant}]₄(BF₄)₄ in MeCN. To my surprise, the racemisation proceeds much faster in the cage than the ligand (Fig. 4.21b), contrary to my initial hypothesis that the embedding of the chiral ligand in the coordination cage would slow down its racemisation thanks to steric hinderance. Moreover, the decay of the signal does not follow an exponential decay as expected from a first order reaction but comes closer to a sigmoidal shape. The rapidity of the process, as well as the shape of the decay curve associated to it, would suggest to us a multifactorial cooperative process between the ligands and the solvent. Indeed, starting from the homochiral cage, if one ligand switches absolute configuration, this would bring the cage in

a more energetically unfavourable *RRRS* configuration, as calculated by DFT. Next, a second ligand could then switch to yield a cage with a *meso* configuration. As the *meso-trans* cage is much more favoured this time, one could imagine a fast energetically downhill process to yield the thermodynamic minimum. Moreover, one needs to consider the breaking and reformation of the hydrogen bonds network between the cage and the solvent, and the potential ligand exchange between the cages. Finally, as X-ray structures have revealed, the homochiral cage can accommodate a BF_4^- counteranion in its cavity, while the *meso-trans* cannot. Thus, the ejection of the anion to allow the transformation has also to be considered.

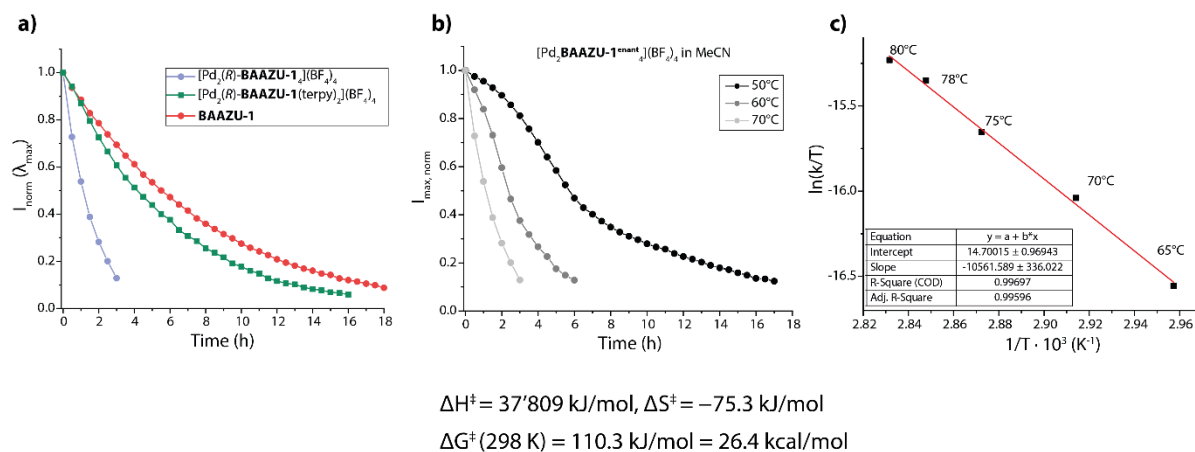


Figure 4.22: (a) comparison between the decay of the CD signal over time between **BAAZU-1**, $[\text{Pd}_2\text{BAAZU-1}^{\text{enant}}(\text{terpy})_2](\text{BF}_4)_4$, and $[\text{Pd}_2\text{BAAZU-1}^{\text{enant}}]_4(\text{BF}_4)_4$ in MeCN at 70°C. (b) Normalised decay of the CD signal over time of $[\text{Pd}_2\text{BAAZU-1}^{\text{enant}}]_4(\text{BF}_4)_4$ in MeCN at 50°C, 60°C, and 70°C. (c) Eyring plot of the racemisation of **BAAZU-1** and the calculated kinetic parameters.

In conclusion, when looking at the system in a broad view, it is difficult to pinpoint an exact reason for the accelerated racemisation of the ligand when part of the cage. More experiments and possibly molecular mechanics calculations would be needed to elucidate the reaction pathway.

A first experiment I performed to assess the possible reasons for the acceleration of the racemisation was to form the coordination complex $[\text{Pd}_2\text{BAAZU-1}^{\text{enant}}(\text{terpy})_2](\text{BF}_4)_4$, where the ligand is coordinated to two Pd(terpy) complexes. This structure was used to mimic the coordination of the ligand to the Pd(II) centres of the cage, but at the same time negating the effects that the neighbouring ligands might have on the racemisation rate. Thus, this complex was prepared to study the effect that the electron-withdrawing Pd(II) might have on the racemisation of the ligand.

To prepare this species, firstly $\text{Pd}(\text{MeCN})_4(\text{BF}_4)_2$ was reacted with 1 equivalent of 2,2';6',2''-terpyridine (terpy), to form $[\text{Pd}(\text{terpy})](\text{BF}_4)_2$.^[34] Then, to **BAAZU-1**^{enant} were added two equivalents of the previously made complex to form the final $[\text{Pd}_2\text{BAAZU-1}^{\text{enant}}(\text{terpy})_2](\text{BF}_4)_4$ complex.

The decay of its CD signals was measured in acetonitrile, like the free ligand. The racemisation was measured to proceed slightly faster than the free ligand at the same temperature, but not to the dramatic extent the cage did (Fig. 4.21a). Therefore, I can exclude that the electronic influence of the palladium cations has a significant effect on the accelerated racemisation rate of the ligand in

cage [Pd₂**BAAZU-1**^{enant}₄]. As explained before, a deeper study is therefore required if one wants to understand the precise mechanism of the racemisation of the cage. For example, one could measure the racemisation with different sizes of counter-anions (BF₄⁻, ClO₄⁻, PF₆⁻, BArF⁻) to understand the extent of their influence on the process. Next, molecular mechanics might be employed to understand the cooperativity between the ligands and the solvent molecules upon a racemisation event. However, it would be limited to a static model of the cage, not taking into account the ligand exchanges happening between the supramolecular coordination assemblies.

4.7 PERSPECTIVE

The BAAZU backbone promises many more discoveries in the next years, may it be in the domain of coordination cages, or for example as a *cis*-chelating group, or used as an alternative for BINOL. In coordination cages, the two amino groups per ligands offer many potential areas of research; for example, one could study the effect that protonation of the endohedral amino groups has on the stability of the cage and on its guest binding abilities. Moreover, chemically modifying the amino group to a urea or a thiourea group could be interesting to increase the neutral guest binding ability of the cage. All of those properties combined with the chromophoric nature of azulene and the potential integration of the ligands in low-symmetry cages may lead to a multifunctional system combining the chirotopic pockets of enzymes with the naked eye detection of specific analytes.

4.8 CONCLUSION

In conclusion, I have prepared new Pd₂**L**₄ assemblies based on an original 2,2'-diamino-[1,1'-biazulene] chiral backbone. A first ligand with pyridine donors, **BAAZU-1**, self-assembles into two different cages depending on its enantiomeric purity: when used as a racemate, a *meso-trans* cage is formed, and when the enantiomerically pure ligand is used, the homochiral cage is formed instead. Crystal structures revealed a peculiar arrangement of solvent molecules around the cage, acting as hydrogen bond bridges between the amino groups of neighbouring ligands. Further experiments and computations confirmed that those bridges between the ligands and the solvent molecules were responsible for the observed chiral self-sorting.

In addition, a second, larger, ligand with isoquinoline donor groups was synthesised. As a racemate, it forms only a mixture of different diastereoisomers of the Pd₂**BAAZU-2**₄ cage. This behaviour again underlines the importance of the size of **BAAZU-1** for optimal interactions between the cage and the solvent molecules to drive the self-sorting forward. In addition, the enantiopure cage Pd₂**BAAZU-2**^{enant}₄ is capable of guest binding, notably of neutral Cr(CO)₆ through H-bonds

between the host and the guest. Moreover, the chirotopic cavity of the cage is capable of differentiating between the two enantiomers of camphorsulfonate in a 1:3 ratio.

Finally, the racemisation rate of the ligands in free solution versus embedded in the cage was studied. Surprisingly, the racemisation of the homochiral cage Pd₂**BAZU-1**^{enant}₄ was much faster than the free ligand. Moreover, its decay did not follow a simple exponential curved, and was closer to a sigmoidal, suggesting a cooperative mechanism.

4.9 EXPERIMENTAL PART

4.9.1 General methods

Where necessary, experiments were performed under argon atmosphere using standard Schlenk techniques. Chemicals and standard solvents were purchased from Sigma Aldrich, Acros Organics, Carl Roth, TCI Europe, VWR, ABCR and used as received, if not mentioned differently. Dry solvents were purchased or purified and dried over absorbent-filled columns on a GS-Systems solvent purification system (SPS). Reactions were monitored with thin layer chromatography (TLC) using silica coated aluminium plates (Merck, silica 60, fluorescence indicator F254, thickness 0.25 mm). For column chromatography, silica (Merck, silica 60, 0.02–0.063 mesh ASTM) was used as the stationary phase. Gel permeation chromatography (GPC) purification of ligands were performed on a JAI 9210-II NEXT GPC System with a JAIGEL HH-2/HH-1 column combination running with CHCl₃ (HPLC grade). UV-vis spectra were recorded on a DAD HP-8453 UV-Vis spectrometer. Cuvette path length 1 cm, unless otherwise stated; wavelength: 270 nm – 900 nm, step size: 1 nm. Fluorescence spectra were recorded on a Jasco FP-8300 fluorescence spectrometer. Cuvette path length 2 mm, step size 0.5 nm.

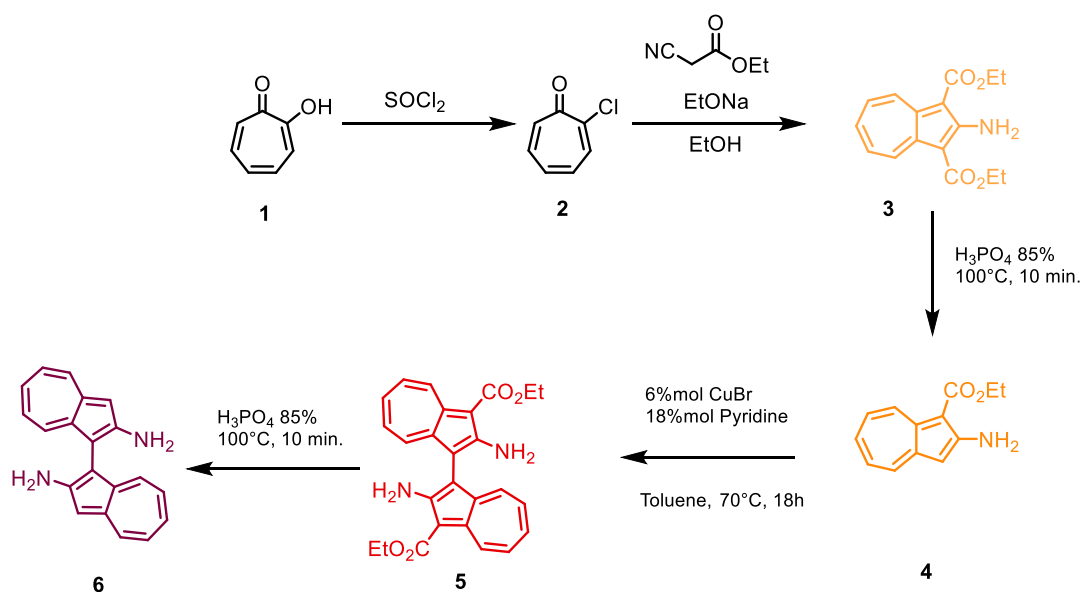
High resolution Electrospray ionization (ESI) mass spectra were recorded on Bruker ESI timsTOF (trapped ion mobility-time of flight) and Compact mass spectrometers (positive mode). All samples were diluted with spectroscopy-grade CH₃CN (1:10).

NMR experiments were performed on Bruker AVANCE III 500, 600 or 700 MHz spectrometers. Chemical shifts for ¹H and ¹³C are reported in ppm with residual solvent as reference: acetonitrile (1.94 ppm for ¹H, 1.32 ppm for ¹³C), DMSO-*d*₆ (2.50 ppm for ¹H, 39.52 ppm for ¹³C) and CDCl₃ (7.26 ppm for ¹H, 77.16 ppm for ¹³C). Abbreviations for signal multiplicity in the ¹H-NMR spectra are indicated as following: s: singlet, d: doublet, t: triplet, dd: doublet of doublets; dt: doublet of triplets; m: multiplet, b: broad.

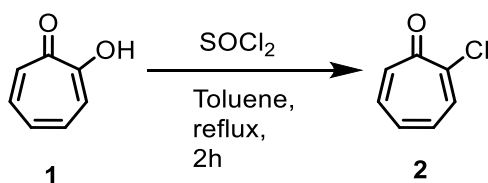
4.9.2 Synthetic procedures

4.9.2.1 Synthesis of [1,1'-biazulene]-2,2'-diamine ("BAAZU")

General scheme



Compounds **2** to **5** were synthesised according to reported literature procedures (cited at the beginning of the following synthetic protocols).

2-chlorotropolone (2):^[20]

Tropolone **1** (1 g, 8.19 mmol) was dissolved in dry toluene (25 ml) and SOCl_2 (0.773 ml, 1.27 g, 10.65 mmol) was added dropwise to the stirring solution which was then refluxed for 2 hours under argon. After cooling down, the solvent was removed under low pressure. The product was purified from the resulting crude dark oil by extraction with hot hexane and recrystallisation, to yield 2-chlorotropolone **2** (1.08 g, 7.67 mmol) as off-white needles. Yield: 72%

$^1\text{H-NMR}$ (500 MHz, DMSO) δ 8.02 (d, $J = 9.4$ Hz, 1H), 7.44 – 7.37 (m, 1H), 7.30 – 7.24 (m, 1H), 7.17 (d, $J = 12.2$ Hz, 1H), 7.10 (t, $J = 10.1$ Hz, 1H).

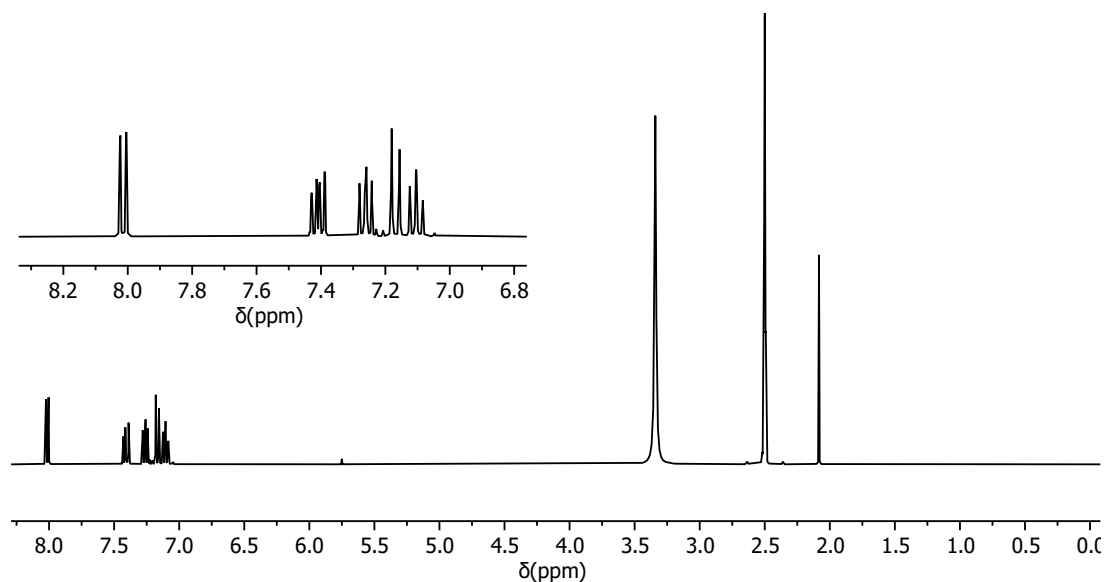
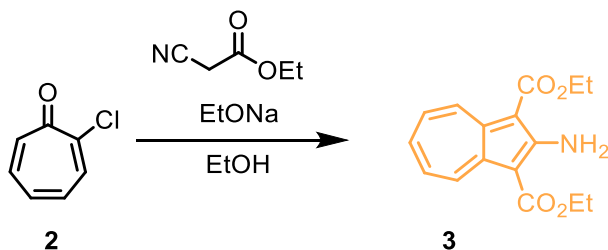


Figure S4.1: $^1\text{H-NMR}$ (500 MHz, 298 K, $\text{DMSO-}d_6$) spectrum of 2-chlorotropone (**2**). The aromatic region is presented in the insert.

Diethyl 2-aminoazulene-1,3-dicarboxylate (**3**):^[21]



Metallic sodium (403 mg, 17.5 mmol) was added to 30 ml of absolute ethanol and was left to react. Once done, the solution was then cooled down in an ice bath and ethyl cyanoacetate (3.2 g, 15.78 mmol, 3 ml) was slowly added to it under an argon atmosphere. A solution of 2-chlorotropone **2** (1 g, 7.11 mmol) in ethanol was then added dropwise. The reaction mixture turned immediately yellow. It was left to stir at RT overnight.

Afterward, the reaction was quenched with water and it was extracted with DCM. The organic layer was dried with MgSO_4 and evaporated under low pressure. The crude was recrystallised from aqueous ethanol to yield the title compound **3** as orange crystals (890 mg, 3.13 mmol). Yield: 44%.

$^1\text{H-NMR}$ (500 MHz, DMSO) δ 9.09 (d, $J = 10.4$ Hz, 2H), 7.83 (s, 2H), 7.69 (t, 2H), 7.57 (t, $J = 9.6$ Hz, 1H), 4.39 (q, $J = 7.1$ Hz, 4H), 1.39 (t, $J = 7.1$ Hz, 6H).

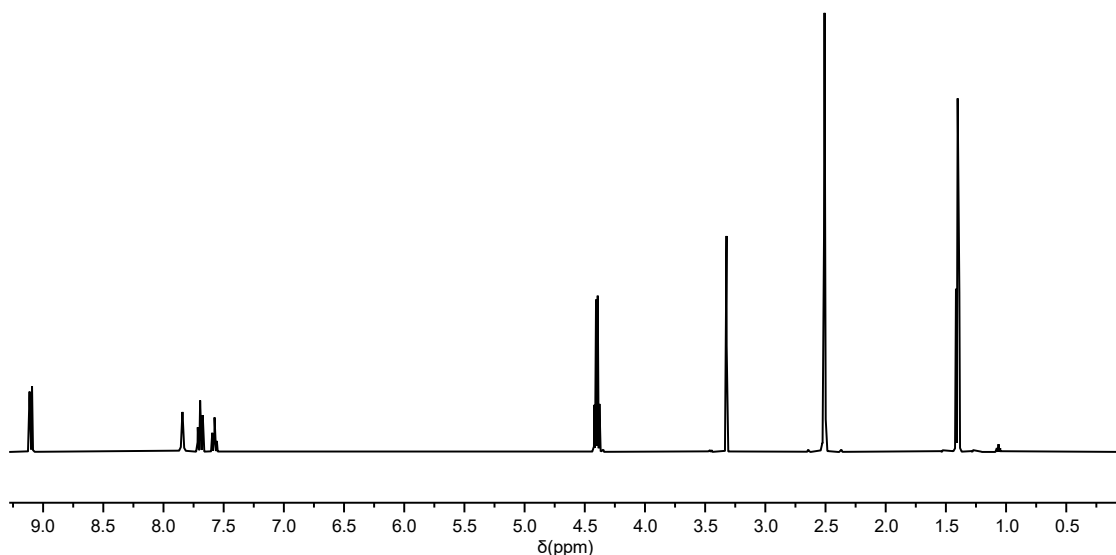
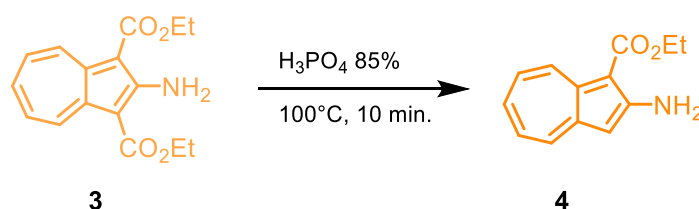


Figure S4.2: $^1\text{H-NMR}$ (500 MHz, 298 K, $\text{DMSO-}d_6$) spectrum of **3**.

Ethyl 2-aminoazulene-1-carboxylate (**4**): ^[22]



Diethyl 2-aminoazulene-1,3-dicarboxylate **3** (1.44 g, 5 mmol) was added to a round-bottom flask containing 10 ml of H_3PO_4 85%. The flask was then added to a pre-heated oil bath at 100°C , and the mixture was stirred 10 minutes. Gas evolution was observed. Afterward, the solution was left to cool down to RT, and was then added to 50 ml of water. The resulting solution was neutralised with NaOH and extracted with EtOAc. The organic layer was dried with MgSO_4 and the solvent was removed under low pressure to yield ethyl 2-aminoazulene-1-carboxylate **4** as an orange product (980 mg, 4.55 mmol). Yield: 91%.

$^1\text{H-NMR}$ (500 MHz, DMSO) δ 8.65 (d, $J = 9.6$ Hz, 1H), 7.85 – 7.77 (m, 1H), 7.31 – 7.24 (m, 1H), 7.22 – 7.12 (m, 2H), 6.56 (s, 1H), 4.33 (q, $J = 7.1$ Hz, 2H), 1.37 (t, $J = 7.1$ Hz, 3H).

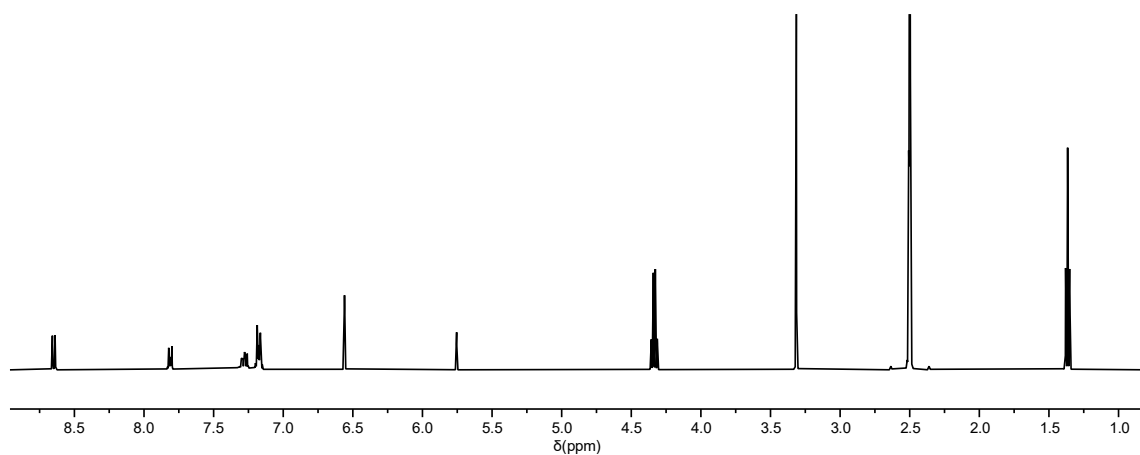
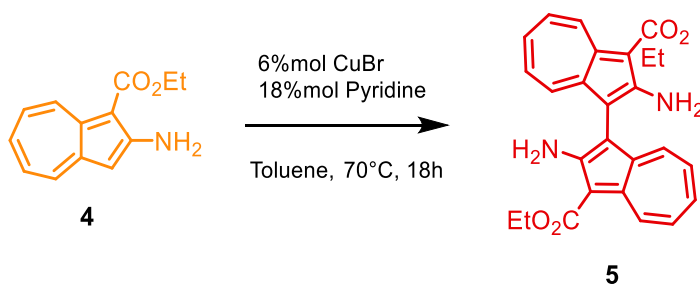


Figure S4.3: $^1\text{H-NMR}$ (500 MHz, 298 K, $\text{DMSO-}d_6$) spectrum of **4**.

Diethyl 2,2'-diamino-[1,1'-biazulene]-3,3'-dicarboxylate (**5**).^[19]



To a round bottom-flask charged with 50 ml of toluene were added ethyl 2-aminoazulene-1-carboxylate **4** (535 mg, 2.5 mmol), CuBr (21 mg, 0.15 mmol) and pyridine (36 mg, 36 μl , 0.45 mmol), and the mixture was stirred under air at 70°C overnight. The toluene was then removed under low pressure, and the crude was chromatographed (DCM, EtOAc 0-10%) to yield diethyl 2,2'-diamino-[1,1'-biazulene]-3,3'-dicarboxylate **5** as a red solid (214 mg, 0.50 mmol). Yield: 41%

The yield can possibly be improved by adding EtOH to the solvent system to better dissolve the catalyst.

$^1\text{H-NMR}$ (500 MHz, CD_2Cl_2) δ 9.03 (d, $J = 9.8$ Hz, 1H), 7.47 (dd, $J = 10.4, 1.0$ Hz, 2H), 7.42 (td, $J = 10.1, 1.2$ Hz, 2H), 7.31 (tt, $J = 10.2, 1.1$ Hz, 2H), 7.16 (ddd, $J = 10.2, 9.1, 1.1$ Hz, 2H), 4.47 (q, $J = 7.1$ Hz, 4H), 1.49 (t, $J = 7.1$ Hz, 6H).

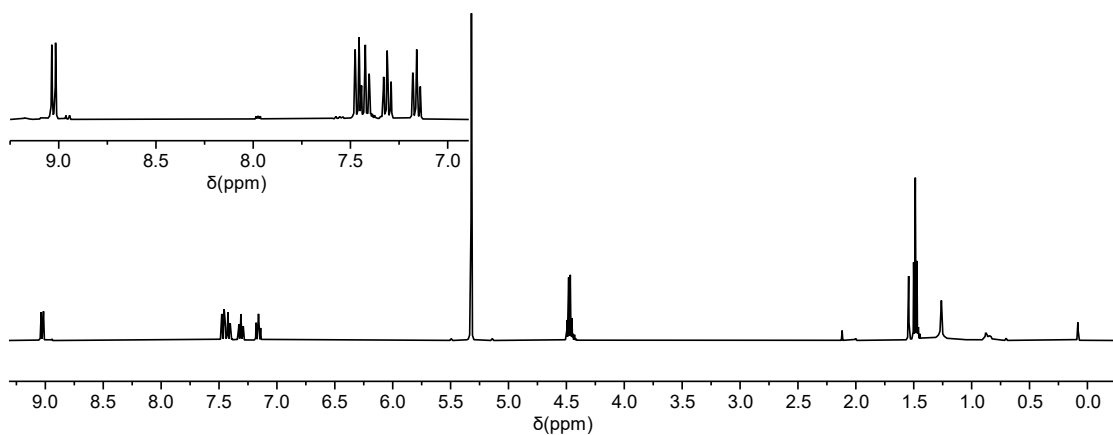
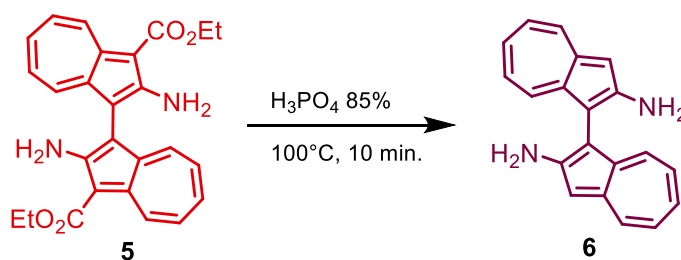


Figure S4.4: $^1\text{H-NMR}$ (500 MHz, 298 K, CD_2Cl_2) spectrum of **5**. The aromatic region is presented in the insert.

[1,1'-biazulene]-2,2'-diamine (**6**):



Diethyl 2,2'-diamino-[1,1'-biazulene]-3,3'-dicarboxylate **5** (300 mg, 0.70 mmol) was added to a round-bottom flask containing 10 ml of H_3PO_4 85%. The flask was then added to a pre-heated oil bath at 100°C , and the mixture was stirred 10 minutes. Gas evolution was observed. Afterward, the solution was left to cool down to RT, and was then added to 50 ml of water. The resulting solution was neutralised with NaOH and extracted with EtOAc. The organic layer was dried with MgSO_4 and the solvent was removed under low pressure to yield [1,1'-biazulene]-2,2'-diamine **6** (“**BAAZU**”) as a dark brown product (181 mg, 0.64 mmol). Yield: 90%.

$^1\text{H-NMR}$ (600 MHz, DMSO) δ 7.80 (dd, $J = 9.5, 1.3$ Hz, 2H), 7.20 (d, $J = 9.8$ Hz, 2H), 7.10 – 7.01 (m, 4H), 6.91 (ddd, $J = 10.5, 8.7, 1.4$ Hz, 2H), 6.77 (s, 2H), 6.01 (s, 4H).

$^{13}\text{C-NMR}$ (126 MHz, DMSO) δ 158.05, 142.62, 139.18, 128.14, 126.53, 125.75, 124.36, 123.90, 107.86, 102.82.

ESI-MS (pos. mode): calculated for $[\text{C}_{20}\text{H}_{16}\text{N}_2+\text{H}]^+$: 285.1386, found 285.1376

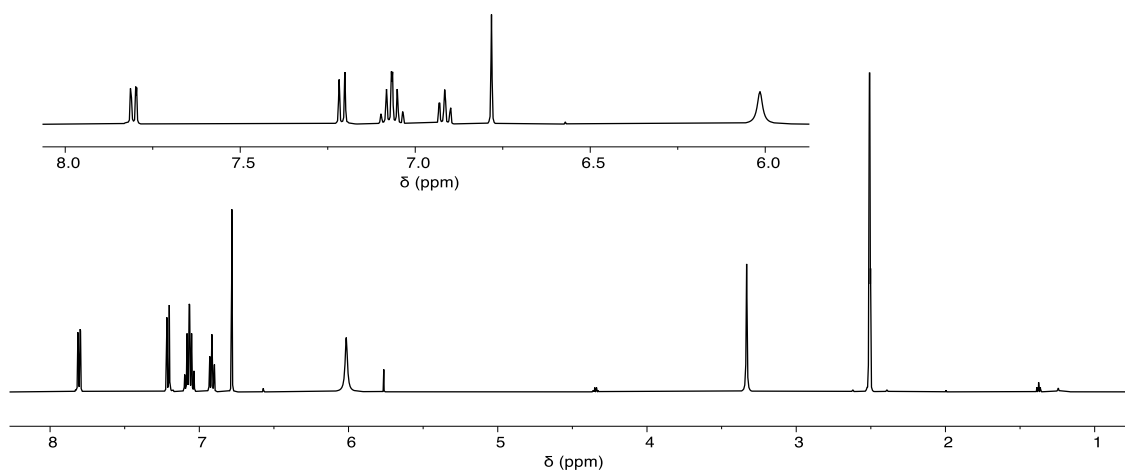


Figure S4.5: ¹H-NMR (600 MHz, 298 K, DMSO-*d*₆) spectrum of **6**.

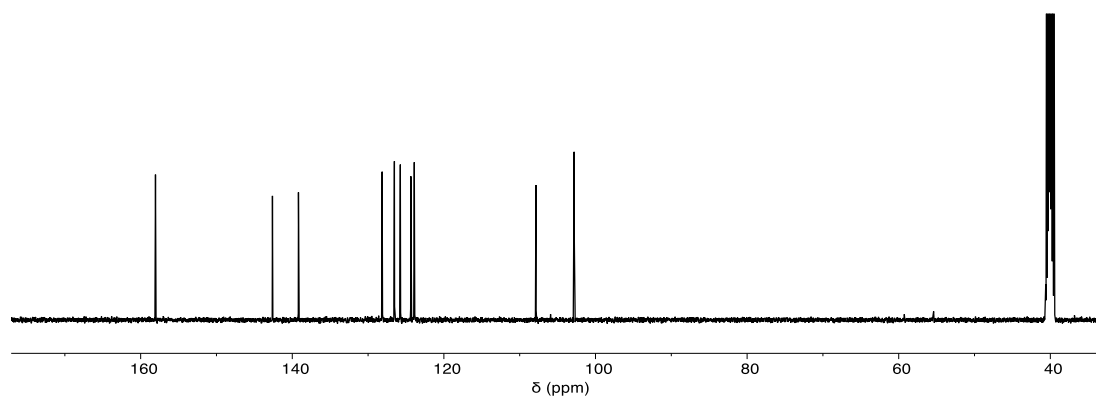


Figure S4.6: ¹³C-NMR (126 MHz, 298 K, DMSO-*d*₆) spectrum of **6**.

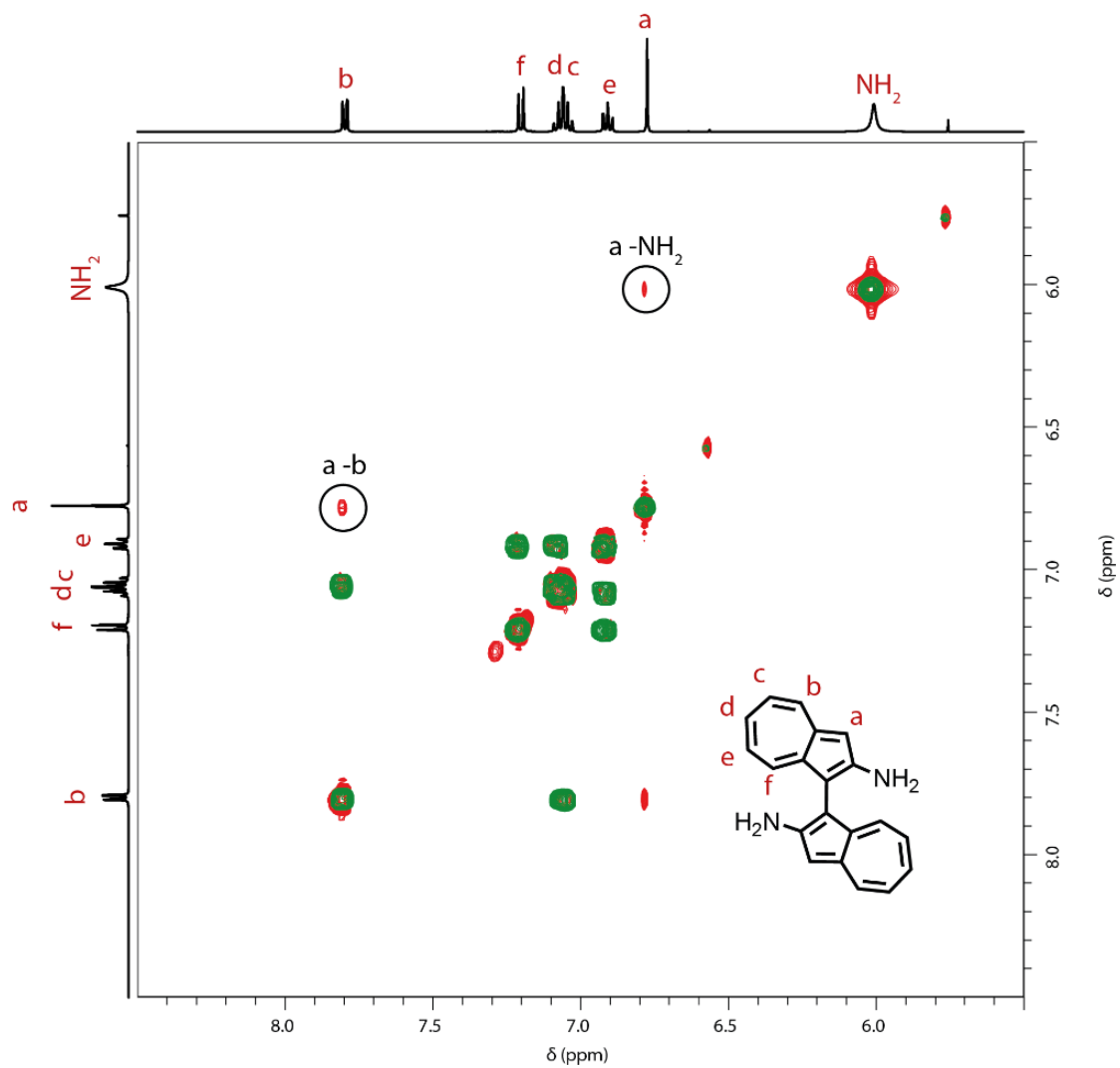
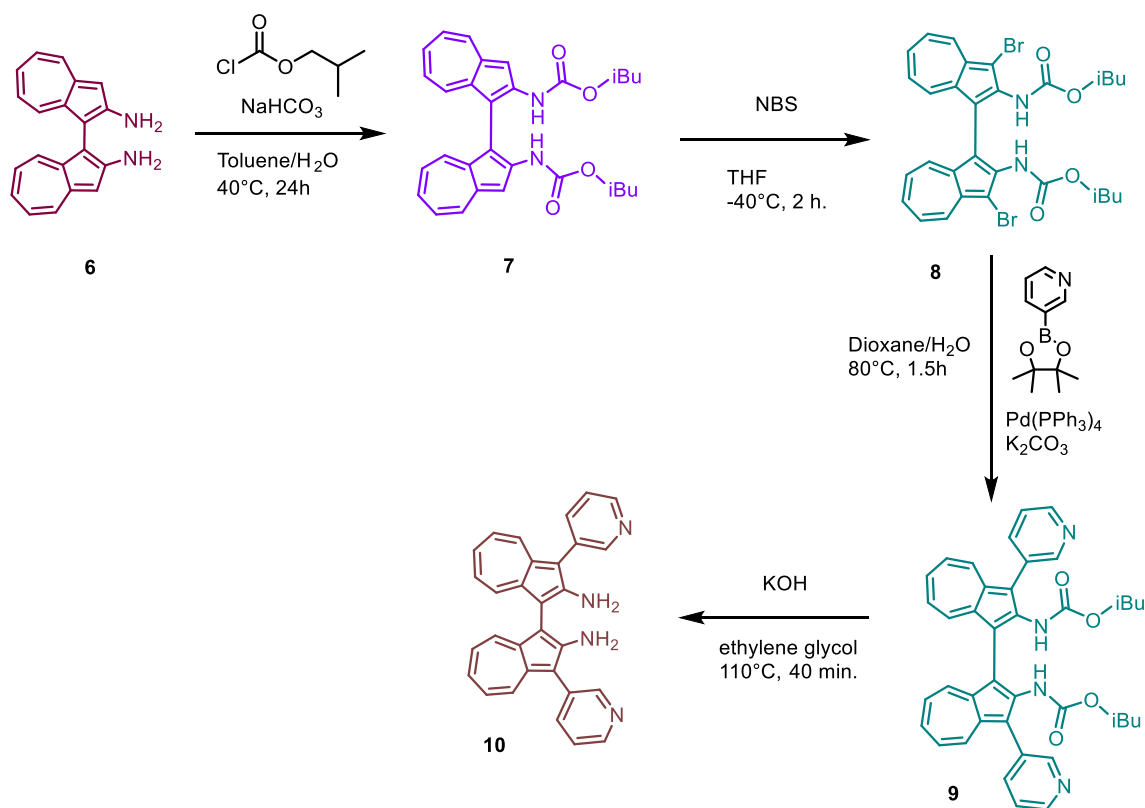
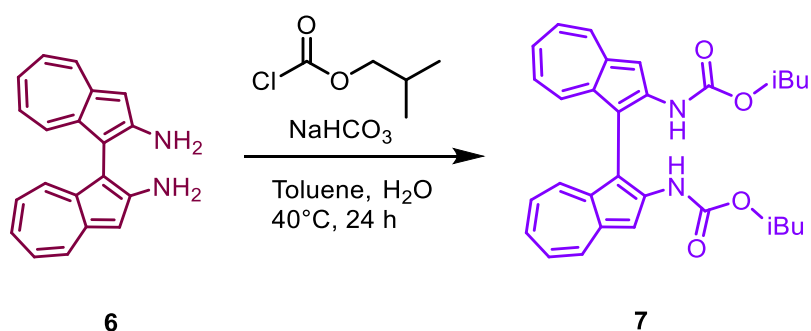


Figure S4.7: ^1H - ^1H COSY (green traces) and NOESY (red traces) NMR (600 MHz, 298 K, $\text{DMSO-}d_6$) spectra **6**. Important NOE correlations are highlighted in the figure.

4.9.2.2 Synthesis of 3,3'-di(pyridin-3-yl)-[1,1'-biazulene]-2,2'-diamine (“**BAAZU-1**”)

General scheme

diisobutyl [1,1'-biazulene]-2,2'-diylidicarbamate (7):

BAAZU (**6**) (455mg, 1.6mmol) was dissolved in a mixture of toluene (50 ml) and water (20 ml) with NaHCO_3 (1.1 g, 13.4 mmol) under argon. Isobutyl chloroformate (1.74 ml, 13.4 mmol) was slowly added as portions over the course of the reaction, and the reaction mixture was stirred strongly at 40°C for 24h. The solvent was then evaporated under low pressure, and the crude was chromatographed on silica gel (DCM). The resulting product was suspended in a 1:1 mixture of DCM and pentane and filtered to yield a purple powder as the title compound **7** (400mg, 0.82mmol, 52% yield).

$^1\text{H-NMR}$ (600 MHz, CDCl_3) δ 8.26 (d, $J = 9.6$ Hz, 2H), 7.96 (s, 2H), 7.59 (d, $J = 9.8$ Hz, 2H), 7.43 (tt, $J = 9.8, 1.0$ Hz, 2H), 7.25 (t, $J = 9.8$ Hz, 2H), 7.04 (t, $J = 9.7$ Hz, 2H), 6.83 (s, 2H), 3.97 – 3.81 (m, 4H), 1.86 (s, 2H), 0.83 (d, $J = 4.7$ Hz, 12H).

$^{13}\text{C-NMR}$ (151 MHz, CDCl_3) δ 153.46, 145.62, 141.69, 137.91, 134.42, 133.92, 132.01, 125.09, 124.69, 105.87, 27.85, 19.04. One nucleus missing.

ESI-MS (pos. mode): calculated for $[\text{C}_{30}\text{H}_{32}\text{N}_2\text{O}_4+\text{H}]^+$: 485.2435, found 485.2437

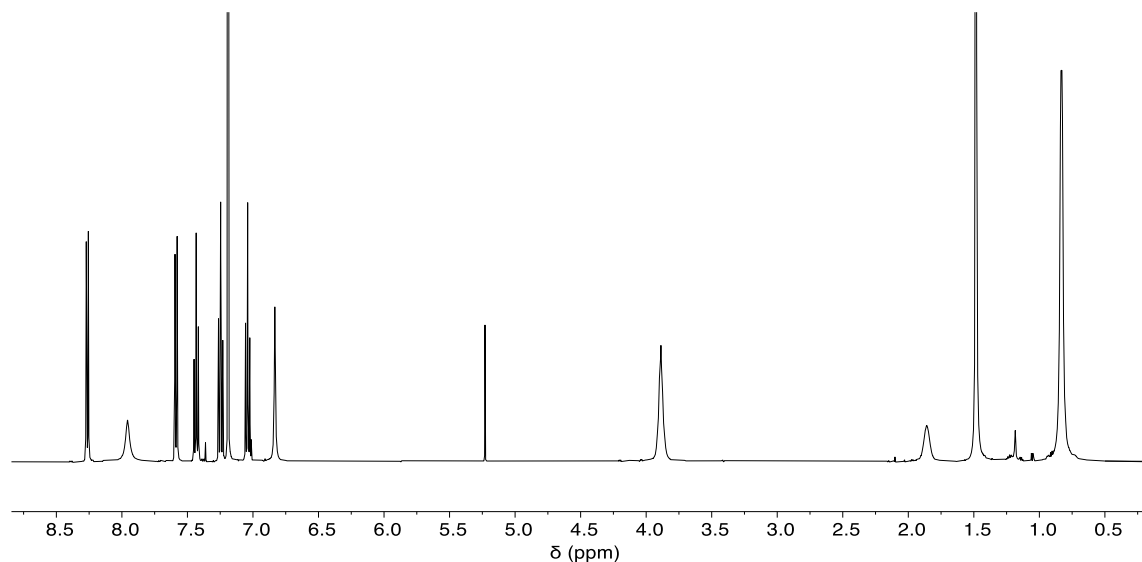
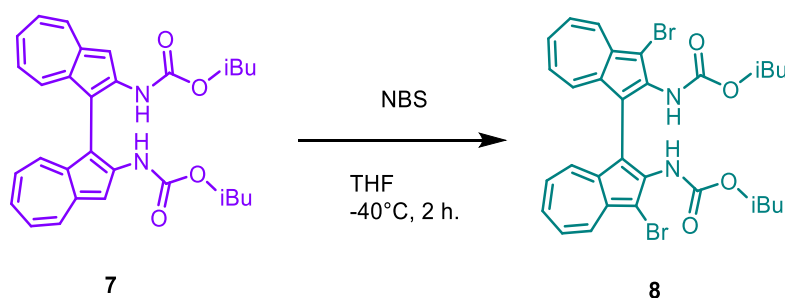


Figure S4.8: $^1\text{H-NMR}$ (600 MHz, 298 K, CDCl_3) spectrum of **7**.

diisobutyl (3,3'-dibromo-[1,1'-biazulene]-2,2'-diyl)dicarbamate (**8**):



7 (400 mg, 0.83 mmol) was added to a two-necked round bottom flask with 10 ml THF. The system was flushed with argon and then cooled to -40°C . A solution of NBS (310 mg, 1.74 mmol) in 10 ml THF was slowly dropped into the flask, and the reaction mixture was left to stir for two hours. Afterward, it was brought to room temperature, water was added to the mixture, and the aqueous phase was extracted with DCM. The organic phase was then dried with MgSO_4 and evaporated under reduced pressure. The crude was chromatographed on silica (pentane, EtOAc 20%) to obtain the title compound as a blue-grey powder (343 mg, 0.53 mmol). Yield: 64%

It is worth noting that a similar reaction with NIS was attempted, but failed to produce the diiodo derivative.

$^1\text{H-NMR}$ (600 MHz, CDCl_3) δ 8.42 (dd, $J = 9.9, 1.0$ Hz, 2H), 7.66 (dd, $J = 9.8, 1.0$ Hz, 2H), 7.57 (tt, $J = 9.9, 1.0$ Hz, 2H), 7.34 (td, $J = 9.8, 0.8$ Hz, 2H), 7.07 (t, $J = 9.7$ Hz, 2H), 6.94 (s, 2H), 3.81 – 3.72 (m, 4H), 1.74 (hept, $J = 6.7$ Hz, 2H), 0.75 (dd, $J = 6.7, 2.4$ Hz, 12H).

$^{13}\text{C-NMR}$ (151 MHz, CDCl_3) δ 153.68, 142.82, 138.34, 137.57, 135.90, 134.94, 134.84, 125.08, 124.94, 115.29, 99.21, 71.99, 28.03, 19.05.

ESI-MS (pos. mode): calculated for $[\text{C}_{30}\text{H}_{30}\text{Br}_2\text{N}_2\text{O}_4+\text{H}]^+$: 663.0465, found 663.0455.

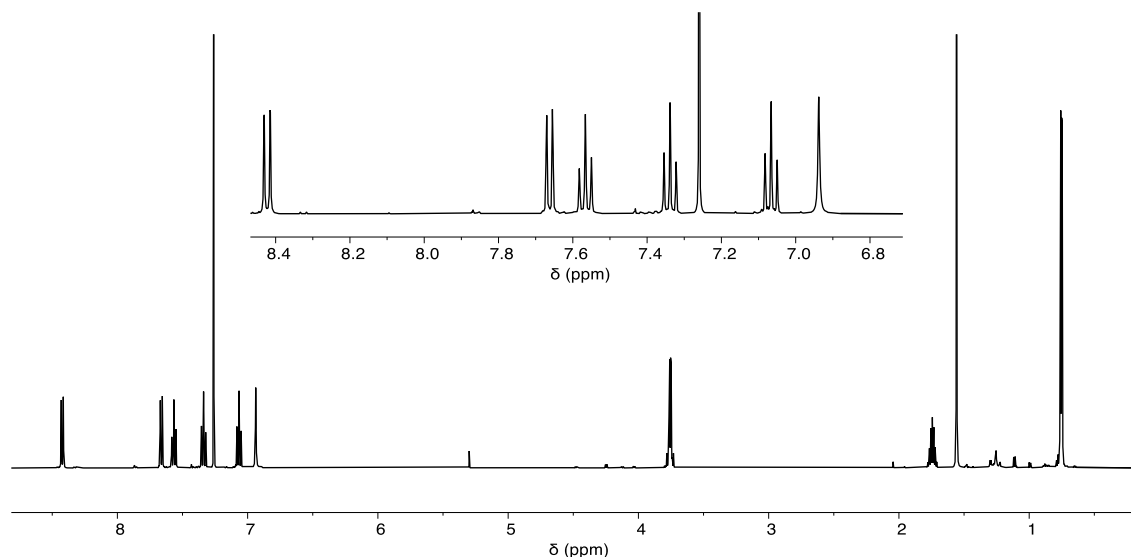
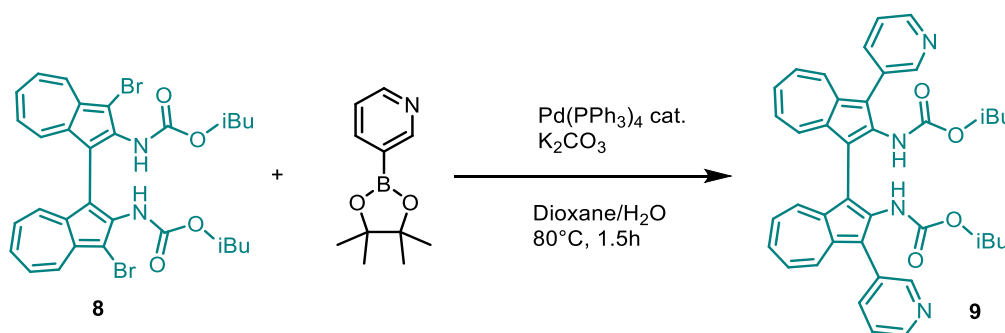


Figure S4.9: $^1\text{H-NMR}$ (500 MHz, 298 K, CDCl_3) spectrum of **8**. The aromatic region is presented in the insert.

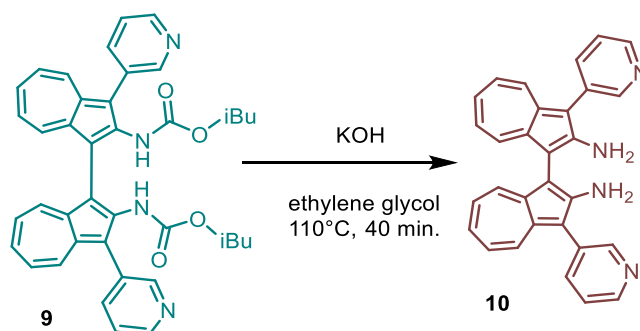
diisobutyl (3,3'-di(pyridin-3-yl)-[1,1'-biazulene]-2,2'-diyl)dicarbamate (**9**):



In a Schlenk flask, **8** (100 mg, 0.156 mmol), 3-pyridine-BPin (128 mg, 0.62 mmol), and K_2CO_3 (86 mg, 0.62 mmol) were added to a mixture of 1,4-dioxane (20 ml) and water (5 ml). The solution was degassed by bubbling argon through it for 30 min. $\text{Pd}(\text{PPh}_3)_4$ (17.3 mg, 0.015 mmol) was added as the catalyst and the flask was closed. The reaction mixture was heated at 80°C and stirred for 1.5 hours. Afterward, the reaction was quenched with water and the product was extracted with DCM. The organic phase was dried with MgSO_4 and evaporated under lower pressure. The crude was chromatographed on silica (EtOAc, MeOH 0-5%) to yield the crude title compound **9** as a blue-grey powder (76 mg, 0.12 mmol), which was used in the next step without further purification.

ESI-MS (pos. mode): calculated for $[C_{40}H_{38}N_4O_4]^+$: 639.2966, found 639.2942

3,3'-di(pyridin-3-yl)-[1,1'-biazulene]-2,2'-diamine (BAAZU-1):



9 (70 mg, 0.11 mmol) was added to a flask with ethylene glycol (10 ml) and powdered KOH (100 mg), and argon was bubbled through the mixture for 15 minutes. Afterward, the flask was stoppered, and the mixture was stirred and heated at 110°C for 40 minutes, or until no starting material was detected by TLC anymore. It was then quenched with water and the crude was extracted with DCM. The crude was chromatographed on silica (DCM, 5% MeOH) to yield **10** as a brown powder. The product was further purified by recycling GPC ($CHCl_3$, 0.5% NEt_3) to yield **BAAZU-1** as a brown powder (36.4 mg, 0.083 mmol, 75%, light spillage).

ESI-MS (pos. mode): calculated for $[C_{30}H_{22}N_4]^+$: 438.1839, found 438.1826

1H -NMR (600 MHz, CD_3CN) δ 8.84 (dd, $J = 2.3, 0.9$ Hz, 2H), 8.60 (dd, $J = 4.8, 1.7$ Hz, 2H), 8.00 (ddd, $J = 7.8, 2.3, 1.7$ Hz, 2H), 7.92 (dd, $J = 9.9, 0.9$ Hz, 2H), 7.57 – 7.49 (m, 4H), 7.27 (tt, $J = 9.6, 1.0$ Hz, 2H), 7.16 (td, $J = 9.8, 1.0$ Hz, 2H), 7.07 (td, $J = 9.7, 1.0$ Hz, 2H), 5.16 (s, 4H)

^{13}C -NMR (151 MHz, CD_3CN) δ 155.10, 151.48, 148.02, 139.75, 139.67, 138.07, 131.99, 130.77, 128.00, 126.20, 125.86, 125.21, 124.49, 110.98, 107.14

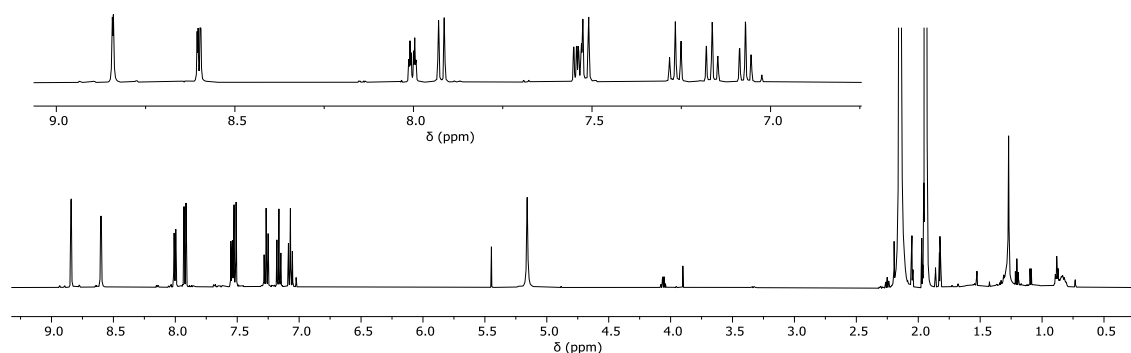


Figure S4.10: 1H -NMR (600 MHz, 298 K, $DMSO-d_6$) spectrum of **BAAZU-1** (**10**). The aromatic region is presented in the insert.

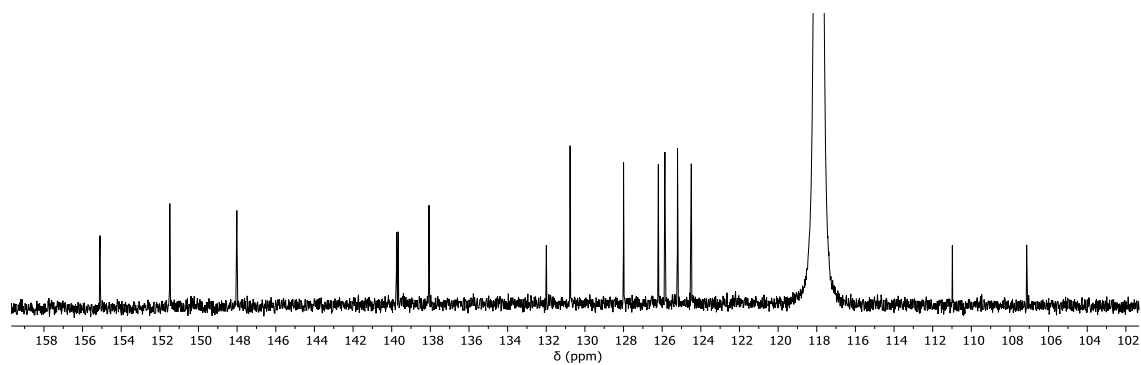


Figure S4.11: ^{13}C -NMR (151 MHz, 298 K, $\text{DMSO-}d_6$) spectrum of **BAAZU-1** (**10**).

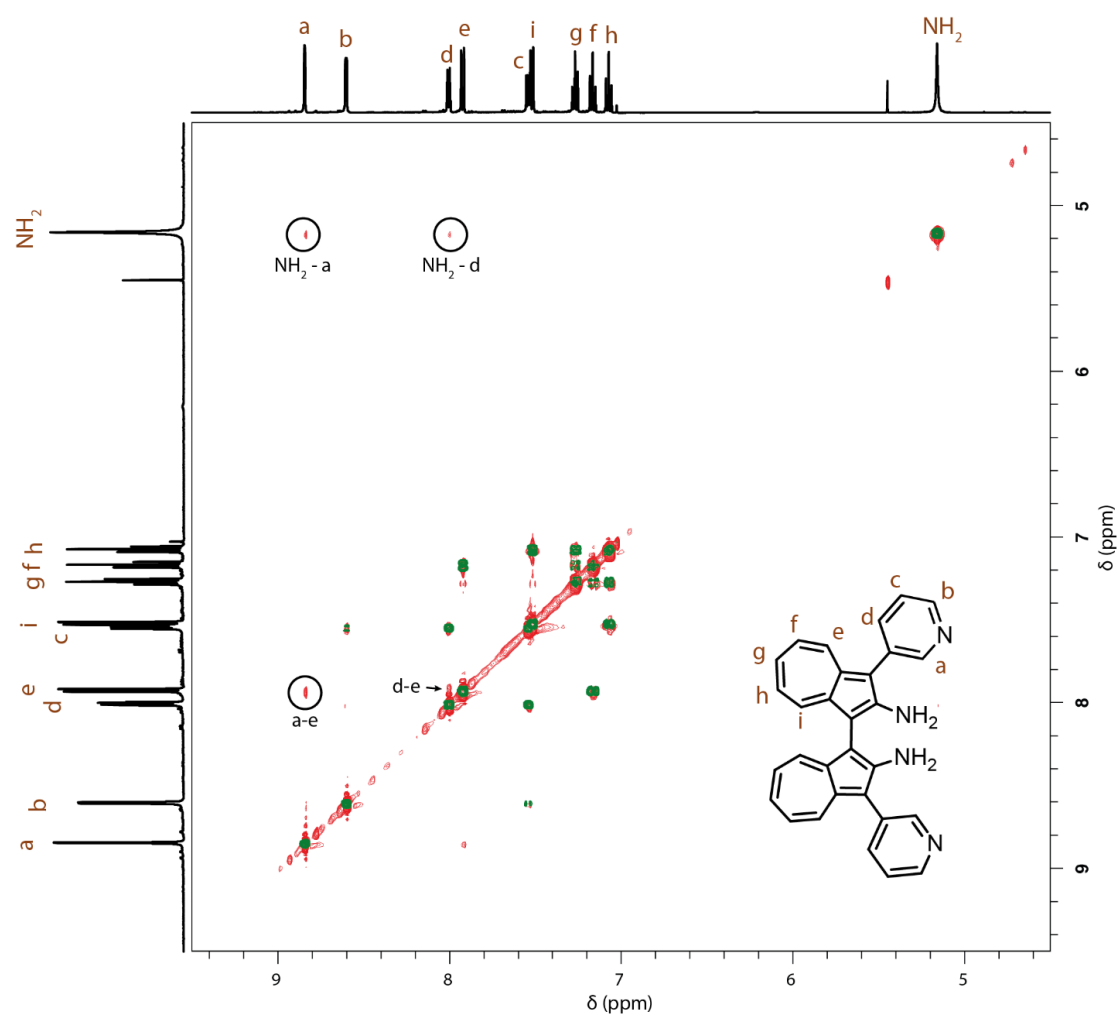
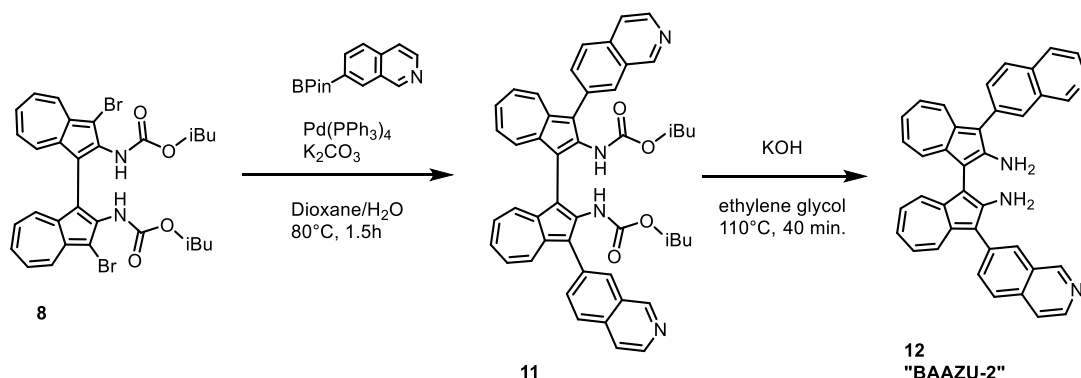


Figure S4.12: ^1H - ^1H COSY (green traces) and NOESY (red traces) NMR (600 MHz, 298 K, $\text{DMSO-}d_6$) spectra of **BAAZU-1** (**10**). Important NOE correlations are highlighted in the figure.

4.9.2.3 Synthesis of 3,3'-di(isoquinolin-7-yl)-[1,1'-biazulene]-2,2'-diamine ("BAAZU-2")

diisobutyl (3,3'-di(isoquinolin-7-yl)-[1,1'-biazulene]-2,2'-diyl)dicarbamate (11):

In a Schlenk flask, **8** (170 mg, 0.260 mmol), isoquinoline-7-boronic acid pinacol ester (230 mg, 0.9 mmol), and Cs_2CO_3 (391 mg, 1.2 mmol) were added to a mixture of 1,4-dioxane (20 ml) and water (5 ml). The solution was degassed by bubbling argon through it for 30 min. $\text{Pd}(\text{PPh}_3)_4$ (35 mg, 0.03 mmol) was added as the catalyst and the flask was closed. The reaction mixture was heated at 80°C and stirred for 1.5 hours. Afterward, the reaction was quenched with water and the product was extracted with DCM. The organic phase was dried with MgSO_4 and evaporated under lower pressure. The crude was chromatographed on silica (DCM, MeOH 1-3%) to yield the title compound **11** as a blue-grey powder (173 mg, 0.234 mmol, 90% yield).

$^1\text{H-NMR}$ (500 MHz, CD_2Cl_2) δ 9.26 (s, 2H), 8.50 (d, $J = 5.7$ Hz, 2H), 8.43 (dd, $J = 10.0, 0.9$ Hz, 2H), 8.16 (d, $J = 1.2$ Hz, 2H), 7.99 (d, $J = 1.2$ Hz, 4H), 7.85 (dd, $J = 9.8, 1.0$ Hz, 2H), 7.75 – 7.69 (m, 2H), 7.58 (tt, $J = 9.8, 1.1$ Hz, 2H), 7.33 – 7.21 (m, 4H), 7.12 (t, $J = 9.7$ Hz, 2H), 5.33 – 5.29 (m, 2H), 3.54 (dd, $J = 10.5, 6.8$ Hz, 2H), 3.45 (dd, $J = 10.6, 6.8$ Hz, 2H), 1.53 (hept, $J = 6.7$ Hz, 2H), 0.61 (dd, $J = 6.7, 2.1$ Hz, 12H).

$^{13}\text{C-NMR}$ (126 MHz, CD_2Cl_2) δ 153.75, 152.42, 143.47, 142.85, 138.13, 137.12, 137.05, 135.05, 134.59, 134.47, 133.88, 132.94, 129.05, 127.90, 126.58, 125.05, 124.65, 121.80, 120.19, 115.28, 71.28, 27.77, 18.45, 18.43.

ESI-MS (pos. mode): calculated for $[\text{C}_{48}\text{H}_{42}\text{N}_4\text{O}_4 + \text{H}]^+$: 739.3279, found 739.3198

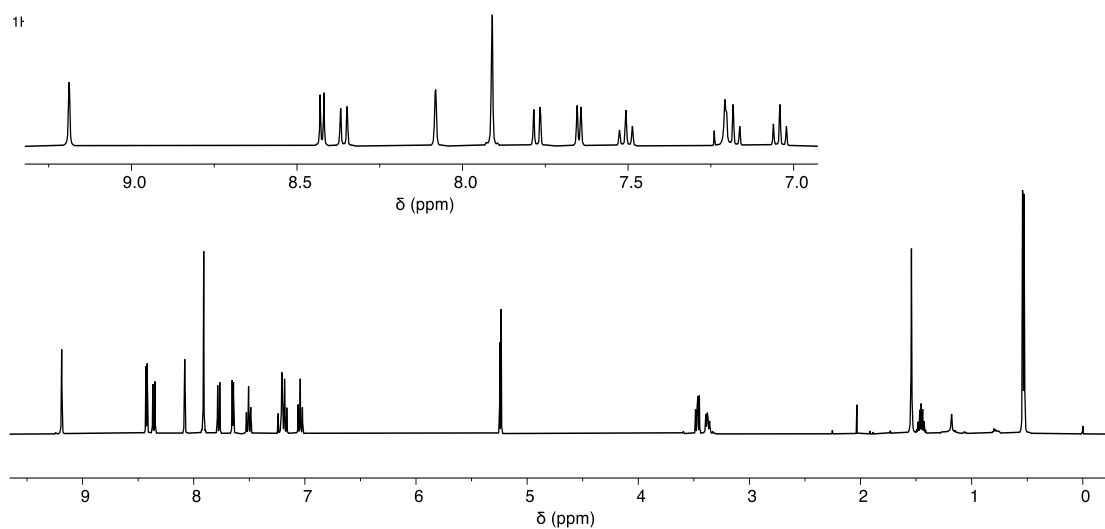


Figure S4.13: $^1\text{H-NMR}$ (500 MHz, 298 K, CD_2Cl_2) spectrum of **11**. The aromatic region is presented in the insert.

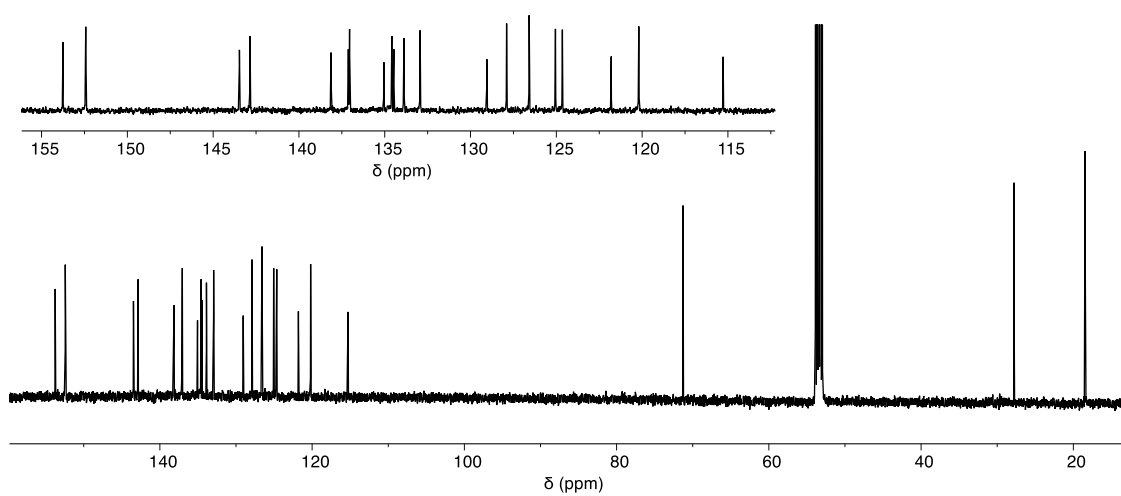


Figure S4.14: $^{13}\text{C-NMR}$ (151 MHz, 298 K, $\text{DMSO-}d_6$) spectrum of **11**. The aromatic region is presented in the insert.

3,3'-di(isoquinolin-7-yl)-[1,1'-biazulene]-2,2'-diamine (“BAAZU-2”):

11 (62 mg, 0.08 mmol) was added to a flask with ethylene glycol (10 ml) and powdered KOH (100 mg), and argon was bubbled through the mixture for 15 minutes. Afterward, the flask was stoppered, and the mixture was stirred and heated at 110°C for 40 minutes, or until no starting material was detected by TLC anymore. It was then quenched with water and the crude was extracted with DCM. The crude was chromatographed on silica (DCM, 5% MeOH) to yield the product as a brown powder. The product was further purified by recycling GPC (CHCl₃, 0.5% NEt₃) to yield **BAAZU-2** as a brown powder (32 mg, 0.06 mmol, yield 75%)

¹H-NMR (500 MHz, DMSO) δ 9.47 (s, 2H), 8.60 (d, *J* = 5.6 Hz, 2H), 8.40 (s, 2H), 8.21 (d, *J* = 8.5 Hz, 2H), 8.14 (dd, *J* = 8.4, 1.7 Hz, 2H), 8.01 (dd, *J* = 9.8, 1.1 Hz, 2H), 7.98 (d, *J* = 5.7 Hz, 2H), 7.51 (dd, *J* = 9.9, 0.8 Hz, 2H), 7.31 – 7.24 (m, 2H), 7.21 (td, *J* = 9.8, 1.2 Hz, 2H), 7.12 (td, *J* = 9.6, 1.2 Hz, 2H), 6.05 (s, 4H).

¹³C-NMR (126 MHz, DMSO) δ 155.46, 152.94, 142.97, 139.22, 139.11, 134.87, 134.21, 133.84, 129.74, 129.39, 128.38, 127.24, 127.00, 125.64, 125.08, 124.94, 120.67, 113.10, 107.01.

ESI-MS (pos. mode): calculated for [C₃₈H₂₆N₄+H]⁺: 539.2230, found 539.2154

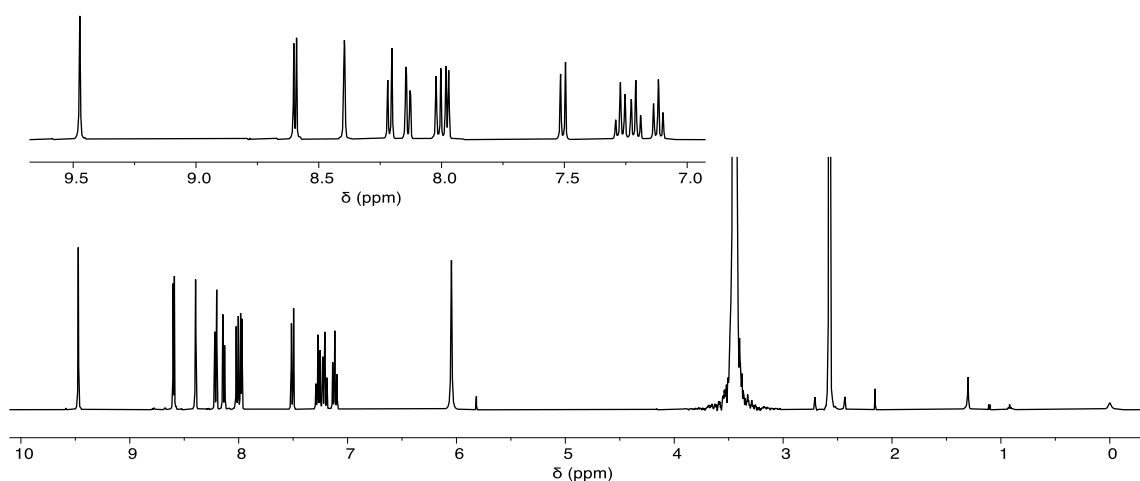


Figure S4.15: ¹H-NMR (500 MHz, 298 K, DMSO-*d*₆) spectrum of **BAAZU-2** (**12**). The aromatic region is presented in the insert.

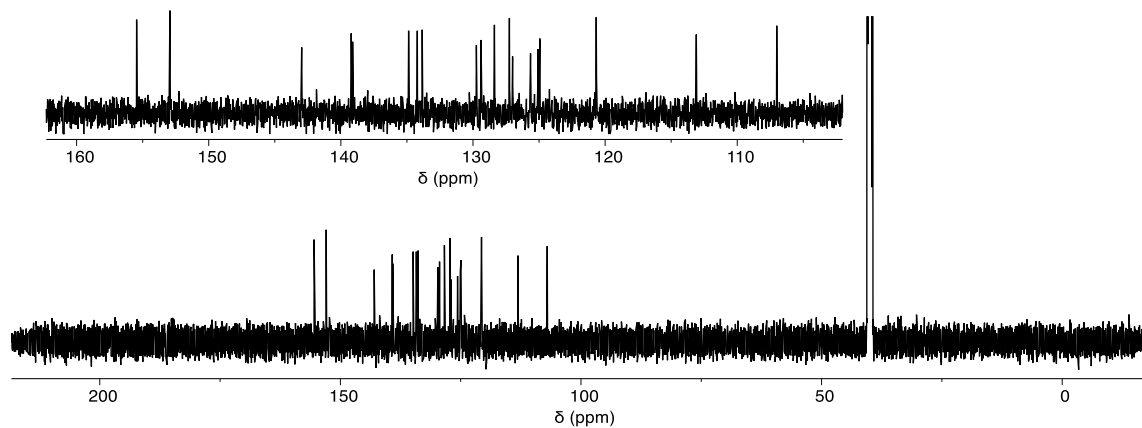


Figure S4.16: ^{13}C -NMR (151 MHz, 298 K, $\text{DMSO-}d_6$) spectrum of **BAAZU-2** (**12**). The aromatic region is presented in the insert.

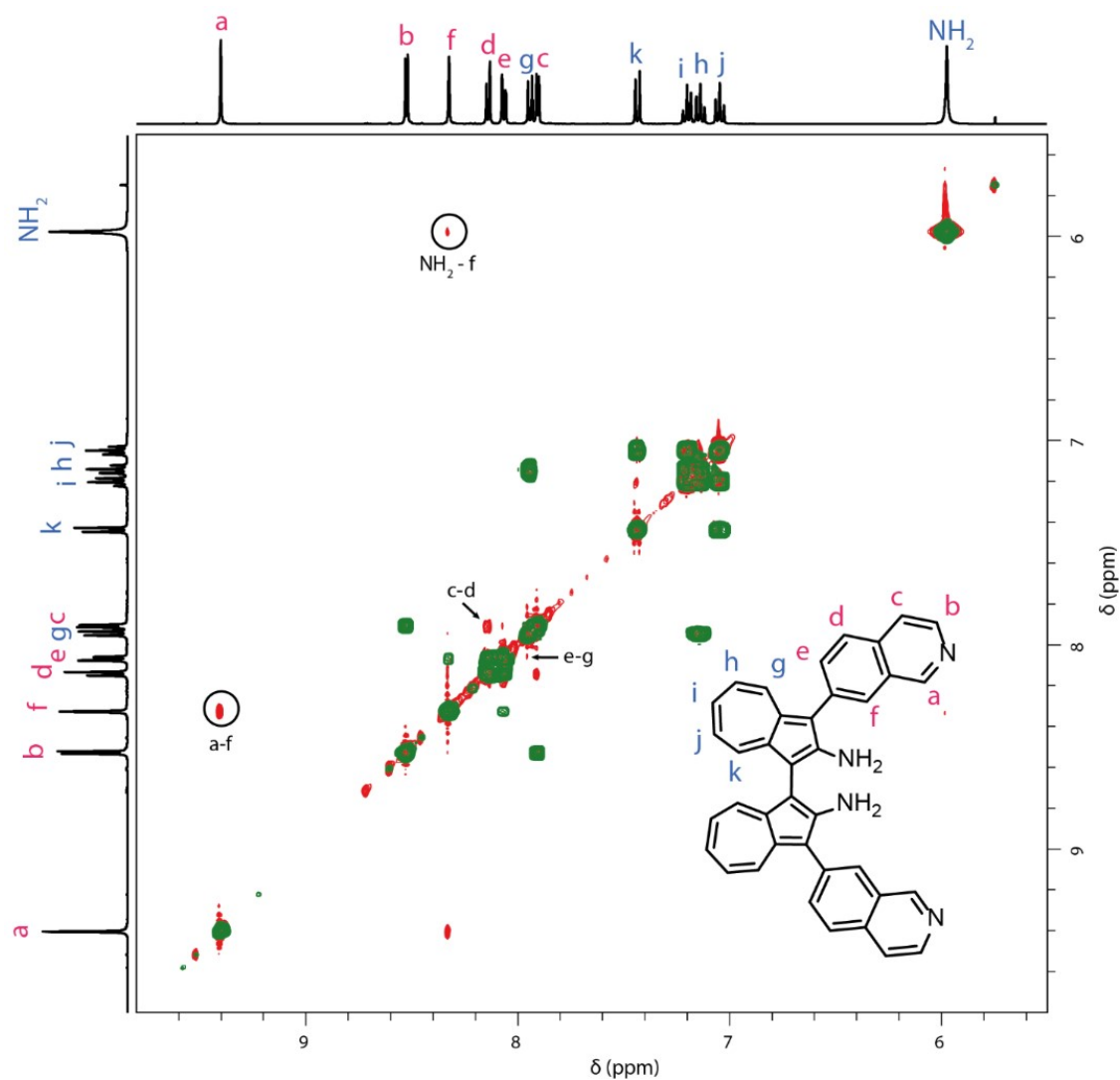


Figure S4.17: ^1H - ^1H COSY (green traces) and NOESY (red traces) NMR (600 MHz, 298 K, $\text{DMSO-}d_6$) spectra of **BAAZU-2** (**12**). Important NOE correlations are highlighted in the figure.

4.9.3 Chiral separation of the ligands by HPLC

Chiral high-performance liquid chromatography was performed on an Agilent Technologies 1260 infinity HPLC system equipped with Daicel CHIRALPAK IC columns [250 x 4.6 mm (analytic) and 250 x 10 mm (semipreparative)]. Flowrates were set up at 1 ml/min for analytics and 4 ml/min for separation.

Intermediate **8** was separated using a dichloromethane/hexane (70%/30%) mixture as eluent.

BAAZU-1 was separated using a dichloromethane (with 0.05% NEt₃)/isopropanol (97%/3%) mixture as eluent.

BAAZU-2 was separated using a dichloromethane (with 0.05% NEt₃)/ isopropanol (92.5%/7.5%) mixture as eluent. The full method is presented on the following table:

Table S4.1: chiral HPLC method for the separation of the two enantiomers of **BAAZU-2**.

Time [min]	DCM (%)	iPrOH (%)	MeOH (%)	n-hexane (%)
0.00	92.5	7.5	0	0
20.00	92.5	7.5	0	0
20.01	0	0	80	20
30.00	0	0	80	20
30.01	92.5	7.5	0	0
40.00	92.5	7.5	0	0

The washing step with methanol and n-hexane was necessary to keep the enantiomers eluting at similar times upon repeated runs. Without the washing step, the peaks would gradually elute earlier and earlier, and overlap after a certain number of cycles.

Chromatograms of 8:

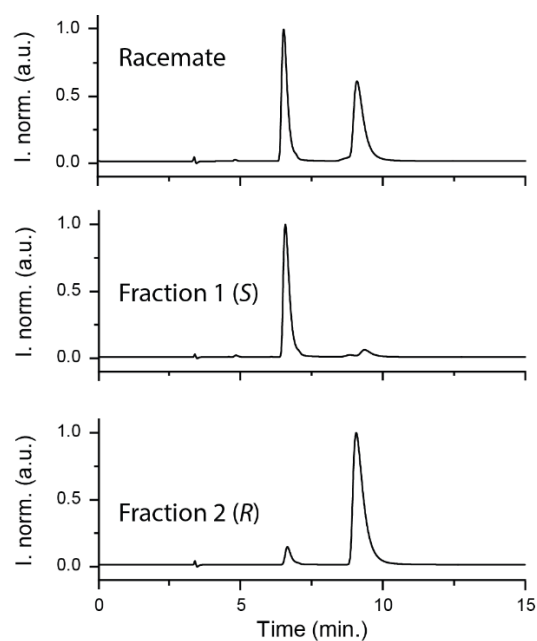


Figure S4.18: chiral HPLC chromatograms of intermediate **8** as racemate (top), of the first fraction (middle), and of the second fraction (bottom).

Chromatograms of BAAZU-1:

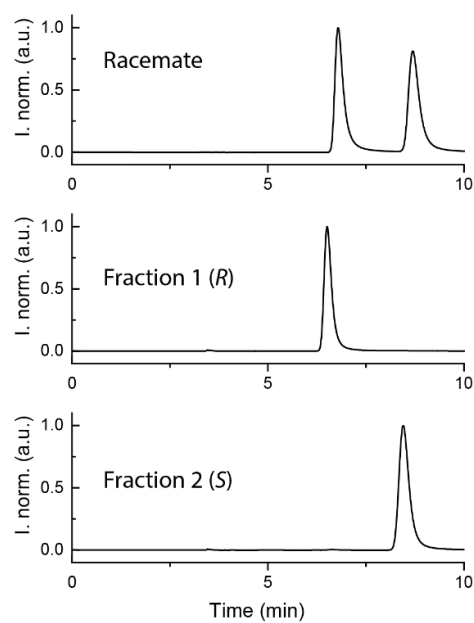


Figure S4.19: chiral HPLC chromatograms of **BAAZU-1** as racemate (top), of the first fraction (middle), and of the second fraction (bottom).

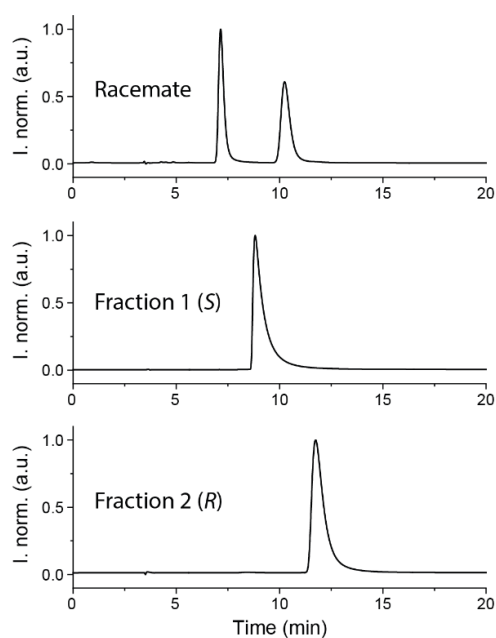
Chromatograms of BAAZU-2:

Figure S4.20: chiral HPLC chromatograms of **BAAZU-2** as racemate (top), of the first fraction (middle), and of the second fraction (bottom).

The chromatograms of the racemates show different retention times compared to the separated enantiomers. The reason is not clear to me. However, the washing step explained above allows me to keep more consistent retention times in-between runs.

4.9.4 Preparation of the cages

All of the Pd₂L₄ species were assembled according to the same procedure: to 450 μl of a 3.11 mM solution of the ligand in CD₃CN, DMSO-*d*₆, or CD₃NO₂, 50 μl of 15 mM solution of the Pd(II) salt in the same solvent were added. The solutions were then heated at 70 °C.

4.9.4.1 Pd₂BAAZU-1^{rac}₄

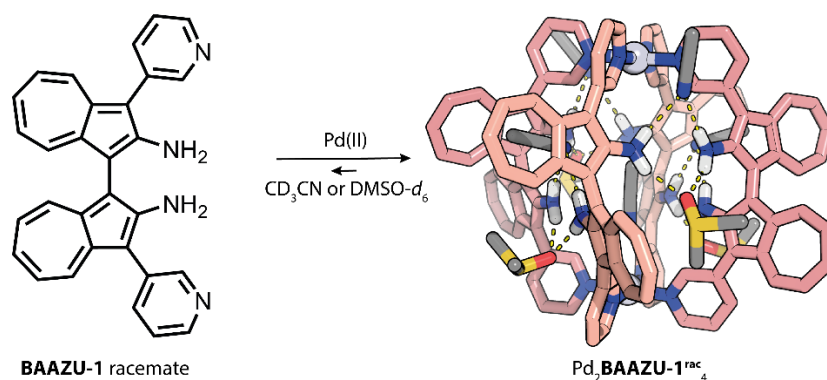


Figure S4.21: Formation of Pd₂BAAZU-1^{rac}₄ from the racemate of BAAZU-1.

The coordination cage [Pd₂BAAZU-1^{rac}₄](BF₄)₄ was synthesised as a 0.7 mM solution in CD₃CN, DMSO-*d*₆, or CD₃NO₂ according to the general procedure, using [Pd(CH₃CN)₄](BF₄)₄ as the palladium (II) salt and the racemate of BAAZU-1. The *trans-meso* cage was obtained after heating for 24 hours in CD₃CN, or for 5 hours in DMSO-*d*₆. Only a mixture of diastereomers was obtained from CD₃NO₂. The following characterisation was made from the CD₃CN solution.

¹H-NMR (600 MHz, CD₃CN) δ 9.53 (dd, *J* = 5.7, 1.1 Hz, 2H), 9.46 (s, 2H), 8.31 (ddd, *J* = 7.8, 2.0, 1.4 Hz, 2H), 7.97 – 7.90 (m, 4H), 7.23 – 7.17 (m, 2H), 7.18 (dd, *J* = 9.4, 0.9 Hz, 2H), 7.11 (t, *J* = 9.7 Hz, 2H), 6.94 (ddd, *J* = 10.2, 9.1, 0.9 Hz, 2H), 5.30 (s, 4H).

¹³C-NMR (151 MHz, CD₃CN) δ 156.15, 151.01, 148.24, 142.60, 141.42, 139.74, 137.14, 132.70, 129.05, 128.74, 127.58, 126.98, 126.86, 118.26, 108.51, 108.02, 55.28.

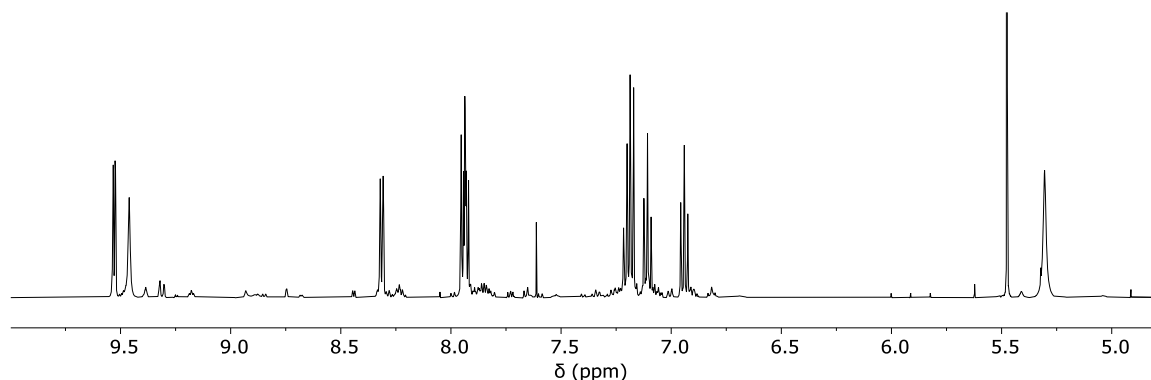


Figure S4.22: ¹H-NMR (600 MHz, 298 K, CD₃CN) spectrum of [Pd₂(BAAZU-1^{rac})₄](BF₄)₄.

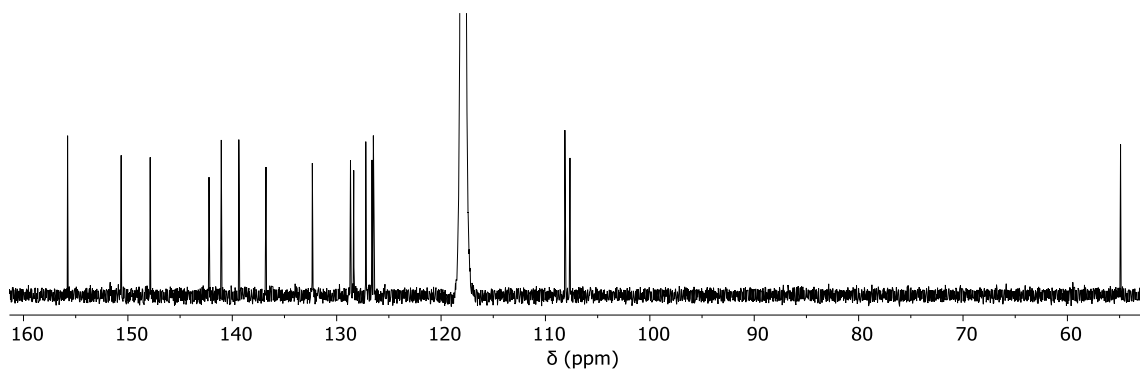


Figure S4.23: ^{13}C -NMR (151 MHz, 298 K, CD_3CN) spectrum of $[\text{Pd}_2\text{BAAZU-1}^{\text{rac}}_4](\text{BF}_4)_4$.

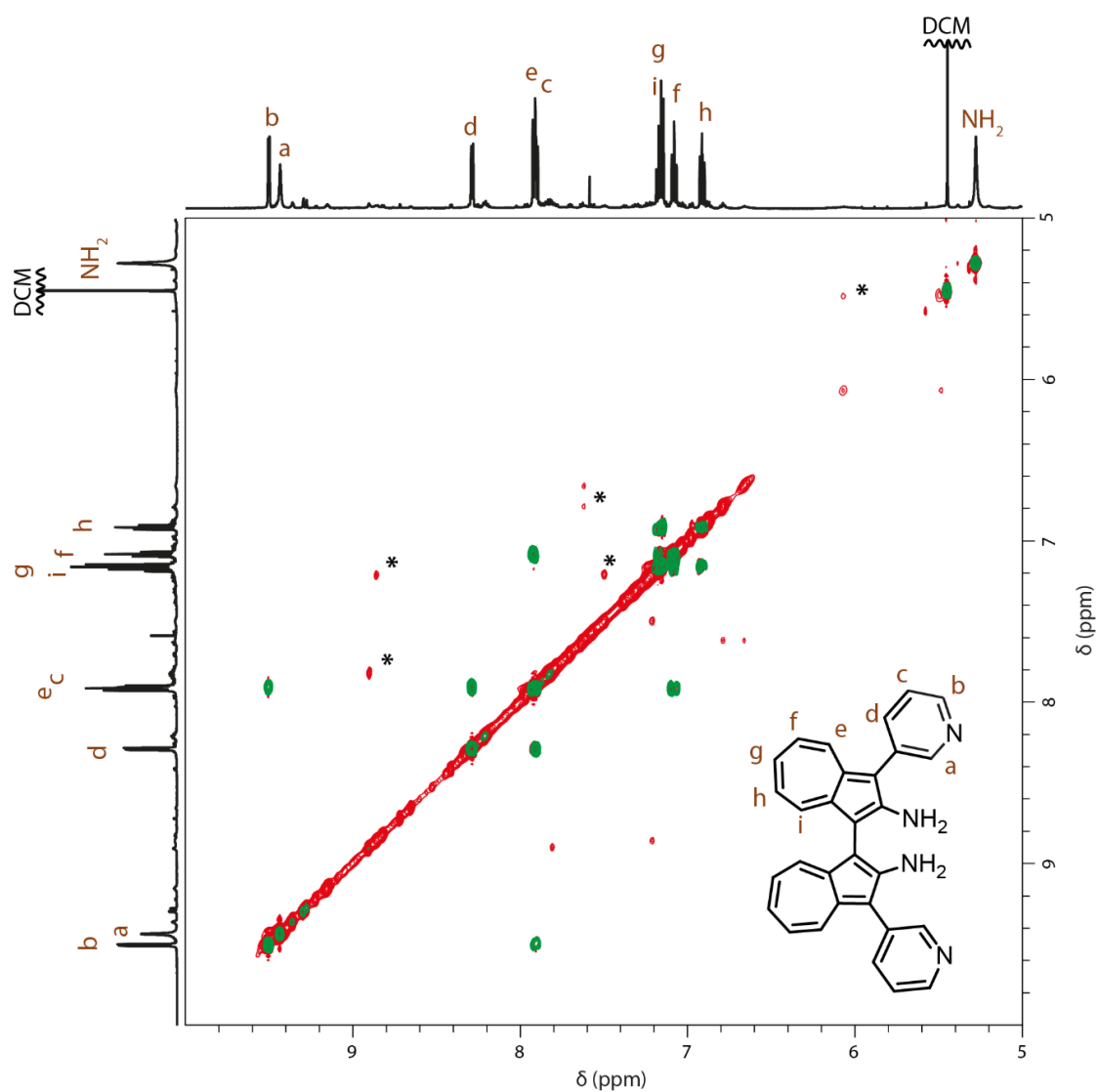


Figure S4.24: ^1H - ^1H COSY (green traces) and NOESY (red traces) NMR (600 MHz, 298 K, CD_3CN) spectra of $[\text{Pd}_2\text{BAAZU-1}^{\text{rac}}_4](\text{BF}_4)_4$. NOE correlation belonging to trace species are highlighted with an asterisk.

4.9.4.1.1 Evolution over time

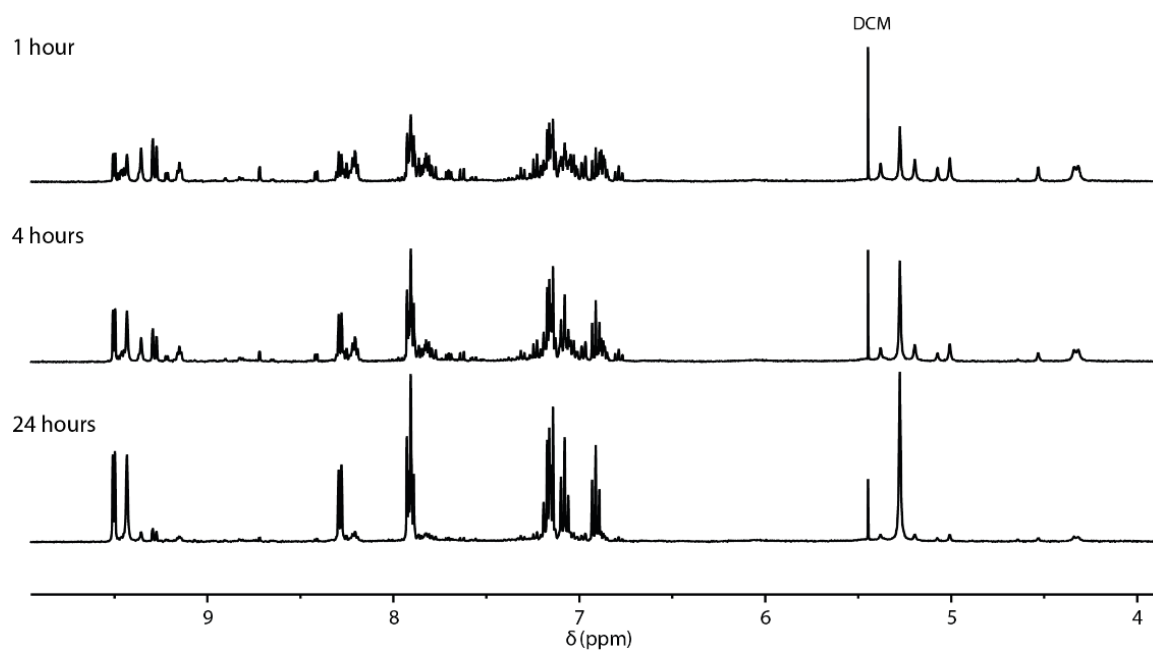


Figure S4.25: $^1\text{H-NMR}$ (500 MHz, CD_3CN , 298 K) of cage $[\text{Pd}_2\text{BAAZU-1}^{\text{rac}}_4](\text{BF}_4)_4$ over time while heating at 70°C .

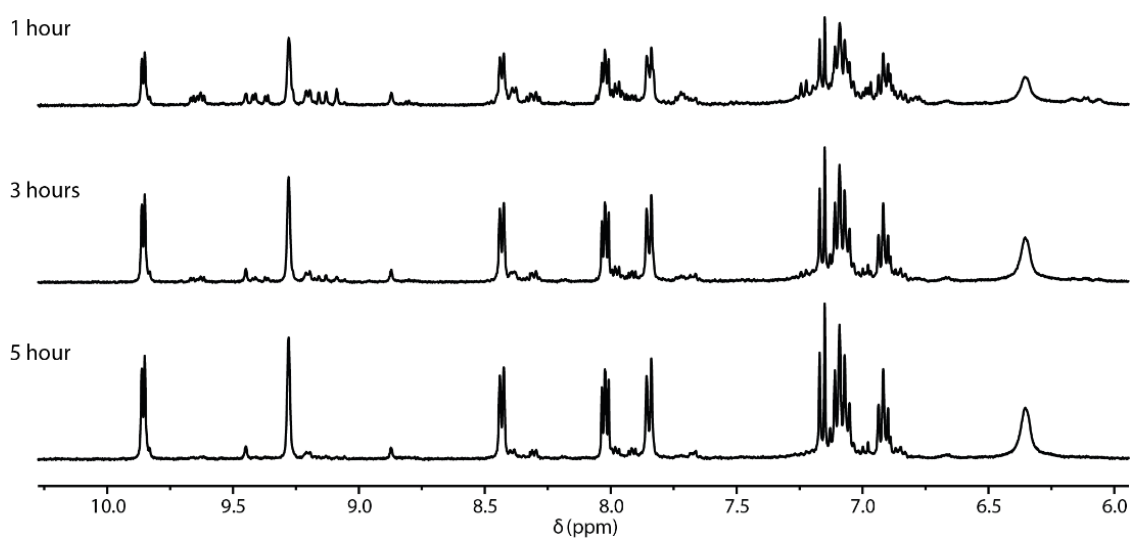


Figure S4.26: $^1\text{H-NMR}$ (500 MHz, $\text{DMSO-}d_6$, 298 K) of cage $[\text{Pd}_2\text{BAAZU-1}^{\text{rac}}_4](\text{BF}_4)_4$ over time while heating at 70°C .

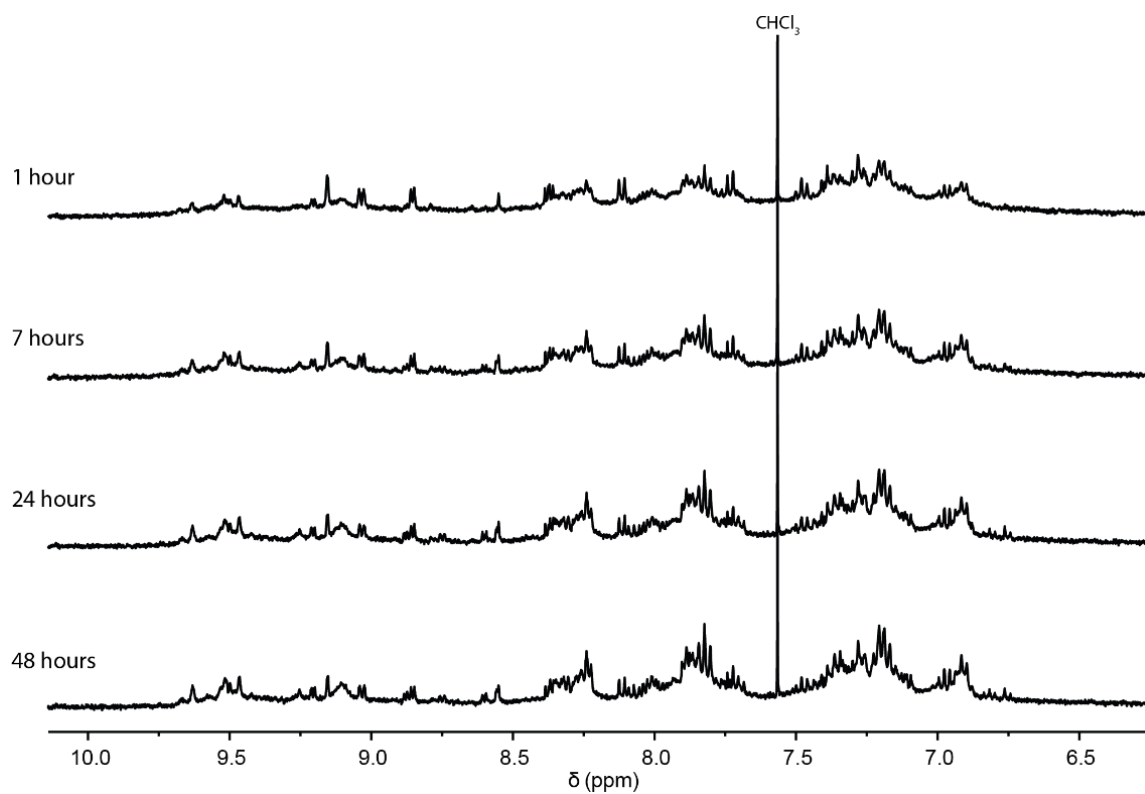


Figure S4.27: $^1\text{H-NMR}$ (500 MHz, CD_3NO_2 , 298 K) of cage $[\text{Pd}_2\text{BAAZU-1}^{\text{rac}}_4](\text{BF}_4)_4$ over time while heating at 70°C .

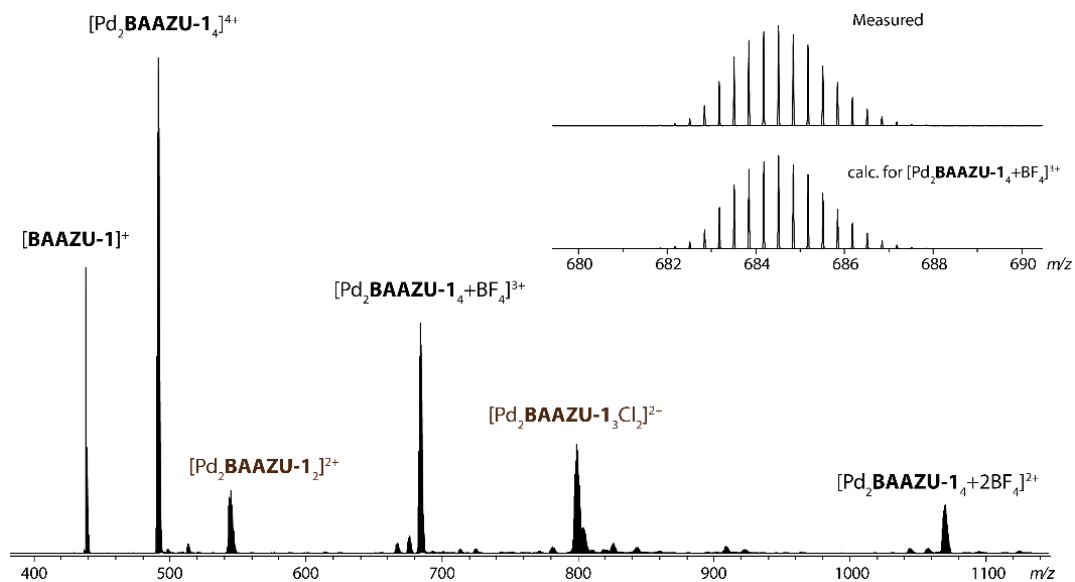


Figure S4.28: ESI-MS spectrum of cage $[\text{Pd}_2\text{BAAZU-1}^{\text{rac}}_4](\text{BF}_4)_4$ after 1 hour.

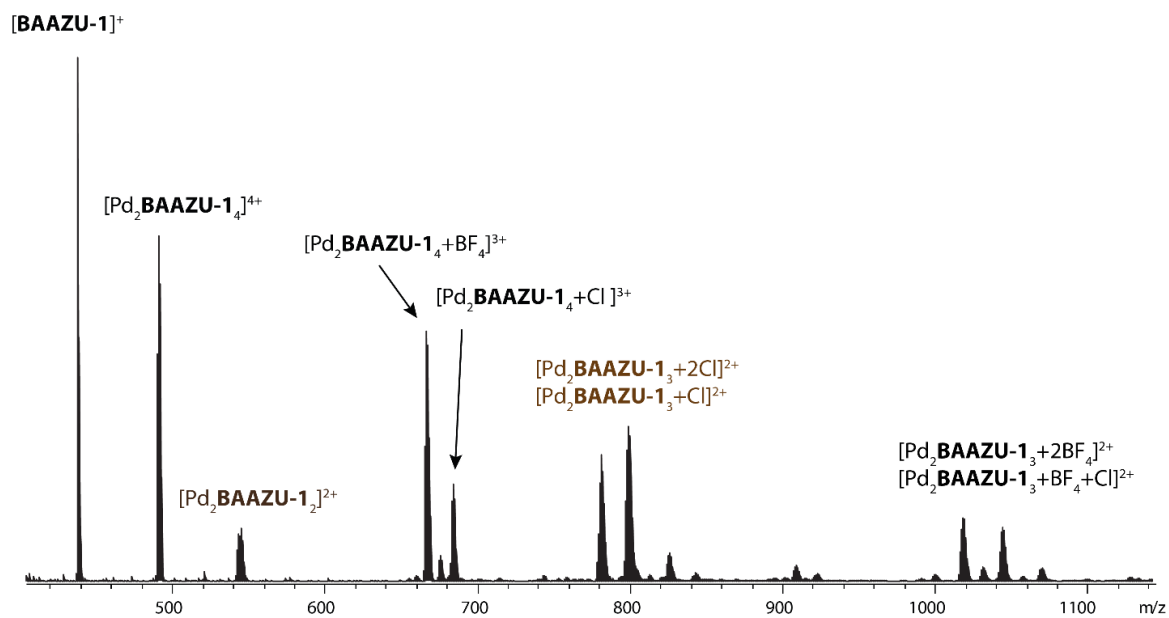


Figure S4.29: ESI-MS spectrum of cage $[Pd_2BAAZU-1^{rac_4}](BF_4)_4$ after 24 h in CD_3CN , at $70^\circ C$. The chloride adducts are probably formed because of a contamination in the spectrometer.

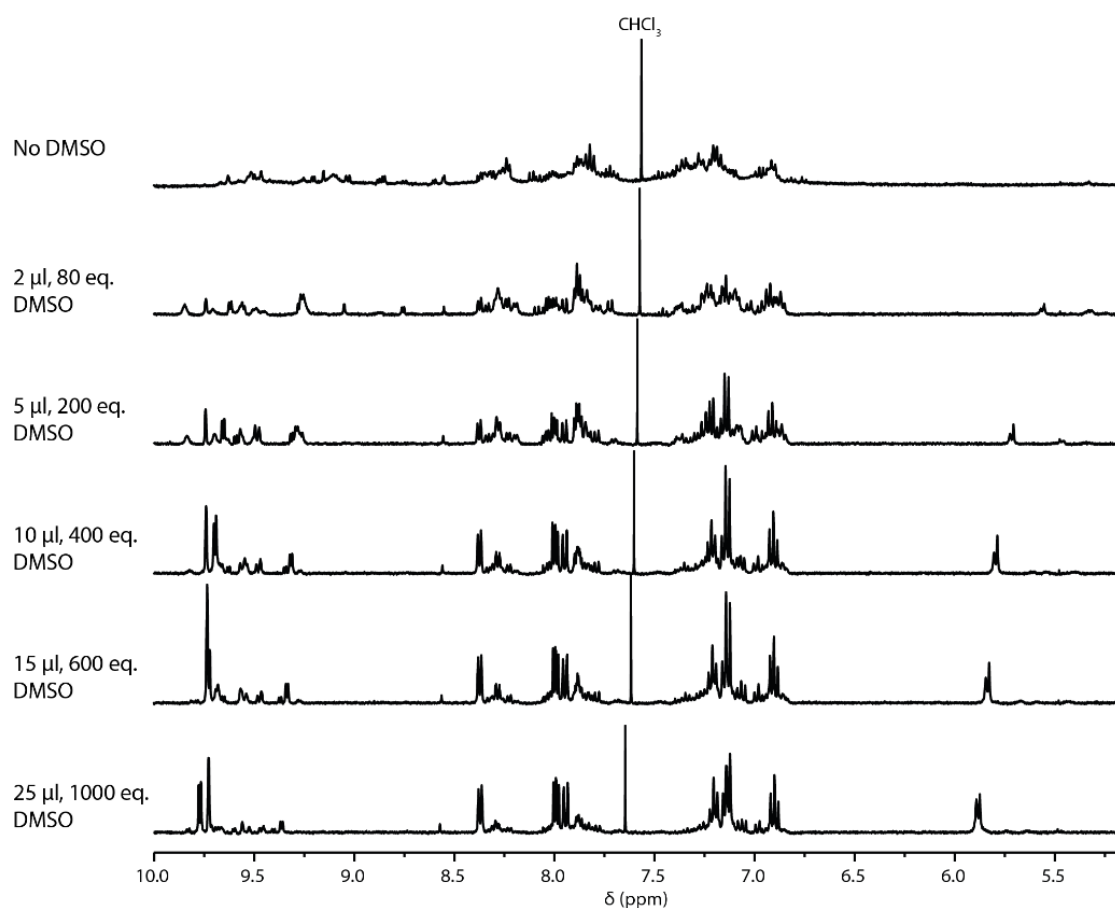
4.9.4.1.2 Titration of Pd₂BAAZU-1^{rac}₄ in CD₃NO₂ with DMSO

Figure S4.30: ¹H-NMR (500 MHz, CD₃NO₂, 298 K) of [Pd₂BAAZU-1^{rac}₄](BF₄)₄ (1.4 mM in ligand equivalent) titrated with DMSO-*d*₆. The DMSO amount is expressed as equivalents to the cage.

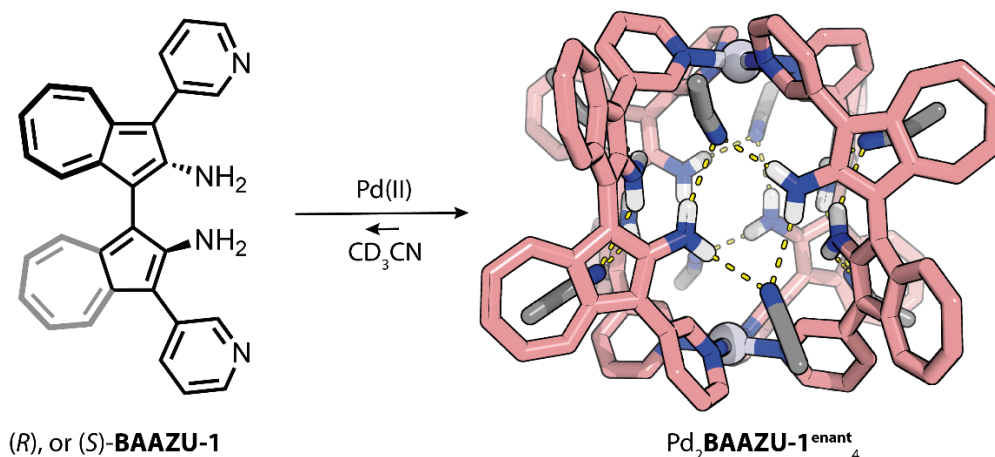
4.9.4.2 $\text{Pd}_2\text{BAAZU-1}^{\text{enant}}_4$ 

Figure S4.31: Formation of $\text{Pd}_2\text{BAAZU-1}^{\text{enant}}_4$ from the enantiopure (*R*) or (*S*)-**BAAZU-1**.

The coordination cage $[\text{Pd}_2\text{BAAZU-1}^{\text{enant}}_4](\text{BF}_4)_4$ was synthesised as a 0.7mM solution in CD_3CN according to the general procedure, using $[\text{Pd}(\text{CH}_3\text{CN})_4](\text{BF}_4)_4$ as the palladium (II) salt and enantiopure (*R*)- or (*S*)-**BAAZU-1**.

$^1\text{H-NMR}$ (600 MHz, CD_3CN) δ 8.75 (s, 2H), 8.44 (dd, $J = 5.9, 1.3$ Hz, 2H), 8.33 (dd, $J = 7.9, 1.7$ Hz, 2H), 7.90 (d, $J = 10.0$ Hz, 2H), 7.73 (dd, $J = 7.9, 5.9$ Hz, 2H), 7.66 (d, $J = 10.0$ Hz, 2H), 7.34 (t, $J = 9.5$ Hz, 2H), 7.20 (t, $J = 10.0$ Hz, 2H), 7.10 (t, $J = 9.6$ Hz, 2H), 5.41 (s, 4H).

Due to the very long acquisition needed for $^{13}\text{C-NMR}$ and concerns over partial epimerisation of the compound over this period, the $^{13}\text{C-NMR}$ spectrum was not measured in this case.

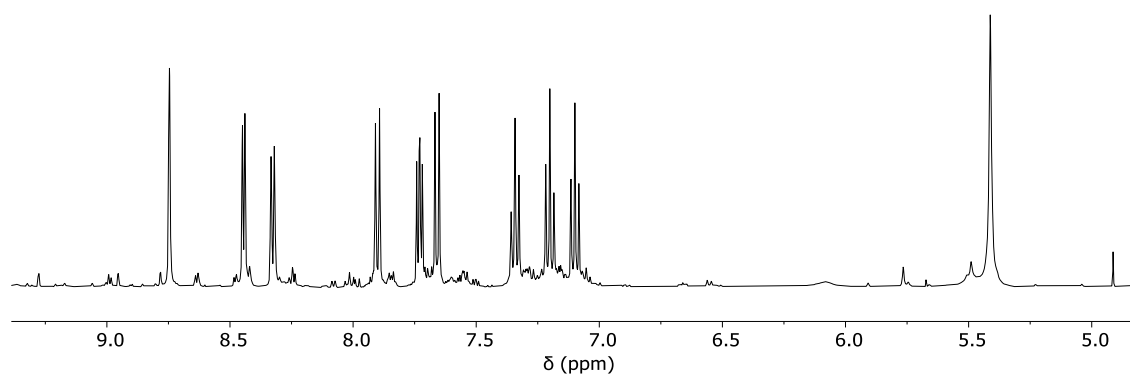


Figure S4.32: $^1\text{H-NMR}$ (600 MHz, 298 K, CD_3CN) spectrum of $[\text{Pd}_2\text{BAAZU-1}^{\text{enant}}_4](\text{BF}_4)_4$.

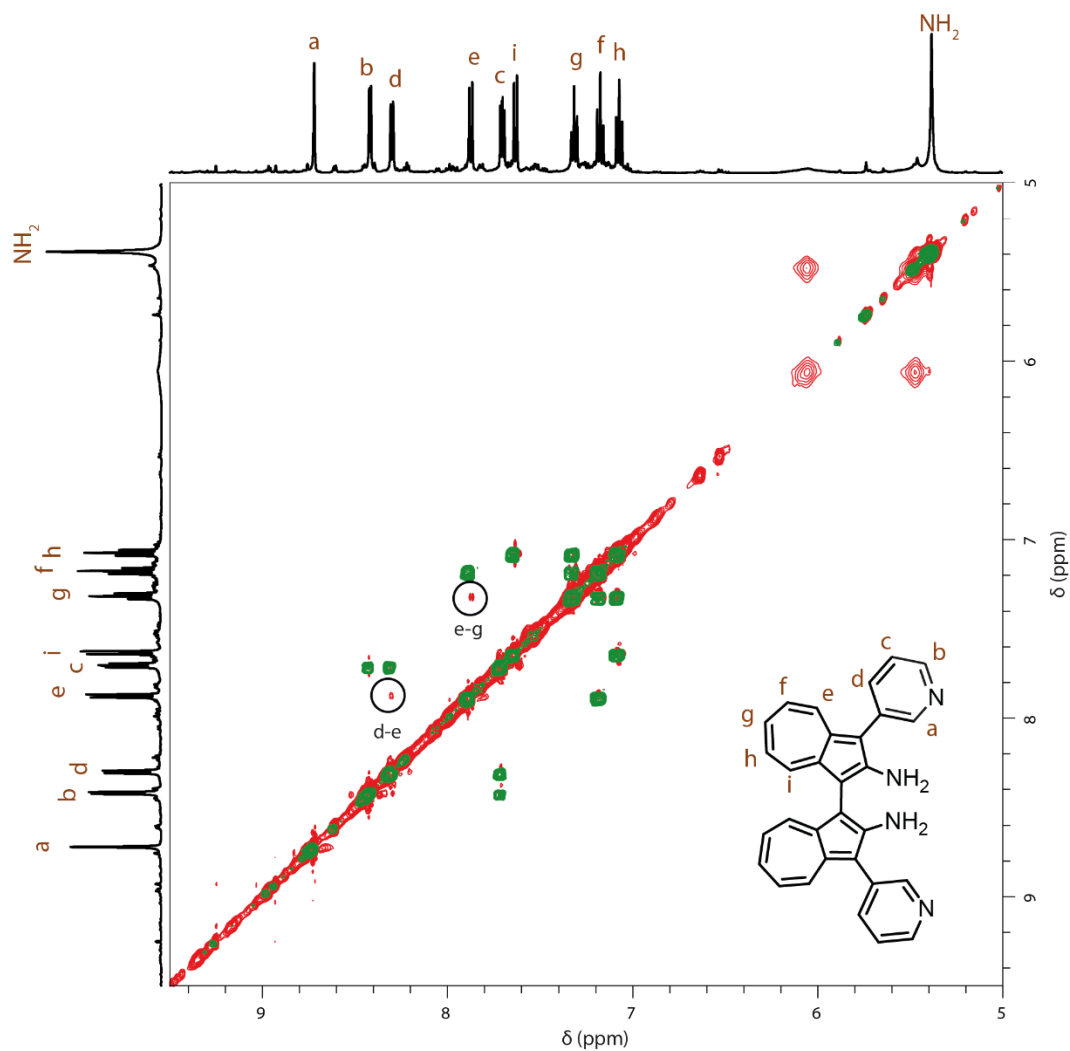


Figure S4.33: ¹H-¹H COSY (green traces) and NOESY (red traces) NMR (600 MHz, 298 K, CD₃CN) spectra of [Pd₂BAAZU-1^{enant}₄](BF₄)₄.

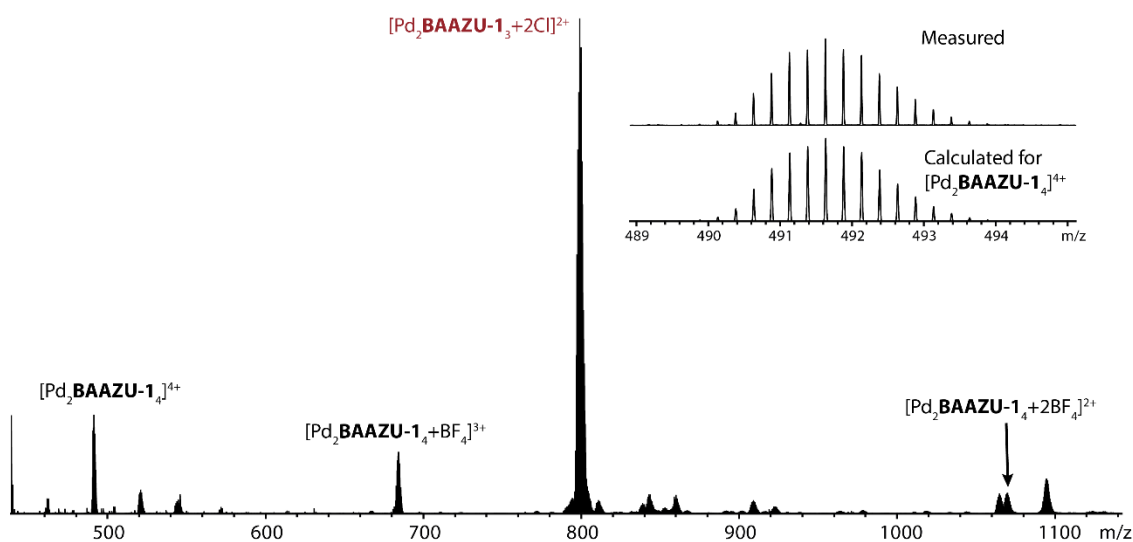


Figure S4.34: ESI-MS spectrum of cage [Pd₂BAAZU-1^{enant}₄](BF₄)₄ after 24 h in CD₃CN, at 70°C. The chloride adducts are probably formed because of a contamination in the spectrometer.

4.9.4.3 $\text{Pd}_2\text{BAAZU-2}^{\text{rac}}_4$

The coordination cages $[\text{Pd}_2\text{BAAZU-2}^{\text{rac}}_4](\text{BF}_4)_4$ were synthesised as a 0.7 mM solution in CD_3CN , $\text{DMSO-}d_6$, or CD_3NO_2 according to the general procedure, using $[\text{Pd}(\text{CH}_3\text{CN})_4](\text{BF}_4)_4$ as the palladium (II) salt and the racemate of **BAAZU-2**. A mixture of isomers was obtained in every tested solvent.

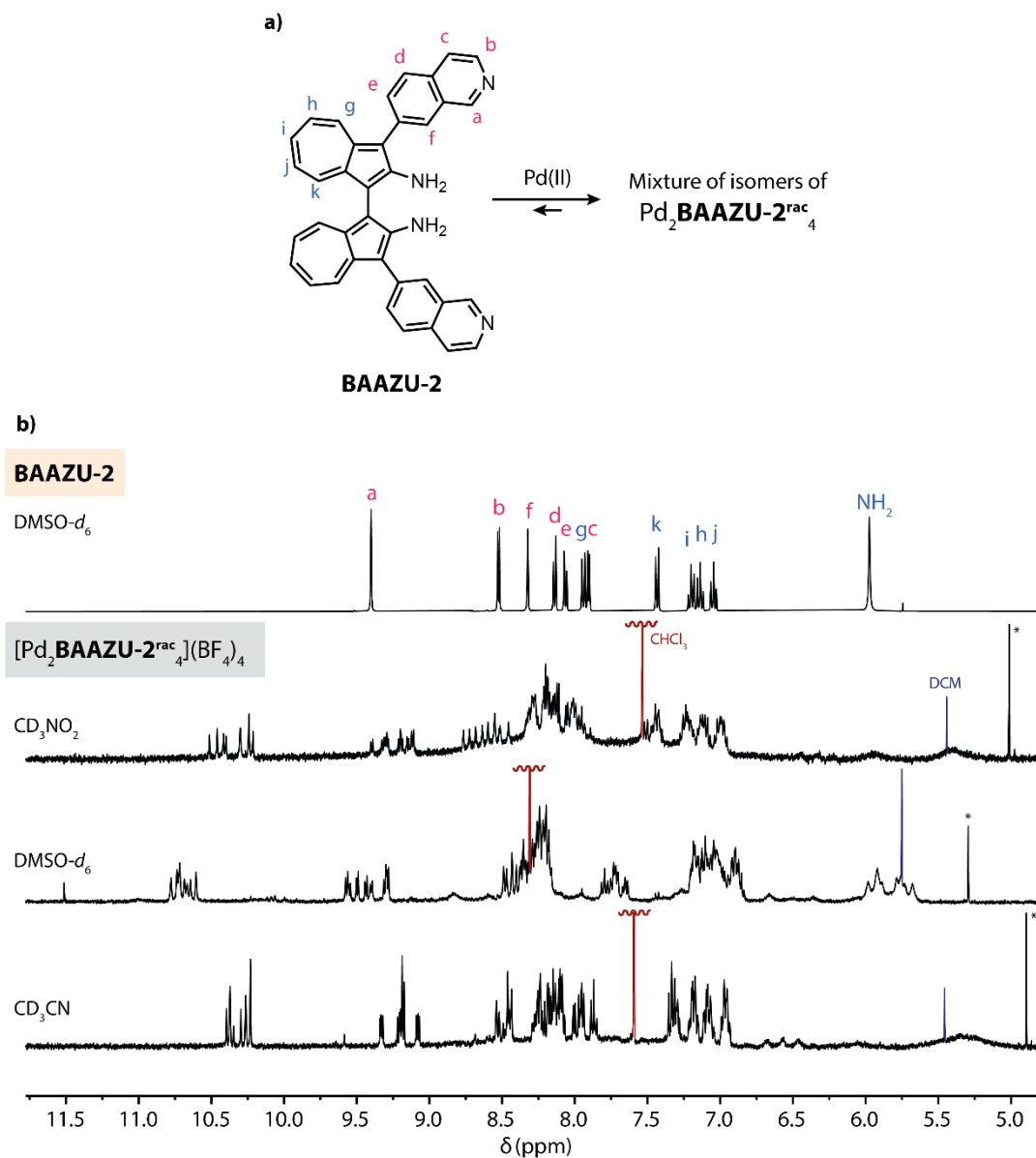


Figure S4.35: a) Scheme of the synthesis of the mixture of the isomers of $\text{Pd}_2\text{BAAZU-2}^{\text{rac}}_4$. b) $^1\text{H-NMR}$ (500 MHz, 298 K) of **BAAZU-2**, and of the $[\text{Pd}_2\text{BAAZU-2}^{\text{rac}}_4](\text{BF}_4)_4$ mixtures in CD_3NO_2 , $\text{DMSO-}d_6$, and CD_3CN .

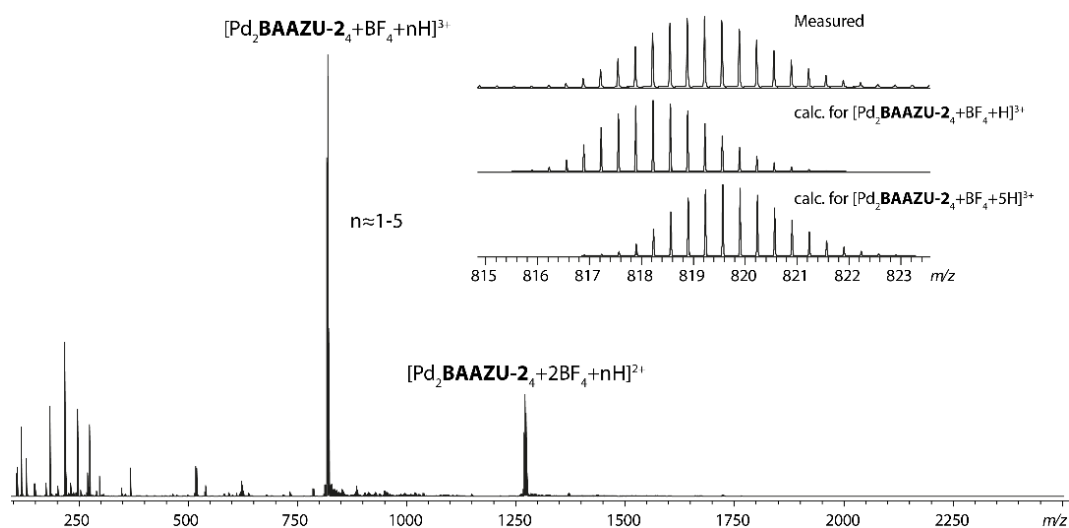


Figure S4.36: ESI-MS spectrum of cage $[\text{Pd}_2\text{BAAZU-2}^{\text{rac}}_4](\text{BF}_4)_4$ prepared in CD_3NO_2 .

4.9.4.4 $\text{Pd}_2\text{BAAZU-2}^{\text{enant}}_4$

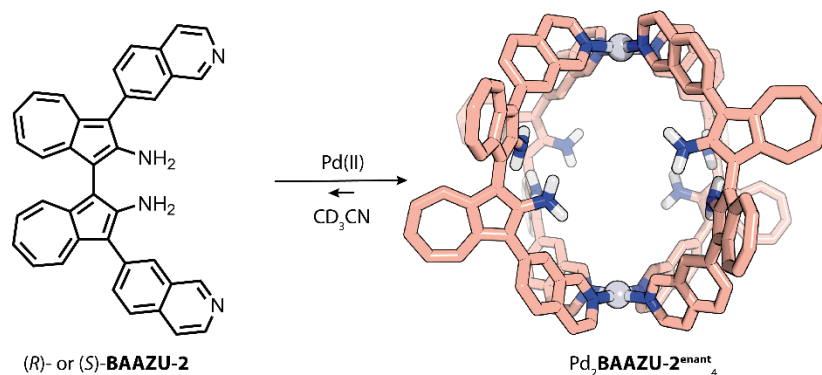


Figure S4.37: Formation of $\text{Pd}_2\text{BAAZU-2}^{\text{enant}}_4$ from the enantiopure (*R*) or (*S*)-**BAAZU-2**.

The coordination cage $[\text{Pd}_2\text{BAAZU-2}^{\text{enant}}_4]$ was synthesised from the enantiopure ligand **BAAZU-2** with either BF_4^- or BArF_{20}^- counteranions from the corresponding Pd(II) salt in CD_3CN as a 0.7 mM solution. The following shifts are from the BArF_{20}^- species.

$^1\text{H-NMR}$ (600 MHz, CD_3CN) δ 10.08 (s, 2H), 9.18 (d, $J = 6.7$ Hz, 2H), 8.42 – 8.39 (m, 2H), 8.26 (dd, $J = 8.3, 1.7$ Hz, 2H), 8.15 (d, $J = 8.3$ Hz, 2H), 8.11 (d, $J = 6.8$ Hz, 2H), 8.00 – 7.95 (m, 2H), 7.35 (dd, $J = 10.2, 1.0$ Hz, 2H), 7.23 – 7.17 (m, 2H), 7.10 (t, $J = 9.8$ Hz, 2H), 6.98 (ddd, $J = 10.0, 9.0, 0.9$ Hz, 2H), 5.29 (s, 4H).

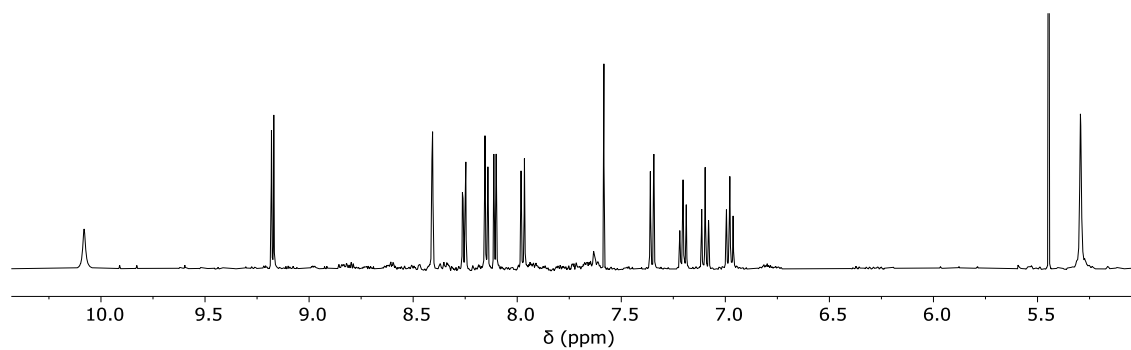


Figure S4.38: ^1H -NMR (600 MHz, 298 K, CD_3CN) spectrum of $[\text{Pd}_2\text{BAAZU-2}^{\text{enant}}_4](\text{BArF}_{20})_4$.

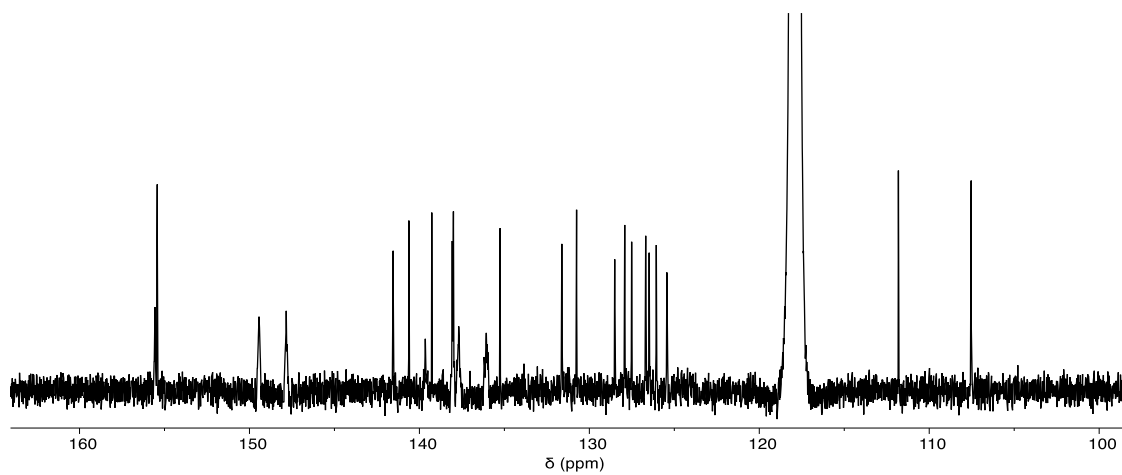


Figure S4.39: ^{13}C -NMR (151 MHz, 298 K, CD_3CN) spectrum of $[\text{Pd}_2\text{BAAZU-2}^{\text{enant}}_4](\text{BArF}_{20})_4$.

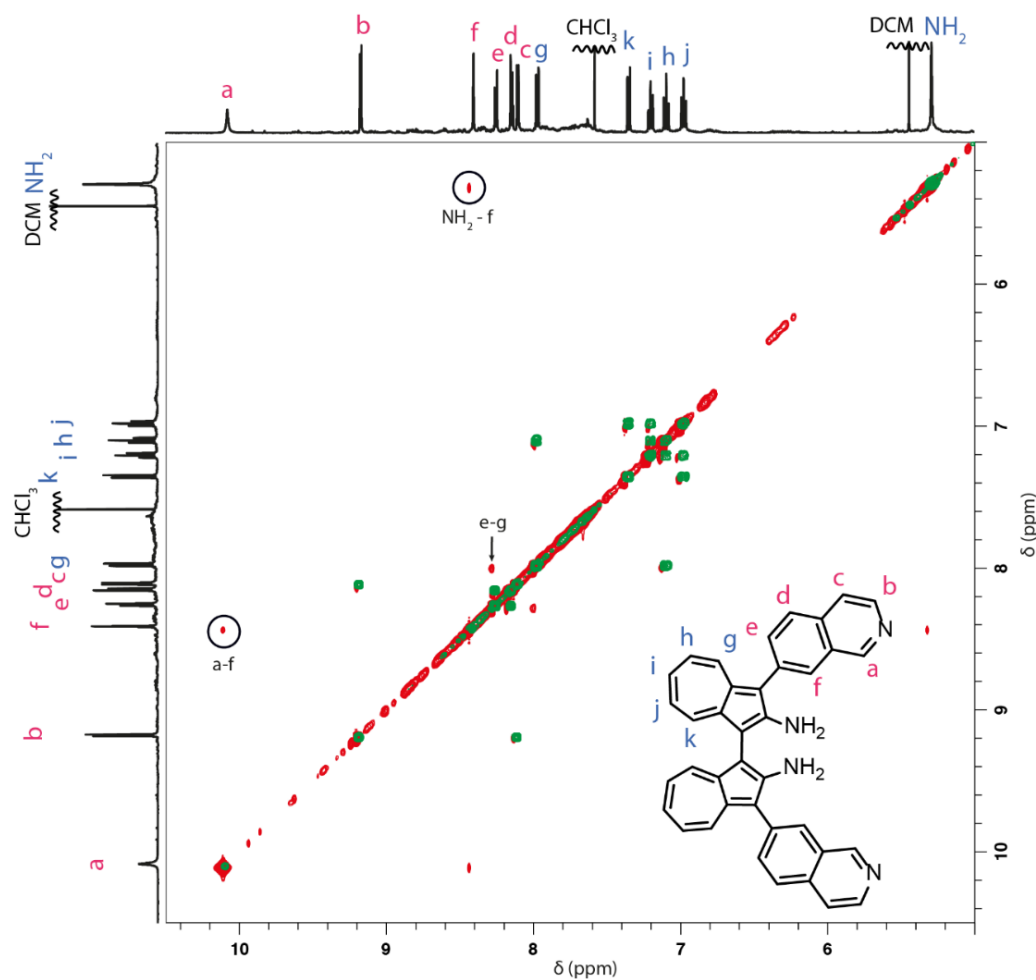


Figure S4.40: ^1H - ^1H COSY (green traces) and NOESY (red traces) NMR (600 MHz, 298 K, CD_3CN) spectra of $[\text{Pd}_2\text{BAAZU-2}^{\text{enant}}_4](\text{BARF}_{20})_4$. Important NOE correlations are highlighted.

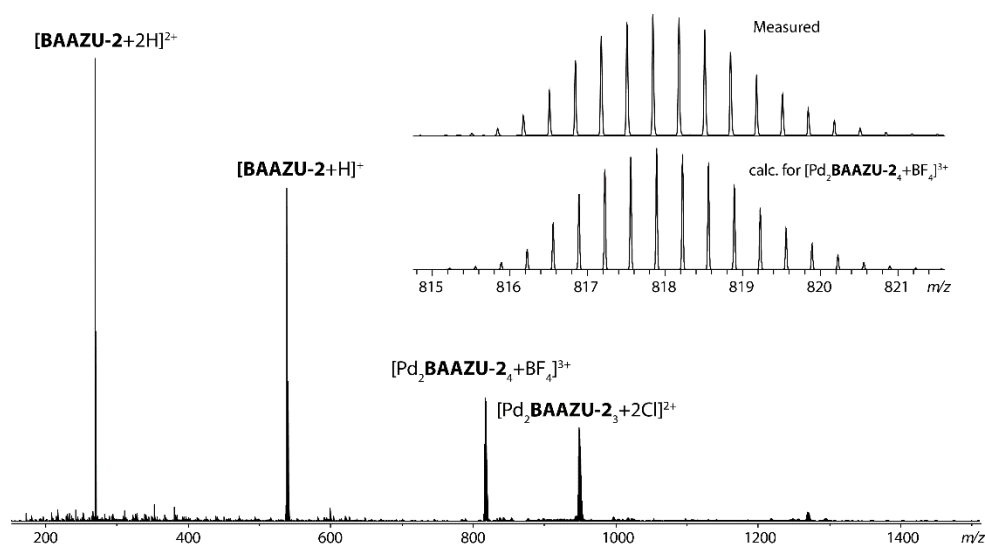


Figure S4.41: ESI-MS spectrum of cage $[\text{Pd}_2\text{BAAZU-2}^{\text{enant}}_4](\text{BF}_4)_4$.

4.9.5 Circular dichroism

Cuvette path length: 2mm (except when noted). Concentration in ligand: 1.25 mM or 0.125 mM.

Intermediate 8

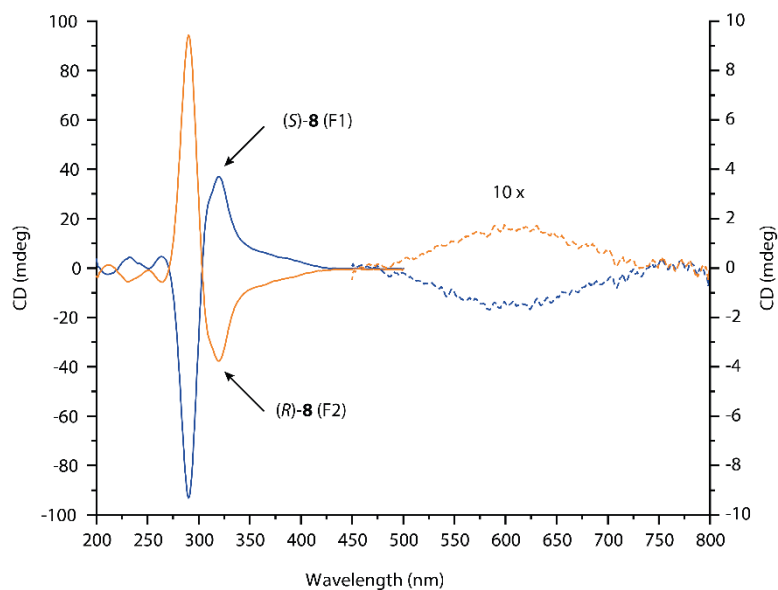


Figure S4.42: Circular dichroism of the two fractions of the intermediate **8**. The 450-800 nm concentrated spectra are plotted on the right y-axis.

BAAZU-1

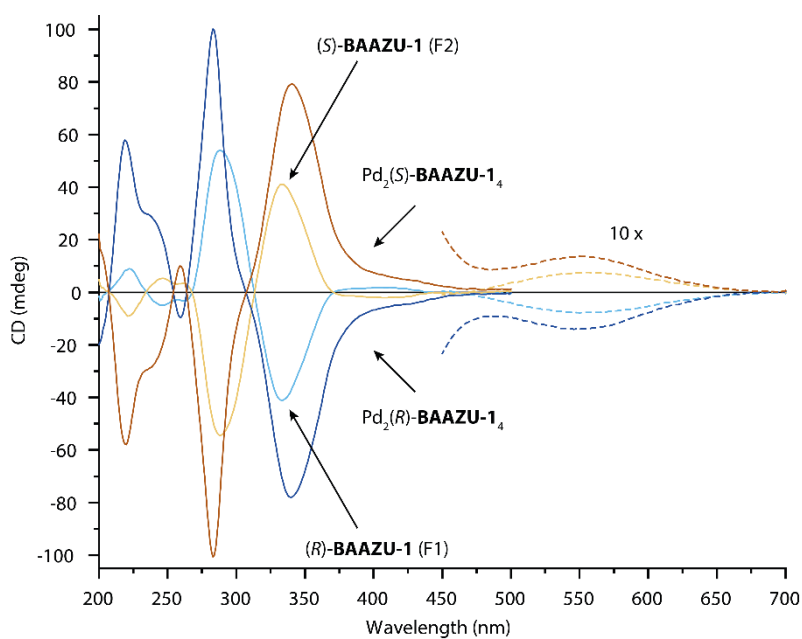


Figure S4.43: Circular dichroism of the two fractions of the **BAAZU-1** ligand and of the corresponding $[\text{Pd}_2\text{BAAZU-1}^{\text{enant}_4}](\text{BF}_4)_4$ in acetonitrile (0.125 mM: continuous lines, 1.25 mM: dashed lines). Due to its low solubility, the higher concentration data for pure ligand **BAAZU-1** was recorded at 0.25 mM with a cuvette with a 1 cm path length.

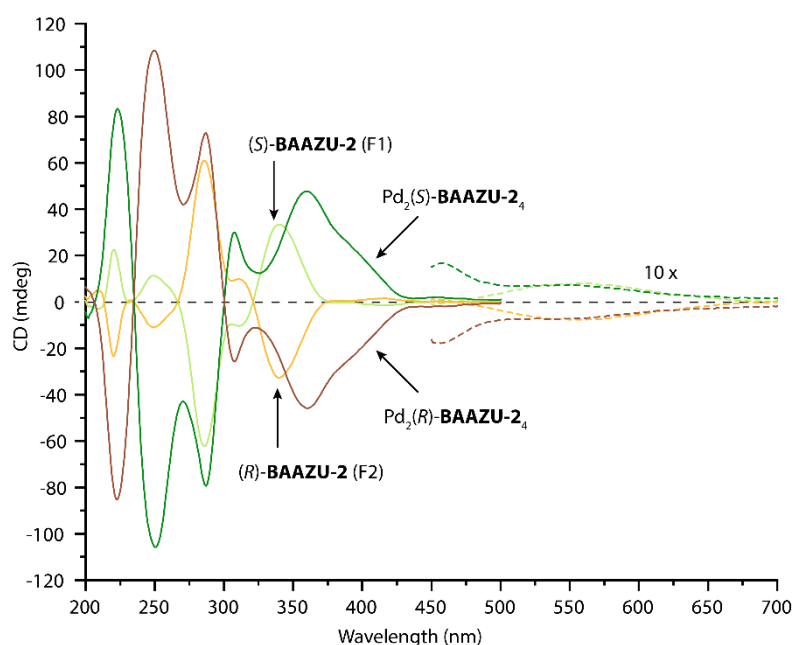
BAAZU-2

Figure S4.44: Circular dichroism of the two fractions of the **BAAZU-2** ligand and of the corresponding $[\text{Pd}_2\text{BAAZU-2}^{\text{enant}}_4](\text{BF}_4)_4$ in acetonitrile (0.125 mM: continuous lines, 1.25 mM: dashed lines).

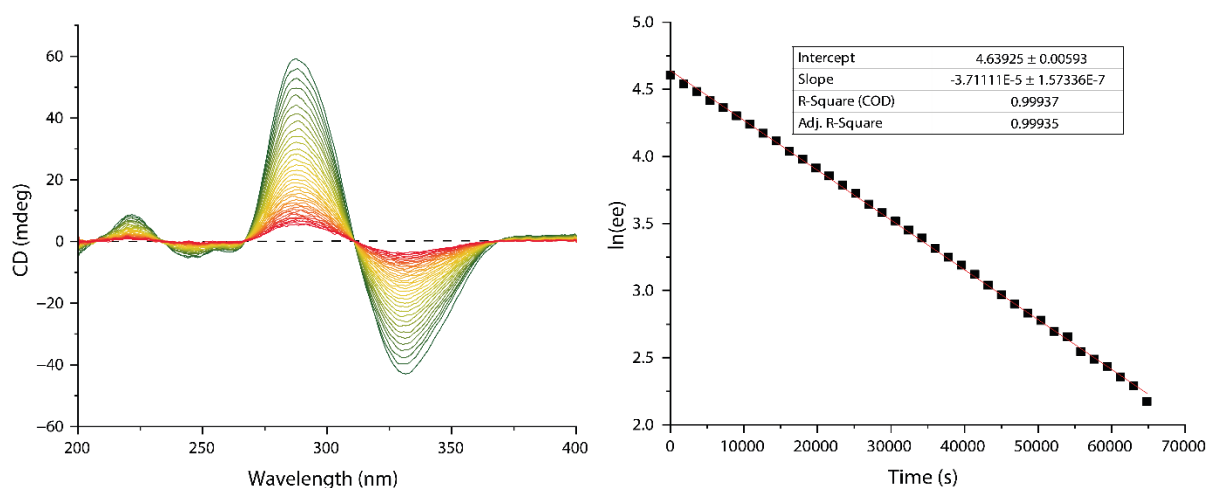
4.9.6 Racemisation4.9.6.1 **BAAZU-1**

Figure S4.45: (left) CD spectra of *S*-**BAAZU-1** in acetonitrile at 70°C. Each curve is measured with a 30 min. interval over 20.5 h. (right) natural logarithm of the enantiomeric excess (*ee*) over time. Red line: linear fit of the data.

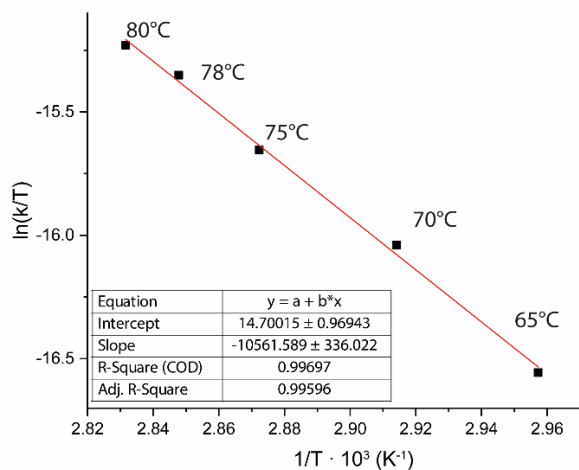


Figure S4.46: Eyring plot of the racemisation of **BAAZU-1** in acetonitrile.

The calculated kinetic parameters for the racemisation of **BAAZU-1** in acetonitrile are:

$$\Delta H^\ddagger = 87'809 \text{ kJ/mol}$$

$$\Delta S^\ddagger = -75.3 \text{ kJ/mol}$$

$$\Delta G^\ddagger(RT) = 110.3 \text{ kJ/mol} = 26.4 \text{ kcal/mol}$$

4.9.6.2 Racemisation of $[\text{Pd}_2\text{BAAZU-1}(\text{terpy})_2](\text{BF}_4)_4$

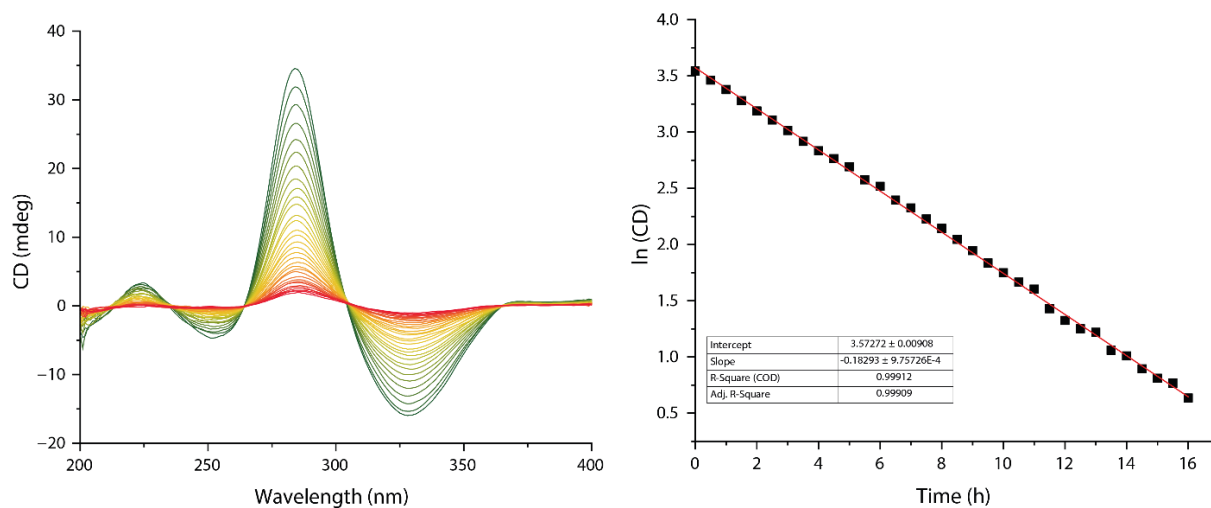


Figure S4.47: CD spectra of $[\text{Pd}_2(R)\text{-BAAZU-1}(\text{terpy})_2](\text{BF}_4)_4$ in acetonitrile at 70°C. Each curve is measured with a 30 min. interval over 16 h

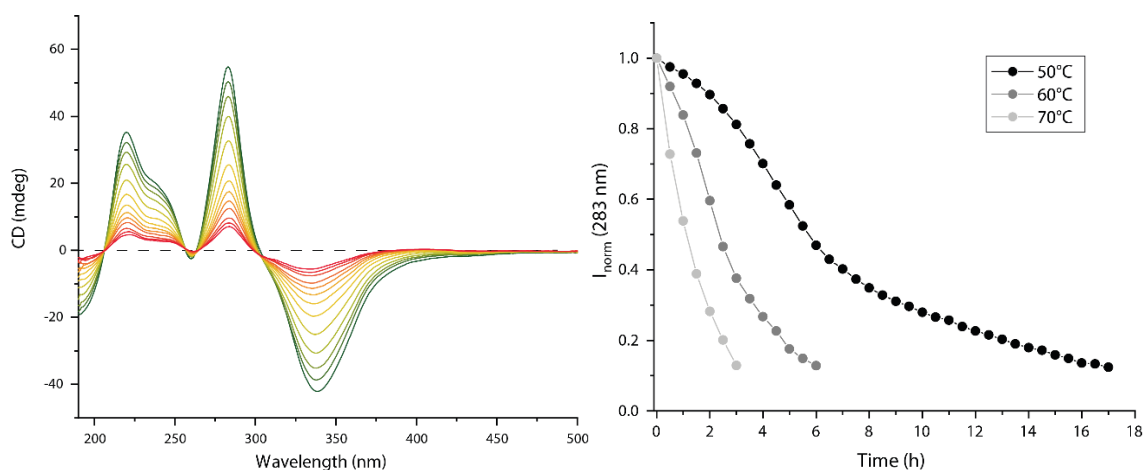
4.9.6.3 Racemisation of $[\text{Pd}_2\text{BAAZU-1}_4](\text{BF}_4)_4$ 

Figure S4.48: (left) CD spectra of $[\text{Pd}_2(R)\text{-BAAZU-1}_4](\text{BF}_4)_4$ in acetonitrile at 60°C . Each curve is measured with a 30 min. interval over 6 h. (right) plot of the normalised intensity of the band at 283 nm at 50°C , 60°C , and 70°C .

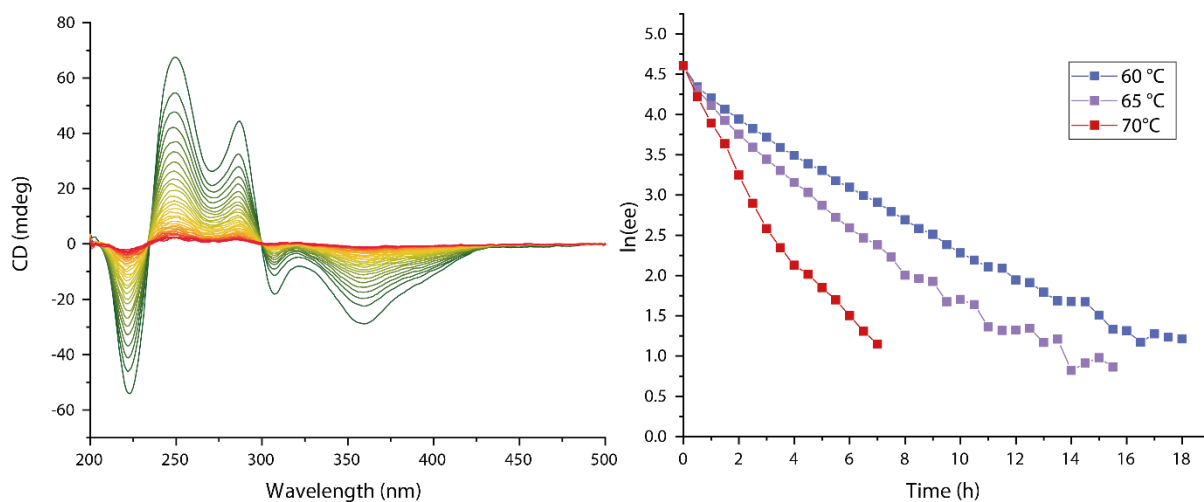
4.9.6.4 Racemisation of $[\text{Pd}_2\text{BAAZU-2}_4](\text{BF}_4)_4$ 

Figure S4.49: (left) CD spectra of $[\text{Pd}_2(R)\text{-BAAZU-2}_4](\text{BF}_4)_4$ in acetonitrile at 60°C . Each curve is measured with a 30 min. interval over 6 h. (right) plot of the normalised intensity of the band at 283 nm at 60°C , 65°C , and 70°C .

4.9.7 Host-guest experiments

Titration experiments were performed with $[\text{Pd}_2\text{BAAZU-2}^{\text{enant}}_4](\text{BArF}_{20})_4$ in CD_3CN solution. Association constants were calculated with BindFit (<http://app.supramolecular.org/bindfit/>). The effective concentration of the cage in the sample was compared by integration of the signals of the cage and of the tetrabutylammonium counterions of the guests. All titrations were done using aliquots of the same batch of cage solution.

4.9.7.1 $\text{Cr}^0(\text{CO})_6$

The titration was recorded by $^1\text{H-NMR}$, with a cage concentration of 0.16 mM. Calculated association constant: $111.4 \text{ M}^{-1} \pm 4.6 \%$. Due to the low binding affinity, the host-guest complex could not be detected by ESI-MS. Due to the absence of the signals from counterions, the effective concentration of the cage was determined from the calculated values of the next experiments.

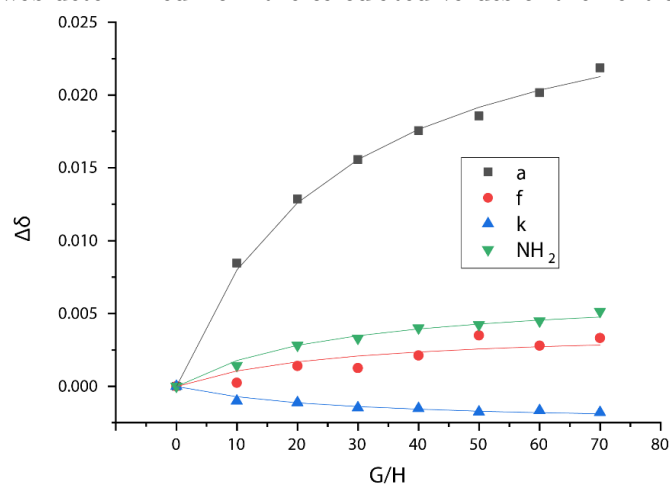


Figure S4.50: $^1\text{H-NMR}$ peak shifts upon addition of $\text{Cr}(\text{CO})_6$ to $[\text{Pd}_2\text{BAAZU-2}^{\text{enant}}_4](\text{BArF}_{20})_4$ in CD_3CN . Solid lines: fitting curves.

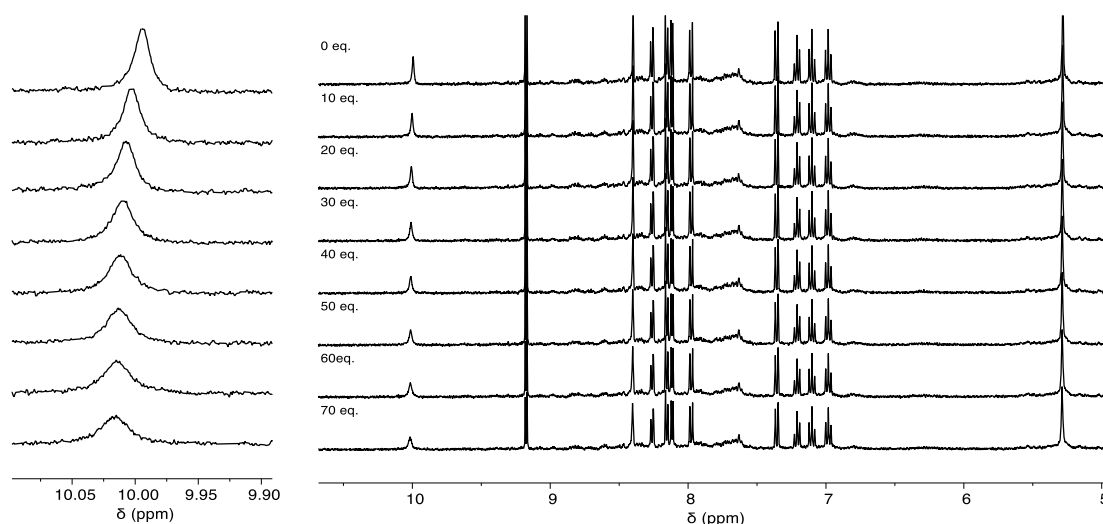


Figure S4.51: $^1\text{H-NMR}$ (500 MHz, 298 K, CD_3CN) titration of $[\text{Pd}_2\text{BAAZU-2}^{\text{enant}}_4](\text{BArF}_{20})_4$ upon addition of $\text{Cr}(\text{CO})_6$. The region of the **a** proton is zoomed in in the insert on the left.

4.9.7.2 $(\text{NBu}_4)_2[\text{Pt}^{\text{IV}}(\text{CN})_6]$

The titration was recorded by $^1\text{H-NMR}$, UV-Vis and CD. However, precipitation was directly observed after the addition of more than 1.2 eq. of the guest, preventing us from calculating an accurate binding constant. The binding constant calculated from the NMR data is: $86'681 \text{ M}^{-1} \pm 47\%$.

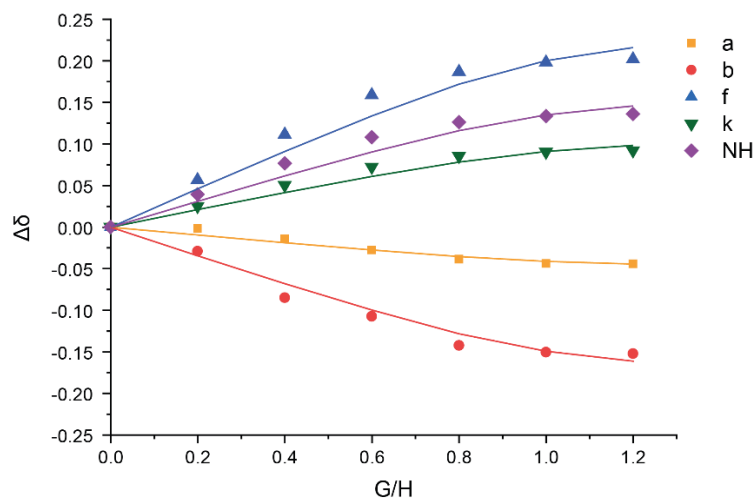


Figure S4.52: $^1\text{H-NMR}$ peak shifts upon addition of $(\text{NBu}_4)_2[\text{Pt}(\text{CN})_6]$ to $[\text{Pd}_2\text{BAAZU-2}^{\text{enant}}_4](\text{BArF}_{20})_4$ in CD_3CN . Solid lines: fitting curves.

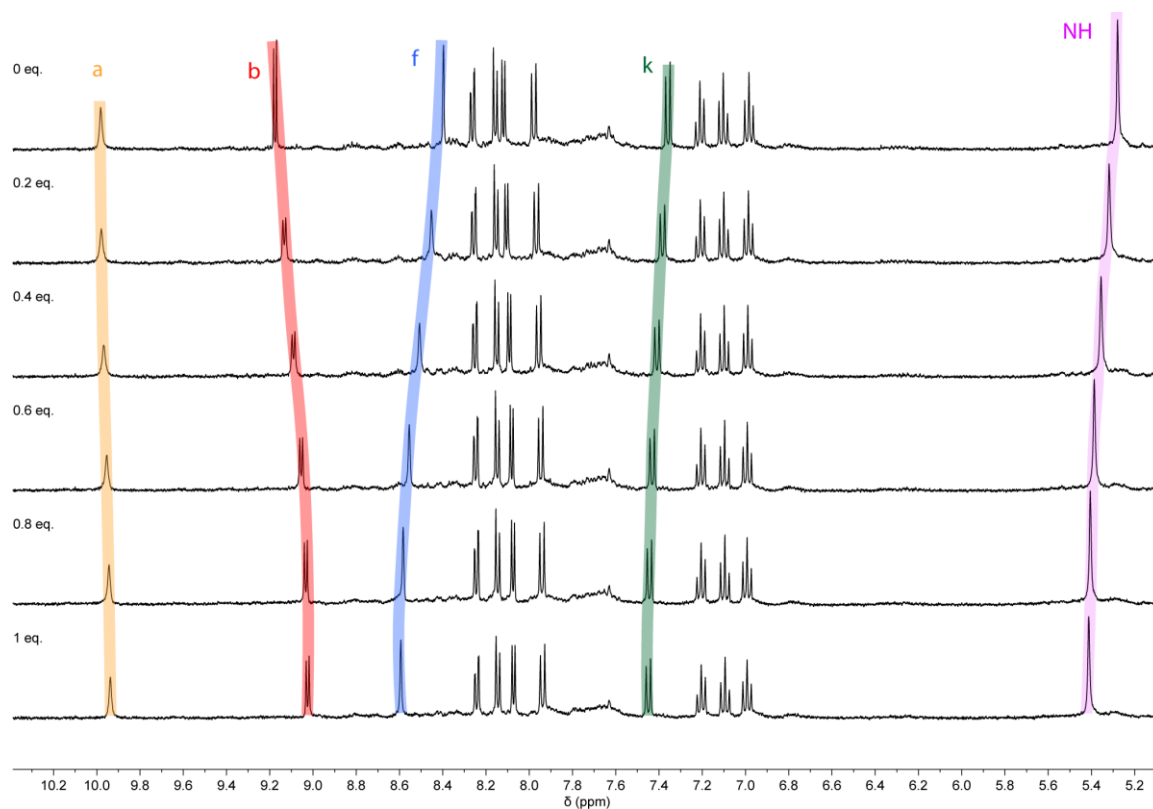


Figure S4.53: $^1\text{H-NMR}$ (500 MHz, 298 K, CD_3CN) titration of $[\text{Pd}_2\text{BAAZU-2}^{\text{enant}}_4](\text{BArF}_{20})_4$ upon addition of $(\text{NBu}_4)_2[\text{Pt}(\text{CN})_6]$.

4 – Solvent-directed chiral self-sorting of an azulene-based coordination cage

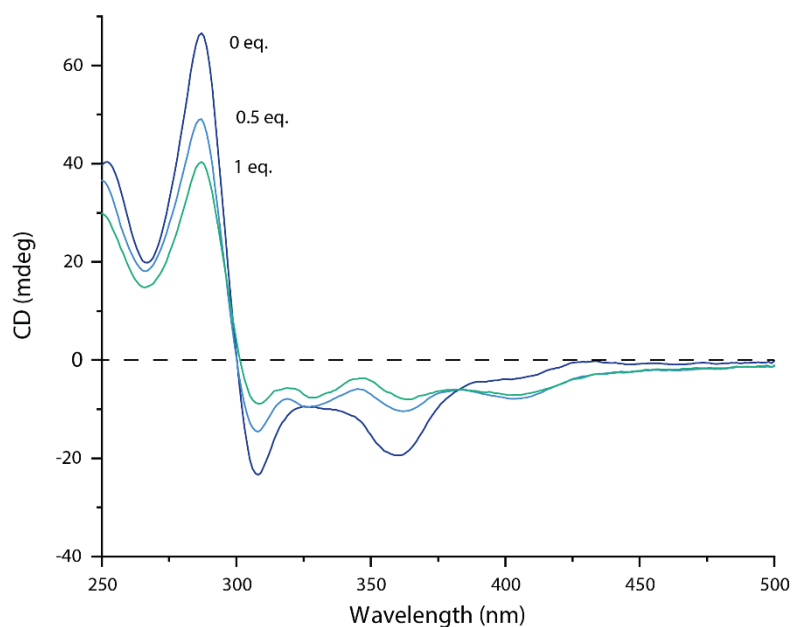


Figure S4.54: partial data of the titration of $[\text{Pd}_2(R)\text{-BAAZU-2}]_4(\text{BArF}_{20})_4$ by $(\text{NBu}_4)_2[\text{Pt}(\text{CN})_6]$ in CD_3CN measured by CD.

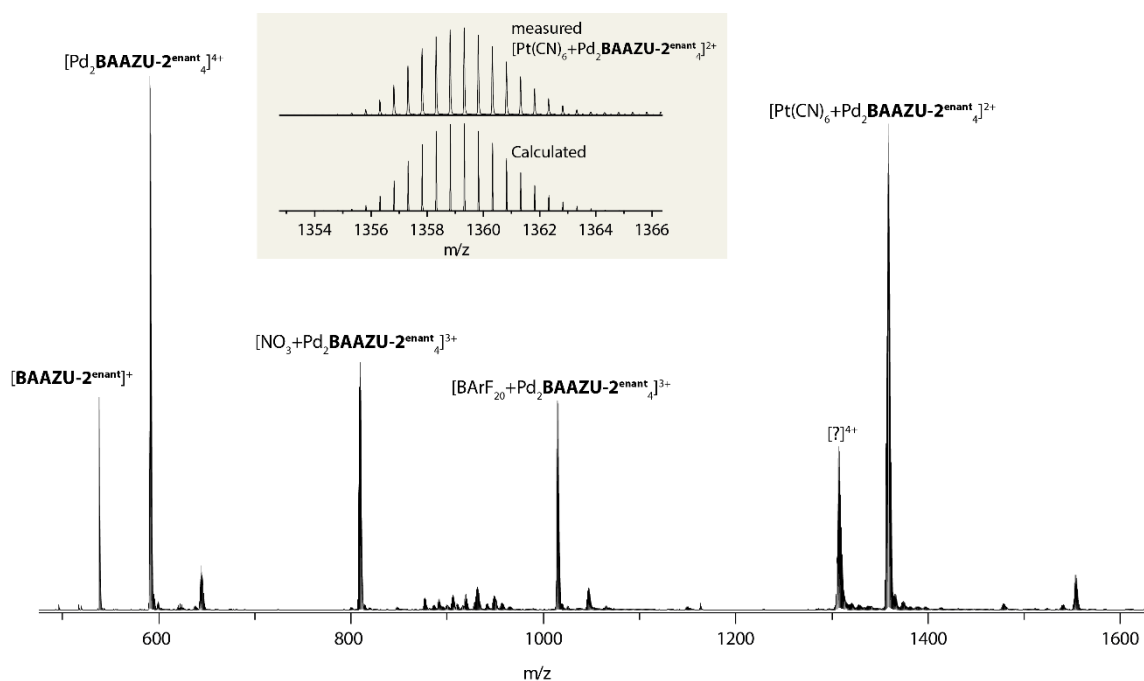


Figure S4.55: ESI-MS spectrum of host-guest complex $[\text{Pt}(\text{CN})_6]_6@[\text{Pd}_2\text{BAAZU-2enant}]_4(\text{BArF}_{20})_2$

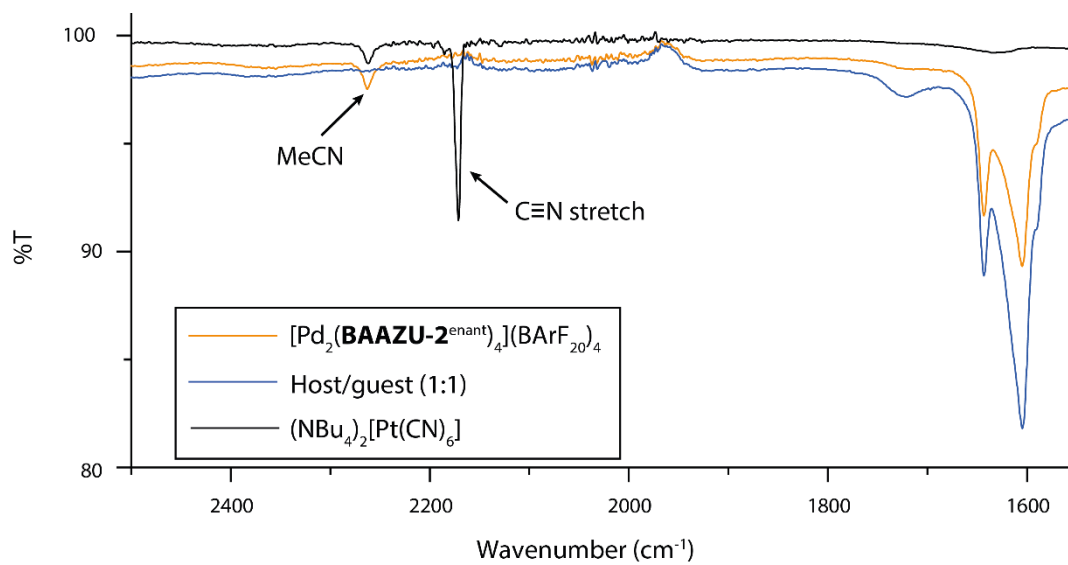


Figure S4.56: FT-IR spectra of (NBu₄)₂[Pt(CN)₆] (black), cage [Pd₂BAAZU-2^{enantiomer}]₄(BArF₂₀)₄ (orange), and their 1:1 host guest complex (blue).

4.9.7.3 Camphorsulfonate

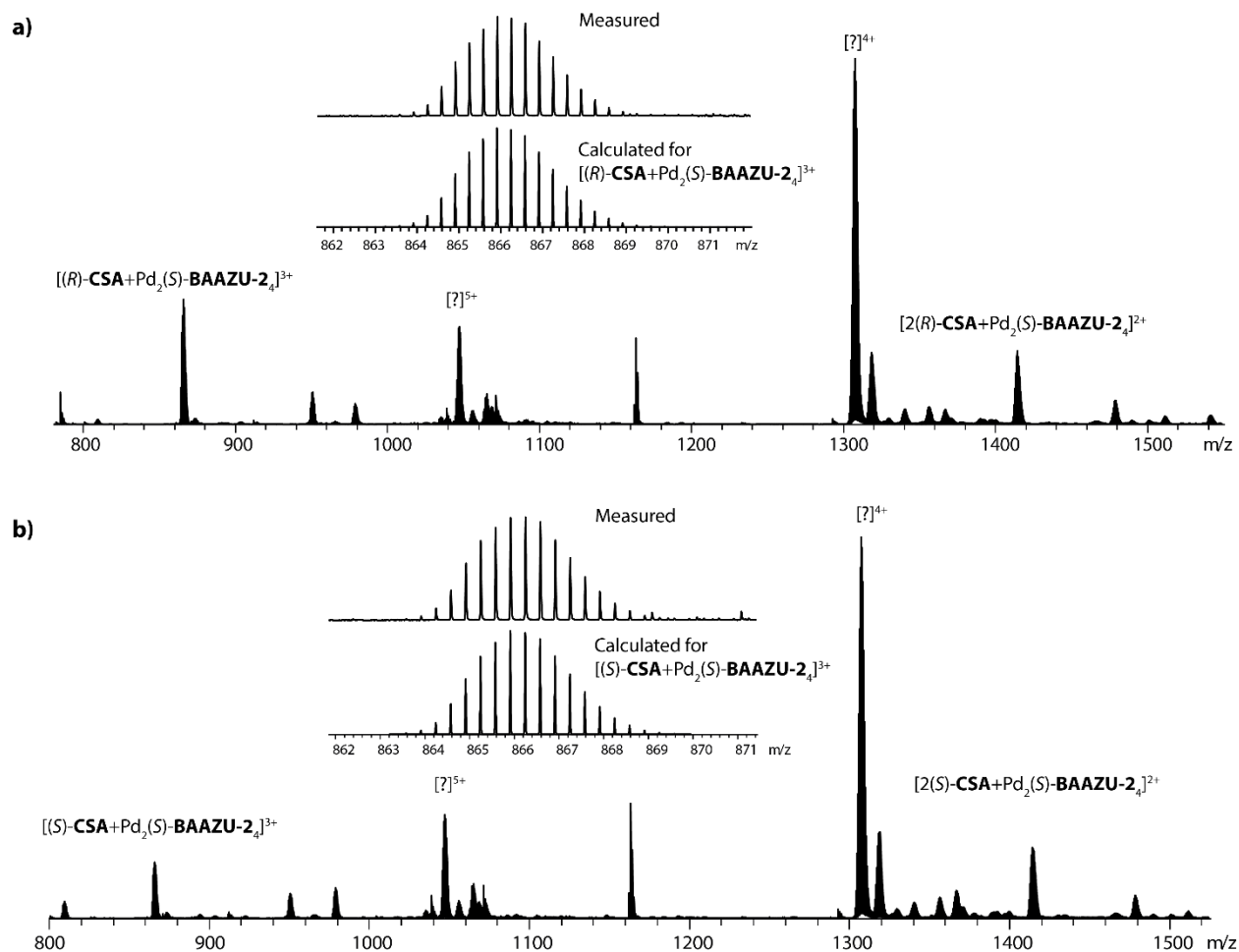


Figure S4.57: ESI-MS spectra of the host-guest complexes of cage $[\text{Pd}_2(\text{S})\text{-BAAZU-2}_4](\text{BARF}_{20})_4$ with (*R*)- and (*S*)-CSA ((a) and (b), respectively). A larger species was detected as well, but could not be identified, but is probably an adduct formed during the measurement.

4.9.8 Computations

All the .xyz files of the structures discussed here can be found on the shared folder of the group, under \User\Thesis_group_members\PhD\2024_10_Alexandre_Walther.

4.9.8.1 Computational investigation of the energetic ranking of the isomers

All geometries of the considered structures have been relaxed at the def2-SVP^[35,36]/ ω B97X-D3^[37] level of theory and harmonic frequencies have been evaluated at the same level of theory in order to verify that the obtained structure is a minimum. When necessary, the harmonic frequencies have been employed to estimate the Gibbs free energy. In order to have accurate single point energies a double hybrid functional has been employed (DSD-PBEP86 D3BJ^[38,39]/def2-TZVP^[35,36]). The CPCM implicit solvation model^[40] was used for both MeCN and DMSO; both solvents deliver the

same energetic ranking. For this reason, we have employed only the MeCN implicit solvation model throughout the investigation. Below an example of the ORCA input file concerning the single point calculations.

```
! DSD-PBEP86 D3BJ
! def2-TZVP def2-TZVP/C
! CPCM(ACETONITRILE)
%MAXCORE 9200
%PAL NPROCS 32 END
%cpcm
surfacetype vdw_gaussian
end
* xyzFILE 4 1 input.xyz
```

The eight explicit solvent molecules have been placed in the cage structure accordingly to the crystal structure of the *RSRS* and *RRRR* isomers and in similar positions around the two other isomers. Both MeCN and DMSO solvent molecules have been taken into account, based on observations from the crystallographic data.

Table S4.2: relative energies of the four different isomers of cage Pd₂BAAZU-1₄ with implicit and explicit solvation models.

Isomers	ΔE (kcal / mol)				ΔG (kcal / mol)		
	Implicit Solvent (MeCN)	8 MeCN	8 DMSO	4 MeCN + 4 DMSO	8 MeCN	8 DMSO	4 MeCN + 4 DMSO
<i>RRRR</i>	0	0	3	0	0	3	2
<i>RRSS</i>	8	7	11	13	4	9	12
<i>RSRS</i>	7	3	0	0	1	0	0
<i>SRRR</i>	4	6	7	8	6	7	5

Introducing explicit solvent molecules in the calculations significantly improves the agreement between the isomers' energetic ranking and the experimental observations: the *RRRR* and *RSRS* cages are the two most stable isomers, the other two isomers are ruled out, confirming experimental results from ¹H-NMR.

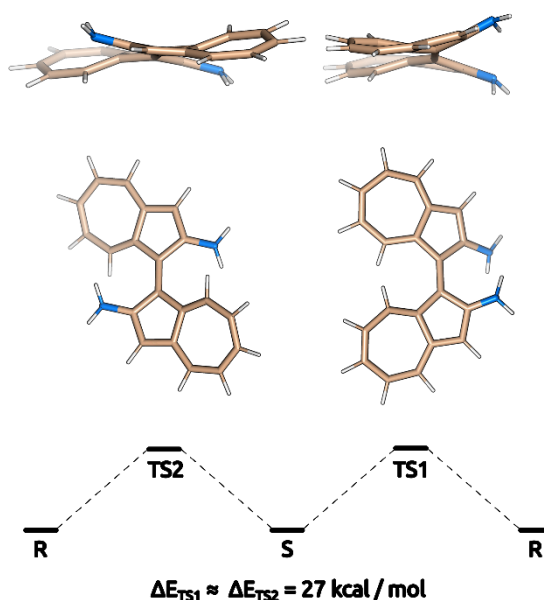
In order to further evaluate which of the two isomers is the most stable, we increased the complexity of our computational models by introducing the BF₄⁻ anion in the structures of the two isomers. The position of the anion was chosen accordingly to the X-ray structures of the two isomers: in the *RRRR* isomer the anion is located within the cage cavity and for *RSRS* isomer it is positioned outside. In order to compare the isomers on the same ground, i.e. having a molecule in the cage cavity for both of them, we consider an additional MeCN molecule, and we position it inside the *RSRS* cage (as observed in the X-ray structure) and on top of the *RRRR* cage, interacting with the Pd atom.

Table S4.3: relative energies of the *RRRR* and *RSRS* isomers of cage Pd₂BAAZU-1₄ with explicit solvent models, and one additional BF₄⁻ anion.

Isomers	ΔE (kcal / mol)	ΔG (kcal / mol)
	8 MeCN + BF ₄ ⁻ + 1 MeCN	8 MeCN + BF ₄ ⁻ + 1 MeCN
<i>RRRR</i>	5	7
<i>RSRS</i>	0	0

The energies of the final models with a total of nine MeCN molecules and one counter-ion are in agreement with the experimental observation that the *RSRS* isomer is the most stable form.

4.9.8.2 Computational investigation of the isomerisation

**Figure S4.58:** calculated transition geometries of the racemisation of BAAZU and their relative energies.

During the investigation, all geometries of the considered structures have been relaxed at the same level of theory as in the previous section in acetonitrile (treated with an implicit solvation model^[40]). All transition states (TS), firstly located with the aid of NEB calculations^[32], have been further optimized with the previously mentioned computational details. In agreement with transition state theory (TST), all transition state structures in our calculations report an imaginary frequency.

Single point energies have been evaluated at the def2-TZVPP/DLPNO-CCSD(T)^[33] level of theory in order to accurately compute the energy barriers associated with the isomerisation process. Below an example of the ORCA input file concerning the single point calculations.

```
! DLPNO-CCSD(T) TightSCF TightPNO RIJCOSX NoPop
! def2-TZVPP def2-TZVPP/C
! CPCM(ACETONITRILE)
%MAXCORE 24000
%PAL NPROCS 64 END
```



```
* xyzFILE 0 1 input.xyz
```

Firstly, the isolated **BAAZU** moiety has been considered. The isomerisation between these two states can occur via two different transition states (Fig. S4.58). Both calculated energy barriers are 27 kcal/mol, suggesting that the two isomerisation pathways are isoenergetic. Nevertheless, the hypothetical formation of TS2 in the cage, would require a large conformational rearrangement of the whole cage. For this reason, we infer that the isomerisation in the cage is preferred to occur through TS1. Then, the isomerisation of the full **BAAZU-1** ligand has been considered, yielding an energy barrier of 28 kcal/mol. This number is comparable within the chemical accuracy to the **BAAZU** moiety considered before, suggesting that the energy barrier of the isomerisation is governed by the steric hindrance of the **BAAZU** unit in the TS. Eventually, a reduced model of the cage has been designed. The same model has been studied experimentally. The transition state for the reduced model has been considered (picture below, distance between the Pd atoms is highlighted in Angstrom) with a BF_4^- anion (present also in the experiments), leading to an energy barrier of 28 kcal/mol. These computations show that the perturbation of palladium to the electronic structure of the **BAAZU-1** ligand has little to no effect on the isomerisation barrier. Hence, the experimentally observed rate acceleration of the cage isomerisation has not origin from a perturbation of the electronic structure.

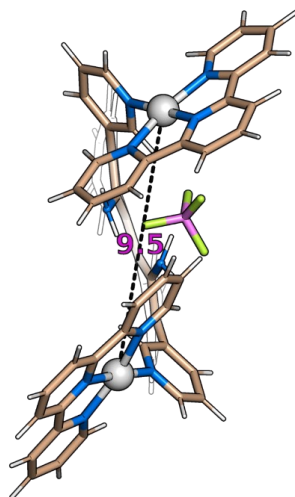


Figure S4.59: model of the $\{[\text{Pd}_2\text{BAAZU-1}(\text{terpy})_2](\text{BF}_4)\}^{3+}$ complex used for the racemisation barrier calculation.

4.9.8.3 ECD

The ECD of intermediate **8**, **BAAZU-1**, and **BAAZU-2** were calculated from DFT models of the compounds optimised at the def2-TZVP/ ω B97X-D3 level of theory. TD-DFT was performed with the same basis set, with both ω B2PLYP^[28] and BHandHLYP^[29] functionals. The resulting spectra were obtained through gaussian broadening. Below is an example of the ORCA input file concerning the TD-DFT calculations.

```

! wB2PLYP Def2-TZVP VeryTightSCF
! AUTOAUX
! CPCM(ACETONITRILE)
! LARGEPRINT
%TDDFT
      Mode sTDDFT
      NROOTS 25
      TDA FALSE
END
%MAXCORE 8000
%PAL NPROCS 32 END
%cpcm
surfacetype vdw_gaussian
end
* xyzFILE 0 1 input.xyz

```

4.9.8.4 **BAAZU-2** cage and host-guest complexes

The DFT models are based on an initial model constructed in Wavefunction SPARTAN'18,^[41] and then optimised by the semi-empirical PM6 method in Gaussian 16.^[42] The final DFT model was geometry-optimised in the gas-phase at the def2-SVP/ ω B97X-D level. The models as .xyz files can be found as supplementary data.

Due to convergence issues when using Gaussian, the cage-**CSA** host-guest complexes were optimised in Orca, at the ω B97X-D3/def2-SVP level.

4.9.9 X-ray crystallography

Six compounds were studied by single crystal X-ray crystallography in this chapter: **BAAZU (6)**, **BAAZU-1 fraction 1**, **BAAZU-2 fraction 2**, diisobutyl (3,3'-dibromo-[1,1'-biazulene]-2,2'-diyl)dicarbamate (**8**) fractions 1 & 2, Pd₂**BAAZU-1**^{rac} and Pd₂(*R*)-**BAAZU-1**. Crystals of suitable quality and size to be measured in-house were obtained for **BAAZU (6)**, **8** fractions 1 & 2, **BAAZU-1 fraction 1**, Pd₂**BAAZU-1**^{rac}₄ and Pd₂(*S*)-**BAAZU-1**₄. They were measured on a Bruker D8 venture diffractometer equipped with an INCOATEC microfocus sealed tube (λ 3.0) at 100 K. The data was integrated with APEX3 and the structure was solved by intrinsic phasing/direct methods using SHELXT^[43] and refined with SHELXL^[44] for full-matrix least-squares routines on F^2 and ShelXle^[45] as a graphical user interface.

Small crystals of **BAAZU-2 fraction 2** were obtained and were measured at the MAX IV synchrotron, in Lund, Sweden.^[46]

Table S4.4: crystallographic tables of BAAZU and BAAZU-1 F1

Compound	BAAZU (6)	(R)-BAAZU-1
CIF ID	aw35high	aw117_fl_j
CCDC number	2356504	2356507
Empirical formula	C ₂₀ H ₁₆ N ₂	C ₃₀ H ₂₂ N ₄
Formula weight	284.35	438.51
Temperature [K]	100(2)	100(2)
Crystal system	orthorhombic	monoclinic
Space group (number)	<i>Pca</i> 2 ₁ (29)	<i>P</i> 2 ₁ (4)
<i>a</i> [Å]	19.9343(7)	8.5359(2)
<i>b</i> [Å]	11.1774(4)	23.0569(6)
<i>c</i> [Å]	6.7622(2)	11.3375(3)
α [°]	90	90
β [°]	90	90.0470(10)
γ [°]	90	90
Volume [Å ³]	1506.71(9)	2231.35(10)
<i>Z</i>	4	4
ρ_{calc} [gcm ⁻³]	1.254	1.305
μ [mm ⁻¹]	0.074	0.610
<i>F</i> (000)	600	920
Crystal size [mm ³]	0.150×0.150×0.150	0.500×0.120×0.120
Crystal colour	red	brown
Crystal shape	block	block
Radiation	MoK α (λ =0.71073 Å)	CuK α (λ =1.54178 Å)
2 θ range [°]	4.09 to 125.42 (0.40 Å)	3.83 to 159.91 (0.78 Å)
Index ranges	-49 ≤ <i>h</i> ≤ 45 -27 ≤ <i>k</i> ≤ 27 -16 ≤ <i>l</i> ≤ 15	-9 ≤ <i>h</i> ≤ 10 -29 ≤ <i>k</i> ≤ 29 -14 ≤ <i>l</i> ≤ 14
Reflections collected	190669	124991
Independent reflections	22926 <i>R</i> _{int} = 0.0724 <i>R</i> _{sigma} = 0.0330	9595 <i>R</i> _{int} = 0.0371 <i>R</i> _{sigma} = 0.0144
Completeness to $\vartheta = 67.679^\circ$	99.7 %	100.0 %
Data / Restraints / Parameters	22926/1/263	9595/1/746
Goodness-of-fit on <i>F</i> ²	1.109	1.024
Final <i>R</i> indexes [<i>I</i> ≥ 2 σ (<i>I</i>)]	<i>R</i> ₁ = 0.0457 <i>wR</i> ₂ = 0.1103	<i>R</i> ₁ = 0.0246 <i>wR</i> ₂ = 0.0632
Final <i>R</i> indexes [all data]	<i>R</i> ₁ = 0.0567 <i>wR</i> ₂ = 0.1182	<i>R</i> ₁ = 0.0248 <i>wR</i> ₂ = 0.0634
Largest peak/hole [eÅ ⁻³]	0.60/-0.28	0.14/-0.17
Flack X parameter	-	0.05(8)

Table S4.5: crystallographic tables of **8 F1** and **8 F2**

Compound	8 F1	8 F2
CIF ID	aw143f1	aw143f2
CCDC number	2356506	2356502
Empirical formula	C ₃₀ H ₃₀ Br ₂ N ₂ O ₄	C ₃₀ H ₃₀ Br ₂ N ₂ O ₄
Formula weight	642.38	642.38
Temperature [K]	100(2)	100(2)
Crystal system	orthorhombic	orthorhombic
Space group (number)	<i>P</i> 2 ₁ 2 ₁ 2 ₁ (19)	<i>P</i> 2 ₁ 2 ₁ 2 ₁ (19)
<i>a</i> [Å]	9.4436(5)	9.4452(5)
<i>b</i> [Å]	12.2584(7)	12.2541(6)
<i>c</i> [Å]	24.0877(14)	24.1005(13)
α [°]	90	90
β [°]	90	90
γ [°]	90	90
Volume [Å ³]	2788.5(3)	2789.5(3)
<i>Z</i>	4	4
ρ_{calc} [gcm ⁻³]	1.530	1.530
μ [mm ⁻¹]	3.999	3.998
<i>F</i> (000)	1304	1304
Crystal size [mm ³]	0.100× 0.050× 0.050	0.200× 0.050× 0.050
Crystal colour	blue	blue
Crystal shape	block	block
Radiation	CuK α (λ =1.54178 Å)	CuK α (λ =1.54178 Å)
2 θ range [°]	7.34 to 148.98 (0.80 Å)	7.34 to 158.03 (0.79 Å)
Index ranges	-11 ≤ <i>h</i> ≤ 9 -15 ≤ <i>k</i> ≤ 15 -30 ≤ <i>l</i> ≤ 30	-8 ≤ <i>h</i> ≤ 11 -15 ≤ <i>k</i> ≤ 15 -30 ≤ <i>l</i> ≤ 29
Reflections collected	56365	51795
Independent reflections	5694 <i>R</i> _{int} = 0.0415 <i>R</i> _{sigma} = 0.0224	5975 <i>R</i> _{int} = 0.0424 <i>R</i> _{sigma} = 0.0271
Completeness to $\vartheta = 67.679^\circ$	100.0 %	100.0 %
Data / Restraints / Parameters	5694/537/353	5975/0/349
Goodness-of-fit on <i>F</i> ²	1.026	1.061
Final <i>R</i> indexes [<i>I</i> ≥ 2 σ (<i>I</i>)]	<i>R</i> ₁ = 0.0179 <i>wR</i> ₂ = 0.0447	<i>R</i> ₁ = 0.0218 <i>wR</i> ₂ = 0.0542
Final <i>R</i> indexes [all data]	<i>R</i> ₁ = 0.0183 <i>wR</i> ₂ = 0.0449	<i>R</i> ₁ = 0.0225 <i>wR</i> ₂ = 0.0546
Largest peak/hole [eÅ ⁻³]	0.25/-0.40	0.58/-0.48
Flack X parameter	0.044(4)	0.059(5)

Table S4.6: crystallographic tables of Pd₂BAAZU-1^{rac}₄ and Pd₂(S)-BAAZU-1₄

Compound	Pd ₂ BAAZU-1 ^{rac} ₄	Pd ₂ (S)-BAAZU-1 ₄
CIF ID	aw82j	aw98j
CCDC number	2356505	2356503
Empirical formula	C ₁₆₃ H _{169.09} B ₄ F ₁₆ N _{30.64} O _{4.86} Pd ₂ S _{3.86}	C ₁₄₀ H ₁₂₂ B ₃ F ₁₂ N ₂₄ OPd ₂
Formula weight	3318.98	2629.84
Temperature [K]	100(2)	100(2)
Crystal system	triclinic	triclinic
Space group (number)	$P\bar{1}$ (2)	$P1$ (1)
<i>a</i> [Å]	17.4805(6)	15.6000(8)
<i>b</i> [Å]	22.5706(8)	17.1715(10)
<i>c</i> [Å]	22.7915(8)	17.7204(9)
α [°]	92.3420(10)	96.809(2)
β [°]	100.2940(10)	115.622(2)
γ [°]	110.8380(10)	111.923(2)
Volume [Å ³]	8215.3(5)	3741.5(4)
<i>Z</i>	2	1
ρ_{calc} [gcm ⁻³]	1.342	1.167
μ [mm ⁻¹]	2.904	2.502
<i>F</i> (000)	3437	1353
Crystal size [mm ³]	0.300× 0.150× 0.100	0.100× 0.100× 0.040
Crystal colour	brown	brown
Crystal shape	block	block
Radiation	CuK α (λ =1.54178 Å)	CuK α (λ =1.54178 Å)
2 θ range [°]	3.97 to 158.47 (0.78 Å)	5.87 to 132.89 (0.84 Å)
Index ranges	-22 ≤ <i>h</i> ≤ 22 -28 ≤ <i>k</i> ≤ 28 -27 ≤ <i>l</i> ≤ 29	-15 ≤ <i>h</i> ≤ 18 -18 ≤ <i>k</i> ≤ 18 -21 ≤ <i>l</i> ≤ 18
Reflections collected	190543	93122
Independent reflections	34821 $R_{\text{int}} = 0.1654$ $R_{\text{sigma}} = 0.0754$	18292 $R_{\text{int}} = 0.0815$ $R_{\text{sigma}} = 0.0644$
Completeness to $\vartheta = 67.679^\circ$	100.0 %	74.1 %
Data / Restraints / Parameters	34821/3682/2289	18292/3423/1732
Goodness-of-fit on F^2	1.081	1.264
Final <i>R</i> indexes [$I \geq 2\sigma(I)$]	$R_1 = 0.0557$ $wR_2 = 0.1583$	$R_1 = 0.1030$ $wR_2 = 0.2742$
Final <i>R</i> indexes [all data]	$R_1 = 0.0582$ $wR_2 = 0.1615$	$R_1 = 0.1226$ $wR_2 = 0.2940$
Largest peak/hole [eÅ ⁻³]	1.40/-1.63	2.08/-0.81
Flack X parameter		0.228(5)

Table S4.7: crystallographic table of BAAZU-2 fraction 2

Compound	BAAZU-2 f2
CIF ID	aw139f2
CCDC number	2356508
Empirical formula	C ₃₈ H ₂₆ N ₄
Formula weight	538.63
Temperature [K]	100(2)
Crystal system	monoclinic
Space group (number)	<i>P</i> 2 ₁ (4)
<i>a</i> [Å]	14.2400(11)
<i>b</i> [Å]	7.1410(15)
<i>c</i> [Å]	15.859(4)
α [°]	90
β [°]	94.206(11)
γ [°]	90
Volume [Å ³]	1608.3(5)
<i>Z</i>	2
ρ_{calc} [gcm ⁻³]	1.112
μ [mm ⁻¹]	0.047
<i>F</i> (000)	564
Crystal size [mm ³]	0.250×0.015×0.005
Crystal colour	brown
Crystal shape	needle
Radiation	synchrotron ($\lambda=0.5904$ Å)
2 θ range [°]	2.14 to 50.48 (0.69 Å)
Index ranges	–16 ≤ <i>h</i> ≤ 16 –8 ≤ <i>k</i> ≤ 8 –18 ≤ <i>l</i> ≤ 18
Reflections collected	45807
Independent reflections	7079 $R_{\text{int}} = 0.0341$ $R_{\text{sigma}} = 0.0222$
Completeness to $\vartheta = 67.679^\circ$	97.0 %
Data / Restraints / Parameters	7079/668/391
Goodness-of-fit on F^2	0.822
Final <i>R</i> indexes [$I \geq 2\sigma(I)$]	$R_1 = 0.0519$ $wR_2 = 0.1686$
Final <i>R</i> indexes [all data]	$R_1 = 0.0549$ $wR_2 = 0.1789$
Largest peak/hole [eÅ ⁻³]	0.17/–0.26
Flack X parameter	–4.3(10)

4.9.9.1 BAAZU (6)

Brown block-shaped crystals of **6** (racemate) were grown by slow vapour diffusion of n-pentane into a DCM solution of **6** at room temperature. Single crystals in mother liquor were pipetted onto a glass slide containing NVH oil. To avoid collapse of the crystal lattice, the chosen crystal was quickly mounted on a micro loop and mounted on the diffractometer under a flow of N₂ at 100 K. The data collection was performed using a MoK_α radiation source.

Specific refinement details

The compound crystallises in the orthorhombic Pca2₁ (29) space group, with one molecule per asymmetric unit cell, and four per unit cell. Every hydrogen atom could be resolved.

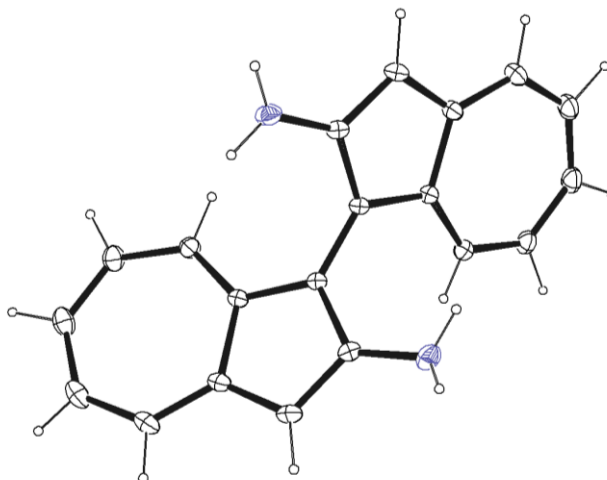


Figure S4.60: ORTEP representation of **BAAZU**. Ellipsoids drawn at 50% probability.

4.9.9.2 **BAAZU-1** Fraction 1

Brown block-shaped crystals of **BAAZU-1** (fraction 1) were grown by slow vapour diffusion of diethyl ether (Et₂O) into a DCM solution of the ligand at room temperature. Crystals in mother liquor were pipetted onto a glass slide containing NVH oil and the chosen crystal was quickly mounted on a micro loop and mounted on the diffractometer under a flow of N₂ at 100 K. The data collection was performed using a CuK_α radiation source.

Specific refinement details

The compound crystallises in the monoclinic P2₁ (4) space group. Two ligands are present in the asymmetric unit cell. Twinning of the crystal was taken into account with the following instructions:

TWIN -1 0 0 0 -1 0 0 1

BASF 0.41872

A Flack parameter of 0.05 (8) was measured according to Parson's method. Therefore, the absolute configuration of fraction 1 of the ligand was assigned to the *R* enantiomer. This result was further confirmed by comparison of the experimental and DFT-calculated CD spectra (see section 4.9.7.).

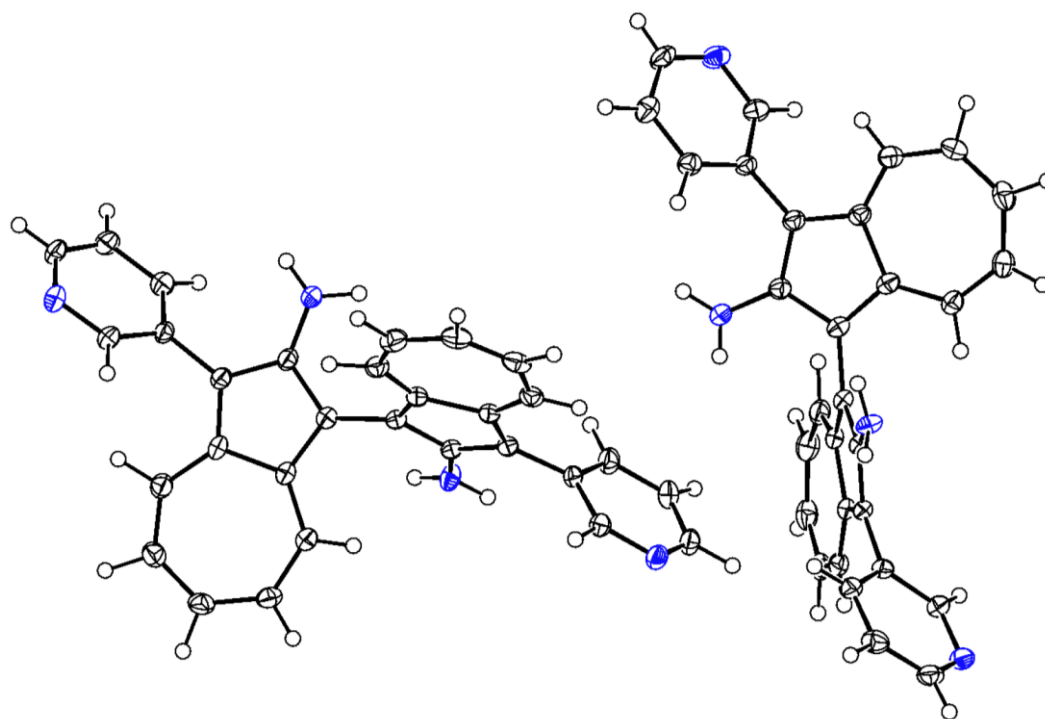


Figure S4.61: ORTEP representation of the asymmetric cell of (*R*)-**BAAZU-1**. Ellipsoids drawn at 50% probability.

4.9.9.3 diisobutyl (3,3'-dibromo-[1,1'-biazulene]-2,2'-diyl)dicarbamate (8) fractions 1 & 2

Blue block-shaped crystals of intermediate **8** (the two enantiomers separated by chiral HPLC) were grown by layering a DCM solution of the title compound with n-hexane at 4°C. Crystals in mother liquor were pipetted onto a glass slide containing NVH oil and the chosen crystal was quickly mounted on a micro loop and then mounted on the diffractometer under a flow of N₂ at 100 K. The data collection was performed using a CuK_α radiation source.

Specific refinement details

The compound crystallises in the orthorhombic P2₁2₁2₁ (19) space group, with one molecule per asymmetric unit cell. Most hydrogens were added through the **AFIX** instruction, except for the two NH groups.

Fraction 1 was assigned to the *S* enantiomer, with a Flack parameter according to Parson's method of 0.044 (4). Fraction 2 was assigned to the *R* enantiomer, with a Flack parameter according to Parson's method of 0.059 (5).

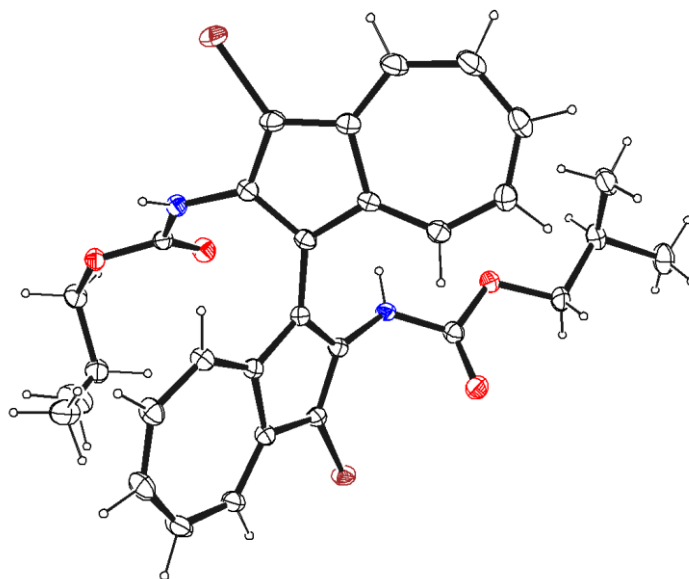


Figure S4.62: ORTEP representation of (*S*)-**8** (fraction 1). Ellipsoids drawn at 50% probability.

4.9.9.4 $[\text{Pd}_2\text{BAAZU-1}^{\text{rac}}_4](\text{BF}_4)_4$

Brown block-shaped crystals of $[\text{Pd}_2\text{BAAZU-1}^{\text{rac}}_4](\text{BF}_4)_4$ were grown by slow vapour diffusion of diisopropylether (iPr_2O) into an acetonitrile (ACN) solution of the supramolecular species with 10% DMSO at room temperature. Single crystals in mother liquor were pipetted onto a glass slide containing NVH oil. To avoid collapse of the crystal lattice, the chosen crystal was quickly mounted on a micro loop and mounted on the diffractometer under a flow of N_2 at 100 K. The data collection was performed using a $\text{CuK}\alpha$ radiation source.

Specific refinement details

Stereochemical restraints for dimethyl sulfoxide (residue DMS), acetonitrile (residue ACN), and diisopropyl ether (residue DIP) solvent molecules, and tetrafluoroborate (residue BF_4) counter anion were generated by the GRADE program using the GRADE Web Server (<http://grade.globalphasing.org>) and applied in the refinement. A GRADE dictionary for SHELXL contains target values and standard deviations for 1,2-distances (DFIX) and 1,3-distances (DANG), as well as restraints for planar groups (FLAT). All displacements for non-hydrogen atoms were refined anisotropically. The refinement of ADPs for every element except hydrogen was enabled by a combination of similarity restraints (SIMU) and rigid bond restraints (RIGU)^[47].

The compound crystallised in the triclinic space group P-1 (2). The cage was modelled in its entirety, and the protons of the amino groups could be placed manually. Those amino groups are bridged by DMSO and ACN molecules. Those solvents molecules overlap in two positions, necessitating to be modelled as disordered over the same positions using free individual variables for refinement of occupancy factors. Moreover, three out of the four BF_4 residues had to be modelled as disordered over two conformations using free individual variables for refinement of occupancy factors. Finally, one ACN residue had to be modelled on a special position, with half-occupancy.

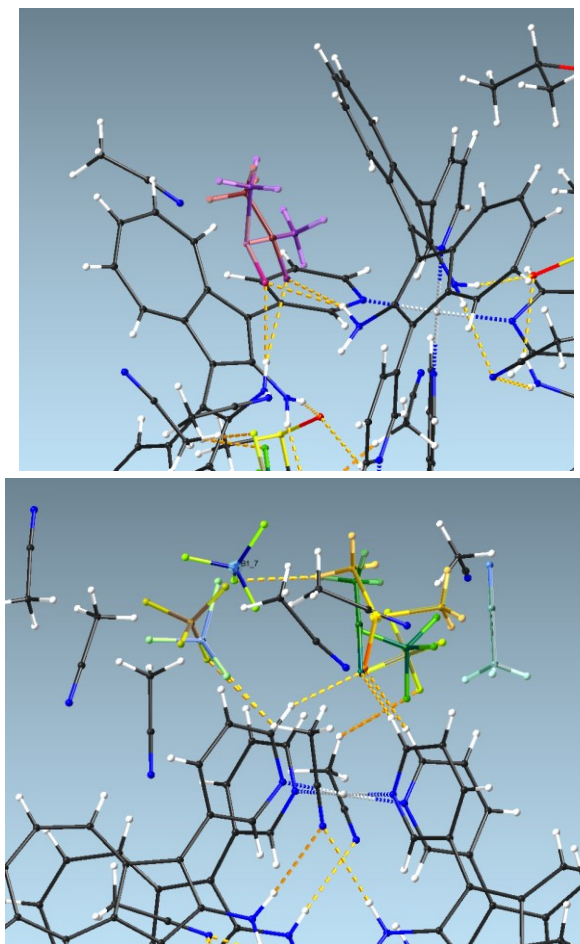


Figure S4.63: disorders in some of the solvent and counteranions in the X-ray structure of $[\text{Pd}_2\text{BAAZU-1}^{\text{rac}}_4](\text{BF}_4)_4$

4.9.9.5 $[\text{Pd}_2(S)\text{-BAAZU-1}_4](\text{BF}_4)_4$

Brown block-shaped crystals of $[\text{Pd}_2(S)\text{-BAAZU-1}_4](\text{BF}_4)_4$ (fraction 2 of **BAAZU-1**) were grown by slow vapour diffusion of diethylether (Et_2O) into an acetonitrile (ACN) solution of the supramolecular species prepared with fraction 2 at room temperature. Single crystals in mother liquor were pipetted onto a glass slide containing NVH oil. To avoid collapse of the crystal lattice, the chosen crystal was quickly mounted on a micro loop and mounted on the diffractometer under a flow of N_2 at 100 K. The data collection was performed using a $\text{CuK}\alpha$ radiation source.

Specific refinement details

Stereochemical restraints for the **BAAZU-1** ligand (residue BAA), acetonitrile (residue ACN) and diethyl ether (residue ETO) solvent molecules, and tetrafluoroborate (residue BF_4) counter anion were generated by the GRADE program using the GRADE Web Server (<http://grade.globalphasing.org>) and applied in the refinement. A GRADE dictionary for SHELXL contains target values and standard deviations for 1,2-distances (DFIX) and 1,3-distances (DANG), as well as restraints for planar groups (FLAT). All displacements for non-hydrogen atoms were refined anisotropically. The refinement of ADPs for every element except hydrogen was enabled by a

combination of similarity restraints (SIMU) and rigid bond restraints (RIGU).^[47] The contribution of the electron density from disordered counterions and solvent molecules, which could not be modelled with discrete atomic positions were handled using the SQUEEZE^[48] routine in PLATON.^[49] The solvent mask file (.fab), computed by PLATON, was included in the SHELXL refinement via the ABIN instruction leaving the measured intensities untouched.

The compound crystallised in the triclinic space group P1 (1), with one full cage per unit cell, as well as three BF₄ counter anions and one diethylether counter solvent molecule. One out of the three BF₄ residues and the ETO residue had to be modelled as disordered over two conformations using free individual variables for refinement of occupancy factors. The measured Flack parameter according to Parson's method before SQUEEZE was 0.208 (5), with the ligands in the *S*-conformation.

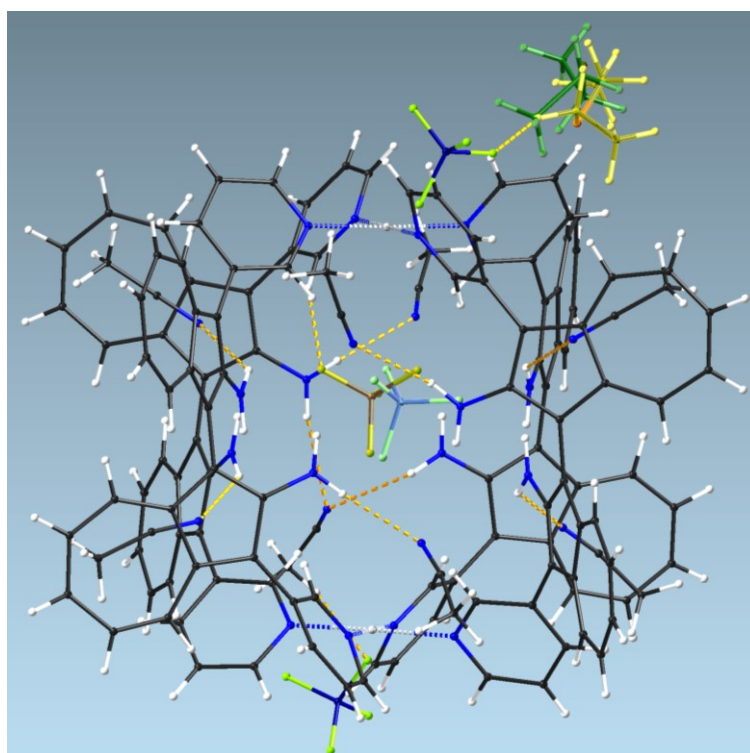


Figure S4.64: full model of the Pd₂(*S*)-BAAZU-1₄ cage, with cavity-bound disordered BF₄⁻ residue, and disordered diethyl ether counter solvent (top right).

4.9.9.6 BAAZU-2 Fraction 2

Brown needle-shaped of **BAAZU-2** fraction 2 were grown by slow vapour diffusion of pentane into a DCM solution of the ligand at 4°C. Single crystals in mother liquor were pipetted onto a glass slide containing NVH oil. To avoid collapse of the crystal lattice, several crystals were quickly mounted on micro loops and immediately flash-cooled in liquid nitrogen. Crystals were stored at cryogenic temperature in dry shippers, in which they were safely transported to macromolecular

beamline BioMAX^[50] at the MAX IV synchrotron, Lund, Sweden. A wavelength of $\lambda = 0.5904 \text{ \AA}$ was chosen using a liquid N₂ cooled double crystal monochromator. Single crystal X-ray diffraction data was collected at 100(2) K on Arinax MD3 microdiffractometer with minikappa axis, equipped with Oxford Cryostream 800, Eiger1 16M detector and Irelec Isara sample changing robot. 3600 diffraction images were collected in a single 360° φ sweep using local MXCube3^[51] and ISPyB^[52] implementation and a detector distance of 188.5 mm, 100% filter transmission, 0.1° step width and 40 milliseconds exposure time per image. Data integration and reduction were undertaken using autoProc^[53] and XDS.^[54]

Specific refinement details

All displacements for non-hydrogen atoms were refined anisotropically. The refinement of ADPs for every element except hydrogen was enabled by a combination of similarity restraints (SIMU) and rigid bond restraints (RIGU).^[47] The contribution of the electron density from disordered counterions and solvent molecules, which could not be modelled with discrete atomic positions were handled using the SQUEEZE^[48] routine in PLATON.^[49] The solvent mask file (.fab), computed by PLATON, was included in the SHELXL refinement via the ABIN instruction leaving the measured intensities untouched.

The compound crystallised in the monoclinic space group P2₁ (4), with one molecule per asymmetric unit cell. Every hydrogen atom was added by the **AFIX** instruction. The crystal possesses voids occupied by disordered solvent molecules, amounting to approx. 14% of the total volume.

The Flack parameter was calculated to be $-4.3(10)$, which is very high and hence does allow us to determine the absolute structure to derive the absolute configuration of the compound by X-ray crystallography.

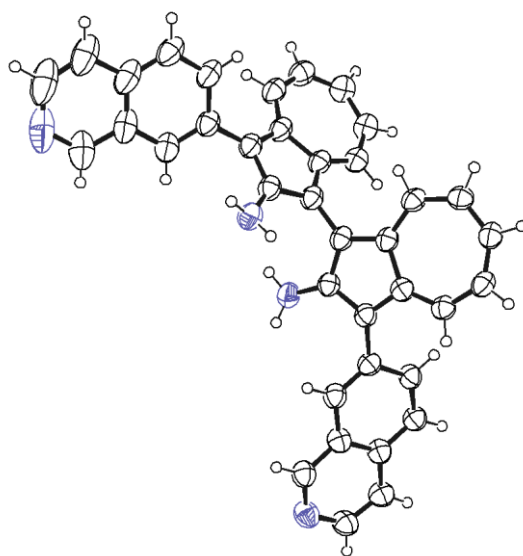


Figure S4.65: ORTEP representation of **BAAZU-2**. Ellipsoids drawn at 50% probability.

4.10 REFERENCES

- [1] P. J. Stang, B. Olenyuk, D. C. Muddiman, R. D. Smith, *Organometallics* **1997**, *16*, 3094–3096.
- [2] Y. Kubota, K. Biradha, M. Fujita, S. Sakamoto, K. Yamaguchi, *Bull. Chem. Soc. Jpn.* **2002**, *75*, 559–565.
- [3] Y. Nishioka, T. Yamaguchi, M. Kawano, M. Fujita, *J. Am. Chem. Soc.* **2008**, *130*, 8160–8161.
- [4] T. Murase, S. Peschard, S. Horiuchi, Y. Nishioka, M. Fujita, *Supramol. Chem.* **2011**, *23*, 199–208.
- [5] I. A. Bhat, A. Devaraj, P. Howlader, K.-W. Chi, P. S. Mukherjee, *Chem. Commun.* **2018**, *54*, 4814–4817.
- [6] P. Howlader, E. Zangrando, P. S. Mukherjee, *J. Am. Chem. Soc.* **2020**, *142*, 9070–9078.
- [7] Y. Zhou, H. Li, T. Zhu, T. Gao, P. Yan, *J. Am. Chem. Soc.* **2019**, *141*, 19634–19643.
- [8] O. Chepelin, J. Ujma, X. Wu, A. M. Z. Slawin, M. B. Pitak, S. J. Coles, J. Michel, A. C. Jones, P. E. Barran, P. J. Lusby, *J. Am. Chem. Soc.* **2012**, *134*, 19334–19337.
- [9] N. Ousaka, J. K. Clegg, J. R. Nitschke, *Angew. Chem. Int. Ed.* **2012**, *51*, 1464–1468.
- [10] T. K. Ronson, S. Zarra, S. P. Black, J. R. Nitschke, *Chem. Commun.* **2012**, *49*, 2476–2490.
- [11] Z. Lu, T. K. Ronson, A. W. Heard, S. Feldmann, N. Vanthuyne, A. Martinez, J. R. Nitschke, *Nat. Chem.* **2023**, *15*, 405–412.
- [12] G. Li, T. K. Ronson, R. Lavendomme, Z. Huang, C. Fuertes-Espinosa, D. Zhang, J. R. Nitschke, *Chem* **2023**, *9*, 1549–1561.
- [13] M. Meyer, B. Kersting, R. E. Powers, K. N. Raymond, *Inorg. Chem.* **1997**, *36*, 5179–5191.
- [14] E. J. Enemark, T. D. P. Stack, *Angew. Chem. Int. Ed.* **1998**, *37*, 932–935.
- [15] C. Klein, C. Gütz, M. Bogner, F. Topić, K. Rissanen, A. Lützen, *Angew. Chem. Int. Ed.* **2014**, *53*, 3739–3742.
- [16] C. Gütz, R. Hovorka, C. Klein, Q. Jiang, C. Bannwarth, M. Engeser, C. Schmuck, W. Assenmacher, W. Mader, F. Topić, K. Rissanen, S. Grimme, A. Lützen, *Angew. Chem. Int. Ed.* **2014**, *53*, 1693–1698.
- [17] C. Klein, C. Gütz, M. Bogner, F. Topić, K. Rissanen, A. Lützen, *Angew. Chem. Int. Ed.* **2014**, *53*, 3739–3742.
- [18] T. R. Schulte, J. J. Holstein, G. H. Clever, *Angew. Chem. Int. Ed.* **2019**, *58*, 5562–5566.
- [19] T. Shoji, A. Maruyama, A. Yamamoto, Y. Fujiwara, S. Ito, T. Okujima, N. Morita, *Chem. Lett.* **2014**, *43*, 1122–1124.
- [20] M. Li, D.-H. Wang, *Org. Lett.* **2021**, *23*, 6638–6641.
- [21] T. Nozoe, Y. Kitahara, K. Takase, M. Sasaki, *Proc. Jpn. Acad.* **1956**, *32*, 349–352.
- [22] T. Nozoe, S. Seto, S. Matsumura, Y. Murase, *Bull. Chem. Soc. Jpn.* **1962**, *35*, 1179–1188.
- [23] T. R. Schulte, J. J. Holstein, G. H. Clever, *Angew. Chem. Int. Ed.* **2019**, *58*, 5562–5566.
- [24] L. R. MacGillivray, J. L. Atwood, *Nature* **1997**, *389*, 469–472.
- [25] S. K. Sen, R. Natarajan, *Inorg. Chem.* **2019**, *58*, 7180–7188.
- [26] P. Molinska, A. Tarzia, L. Male, K. E. Jelfs, J. E. M. Lewis, *Angew. Chem. Int. Ed.* **2023**, *62*, e202315451.
- [27] A. L. Spek, *J. Appl. Crystallogr.* **2003**, *36*, 7–13.
- [28] M. Casanova-Páez, M. B. Dardis, L. Goerigk, *J. Chem. Theory Comput.* **2019**, *15*, 4735–4744.
- [29] A. D. Becke, *J. Chem. Phys.* **1993**, *98*, 1372–1377.
- [30] M. D. Johnstone, E. K. Schwarze, J. Ahrens, D. Schwarzer, J. J. Holstein, B. Dittrich, F. M. Pfeffer, G. H. Clever, *Chem. Eur. J.* **2016**, *22*, 10791–10795.
- [31] C. Desmarets, G. Gontard, A. L. Cooksy, M. N. Rager, H. Amouri, *Inorg. Chem.* **2014**, *53*, 4287–4294.
- [32] V. Ásgeirsson, B. O. Birgisson, R. Björnsson, U. Becker, F. Neese, C. Riplinger, H. Jónsson, *J. Chem. Theory Comput.* **2021**, *17*, 4929–4945.
- [33] C. Riplinger, F. Neese, *J. Chem. Phys.* **2013**, *138*, 034106.
- [34] S. Pullen, S. Löffler, A. Platzek, J. J. Holstein, G. H. Clever, *Dalton Trans.* **2020**, *49*, 9404–9410.
- [35] F. Weigend, R. Ahlrichs, *Phys. Chem. Chem. Phys.* **2005**, *7*, 3297–3305.
- [36] F. Weigend, *Phys. Chem. Chem. Phys.* **2006**, *8*, 1057–1065.
- [37] Y.-S. Lin, G.-D. Li, S.-P. Mao, J.-D. Chai, *J. Chem. Theory Comput.* **2013**, *9*, 263–272.
- [38] S. Kozuch, J. M. L. Martin, *Phys. Chem. Chem. Phys.* **2011**, *13*, 20104–20107.
- [39] S. Grimme, J. Antony, S. Ehrlich, H. Krieg, *J. Chem. Phys.* **2010**, *132*, 154104.
- [40] V. Barone, M. Cossi, *J. Phys. Chem.* **1998**, *102*, 1995–2001.
- [41] Spartan'18, Wavefunction Inc., Irvine.
- [42] M. J. Frisch, G. W. Trucks, H. B. Schlegel, G. E. Scuseria, M. A. Robb, J. R. Cheeseman, G. Scalmani, V. Barone, G. A. Petersson, H. Nakatsuji, X. Li, M. Caricato, A. V. Marenich, J. Bloino, B. G. Janesko, R. Gomperts, B. Mennucci, H. P. Hratchian, J. V. Ortiz, A. F. Izmaylov, J. L. Sonnenberg, D. Williams-Young,

- F. Ding, F. Lipparini, F. Egidi, J. Goings, B. Peng, A. Petrone, T. Henderson, D. Ranasinghe, V. G. Zakrzewski, J. Gao, N. Rega, G. Zheng, W. Liang, M. Hada, M. Ehara, K. Toyota, R. Fukuda, J. Hasegawa, M. Ishida, T. Nakajima, Y. Honda, O. Kitao, H. Nakai, T. Vreven, K. Throssell, Jr. Montgomery, J. E. Peralta, F. Ogliaro, M. J. Bearpark, J. J. Heyd, E. N. Brothers, K. N. Kudin, V. N. Staroverov, T. A. Keith, R. Kobayashi, J. Normand, K. Raghavachari, A. P. Rendell, J. C. Burant, S. S. Iyengar, J. Tomasi, M. Cossi, J. M. Millam, M. Klene, C. Adamo, R. Cammi, J. W. Ochterski, R. L. Martin, K. Morokuma, O. Farkas, J. B. Foresman, D. J. Fox, *Gaussian'16 Revision C.01*, Gaussian Inc., Wallingford CT.
- [43] G. M. Sheldrick, *Acta Crystallogr., Sect. A: Found. Adv.* **2015**, *71*, 3–8.
- [44] G. M. Sheldrick, *Acta Crystallogr., Sect. C: Struct. Chem.* **2015**, *71*, 3–8.
- [45] C. B. Hübschle, G. M. Sheldrick, B. Dittrich, *J. Appl. Crystallogr.* **2011**, *44*, 1281–1284.
- [46] T. Ursby, K. Åhnberg, R. Appio, O. Aurelius, A. Barczyk, A. Bartalesi, M. Bjelčić, F. Bolmsten, Y. Cerenius, R. B. Doak, M. Eguiraun, T. Eriksson, R. J. Friel, I. Gorgisyan, A. Gross, V. Haghighat, F. Hennies, E. Jagudin, B. N. Jensen, T. Jeppsson, M. Kloos, J. Lidon-Simon, G. M. A. de Lima, R. Lizatovic, M. Lundin, A. Milan-Otero, M. Milas, J. Nan, A. Nardella, A. Rosborg, A. Shilova, R. L. Shoeman, F. Siewert, P. Sondhauss, V. O. Talibov, H. Tarawneh, J. Thånell, M. Thunnissen, J. Unge, C. Ward, A. Gonzalez, U. Mueller, *J. Synchrotron Radiat.* **2020**, *27*, 1415–1429.
- [47] A. Thorn, B. Dittrich, G. M. Sheldrick, *Acta Crystallogr., Sect. A: Found. Crystallogr.* **2012**, *68*, 448–451.
- [48] A. L. Spek, *Acta Crystallogr., Sect. C: Struct. Chem.* **2015**, *71*, 9–18.
- [49] A. L. Spek, *Acta Crystallogr., Sect. D: Biol. Crystallogr.* **2009**, *65*, 148–155.
- [50] T. Ursby, K. Åhnberg, R. Appio, O. Aurelius, A. Barczyk, A. Bartalesi, M. Bjelčić, F. Bolmsten, Y. Cerenius, R. B. Doak, M. Eguiraun, T. Eriksson, R. J. Friel, I. Gorgisyan, A. Gross, V. Haghighat, F. Hennies, E. Jagudin, B. N. Jensen, T. Jeppsson, M. Kloos, J. Lidon-Simon, G. M. A. de Lima, R. Lizatovic, M. Lundin, A. Milan-Otero, M. Milas, J. Nan, A. Nardella, A. Rosborg, A. Shilova, R. L. Shoeman, F. Siewert, P. Sondhauss, V. O. Talibov, H. Tarawneh, J. Thånell, M. Thunnissen, J. Unge, C. Ward, A. Gonzalez, U. Mueller, *J. Synchrotron Radiat.* **2020**, *27*, 1415–1429.
- [51] U. Mueller, M. Thunnissen, J. Nan, M. Eguiraun, F. Bolmsten, A. Milàn-Otero, M. Guijarro, M. Oscarsson, D. de Sanctis, G. Leonard, *Synchrotron Radiat. N.* **2017**, *30*, 22–27.
- [52] S. Delagenière, P. Brechereau, L. Launer, A. W. Ashton, R. Leal, S. Veyrier, J. Gabadinho, E. J. Gordon, S. D. Jones, K. E. Levik, S. M. McSweeney, S. Monaco, M. Nanao, D. Spruce, O. Svensson, M. A. Walsh, G. A. Leonard, *Bioinformatics* **2011**, *27*, 3186–3192.
- [53] C. Vonnrhein, C. Flensburg, P. Keller, A. Sharff, O. Smart, W. Paciorek, T. Womack, G. Bricogne, *Acta Crystallogr., Sect. D: Biol. Crystallogr.* **2011**, *67*, 293–302.
- [54] W. Kabsch, *Acta Crystallogr., Sect. D: Biol. Crystallogr.* **2010**, *66*, 133–144.

5 THIENO[3,4-B]PYRAZINE-BASED Pd₂L₄ LUMINESCENT ASSEMBLIES

5.1 REPRODUCING THE CAGE-TO-TETRAHEDRON TRANSFORMATION

Chapter 3 described the transformation of an azulene-based Pd₂**AZU1**₄ cage undergoing a transformation to a Pd₄**AZU1**₈ tetrahedron upon guest binding with **BEN13** or **BEN14**. As a unique event, the guest-triggered transformation was thoroughly studied, and the reproduction of this result was attempted with other azulene-based ligands, **AZU4** and **AZU5**. However, no cage-guest combination was found to trigger a similar transformation, despite the ligands only differing from **AZU1** by the length of their linkers. Those negative results showed that the transformation was relying on a very specific geometry of the ligand, and that azulene itself was not the decisive factor in the observed phenomenon. If the transformation was only occurring with the ligand with alkyne linkers and a 3-pyridine donor group, it is possible that swapping the azulene backbone with another five-membered aromatic ring could yield another cage capable of undergoing a similar transformation upon addition of guests **BEN13** or **BEN14**.

Several heteroaromatic backbones such as pyrrole or furan were considered as a backbone for the new ligand, but thiophene was chosen in the end for the ease of synthesis in one step of the final compound, which has already been reported.^[1,2]

Ligand **THO** (2,5-bis(pyridin-3-ylethynyl)thiophene) was prepared in one step through Sonogashira coupling between 2,5-dibromothiophene and 3-ethynylpyridine. Cage Pd₂**THO**₄ was assembled similarly as the previously described species and was characterised by NMR spectroscopy (Fig. 5.1b) and ESI-MS (Fig S5.26). Single crystals of the cage were obtained from slow diffusion of benzene into an acetonitrile solution of the cage. The X-ray structure shows as expected the lantern shape of the cage (Fig. 5.1a).

Next, the outcome of the addition of guest **BEN14** was monitored by NMR in DMSO-*d*₆. Delightfully, like its azulene cousin, a split of the signals was observed after only 5 minutes at 70°C. However, unlike the previous species, the signals split in four (1:1:1:1), indicating the formation of an even lower symmetry species. ESI-MS confirmed the formation of a 2**BEN14**@Pd₄**THO-P**₈ host-

guest complex (Fig. 5.1c). Moreover, a DOSY experiment yielded a Stokes-Einstein radius of 13.7 Å (Fig. 5.1b), a similar value to the one measured for the 2BEN14@Pd₄AZU1₈ species in Chapter 3.

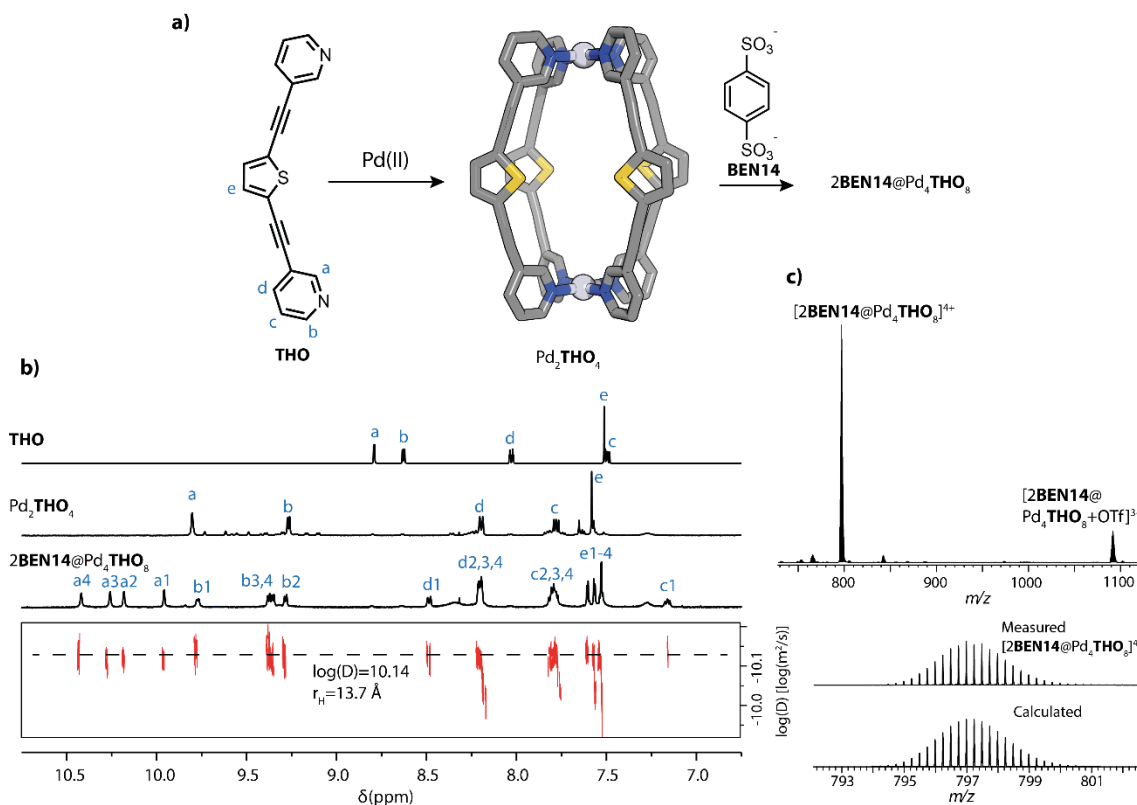


Figure 5.1: (a) formation of the cage Pd₂THO₄ (X-ray structure) and the transformation upon addition of guest BEN14. (b) ¹H-NMR (500 MHz, 298 K, DMSO-*d*₆) of the three species and the DOSY of host-guest complex 2BEN14@Pd₂THO₄. (c) ESI-MS of host-guest complex 2BEN14@Pd₄THO₈.

Sadly, despite my best efforts, no crystals of the newly formed species could be grown. Its structure remains unknown, despite the bits of evidence gleaned from 2D-NMR, which I will expose now.

The four-way split of the species is mostly evident on the **a** and **b** protons, the rest of the signals overlapping too closely to each other to make them out individually. The **a** protons were numbered from 1 to 4 and the COSY contacts were used to assign their corresponding pyridine protons **b**, **c**, and **d**. Only set 1 has very distinct signals from the rest. From the NOESY spectrum, I could determine that contacts occurred between **a1** and **a2**, and between **a3** and **a4**, but not between **a1** & **a3** and **a2** & **a4**, meaning that **a1** and **a2** belong to pyridines coordinated to the same palladium centres, distinct from the ones where **a3** and **a4** are located. Further NOE peaks confirm contacts between pyridine 1 and 2 (Fig. S5.27). The **e** protons are bundled too close to each other to reveal much of importance, except their change of multiplicity from singlets to doublets, and one NOE contact between an **e** and a **d** proton. What can be concluded from this analysis is that the structure possesses two symmetrically distinct Pd(II) coordination centres, counting each for two Pd cations.

As the structure could not be well determined despite extensive crystallisation attempts, I searched for potential derivatives of thiophene to prepare the same type of host-guest complex, and chose thieno[3,4-*b*]pyrazine-based ligands for their chromophoric properties, bulkier backbone potentially better at mimicking azulene, and their ease of synthetic access.

5.2 THIENO[3,4-*B*]PYRAZINE-BASED LIGANDS AND CAGES

Thieno[3,4-*b*]pyrazine (hereafter just thienopyrazine or TP) derivatives are part of a broader family of thiophene-substituted products investigated for their optoelectronic properties and for the preparation of organic polymers of potential use in organic solar cells.^[3-8] Interestingly, they can show intramolecular charge transfer phenomena between the thiophene ring acting as the donor and the pyrazine group acting as the acceptor.^[9] Moreover, while the unsubstituted backbone is of an off-white colour, its substituted cousins can show a much broader range of intense colours^[10-12] and emission.^[13] Due to their interesting electronic properties and their strong emission, I therefore chose to integrate them into our coordination assemblies for sensing and molecular recognition purposes, as well as to potentially serve as new optoelectronic materials.

The thieno-pyrazine (TP) backbone **3** can be easily accessed by aromatic cyclisation between thiophene-3,4-diamine (**1**) and a choice of diketones **2**, for example benzil (**2a**).^[14] Initially, a synthesis attempt was made with glyoxal, but the low stability of the resulting compound made me give up on this approach. Instead, the use of aromatic side groups stabilised the molecule, and this type of thienopyrazine was used in the rest of this section.

Backbone **1** can then be brominated by NBS on the 2- and 5-positions to yield intermediate **4**, followed by a Sonogashira coupling with 3-ethynylpyridine (**P**) or 8-ethynylisoquinoline (**IQ**) to yield the family of ligands **TP** (Fig. 5.2). All ligands were thoroughly purified by Gel Permeation Chromatography (GPC) before the preparation of the coordination species. Every ligand synthesised here showed bright yellow and orange fluorescence, even red for **TPd-P**. Furthermore, the structure of the last ligand could be confirmed by X-ray crystallography (Fig. 5.3).

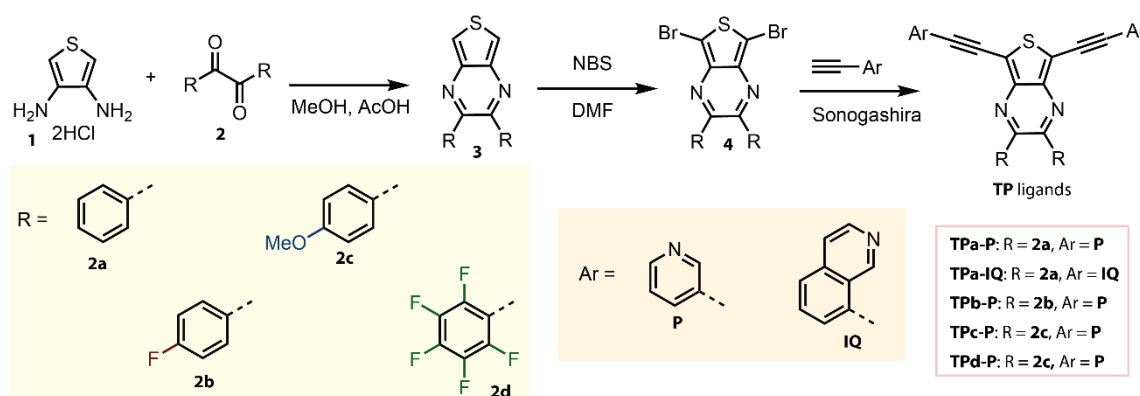


Figure 5.2: synthesis pathway of the ligands based on the TP backbone.

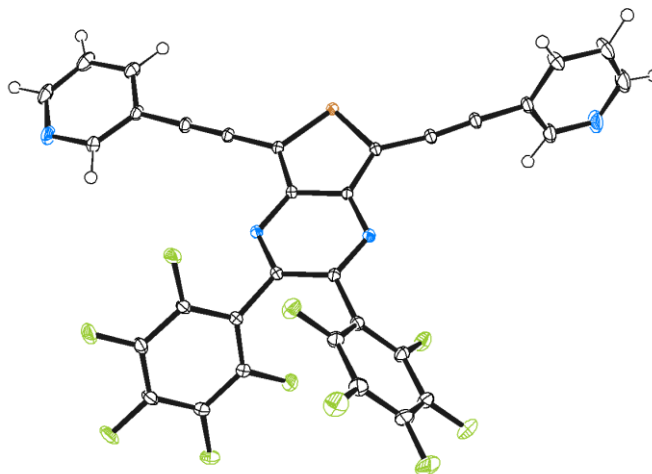


Figure 5.3: ORTEP representation of the X-ray structure of ligand **TPd-P** (ellipsoids drawn at 50% probability, black: C, blue: N, gold: S, green: F)

5.2.1 Synthesis of TPa-P cage

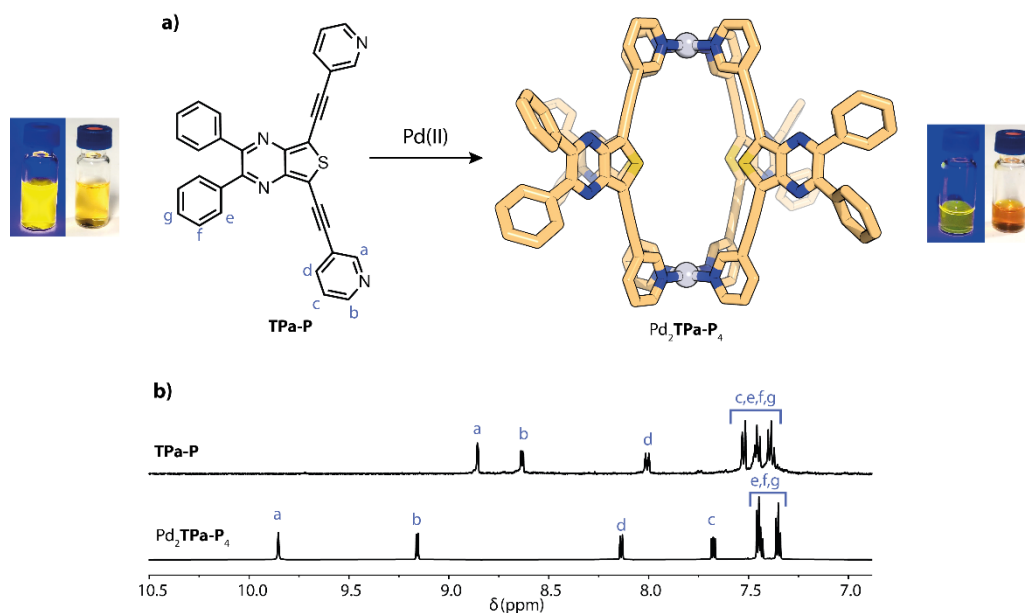


Figure 5.4: (a) preparation of cage Pd₂TPa-P₄ (DFT structure, ωB97XD/def2-SVP) from the corresponding ligand, with photographs of the corresponding species under normal and UV light, showing their emissive properties. (b) ¹H-NMR (500 MHz, 298 K, CD₃CN) of ligand **TPa-P** and of cage [Pd₂TPa-P₄](OTf)₄

The synthesis of the thienopyrazine-based cages was performed according to the general procedure (see sub-section 3.2.1) in acetonitrile (CD₃CN). Cage Pd₂TPa-P₄ was characterised by NMR (Fig 5.4) and ESI-MS (Fig S5.29). Despite my best efforts, no crystals of the homoleptic assemblies could be grown.

To my pleasant surprise, the cage formed from the highly luminescent **TPa-P** ligand still showed decent light emission, despite being visibly weaker. The quantum yield of ligand **TPa-P** was measured to be 55%, while the one of the Pd₂TPa-P₄ cage was measured to be 11-19% (depending

on the sample), a marked improvement from the examples of luminescent Pd₂L₄ cages discussed in Chapter 1.4.2. The reason such a strong luminescence is observed here probably stems from an already strong emission of the free ligand, as observed in the case of the unstacked DPP Pd₃L₆ structure discussed previously.^[15] Further details on Section 5.4.2.

The formation of Pd₂TPa-P₄ in DMSO was only partially successful, as much of free ligand could still be observed in the NMR spectrum after the addition of 0.5 eq. of Pd(II). The addition of more metal salt did not ameliorate the situation (Fig. S5.30). The addition of guest BEN14 to the partially formed cage solution triggered the partial transformation to another species with a 1:1:1:1 splitting (Fig. S5.31). However, free ligand was still a large part of the solution. Moreover, the prolonged heating of the DMSO solution turned the colour from yellow to brown, suggesting a degradation of the ligand. In addition, the same observation was made during crystallisation attempts from the DMSO solution. Therefore, DMSO was deemed unsuitable for the formation and study of this family TP-based cages. DMF was also tested but the addition of BEN14 to the cage solution caused precipitation, as was observed in the case of AZU1. Despite this failure in replicating the cage-to-cage transformation with TP ligands, they still offered many interesting emissive properties that could be studied on their own.

5.2.2 Synthesis of TPa-IQ helicite

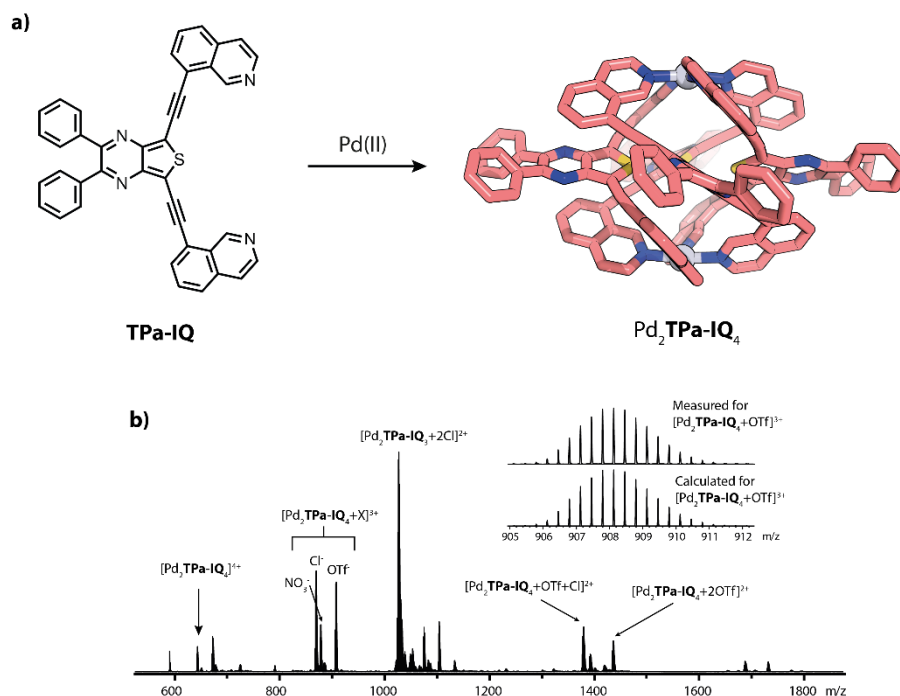


Figure 5.5: (a) formation of helicite Pd₂TPa-IQ₄ (DFT structure, ωB97XD/def2-SVP) (b) ESI-MS of the helicite.

Ligand TPa-IQ was prepared by replacing the donor with an 8-isoquinolinyl group with convergent vectors (Fig. 5.2). It was self-assembled according to the general procedure into a Pd₂TPa-IQ₄ quadruply-stranded helicite (Fig. 5.5a), as measured by ESI-MS (Fig. 5.5b) and NMR (Fig.

S5.32). Some other minor species were also detected in solution; they were determined to be of a similar size to the main species by DOSY analysis. Possibly due to the larger π -system compared to the pyridyl-capped species, the present ligand shows an orange emission and a darker colour (Fig. 5.6 & 5.13). Disappointingly, the emission of the helicate is noticeably quenched, compared to cage Pd₂TPa-P₄. The quantum yield was not measured however.

5.2.3 Synthesis of substituted TP cages

The substitution of the ligands on the pending phenyl groups was attempted in order to modulate the photophysical properties of the products by simple chemical modifications. Indeed, if adding electron donating or withdrawing groups to the phenyl groups could modify the electronic levels of the chromophore, a family of differently emitting ligands could simply be prepared by changing their side-chains. Thus, ligands TPb-P to TPd-P were synthesised starting from substituted benzil precursors (Fig. 5.2). TPb-P (with phenyl-4-F) and TPc-P (with phenyl-4-OMe) did not show significant difference in colour of both absorbance or emission compared to TPa-P (Fig. 5.6). However, the ligand TPd-P, with penta-fluorinated phenyl groups, showed a marked red shift of both absorbance and emission. Therefore, the initial assumption that the photophysical properties of the ligands could be tuned by substituting the side groups was confirmed. However, as a caveat, the modification has to be significant to yield appreciable results.

Cage Pd₂TPc-P₄ kept part of its luminescence, like Pd₂TPa-P₄, but was visibly quenched to a higher degree. Finally, the formation of Pd₂TPd-P₄ was accompanied with a marked blue shift of both the absorbance and the emission, turning from a bright red to an orange colour. Moreover, I was happily surprised to see that the fluorescence was still intense.

5.2.4 Photophysical properties of the homoleptic thienopyrazine assemblies

The absorption and emission spectra of the species previously discussed in this chapter have all been measured and analysed.

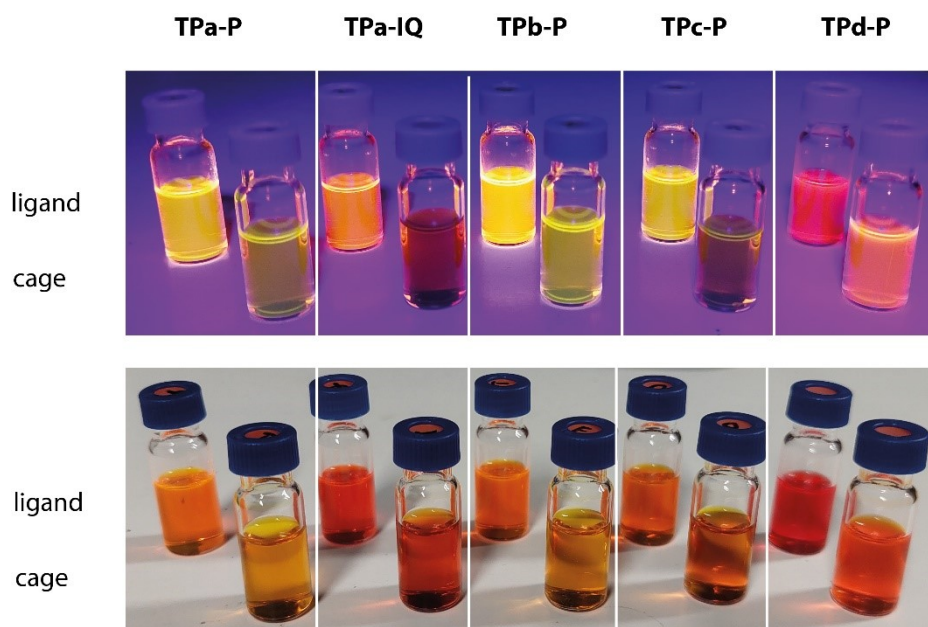


Figure 5.6: photographs of solutions of the ligands (in CHCl₃) and cages (in CD₃CN) discussed in this section under UV light (top) and white light (bottom).

A general first observation one can make is that the formation of the cages from the ligands is systematically accompanied by a blue shift of both the first band of the absorbance and of the emission (Fig. 5.7 & 5.8). Due to the systematic nature of the shift, it is probably attributable to the electron withdrawing nature of the coordinating Pd(II). In what way this influences the shift of the absorbance and of the emission is still unknown and would probably need to be investigated by computational means. This behaviour is similar to the one observed for the fluorenone-based assemblies we published earlier.^[16] However, it is inverse to the behaviour of our previously prepared DPP ligands, which experienced a bathochromic shift of both absorption and emission upon coordination with Pd(II).^[15] **AZU1**, as discussed in Section 3.7.6, also undergoes a blue-shift upon coordination with Pd(II).

Few differences were observed between the absorption spectra of ligands **TPa-P** and **TPb-P**, both having a first local maximum at around 465 nm. The methoxy-substituted **TPc-P** ligand showed a bigger difference by having a shifted local maximum at 425 nm. It does however possess a shoulder centred around 465 nm. The perfluorinated phenyl ligand **TPd-P** shows a broad isolated band at around 497 nm. Finally, ligand **TPa-IQ** possesses a local absorption maximum close to the last one at 500 nm, probably attributable to the overall larger π surface of the two isoquinoline donors (Fig. 5.7a).

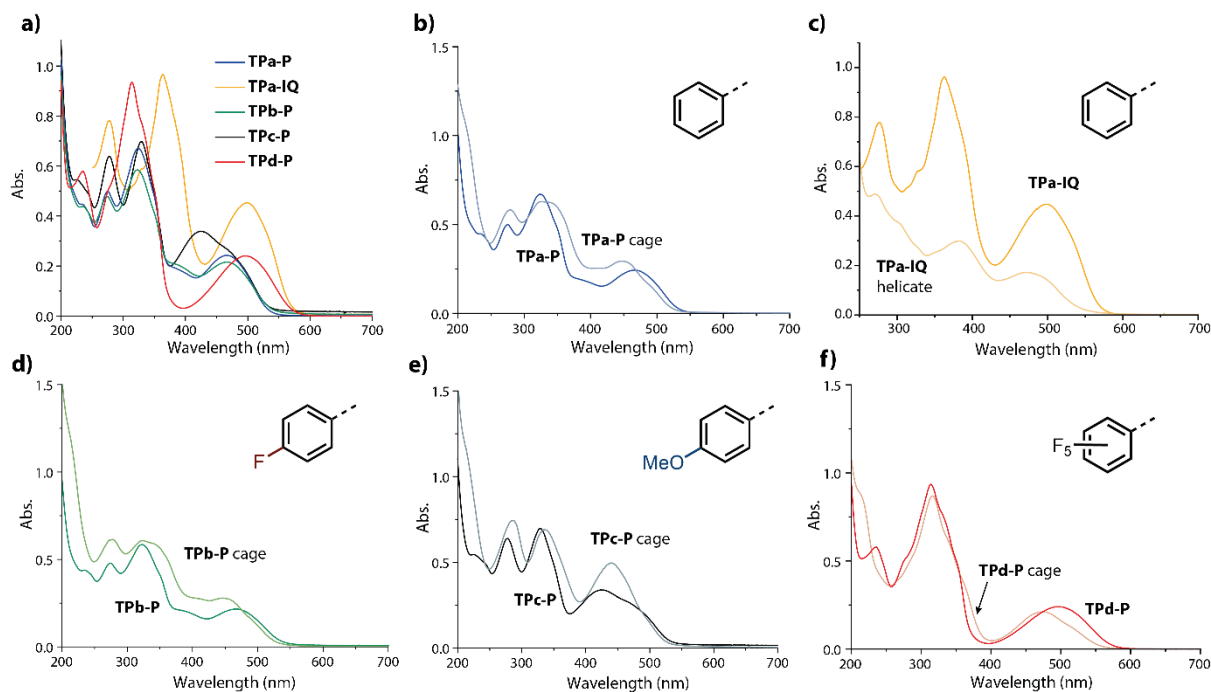


Figure 5.7: (a) Overlay of the absorption spectra of the TP ligands (b)-(f) spectra of the ligands and of their corresponding coordination cages and helicate. Concentration in ligand: 0.1 mM, 2 mm cuvette, solvent MeCN (except **TPa-IQ** in DMSO).

The corresponding cages all show a blue shift of the first local maxima of around 15-25 nm, but their overall spectra do not appear dramatically changed compared to the ligands, to the exception of helicate Pd₂TPa-IQ₄ whose absorption in the whole measured range is visibly reduced compared to the free ligand. Moreover, the maximum is blue-shifted by 28 nm (500 nm to 472 nm, Fig. 5.7c). The biggest visible change happens with the formation of Pd₂TPd-P₄, the solution of the ligand turning from red to orange upon addition of Pd(II). Moreover, the shift of the maxima is the largest observed with the pyridine-based cages, with a difference of 25 nm at the local maxima (500 nm for the ligand to 475 nm for the cage).

The emission spectra paint a clearer picture of the influence of the substituents on the phenyl side groups over the S₁-S₀ transition energy. Indeed, the electron-donating methoxy group blue shifts the emission of the unsubstituted ligand by around 7 nm compared to the unsubstituted one. On the opposite, the singly fluorinated ligand's emission is only slightly red shifted by 2 nm. However, the effect is enhanced manyfold when the phenyl rings become perfluorinated; there, the emission of the ligand is shifted by 52 nm (Fig. 5.8a).

The emission of the cages was partially quenched as expected by the coordination of Pd(II). However, this effect was the most marked in Pd₂TPc-P₄ and the reason is not clear by simple examination of the spectra. An explanation may be found in computational models. Moreover, by measuring the emission of the ligand at different excitation wavelengths, I found that the band creating the shoulder centred at 460 nm is probably the sole responsible for the emission of the ligand. Indeed, irradiating at different wavelengths yielded the same excitation spectrum. The local maximum at 425 nm thus probably corresponds to a dark state. Every pyridine-based assembly show an approx.

10-15 nm shift in emission upon coordination with Pd(II), except for **TPd-P**, where the shift is of 25 nm.

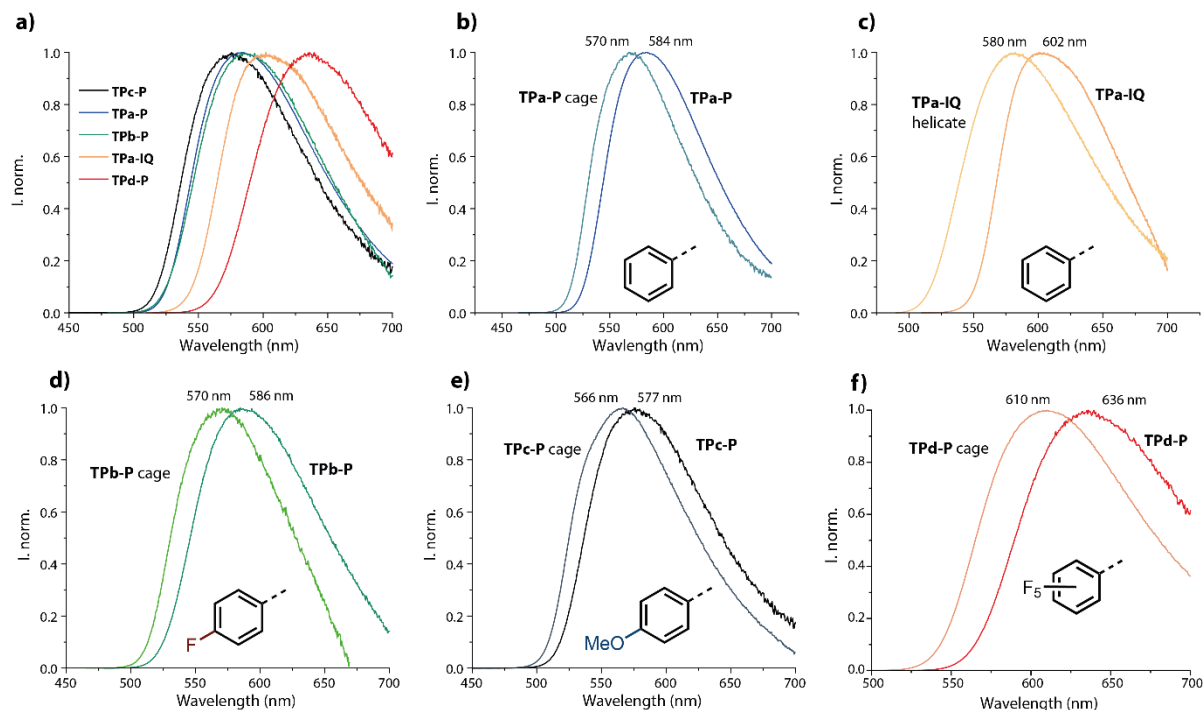


Figure 5.8: Normalised fluorescence spectra of: (a) every ligand prepared in this chapter and (b)-(f) overlay of the spectra of each ligand and of their corresponding Pd₂L₄ species. Solvent: acetonitrile, except **TPa-IQ** in DMSO.

Finally, the emission of helicate Pd₂**TPa-IQ**₄ was also more noticeably quenched and was the one with the strongest hypsochromic shift compared to its ligand (Fig. 5.8c), although it could be explained by the difference in solvents between the ligand (DMSO) and the helicate (MeCN). The DFT structure of the assembly shows a very tight structure (Fig. 5.5a), bringing the TP dyes close together, in a way that might facilitate ligand-to-ligand interactions and therefore, akin to an H-aggregate, lead to an hypsochromic shift and a quenching of the luminescence.^[17] More precise experiments would however be needed to validate this hypothesis.

To help us shed some light into the reason the luminescence of the ligand was not fully quenched upon self-assembly with Pd(II), a DFT calculation of the orbitals of Pd₂**TPa-P**₄ was performed (ω B97XD/def2-TZVP). Indeed, in a previous work of our lab, we observed that the luminescence of a phenoxazine-based ligand was fully quenched upon formation of its corresponding Pd₂L₄ cage.^[18] DFT models showed that the HOMO of this assembly was located on the phenoxazine backbone, while the LUMO was located on and around the Pd(II) centres. Thus, upon photoexcitation, electrons are transferred to the metal, and the overall fluorescence of the assembly is quenched. In the present case, the HOMO of the **TPa-P** ligand is located on the pending phenyl groups and the thienopyrazine core, while the LUMO is not located around the Pd(II) centres, but largely distributed on the core and on the arms of the ligand, a demonstration of the intramolecular donor-acceptor character of the thienopyrazine. The closest unoccupied molecular orbital centred on

Pd(II) is the LUMO+4 (LUMO+1 and +2 are degenerate) (Fig. 5.9). Therefore, the larger energy difference between the HOMO and the LUMO+4 may explain why the fluorescence of the assembly is not fully quenched, unlike many Pd(II)-based cages.

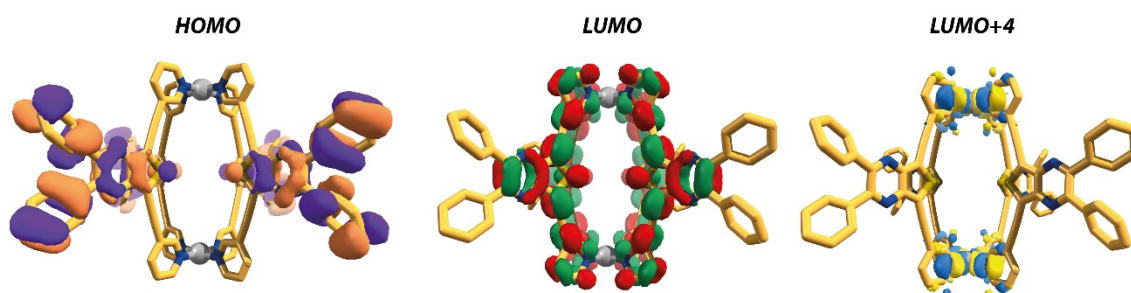


Figure 5.9: Frontier molecular orbital visualisation for cage Pd₂TPaP₄. LUMO: orange and purple, LUMO: red and green, LUMO+4: yellow and azure. DFT computation (ω B97XD/def2-TZVP).

By carefully tailoring the orbital energies of the assemblies, one might in the future be able to easily prepare highly luminescent assemblies, even when using Pd(II) as a metal node. Moreover, the integration of multiple chromophores inside of a single assembly might enhance even more the emissive properties of the cage.

5.3 HETEROLEPTIC ASSEMBLIES

Having observed the particularly interesting luminescent properties of the present family of thienopyrazine dyes and of their corresponding homoleptic cages, I sought next to incorporate them into heteroleptic assemblies to test their interactions with other types of ligands.

5.3.1 Carbazole and fluorenone

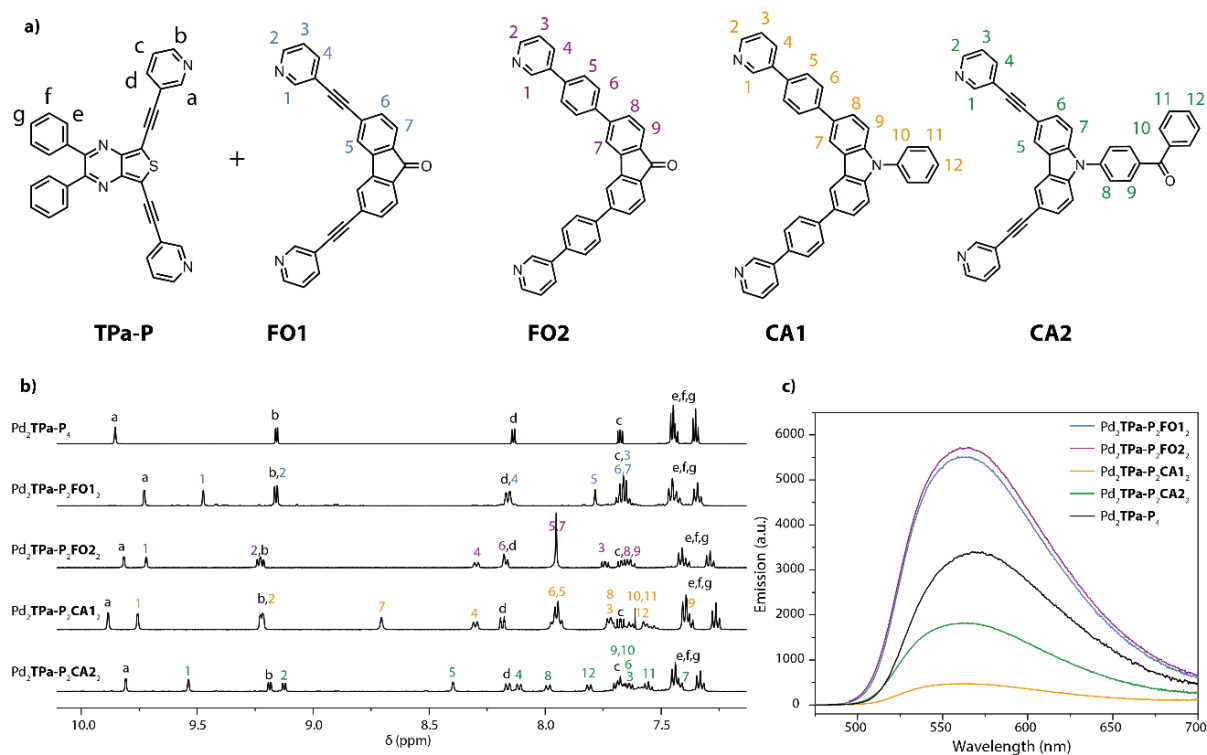


Figure 5.10: (a) structure of the ligands tested for heteroleptic combinations with **TPa-P**. (b) ¹H-NMR (500 MHz, CD₃CN, 298 K) of the homo- and heteroleptic cages with formed from the ligands above. (c) Fluorescence spectra of the cages measured at the same conditions (concentration in cage: 70 μM, MeCN) showing the relative increase of luminescence when using fluorenone ligands, and a quenching when using carbazole ligands.

As observed previously, the combination of a carbazole^[15] or of a fluorenone^[19] with a DPP-based ligand could yield extremely bright heteroleptic assemblies through ligand-to-ligand energy transfer.^[19] Thanks to good shape- and size-complementarity between ligand **TPa-P** (divergent vectors) and of certain of the carbazole and fluorenone ligands previously synthesised in our lab (convergent vectors), four different Pd₂TPa-P₂L₂ heteroleptic cages could be assembled (Fig. 5.10a). The newly formed cages were characterised by NMR (Fig 5.10b) and ESI-MS (Fig. S5.33, 35, 37, and 39).

By simple eye inspection, it was apparent that the emission of the fluorenone-TP heteroleptic cages was increased compared to the homoleptic Pd₂TPa-P₄. However, the emission of the carbazole-TP species was, on the opposite, quenched. Interestingly, the emission spectra of every species only showed the emission band of **TPa-P**, and nothing corresponding to the second ligand. This fact may be evidence of energy transfer between the two chromophores present in the same assembly, like in the fluorenone-DPP cages.^[20] Indeed, the emission of the fluorenone ligand ($\lambda_{\max, \text{em}} \approx 490 \text{ nm}$)^[21] overlaps with the S₀-S₁ absorption band of **TPa-P** ($\lambda_{\max, \text{ex}} \approx 480 \text{ nm}$), potentially leading to FRET (or another similar form of energy transfer) between the two chromophores. This would explain why only the emission of **TPa-P** is observed in every heteroleptic system studied here. However, a deeper inspection of the system through more advanced experiments is needed to confirm if a similar process

is at play in the present system. Quantum yields of the species were measured and confirmed the trends observed by eye, with a 20% QY for the fluorenone-TP assemblies, and a QY as low as 1% for the carbazole-TP cages.

5.3.2 Pd₂TPa-P₂FRQ₂

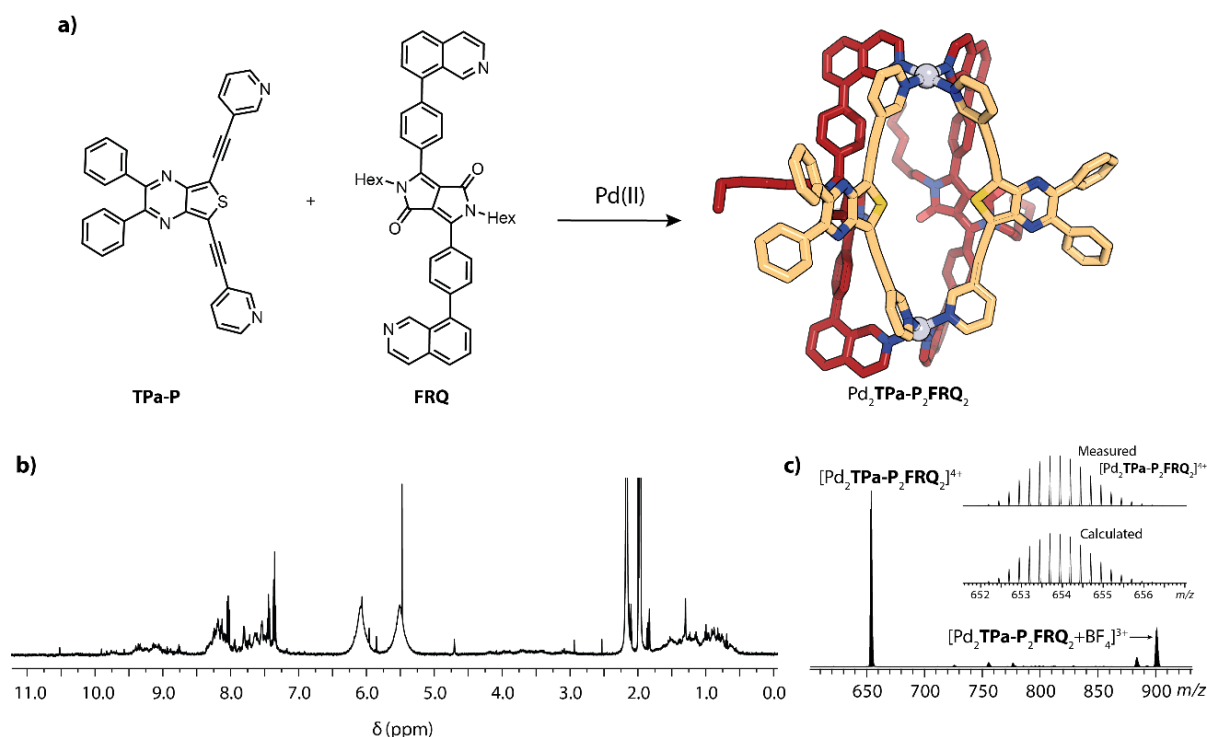


Figure 5.11: (a) preparation of cage Pd₂TPa-P₂FRQ₂ (X-ray structure) from the corresponding ligands. (b) ¹H-NMR (500 MHz, 298 K, CD₃CN) of cage [Pd₂TPa-P₂FRQ₂](BF₄)₄ and (c) ESI-MS of the same species.

The combination of **TPa-P** with another highly luminescent ligand previously synthesised in the group by Dr. Irene Regeni based on the DPP backbone, **FRQ** (Fig. 5.11a),^[15] was also tested. The two ligands were mixed in CD₃CN and 0.5 eq. of [Pd(CH₃CN)₄](BF₄)₂ was added as a solution. The mixture was heated and stirred overnight and afterward its NMR spectrum was measured. To my surprise, only a forest of peaks of low intensity was observed (Fig. 5.11b), making it impossible to assign it to a specific species. Additionally, the intense fluorescence characterising both ligands was now mostly quenched. The experiment was attempted a second time, to the same outcome. However, the ESI-MS revealed that a clean heteroleptic assembly Pd₂TPa-P₂FRQ₂ had formed (Fig. 5.11c). The very messy NMR of the otherwise clean cage may be explained by the bulk and lower symmetry of **FRQ**, which may cause the presence in solution of slowly exchanging conformational isomers of the cage. A VT NMR experiment could be performed in the future to try to clean-up the spectrum.

Crystals of the species could also be grown from the acetonitrile solution by slow diffusion of diethylether. The compound crystallises in the triclinic P-1 (no.2) space group and is, as expected, the heteroleptic cage Pd₂TPa-P₂FRQ₂ (Fig. 5.11a), with the ligands in a *cis* configuration. Despite some disorder in the hexyl chains of FRQ and on the side phenyl groups of **TPa-1** (Fig. S5.45, 46),

only one major configuration of the cage was observed in the crystal and cannot explain the many weak signals of the NMR spectrum. However, despite its interesting dichotomy between the MS and NMR spectra, no other interesting properties were found for the cage, and it will not be discussed further.

5.3.3 Pd₂TPa-P₂TRO₂

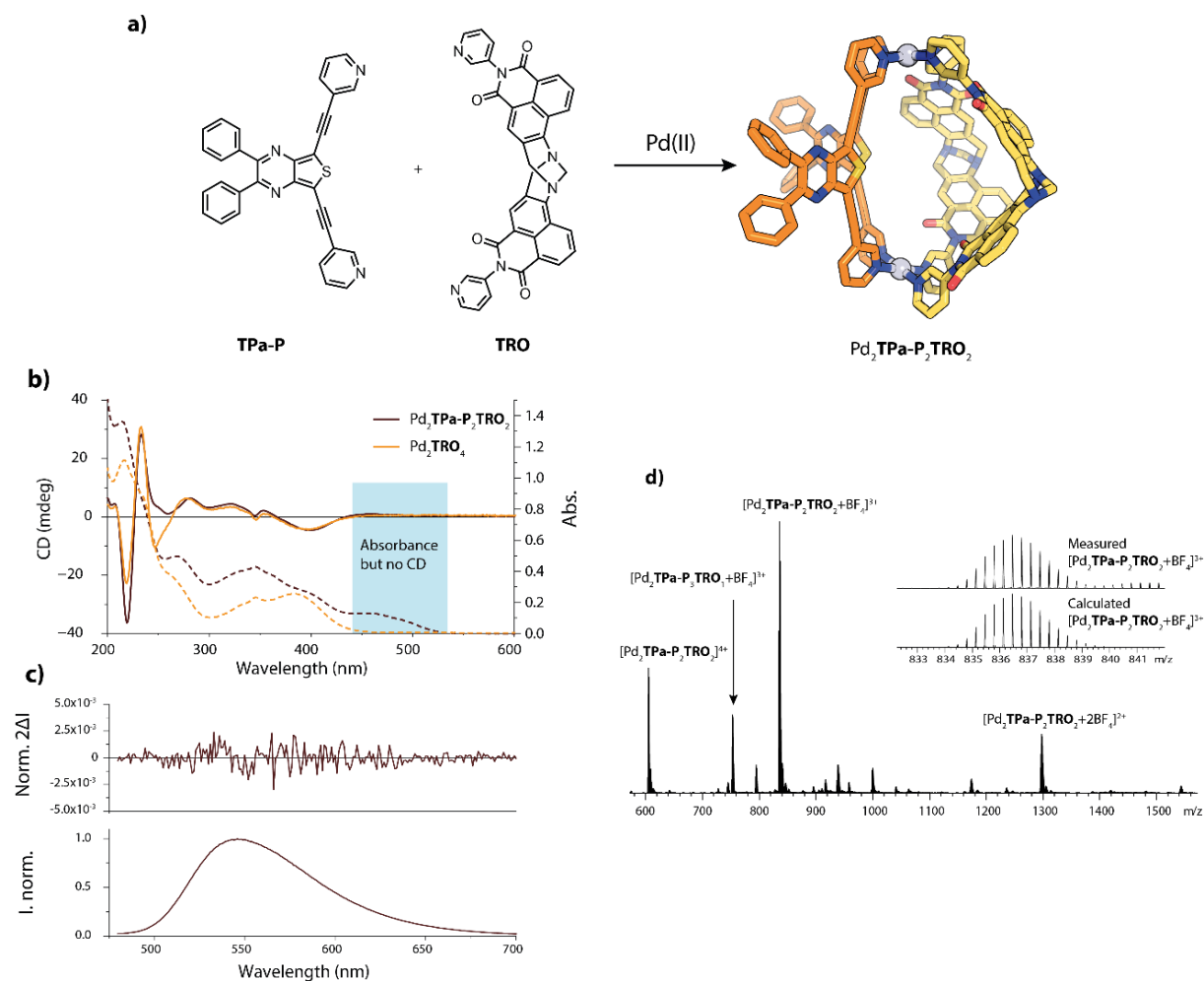


Figure 5.12: (a) formation of cage Pd₂TPa-P₂TRO₂ (PM6 model) from its components. (b) overlap of the CD and absorbance spectra of Pd₂TPa-P₂TRO₂ and Pd₂TRO₄ (0.116 mM in TRO, 1 mm cuvette), showing the almost complete lack of chirality transfer from TRO to TPa-P from 275 nm to 525 nm. (c) CPL (top) and emission (bottom) spectra of Pd₂TPa-P₂TRO₂ (d) ESI-MS spectrum of Pd₂TPa-P₂TRO₂.

A combination of TPa-P with a chiral ligand based on Tröger's base, TRO, was tested for its potential to show ligand-to-ligand chirality transfer which might lead to CPL emission of the cage (Fig. 5.12a).^[21,22] While the homoleptic cage Pd₂TRO₄ is also slightly luminescent, I hoped that the inclusion of the highly emissive TPa-P would boost the luminescent properties of the heteroleptic assembly.

The cage was assembled according to the general protocol, and it was heated at 70°C overnight. The ¹H-NMR spectrum revealed one main species with a splitting pattern (2 different

After the previous CPL-silent system, I made a second attempt to prepare a CPL-emitting thienopyrazine-based system. Looking at their size and shape complementarity, a combination of **TPa-IQ** and chiral ligand **ST5**^[21] was used. The ligands and Pd(II) were mixed according to the general protocol and the solution was heated overnight (Fig. 5.13a). The resulting ¹H-NMR spectrum showed the expected splitting pattern for a chiral Pd₂A₂B₂ cage (although some subspecies could still be observed) (Fig. S4.42), and this nuclearity was confirmed by ESI-MS (Fig. 5.13b). The absorbance spectra of the ligand and of the homo- and heteroleptic species were measured by keeping the chromophoric ligand at a constant concentration (0.1 mM). Interestingly, the absorption coefficient of the chromophore is lowered upon coordination with Pd(II) in both assemblies, but even more so in the homoleptic helicate (Fig. 5.14a).

This time, a CD signal corresponding to **TPa-IQ** was observed in the visible and near-UV, where **ST5** does not absorb (300-600 nm) (Fig. 5.14b), and a CPL signal was measured as well, confirming in this case a chirality transfer between the chiral ligand and the emissive one (Fig. 5.14c). The maximal g_{lum} of the heteroleptic cage was measured to be $2.0 \cdot 10^{-4}$ at 572 nm, a weak value compared to the previously reported values for cages.^[19,21,22] Due to time constraints, further tests were not conducted. However, the effect of chiral guests on the CPL emission could be studied in the future.

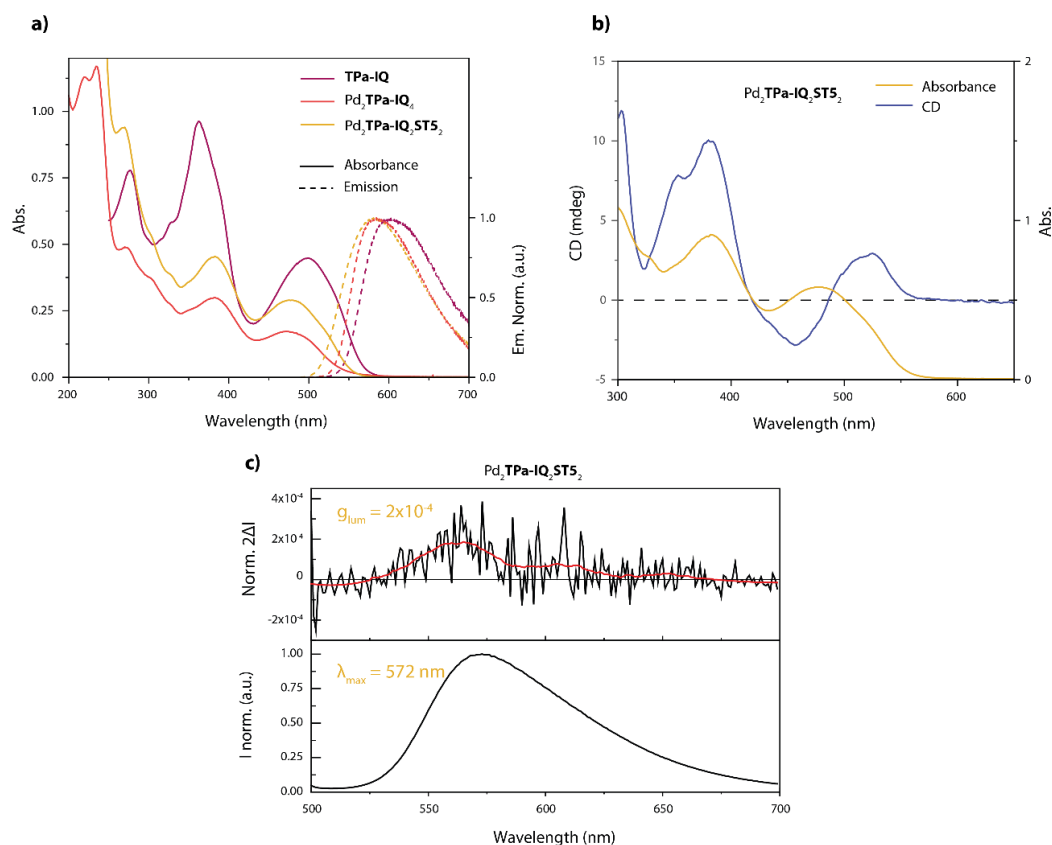


Figure 5.14: (a) Absorbance (full lines) and normalised emission (dashed lines) of the ligand **TPa-IQ** (in DMSO) and Pd₂TPa-IQ₄ and Pd₂TPa-IQ₂ST₅₂ (CH₃CN). (b) Absorbance (yellow) and CD (blue) spectra of Pd₂TPa-IQ₂ST₅₂. (c) CPL (top) and normalised emission (bottom) spectra of cage Pd₂TPa-IQ₂ST₅₂. Concentration in **TPa-IQ**: 0.1 mM, 2 mm cuvette.

5.4 PERSPECTIVE

While no concrete applications to the present thieno-pyrazine cages have been found for now, the chemical flexibility of the backbone may be harnessed to create more interesting highly luminescent assemblies by varying the linkers of the ligands for example. A brief attempt was made to replace the alkyne linkers by phenyl groups. The resulting ligand was sadly fully insoluble in most solvents (except very sparsely in hot DMSO), and did not create any easily determined assembly upon coordination to Pd(II). It showed however a very nice pinkish-red emission, and its colour and emission were fully stable in DMSO upon heating, a certain advantage over the ligands presented in this chapter which decompose in the same solvent. Substituting the side phenyl groups with alkyl chains may help with the solubility issues. Moreover, the phenyl linkers could potentially be replaced by triazoles by assembling the final ligand through a copper-catalysed click reaction. Thus, the donor vectors would be much more favourable to the formation of a Pd₂L₄ cage. Moreover, the rotation of the triazoles may lend this new cage a significant plasticity upon guest binding for example.

In addition, the substituted side phenyl groups could also be used in the future to add two more donor groups and create a tetratopic ligand, similar to the ones used by the Mukherjee group.^[23] If problems of solubility can be mitigated, highly luminescent barrel-like assemblies could be prepared and potentially serve as CPL-active supramolecular hosts for the detection of chiral guests in aqueous solutions.

Finally, the emissive properties, as well as the interesting properties of intramolecular charge transfer of the thienopyrazine backbone can be studied in deeper detail and serve as the basis for novel optoelectronic materials based on coordination assemblies.

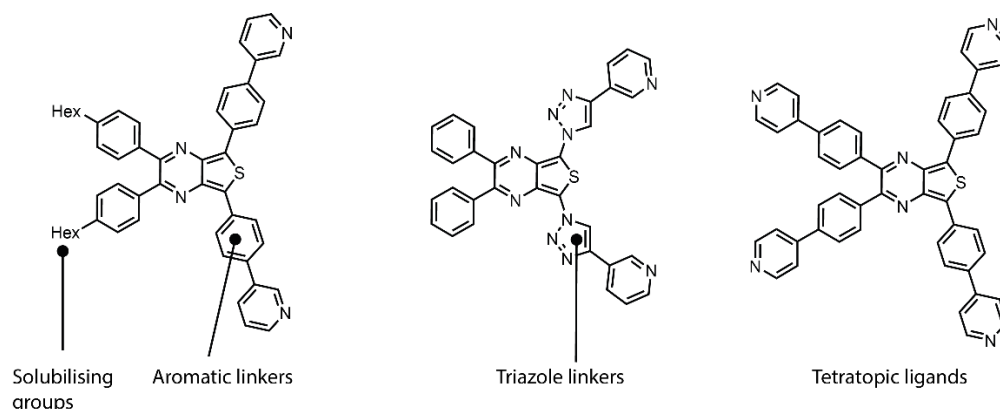


Figure 5.15: potential modifications that could be brought to the TP ligands in the future.

5.5 CONCLUSION

As a first step, I prepared a thiophene-based ligand **THO** that self-assembles into a Pd₂THO₄ cage. In turn, this cage can undergo a transformation to a larger Pd₄THO₈ species upon addition of

guest **BEN14**. This change in size and shape is identical to what was described in Chapter 3 with an azulene-based cage transforming into a tetrahedron. Unfortunately, a difference in the pattern of the ¹H-NMR spectrum between the two species meant that I could not assign with certainty a tetrahedral geometry to Pd₄**THO**₈ in the absence of crystallographic data. On the other hand, it is possible to envision a tetrahedral species with ligands locked into certain positions which could in turn result into the four-way split of the NMR, instead of the expected two-way split. Despite my best efforts, sadly I could not model such a complex. However, with this experiment I could show that small cages with a five-membered ring backbone and alkyne linkers could repeatedly undergo transformation towards a larger species upon the addition of a benzene disulfonate guest.

Next, I attempted to prepare the same kind of system with a larger thiophene derivative as a backbone. A series of luminescent thienopyrazine ligands were prepared. The cages prepared with those ligands were still luminescent, unlike many other Pd(II)-based cages. By substituting the pending phenyl groups, I could fine-tune the emission of the ligands and of their cage. Moreover, the formation of heteroleptic cages with this new family of ligands was studied. First, I could show that heteroleptic cages formed with fluorenone ligands increased the luminescence of the overall assembly, while carbazole ligands quenched the emission. Next, I also prepared two systems with chiral ligands, and unexpectedly only one showed the expected chirality transfer to the luminescent unit.

While incomplete, this study may be a stepping stone for the preparation of a vast array of luminescent cages for sensing applications. Moreover, thanks to the optoelectronic properties of thienopyrazines, one could find further uses for those assemblies in light-harvesting materials, such as artificial photosynthetic systems.

5.6 EXPERIMENTAL PART

5.6.1 General methods

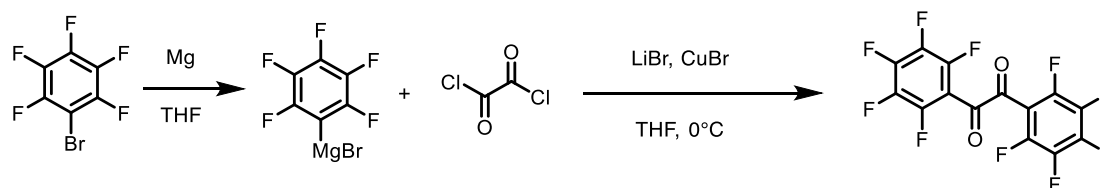
Where necessary, experiments were performed under argon atmosphere using standard Schlenk techniques. Chemicals and standard solvents were purchased from Sigma Aldrich, Acros Organics, Carl Roth, TCI Europe, VWR, ABCR and used as received, if not mentioned differently. Dry solvents were purchased or purified and dried over absorbent-filled columns on a GS-Systems solvent purification system (SPS). Reactions were monitored with thin layer chromatography (TLC) using silica coated aluminium plates (Merck, silica 60, fluorescence indicator F254, thickness 0.25 mm). For column chromatography, silica (Merck, silica 60, 0.02–0.063 mesh ASTM) was used as the stationary phase. Gel permeation chromatography (GPC) purification of ligands were performed on a JAI 9210-II NEXT GPC System with a JAIGEL HH-2/HH-1 column combination running with CHCl₃ (HPLC grade). UV-vis spectra were recorded on a DAD HP-8453 UV-Vis spectrometer. Cuvette path length 1 cm, unless otherwise stated; wavelength: 270 nm – 900 nm, step size: 1 nm. Fluorescence spectra were recorded on a Jasco FP-8300 fluorescence spectrometer. Cuvette path length 2 mm, step size 0.5 nm.

High resolution Electrospray ionization (ESI) mass spectra were recorded on Bruker ESI timsTOF (trapped ion mobility-time of flight) and Compact mass spectrometers (positive mode). All samples were diluted with spectroscopy-grade CH₃CN (1:10).

NMR experiments were performed on Bruker AVANCE III 500, 600 or 700 MHz spectrometers. Chemical shifts for ¹H and ¹³C are reported in ppm with residual solvent as reference: acetonitrile (1.94 ppm for ¹H, 1.32 ppm for ¹³C), DMSO-*d*₆ (2.50 ppm for ¹H, 39.52 ppm for ¹³C) and CDCl₃ (7.26 ppm for ¹H, 77.16 ppm for ¹³C). Abbreviations for signal multiplicity in the ¹H-NMR spectra are indicated as following: s: singlet, d: doublet, t: triplet, dd: doublet of doublets; dt: doublet of triplets; m: multiplet, b: broad.

5.6.2 Synthetic procedures

2,3-diphenylthieno[3,4-*b*]pyrazine (**3a**) and 5,7-dibromo-2,3-diphenylthieno[3,4-*b*]pyrazine (**4a**) were prepared according to published procedures.^[24] Benzil (**2a**), 4,4'-difluorobenzil (**2b**), 4,4'-dimethoxybenzil (**2c**), 3,4-diaminothiophene dihydrochloride (**1**), and 3-ethynylpyridine were obtained commercially. Ligands **FO1**, **FO2**, **CA1**, **CA2**, **FRQ**, **TRO**, and **ST5** were previously synthesised in the lab, and used as is.

5.6.2.1 Synthesis of the precursorsPerfluorobenzil (3d):

Magnesium turnings (240 mg, 10 mmol) were added to a dry 2-necked round-bottom flask with an iodine crystal. Then, under argon, the RBF was heated until the iodine evaporated. Then, 8 ml of dry THF were added with a stirrer and 250 μ l (out of 1.247 ml, 2470 mg, 10 mmol) of pentafluorobromobenzene were added to the solution. The flask was then sonicated for 5 minutes, and after that the stirring was turned on. When the yellow colour had faded, a reflux column was fitted to the flask and the rest of the pentafluorobromobenzene was added in portions. After everything had reacted, anhydrous LiBr (1.74 g, 20 mmol) and CuBr (1.43 g, 10 mmol) were added to 10 ml of dry THF in a 2-necked round-bottom flask and stirred at 0°C. The solution of the Grignard reagent was then added dropwise to the solution. After stirring 10 minutes at 0°C, oxalyl chloride (635 mg, 429 μ l, 5 mmol) was added. The solution was then left to stir another 30 minutes. Then, NH₄Cl sat. was added to quench the reaction. The phases were separated, and the aqueous layer was washed with DCM. The organic layers were combined and washed with water, and then dried with MgSO₄, reduced under pressure, and the crude was chromatographed on silica (pentane, EtOAc 5% to 15%) to yield the final product as a yellow oil that solidified upon standing.

Yield: 1'280 mg, 3.28 mmol, 66%

¹³C-NMR (151 MHz, CDCl₃) δ 181.39 (s), 147.69-147.51 (m), 146.46-146.22 (m), 145.96-145.78 (m), 144.71-144.47 (m), 139.09-138.86 (m), 137.39-137.17 (m), 108.99-108.79 (m).

¹⁹F-NMR (565 MHz, CDCl₃) δ -136.91 (dtt, *J* = 19.2, 6.9, 3.9 Hz), -142.43 (tt, *J* = 20.8, 6.2 Hz), -158.69 – -158.83 (m).

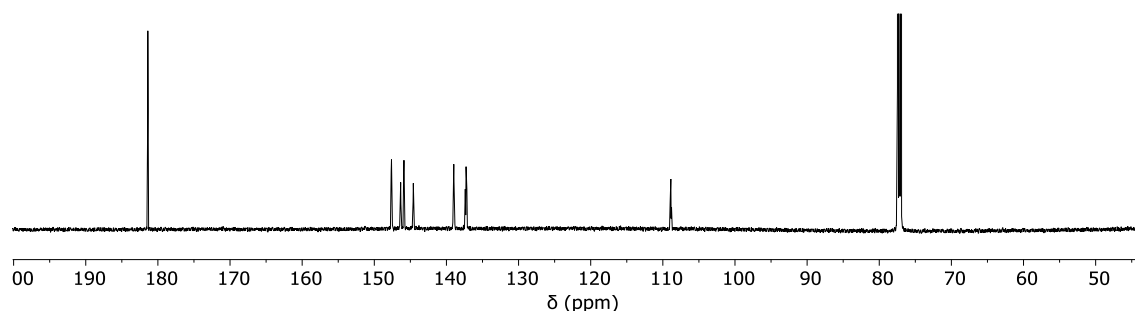


Figure S5.1: ¹³C-NMR (151 MHz, 298 K, CDCl₃) of perfluorobenzil **2d**

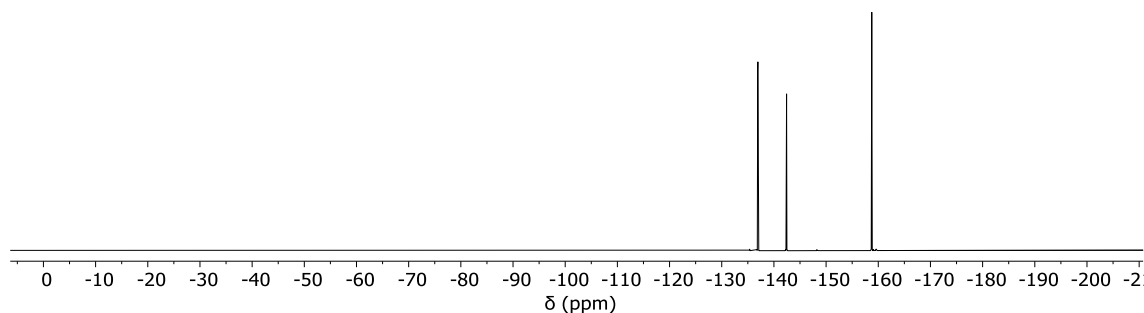
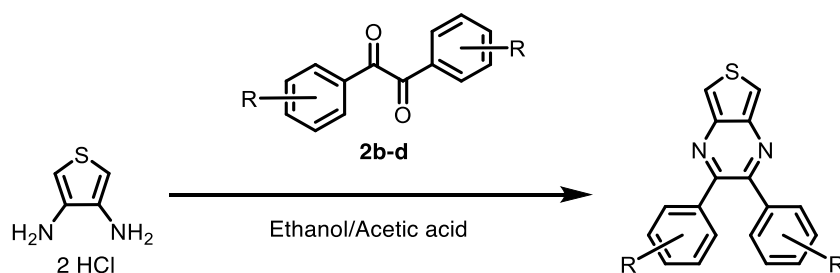


Figure S5.2: ¹⁹F-NMR (565 MHz, 298 K, CDCl₃) of perfluorobenzil **2d**.

Substituted 2,3-diphenylthieno[3,4-*b*]pyrazine (**3b-d**):



The substituted benzil (**2b-d**, 1.5 mmol) was added to a round-bottom flask with 40 ml of ethanol and 1 ml of acetic acid, and a solution of 3,4-diaminothiophene dihydrochloride (**1**, 2.5 mmol) neutralised with the same amount of triethylamine in THF was slowly dropped into the solution under stirring for a few hours. Then the solution was refluxed for 2 hours. The completion of the reaction was monitored by TLC; if a band corresponding to the starting benzil was observed, more of the diaminothiophene was added. Afterward, the solvent was evaporated, and the crude was chromatographed on silica to yield the title products.

- **3b** (R=F): yield: 62 %, tan solid

ESI-MS: calculated for [C₁₈H₁₀F₂N₂S+H]⁺: 325.0606, observed: 325.0566

NMR: too impure

- **3c** (R=OMe): yield: 29 %, bright yellow solid

ESI-MS: calculated for [C₂₀H₁₆N₂O₂S]⁺: 349.1005, observed 349.0947

¹H-NMR (500 MHz, CDCl₃) δ 8.09 (s, 2H), 7.46 – 7.40 (m, 4H), 6.89 – 6.84 (m, 4H), 3.83 (s, 6H).

¹³C-NMR (126 MHz, CDCl₃) δ 160.63, 152.59, 131.36, 117.24, 113.95, 113.80, 55.36 (1 nucleus missing).

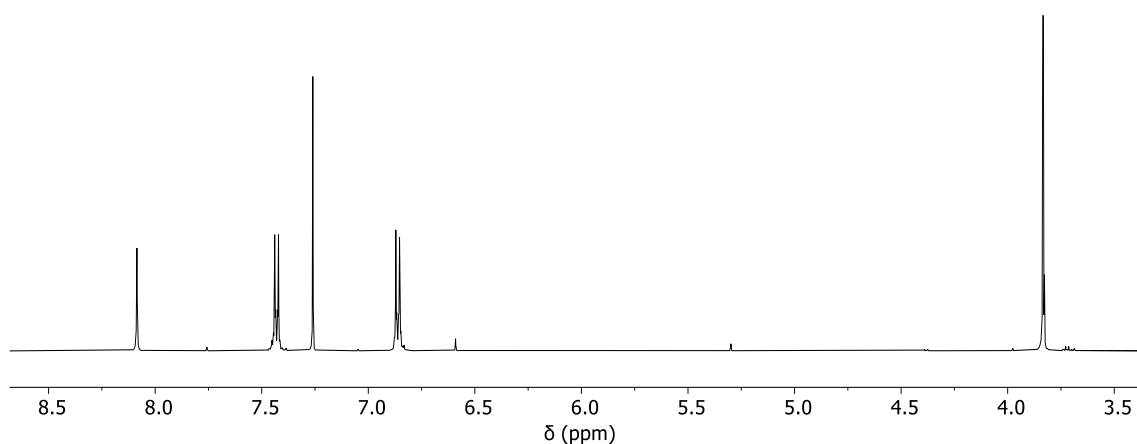


Figure S5.3: ¹H-NMR (500 MHz, 298 K, CDCl₃) spectrum of intermediate **3c**.

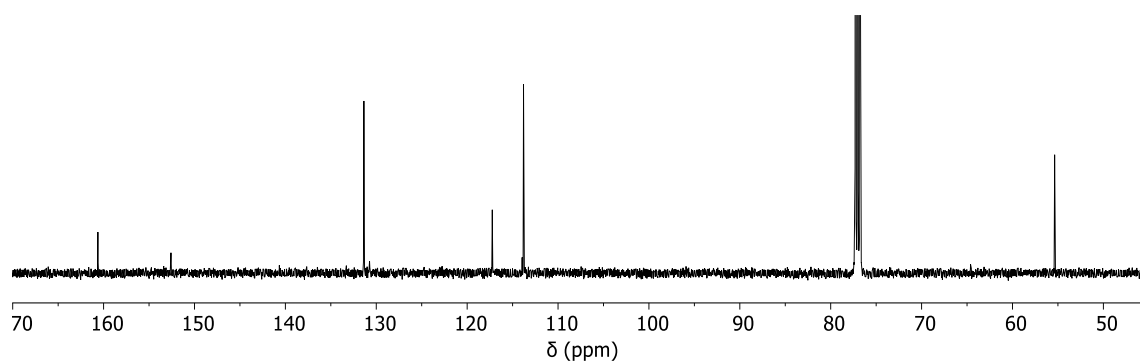


Figure S5.4: ¹³C-NMR (151 MHz, 298 K, CDCl₃) spectrum of intermediate **3c**.

- **3d** (R=F₅): yield: 55%, off-white solid

ESI-MS: could not be detected

¹H-NMR (600 MHz, CDCl₃) δ 8.27 (s, 1H).

¹³C-NMR (151 MHz, CDCl₃) δ 145.76, 144.09, 143.26, 141.96, 141.55, 141.47, 141.46, 138.59, 136.91, 136.80, 120.28, 112.73, 112.62, 112.51. (weak intensity)

¹⁹F-NMR (565 MHz, CDCl₃) δ -140.84 (dt, *J* = 23.5, 4.5 Hz), -150.10 (t, *J* = 20.9 Hz), -159.91 (td, *J* = 22.3, 7.6 Hz).

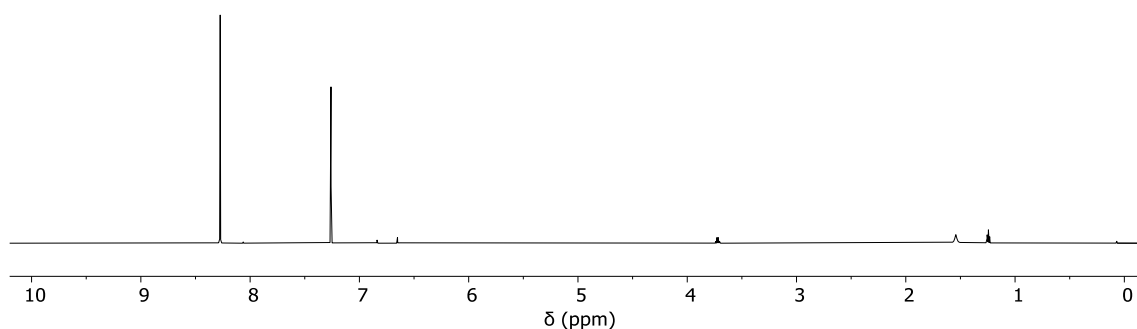


Figure S5.5: ¹H-NMR (500 MHz, 298 K, CDCl₃) spectrum of intermediate **3d**.

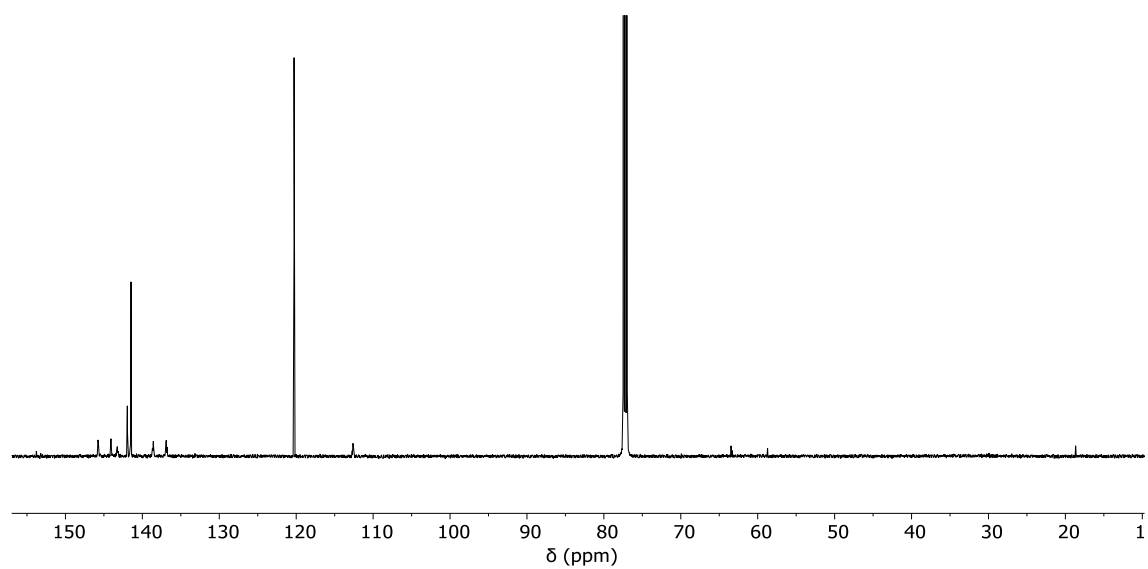


Figure S5.6: ¹³C-NMR (151 MHz, 298 K, CDCl₃) spectrum of intermediate **3d**.

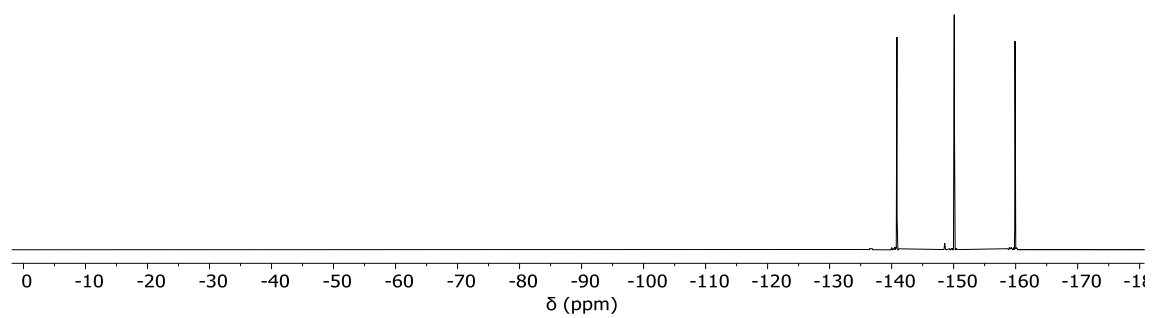
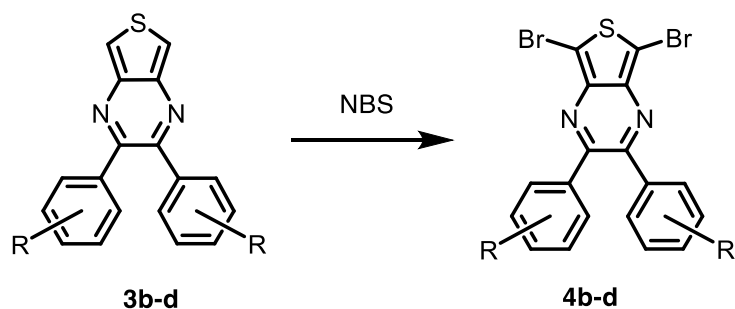


Figure S5.7: ¹⁹F-NMR (565 MHz, 298 K, CDCl₃) of intermediate **3d**.

Substituted 5,7-dibromo-2,3-diphenylthieno[3,4-*b*]pyrazine (**4b-d**):



The starting material **3b-d** (1 mmol) was added to a round-bottom flask with 15 ml of dry DMF and the solution is cooled to -10°C with a salt-ice bath. Then, NBS (356 mmol, 2 mmol) was added portion-wise. The solution was then stirred overnight. The solution was then partitioned in a water-DCM mixture, and the organic layer was isolated. It was then washed five times with water. The organic layer was then reduced under low pressure (keep a low temperature because of decomposition of the product) and the crude was chromatographed on silica to yield the title products.

- **4b** (R=F): yield 66%, yellow-green powder

ESI-MS: could not be detected

¹H-NMR (500 MHz, CDCl₃) δ 7.49 – 7.44 (m, 4H), 7.06 – 7.00 (m, 4H).

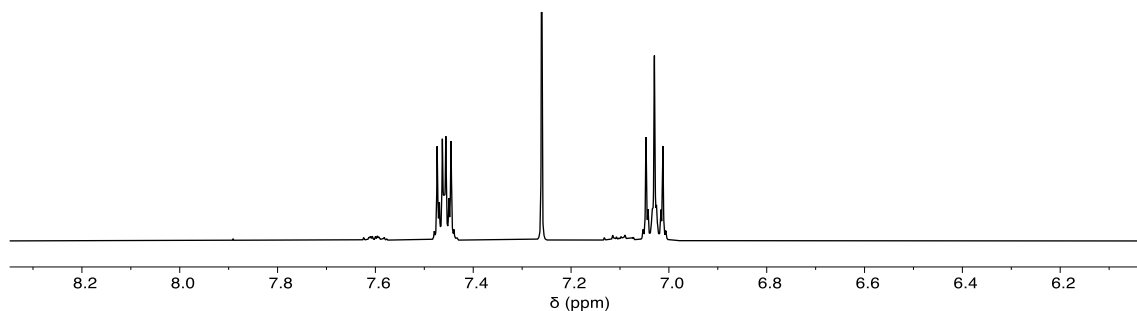


Figure S5.8: ¹H-NMR (500 MHz, 298 K, CDCl₃) spectrum of intermediate **4b**.

- **4c** (R=OMe): yield 48%, yellow powder

ESI-MS: calculated for [C₂₀H₁₄Br₂N₂O₂S+H]⁺: 506.9196, found 506.9112

¹H-NMR (600 MHz, DMSO) δ 7.39 (d, *J* = 8.8 Hz, 4H), 6.93 (d, *J* = 8.8 Hz, 4H), 3.78 (s, 6H).

¹³C-NMR (151 MHz, DMSO) δ 160.68, 154.72, 139.18, 131.69, 130.97, 114.00, 104.56, 55.74.

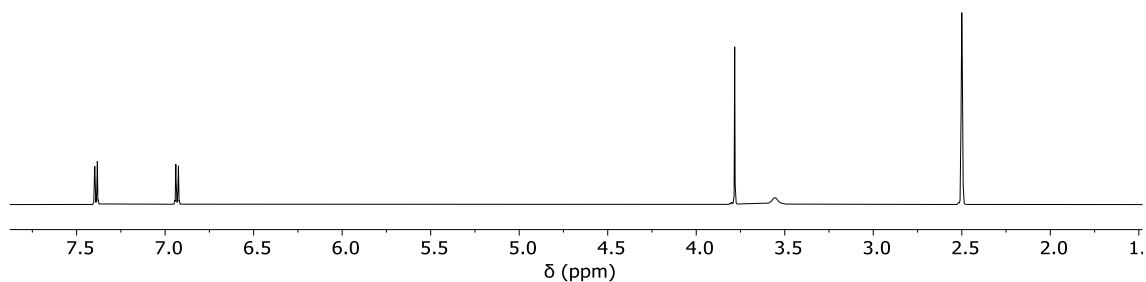


Figure S5.9: ¹H-NMR (600 MHz, 298 K, DMSO) spectrum of intermediate **4c**.

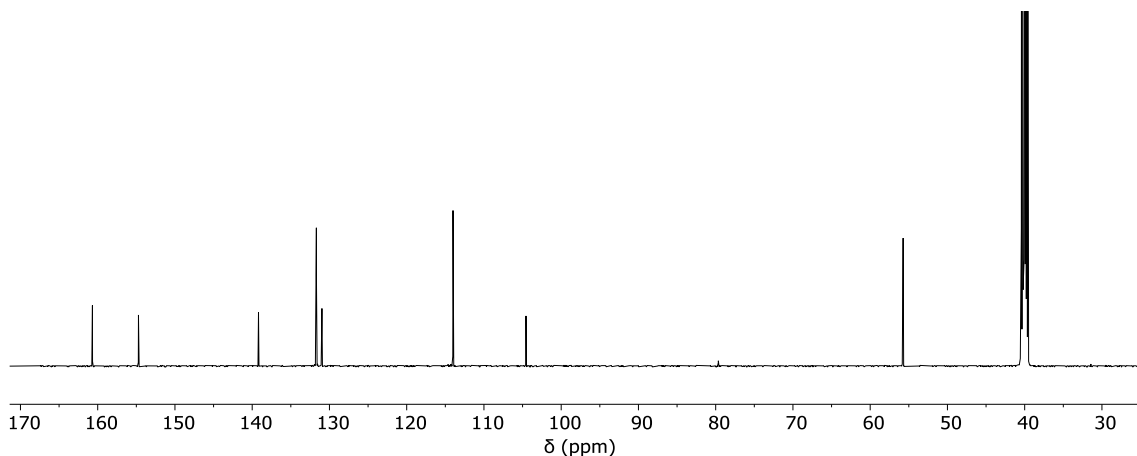
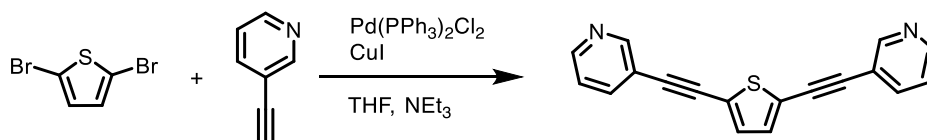


Figure S5.10: ¹³C-NMR (151 MHz, 298 K, DMSO) spectrum of intermediate **4c**.

- **4d** (R=F₅): yield 65%, yellow-orange powder, unstable and used immediately as-is for the next step.

5.6.2.2 Synthesis of the ligands

2,5-bis(pyridin-3-ylethynyl)thiophene (THO):



2,5-dibromothiophene (1 mmol, 242 mg, 113 μ l) and 3-ethynylpyridine (4 mmol, 412 mg) were added to a pressure-proof Schlenk flask with 5 ml of THF and 5 ml of NEt₃. The solution was degassed three times by the freeze-pump-thaw technique, and afterward the catalysts were added under argon: Pd(PPh₃)₂Cl₂ (0.05 mmol, 35 mg) and CuI (0.05 mmol, 9.5 mg). The flask was then sealed, and the solution was heated and stirred at 90°C for 1.5h. After cooling down, the resulting mixture was partitioned between water and EtOAc, and the organic layer was isolated, dried with MgSO₄, and dried under low pressure. The crude was chromatographed on silica (EtOAc) to yield

the ligand as an off-white solid with a blue fluorescence in solution. The ligand was further purified by GPC. Final yield: 137 mg, 48%.

ESI-MS: calculated for [C₁₈H₁₀N₂S]⁺: 286.0559, measured: 286.0548

¹H-NMR (500 MHz, CD₃CN) δ 8.73 (dd, *J* = 2.3, 0.9 Hz, 2H), 8.57 (dd, *J* = 4.9, 1.7 Hz, 2H), 7.89 (dt, *J* = 7.9, 2.0 Hz, 2H), 7.39 (ddd, *J* = 7.9, 4.9, 0.9 Hz, 2H), 7.32 (s, 2H).

¹³C-NMR (126 MHz, CD₃CN) δ 152.73, 150.31, 139.27, 134.16, 125.17, 124.41, 120.24, 91.92, 85.38.

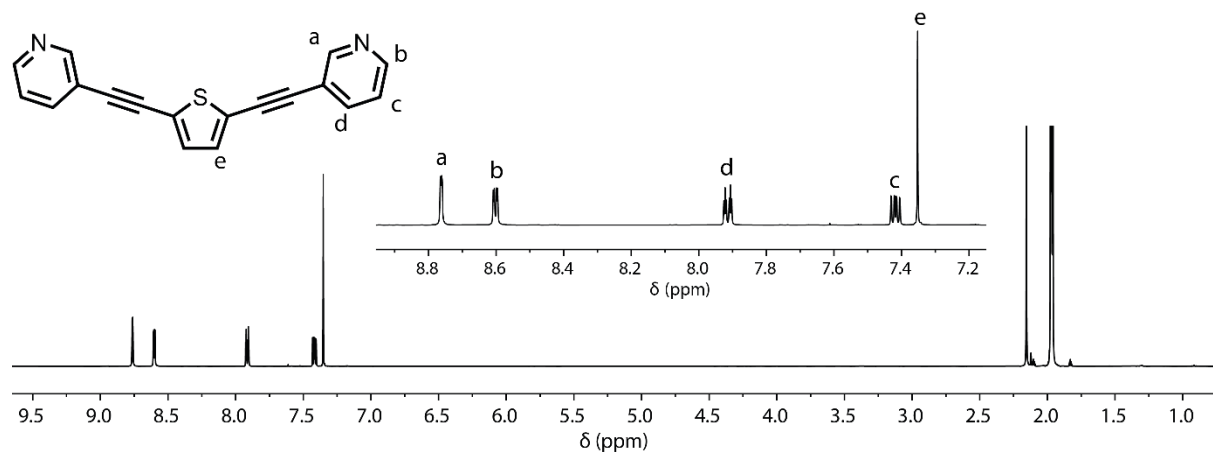


Figure S5.11: ¹H-NMR (500 MHz, 298 K, CD₃CN) spectrum of ligand **THO**.

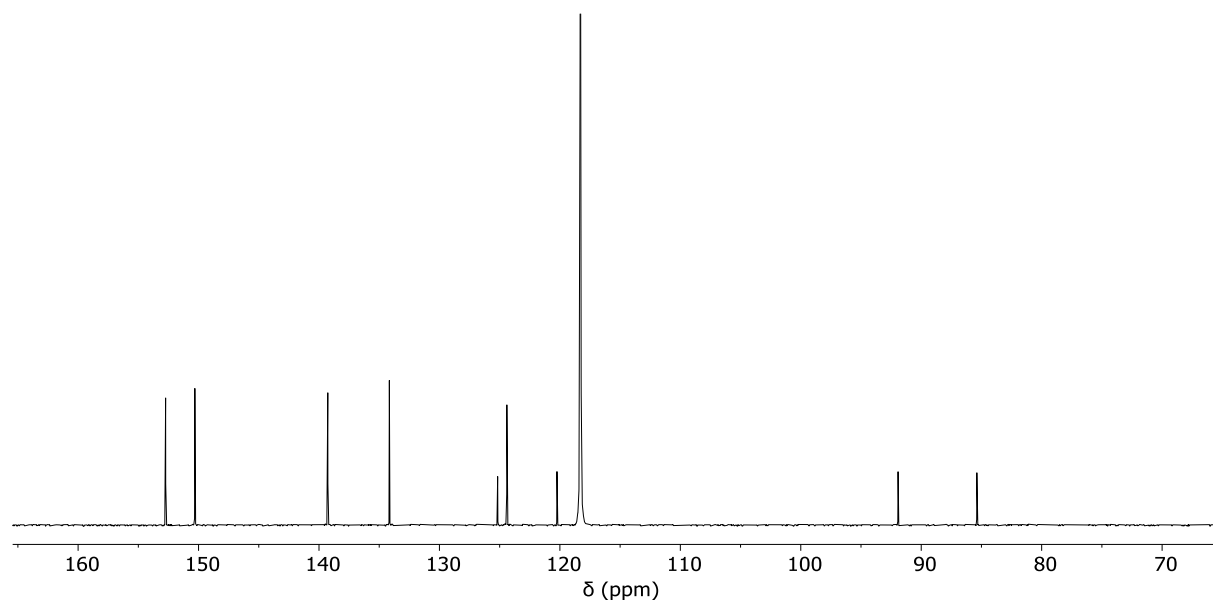
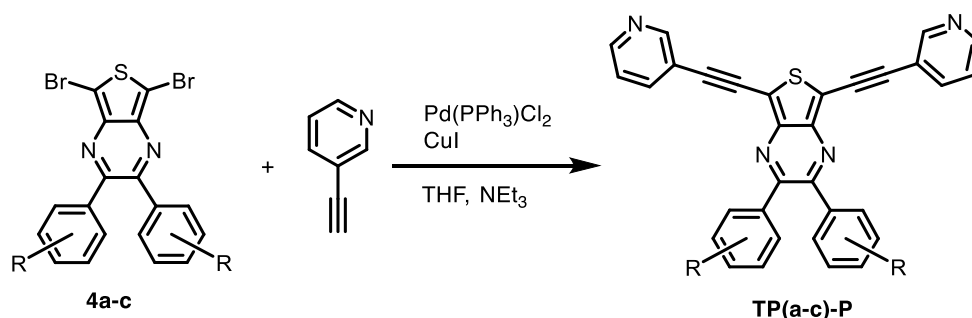


Figure S5.12: ¹³C-NMR (126 MHz, 298K, CD₃CN) of ligand **THO**.

- Ligands TPa-P to TPc-P:



Intermediates **4a-d** (1 mmol) and 3-ethynylpyridine (4 mmol, 412 mg) were added to a pressure-proof Schlenk flask with 5 ml of THF and 5 ml of NEt₃. The solution was degassed three times by the freeze-pump-thaw technique, and afterward the catalysts were added under argon: Pd(PPh₃)₂Cl₂ (0.05 mmol, 35 mg) and CuI (0.05 mmol, 9.5 mg). The flask was then sealed, and the solution was heated and stirred at 90°C for 2.5h. After cooling down, the resulting mixture was partitioned between water and EtOAc, and the organic layer was isolated, dried with MgSO₄, and dried under low pressure. The crude was chromatographed on silica (DCM, MeOH 5%) to yield the ligands, which were further purified by GPC.

This procedure is not suitable for the synthesis of **TPd-P**, as the precursor **4d** instantly turns brown upon contact with the solvent mixture.

- TPa-P: yield: 37%, orange powder

ESI-MS: calculated for [C₃₂H₁₈N₄S+H]⁺: 491.1325, measured: 491.1310

¹H-NMR (500 MHz, CD₃Cl) δ 8.90 – 8.86 (m, 2H), 8.60 (dd, *J* = 4.9, 1.7 Hz, 2H), 7.92 (dt, *J* = 7.9, 1.9 Hz, 2H), 7.57 – 7.51 (m, 4H), 7.42 – 7.35 (m, 2H), 7.36 – 7.29 (m, 6H).

¹³C-NMR (126 MHz, CD₃Cl) δ 154.76, 152.46, 149.26, 143.12, 138.65, 130.18, 129.59, 128.32, 123.23, 120.06, 115.69, 97.71, 84.42. (1 missing nucleus)

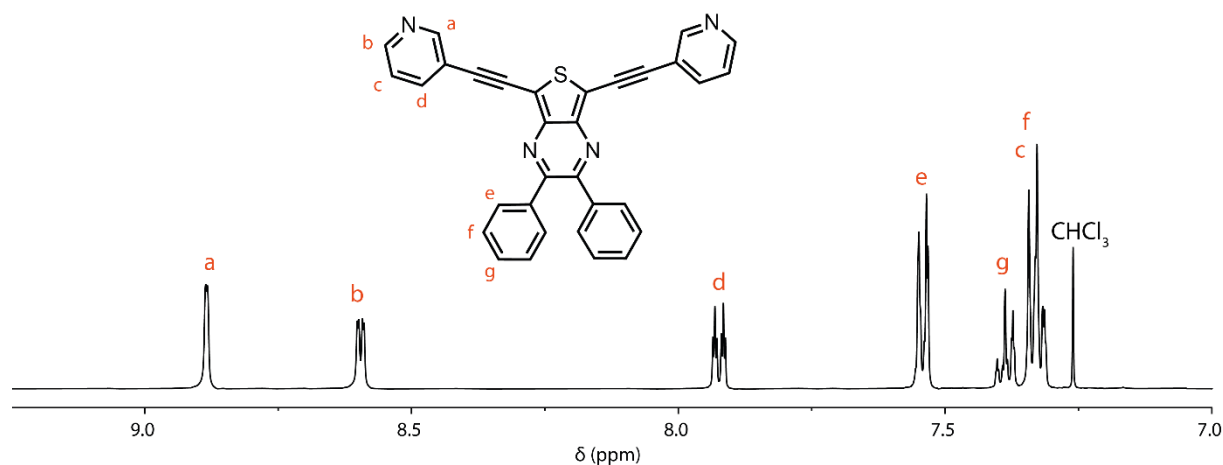


Figure S5.13: ¹H-NMR (500 MHz, 298K, CDCl₃) spectrum of ligand **TPa-P**.

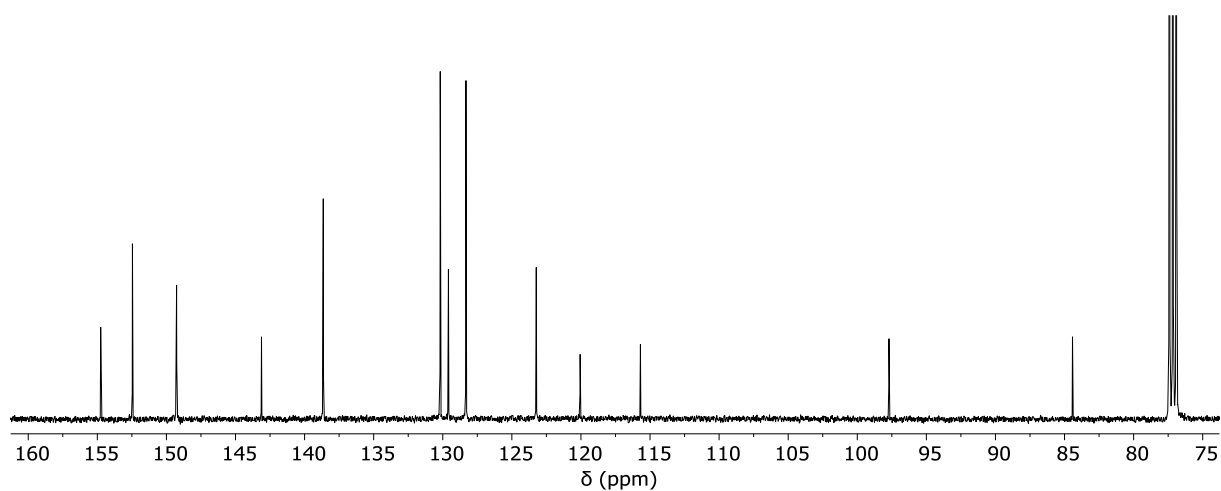


Figure S5.14: ¹³C-NMR (126 MHz, 298K, CDCl₃) spectrum of ligand **TPa-P**.

- **TPb-P**: yield: 22%, orange powder

ESI-MS: calculated for [C₃₂H₁₆N₄SF₂+H]⁺: 527.1137, found 527.1052

¹H-NMR (600 MHz, CD₃CN) δ 8.83 (dd, *J* = 2.2, 0.9 Hz, 2H), 8.61 (dd, *J* = 4.9, 1.7 Hz, 2H), 7.98 (ddd, *J* = 7.9, 2.2, 1.7 Hz, 2H), 7.56 – 7.49 (m, 4H), 7.43 (ddd, *J* = 7.9, 4.9, 0.9 Hz, 2H), 7.16 – 7.09 (m, 4H).

¹³C-NMR (151 MHz, CD₃CN) δ 165.14, 163.50, 154.96, 152.79, 150.54, 143.87, 139.35, 135.85, 135.82, 133.13, 133.07, 124.46, 120.20, 118.45, 118.26, 118.07, 116.30, 116.12, 115.97, 98.25, 84.39.

¹⁹F-NMR (565 MHz, CD₃CN) δ -113.13 (tt, *J* = 9.1, 5.4 Hz).

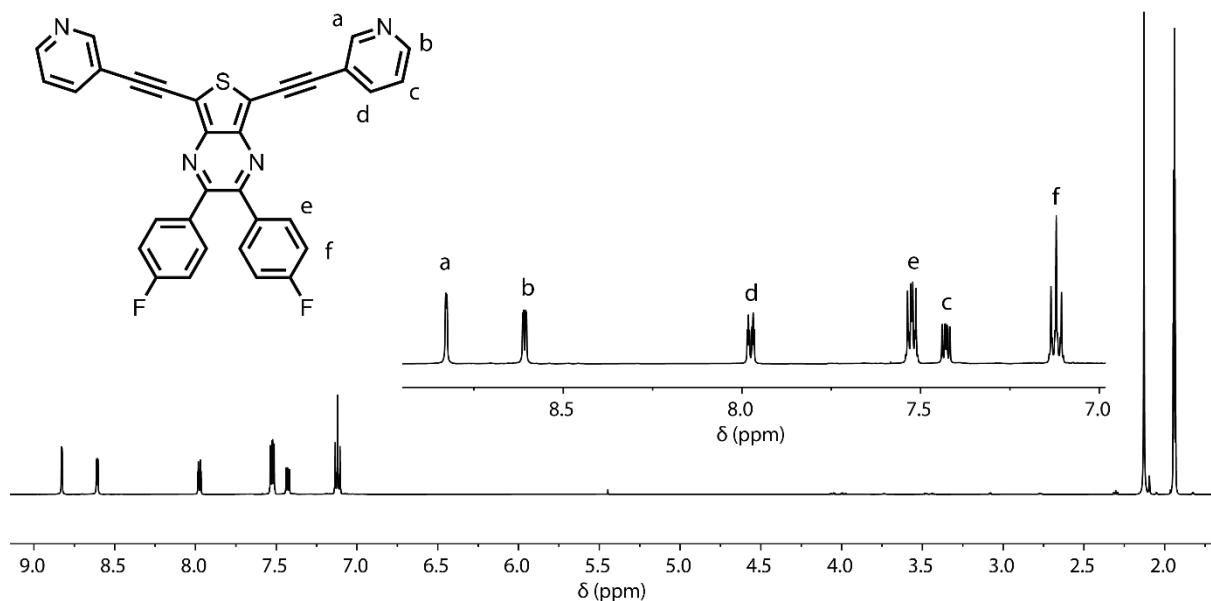


Figure S5.15: ¹H-NMR (600 MHz, 298K, CD₃CN) of ligand **TPb-P**.

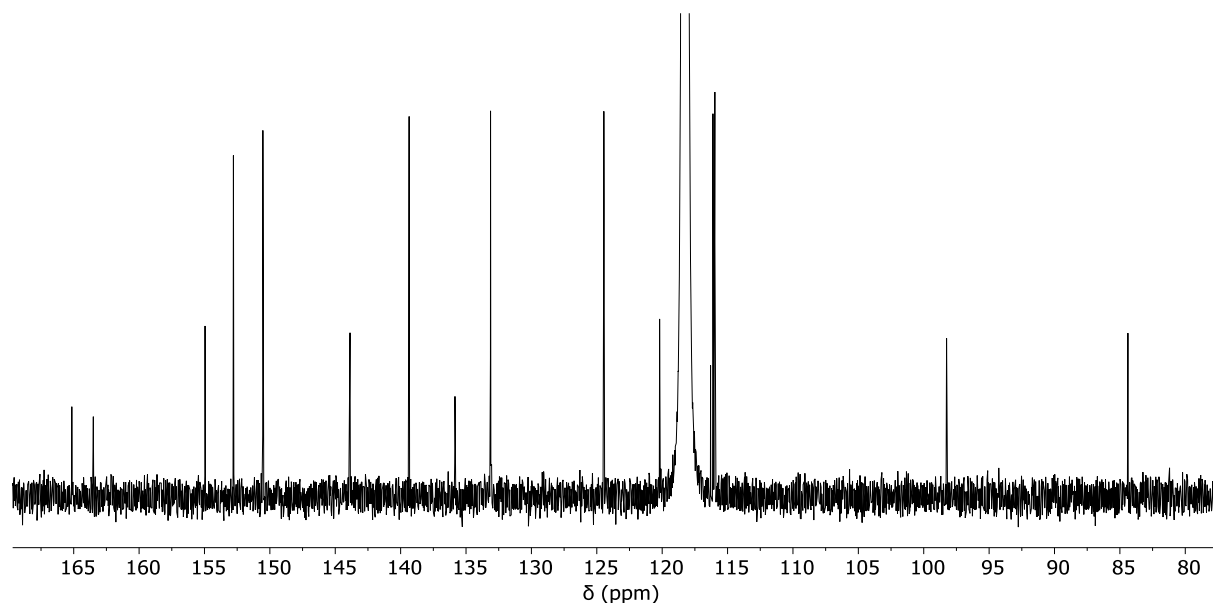


Figure S5.16: ¹³C-NMR (151 MHz, 298K, CD₃CN) of ligand TPb-P.

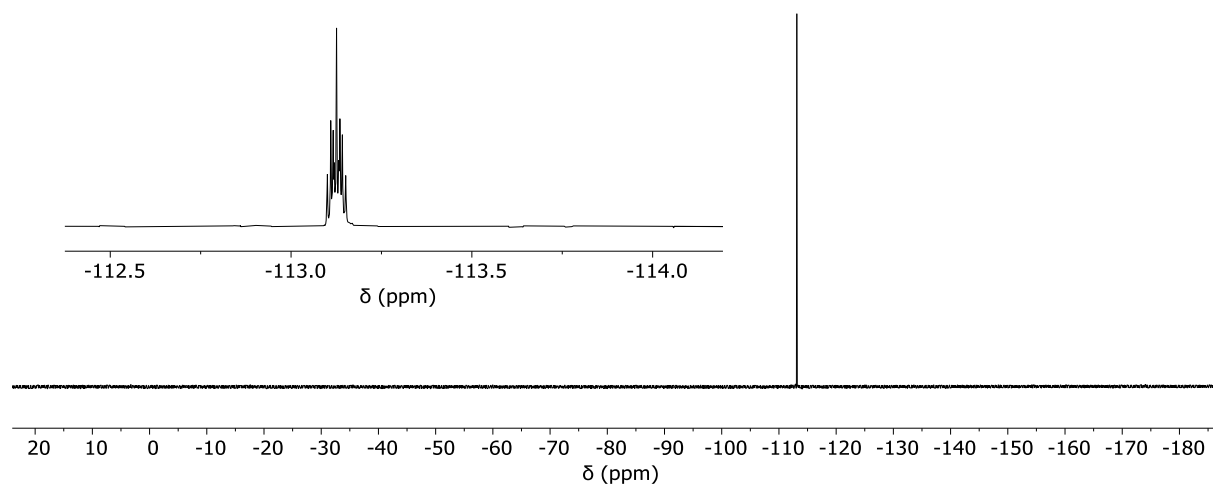


Figure S5.17: ¹⁹F-NMR (565 MHz, 298 K, CD₃CN) of ligand TPb-P.

- **TPc-P**: yield: 54 %, orange powder

ESI-MS: calculated for [C₃₄H₂₂N₄O₂S+H]⁺: 551.1513, found 551.1536

¹H-NMR (600 MHz, CD₂Cl₂) δ 8.85 (dd, *J* = 2.2, 0.9 Hz, 2H), 8.58 (dd, *J* = 4.9, 1.7 Hz, 2H), 7.93 (dt, *J* = 7.9, 1.9 Hz, 2H), 7.53 – 7.48 (m, 4H), 7.35 (ddd, *J* = 7.8, 4.9, 0.9 Hz, 2H), 6.91 – 6.85 (m, 4H), 3.84 (s, 6H).

¹³C-NMR (151 MHz, CD₂Cl₂) δ 160.79, 154.27, 152.16, 149.19, 143.03, 138.29, 131.45, 131.13, 123.13, 119.74, 114.86, 113.57, 97.09, 84.15, 55.34.

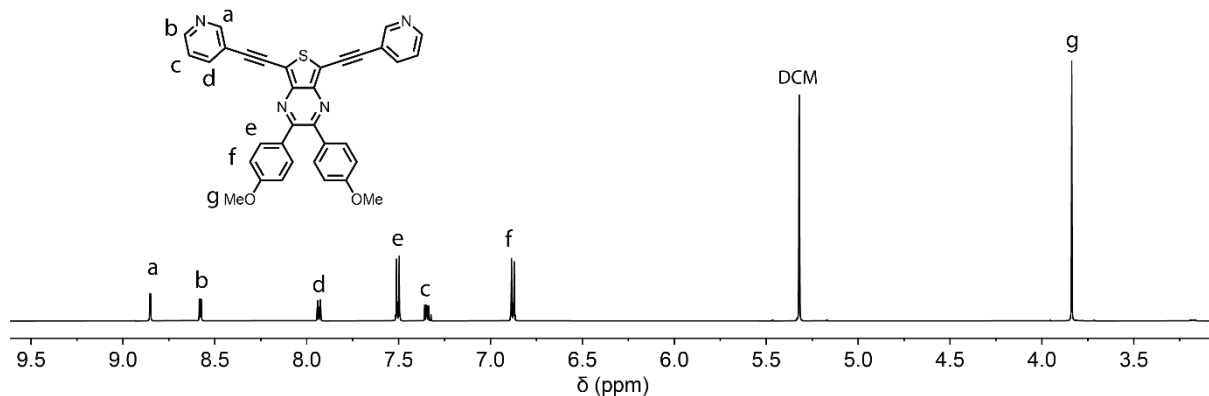


Figure S5.18: ¹H-NMR (600 MHz, 298K, CD₂Cl₂) spectrum of ligand TPc-P.

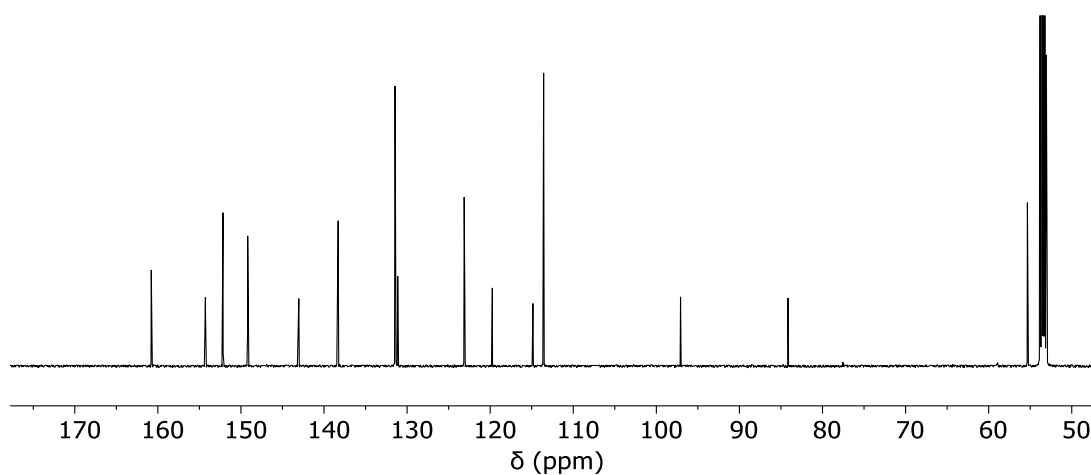
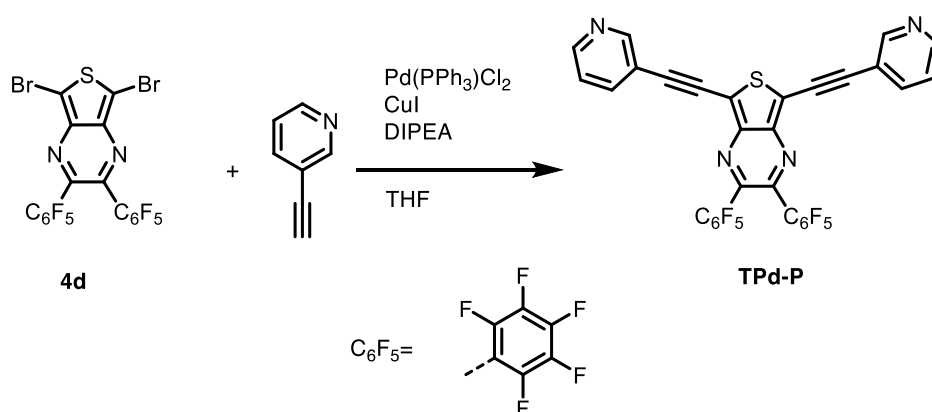


Figure S5.19: ¹³C-NMR (151 MHz, 298 K, CD₂Cl₂) spectrum of ligand TPc-P.

• Ligand TPd-P:



A Schlenk flask with 15 ml of THF and DIPEA (1.6 mmol, 206 mg, 0.278 ml) was prepared, and the solution mixture was degassed three times by the freeze-pump-thaw technique. Afterward, intermediate **4d** (0.2 mmol, 125 mg), 3-ethynylpyridine (0.66 mmol, 412 mg), Pd(MeCN)₂Cl₂ (0.02 mmol, 5.2 mg), CuI (0.02 mmol, 3.8 mg), and [H^tBu₃P]BF₄ (0.08 mmol, 23 mg) were added under a stream of argon. The flask was then sealed, and the solution was heated and stirred at 70°C for 6

hours. After cooling down, the resulting mixture was partitioned between water and EtOAc, and the organic layer was isolated, dried with MgSO₄, and dried under low pressure. The crude was chromatographed on silica (DCM, MeOH 2%) to yield the ligand as a red powder, which was further purified by GPC. It is important to process the crude immediately, as it was observed that the ligand decomposes in the crude overnight. Yield: 26 mg, 19%

ESI-MS: calculated for [C₃₂H₈F₁₀N₄S]⁺: 670.0305, found 670.0290

¹H-NMR (600 MHz, CD₂Cl₂) δ 8.84 (dd, *J* = 2.2, 0.9 Hz, 1H), 8.61 (dd, *J* = 4.9, 1.7 Hz, 1H), 7.92 (dt, *J* = 7.9, 1.9 Hz, 1H), 7.36 (ddd, *J* = 7.9, 4.9, 0.9 Hz, 1H).

¹³C-NMR (151 MHz, CD₂Cl₂) δ 152.22, 149.74, 143.27, 142.51, 138.45, 123.21, 119.08, 117.86, 99.02, 82.82.

¹⁹F-NMR (565 MHz, CD₂Cl₂) δ -141.09 – -141.22 (m), -150.66, -160.61 (d, *J* = 6.5 Hz).

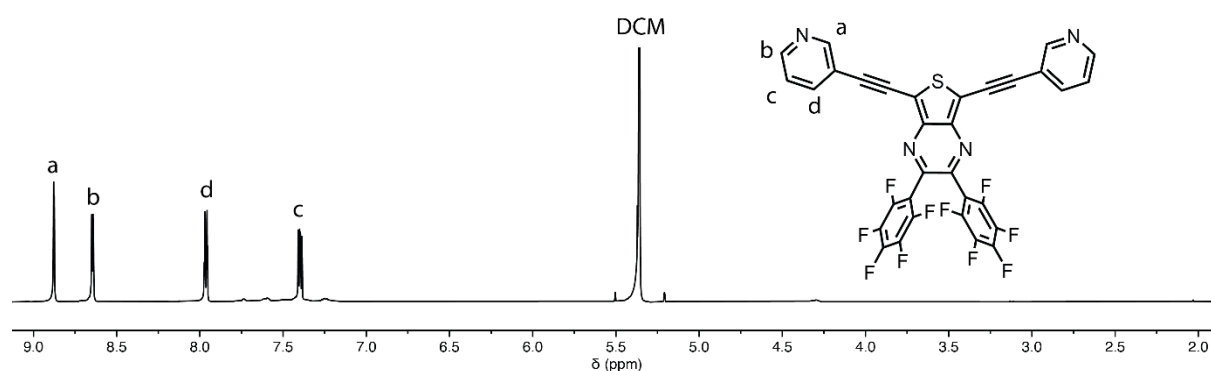


Figure S5.20: ¹H-NMR (600 MHz, 298K, CD₂Cl₂) of ligand TPd-P.

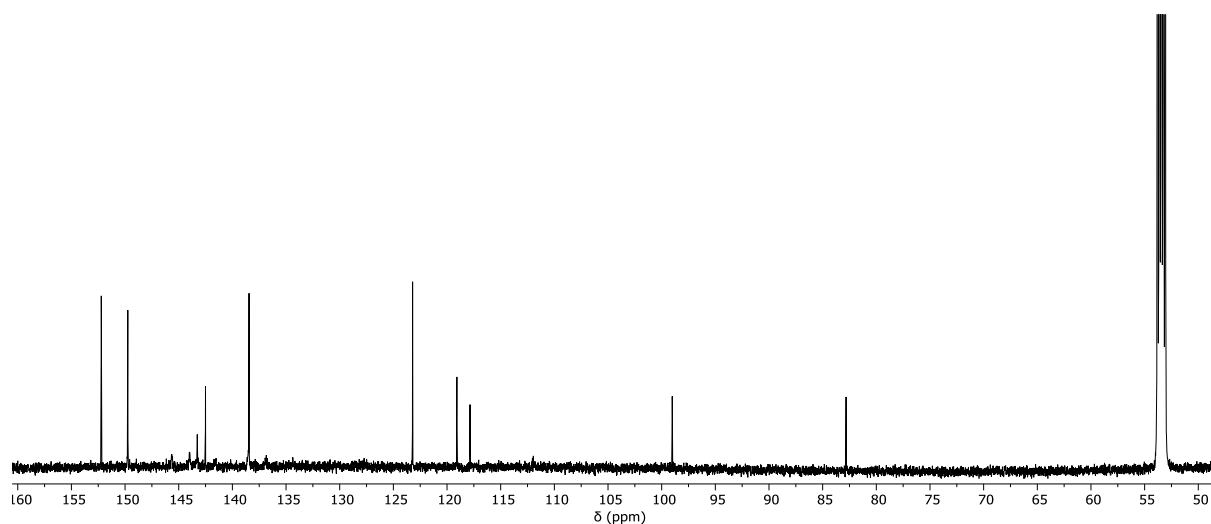


Figure S5.21: ¹³C-NMR (151 MHz, 298K, CD₂Cl₂) of ligand TPd-P.

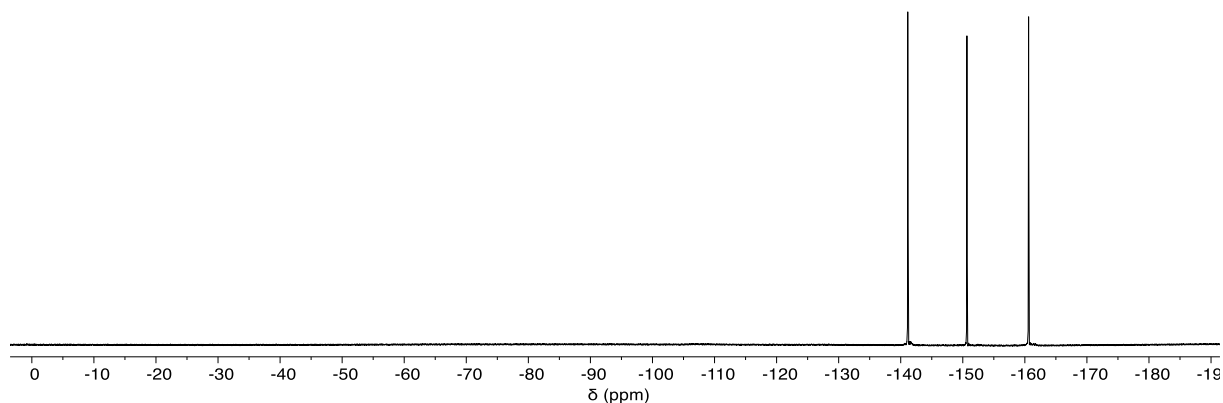
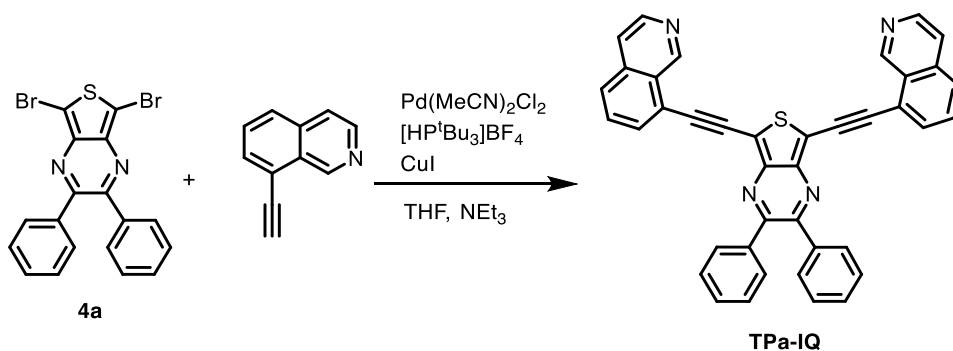


Figure S5.22: ¹⁹F-NMR (565 MHz, 298K, CD₂Cl₂) of ligand TPd-P.

- Ligand TPa-IQ:



Intermediate **4a** (0.25 mmol, 135 mg) and 8-ethynylisoquinoline (0.825 mmol, 126 mg, synthesised in Section 3.7.2.3) were added to a pressure-proof Schlenk flask with 10 ml of THF and 5 ml of NEt₃. The solution was degassed three times by the freeze-pump-thaw technique, and afterward the catalysts were added under argon: Pd(MeCN)₂Cl₂ (0.025 mmol, 6.5 mg), [HP^tBu₃]BF₄ (0.075 mmol, 22 mg) and CuI (0.025 mmol, 4.8 mg). The flask was then sealed, and the solution was heated and stirred at 90°C for 2.5h. After cooling down, the resulting mixture was partitioned between water and DCM, and the organic layer was isolated, dried with MgSO₄, and dried under low pressure. The crude was chromatographed on silica (DCM, MeOH 5%) to yield the ligand as a dark red powder. The ligands were further purified by GPC. Yield: 104 mg, 72%

ESI-MS: calculated for [C₄₀H₂₂N₄S+H]⁺: 591.1638, found 591.1646

¹H-NMR (500 MHz, CDCl₃) δ 10.05 (br, 2H), 8.68 (br, 2H), 7.95 (dd, *J* = 7.2, 1.2 Hz, 2H), 7.85 (dd, *J* = 8.3, 1.2 Hz, 2H), 7.76 – 7.60 (m, 8H), 7.44 – 7.34 (m, 6H).

¹³C-NMR (126 MHz, CDCl₃) δ 154.79, 151.59, 144.17, 143.63, 138.76, 135.91, 131.77, 130.30, 129.87, 129.61, 128.43, 127.82, 121.22, 115.81, 97.92, 87.78 (1 nucleus missing).

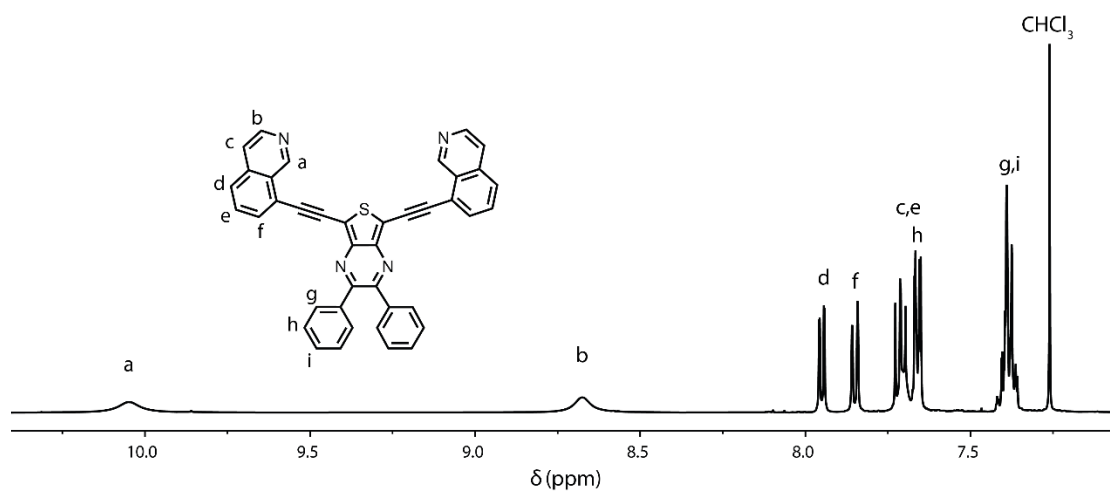


Figure S5.23: ¹H-NMR (500 MHz, 298K, CDCl₃) spectrum of ligand TPa-IQ.

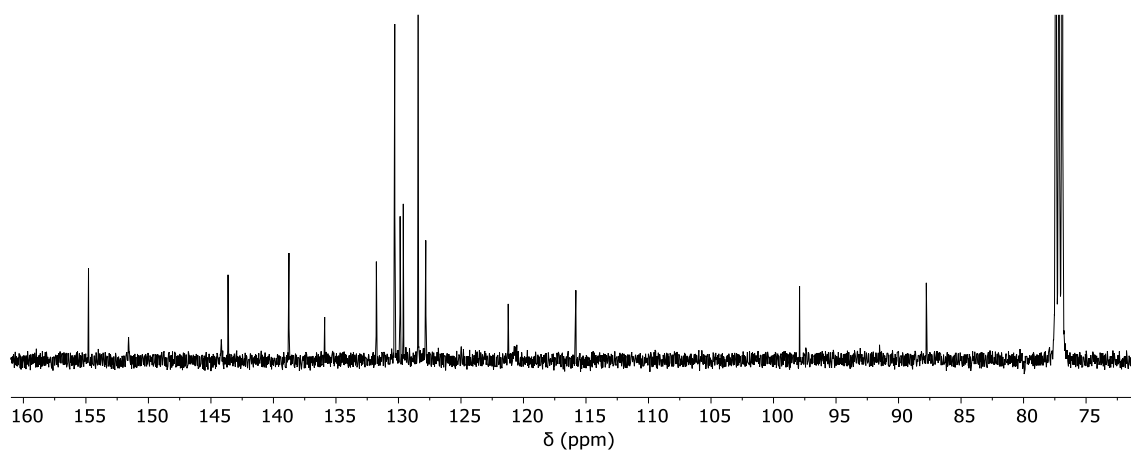


Figure S5.24: ¹³C-NMR (126 MHz, 298 K, CDCl₃) spectrum of ligand TPa-IQ.

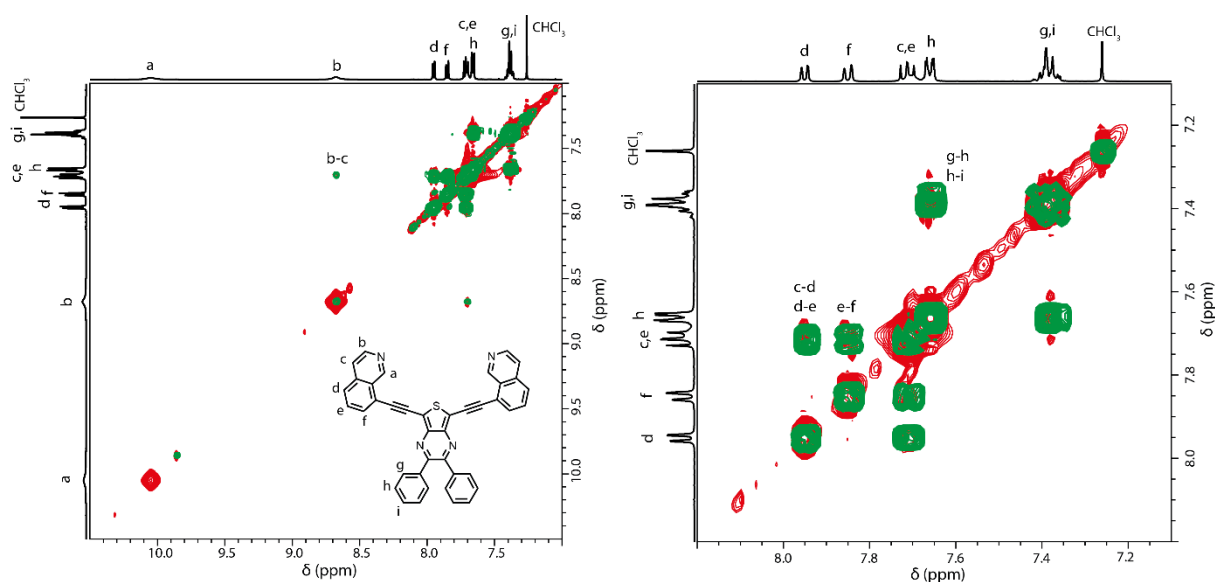


Figure S5.25: (left) ¹H-¹H COSY (green traces) and NOESY (red traces) NMR (500 MHz, 298 K, CDCl₃) spectra of ligand **TPa-IQ**. (right) zoomed-in aromatic region.

5.6.2.3 Assembly of the cages

All of the Pd₂L₄ species were assembled according to the same procedure: to 450 μl of a 3.11 mM solution (or suspension) of the ligand in CD₃CN, 50 μl of a 15mM solution of the Pd(II) salt in the same solvent were added. The mixture was then heated to 70°C for 2 hours to yield the coordination species as a 0.7mM solution. In the case of heteroleptic Pd₂A₂B₂ species, 225 μl of a 3.11 mM solution of each ligand was added and the mixture was heated overnight (unless otherwise stated).

- Pd₂THO₄

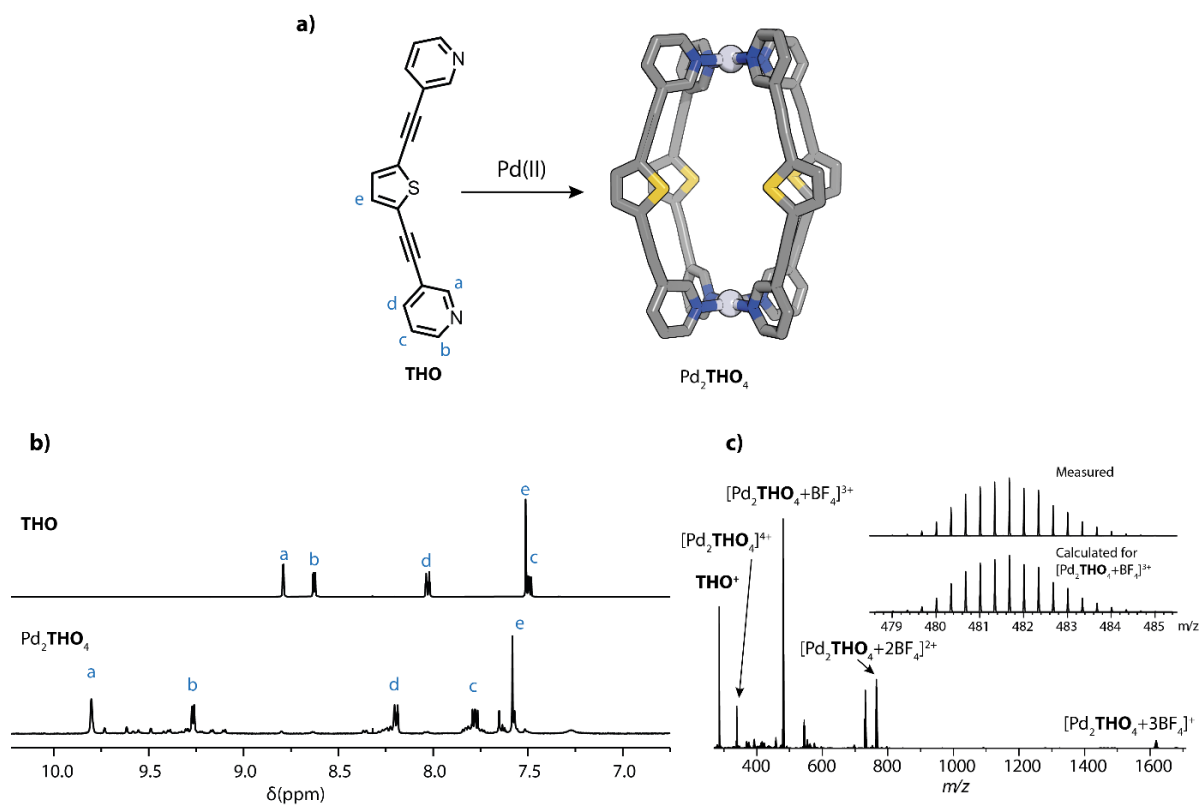


Figure S5.26: (a) Preparation of cage Pd₂THO₄ (X-ray structure). (b) ¹H-NMR (500 MHz, 298K, DMSO-*d*₆) of ligand THO (top) and cage [Pd₂THO₄](BF₄)₄ (bottom). (c) ESI-MS of [Pd₂THO₄](BF₄)₄.

- BEN14 host-guest complex

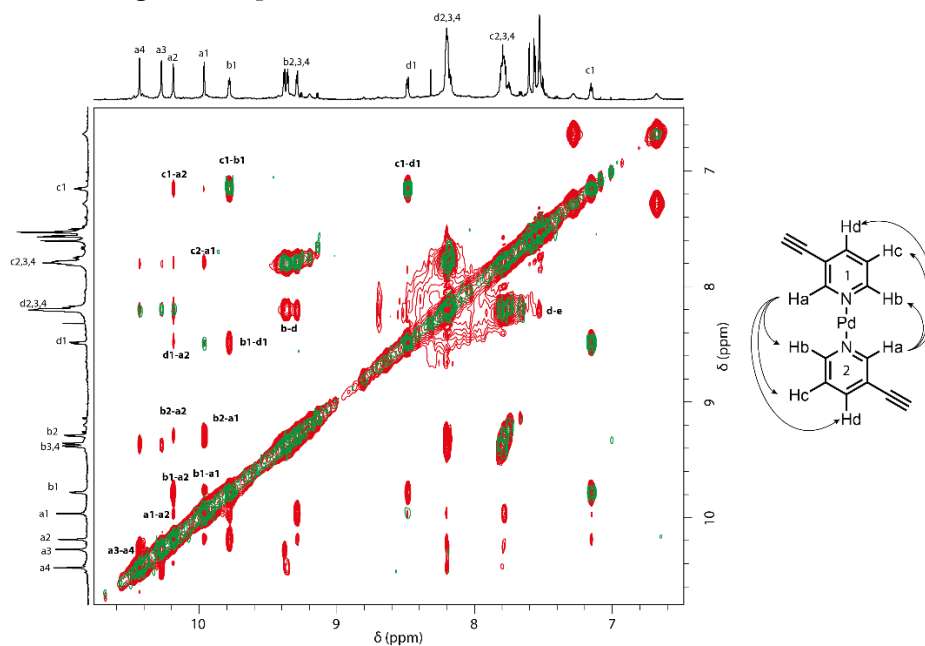


Figure S5.27: ¹H-¹H COSY (green traces) and NOESY (red traces) NMR (600 MHz, 298 K, DMSO-*d*₆) spectra of host-guest complex [2BEN14@Pd₂THO₄](BF₄)₄. The NOE correlations found between the protons of the pyridine donor are highlighted on the scheme on the right side.

- Homoleptic Pd₂TP(a-d)-P₄ cages

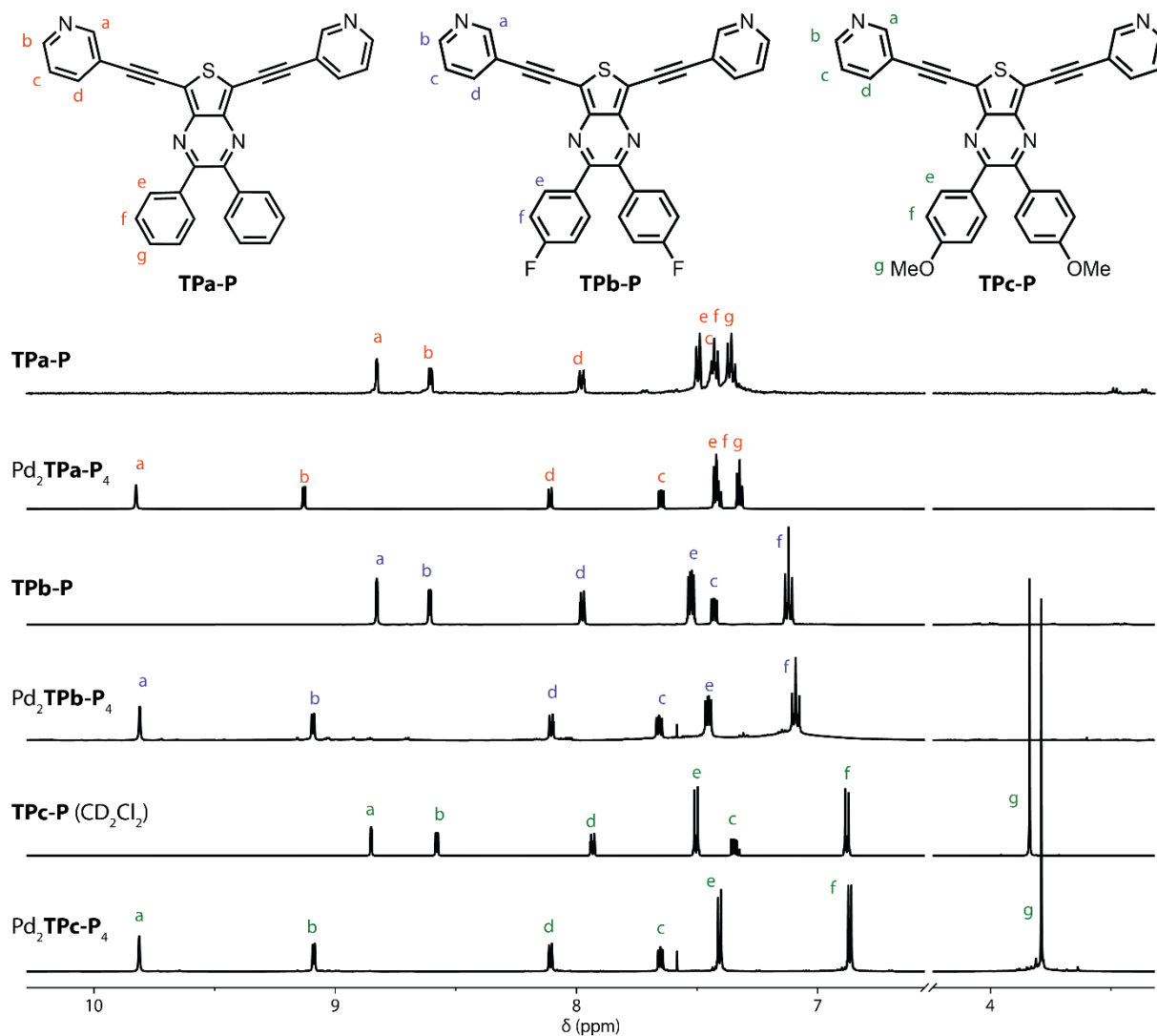


Figure S5.28: ¹H-NMR (500 MHz, 298 K, CD₃CN (unless otherwise stated)) of ligands TP(a-c)-P and cages [Pd₂TP(a-c)-P₄]OTf₄.



¹H-NMR (700 MHz, CD₃CN) δ 9.83 (d, *J* = 2.0 Hz, 2H), 9.13 (dd, *J* = 5.9, 1.3 Hz, 2H), 8.11 (dt, *J* = 7.9, 1.6 Hz, 2H), 7.67 – 7.63 (m, 2H), 7.45 – 7.39 (m, 6H), 7.35 – 7.30 (m, 4H).

¹³C-NMR (176 MHz, CD₃CN) δ 156.57, 154.85, 151.05, 144.22, 142.23, 139.36, 130.66, 130.47, 129.05, 128.37, 124.43, 117.17, 96.61, 88.21.



¹H-NMR (600 MHz, CD₃CN) δ 9.81 (d, *J* = 1.9 Hz, 2H), 9.09 (dd, *J* = 6.0, 1.3 Hz, 2H), 8.10 (dt, *J* = 8.0, 1.5 Hz, 2H), 7.68 – 7.63 (m, 2H), 7.49 – 7.43 (m, 4H), 7.12 – 7.06 (m, 4H).

¹³C-NMR spectrum of too low quality

¹⁹F-NMR (565 MHz, CD₃CN) δ -112.09 – -113.08 (m), -150.66 (CF₃SO₃⁻).

- [Pd₂TPc-P₄]OTf₄

¹H-NMR (700 MHz, CD₃CN) δ 9.81 (d, *J* = 1.8 Hz, 2H), 9.09 (dd, *J* = 6.0, 1.4 Hz, 2H), 8.11 (dt, *J* = 7.9, 1.6 Hz, 2H), 7.65 (dd, *J* = 7.9, 5.9 Hz, 2H), 7.41 (d, *J* = 8.8 Hz, 4H), 6.87 (d, *J* = 8.8 Hz, 4H), 3.79 (s, 6H).

¹³C-NMR (176 MHz, CD₃CN) δ 161.91, 156.18, 154.75, 150.94, 144.27, 142.10, 132.36, 131.71, 128.36, 124.52, 116.43, 114.46, 96.40, 88.40, 56.08.

- [Pd₂TPd-P₄](BF₄)₄

¹H-NMR (600 MHz, CD₃CN) δ 9.87 (d, *J* = 1.9 Hz, 2H), 9.12 (dd, *J* = 6.0, 1.3 Hz, 2H), 8.07 – 8.02 (m, 2H), 7.65 (ddd, *J* = 7.9, 5.9, 0.6 Hz, 2H).

¹³C-NMR (176 MHz, CD₃CN) δ 173.11, 154.68, 151.07, 145.88, 144.47, 143.65, 141.91, 139.25, 137.84, 128.09, 97.61, 86.66.

¹⁹F-NMR (565 MHz, CD₃CN) δ -143.16 – -143.33 (m), -150.83 (d, *J* = 30.7 Hz, BF₄⁻), -151.71 (t, *J* = 20.1 Hz), -161.61 (td, *J* = 21.5, 6.9 Hz).

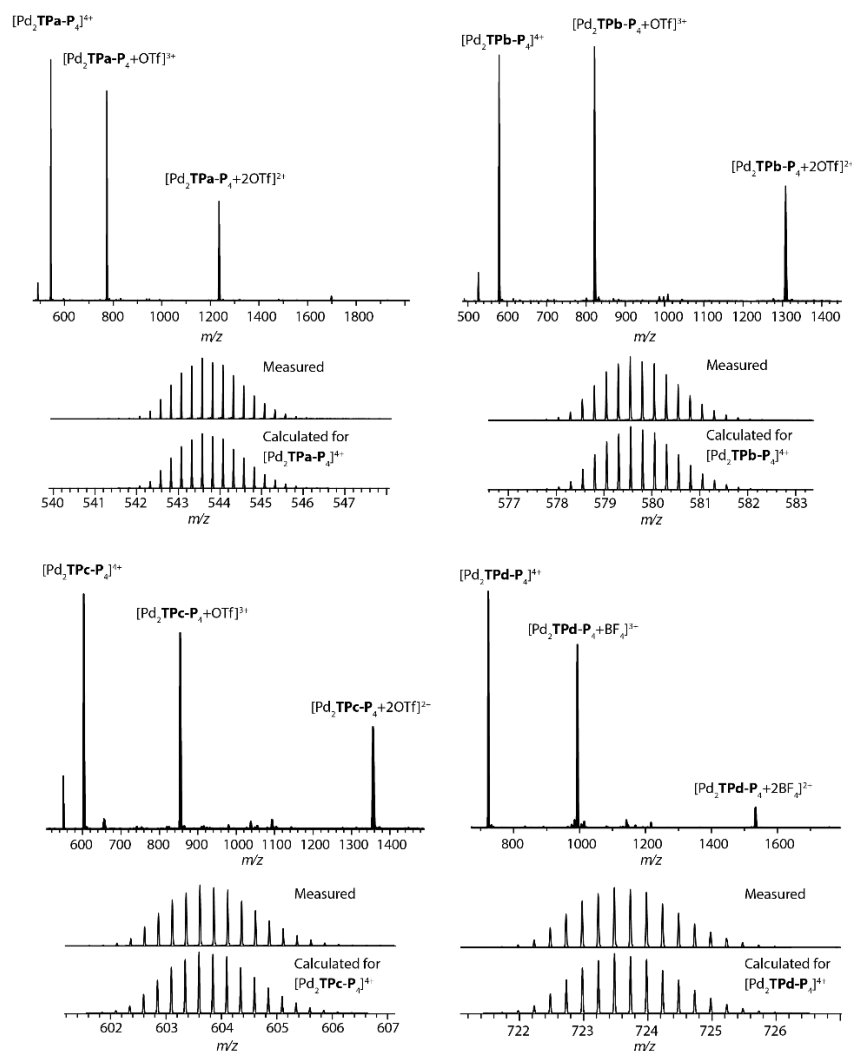


Figure S5.29: ESI-MS spectra of the three cages [Pd₂TPa-P₄](OTf)₄, [Pd₂TPb-P₄](OTf)₄, [Pd₂TPc-P₄](OTf)₄, and [Pd₂TPd-P₄](BF₄)₄

- Cage Pd₂TPa-P₄ in DMSO

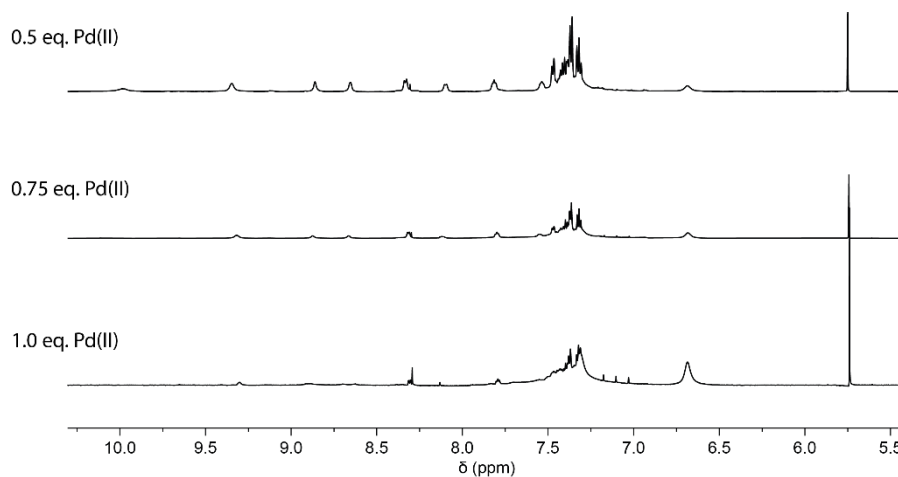


Figure S5.30: ¹H-NMR (500 MHz, 298K, DMSO-*d*₆) of the mixture of ligand TPa-P with an increasing amount of Pd(II). With 0.5 eq. a mixture of free ligand and other species is observed, while they mostly disappear upon addition of more Pd(II).

- Cage Pd₂TPa-P₄ in DMSO + 1 eq. BEN14

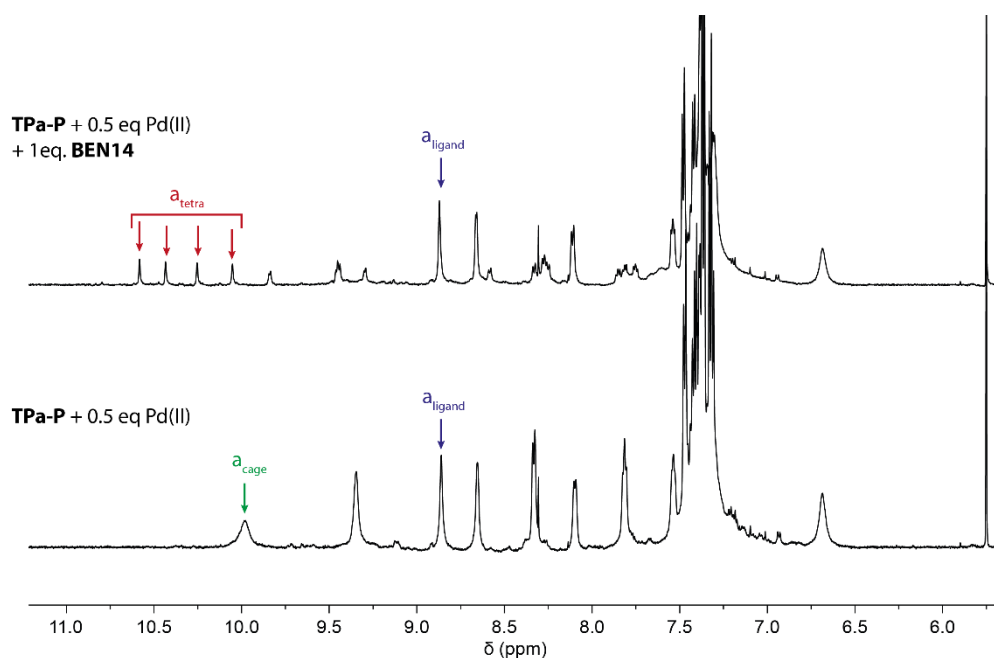


Figure S5.31: ¹H-NMR (500 MHz, 298K, DMSO-*d*₆) of the mixture of ligand TPa-P with 0.5 eq of Pd(II) (bottom), with the addition of 1 eq. of guest BEN14 (top). The a protons of each species are labelled with arrows.

- Helicate Pd₂TPa-IQ₄

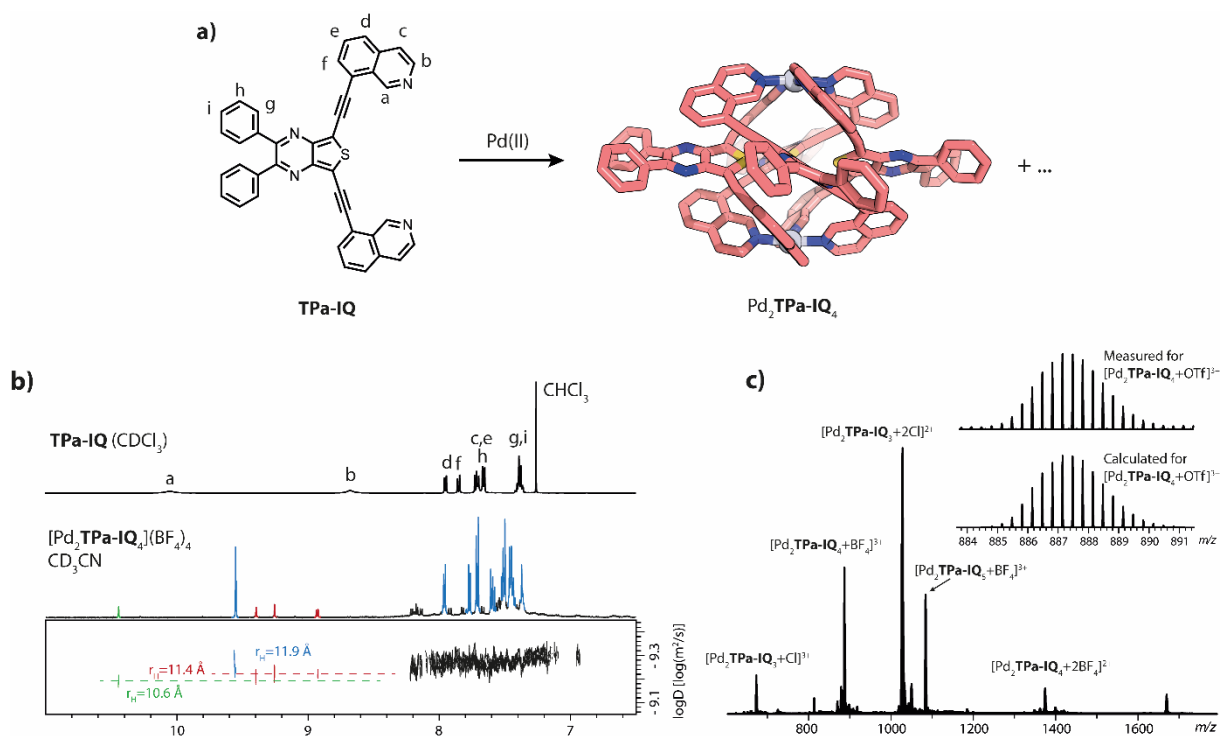


Figure S5.32: (a) Preparation of cage Pd₂TPa-IQ₄ (DFT model). (b) ¹H-NMR (500 MHz, 298K) of ligand TPa-IQ (top, CDCl₃) and of cage [Pd₂TPa-IQ₄](BF₄)₄ (bottom, CD₃CN), with its corresponding DOSY trace. The Stokes-Einstein radius of each species is indicated. The different species were differentiated from their diffusion coefficient and by integration of the signals. (c) ESI-MS of [Pd₂TPa-IQ₄](BF₄)₄, showing some Pd₂TPa-IQ₃ and Pd₂TPa-IQ₅.

Heteroleptic assemblies

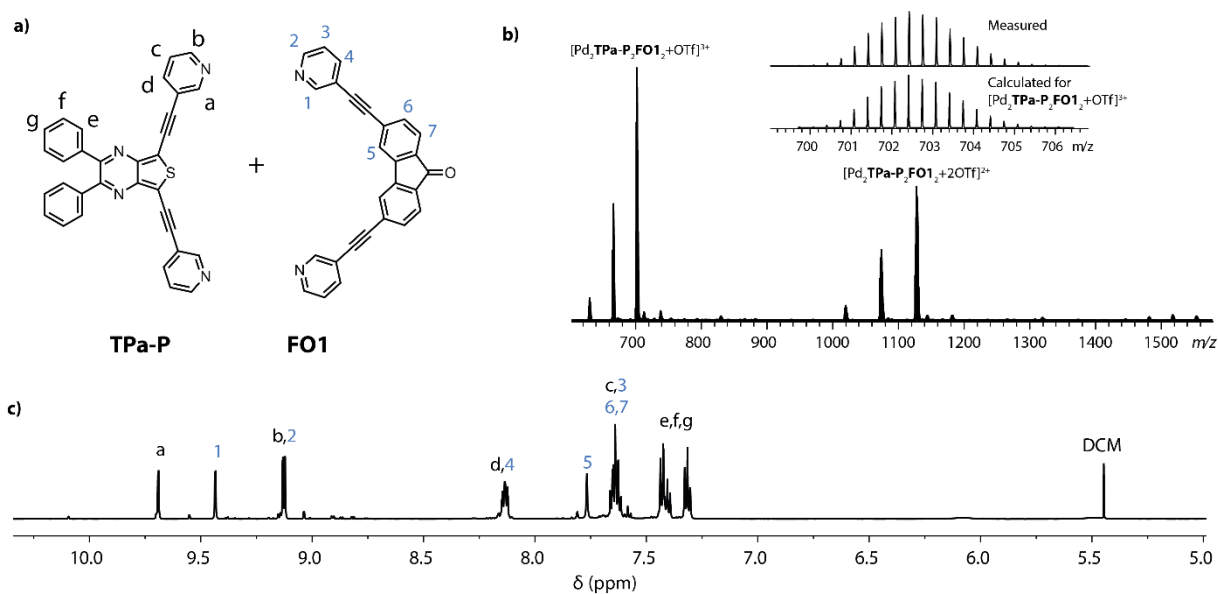
• [Pd₂TPa-P₂FO1₂]OTf₄

Figure S5.33: (a) Structure of the ligands. (b) ESI-spectrum of [Pd₂TPa-P₂FO1₂]OTf₄. (c) ¹H-NMR (600 MHz, 298K, CD₃CN) of cage [Pd₂TPa-P₂FO1₂]OTf₄.

¹H-NMR (600 MHz, CD₃CN) δ 9.69 (d, *J* = 1.9 Hz, 2H), 9.43 (d, *J* = 1.9 Hz, 2H), 9.13 (dd, *J* = 6.1, 1.4 Hz, 4H), 8.16 – 8.11 (m, 4H), 7.77 (s, 2H), 7.68 – 7.60 (m, 8H), 7.45 – 7.41 (m, 2H), 7.44 – 7.38 (m, 4H), 7.34 – 7.29 (m, 4H).

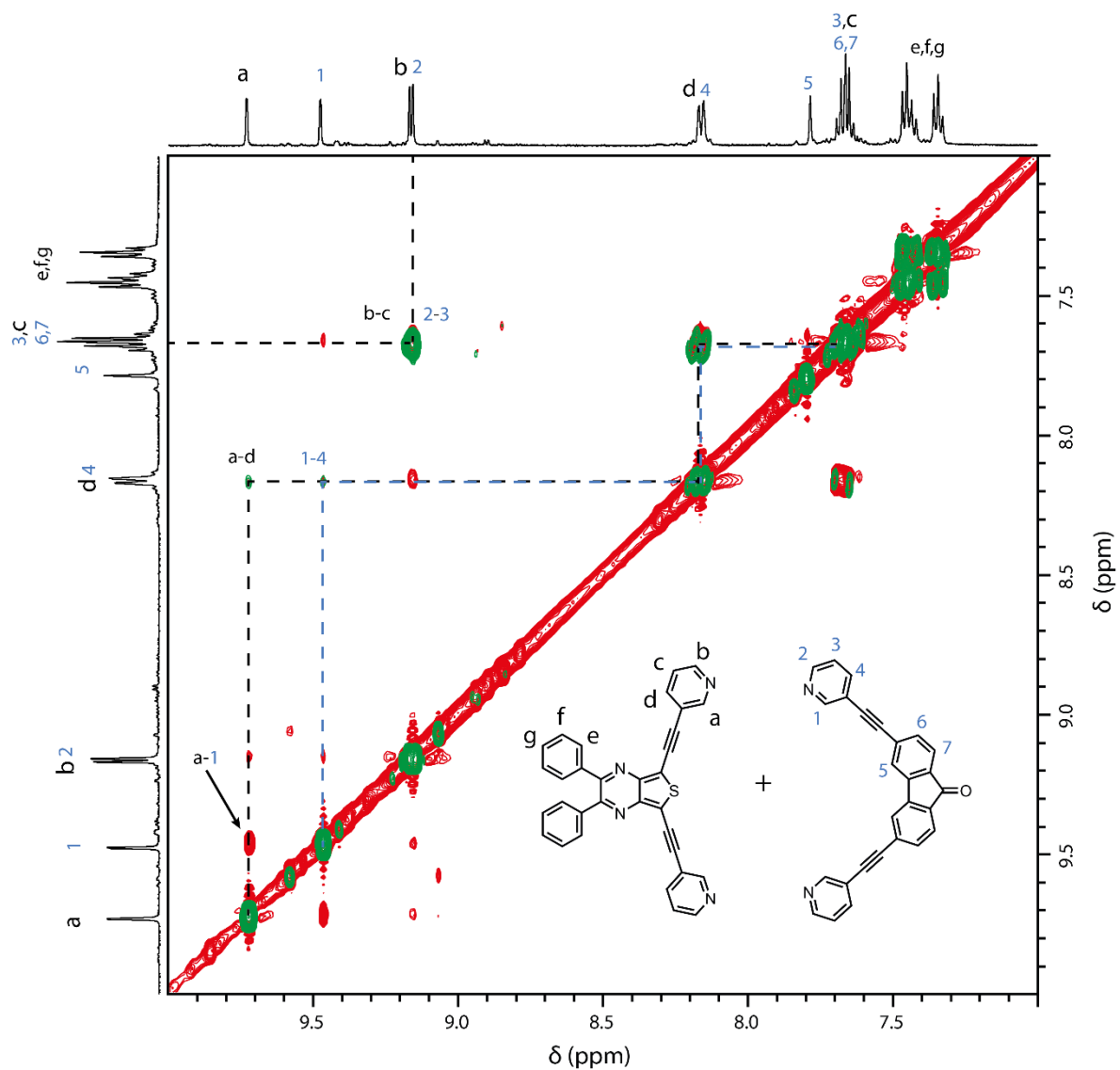


Figure S5.34: ¹H-¹H COSY (green traces) and NOESY (red traces) NMR (600 MHz, 298 K, CD₃CN) spectra of cage [Pd₂TPa-P₂FO₁₂]⁺OTf₄⁻.

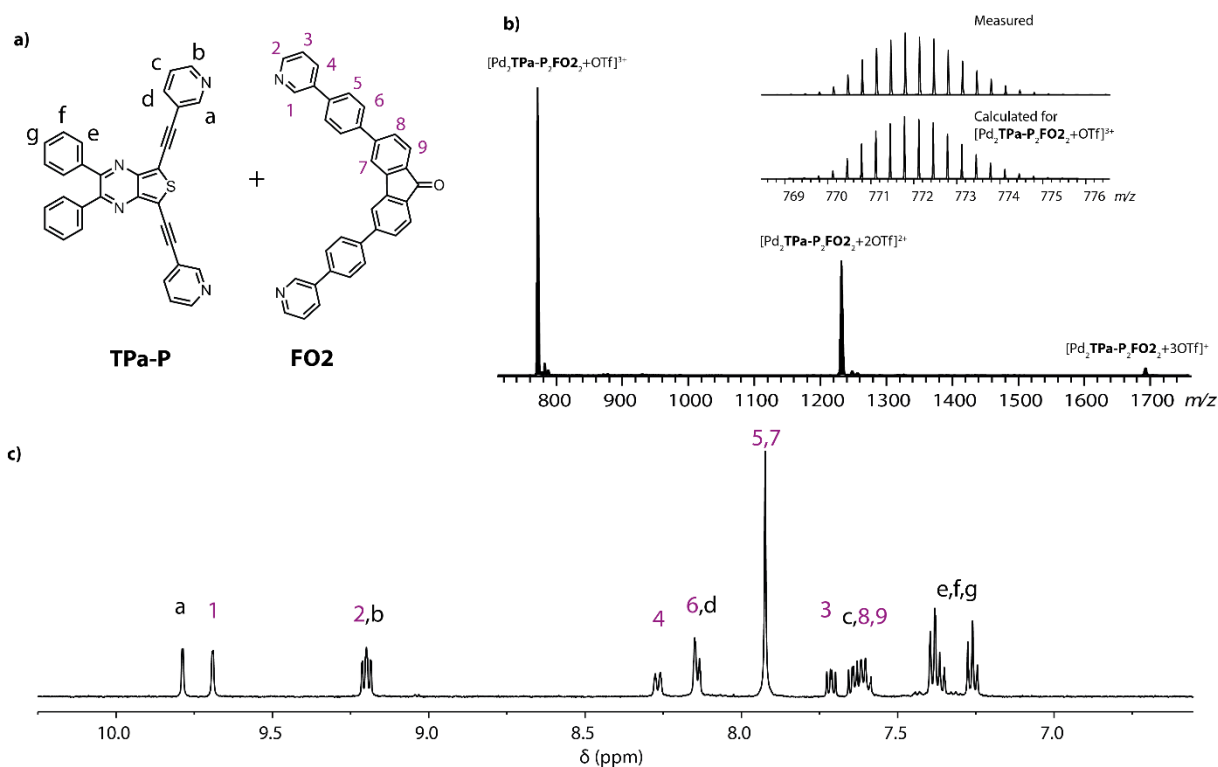
• [Pd₂TPa-P₂FO₂]₂OTf₄

Figure S5.35: (a) Structure of the ligands. (b) ESI-spectrum of [Pd₂TPa-P₂FO₂]₂OTf₄. (c) ¹H-NMR (600 MHz, 298K, CD₃CN) of cage [Pd₂TPa-P₂FO₂]₂OTf₄.

¹H-NMR (500 MHz, CD₃CN) δ 9.79 (d, *J* = 1.9 Hz, 2H), 9.69 (d, *J* = 2.1 Hz, 2H), 9.20 (ddd, *J* = 7.7, 5.8, 1.3 Hz, 4H), 8.27 (d, *J* = 8.1 Hz, 2H), 8.14 (dt, *J* = 7.9, 1.6 Hz, 4H), 7.92 (s, 6H), 7.71 (dd, *J* = 8.1, 5.7 Hz, 2H), 7.68 – 7.57 (m, 6H), 7.42 – 7.33 (m, 6H), 7.26 (t, *J* = 7.7 Hz, 4H).

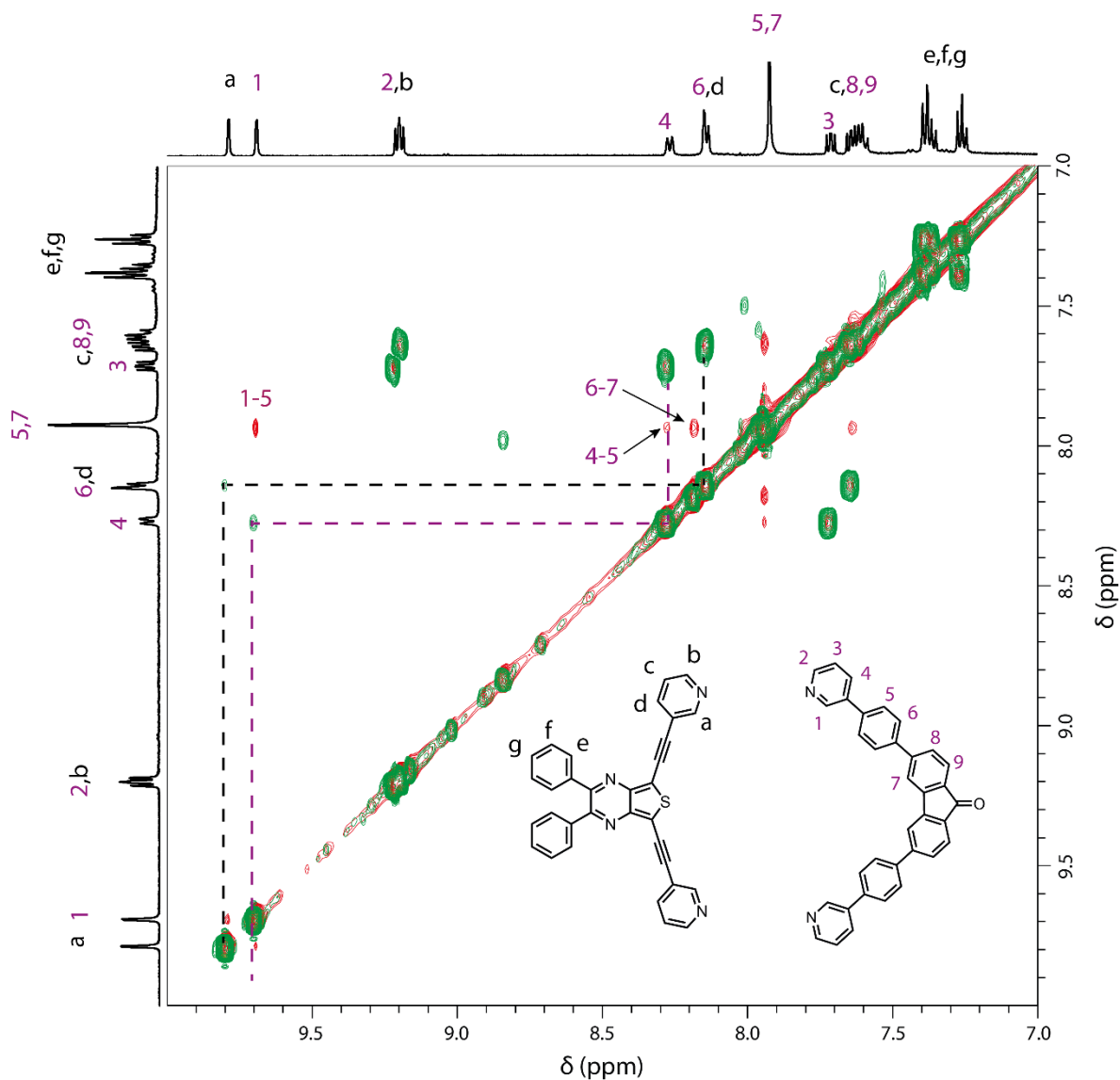


Figure S5.36: ¹H-¹H COSY (green traces) and NOESY (red traces) NMR (600 MHz, 298 K, CD₃CN) spectra of cage [Pd₂TPa-P₂FO₂]₄OTf₄.

• [Pd₂TPa-P₂CA1₂]OTf₄

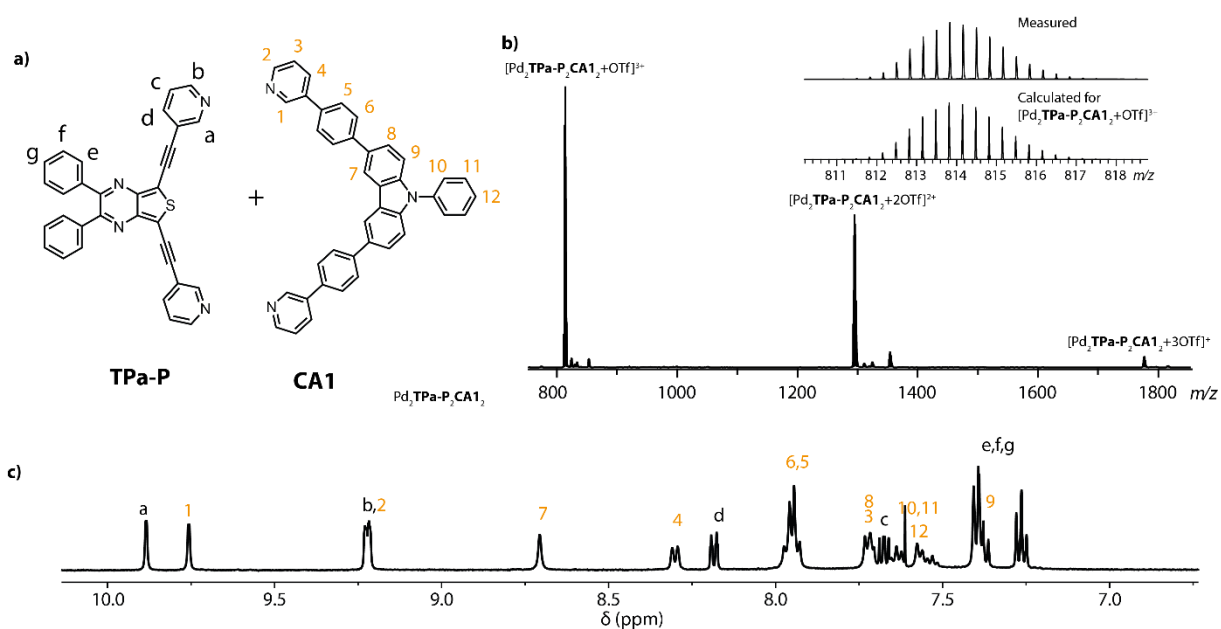


Figure S5.37: (a) Structure of the ligands. (b) ESI-spectrum of [Pd₂TPa-P₂CA1₂]OTf₄. (c) ¹H-NMR (600 MHz, 298K, CD₃CN) of cage [Pd₂TPa-P₂CA1₂]OTf₄.

¹H-NMR (500 MHz, CD₃CN) δ 9.88 (d, *J* = 1.9 Hz, 2H), 9.76 (d, *J* = 2.1 Hz, 2H), 9.31 – 9.18 (m, 4H), 8.71 (s, 2H), 8.30 (d, *J* = 8.2 Hz, 2H), 8.18 (dt, *J* = 8.0, 1.5 Hz, 2H), 7.99 – 7.91 (m, 8H), 7.72 (t, *J* = 6.9 Hz, 4H), 7.68 (dd, *J* = 8.0, 5.9 Hz, 2H), 7.66 – 7.62 (m, 1H), 7.60 – 7.50 (m, 4H), 7.43 – 7.34 (m, 8H), 7.26 (t, *J* = 7.7 Hz, 4H).

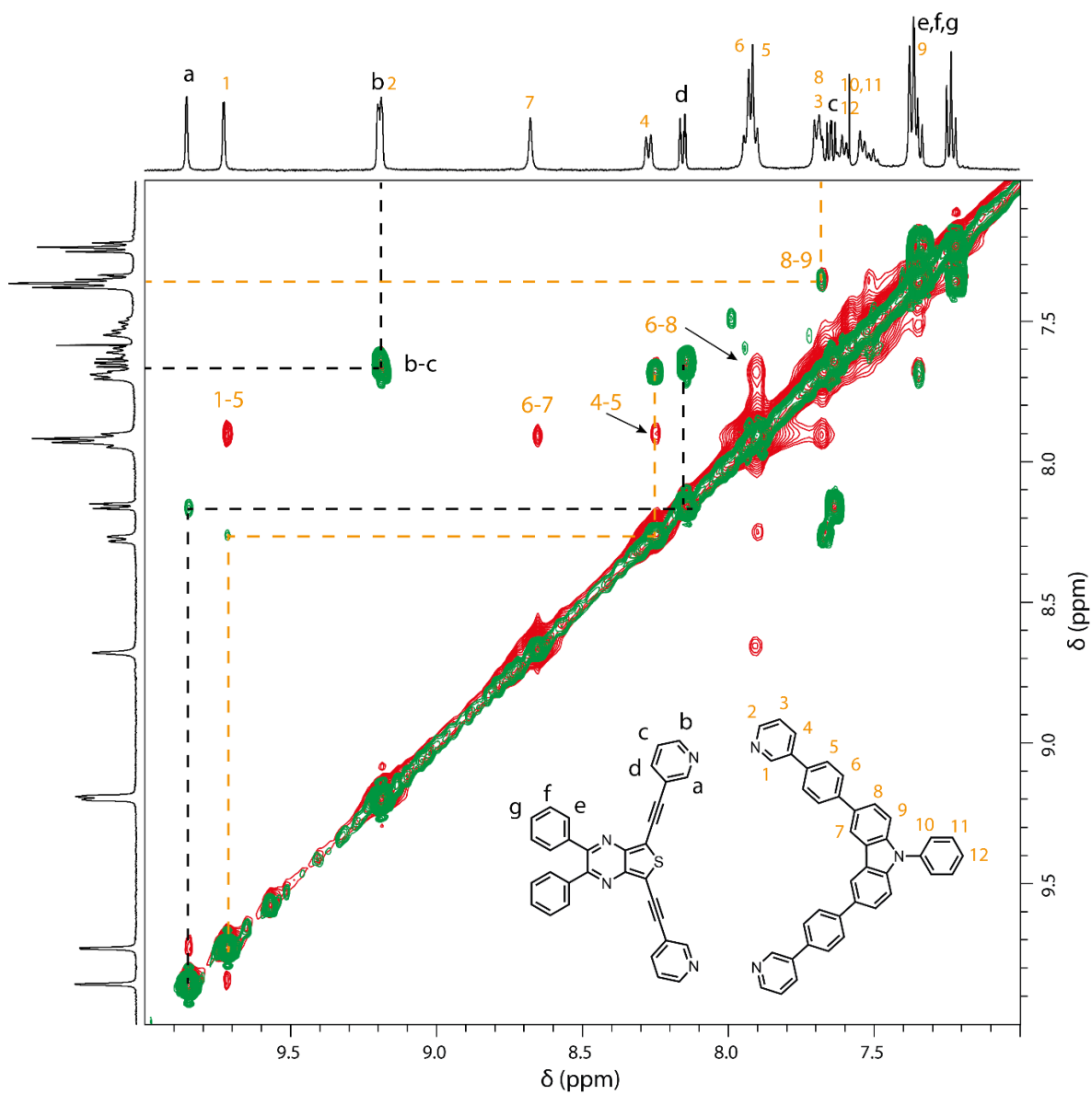


Figure S5.38: ¹H-¹H COSY (green traces) and NOESY (red traces) NMR (600 MHz, 298 K, CD₃CN) spectra of cage [Pd₂TPa-P₂FO₂]₄OTf₄.

• [Pd₂TPa-P₂CA2₂]OTf₄

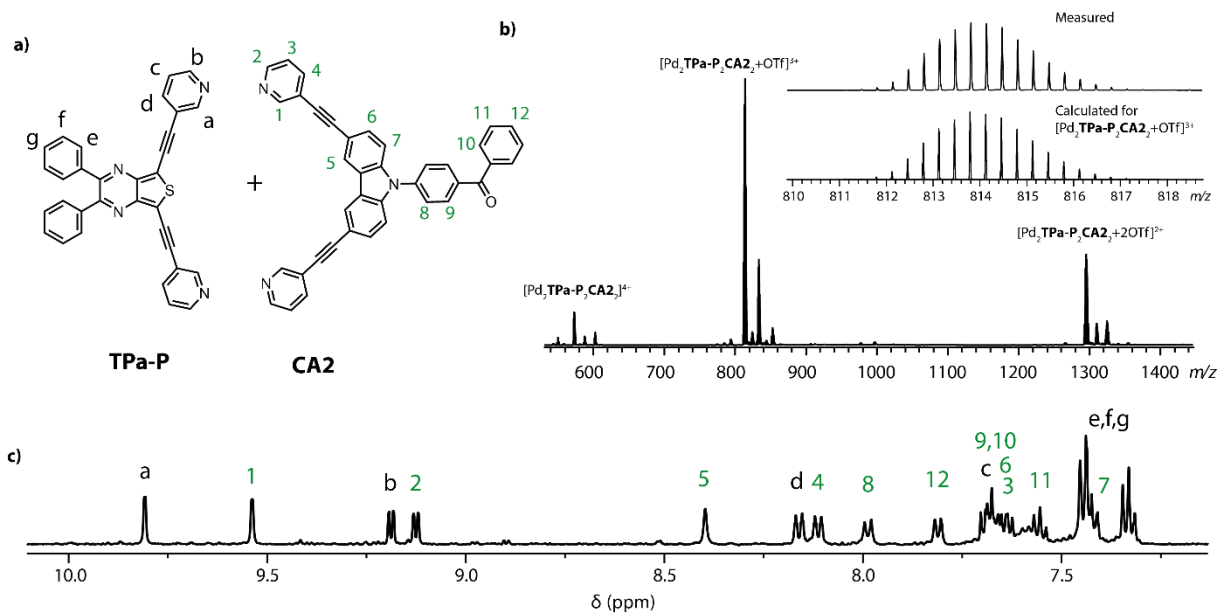


Figure S5.39: (a) Structure of the ligands. (b) ESI-spectrum of [Pd₂TPa-P₂CA₂₂]OTf₄. (c) ¹H-NMR (600 MHz, 298K, CD₃CN) of cage [Pd₂TPa-P₂CA₂₂]OTf₄.

¹H-NMR (500 MHz, CD₃CN) δ 9.81 (d, *J* = 2.0 Hz, 2H), 9.54 (d, *J* = 1.7 Hz, 2H), 9.19 (dd, *J* = 5.9, 1.4 Hz, 2H), 9.15 – 9.11 (m, 2H), 8.40 (s, 2H), 8.16 (dt, *J* = 7.8, 1.6 Hz, 2H), 8.14 (dt, *J* = 8.1, 1.5 Hz, 2H), 8.10 (dt, *J* = 8.0, 1.6 Hz, 2H), 7.99 (d, *J* = 8.2 Hz, 2H), 7.81 (d, *J* = 7.7 Hz, 2H), 7.72 – 7.53 (m, 11H), 7.49 – 7.39 (m, 8H), 7.33 (t, *J* = 7.7 Hz, 4H).

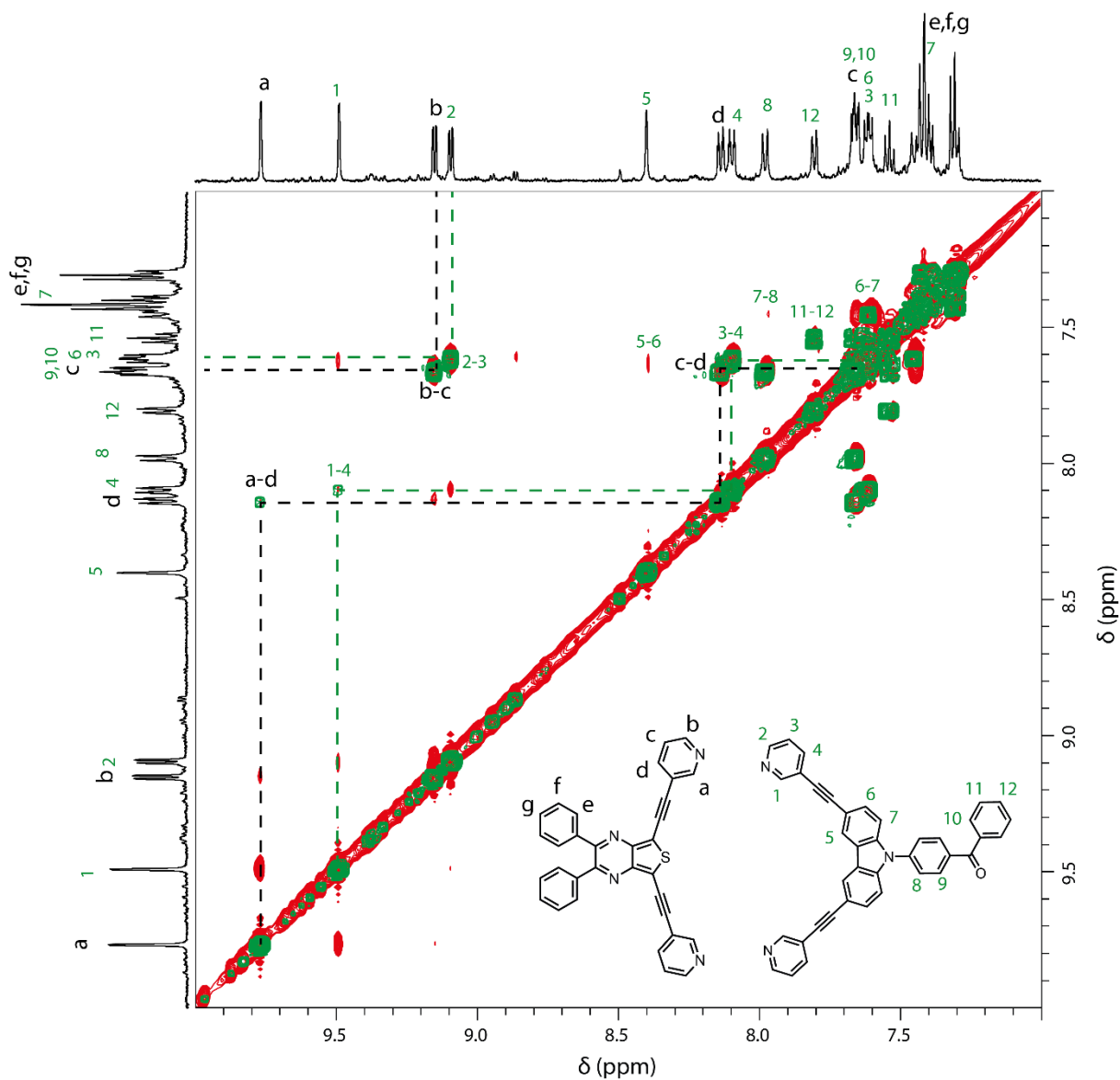


Figure S5.40: ¹H-¹H COSY (green traces) and NOESY (red traces) NMR (600 MHz, 298 K, CD₃CN) spectra of cage [Pd₂TPa-P₂CA₂]₂OTf₄.

- Pd₂TPa-P₂TRO₂

Due to a lack of time, more NMR experiments were not conducted.

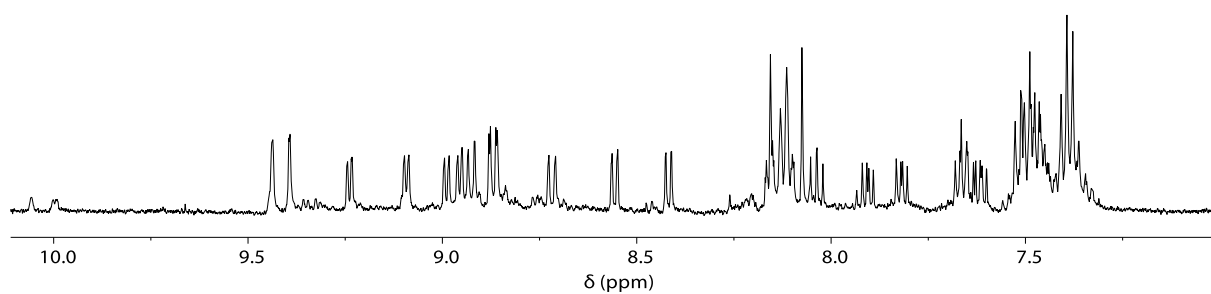


Figure S5.41: ¹H-NMR (500 MHz, 298K, CD₃CN) of cage [Pd₂TPa-P₂CA₂]₂(BF₄)₄.

- Pd₂TPa-IQ₂ST5₂

Due to a lack of time, more NMR experiments were not conducted.

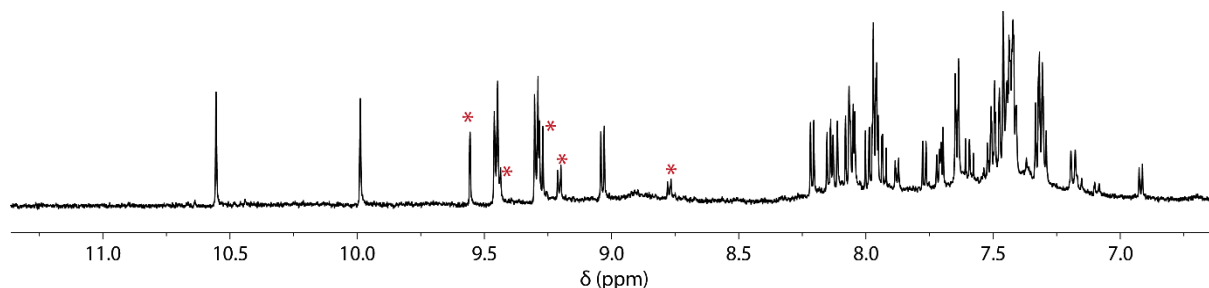


Figure S5.42: ¹H-NMR (500 MHz, 298K, CD₃CN) of cage [Pd₂TPa-IQ₂ST5₂](BF₄)₄. Despite several trials, secondary species (labelled with *) could not be avoided.

5.6.3 X-ray structures

In this chapter, three compounds were studied by X-ray crystallography: ligand **TPd-P**, and cages [Pd₂THO₄](BF₄)₄ and [Pd₂TPa-P₂FRQ₂](BF₄)₄. Crystals of suitable quality and size of the first and third species could be obtained to be measured in-house. They were measured on a Bruker D8 venture diffractometer equipped with an INCOATEC microfocus sealed tube (I_μs 3.0) at 100 K. The data was integrated with APEX3 and the structure was solved by intrinsic phasing/direct methods using SHELXT^[25] and refined with SHELXL^[26] for full-matrix least-squares routines on *F*² and ShelXle^[27] as a graphical user interface.

Crystals of the second species were extremely sensitive to organic solvent loss. Moreover, due to small block or thin plate shaped crystals, the analysis required cryogenic handling and highly brilliant synchrotron radiation. Hence, diffraction data of most of supramolecular assemblies was collected during four beamtime shifts at macromolecular synchrotron beamline P11, PETRA III, DESY.^[28]

As the data is yet unpublished, the cif files will be stored in the shared folder of the group, under \User\Thesis_group_members\PhD\2024_10_Alexandre_Walther.

Table S5.1: Crystal data and structure refinement for species **TPd-P** and Pd₂**THO**₄.

Compound	TPd-P ligand	Pd ₂ THO ₄
CIF ID	aw141	aw55b
CCDC number	Unpublished	Unpublished
Empirical formula	C ₃₂ H ₈ F ₁₀ N ₄ S	C ₇₈ H ₄₆ B ₄ F ₁₆ N ₈ Pd ₂ S ₄
Formula weight	670.48	1783.51
Temperature [K]	100(2)	100(2)
Crystal system	monoclinic	monoclinic
Space group (number)	<i>C</i> 2/ <i>c</i> (15)	<i>P</i> 2 ₁ / <i>n</i> (14)
<i>a</i> [Å]	26.2190(12)	27.652(14)
<i>b</i> [Å]	6.8421(3)	9.5670(14)
<i>c</i> [Å]	29.7415(13)	31.952(4)
α [°]	90	90
β [°]	94.373(2)	90.50(2)
γ [°]	90	90
Volume [Å ³]	5319.9(4)	8452(5)
<i>Z</i>	8	4
ρ _{calc} [gcm ⁻³]	1.674	1.402
μ [mm ⁻¹]	0.225	1.083
<i>F</i> (000)	2672	3560
Crystal size [mm ³]	0.250×0.200×0.200	0.100×0.005×0.005
Crystal colour	red	colourless
Crystal shape	block	needle
Radiation	MoK _α (λ=0.71073 Å)	synchrotron (λ=0.88561 Å)
2θ range [°]	3.99 to 90.68 (0.50 Å)	2.42 to 53.11 (0.99 Å)
Index ranges	-52 ≤ <i>h</i> ≤ 52 -13 ≤ <i>k</i> ≤ 13 -59 ≤ <i>l</i> ≤ 59	-27 ≤ <i>h</i> ≤ 27 -9 ≤ <i>k</i> ≤ 9 -32 ≤ <i>l</i> ≤ 32
Reflections collected	290822	48300
Independent reflections	22251 <i>R</i> _{int} = 0.0708 <i>R</i> _{sigma} = 0.0301	8033 <i>R</i> _{int} = 0.0811 <i>R</i> _{sigma} = 0.0514
Completeness to ϑ = 25.242°	99.9 %	88.0 %
Data / Restraints / Parameters	22251/0/448	8033/1724/1056
Absorption correction T _{min} /T _{max} (method)	0.666/0.7489 (multi-scan)	?/? (none)
Goodness-of-fit on <i>F</i> ²	1.114	1.034
Final <i>R</i> indexes [<i>I</i> ≥ 2σ(<i>I</i>)]	<i>R</i> ₁ = 0.0485 w <i>R</i> ₂ = 0.1165	<i>R</i> ₁ = 0.0727 w <i>R</i> ₂ = 0.2071
Final <i>R</i> indexes [all data]	<i>R</i> ₁ = 0.0691 w <i>R</i> ₂ = 0.1257	<i>R</i> ₁ = 0.1037 w <i>R</i> ₂ = 0.2358
Largest peak/hole [eÅ ⁻³]	0.68/-0.49	0.71/-0.74

Table S5.2: Crystal data and structure refinement for cage and Pd₂ **TPa-P₂FRQ₂**.

Compound	Pd ₂ TPa-P₂FRQ₂
CIF ID	aw89j
CCDC number	Unpublished
Empirical formula	C _{181.11} H _{161.87} B ₄ F ₁₆ N _{25.45} O _{4.55} Pd ₂ S ₂
Formula weight	3391.75
Temperature [K]	100(2)
Crystal system	triclinic
Space group (number)	$P\bar{1}$ (2)
<i>a</i> [Å]	18.7788(9)
<i>b</i> [Å]	20.1792(10)
<i>c</i> [Å]	25.0027(12)
α [°]	92.540(3)
β [°]	90.931(3)
γ [°]	101.609(3)
Volume [Å ³]	9268.6(8)
<i>Z</i>	2
ρ_{calc} [gcm ⁻³]	1.215
μ [mm ⁻¹]	2.388
<i>F</i> (000)	3502
Crystal size [mm ³]	0.100 × 0.100 × 0.030
Crystal colour	orange
Crystal shape	square
Radiation	CuK α (λ =1.54178 Å)
2 θ range [°]	4.48 to 138.73 (0.82 Å)
Index ranges	-22 ≤ <i>h</i> ≤ 22 -23 ≤ <i>k</i> ≤ 23 -29 ≤ <i>l</i> ≤ 29
Reflections collected	379845
Independent reflections	32721 $R_{\text{int}} = 0.1218$ $R_{\text{sigma}} = 0.0570$
Completeness to $\vartheta = 67.679^\circ$	97.4 %
Data / Restraints / Parameters	32721/5182/2490
Absorption correction T _{min} /T _{max} (method)	0.6384/0.7528 (multi-scan)
Goodness-of-fit on F^2	0.951
Final <i>R</i> indexes [$I \geq 2\sigma(I)$]	$R_1 = 0.0851$ $wR_2 = 0.2487$
Final <i>R</i> indexes [all data]	$R_1 = 0.1172$ $wR_2 = 0.2766$
Largest peak/hole [eÅ ⁻³]	1.02/-0.94

5.6.3.1 Crystal structure of TPd-P

Red block-shaped crystals of **TPd-P** were grown by layering a DCM solution of the ligand with hexane, and leaving to diffuse at 4°C. Single crystals in mother liquor were pipetted onto a glass slide containing NVH oil. The chosen crystal was quickly mounted on a micro loop and mounted on the diffractometer under a flow of N₂ at 100 K. The data collection was performed using a MoK_α radiation source.

Specific refinement details

The compound crystallises in the monoclinic *C2/c* (15) space group, with one molecule per asymmetric unit cell. Every hydrogen atom could be resolved. No further refinement was needed.

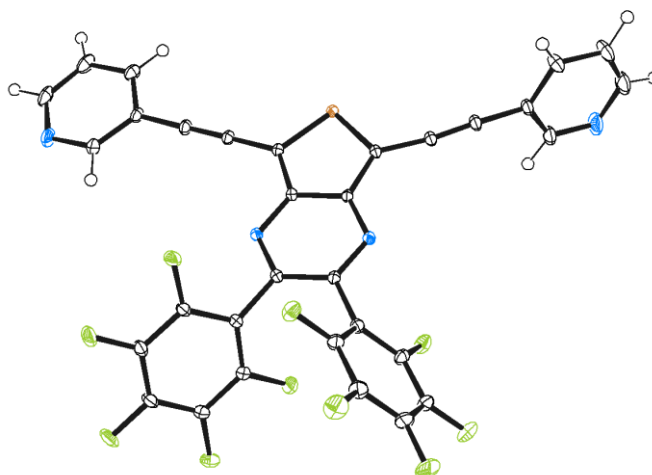


Figure S5.43: ORTEP representation of the X-ray structure of ligand **TPd-P** (ellipsoids drawn at 50% probability, black: C, blue: N, gold: S, green: F)

5.6.3.2 Crystal structure of [Pd₂THO₄](BF₄)₄

White needle-shaped crystals of cage Pd₂THO₄ were grown by slow diffusion of benzene (BEN) into an acetonitrile (ACN) solution of the supramolecular structure. Single crystals in mother liquor were pipetted onto a glass slide containing NVH oil. To avoid collapse of the crystal lattice, several crystals were quickly mounted on micro loops and immediately flash-cooled in liquid nitrogen. Crystals were stored at cryogenic temperature in dry shippers, in which they were safely transported to macromolecular beamline P11 at Petra III,^[28] DESY, Hamburg, Germany. A wavelength of $\lambda = 0.6888 \text{ \AA}$ was chosen using a liquid N₂ cooled double crystal monochromator. Single crystal X-ray diffraction data was collected at 100(2) K on a single axis goniometer, equipped with an Oxford Cryostream 800 and an Eiger2x 16M detector. 3600 diffraction images were collected in a 360° φ sweep at a detector distance of 154 mm, 100% filter transmission, 0.1° step width and 0.05 seconds exposure time per image. Data integration and reduction were undertaken using XDS.^[29] The structure was solved by intrinsic phasing/direct methods using SHELXT^[25] and refined with

SHELXL^[26] using 22 CPU cores for full-matrix least-squares routines on F^2 and ShelXle^[27] as a graphical user interface and the DSR program plugin was employed for modeling.^[30,31]

Specific refinement details

Stereochemical restraints for ligand **THO**, counteranion tetrafluoroborate (residue BF₄), and solvent benzene (residue BEN), were generated by the GRADE program using the GRADE Web Server (<http://grade.globalphasing.org>) and applied in the refinement. A GRADE dictionary for SHELXL contains target values and standard deviations for 1,2-distances (DFIX) and 1,3-distances (DANG), as well as restraints for planar groups (FLAT). All displacements for non-hydrogen atoms were refined anisotropically. The refinement of ADPs for every element except hydrogen was enabled by a combination of similarity restraints (SIMU) and rigid bond restraints (RIGU)^[32]. The contribution of the electron density from disordered counterions and solvent molecules, which could not be modeled with discrete atomic positions were handled using the SQUEEZE^[33] routine in PLATON.^[34] The solvent mask file (.fab), computed by PLATON, was included in the SHELXL refinement via the ABIN instruction leaving the measured intensities untouched.

The cage crystallises in the monoclinic $P2_1/n$ (14) space group. One cage is present in the asymmetric unit cell, accompanied by one benzene molecule, and the four expected BF₄ counteranions.

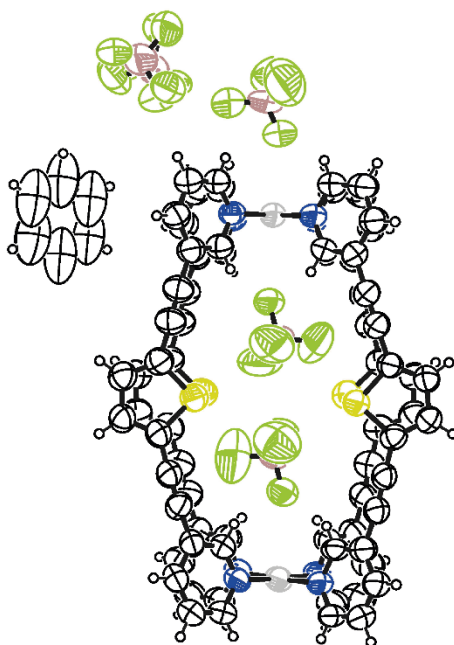


Figure S5.44: ORTEP representation of the X-ray structure of cage Pd₂THO₄ (ellipsoids drawn at 50% probability, black: C, blue: N, gold: S, green: F, purple: B)

5.6.3.3 Crystal structure of [Pd₂TPa-P₂FRQ₂](BF₄)₄

Red block-shaped crystals of cage Pd₂TPa-P₂FRQ₂ could be grown by slow diffusion of diethylether (Et₂O) into an acetonitrile (ACN) solution of the supramolecular structure. Single

crystals in mother liquor were pipetted onto a glass slide containing NVH oil. To avoid collapse of the crystal lattice, the chosen crystal was quickly mounted on a micro loop and mounted on the diffractometer under a flow of N₂ at 100 K. The data collection was performed using a CuK_α radiation source.

Specific refinement details

Stereochemical restraints for ligands **TPa-P** (residue TP1) and **FRQ** (residue QPD), as well as for acetonitrile (residue ACN) and diethyl ether (residue ETO) solvent molecules, and tetrafluoroborate (residue BF4) counter anion were generated by the GRADE program using the GRADE Web Server (<http://grade.globalphasing.org>) and applied in the refinement. A GRADE dictionary for SHELXL contains target values and standard deviations for 1,2-distances (DFIX) and 1,3-distances (DANG), as well as restraints for planar groups (FLAT). All displacements for non-hydrogen atoms were refined anisotropically. The refinement of ADPs for every element except hydrogen was enabled by a combination of similarity restraints (SIMU) and rigid bond restraints (RIGU)^[32]. The contribution of the electron density from disordered counterions and solvent molecules, which could not be modelled with discrete atomic positions were handled using the SQUEEZE^[33] routine in PLATON.^[34] The solvent mask file (.fab), computed by PLATON, was included in the SHELXL refinement via the ABIN instruction leaving the measured intensities untouched.

The compound crystallised in the triclinic space group $P\bar{1}$ (2). The cage was modelled in its entirety, although several disordered positions were observed. Residue 4 (TP1) was disordered over two positions on its side phenyl groups. Consequently, one molecule of ACN (residue 27) was modelled as co-disordered, and could only be found in one of the disordered structures (PART 1). In a similar way, one BF4 counteranion (residue 13) was modelled with the same free variable as for the previous species, as they share a very close proximity, and their positions would be influenced by the others. Next to it, the alkyl chain of residue 2 (ligand QPD) was similarly influenced by the position of the BF4 counteranion. Finally, one molecule of counter-solvent Et₂O could only be modelled in PART 1. Therefore, five distinct disorders could be modelled with only one free variable, as each position influenced the others. The four expected BF4 counteranions could be modelled.

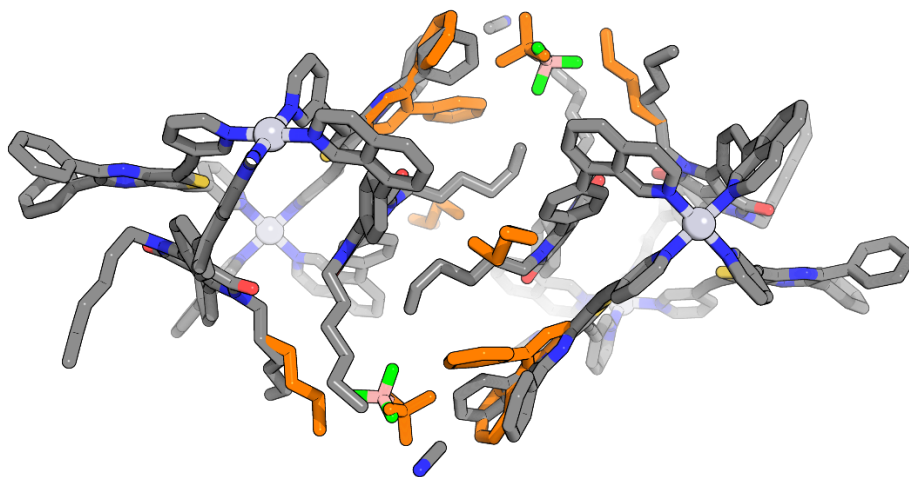


Figure S5.45: X-ray structure of the unit cell of Pd₂TPa-P₂FRQ₂ with some of the disorders indicated in orange. Some solvent and counteranions were omitted for clarity.

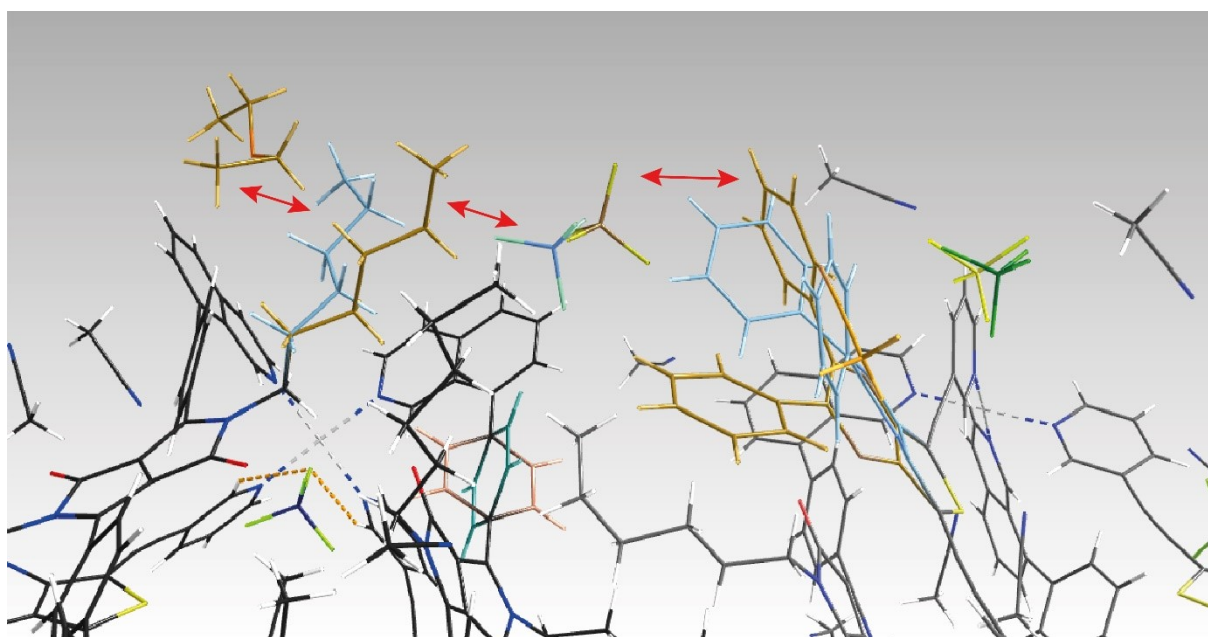


Figure S5.46: Partial view of the cell contents of the X-ray structure of cage Pd₂TPa-P₂FRQ₂. The disorders are highlighted in colour over the bonds. The red arrows show the influence that each disorder has on its neighbours.

5.6.4 Computations

All the .xyz files of the structures discussed here can be found on the shared folder of the group, under \User\Thesis_group_members\PhD\2024_10_Alexandre_Walther. The DFT models are based on initial models constructed in Wavefunction SPARTAN'18,^[35] and then optimised by the semi-empirical PM6 method in Gaussian 16.^[36] The final DFT model was geometry-optimised in the same programme.

5.7 REFERENCES

- [1] E. Paegle, S. Belyakov, M. Petrova, E. Liepinsh, P. Arsenyan, *Eur. J. Org. Chem.* **2015**, 2015, 4389–4399.
- [2] E. Podda, S. J. Coles, P. N. Horton, P. D. Lickiss, O. S. Bull, J. B. Orton, A. Pintus, D. Pugh, M. C. Aragoni, R. P. Davies, *Dalton Trans.* **2021**, 50, 3782–3785.
- [3] M. Pomerantz, B. Chaloner-Gill, L. O. Harding, J. J. Tseng, W. J. Pomerantz, *J. Chem. Soc., Chem. Commun.* **1992**, 0, 1672–1673.
- [4] J. Kastner, H. Kuzmany, D. Vegh, M. Landl, L. Cuff, M. Kertesz, *Macromolecules* **1995**, 28, 2922–2929.
- [5] C. Kitamura, S. Tanaka, Y. Yamashita, *J. Chem. Soc., Chem. Commun.* **1994**, 0, 1585–1586.
- [6] Y. Liang, D. Feng, Y. Wu, S.-T. Tsai, G. Li, C. Ray, L. Yu, *J. Am. Chem. Soc.* **2009**, 131, 7792–7799.
- [7] C. Zhang, X. Zhu, *Acc. Chem. Res.* **2017**, 50, 1342–1350.
- [8] D. Franchi, M. Bartolini, F. D’Amico, M. Calamante, L. Zani, G. Reginato, A. Mordini, A. Dessì, *Processes* **2023**, 11, 1542.
- [9] Z.-W. He, Q. Zhang, C.-X. Li, H.-T. Han, Y. Lu, *Chin. J. Polym. Sci.* **2022**, 40, 138–146.
- [10] H. H. Shah, R. A. Al-Balushi, M. K. Al-Suti, M. S. Khan, C. H. Woodall, K. C. Molloy, P. R. Raithby, T. P. Robinson, S. E. C. Dale, F. Marken, *Inorg. Chem.* **2013**, 52, 4898–4908.
- [11] L. E. McNamara, N. Liyanage, A. Peddapuram, J. S. Murphy, J. H. Delcamp, N. I. Hammer, *J. Org. Chem.* **2016**, 81, 32–42.
- [12] G. Goti, M. Calamante, C. Coppola, A. Dessì, D. Franchi, A. Mordini, A. Sinicropi, L. Zani, G. Reginato, *Eur. J. Org. Chem.* **2021**, 2021, 2655–2664.
- [13] J. Li, Q. Li, D. Liu, *ACS Appl. Mater. Interfaces* **2011**, 3, 2099–2107.
- [14] D. D. Kenning, K. A. Mitchell, T. R. Calhoun, M. R. Funfar, D. J. Sattler, S. C. Rasmussen, *J. Org. Chem.* **2002**, 67, 9073–9076.
- [15] I. Regeni, R. Chowdhury, K. Terlinden, S. Horiuchi, J. J. Holstein, S. Feldmann, G. H. Clever, *Angew. Chem. Int. Ed.* **2023**, 62, e202308288.
- [16] J. Tessarolo, H. Lee, E. Sakuda, K. Umakoshi, G. H. Clever, *J. Am. Chem. Soc.* **2021**, 143, 6339–6344.
- [17] N. J. Hestand, F. C. Spano, *Chem. Rev.* **2018**, 118, 7069–7163.
- [18] S. Ganta, J.-H. Borter, C. Drechsler, J. J. Holstein, D. Schwarzer, G. H. Clever, *Org. Chem. Front.* **2022**, 9, 5485–5493.
- [19] K. Ebbert, **2024**, PhD thesis.
- [20] I. Regeni, R. Chowdhury, N. Bogo, K. E. Ebbert, J. Tessarolo, A. Platzek, E. Yalcin, C. Stein, S. Feldmann, G. H. Clever, *In preparation*
- [21] J. Tessarolo, E. Benchimol, A. Jouaiti, M. W. Hosseini, G. H. Clever, *Chem. Commun.* **2023**, 59, 3467–3470.
- [22] K. Wu, J. Tessarolo, A. Baksi, G. H. Clever, *Angew. Chem. Int. Ed.* **2022**, 61, e202205725.
- [23] P. Howlader, B. Mondal, P. C. Purba, E. Zangrando, P. S. Mukherjee, *J. Am. Chem. Soc.* **2018**, 140, 7952–7960.
- [24] J. Jeong, R. S. Kumar, M. Naveen, Y.-A. Son, *Rsc Adv.* **2016**, 6, 78984–78993.
- [25] G. M. Sheldrick, *G. M. Sheldrick, Acta Crystallogr., Sect. A: Found. Adv.* **2015**, 71, 3–8.
- [26] G. M. Sheldrick, *Acta Crystallogr., Sect. C: Struct. Chem.* **2015**, 71, 3–8.
- [27] C. B. Hübschle, G. M. Sheldrick, B. Dittrich, *J. Appl. Crystallogr.* **2011**, 44, 1281–1284.
- [28] A. Burkhardt, T. Pakendorf, B. Reime, J. Meyer, P. Fischer, N. Stübe, S. Panneerselvam, O. Lorbeer, K. Stachnik, M. Warmer, P. Rödiger, D. Göries, A. Meents, *Eur. Phys. J. Plus* **2016**, 131, 56.
- [29] W. Kabsch, *Acta Crystallogr., Sect. D: Biol. Crystallogr.* **2010**, 66, 125–132.
- [30] D. Kratzert, J. J. Holstein, I. Krossing, *J. Appl. Crystallogr.* **2015**, 48, 933–938.
- [31] D. Kratzert, I. Krossing, *J. Appl. Crystallogr.* **2018**, 51, 928–934.
- [32] A. Thorn, B. Dittrich, G. M. Sheldrick, *Acta Crystallogr., Sect. A: Found. Crystallogr.* **2012**, 68, 448–451.
- [33] A. L. Spek, *Acta Crystallogr., Sect. C: Struct. Chem.* **2015**, 71, 9–18.
- [34] A. L. Spek, *Acta Crystallogr., Sect. D: Biol. Crystallogr.* **2009**, 65, 148–155.
- [35] Spartan’18, Wavefunction Inc., Irvine.
- [36] M. J. Frisch, G. W. Trucks, H. B. Schlegel, G. E. Scuseria, M. A. Robb, J. R. Cheeseman, G. Scalmani, V. Barone, G. A. Petersson, H. Nakatsuji, X. Li, M. Caricato, A. V. Marenich, J. Bloino, B. G. Janesko, R. Gomperts, B. Mennucci, H. P. Hratchian, J. V. Ortiz, A. F. Izmaylov, J. L. Sonnenberg, D. Williams-Young, F. Ding, F. Lipparini, F. Egidi, J. Goings, B. Peng, A. Petrone, T. Henderson, D. Ranasinghe, V. G. Zakrzewski, J. Gao, N. Rega, G. Zheng, W. Liang, M. Hada, M. Ehara, K. Toyota, R. Fukuda, J. Hasegawa, M. Ishida, T. Nakajima, Y. Honda, O. Kitao, H. Nakai, T. Vreven, K. Throssell, Jr. Montgomery, J. E. Peralta,

F. Ogliaro, M. J. Bearpark, J. J. Heyd, E. N. Brothers,
K. N. Kudin, V. N. Staroverov, T. A. Keith, R.
Kobayashi, J. Normand, K. Raghavachari, A. P.
Rendell, J. C. Burant, S. S. Iyengar, J. Tomasi, M.
Cossi, J. M. Millam, M. Klene, C. Adamo, R. Cammi, J.
W. Ochterski, R. L. Martin, K. Morokuma, O. Farkas,
J. B. Foresman, D. J. Fox, *Gaussian'16 Revision C.01*,
Gaussian Inc., Wallingford CT.

6 CONCLUSION AND OUTLOOK

Through my work in this thesis, I have prepared cage systems bearing two different chromophores as backbones: firstly, azulene and its chiral derivative biazulene, and secondly, thieno[3,4-b]pyrazine. The systems prepared from azulene backbones were shown to be dynamic and exhibit unexpected structural properties. Indeed, in the first chapter, I showed that a Pd₂L₄ lantern-shaped cage could quickly and efficiently transform into a Pd₄L₈ tetrahedral host-guest complex upon addition of a benzene-disulfonate guest. In a second step, the reaction was shown to be reversible through the addition of a second cage capable of stealing the guest and forming a new host-guest complex and by consequence reforming the initial cage. This reaction demonstrated the combination of several lines of research the Clever lab had been following over the last decade or so: firstly, the transformation of lantern-shaped cages upon the addition of halide guests, to form new quadruply catenated Pd₄L₈ species. In the present work, the complexity of the cage-to-cage transformation has been expanded upon, and a new topology resulting from it has been introduced by the use of a specific ligand and guest combination. Secondly, the narcissistic cohabitation of two or more different cages in a single system, as well as their dynamic transformation through guest exchange has also been studied in parallel by Elie Benchimol, and one can imagine in the future complex systems of multiple cages undergoing orthogonal guest and component exchange, as well as dramatic size and topology changes, all the while being able to keep a tight control on the system and fully understanding it in terms of driving forces, thermodynamics and kinetics.

The second project, focussing on the chiral biazulene moiety focussed more on the synthesis and characterisation of a wholly new backbone and its derived ligands and cages. Unexpectedly, chiral integrative self-sorting of a cage was observed in one case. Through X-ray crystallography, I was able to observe a phenomenon that had never been observed before for coordination cages: solvent molecules were forming hydrogen-bond bridges between the adjacent amino groups, acting as tethers that kept the cage formed from the racemate of the ligand in a single *meso-trans* isomer. While supramolecular systems often highly depend on non-covalent interactions such as H-bonds, those interactions have sometimes been sidelined in the design of coordination cages. With this new system, I hoped to show that complex cage systems that take into account multiple covalent and non-covalent interactions can lead to surprising results. In that sense, decorating the ligands of the cages with more hydrogen bond donors and/or acceptors, and combining several carefully designed components with complementary substituents, may lead to the directed formation of new highly unsymmetric cages suitable to act as artificial enzymes.

Finally, in the third project, I present a new fluorescent backbone, thieno[3,4-b]pyriazine, whose emissive properties are not fully quenched by coordination to Pd(II) cations. This is an important fact, as the emission of many of the fluorescent ligands previously used to construct coordination cages is fully or at least almost fully quenched once the supramolecular species are constructed. Therefore, cages derived from this new backbone could in the future be more reliably used as fluorophores and luminescent probes for the detection of analytes in solution.

List of abbreviations

ACN, MeCN: acetonitrile	GPC: Gel Permeation Chromatography
AcOH: Acetic Acid	HOMO: Highest Occupied Molecular Orbital
ABI: Adjacent Backbone Interaction	LUMO: Lowest Unoccupied Molecular Orbital
BAAZU: [1,1'-biazulene]-2,2'-diamine	MB: Methylene Blue
BINAP: 2,2'-bis(diphenylphosphino)-1,1'-binaphthyl	MeOH: Methanol
BINOL: 1,1'-bi-2-naphthol	MLCT: Metal-to-Ligand Charge Transfer
BODIPY: 4,4-difluoro-4-bora-3a,4a-diazas-indacene	NBS: <i>N</i> -bromo Succinimide
BPin: Boronic acid, pinacol ester	NMR: Nuclear Magnetic Resonance
CD: Circular Dichroism	OTf: triflate, trifluoromethanesulfonate
CPL: Circularly Polarised Light	PAH: Polyaromatic Hydrocarbon
CSE: Coordination Sphere Engineering	PDI: Perylene Diimide
DCM: Dichloromethane	PMMA: Poly(methacrylic acid)
DFT: Density Functional Theory	RT: Room Temperature
DMF: <i>N,N'</i> -dimethylformamide	SCA: Shape Complementary Assembly
DMSO: Dimethylsulfoxide	SCXRD: Single-Crystal X-ray Crystallography
DPP: Diketopyrrolopyrrole	THF: Tetrahydrofuran
ESI-MS: Electrospray Ionisation Mass Spectrometry	TPE: Tetraphenylene
EtOAc: Ethyl Acetate	UV: Ultra-violet
EtOH: Ethanol	Vis: visible light
FRET: Forster Resonance Energy Transfer	VT: Variable Temperature

ACKNOWLEDGEMENT

Everyone who knows me, even a bit, knows I am not the most expansive person in the world. Far from it. Therefore, even if those thanks might feel a bit stunted, please know that I truly am grateful for everyone I mention here, and even the ones I might have forgotten (which I hope doesn't happen). Firstly, I would like to thank Prof. Guido Clever as my supervisor. You accepting my application just before COVID struck was truly a shining moment after the uncertainty of my post-Master months. Joining your group and learning from all its members was a real game-changer for me, in terms of scientific enquiry in one hand, but it also allowed me to learn the best ways to communicate my science. I would also like to thank you for the trust you gave to me, allowing me to fully grow into my work, without micromanagement, and the freedom you gave me to explore wherever my chemistry would lead me. However, you also were always there to give me the inspiration and the little push when it seemed that I was going nowhere. For all those reasons, you have been an exceptional supervisor, and I will always cherish the time I spent at the AK Clever.

I would like to also thank Prof. Arne Lützen for accepting to be a co-examiner at my defence. It was extremely generous of you to agree to my request, even more knowing that your work on chiral coordination cages was an enormous influence on my own work.

I am also grateful for the funding provided by the graduate school GRK2376. The travel opportunities that were offered to travel to all of those wonderful conferences around Europe to present my work and meet with so many inspiring people was truly a highlight of my time as a PhD student. Outside of the travels, I also got to meet so many inspiring PhD students, even if to me they sometimes spoke in gibberish (I will probably never be a physical chemist, what a shame).

In the lab itself, I have so many people to thank. So let's start (in no particular order)! Thanks Jacopo, you were one of the first faces of the lab I saw (together with Gabi and Guido during my first Skype interview) and one of the early guides I had in my time here. Yes, you could be sometimes annoying, but you truly have a heart of gold, and I learnt so much from you (in chemistry yes, but also in northern Italian swears). Thank you, Irene, the second Italian, your energy was such a driving force to the group and you truly made me feel home, despite the less than ideal conditions of my first year or so in Dortmund. Even away following your adventures in Leiden, your influence and joy are still being felt, and I wish you all the best for your biggest adventure yet in Strasbourg! Thank you, Elie, the Frenchie, your explosions of south-western "language" was always among the funniest things to happen in the lab. Despite that, being able to still speak French almost everyday in the land of the Teutons was a breath of fresh air. And after we both do our theses in parallel, you now go to Groningen to Sijbren Otto's lab; well that is one way to tie a knot with our lives. Danke schön David O, you really brought a joy of life and carelessness (in a very good way) that I could really benefit and learn from (Ya man!). Grazie, Armin, the Bosnian-German-Italian (nationalities are not like Pokémons, you don't have to catch them all), you were truly a great mate, and I spent such good

moments with you and the other boys. Laura N, thank you for all the great moments and discussions in the “Boys’ office” (not so much anymore). I know you want to make everything perfect, but please take your holidays! And thanks Lars for taking a look at my abstract and correcting my German. Thank you, Julian, for introducing me to X-ray crystallography, and patiently teaching me what makes a great crystallographer. Thank you Malavika for the amazing journey in Iceland. I really hope you enjoyed camping, despite the less-than-ideal weather (well, it was Iceland, why was I surprised?). And thanks as well for sharing with me your love on Indian cooking, I am truly thankful. Thanks finally to Christoph for your help with any computational problem I could have had, you were really generous with our time.

Thanks to all the people who were there when I joined, and who left in the meantime: Sudhakar, Pedro (Où cabron!), Qianqian (eh?) and Kai. Also the improbable team of André (Ja, Ja), Kristina (I refuse to google that), and Shota (Ehhh? Etooo... Musukashi desu). You really made life here sweeter. I also would like to mention the people who came to the lab to visit us, and still left a bit of themselves here: Ana (in faaact), Weichhao, Andrea, Alvaro, and Wojtek.

Thanks to the team that kept the lab running from behind: Gabi, Birgit, and later Astrid and Christina. Your help was invaluable, especially when it was about navigating the mysterious and deep waters of the German administration.

And finally, I would like to thank my family back in Switzerland. I know it was a somewhat crazy idea to leave for four years, but you were always supportive and that mattered infinitely to me. Maman and Papa, thanks for having been there for every step of my life, and always picking me up and putting me back on my feet when I stumbled (very often literally), I owe you a debt I could never repay. But I’ll try nonetheless, by living the best life I possibly could. Dorine, what an amazing sister you are! Thanks for always being a ray of sunshine in my life. Now that you start to fly from your own wings, I can truly see what an incredible woman you’ll soon become. Thanks to you three. Now something ends, and something begins, and I’ll get to see what it is, with you by my side.

Le vent se lève! ... il faut tenter de vivre

